U.S. DEPARTMENT OF ENERGY | Energy Efficiency & Renewable Energy

Lightweight Materials R&D

2015 Annual Report

Vehicle Technnologies Office

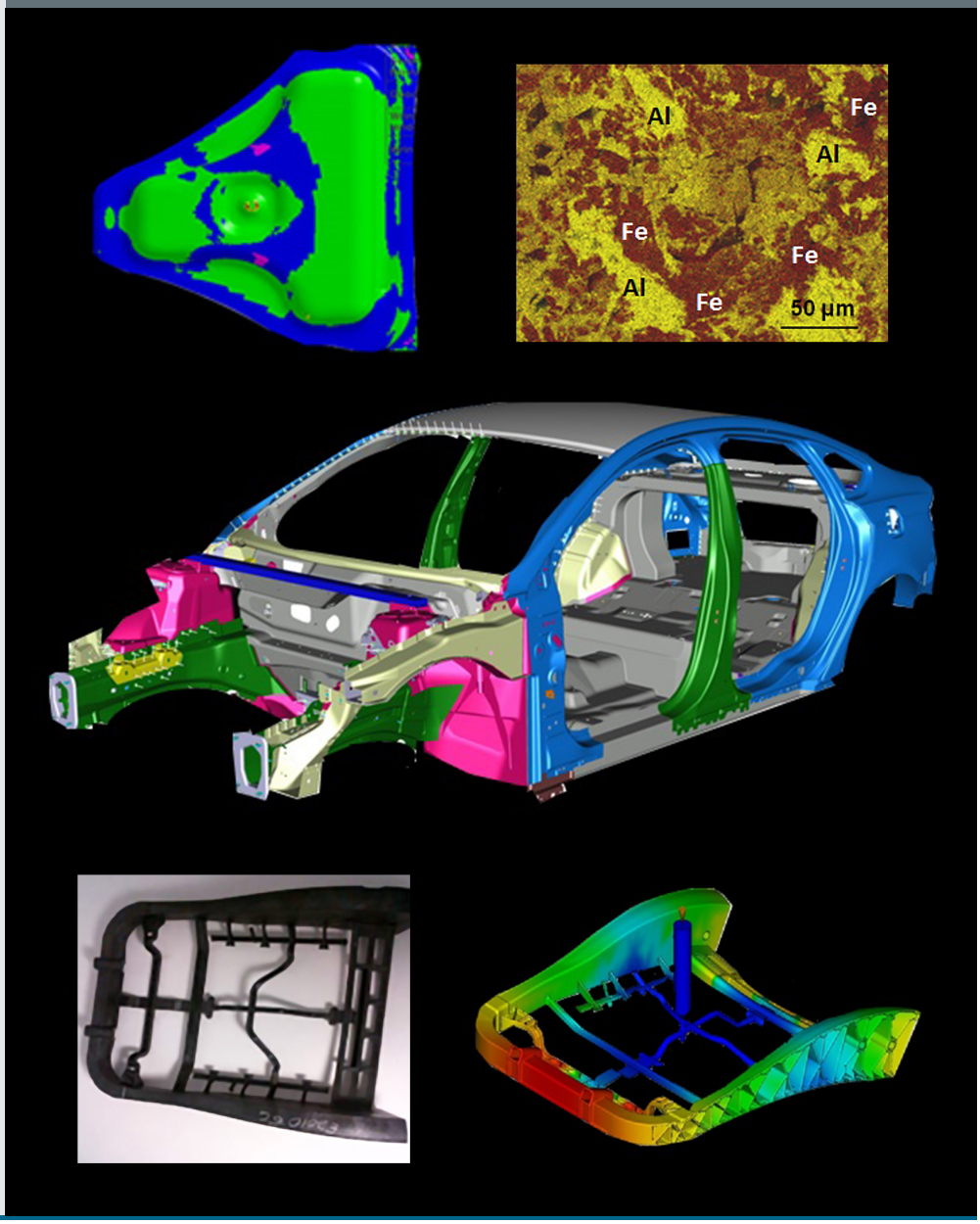

Disclaimer

Foreword

The Lightweight Materials subprogram supports the mission of the Vehicles Technologies Office to reduce petroleum consumption and greenhouse gas emissions while meeting or exceeding vehicle performance and safety requirements. Lightweight structural materials—advanced high-strength steel (AHSS), aluminum (Al), magnesium (Mg), and carbon-fiber (CF) polymer composites—enable improvements in fuel economy by providing properties that are equal to or better than traditional materials and by providing flexibility in design that enables additional lightweighting. Because it takes less energy to accelerate a lighter vehicle, designing for and manufacturing with lightweight materials reduces a vehicle's fuel consumption compared to vehicles made from heavier cast iron and traditional steel components. Lightweighting of an electric vehicle could enable a farther travel distance with the same charge or enable a downsized battery for an equivalent range. One of the Lightweight Materials subprograms' goals is to enable cost-effective reduction of vehicle weight by 30% in 2022 compared to a 2012 baseline vehicle.[1] Considering that a 10% reduction in vehicle weight results in a 6 to 8% reduction in fuel consumption, achieving this goal could result in an 18 to 24% decrease in fuel consumption. If applied to every light duty car and truck on the road, a 30% weight reduction represents potential savings of 1.85 million barrels of oil per day.

Although AHSS and Al are both growing in industry acceptance for use in vehicle lightweighting, many technology gaps still prevent widespread adoption of these lightweight metals. These gaps include high cost, lack of an adequate supply chain, and inadequate materials properties to meet the requirements of specific applications. Earlier stage lightweight materials, specifically Mg and CF composites, have the potential to save greater weight than the more mature AHSS and Al; however, technology gaps that limit the use of these materials include the high cost of CF precursor materials, scaling up raw material production, and validating their use in automotive applications. In addition, cost, manufacturability, formability and other challenges limit their use.

The Lightweight Materials subprogram supports research and development (R&D) to help overcome the many technology gaps; the papers included in this report illustrate progress against these gaps. We organize the lightweight materials R&D by automotive metals, carbon fiber and composites, multi-material joining, and crosscutting research. Within these families of materials and technologies, our taxonomy categorizes the R&D in three sub-areas: (1) properties and manufacturing, (2) multi-material enabling, and (3) modeling and computational materials science. Work within properties and manufacturing aims to improve material mechanical properties and performance, where manufacturability R&D addresses formability, cycle time, ductility, and cost. Work within multi-material enabling targets novel processes, designs, materials, and technologies that enable assembly of disparate material systems (dissimilar metals and composites to metals) into lightweight structures. Understanding corrosion and how to mitigate it is also a focus for this area. The technologies developed seek to enable facile integration and joining of components into a vehicle system while avoiding performance degradation, corrosion, and other compatibility issues. Computational materials science and integrated computational materials engineering (ICME) continue to mature predictive tools to speed up the development to deployment cycle. This area directly supports the President's Materials Genome Initiative.[2] This effort is focused on shortening the product development cycle time for improved performance in lightweight structures through use of predictive tools. These tools are developed by integrating validated models on structure/property and process/property relationships while taking into account uncertainty that can result in predicting energy absorption in a crash, for example. Ultimately, this area seeks to tie materials development from composition through processing and performance. The challenges for integrating and validating models are addressed directly in the work documented in this report.

---

[1] Idaho National Laboratory, *Vehicle Lightweighting: 40% and 45% Weight Savings Analysis: Technical Cost Modeling for Vehicle Lightweighting* (INL/EXT-14-33863), Anthony Mascarin, IBIS Associates, Inc.; Ted Hannibal, IBIS Associates, Inc.; Anand Raghunathan, Energetics Incorporated; Ziga Ivanic, Energetics Incorporated; and Jim Francfort, Idaho National Laboratory, April 2015.

[2] "Materials Genome Initiative for Global Competitiveness," National Science and Technology Council, Executive Office of the President, Washington, DC, June 24, 2011, accessed on March 23, 2016: http://www.whitehouse.gov/mgi.

Preface

The following reports provide the current status and technical accomplishments made during Fiscal Year 2015 to overcome challenges for expanding use of lightweight structural materials for enabling enhanced vehicle efficiency. This document organizes the reports by material class: Automotive Metals, Carbon Fiber and Polymer Composites, and Multi-Material Joining followed by Crosscutting Research, which is applicable to all lightweighting strategies. These efforts support building the foundation of technologies—and technology manufacturers—that tomorrow's vehicles need to achieve ultra-high efficiency and that result in reductions in petroleum use and greenhouse gas emissions.

Acknowledgements

First and foremost, we acknowledge the teams of investigators and the principal investigators from industry, academia, and national laboratories who are working to realize their innovative ideas and deploy them broadly in vehicles to enable better fuel economy and reduced environmental impact.

Thank you to the project managers at the National Energy Technology Laboratory for continued support in administering these projects.

We would like to acknowledge Mark Carroll of Idaho National Laboratory for his leadership in managing this report.

We would also like to acknowledge Energetics Incorporated for their help in preparing and publishing this report.

Will Joost, Ph.D.
Technology Development Manager, Metals
Vehicle Technologies Office

Sarah Ollila
Technology Development Manager, Joining
Vehicle Technologies Office

Carol Schutte, Ph.D.
Technology Development Manager, Composites
Vehicle Technologies Office

Acronyms and Abbreviations

α_a and α_c	the so-called anodic and cathodic charge transfer coefficients in mesoscale electrochemical kinetics calculations
β	a term that is used to turn on (β=1) and off (β=0) solute drag in solidification equations
β_a	symbol for the anodic Tafel slope in mesoscale electrochemical kinetics calculations
°C	degrees Centigrade
°C/min	degrees Centigrade per minute
°C/s	degrees Centigrade per second
$\delta_{Eu\ \alpha}(\xi)$	the number density per square millimeter of the eutectic α phase in microstructural analysis calculations
ΔE	symbol for the overpotential in mesoscale electrochemical kinetics calculations
φ	Euler angle; one of three angles introduced by Leonhard Euler to describe the orientation of a rigid body
Δt	change in time
ΔT	change in temperature
ε	accumulated strain in stress-strain calculations and plots
ε_0	symbol for the electric constant (8.854×10-12 F/m) in macroscale pitting corrosion calculations
ϕ	symbol for the damage parameter (when referring to macroscale corrosion damage equations)
ϕ_{ic}	symbol for the intergranular corrosion rate in macroscale intergranular corrosion calculations
η_p	symbol for pit nucleation (when referring to macroscale corrosion damage equations)
μ	microns
μA	microamps
μA/cm^2	microamps per square centimeter (current density)
μL	microliter
μm	micrometers or microns
μm/hr	micrometers per hour
μm^2	micrometer square
μs	microseconds
υ	Poisson's ratio
υ	symbol for the average pit volume on the specimen surfaces in macroscale pitting corrosion calculations
υ	symbol for the stoichiometric number, or the number of times that the rate-determining step must occur for the overall reaction to occur once in mesoscale electrochemical kinetics calculations
υ_p	symbol for pit growth related to the pit in-plane area, pit depth, and pit volume (when referring to macroscale corrosion damage equations)
Ω cm^{-2}	Ohm per centimeter squared
σ	stress in stress-strain calculations and plots
ξ	aluminum weight percent in microstructural analysis calculations
$/kg	dollars per kilogram

$/lb	dollars per pound
%RX	percent recrystallization
1D	one dimensional
2D	two dimensional
3D	three dimensional
3GAHSS	third generation advanced high strength steel
5xxx	series designation of aluminum alloyed with magnesium
6xxx	series designation for aluminum alloyed with magnesium and silicon, are easy to machine, and can be precipitation hardened, but not to the high strengths that 2000 and 7000
7xxx	series designation for aluminum alloyed with zinc, and can be precipitation hardened to the highest strengths of any aluminum alloy

A

a_0	a solute trapping parameter in a numerical model for solidification
A	the surface area of the dissolving hydroxide in the Nernst-Brunner equation
$Å^3$	cubic angstroms
$Å^2/s$	angstroms squared per second (effective prefactor)
AA	aluminum alloy
AA5182	wrought work hardenable aluminum alloy in the 5000 series composed of 4.5% magnesium and 0.35 manganese
AA6022	a heat treatable low copper precipitation hardenable aluminum sheet alloy composed of 0.8 - 1.5% Si and 0.45 - 0.70% Mg
AA6061	a precipitation hardening aluminum alloy containing 0.8-1.2% magnesium and 0.4 – 0.8% silicon as its major alloying elements
AA7075	an aluminum allow that is strong, with a strength comparable to many steels, and good fatigue strength and average machinability, but has less resistance to corrosion than many other Al alloys composed of 5.6% zinc, 2.5% magnesium and 1.6% copper
ABAQUS	software suite for finite element analysis and computer-aided engineering
ab initio	from the beginning
ABS	anti-lock braking system
AC	alternating current
ACC	Automotive Composites Consortium
ACC45TO60	value for the time (in seconds) for the vehicle to accelerate from 45 to 60 miles per hour
ACM	area contact method
A/cm^2	amps per square centimeter
ADP980	DP980 steel produced by AK Steel
AE	aliphatic epoxy
AE42	a die cast magnesium alloy with good strength, and creep resistance of up to 150°C (316°F) that contains 93.5% magnesium, 4% aluminum, and 2.5% rare earth metals.
AE44	a magnesium alloy with high temperature mechanical properties, diecastability, corrosion resistance that contains magnesium, aluminum, cerium and lanthanum and is typically used in the automotive industry for structural components working at elevated temperature (150÷175°C).

AET Integration Inc.	Advanced research, Engineering and Testing Integration - A research, development, and testing firm specializing in advanced material joining/welding technologies and related materials engineering services.
AFM	atomic force microscope (or microscopy)
Ag	chemical symbol for silver
AgCl	silver chloride
A-hr/L	amp-hour per liter
AHSS	advanced high-strength steel
AIW	adaptable insert welding
AK Steel	producer of flat-rolled carbon, stainless and electrical steel products, primarily for automotive, infrastructure and manufacturing, construction and electrical power generation and distribution markets.
AKSOME	atomistic-kinetic simulations of microstructural evolution
Al	chemical symbol for aluminum
Al 3003	an alloy in the wrought aluminum-manganese family (3000 or 3xxx series) that can be cold worked to produce tempers with a higher strength but a lower ductility and normally has moderate strength, good workability, and good corrosion resistance.
Al 6013	Alcoa alloy 6013 is a weldable high strength 6XXX series alloy that exhibits 7XXX strength levels in the T6 temper. Compared to 6061-T6, alloy 6013 provides higher strength (25%) and improved toughness and fatigue properties with equivalent corrosion resistance.
Al 6022	6022 is a heat treatable low copper, Al-Si-Mg sheet alloy developed by Alcoa for automotive manufacturers used in closure panels, such as a hood, deck lid or a door and provides improved corrosion resistance, higher formability and greater strength.
Al 6082	6082 is a medium strength alloy with excellent corrosion resistance and has the highest strength of the 6000 series alloys. Alloy 6082 is known as a structural alloy most commonly used for machining.
Al:CuO	aluminum:copper (II) oxide
Al:Cu_2O	aluminum:copper (I) oxide
AlMn	aluminum-manganese
Al:NiO	aluminum:nickel(II) oxide
Al_2O_3	aluminum oxide
Alodine® 5200	Alodine® 5200 treatment is a chromium free product and specifically formulated for treating aluminum and its alloys.
AM	magnesium alloy designation where the two principal alloying metals are aluminum and manganese
AM40	magnesium alloy that is 3.5% aluminum, 0.5% manganese, and 0.4% strontium
AM50	magnesium alloy that is 5% aluminum and less than 0.5% manganese
AM60	magnesium alloy that is 5.6-6.5% aluminum and less than 0.25% manganese
AM70	magnesium alloy that is 7.2% aluminum and 0.4% manganese
aMT	annual metric ton
APLAIR	APLAIR Manufacturing Systems
APT	atom probe tomography
Ar	chemical symbol for argon
ARM	Atomic Resolution Analytical Electron Microscope
A/SP	Auto/Steel Partnership

ASPM	All Service Plastic Molding
ASTM	shortened name for standards governing body ASTM International, formerly American Society for Testing and Materials
ASU	Arizona State University
at.%	atomic percent
AWD	all-wheel drive
AZ	magnesium alloy designation where the two principal alloying metals are aluminum and zinc
AZ31B	the most widely available of the magnesium grade alloys, AZ31B is commonly used as an alternative to aluminum alloys due to its high strength to weight ratio with 2.5-3.5% aluminum and 0.7-1.3% zinc
AZ91	magnesium alloy with nine weight percent aluminum and one weight percent zinc

B

$b_{i(i = 1,2,3,4,5)}$	A scalar constant used in calculation of tensor values
B117	ASTM Salt Spray (Fog) Testing
BASF	The largest chemical company in the world headquartered in Ludwigshafen, Germany. BASF originally stood for Badische Anilin- und Soda-Fabrik (English: Baden Aniline and Soda Factory)
BES	Basic Energy Sciences (U.S. Department of Energy)
BETAFORCE™	two-component composite bonding adhesive made by Dow Chemical Company to permanently bond coated metals such as steel to aluminum, carbon-fiber panels to steel or aluminum, and sheet molding compound to aluminum.
BF	bright field
BIW	body-in-white (a car body's sheet metal components have been welded together)
BLOCKER	a control variable used in a crash frequency analysis that represents a secondary energy-absorbing structure (known as a "blocker beam") behind and below the bumper, so that it engages
Bluestar	company previously known as Akzo Nobel and Acordis which produced the Fortafil precursor.
BM	ball milled
BMW	Bayerische Motoren Werke AG is a German luxury automobile, motorcycle and engine manufacturing company
BPR	ball-to-powder mass ratio
BSE	backscattered electron
BU	Brown University

C

C	carbon (when referring to a fiber material or to the chemical element)
C	the concentration of solute in the Nernst-Brunner equation
$\dot{C}$	the coalescence rate in macroscale pitting corrosion calculations
C_0	the initial concentration of the liquid in the Scheil equation
C_1, C_2	parameters that are determined by the material properties in a modified Faraday's Law equation for calculating a macroscale general corrosion rate

C_8, $C_{9,\ldots}C_{14}$	material parameters that change as a function of temperature, pH level, and materials microstructural characteristics in macroscale pitting corrosion calculations
C_b	shear rate constant
C_B	breakage factor in the Phelps-Tucker model
C_D	drag coefficient in the Phelps-Tucker model
c_{Le}	the liquidus composition from an equilibrium phase diagram
c_{Lv}	the velocity dependent liquidus composition in a numerical model for solidification
c_p	symbol for the pit coalescence term related to the nearest neighbor distance between pits
C_S	the concentration of solute in the solid in the Scheil equation
C_s	the saturation concentration in the Nernst-Brunner equation
c_{Se}	the solidus composition from an equilibrium phase diagram
Ca	chemical symbol for calcium
CAD	computer-aided design
CAE	computer-aided engineering
CAI	compression-after-impact
CALPHAD	CALculation of PHAse Diagrams
CANMET	Canada Center for Mineral and Energy Technology
CANMET MTL	Canadian federal laboratory in the energy sector with a focus on research in metals and materials in automotive, energy distribution, and power generation
CARB	California Air Resources Board
CAVS	Center for Advanced Vehicular Systems, Mississippi State University
CBTN	carboxyl-terminated butadiene acrylonitrile rubber
cc	cubic centimeter
cc/s	cubic centimeter per second
CC:urea	choline-chloride:urea
Ce	chemical symbol for cerium
Century	Century Tool and Gage Company, Fenton, MI.
CF	carbon fiber
CFRP	carbon fiber reinforced polymer
CI	core image (when referring to photo micrographs)
CI-NEB	climbing image nudge-elastic band
cm	centimeter
CM	compression molding
CMAT	CANMET Materials
CO_2	carbon dioxide
Co-Kriging	a model that calculates estimates or predictions for a poorly sampled variable (the predictand) with help of a well-sampled variable (the covariable)
COMBO	a control variable used in crash frequency analyses that represents a combination of air bag technologies
CompuTherm	CompuTherm LLC is a spin-off company from University of Wisconsin-Madison that develops software and databases for thermodynamic and phase diagram calculation.
COSMA	Cosma International, a subsidiary of the metal forming group of Magna.
COV	coefficient of variation
cP	centipoise

CP	commercial purity (when referring to content of commercial materials)
CP	corrosion potential (when referring to corrosion of metals)
CPM	crystal plasticity model
Cr	chemical symbol for chromium
CRISPRs	clustered regularly interspaced short palindromic repeats - segments of prokaryotic DNA containing short repetitions of base sequences.
C-RTM	continuous resin transfer molding
CSM	Colorado School of Mines
CSP	Continental Structural Plastics
CT	computed tomography (when referring to non-destructive evaluation)
CT	computerized thermography (when referring to materials analysis)
CT	cross tension (when referring to material design)
Cu	chemical symbol for copper
CU	Clemson University
CURTAIN	a control variable used in crash frequency analyses that represents a side curtain airbag designed for protection from driver or passenger side impacts
CUV	crossover utility vehicle
CV	coefficient of variation (when referring to statistical analysis)
Cytec	short name for Cytec Solvay Group

D

D	diffusivity in meters square per second (when referring to the rate at which particles or heat or fluids can spread)
D	deuterium (when referring to the isotope of hydrogen with mass number 2)
D	the diffusion coefficient (when referring to the Nernst-Brunner equation)
$D_{Eu\,\alpha}(\xi)$	the particle size/phase size in microns of the eutectic α phase in microstructural analysis calculations
D_i	the diffusion coefficient of the solute at the solid/liquid interface in a numerical model for solidification
D_2O	deuterium oxide
$D_2{}^{16}O$	atomic oxygen isotope of deuterated water
DACA	DACA Instruments is a supplier of micro-scale polymer processing instruments
DC	direct current
DDS	diaminodiphenyl sulfone -3,3 indicates position of molecules on the cyclic structure
DEFORM 3D	DEFORM is an engineering software that enables designers to analyze metal forming, heat treatment, machining and mechanical joining processes on the computer rather than the shop floor using trial and error.
Delsen	Delsen Testing Laboratories, currently Element Materials Technology, is an independent laboratory engaged in the mechanical, electrical, and flammability testing.
DETDA	diethyltoluene-diamine
DFT	density functional theory
DIC	digital image correlation
Digimat®	a nonlinear multi-scale material and structure modeling platform by MSC Software

D-LFT	direct-injection long-fiber technology molding process, Pushtrusion™, is a PlastiComp, Inc. exclusive, patented and proprietary in-line manufacturing technology for injection and compression molding that eliminates pre-compounding
DMTA	dynamic mechanical thermal analyzer
DOE	U.S. Department of Energy
Dow	commonly used name for Dow Chemical Company
DP	dual phase
DP780	a grade of high-strength dual-phased steel having good fatigue properties
DP980	a dual phase steel consisting of a ferrite matrix containing a hard second phase, usually islands of martensite.
DREAM 3D	data analysis tools (filters) that allow for the construction of customized workflows (pipelines) to analyze data.
DREIDING	a generic force field for molecular simulation
DRI	Dynamic Research Incorporated
DRVMALE	a control variable used in crash frequency analyses that represents which the driver's gender and age group (i.e. M14_30 for males 14 to 30 years old or F14_30 for females)
DRX	dynamic recrystallization
DSC	differential scanning calorimeter
DSM	English translation of the company's original name, Nederlandse Staatsmijnen (Dutch State Mines)
DSpace	online data repository at NIST
Dupont®	E. I. du Pont de Nemours and Company, commonly referred to as DuPont, is an American chemical company founded in 1802 as a gunpowder mill by Éleuthère Irénée du Pont but in the 20th century, DuPont developed many polymers such as Vespel, neoprene, nylon, Corian, Teflon, Mylar, Kevlar, Zemdrain, Nomex, Tyvek, Sorona and Lycra

E

E	Young's Modulus (when referring to mechanical properties of materials)
E	electrode potential (when referring to polarization curves)
$E(\xi)$	the electrochemical potential value of the magnesium-aluminum solution phase in microstructural calculations
E_{corr}	corrosion potential
E_{eq}	equilibrium/reversible potential
E2SC	Epsilon 2, Sedan, Chevrolet - Epsilon is General Motors' mid-size front-wheel drive automobile platform.
E717	high formability magnesium sheet produced by Magnesium Elektron North America used for deep drawing automobile and light truck closure panels (also known as ZE10A)
EAM	embedded atom method
EATON	EATON is a diversified industrial products manufacturer in the fluid power, industrial and commercial controls, automotive, and truck industries.
EBSD	electron backscatter diffraction
EC^{2} ™	Alodine® EC^{2} ™, an electroceramic coating provided by Henkel Corporation
ECSA	electrochemical surface area
e-coating	electrostatic coating
E. coli	Escherichia coli

EDAG	Engineering + Design AG Inc.
EDS or EDX	energy dispersive spectroscopy or energy dispersive x-ray spectroscope (or spectroscopy)
EELS	electron energy loss spectroscopy
e.g.	abbreviation meaning “for example”; a Latin phrase, “exempli gratia” meaning “for the sake of example”
EPMA	electron probe microanalysis
EPMA	electron probe micro-analysis
EPSC	elastic plastic self-consistent
EPSCCP	elastic-plastic self-consistent crystal plasticity
ER100-2	a low alloy, copper-coated welding wire suited for metal inert gas or tungsten inert gas welding
ER70S-3	a general purpose welding wire for fabrication of mild steel that contains silicon and manganese as deoxidizers.
ES3	an engineering firm specializing in engineering and design for several applications including computational methods for structural dynamic analysis.
ESC	electronic stability control
ESCs	externally solidified crystals (when referring to the microstructure of alloys)
ESI	Engineered Solutions, Inc.
et al.	abbreviation for the Latin phrase “et alia” which means "and others"
etc.	abbreviation for the Latin phrase “et cetera” which means “and so forth”
eV	electron volts
exp. or expt.	experimental

F

$f_{Eu\,\alpha}(\xi)$	area fraction of the eutectic α phase in the material in microstructural analysis calculations
F_c	the electrostatic interaction force between pits in Coulomb’s Law
FARS	Fatality Analysis Reporting System
FBCC	front bumper and crash can
FBG	Fiber Bragg Grating (sensors) record within the core of a single mode optical fiber only 9 microns in diameter
FCA US LLC	Fiat Chrysler Automobiles U.S. LLC, formerly Chrysler Group LLC
Fe	chemical symbol for iron
FE	finite element
FEA	finite element analysis
FEI	FEI Company, founded in 1971 as Field Electron and Ion Co., is a supplier of electron and ion beam sources for field emission research and electron microscopy
FEM	finite element model
FEV	FEV, Incorporated (not an acronym) is in international company that designs and develops internal combustion engines, conventional, electric, and alternative vehicle drive systems, energy technologies, and is a major supplier of advanced testing and instrumentation products and services
FIB	focus ion beam
Fibersim	software by Siemens for composites engineering in the aerospace, automotive, marine, and wind energy industries to engineer innovative, durable, and lightweight composite products and parts

FLD	fiber length distribution (when referring to composite materials)
FLD	forming (or formability) limit diagrams (when referring to modeling of metal structures)
FMC	Ford Motor Company
FMVSS	Federal Motor Vehicle Safety Standards
FOA	Funding Opportunity Announcement
FOD	fiber orientation distribution
FOOTPRNT	value for the vehicle footprint (in square feet) in crash models
FPA	focal-plane array
fps	frames per second
F/R	front/rear
freq.	frequency
FRP	fiber reinforced polymer
fs	fraction solid
FSW	friction stir welding
FSLW	friction-stir linear welding
ft	foot or feet
FY	fiscal year

G

g	gram(s)
g/cc	gram(s) per cubic centimeter
g/L	gram(s) per liter
Ga	chemical symbol for gallium
gal	gallon
Gatan	Gatan, Inc., is manufacturer of state of the art cameras, imaging energy filters, specimen preparation equipment and other electron microscope products and solutions
Gleeble®	Registered trademark by Dynamic Systems, Inc. for a fully integrated digital closed loop control thermal and mechanical testing system
GM	General Motors
GnP	graphene nanoplatelets
GPa	gigapascals
$GS(\xi)$	the grain size in microns in microstructural analysis calculations
G_T	transverse shear modulus

H

h or hr	hour(s)
h	the thickness of the diffusion boundary layer in the Nernst-Brunner equation
H	chemical symbol for elemental hydrogen
H_2	chemical symbol for molecular hydrogen
$H_2{}^{16}O$	atomic oxygen isotope of water
HAADF-STEM	high-angle annular dark field-scanning transmission electron microscope
HAZ	heat-affected zone
HC	heavy chain

HCP or hcp	hexagonal close-packed
HEXRD	high energy x-ray diffraction
HPDC	high-pressure die casting
HP-RTM	high pressure resin transfer molding
HRA	Honda R&D America
HSBS	hot stamped boron steel
HSS	high-strength steel
HT	high temperature
HV	Vickers Pyramid Number

I

i	electrode current density in mesoscale electrochemical kinetics calculations
i_{corr}	exchange corrosion current density in amps per square centimeter used in mesoscale electrochemical kinetics calculations
i3	a five-door urban electric car developed by the German manufacturer BMW that is part of BMW's "Project i" and was launched as a new brand, BMW i
IBIS	short name for IBIS Associates, Inc.
ICME	integrated computational materials engineering
I-Corps@Ohio	a statewide program to assist faculty and graduate students from Ohio universities and colleges to validate the market potential of their technologies and validate and launch startup companies
ICP-MS	inductively coupled plasma - mass spectroscopy
ID	identification
i.e.	abbreviation for “id est,” a Latin phrase meaning “that is.”
IIHS	Insurance Institute for Highway Safety
iL or iLs	ionic liquid(s)
IMC(s)	intermetallic compound(s)
InSb	indium-antimony
in situ	on site or in place
IP	intellectual property (when referring to an idea, invention, or process that derives from the work of the mind or intellect
IPTG	isopropyl-β-D-thiogalactoside
Ir	chemical symbol for iridium
IR	infrared
ISO	International Organization for Standardization
ISV	internal state variable
Izod	ASTM standard method of determining the impact resistance of materials

J

JAC	Japanese Iron and Steel Federation Standard (JFS) A3011 material designation for hot-dip galvannealed steel sheet and strip products, grade from commercial quality to deep drawing quality, which can be used in various applications such as automobiles because of their deforming properties
JAC270F	a galvannealed extra deep drawing steel with a nominal tensile strengths of 270MPa

JAC980	a galvannealed extra deep drawing steel with a nominal tensile strengths of 980MPa
JEOL	company founded in 1949 as the Japan Electron Optics Laboratory Company, Limited in Mitaka, Tokyo; a manufacturer of scanning electron microscopes, transmission electron microscopes and scanning probe microscopes, along with related equipment
J/g	joules per gram
J/kg-K	joules per kilogram-degree Kelvin

K

K or k	thousand (when used with a number preceding the K or k)
k	partition coefficient in Scheil equation
k_e	Coulomb's constant ($k_e = 8.987 \times 10^9$ Nm^2/C^2)
κ_e	a partitioning parameter in a numerical model for solidification
Kapton®	a polyimide film developed by DuPont® that remains stable across a wide range of temperatures, from −269 to +400 °C (−452 – 752 °F / 4 – 673 K) used in flexible printed circuits (flexible electronics) and thermal micrometeoroid garments (the outside layer of space suits); the chemical name for Kapton K and HN is poly (4,4'-oxydiphenylene-pyromellitimide)
kD	kilodalton
Kevlar®	the registered trademark for a para-aramid synthetic fiber
kg	kilogram
kg/m^3	kilogram per cubic meter
kJ	kilojoules
kJ/mol	kilojoule per mole
kMC	kinetic Monte Carlo
kN	kilonewton
kN-m/kg	killonewton-meter(s) per kilogram
K/s	degree Kelvin per second
Ksi/ksi/kpsi	kilopound per square inch
KUKA	Keller und Knappich Augsburg
KWN	Kampmann-Wagner numerical (model)
kWh	kilowatt hour(s)
kWh/kg	killowatt hours per kilogam

L

L	tow name when referring to carbon fiber processing
L	longitudinal reference when referring to a section of sample taken for microscopic analysis
LabVIEW	acronym for Laboratory Virtual Instrument Engineering Workbench which is a system-design platform and development environment for a visual programming language from National Instruments
LAMMPS	Large-scale Atomic/Molecular Massively Parallel Simulator
lb(s)	pound(s)
LBS100	value for 100 pounds of weight reduction in crash models
l-DOPA	L-3,4-dihydroxyphenylalanine
LDH	limiting dome height

Li	chemical symbol for lithium
LiCl	lithium chloride
$LiClO_4$	lithium perchlorate
LLC	Limited Liability Company
LS-DYNA	an advanced general-purpose multiphysics simulation software package developed by the Livermore Software Technology Corporation
LS-OPT	a standalone design optimization and probabilistic analysis package with interface to LS-DYNA
LSTC	Livermore Software Technology Corporation
LT	low temperature
LTT	low temperature transformation
LVDT	linear variable differential transformer
LVDT	linear variable distance transducers (device used to measure displacement)

M

m	mass change of an electrode in grams (in Faraday's Law)
M	molar mass of a substance (in Faraday's Law0
M	meter(s)
M	molarity (moles of solute per liter of solution)
MagGen™	INFINIUM Inc. process for magnesium production
MAGMASOFT®	modular simulation software supplied by MAGMA, a developer and supplier of software for casting process simulation
MANEUVER	value for the maximum speed (in miles per hour) a vehicle obtained on the avoidance maneuver test
MARS	Multiscale-multiphysics Analysis of the Response of Structures
MaSp1	major ampullate spidroin 1 - Spidroin, the main protein in a spider's dragline silk, with a very low proline content
MaSp2	major ampullate spidroin 2 - Spidroin, the main protein in a spider's dragline silk, with a significant proline content
MAT131	a material model for multi-layered shell elements in PAM-CRASH
MAT277	a thermos-chemo-mechanical material model in LS-DYNA
MCMC	Markov Chain Monte Carlo
MD	molecular dynamics
MDA	molecular dynamic analysis
MDS	Multiscale Design System
MEAM	modified embedded atom method
MEMS	microelectromechanical systems
MENA	Magnesium Elektron North America
METALAST	METALAST International, Inc. trivalent chromium post-treatment, hexavalent free
TCP -HF®	alternative and a drop-in replacement for products containing hexavalent chromates
MFERD	Magnesium Front End Research and Development
Mg	chemical symbol for magnesium
$MgCl_2$	magnesium chloride
$Mg(ClO_4)_2$	magnesium perchlorate

MgO	magnesium oxide
$Mg(OH)_2$	magnesium hydroxide
MGI	Materials Genome Initiative
MIL-DTL	military detail specification
min	minute(s)
MiSp	minor ampullate spidroin
MLG	multilayer graphene
mm	millimeters
m/min	meters per minute
mm/s	millimeter(s) per second
MMLV	Multi-Material Lightweight Vehicle
mN	millinewtons
Mn	manganese
$(MO/MO_0)^{z_{ic}}$	grain misorientation factor in macroscale intergranular corrosion calculations
MPa	megapascals
mph	miles per hour
MPS	Material and Process Selection
m/s	meter(s)/second
MSI or Msi	million pounds per square inch
MS&T	Missouri University of Science and Technology
MSU	Mississippi State University
MSU	Michigan State University
MTHPA	methyltetrahydrophthalic anhydride
MTM	Microplane Triad Model
mtorr	millitorr (approximately 133.3 pascals)
MTS	MTS Systems Corporation
MuCell®	a microcellular foam injection molding process for thermoplastics materials that provides unique design flexibility and cost savings opportunities not found in conventional injection molding and allows for plastic part design with material wall thickness optimized for functionality and not for the injection molding process
M/W or MW	microwave (when referring to a type of energy)
MY	model year (referring to automobiles)

N

n	sample number when referring to statistical results
N	newtons
Na	chemical symbol for sodium
NaCl	sodium chloride
Nano Al	nanostructured aluminum alloys
NanoBond®	Indium Corporation's patented process for bonding components utilizing NanoFoil®
NCAP	New Car Assessment Program
NCF	non–crimped fabric
nCode	engineering data analysis tool with special concentration in fatigue and durability

Nd	chemical symbol for neodymium
ND	normal direction
NDE	nondestructive evaluation
NDSU	North Dakota State University
NHE	normal hydrogen electrode
NHTS	National Household Transportation Survey
NETL	National Energy Technology Laboratory
NHTSA	National Highway Traffic Safety Administration
NiO	nickel oxide
NIST	National Institute of Standards and Technology
NITE	a control variable used in crash a frequency analysis that represents crashes occurring at night
nm	nanometers
NND	nearest neighbor distance
NRC	National Research Council
NWU or NU	Northwestern University

O

O	chemical symbol for elemental oxygen
O_2	chemical symbol for the oxygen molecule
OCP	open circuit (or cell) potential - The potential of the working electrode relative to the reference electrode when no potential or current is being applied to the cell
OEM	original equipment manufacturer
OH	chemical symbol for hydroxide
OIM	orientation imaging microscopy
OPF	oxidized polyacrylonitrile fiber
ORNL	Oak Ridge National Laboratory
OSU	Ohio State University
OVERWT00	value for the mass reduction in heavier-than-average cars

P

P	perpendicular reference when referring to a section of sample taken for microscopic analysis
$P_{Eu\,\alpha}(\xi)$	the aluminum weight percent content in the eutectic α phase in microstructural analysis calculations
Pa	pascal
PA	polyamide
PAM-CRASH	software package from ESI Group used for crash simulation and the design of occupant safety systems, primarily in the automotive industry

PAM-RTM	pluggable authentication module - resin transfer molding; a cost effective simulation tool by ESI that covers a wide range of liquid composites molding (LCM) manufacturing processes including Resin Transfer Molding (RTM), Vacuum Assisted RTM (VARTM), Vacuum Assisted Resin Infusion (VARI), and Compression Resin Transfer Molding (CRTM)
PAM-FORM	software program by ESI that enables the realistic and predictive simulation of dry textiles or prepregs forming processes
PAN	polyacrylonitrile (traditional vs textile)
Pandat™	an integrated computational tool from CompuTherm LLC for multi-component phase diagram calculation and materials property simulation
PanMagnesium	a thermodynamic and atomic mobility database for magnesium
PanPrecipitation	a module in the Pandat™ software that provides simulation of precipitation kinetics during heat treatment process
PB	paint bake
PF	pole figure
PCE	polynomial chaos expansion
PE	predictive engineering (when referring to a modeling tool)
pH	potential of hydrogen; the negative logarithm of the effective hydrogen-ion concentration
Pi joint	material joint shaped like an upside-down Greek letter “pi” (□□
PI	principal investigator
PJ	pulse joining
PNNL	Pacific Northwest National Laboratory
POSCO	formerly Pohang Iron and Steel Company, is a multinational steel-making company headquartered in Pohang, South Korea
POWERCRON® 6000CX	PPG’s high performing black cationic epoxy finish approved for use on automotive parts
PP	polypropylene
ppb	parts per billion
PPG	PPG Industries, originally Pittsburgh Plate Glass Co.
prepreg	a term for "pre-impregnated" composite fibers
PRISMS	PRedictive Integrated Structural Materials Science
ProCAST	software provided by Engineered Solutions, Inc. that is based on Finite Element technology and is able to predict deformations and residual stresses as well as specific processes like semi-solid modeling, core blowing, centrifugal casting, lost foam and continuous casting
psi	pounds per square inch
PUs	pickups (trucks)

Q

q_1, q_2	symbols for point charges in Coulomb’s Law
Q	total electric charge passed through a substance (in Faraday’s Law)
Q&P	quench and partition
QI	quasi-isotropic
QP	quench and partitioned (for processing steel)
QP980	Baosteel Group Corporation’s ultra-high strength galvanized steel with resistance to corrosion for use in automotive applications

R

r	the symbol for the separation distance between two neighboring pits in Coulomb's Law
r	rate of material loss in grams per hour when referring to surface corrosion rates
R	the gas constant equal to 8.314 joules per mole-degree Kelvin
R^2	correlation coefficient of the linear regression line
R&D	research and development
RADIOSS	a multidisciplinary finite element solver developed by Altair Engineering that can solve both linear and non-linear problems using implicit and explicit integration schemes for the solution of engineering problems, from linear statics and linear dynamics to nonlinear transient dynamics and mechanical systems, and enables designers to maximize performance related to durability, NVH, crash, safety, manufacturability, and fluid-structure interaction
RD	rolling direction
RDE	rotation disk electrode
RE	rare earth
redox	reduction-oxidation
ROLLCURT	a control variable used in crash a frequency analysis that represents a special type of side curtain airbag that deploys in response to a vehicle's side movement or tilting during rollover crashes involving cars or CUVs/minivans
RNA	ribonucleic acid
RPM or rpm	rotation(s) per minute
RR	right rear
RRR	run number designation
RT	room temperature
RTM	resin transfer molding
RUC	representative unit cell
RURAL	a control variable used in crash a frequency analysis that represents crashes occurring in rural areas
RVE	representative volume element

S

S	scalar factor in the Phelps-Tucker model
s^{-1}	per second
SA	simulated annealing
SAE	Society of Automotive Engineers
SAIE	shear assisted indirect extrusion
SANS	small angle neutron scattering
SBM	styrene-butadiene-methyl-methacrylate
SCE	saturated calomel electrode

Scheil Model	model making the assumption that diffusion rates are infinite in the liquid and zero in the solid; that local equilibrium is maintained at the advancing solidification interface, and the ratio of the liquidus composition to the solidus composition remains constant; and that there is negligible undercooling due to curvature or kinetics; can be used to describe the microsegregation present in primary phase dendritic growth and directional solidification
SciDAC	Scientific Discovery through Advanced Computing
SD	shear direction
SDAS	secondary dendrite arm spacing
SDS-PAGE	sodium dodecyl sulfate - polyacrylamide gel electrophoresis
SECM	scanning electro-chemical microscope (or microscopy)
SEM	scanning electron microscope (or microscopy)
SGL Group	SGL Carbon AG originated in 1992 from a merger between SIGRI GmbH, Germany, and Great Lakes Carbon, USA, to share a company according to German law; since March 2007, SGL Carbon AG has operated on the market as SGL Group - The Carbon Company
SHM	structural health monitor
Si	chemical symbol for silicon
SIMS	secondary ion mass spectrometry
Si_3N_4	silicon nitride
SLA or SL	stereolithographic analysis or stereolithography
SLKMC	self-learning kinetic Monte Carlo
SMC	sheet molding compound
SMD	steered molecular dynamics
SMDI	Steel Market Development Institute
S-N or S/N	an S-N curve, also known as a Wöhler curve, is a graph of the magnitude of a cyclic stress (S) against the logarithmic scale of cycles to failure (N)
Sn	chemical symbol for tin
SPD	severe plastic deformation
SPDLIM55	a control variable used in crash a frequency analysis that represents a crash that occurred in excess of the 55 mile per hour speed limit
SPN	shear plane normal
SPR	self-pierce riveting or self-piercing rivets
Sr	chemical symbol for strontium
SSMM	Spectral Stiffness Microplane Model
STEM	scanning transmission electron microscope (or microscopy)
SUV	sports utility vehicle
SVDC	super vacuum die casting
SVE	statistical volume element
SVM	State Variable Model

T

T	transverse reference when referring to a section of sample taken for microscopic analysis
t_c	the transition time from pit nucleation dominated to pit coalescence or general corrosion dominated in macroscale pitting corrosion calculations
T_g	glassy transition temperature

T joint	material joint shaped like the letter "T"
T4	Temper designation for solution heat-treated and naturally aged to a substantially stable condition; applies to products which are not cold worked after solution heat-treatment, or in which the effect of cold work in flattening or straightening does not affect mechanical properties
T5	temper designation for cooled from hot working and artificially aged (at elevated temperature)
T6	Temper designation for solution heat treated and artificially aged aluminum alloy
TALEN	transcription activator-like effectors to nucleases
TARDEC	U.S. Army Tank Automotive Research Development and Engineering Center
TCM	Technical Cost Models
TD	transverse direction
TEM	transmission electron microscope (or microscopy)
Terokal® 5089	a heat curing, solvent free, metal-to-metal adhesive with good storage stability based on epoxy resins that exhibits excellent strength and corrosion resistance at temperature extremes or after extensive aging and weathering and exceptional impact resistance over a wide temperature range; can be spot-welded and will reach maximum strength with curing temperatures between 155° and 190°C
TEROSON® PV 1097™	Henkel's TEROSON® PV 1097™ is a paintable seam sealer used on body panels to prevent water, dirt and fumes from entering passenger vehicles
TGA	thermogravimetric analysis
Ti	chemical symbol for titanium
TORSO	a control variable used in a crash frequency analysis that represents side-impact airbag or side torso airbag (side thorax/abdomen airbag) which is a category of airbag usually located in the seat, and inflate between the seat occupant and the door; these airbags are designed to reduce the risk of injury to the pelvic and lower abdomen regions
TP	thermoplastic
tRNA	transfer ribonucleic acid(s)
TRIP	transformation induced plasticity (for processing steel)
T.S. or TS	tensile strength
TSP	thermal signal reconstruction
TWB	tailor-welded blanks

U

U	the equilibrium potential or electric potential energy in a mathematical equation
UCR	upset cast riveting
UD	unidirectional
UDP980	DP980 steel produced by U.S. Steel
UHF	ultra-high frequency
UHP	ultrahigh purity
UHSS	ultra-high strength steel
UIUC	University of Illinois at Urbana-Champaign
UM	University of Michigan-Dearborn
UNDRWT00	Value for the mass reduction in lighter-than-average cars
UPJ	upset protrusion joining

USAMP	United States Automotive Materials Partnership
USC	University of Southern California
USU	Utah State University
UTS	universal testing system (when referring to a test methodology)
UTS	ultimate tensile strength (when referring to properties of materials)
UVW	unloaded vehicle weight

V

v	solidification front velocity in microsegregation models
v_0	parameter describing the maximum speed of crystallization in solidification equations
V	volt, voltage, or potential (when referring to an electrical property)
V	the volume of electrolyte in the Nernst-Brunner equation
VAC	vacuum
VFAW	vaporizing foil actuator welding
VFMW	variable frequency microwave
viz.	synonym for "namely", "that is to say", and "as follows"
VMM	validation of materials and models
VMT	vehicle mile(s) of travel
Voronoi	In mathematics, a partitioning of a plane into regions based on distance to points in a specific subset of the plane
vs.	versus
VTO	Vehicle Technologies Office

W

WE43	high strength casting alloy produced by Magnesium Elektron North America that can be used in temperatures of up to 300°C (572°F) with good mechanical properties and corrosion resistance; the composition of WE43 is 3.7-4.3% yttrium, 2.4-4-4% rare earths, 0.4% zirconium, and the remainder magnesium
W/g	watts per gram (heat flow)
w(l)	the weight distribution of fibers as a function of length.
W/mK	watts per meter - degree Kelvin
WSU	Wayne State University
wt%	percent by weight

X

x_1	the axis parallel to the shear direction as used in Beausir's equation for the persistence parameter for hexagonal materials
x2	the shear plane axis normal (z axis) as used in Beausir's equation for the persistence parameter for hexagonal materials
x3	the radial axis (r) as used in Beausir's equation for the persistence parameter for hexagonal materials
XPS	x-ray photoelectron spectroscopy
XRD	x-ray diffraction

Y

yr	year
YS	yield strength

Z

z	valency number of ions of a substance (in Faraday's Law)
ZE20	an alloy melt containing, by weight, 2 percent zinc and 0.2 percent cerium and the balance magnesium cast into a round cylindrical billet for in-line extrusion
ZEK100	a novel magnesium alloy with reduced content of rare earth metals with a composition of Mg plus 1.0 wt% zinc, 0.1 wt%, rare earth metals, and 0.1 wt% zirconium
ZK60	a magnesium wrought alloy consisting of primary matrix α (Mg) and the eutectic (solid solution α and MgZn (5.5% ZN) and Zn2Zr (0.6% Zr) compounds) with good formability used because its compressive proof strength is smaller than its tensile proof strength
Zircobond® 4200	a zirconium oxide coating which provides excellent liquid paint adhesion and e-coat applications for corrosion protection
Zn	chemical symbol for zinc
Zr	chemical symbol for zirconium

Table of Contents

List of Figures

List of Tables

I. Executive Summary

Within the automotive metals portfolio, advanced high strength steel (AHSS) is the most mature material in terms of widespread use in industry due to its compatibility with existing manufacturing infrastructure and vehicle materials. The exceptional strength and ductility of advanced steels offer potential for efficient structural designs and reduced weight. Application of a new generation of advanced high-strength steels has the potential to reduce component weight by up to 25%, particularly in strength-limited designs. Steel development and research in the Lightweight Materials subprogram is focused on introducing "3rd generation AHSS" (3GAHSS), which targets two different property sets: (1) exceptional strength and high ductility (>1,500 MPa ultimate tensile strength [UTS], >1,200 MPa yield strength [YS], and >25% elongation) and high strength and exceptional ductility (>1,200 MPa UTS, >800 MPa YS, and >30% elongation). The integrated computational materials engineering (ICME) approach used to deliver these results will accelerate development and widespread deployment of 3GAHSS through modeling of multi-scale metallurgical, thermal, and mechanical processes in coil sheet development, in automotive part and assembly manufacturing, and, ultimately, in vehicle performance.

Aluminum (Al) is also increasingly selected as a lightweight material for vehicle components, especially hoods, trunk lids, and doors. Representing a potential for 55% weight reduction when replacing traditional steel, precipitation-hardened grades have also found applications in body-in-white components. However, there are several challenges to the increased use of Al in vehicle weight reduction applications, including material cost, room temperature formability, and limitations within the existing manufacturing infrastructure. Lightweight Materials has funded several projects advancing manufacturing methods in both forming and welding to enable further use of Al.

With the lowest density of all structural metals, magnesium (Mg) has the potential to reduce component weight by greater than 60%. However, significant technical barriers limit the use of Mg to approximately 1% of the average vehicle by weight. These barriers include high raw material cost and price volatility, relatively low specific stiffness, difficulty in forming sheet at low temperatures, low ductility of finished components, and a limited alloy set, among others. High performance cast Mg alloys with improved strength and corrosion resistance are desirable for automotive applications; however, a major technical gap exists in the scientific foundation for developing such materials. By supporting improved scientific comprehension in the area of kinetics, diffusion, and corrosion behavior, the Lightweight Materials subprogram is identifying development paths toward novel Mg alloys, which allow greater impact on weight reduction in the U.S. fleet.

Carbon-fiber (CF) composites also have the potential to reduce component weight by more than 60%. One of the main barriers to this widespread implementation is the high cost of CFs, which is due, in large part, to the cost of both the raw material (fiber precursor) and the manufacturing processes that oxidize the precursor and then carbonizes the oxidized precursor to produce CF. Nature's strongest fiber, spider silk, may have the potential to serve as a lower+cost, non-petroleum precursor for CF; this report provides preliminary work on scaling up spider silk. Novel technologies that have the potential to reduce the cost of manufacturing carbon fiber are also addressed. In addition, the cost of manufacturing CF composites contributes to the high cost of structural components and subcomponents. In order to optimize the CF composite for cost and performance, industry needs reliable predictive tools to not only design but also predict performance in a crash. When fully developed, these tools will integrate models from the microscale to the macroscale, predicting structure/property and process/property relationships while taking into account uncertainty (e.g., fiber misalignment, defects, and the probabilistic nature of materials) that ultimately allows accurate pre-assessments of the performance of the structural component in a crash. This direct link from design to validation has the potential to signficantly speed up the development-to-deployment cycle in a reliable way.

Although each lightweight structural material has strengths and weaknesses that render it more suitable for certain applications than others, the most effective way of reducing the overall weight of a vehicle is to use the right structural material for the right application. The resulting multi-material structures have challenges of their own. Traditional joining methods used in automotive assembly, such as resistance spot welding, are

inefficient for joining of dissimilar metals. In the near term, joining of AHSS and Al (the more mature lightweight metals) is the highest priority challenge that needs to be addressed, with friction stir and friction stir scribe welding showing promising advances. As the barriers to introduction of Mg and CFRP are overcome, breakthroughs in joining technology are also necessary. The scope of this subprogram included five early stage projects to supplement the overall effort with solutions for dissimilar joining of light metal to light metal and light metal to CF composites.

Finally, multi-material crosscutting endeavors must include evaluations of both safety and cost. One study utilizes statistical analyses of crash safety data to illuminate the impact of lighter weight on vehicle safety based on real-world crash data. Another study is evaluating the full spectrum of lightweighting strategies and their potential impacts on cost. These two studies support addressing barriers to implementation from a holistic, vehicle systems approach.

II. Major Accomplishments for Fiscal Year 2015

II.1. Industry Impact

- Developed and deployed Al friction stir-welded, tailor-welded blank process technology with a weight reduction potential of up to 60% versus conventional techniques. This technology is now implemented in production at the tailor-welded blanks facility in Monroe, Michigan with a capacity of up to 250,000 parts per year.
- Developed a non-contact, non-destructive infrared weld inspection technology suitable for use in a production environment. This technology is licensed by ALPAIR Manufacturing Systems for development into a commercial product.
- Completed prototype design, build, and testing of a multi-material lightweight vehicle (MMLV) demonstrating more than 23.5% weight reduction versus a conventional baseline. Investigations and early testing of the MMLV carbon-fiber wheels helped speed the development of the carbon-fiber wheel available for the new Mustang Shelby GT350R.
- Matured plasma oxidation technology, which reduces energy use by 75% and increases throughput by a factor of three, decreases the cost of manufacturing oxidized carbon-fiber precursors. This technology has the potential to reduce the cost of carbon fiber by 20%. 4M Industrial Oxidation has announced commercialization of this technology due to the demonstrated scalability, robustness, and low variability of this process.
- Completed and validated a magnesium-intensive demonstration structure for under-hood applications; investigated a wide range of processing, joining, corrosion protection, design, and testing procedures for magnesium-intensive structures and validated modeling methodologies to the automotive lightweighting community.

II.2. Technology Pipeline

- Initiated a major thrust in developing ICME tools for carbon-fiber composites in order to speed up the product development cycle time with robust predictive modeling tools for structure/property and process/property relationships. These tools are meant to predict systems-level performance in a crash while taking into account uncertainty.
- Laid the foundation for a potential lower cost using an alternative and non-petroleum precursor for carbon fiber by investing in early stage research on spider silk.
- Developed and demonstrated new high-strength, exceptional ductility advanced steel with greater than 1,200 MPa tensile strength and greater than 30% elongation to failure, while simultaneously building an initial integrated computational modeling framework to predict properties of advanced steels.
- Completed detailed characterization of diffusion kinetics, microsegregation, and phase transformations of Mg alloys processed at a wide range of cooling rates. Produced new data and insight essential for development of next-generation, high-performance Mg alloys and began distributing these data to the broader materials community through established materials data repositories.
- Demonstrated technical feasibility of breakthrough joining techniques (such as collision welding by vaporizing foil actuator) by successfully welding more than 14 dissimilar metal combinations consisting of Mg, steel, and Al alloys. Laser-assisted adhesive joining of CFRP to Al (another breakthrough technique) showed a 40% increase in lap shear strength when compared to a non-laser-assisted baseline.

III. Automotive Metals

III.1. Development and Demonstration of a Magnesium-Intensive Vehicle Front-End Substructure – United States Automotive Materials Partnership LLC (USAMP)

Project Details

Stephen D. Logan, Principal Investigator
FCA US LLC
800 Chrysler Drive
Auburn Hills, MI 48326-2757
Phone: 248-512-9485
E-mail: stephen.logan@fcagroup.com

Joy H. Forsmark, Principal Investigator
Ford Motor Company
Ford Research and Innovation Center
2101 Village Road
Dearborn, MI 48124
Phone: 313-845-3056
E-mail: jforsma5@ford.com

Richard Osborne, Principal Investigator
General Motors Company
Materials and Appearance Engineering Center
MC 480-210-3B1
30001 Van Dyke
Warren, MI 48090
Phone: 248-202-6963
E-mail: richard.osborne@gm.com

Aaron Yocum, Project Manager
National Energy Technology Laboratory
3610 Collins Ferry Road
Morgantown, WV 26505
Phone: 304-285-4852
E-mail: aaron.yocum@netl.doe.gov

William Joost, Technology Area Development Manager
U.S. Department of Energy
1000 Independence Avenue, SW
Washington, DC 20585
Phone: 202-287-6020
E-mail: william.joost@ee.doe.gov

Contractor: USAMP
Contract No.: DE-EE0005660

Executive Summary

The goal of this project is the design, manufacture, and performance evaluation of magnesium (Mg)-intensive demonstration vehicle front-end substructures that are enabled through the incorporation of Mg alloys, advanced materials processing, joining, finishing, and use of computer-aided engineering (CAE). The demonstration structure concept provides a common geometric platform that is adaptable to investigation of alternative materials and processes, whereby computer-aided design (CAD) renderings and fixtures for processing and testing are virtually the same. The structures designed for this project employ a central, super-vacuum die cast (SVDC) AM60B Mg shock tower component to which upper and lower crush rail pieces are joined; this is typical of structural archetypes seen in unibody passenger vehicle front-end construction. A focal point of this work has been development and subsequent study of mixed-metal structures, including galvanized steel and wrought aluminum (Al) to demonstrate multi-material joining and finishing techniques as well as durability performance (including fatigue and corrosion). The project includes efforts in the integrated computational materials engineering (ICME) of die cast and extruded Mg alloys and components fabricated from them. The awardee participates in an international collaboration with Canada and The People's Republic of China to further advance Mg technology aimed at similar automotive applications.

Accomplishments

- Produced over 200 multi-material demonstration structures in four configurations: (1) steel upper rail (lower half only) for corrosion testing, (2) steel upper rail (complete assembled lower half and upper half) for durability testing, (3) Al upper rail (lower half only) for corrosion testing, and (4) Al upper rail (complete assembled lower half and upper half) for durability testing. All structures incorporated an extruded Al lower rail affixed to the central die cast AM60B Mg shock tower by self-piercing rivets (SPR).
- Incorporated novel dissimilar metal joining techniques for steel-to-Mg (adaptable insert welding [AIW]) and Al-to-Mg friction-stir linear welding (FSLW) in demonstration structures.
- Determined limitations of FSLW for the thin (i.e., 1.5 millimeter [mm] gauge) Al-to-Mg upper rail joint with respect to peel-type loading.
- Measured the deformation, fatigue, and corrosion properties of a novel ZE20 Mg alloy developed for improved extrusion speed and component performance in crashworthiness.
- Conducted fatigue and overload capacity measurements for three orthogonal loading directions on multiple steel-upper version demonstration structures joined by AIW and SPRs.
- Assessed the validity of several CAE approaches to the durability (i.e., fatigue) of dissimilar metal joints employed in the steel version demonstration structures.
- Determined the corrosion resistance performance of various commercial pretreatments and coatings on novel alloys ZEK100 and ZE20.
- Developed characterization tools for assessing the extent of galvanic corrosion for dissimilar metal couples, including junctions between steel SPRs and Mg and overlaps of galvanized steel sheet over die cast Mg.
- Constructed fixtures and conducted crash testing of exemplary SVDC AM60B shock tower components for comparison with predicted deformation behaviors using the three-dimensional solid element materials card developed for LS-DYNA®.
- Determined the elevated temperature deformation characteristics of ZE20 Mg using a Gleeble® device for development of parameters used in modeling of the extrusion process. Applied such models to extrusion of simple I-beam profiles with comparison to predictions using the DEFORM® three-dimensional forming software, with reasonable agreement.

Future Directions

- Complete all vehicle original equipment manufacturer (OEM) corrosion testing of painted demonstration structures.
- Complete all sub-awardee contracts.
- Provide all close-out reports and project documentation.

Technology Assessment

Many of the technology "gaps" identified in the Fiscal Year (FY) 2014 annual progress report have now been closed by ongoing project research and were removed from the target/status report updated as follows:

- Target: **Design**. Create a design for an Mg plus dissimilar metal demonstration structure to evaluate candidate joining methods, durability, and corrosion mitigation strategies while improving the Mg shock tower design. Design this demonstration structure for robust fixtures for durability testing.
- Status: Complete.
- Target: **Crashworthiness**. Analytically predict peak load and displacement at peak load within 5% (or within test scatter band) of physical test average for a selected Mg AM60B SVDC component.
- Gap: Lack of accurate material property input cards for LS-DYNA® to permit finite element calculation of deformations at high strain rates for cast and wrought Mg alloys in component applications.
- Status: Both two-dimensional shell element and three-dimensional solid element models for die cast AM60B, incorporating tensile/compression yield strength asymmetry, were developed and implemented in the LS-DYNA® software. Material deformation property data for extruded novel alloy ZE20 alloy were also developed.
- Target: **Durability (Fatigue).** Achieve capability for CAE prediction of fatigue life of similar and dissimilar metal joints (incorporating Mg) within a factor of two with respect to experimentally obtained values.
- Status: The fatigue life of a die cast AM60B Mg component (demonstration structure shock tower) was predicted within a factor of ±3of the median value, as well as fracture or failure location. Models for joint failure of AIW for steel to Mg and the SPR joint for Mg to Al were developed and lifetimes were predicted within a factor of three compared to experimental values. A subtask for assessing the role of residual stresses in fatigue of SPR joints was initiated employing neutron diffraction to determine the residual stresses within the interiors of such joints.
- Target: **Corrosion**. Achieve minimal (ideally zero) galvanic corrosion associated with coated, hardened steel SPRs in Mg.
- Status: A coating system was identified that greatly reduced the galvanic coupling of steel SPRs and Mg. New research suggests that for painted and riveted assemblies, localized corrosion may be affected by polymer topcoat thinning in the vicinity of the SPR joint.
- Target: **Extrusion.** Produce an Mg-extruded alloy with improved ductility, resistance to recrystallization and grain growth, and limited imposed texturing during forming in order to enhance performance in high strain-rate deformation (e.g., crash) and extrusion speed (e.g., manufacturing).
- Status: A ZE20 Mg alloy was selected for study. Billets and extrusions were acquired. Characterization of the lower rail component and several model profiles were conducted, including detailed analysis of extrusion textures in the extrudates, microstructure, and the resulting mechanical properties. The results suggested a slight improvement in extrusion speed over conventional alloys and reductions in texture, which are desirable for crashworthiness performance.

- Target: **Casting.** Acquire sufficient SVDC AM60B shock tower castings for production of the requisite demonstration assemblies.
- Status: Complete.
- Target: **Joining.** Identify and demonstrate joining technologies that are compatible with the dissimilar material combinations included in the present generation of demonstration structures. Assembly of approximately 200 demonstration structures for use by the project in durability and corrosion testing.
- Status: Three candidate joining methods (i.e., SPR, FSLW, and AIW) were developed and employed to fabricate the demonstration structures. Limitations on the use of FSLW for thin Al sheet to Mg couples were identified. Several alternative joining methods for this stackup were explored.
- Target: **ICME**. There were two subtargets: (1) development of an ICME framework for fatigue and durability of an SVDC AZ91D Mg shock tower casting, and (2) development of an ICME framework for ZE20 Mg extrusion alloy permitting mechanical property prediction in wrought profiles.
- Status: (1) For die cast AZ91D shock towers, all work is complete. Analyses indicate capability to determine the probable locus for fatigue failure of the shock tower component under cyclic loading. (2) For extruded ZE20, the extensive characterization of initial billet material and extruded forms was developed; deformation data for ambient and elevated temperatures was aquired and deformation models were developed for use in CAE simulations of the extrusion process for Mg alloys based on a crystal plasticity model incorporating the effects of dynamic recrystallization.

Introduction

This project builds on developments from several prior, interrelated USAMP Mg front-end research and development (MFERD) projects (identified by participants as Phases I and II). The overarching goal has been development of robust, enabling technologies permitting greater utilization of Mg alloys in lightweight vehicle body structures, of which the demonstration front-end substructure is exemplary [1,2]. The precursor projects included design, manufacture, and evaluation of all-Mg demonstration structures employing FSLW and SPR as the principal joining methods, with commercially available surface pretreatments and cathodic electrocoat as the protective finish. SPR, while offering substantial joint strength, had disadvantages of (a) a requirement for preheating when Mg is the underlying substrate in lap joints and (b) susceptibility to apparent galvanic corrosion attack in regions adjacent to the rivets. FSLW of similar and dissimilar alloys of Mg was found to be generally acceptable for creating joints in all Mg structures.

The current project, employing a nearly identical design envelope to the “all-Mg” demonstration structures of Phase II, explored mixed-metal construction. Specifically, high-strength, low-alloy 350 electrogalvanized steel and wrought Al (6022-T4) in the form of press-brake-formed pieces were used for the upper rail components and high-strength extrusions (Al 6082-T4) were used for the lower rails. Figure III-1 illustrates the layout and nomenclature for the Phase III demonstration structures. This approach addresses concerns from the earlier phases, wherein the commercially available wrought grades of Mg used in crush-sensitive applications were more prone to early fracture, particularly in high-strain rate (i.e., crash) loadings. Integration of large Mg structural castings in predominantly steel or Al body-in-white structures is a more likely scenario for the near-term and suggests an increased study of joining, finishing, and durability of such mixed metal assemblies that include Mg. the overall project, however, has focused on improving and understanding Mg alloys and their processing at a fundamental level. Aims have been to reduce the production cost and improve mechanical properties to be more competitive with current lightweighting materials such as Al and advanced high-strength steels. The project has also maintained a longstanding (since 2007) international (i.e., United States, Canada, and China) cooperative effort aimed at advancing the knowledge base and technologies required for enabling greater use of Mg alloys in automotive structures.

Approach

In its FY 2014 annual progress report [3], USAMP presented a restructuring of its approach by identifying two technology clusters, each incorporating relevant disciplines that had previously defined the organizational structure of the project as individual tasks (e.g., crashworthiness, durability, and corrosion). The first cluster incorporated joining, durability, and corrosion as overlapping entities, because any technology selected for dissimilar metal joining would also be subject to both durability (i.e., fatigue) and corrosion concerns. The second cluster considered ICME of Mg for two methods of forming components: die casting and extrusion. In particular, the selected performance metrics for this cluster were in the domain of crashworthiness, specifically aiming at improving high-rate deformation characteristics through improvements and characterization of microstructures as develop during material processing. In FY 2015, this cluster focused primarily on the characterization of a novel ZE20 extrusion alloy for crashworthiness applications.

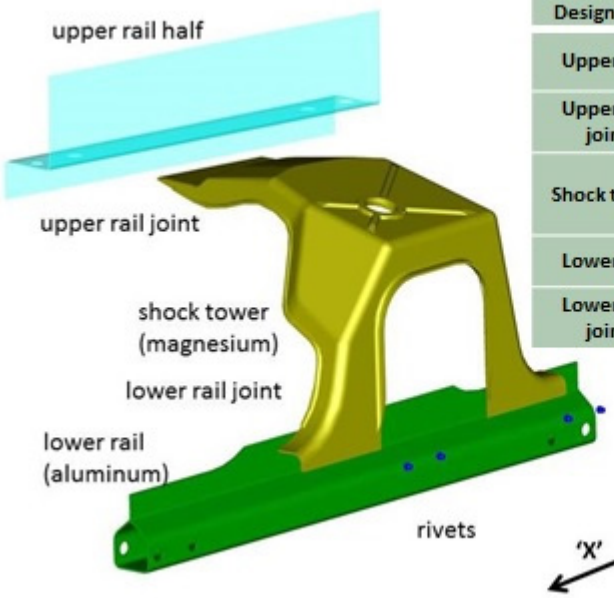

Structure Designation	Steel	Aluminum
Upper rail	HSLA 350 70x70EG 1.0mm sheet	6022-T4 Al 1.5mm sheet
Upper rail joint	Adaptable insert weld (AIW)	Friction-stir weld (FSW)
Shock tower	SVDC AM60B magnesium	SVDC AM60B magnesium
Lower rail	6082-T4 Al extrusion	6082-T4 Al extrusion
Lower rail joint	Self-piercing rivets (4)	Self-piercing rivets (4)

Figure III-1: MFERD Phase III demonstration structure technologies layout and component nomenclature.

Results and Discussion

The following tasks (i.e., Tasks 2, 7, and 8) are complete.

Design (Task 2). In FY 2015, the team has provided all essential computer-aided design data for the two versions of the demonstration structures, including details as needed for modification and development of any fixtures for use in testing or assembly. The design task team provided the project timing grid and participated in the logistics aspects of parts delivery, storage, and queuing for assembly of the various structures.

Sheet and Forming (Task 7). Work by this team is complete.

Casting (Task 8). Work by this team is complete.

Cluster I – Joining (Task 9), Durability (Task 4), and Corrosion (Task 5)

Figure III-2 illustrates the synergy between the joining, durability, and corrosion tasks with respect to the technologies selected for assembly of the Phase III demonstration structures and additional development. AIW was selected for the steel upper to Mg shock tower joints, and FSLW was selected for the Al upper to Mg shock tower joints. Both steel and Al upper rail structures incorporated a lower rail comprised of extruded 6082-T4 Al, joined by zinc-tin coated steel SPRs. It was previously shown that by placing the die cast Mg component in the top (i.e., first to be pierced) position of the couple, preheating of the joint area was not required. No further development was required for this joint and the technology was implemented by the supplier (i.e., Vehma International) using standard procedures and parameters supplied by Henrob Corporation of New Hudson, Michigan.

Joining (Task 9). In FY 2015, the joining task focused primarily on the upper rail to shock tower joints incorporating AIW and FSLW for the demonstration structures. AIW was developed and implemented for the demonstration structures by AET Integration, Inc. of Troy, Michigan. This technology was described in detail in the FY 2014 progress report [3]. AET Integration provided the AIW joints for over 100 substructures.Final assembly of the upper rail second half (where required for durability studies) and the lower rail was accomplished at Vehma International of Troy, Michigan. The corrosion test versions of the demonstration structures for both the steel and Al upper rails, control assemblies with no top-coating or sealing technologies included, versions having adhesive placement in the joint areas, and post-joining applied sealant (following any painting). Any instances involving adhesive required pretreatment processing with either Henkel Alodine® 5200 (Al and, Mg) or PPG Industries Zircobond® 4200 (steel and Mg). In theory, the Henkel Terosan® 5089 adhesive is designed to work with galvanized steel, absent any pretreatment processing. Any use of adhesives or sealants for the demonstration structures required an additional curing step, usually at automotive paint-bake conditions of 20 to 30 minutes at 180°C. The effect of multiple curing treatments on adhesives or sealants was not studied.

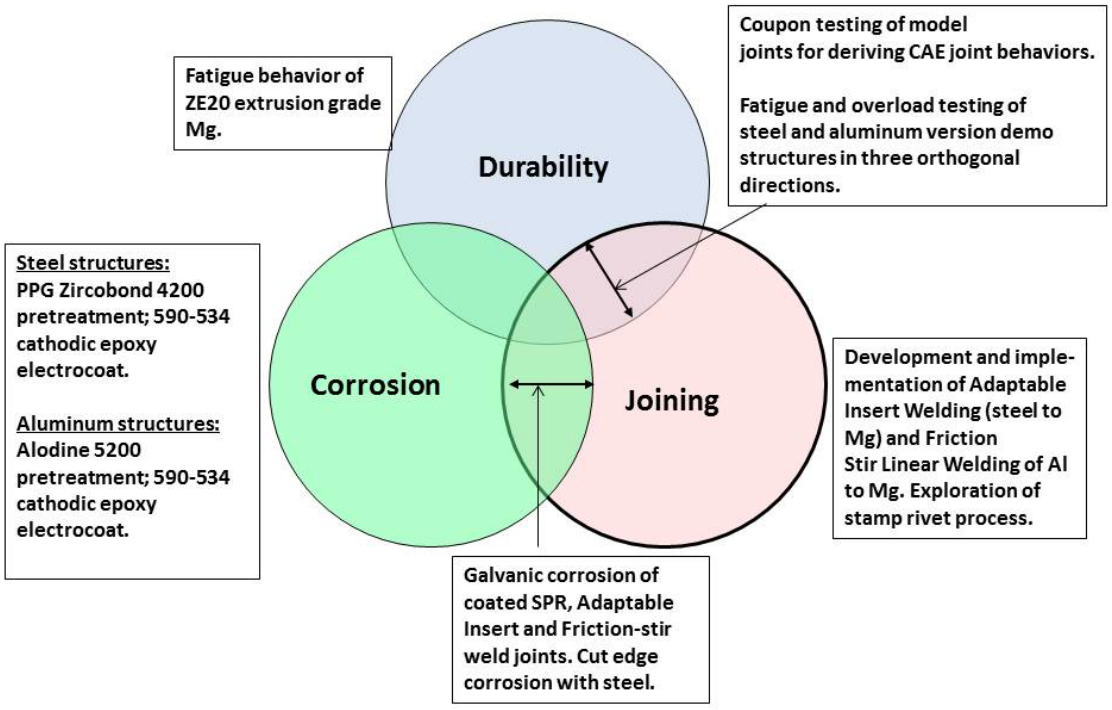

Figure III-2: Synergies among joining, durability and corrosion tasks for demonstration structure technologies.

During FY 2015, Hitachi Automotive Systems Americas, Inc. of Farmington Hills, Michigan continued development of the FSLW process specifically for joining of the 6022 Al upper rail half to the AM60B Mg shock tower for demonstration structures. This joining technique was chosen for the Al upper rail structures, with future potential for joining 3-mm AM60B (die casting) to 3-mm 6082 Al as might be later developed for the lower rail attachment. Hitachi also demonstrated the capability of incorporating adhesive into the upper rail joint. This was a desired feature primarily for corrosion mitigation in this joint, but also for providing additional overload and fatigue strength in this region.

FSLW provided adequate strength (about 3,000 newtons) in lap-shear (LS) coupon testing for the Al-Mg upper rail joint. It was later learned in fatigue studies at the University of Alabama, Tuscaloosa, Alabama that the joining resulted in peel strengths that were likely unacceptable for a mixed-loading condition of the joint. This means that it could not be assured that loading of the joint was strictly in shear with respect to the particular layup, and that any peel component could lead to lower than acceptable joint strength. This was particularly true for fatigue (cyclic) loading of the joint. The results showed low strengths and a proclivity for fracture running through the mixed Al-Mg zone, where formation of intermetallic compounds and associated brittleness is most likely to occur. Results from this study are presented later in the durability section.

Additional Joining Studies for Dissimilar Metals

Studies of alternative joining methods for the 6022 Al upper rail half to the AM60 shock tower flange continued with an emphasis on stamp rivets provided by the AKH, Inc. of Indianapolis, Indiana. Studies of the limitations on SPRs for such a thin ‘lower’ sheet of Al to be affixed to thicker die cast Mg were also initiated with Henrob Corporation with support from the Al supplier, Novelis Inc. of Atlanta, Georgia. For the stamp rivet testing, cross-tension (CT) and LS joints were constructed in both 1.5 and 3.0-mm gauges of Al (sheet or extrusion) to 3-mm AM60 and provided shear and tension strengths assessed to be adequate. The aim of studying thin Al to 3-mm AM60B die castings joints using SPR was to determine the minimum gauge of Al that could be joined to 3-mm die cast Mg (i.e., typical of the shock tower) with this technology.

Durability and Fatigue (Task 4). The objectives of this task are (a) to develop fatigue characteristics for monolithic samples of novel Mg alloys (e.g., ZE20), (b) to acquire fatigue data from coupon samples of selected demonstration structure joining methods for Mg and dissimilar metals, (c) to advance CAE methodologies for improved prediction of fatigue at joint locations in complex structures, and (d) to provide for fatigue testing of the project’s demonstration structures, with emphasis on durability of the joints.

Fatigue Modeling Capability Development (University of Michigan-Dearborn, Dearborn, Michigan)

The information and calculation flow for predicting the location and cycles-to-failure for joints and materials (die cast Mg) in the demonstration structure are illustrated in Figure III-3. Two approaches were considered (depending largely on the nature of the joint and the accuracy of its representation using the finite element method). Both formalisms, the maximum principal stress method and the structural stress method, begin with load versus cycles-to-failure data for coupon specimens as measured from partner laboratories (e.g., AET Integration or the University of Alabama). For the maximum principal stress method (based on stress-life metal-fatigue analysis), a tied-contact representation defines the transmission of stresses and strains across the joint with elements of the second material effectively tied to those of the first at the junction. The modeling assumes no particular mechanical properties of the interface. The structural stress method (typically used for fatigue analysis of spot welds) employs the use of the area-contact method (ACM) to define transmission of loads across the junction. For the joints of interest, both tied contacts and ACM could be used for SPR and AIW joints. ACM was preferred for FSLW joints depicted using shell elements.

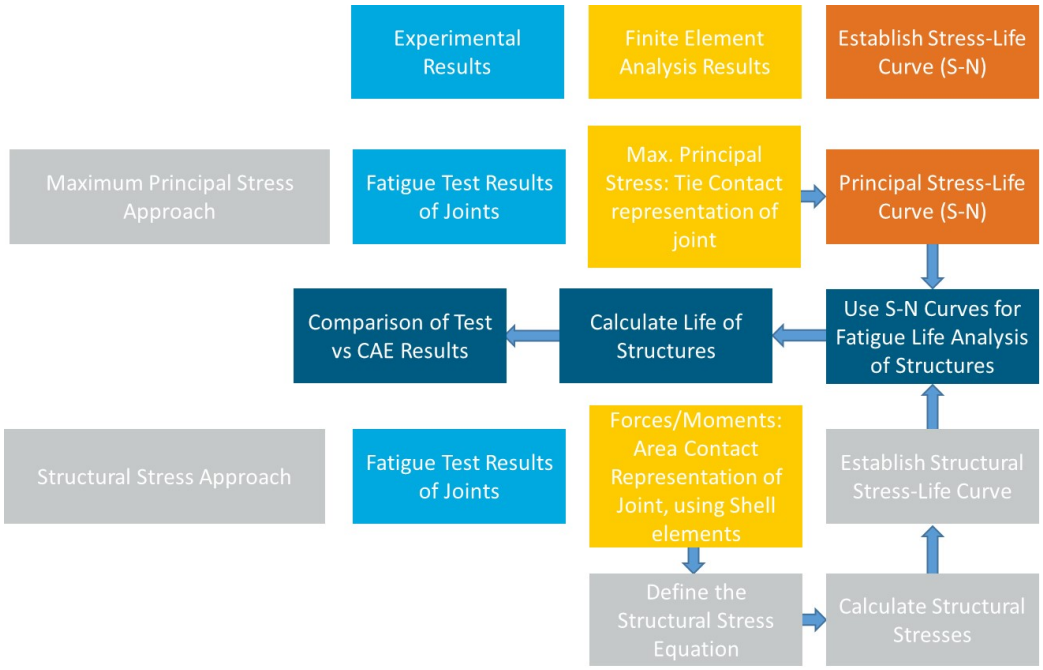

Figure III-3: Computational scheme for the prediction of structure fatigue performance from coupon data.

Finite element analysis was used with a physical model of the particular joint (with the contact formalisms described above) to obtain the forces and moments. These were then used to develop a local stress versus cycles-to-failure, or S/N, curve for the particular joint of interest. Figure III-4 illustrates an S/N curve for the AIW, securing 1-mm sheet steel to 3-mm AM60B die cast Mg and employing analyses from both lap-shear and cross-tension coupon samples. The greater demonstration structural model, with specified joints and loads, was then explored for failure cycles given the magnitude of the cyclic loading of the structure and its local valuation obtained from the finite element method. The applicability of the S/N curve for a particular joint is improved with characterization for multiple loading orientations (e.g., LS, CT, or coach peel). The requirement for such coupon loadings to obtain the S/N joint behavior becomes more complex, because such joints may be difficult to both construct and test.

With S/N behaviors developed for various types of joints in the structure, it becomes possible to predict joint fatigue life under externally applied cyclic loading. All cyclic testing of the steel upper demonstration structures was conducted by Exova of Warren, Michigan. Fatigue-life testing for the various loading conditions was compared to predictions from coupon samples of the particular joints with the different modeling techniques for the contact (e.g., ACM or tied contact). In designing mechanical testing for the demonstration structures, the focus was on defining loading conditions to cause failure for joints of interest or the parent material. With reference to Figure III-1, ‘X’ direction loading was intended to impart the maximum stress for the SPR joints securing the lower rail to shock tower, while the ‘Y’ loading was intended to cause the maximum stress on the upper-rail to shock tower joint. The ‘Z’ loading was intended to stress the base AM60B Mg of the shock tower casting. These assumptions were borne out by experiments.

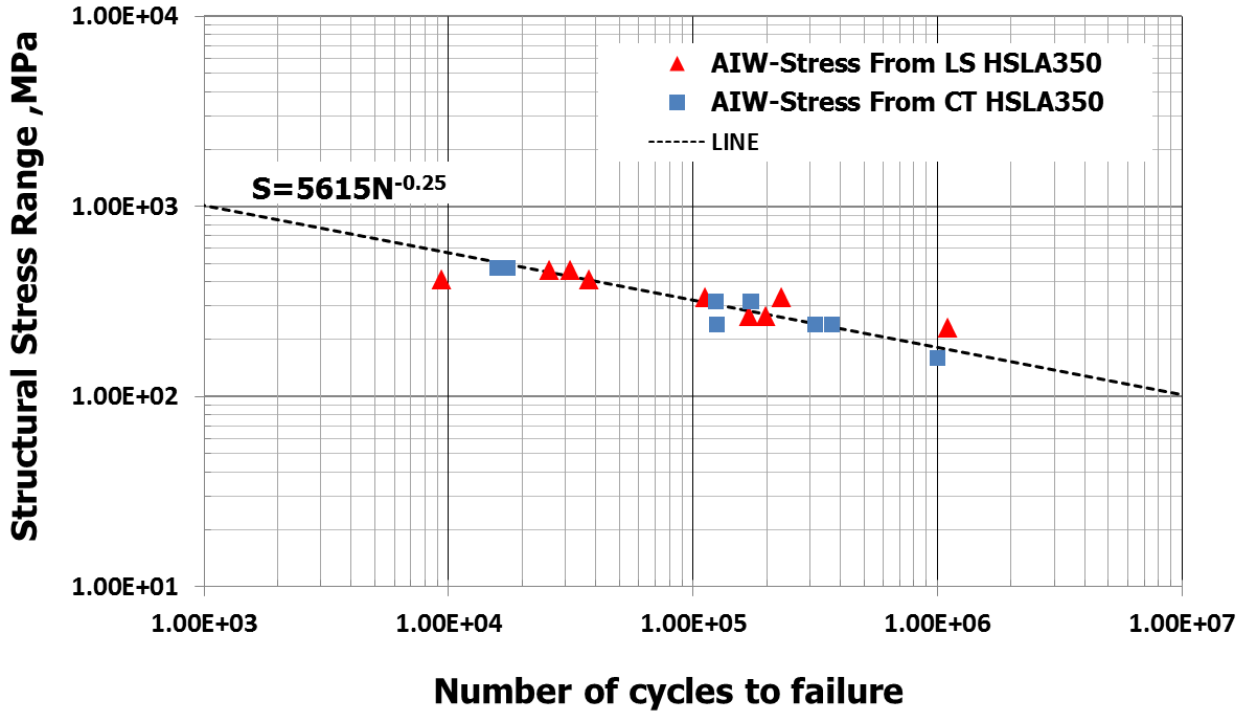

Figure III-4: Composite stress/cycles-to-failure data for LA and CT joints of HSLA 350 steel sheet (1-mm gauge) to the AM60B die cast Mg shock tower.

Fatigue Lifetime Determination for FSLW Joints (University of Alabama)

The focus of work at the University of Alabama was the development of load life data for the coupon specimens of the FSLW joints. These data were then parameterized for the University of Michigan-Dearborn structure analysis described above. Concern had previously arisen over an apparent tendency for the FSLW joints between Al and Mg to fracture in a brittle manner via interfacial cracks traversing the stir zone where there was substantial formation of intermetallic compounds of Al and Mg and associated brittleness. Figure III-5 illustrates the great disparity in joint strength as measured by load/cycles-to-failure from which the S/N curves are calculated for the structural-stress approach outlined previously. The relatively low strength in tensile or peel loading of the joints later manifested itself in the poor mechanical strength of the demonstration structures where this joining method was employed. An exception to this was for structures where a supplementary adhesive was applied, principally for joint corrosion improvement.

Fatigue Testing of Steel-Upper Demonstration Structures

Steel-upper demonstration structures having the AIW (upper) and SPR (lower) joints were subjected to overload and fatigue testing at Exova. As indicated above, 'X' and 'Y' loadings were intended to stress the joined areas, while 'Z' direction loading was employed to evaluate the fatigue strength of the base vacuum die-cast AM60B alloy of the shock towers. Figure III-6 illustrates the correlation between predicted results and actual test results using ACM and tied-contact finite-element analysis representations of the joints. Fixture layouts are shown in the insets. Excellent correlation was achieved between modeling and experiment. The fatigue test results were within a factor of three (i.e., one-third to three times) of the median value when compared to predictions, with the predictions typically being conservative. Predictive analysis was conducted in advance of testing.

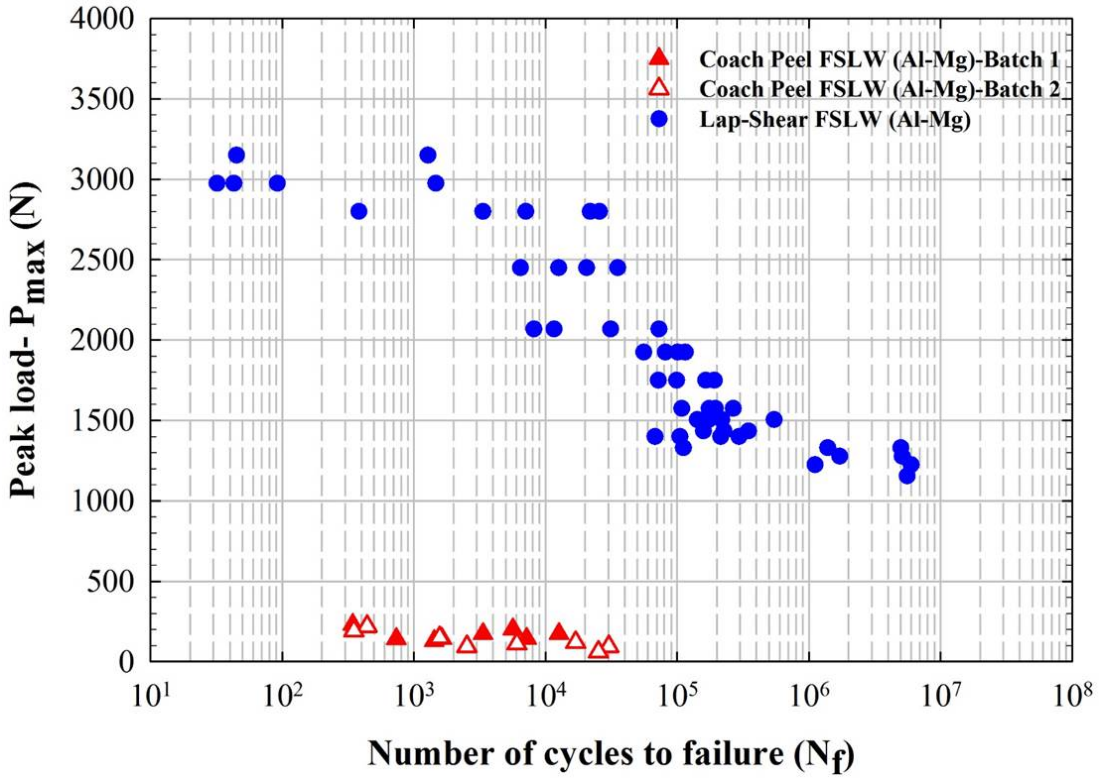

Figure III-5: Comparison of coupon fatigue test data for FSLW 6022 Al to AM60B Mg in both coach peel (two data sets) and lap-shear modes.

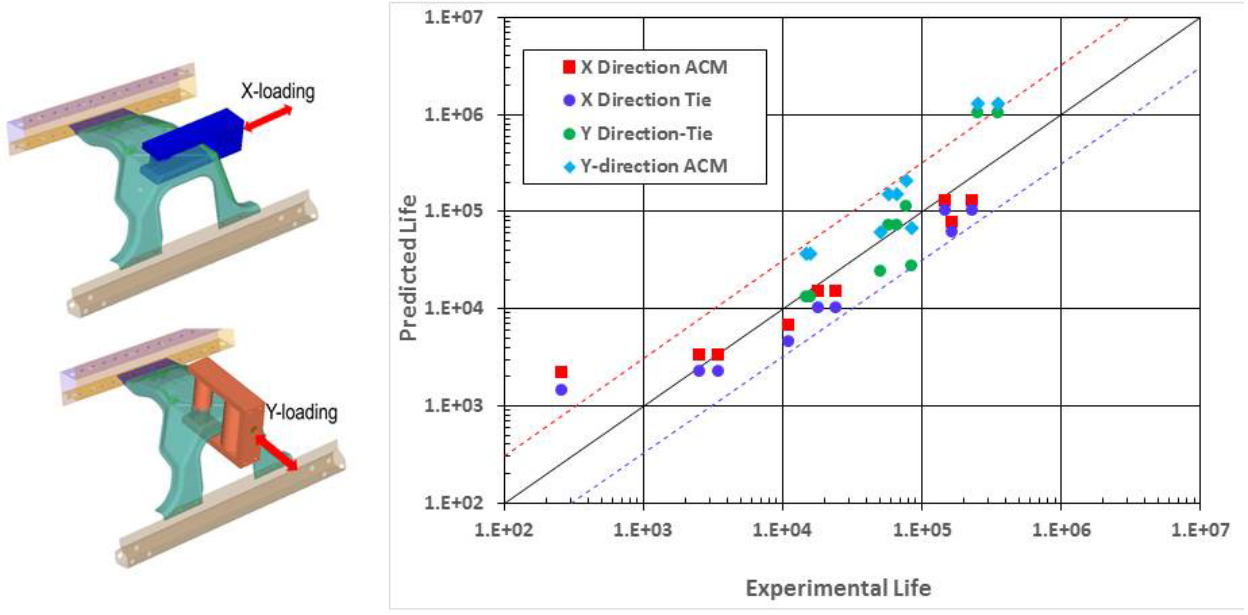

Figure III-6: Demonstration structure loading arrangements and comparison of predicted and observed lifetimes using either "tied contacts" or the ACM for characterization of the joints in the finite element method.

Task 5 – Corrosion and Surface Treatment

Corrosion testing of an extensive test matrix (i.e., over 640 multi-plate assemblies) of various materials, joining methods, and finishes that were previously reported [3] was concluded. Corrosion performance of selected pretreatments, topcoatings, and alternative rivets and coatings was assessed. Very few combinations of metal pretreatment and topcoating provided corrosion performance that would have passed OEM qualifications predicated solely on scribe creep over the test duration. Ion-vapor-deposited Al coating of the hardened steel SPRs was found to be unsatisfactory when compared to the baseline Henrob zinc-tin barrel coating. Cyclic (Society of Automotive Engineers (SAE) J2334, "Laboratory Cyclic Corrosion Test") and salt-spray (American Society for Testing and Materials (ASTM) B117, "Standard Practice for Operating Salt Spray (Fog) Apparatus") testing of candidate pretreatments and topcoatings was conducted for novel alloys ZE20 (extrusion) and ZEK100 (sheet). Combinations of pretreatment and topcoating were identified that either met OEM acceptance criteria or suggested they were within the range of acceptance criteria through minor processing improvements. This testing of ZE20 and ZEK100 alloys did not include multiple material combinations or joining methods.

Demonstration structures having only the lower-half upper rail (i.e., joint to die cast Mg) were conversion coated and painted by cathodic electrocoat (PPG Powercron® 590-534) following assembly. Table III-1 provides the processing details and nomenclature for structures designated as controls (i.e., having no electrocoat topcoating), 'standard' (i.e., having pre-placed adhesive in joint areas as a corrosion deterrent), and 'sealed' versions (i.e., having a Henkel TEROSON® PV-1097™ paint shop sealant applied to rivet caps and lapped junctions and cured following all assembly and painting of the underlying structures). The corrosion test versions were substantially different than durability test versions in that (a) there was not a second half upper rail (required for durability tests) and b) adhesive was placed in all joints near exposed regions to minimize fluid ingress in the joints. This was deemed a likely scenario in actual vehicle assembly. Durability versions used selective placement of adhesive only for purposes of stressing particular joint areas. Corrosion testing of the various demonstration structure versions is underway at the OEM test facilities at the time of this writing. The longest of the test cycles requires 24 weeks of cyclic exposure.

Table III-1: Features of Al and steel versions of the demonstration structure and finishing details for corrosion testing by OEMs.

Version	Processing	Control	Standard Corrosion Testing	Sealed Rivets and Joints
Aluminum upper	**Almond Products**: Henkel Alodine 5200 (all pieces); PPG 590-534 cathodic electrocoat	Pretreat upper rail and shock tower; assemble using FSLW (no adhesive)	Pretreat components; assemble with adhesive around exterior of contact	Henkel PV-1097 applied to painted joints and rivet caps
Steel upper	**PPG**: Zircobond 4200 (all pieces); PPG 590-534 cathodic electrocoat	Assemble using AlW; no adhesive; no pretreat of steel	Steel rail is pretreated and electrocoated prior to joining; adhesive in joint area	Henkel PV-1097 applied to painted joints and rivet caps
Both versions	SPR joining of 6082 Al lower rail to Mg shock tower; pretreatment of rail and shock tower components prior to assembly.	No adhesive at SPR joint; pretreat of Mg and 6082 Al only	Henkel Teroson 5089 in SPR joint regions.	Henkel PV-1097 applied to painted joints and rivet caps

Detailed studies of corrosion adjacent to coated steel SPRs were conducted by the Ohio State University, Missouri University of Science and Technology, North Dakota State University, PPG Industries, Henrob Corporation, and Henkel Corporation. Studies at the Ohio State University showed that under the worst case

conditions of galvanic attack of Mg by the steel rivet, loss of joint shear strength could be far less than anticipated from joint appearance. In some instances, severely corroded Mg retained joint strength in shear loading of as much as 95% of its non-corroded value. Missouri University of Science and Technology investigated corrosion products and polymer coating thickness of the electrocoat used to cover embedded rivets. Results showed that polymer thinning around the rivet head (i.e., a geometric feature of cathodic electrocoating) may contribute to early onset of cosmetic corrosion. While there may be a galvanic component of this attack, especially at long exposure times in non-passivating environments, polymer layer thickness appears to be a critical factor in reducing cosmetic corrosion at painted over rivets. USAMP, PPG Industries, and Missouri University of Science and Technology developed a test matrix to explore the effects of polymer type and coating thickness with respect to eliminating cosmetic corrosion at rivet heads. North Dakota State University has studied various coatings to SPRs and electrochemical measurement methods to determine the effectiveness of rivet coatings with regard to halting galvanic attack of Mg adjacent to coated rivets. Highly insulating layers (such as those produced through a combination of Al electroplating and electro-ceramic coating [Henkel EC$^{2®}$]) were shown to be effective for eliminating the galvanic component of attack near SPRs.

Cluster II – Extrusion (Task 6), Crashworthiness (Task 3), and Integrated Computational Materials Engineering (Task 10)

The FY 2014 annual progress report [3] illustrated the synergy between the ICME, extrusion, and crashworthiness tasks. During FY 2015, the extrusion and ICME task groups met concurrently with the objective of developing a framework that specifically addresses the advanced ZE20 alloy under consideration for use in the front-end structure. Improvements in the physical metallurgy of Mg, typified by grain size control and defusing of texture development through microalloying with rare-earth metal addition, were objectives of this approach. The intended usage of improved Mg extrusions was in crash loading. The crashworthiness task provided property measurements of the selected ZE20 material and the protocol for comparing the advanced Mg alloy to the baseline AM30 and AZ31 grades and Al 6082 as a comparator material. The flow chart shown in Figure III-7 illustrates the collective material and information flows in support of this objective.

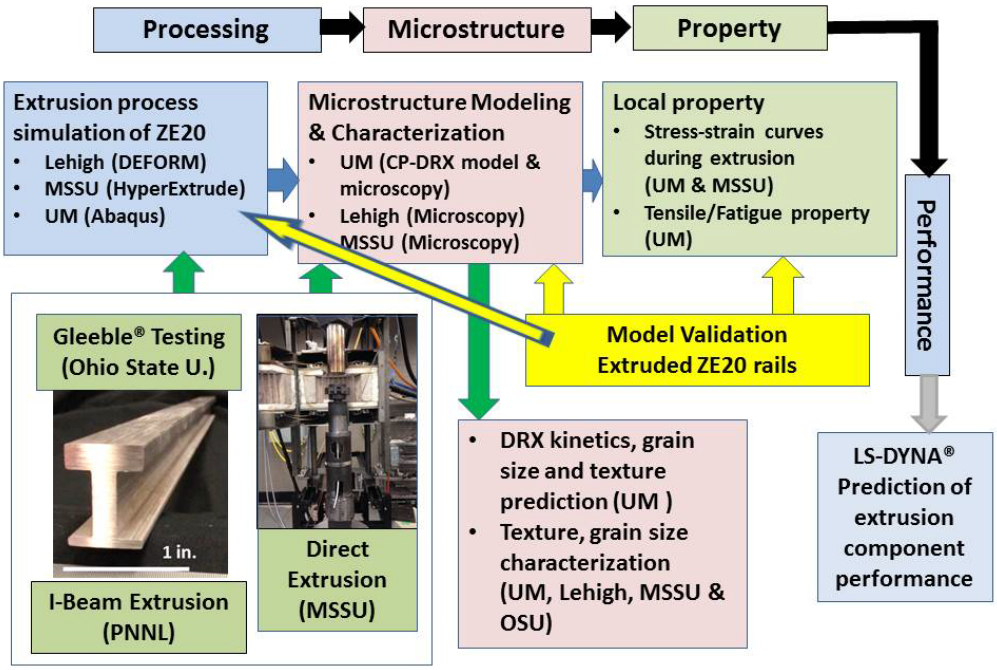

Figure III-7: Experimental and simulation information flows for ZE20 extrusion modeling.

Extrusion (Task 6). This team, in conjunction with Mag Specialties Company of Denver, Colorado, conducted extrusion trials with a ZE20 alloy, using the demonstration structure lower rail profile to determine if the metallurgy of this alloy would permit greater extrusion speeds than the comparator AZ31 for which extensive production data have been acquired. Mag Specialties found they could extrude ZE20 at 14 ft per minute without issues. This is 2 ft per minute faster than a conventional AZ31 extrusion alloy in the same profile. A study was also completed in conjunction with Pacific Northwest National Laboratory for model extrusions with I-beam profiles as shown in Figure III-7. Pacific Northwest National Laboratory has an indirect extrusion press and provided assistance in designing the dies and producing the extrusions for further characterization by the extrusion and ICME teams. Extruded ZE20 I-beams were sectioned and studied by teams at the University of Michigan (Ann Arbor, Michigan), Mississippi State University, the Ohio State University, and Lehigh University. Grain size and texture data were acquired for incorporation into the deformation models being developed by Lehigh University and Mississippi State. The Ohio State University generated elevated temperature stress/deformation data using a Gleeble® apparatus; these data then became an input and validation for materials models used in simulations such as DEFORM® 3D as implemented by Lehigh University. Finally, the University of Michigan combined a prediction for dynamic recrystallization (designated CP-DRX in Figure III-7) during deformation of ZE20 with a previously developed crystal plasticity model and successfully predicted softening in the stress/strain behavior as a consequence of the extrusion process. This was then validated by tensile testing using excised coupons from the Pacific Northwest National Laboratory I-beams.

Crashworthiness (Task 3). High strain rate and large-strain deformation of wrought or cast Mg components and associated limitations remain a concern for vehicle engineers. The crashworthiness team continued acquisition of shear deformation characteristics for extruded ZE20 and die cast AM60B using specially designed coupons that enable shear data to be acquired with conventional tensile loading. These data are then employed in deformation models such as LS-DYNA®. The task team has previously developed specialty material cards for AM60B die cast Mg and has developed new data for the ZE20 extrusion grade. The team conducted deformation studies of the AM60B die cast shock tower component in two different schemes: (1) a quasi-static deformation test as illustrated in Figure III-8(a) with edges of the component secured and (2) a crash-loading test with impacts at specific angles and locations on the component. The team developed CAE models for the component piece and associated fixtures that govern the boundary conditions. Experimental force versus displacement behavior for the component piece were compared to predictions from LS-DYNA® or comparable simulation using material cards developed by the project or alternate data from the software library (Figure III-8(b)). Table III-2 details the ultimate loads predicted by the various material cards with experimental findings. The team developed CAE models for fixtures and deformation testing of the demonstration structure lower rail in the various materials considered (e.g., AZ31, AM30, ZE20 and AA6082-T6 Al) and their profiles.

Integrated Computational Materials Engineering (Task 10)

The ICME task was combined with the extrusion task during FY 2015 because the thrust of both efforts was on the processing-structure-property relationship specifically for the novel ZE20 extrusion alloy. Details of that approach were presented previously in this report. All work related to deformation and fatigue of as-cast and precipitation hardened AZ91D was completed and included in the FY 2014 annual progress report.

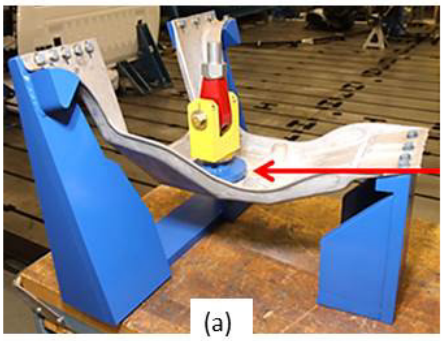

(a)

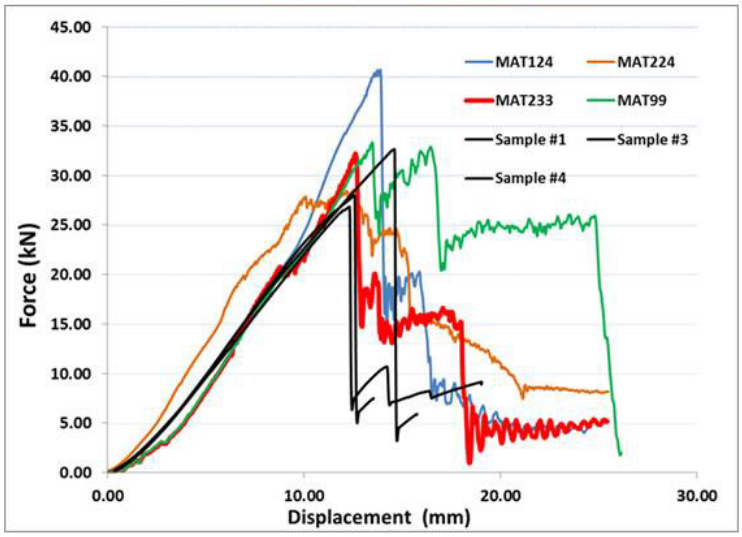

(b)

Figure III-8: (a) Experimental arrangement for quasi-static deformation testing of the AM60B Mg shock tower at General Motors Company. (b) Comparison with deformation characteristics from LS-DYNA® (black lines) using four different models (colored lines) for the Mg deformation parameters.

Table III-2: Comparison of maximum load in quasi-static testing with predictions using the LS-DYNA® material cards as indicated

MAT Model Type	Test	MAT124	MAT224	MAT233	MAT099
Max Load (kN)	30.50	40.66	28.53	32.21	33.32
% Peak Load Difference	N/A	33.3	6.4	5.6	9.2

Technology Transfer Path

Increased use of Mg as a lightweighting material alternative in automotive structural design faces both economic and technical challenges, including material cost, perceived durability concerns, a receding North American supplier base, and manufacturing concerns such as joining and surface treatment. Although incorporation of multiple, individually cast or wrought Mg components into articulated subassemblies (such as the originally envisioned unibody front-end) appears unlikely in the near-term, Mg will continue to have a role in vehicle lightweighting, predicated on its attractive features of low density, high specific stiffness, and amenability to thin-wall die casting and component integration. Because of this, efforts devoted to improving strength and durability (i.e., fatigue) of castings, joining to dissimilar metals, and finishing alternatives will remain quite relevant. Data acquired during this project related to material deformation properties for extrusion

and crashworthiness are documented and, for the case of LS-DYNA®, have resulted in generation of material cards that are currently available to users of the software.

OEMs. Improved material properties models for specific grades of Mg (e.g., AM60B and ZE20) will be of value in various design simulations, including crashworthiness. Developments in the physical metallurgy of advanced grades of Mg (e.g., ZE20 and ZEK100) may eventually permit utilization of lightweight components in load-sensitive applications where more isotropic behavior of the metal is desirable. Knowledge gained in regard to corrosion protection systems and scope of applicability – particularly for novel, multi-material pretreatments – is expected to be of value. Additionally, novel joining methods and parameters such as rivet coatings are of interest. Durability modeling of joining technologies is of general value, as are novel approaches for joining dissimilar metals.

Suppliers. USAMP has enlisted over 50 distinct suppliers of materials, technologies, and services relating to the design, production, and incorporation of Mg components in automotive structures over the course of several MFERD projects dating back to 2006. Through technical committees and web-based tools, suppliers are both engaged in discussion of Mg technologies as well as in providing (often unique) adaptations of existing technologies for deployment with Mg. Suppliers are thus engaged in understanding the particular technical challenges and building their capabilities to meet expanded use of Mg alloys in vehicle lightweighting.

Universities. A long-range MFERD initiative goal is to foster greater Mg technology education and innovation through the university system. To this end, 11 universities have been engaged in the overall project with nine in the current embodiment, focusing on physical metallurgy, ICME, durability, metal deformation, and corrosion. This sponsored university research was intended to instill a greater interest in Mg science and technology among students and provide a means for linking knowledgeable graduating students with possible opportunities in supplier or OEM organizations.

Conclusion

At the end of its third full fiscal year, the project team has assembled over 200 Mg-centered demonstration structures in four configurations and conducted durability (i.e., fatigue) testing on the steel upper versions. Novel joining techniques for steel to Mg (viz. AIW) and FSLW of Al to Mg were explored and developed. Corrosion testing of demonstration structures according to OEM protocols is underway at the OEM test facilities at the time of this writing because the longest test cycles require 24 weeks of cyclic exposure.

References

1. Luo, A. A.; Quinn, J. F.; Wang, Y.-M.; Lee, T. M.; Verma, R.; Wagner, D. A.; Forsmark, J. H.; Su, X.; Zindel, J.; Li, M.; Logan, S. D.; Bilkhu, S.; and McCune, R. C., 2012, "The USAMP Magnesium Front End Research and Development Project," *Light Metal Age*, April 2012, pp. 54-58.
2. Forsmark, J. H.; Li, M.; Wagner, D. A.; Zindel, J. W.; Luo, A. A.; Quinn, J. F.; Verma, R.; Wang, Y.-M.; Logan, S. D.; Bilkhu, S.; and McCune, R.C., 2014, "The USAMP Magnesium Front End Research and Development Project – Results of the Magnesium 'Demonstration' Structure," *Magnesium Technologies*, pp. 517-524.
3. "Lightweight Materials R&D Program," 2014, U.S. Department of Energy Vehicle Technologies Office, Fiscal Year 2014 Annual Progress Report, p9, accessed October 26, 2015: http://energy.gov/sites/prod/files/2015/07/f24/DOE%20VTO%202014%20Materials%20Annual%20report.pdf.

Bibliography

Forsmark, J. H.; McCune, R. C.; Giles, T.; Audette, M.; Snowden, J.; Stalker, J.; Morey, M.; O'Keefe, M.; and Castano, C., 2015, "Investigation of Coating and Corrosion Mitigation Strategies in Magnesium/Mixed Metal Assemblies," in *Magnesium Technology 2015*, Manuel, M. V., Singh, A., Alderman, M., and Neelameggham, N. R. (eds.); The Minerals, Metals and Materials Society, Warrendale, PA; pp. 333-338.

Ma, X.; Huang, Z.; Li, M.; and Allison, J. E., 2015, "Recrystallization Behavior of the Magnesium Alloy ZE20," in *Magnesium Technology 2015*, Manuel, M. V., Singh, A., Alderman, M., and Neelameggham, N. R. (eds.); The Minerals, Metals and Materials Society, Warrendale, PA; pp 177-182.

McClelland, Z.; Li, B.; Horstemeyer, S. J.; Horstemeyer, M. F.; and Oppedal, A. L., 2016, "Effects of Homogenization on Microstructures and Mechanical Properties of a ZE20 Mg Alloy Processed by Indirect Extrusion," accepted for publication in *Magnesium Technology 2016;* The Minerals, Metals and Materials Society, Warrendale, PA. (in press).

McCune, R. C.; Forsmark, J. H.; Upadhyay, V.; and Battocchi, D., 2015, "Characterization of Coatings on Steel Self-piercing Rivets for use with Magnesium Alloys," in *Magnesium Technology 2015*, Manuel, M. V., Singh, A., Alderrman, M., and Neelameggham, N. R. (eds.); The Minerals, Metals and Materials Society, Warrendale, PA; pp. 327-332.

Rao, H. M.; Jordon, J. B.; Yuan, W.; Ghaffari, B.; Su, X.; Khosrovaneh, A. K.; and Lee, Y. L., 2015, "Fatigue Behavior of Friction Stir Linear Welded Dissimilar Aluminum-to-Magnesium Alloys," in *Friction Stir Welding and Processing VIII*, Mishra, R. S.,Mahoney, M. W., Sato, Y.,Hovanski, Y. (eds.); The Minerals, Metals and Materials Society, John Wiley & Sons, Inc., Hoboken, New Jersey; pp 145-152.

Rao, H. M.; Jordon, J. B.; Ghaffari, B.; Su, X.; Khosrovaneh, A. K.; Barkey, M. E.;Yuan, W.; and Guo, M., 2016, "Fatigue and Fracture of Friction Stir Linear Welded Dissimilar Aluminum-to-Magnesium Alloys," *International Journal of Fatigue*, 82; pp. 737-747.

Rao, H. M.; Ghaffari, B.; Yuan, W.; Jordon, J. B.; and Badarinarayan, H., 2016, "Effect of Process Parameters on Lap Shear Strength of Friction Stir Linear Welded Aluminum to Magnesium," *Materials Science and Engineering A*, 651:pp. 27-36.

Sutton, S.; and Luo, A. A., 2015, "Hot Compression Behavior of Magnesium Alloys ZE20 and AM30," in *Magnesium Technology 2015*, Manuel, M. V., Singh, A., Alderrman, M., and Neelameggham, N. R. (eds.); The Minerals, Metals and Materials Society, Warrendale, PA; pp 25-28.

Upadhyay, V.; McCune, R. C.; Forsmark, J. H.; Qi, X.; Wilson, N.; Battocchi, D.; and Bierwagen, G., 2016, "Electrochemical Characterization of Coated Self-Piercing Rivets for Magnesium Applications," *Society of Automotive Engineers International Journal of Materials and Manufacturing*, 9 (1), SAE Paper Number 2015-01-9085.

Yuan, W.; Shah, K.; Ghaffari, B.; and Badarinarayan, H., 2015, "Friction Stir Welding of Dissimilar Light-weight Metals with Addition of Adhesive in Friction Stir Welding and Processing VIII," Mishra, R. S., Mahoney, M. W., Sato, Y., and Hovanski, Y. (eds.); The Minerals, Metals and Materials Society, John Wiley & Sons, Inc., Hoboken, New Jersey; pp 127-134.

III.2. Integrated Computational Materials Engineering Approach to Development of Lightweight 3GAHSS Vehicle Assembly (ICME 3GAHSS) - United States Automotive Materials Partnership, LLC

Project Details

Louis Hector, Jr., Principal Investigator
General Motors R&D Center
Mail Code 480-106-RL1
30500 Mound Road
Warren, MI 48090-9055
Phone: 586-651-2628
E-mail: Louis.hector@gm.com

Jody Hall, Principal Investigator
Vice President, Automotive Market
Steel Market Development Institute
2000 Town Center, Suite 320
Southfield, MI 48075
Phone: 248-945-4761
E-mail: rhall@steel.org

David Ollett, Project Officer
National Energy Technology Laboratory
DOE/NETL/PMC/VTP Division
626 Cochrans Mill Road
Pittsburgh, PA 15236-0940
Phone: 412-386-7339
E-mail: david.ollett@netl.doe.gov

William Joost, Technology Area Development Manager
U.S. Department of Energy
1000 Independence Avenue, SW
Washington, DC 20585
Phone: 202-287-6020
E-mail: william.joost@ee.doe.gov

Contractor: United States Automotive Materials Partnership, LLC
Contract No.: DOE DE-EE0005976

Executive Summary

The goal of the program is to successfully demonstrate the applicability of integrated computational materials engineering (ICME) for the development and deployment of third generation advanced high strength steels (3GAHSS) for immediate weight reduction in passenger vehicles. The ICME approach integrates results from well-established computational and experimental methodologies to develop a suite of material constitutive models (deformation and failure), manufacturing process and performance simulation modules, as well as the computational environment linking them together for both performance prediction and material optimization. The project officially started on February 1, 2013.

Accomplishments (FY 2015)

- In June, the United States Automotive Materials Partnership, LLC signed a Cooperative Research and Development Agreement with the National Institute of Standards and Technology to utilize their dSpace data repository for curating and storage of project data.
- Under Task 4, Livermore Software Technology Corporation (LSTC) completed Milestone #2 (Meso-Scale Computational Predictions) on January 30, 2015. A meso-scale material model was developed and validated using uniaxial tensile data for QP980 steel. Because of the implemented sub-optimization loops, the predicted tensile curve was in general agreement with the experimental QP980 tensile data provided by Clemson University. This milestone effectively demonstrates successful assembly of the crystal plasticity model (CPM) and state variable (homogenized) model (SVM).
- The Auto/Steel Partnership (A/SP) contracted with CanmetMATERIALS (CMAT) to cast, hot roll, and cold roll two 3GAHSS alloys for evaluation. CMAT successfully cold-rolled two alloys, labeled CMAT medium manganese (Mn) 2 and CMAT quench and partition (Q&P) 2, which have mechanical properties close to those specified in the U.S. Department of Energy (DOE) funding opportunity announcement (FOA) for the high-strength, exceptional ductility and the exceptional ductility, high-strength steels.
- In collaboration with Argonne National Laboratory, Pacific Northwest National Laboratories (PNNL), Clemson University, and General Motors coupled digital image correlation (DIC) with the laboratory's synchrotron high-energy x-ray diffraction to measure the in-situ phase transformation of the retained austenite to martensite as a function of strain for the QP980, CMAT medium Mn 2 and CMAT Q&P 2 steels. This work has been integrated into the assembled material models for QP980, enabling the models to accommodate for phase transformation during deformation.
- PNNL, Clemson University, Michigan State University (MSU), LSTC, and A/SP worked together to implement the T-component forming model in the LS-DYNA® software and then integrate it with the assembled material models. This rudimentary ICME model has not yet been validated. The work for accomplishing this is expected to be completed later during the third year of the project.
- A/SP, AK Steel Corporation (AK Steel), and Ford Motor Company designed and built a T-component die for validating forming simulations based on the T-component design. Many T-component forming simulations were run to determine the blank geometries and features for two scenarios: a best-case scenario and worst-case scenario. These best-case scenarios will produce T-components that meet intended dimensions, whereas the worst-case scenario would induce fracture in the T-component. These two scenarios will enable the Task 3 team to validate the integrated material and forming models, starting with the baseline material and ending with 3GAHSS.
- Engineering + Design AG Inc. (EDAG) performed a sensitivity analysis to identify individual component contributions to a 2008 model vehicle side-structure assembly stiffness. This work has enabled the team to determine which components can be reduced in gauge and those for which the gauge should either be maintained or even increased to compensate for gauge reduction elsewhere in the assembly.
- EDAG and General Motors produced a performance neutral side-structure design (Iteration 3 Design) that achieved a 35.8% mass savings (exceeding the FOA target) with an approximately 10% and 20% reduction, respectively, in torsional and bending stiffness. Current work is focused on gauge and design optimization to recover bending and torsional stiffness while maintaining the mass savings.
- Brown University and MSU developed a three dimensional (3D) representative volume element (RVE) for the CMAT medium Mn 2 steel using BlueQuartz Software's Dream.3D software. Work is progressing to produce a 3D RVE for the CMAT Q&P 2 steel, which with the QP980 3D RVE will complete the microstructural characterization of the baseline and 3GAHSS alloys and will enable simulations under complex loading.

- Clemson University completed the following during this period of performance:
  - Completed extraction of full forming limit curves for QP980
  - Completed cyclic loading tests (tension and compression) for QP980
  - Measured the retained austenite volume fraction (RAVF) evolution with plastic strain for QP980 (in-situ of tensile deformation and DIC)
  - Measured the retained austenite volume fraction evolution with plastic strain for 10% Mn steel (in-situ of tensile deformation and DIC)
  - Characterized the tensile flow behavior for the 10% Mn steels developed at the Colorado School of Mines (CSM)/AK Steel and CMAT
  - Characterized the initial microstructure and texture for QP980, CSM/AK steel 10% Mn steel, and CMAT 10% Mn steel
  - Completed development of a set of flow curves for QP980 at different strain rates from a quasi-static to very high rate.

Future Directions

- The Task 2 Team (A/SP) will complete the manufacturing of the 3GAHSS sheet at CMAT.
- With material characterization of the baseline QP980 steel mostly complete, the project will focus on characterizing the 3GHASS produced in the project, CMAT medium Mn 2 and CMAT Q&P 2 steels. Results from this testing will direct material and forming model development and calibration for 3GAHSS.
- Once the ICME model has been calibrated for each 3GAHSS, the team will use the model to predict microstructure-based flow curves for the two FOA-specified 3GAHSS. The project will then seek options to manufacture 3GAHSS with the predicted microstructures to validate the 3GAHSS ICME model.
- The Task 2 team will continue to develop, calibrate, and validate microstructure-based fracture models for QP980 and 3GAHSS. Validated models will be integrated with existing material and forming models.
- The T-component die will be used to validate and calibrate the modified assembled material models (i.e., plastic flow, fracture, and austenite transformation), the forming models, and the preliminary ICME 3GAHSS model. Work will initially start with the baseline QP980 steel before progressing to the 3GAHSS. Validation of the preliminary ICME 3GAHSS model and forming model will be documented in Milestone #3 (Macroscopic Constitutive Models) and Milestone #4 (Initial Forming Model), which are both due January 31, 2016.
- The Task 5 Team will continue to perform gauge and shape optimization of the “Iteration 3” design to recover the stiffness but maintain mass savings. The goal is to deliver a final 3GAHSS side structure design that meets all baseline performance criteria and achieves the target 35% mass savings.
- The Task 5 team will verify the baseline and 3GAHSS side structure joining strategy and document this accomplishment in Milestone #6 (Estimated Joint Properties) due July 31, 2016.
- The combined Task 4/Task 6 team will continue to refine integration of the material and forming models and begin the process of developing the 3GAHSS ICME model user guide.
- The Task 7 team will assess the cost of the two 3GAHSS alloys. Upon completion of the optimized 3GAHSS side structure design, the team will apply the costs to the technical cost model and determine the cost per pound of weight saved versus the baseline design cost.

Technology Assessment

- Target: Model elements must be within 15% of experimental results and the optimized 3GAHSS assembly must achieve 35% weight savings at a cost of no more than $3.18 per pound of weight savings.
- Gap: There is no existing ICME framework that ties together all length scale computer models with forming simulation, fracture modeling, and vehicle design optimization, especially with low and high-level optimization loops. Although a linear input/output connectivity can be achieved between the length-scale material models, the optimization loops will require significant coding that may be complicated by disparate codes used in the individual models.
- Gap: Boundary conditions have been applied to model elements to facilitate assembly and integration within the project's 4-year duration. For example, the number of solutes to be evaluated has been limited, inclusions and precipitates are largely ignored (although they have been measured with atom probe tomography at PNNL for QP980), and dislocation dynamics are superficially treated. These gaps are all opportunities for necessary future work and model improvement, but these boundary conditions (and dissipative processes such as friction in stamping) may adversely affect the model's accuracy.
- Gap: Mass savings targets are aggressive and it is unknown if these targets can be achieved with the selected subassembly using the two proposed FOA 3GAHSS grades while maintaining subassembly performance. Aggressive gauge optimization, joint elimination, and novel shape optimization may be needed. If so, this may create component designs that meet the weight savings target but are difficult and costly to manufacture. The project will assess the formability of optimized component designs through forming simulations.
- Gap: Phase transformations as a function of strain, strain path and complex deformation, and hardening mechanisms (such as twinning) have not been previously modeled. Furthermore, test methodologies may not exist to develop sufficient constitutive information for modeling. The project will adapt the models to accommodate the gaps and document any unresolved technical gaps as opportunities for future work.
- Target: Two different 3GAHSS are defined by the FOA, exceptional strength and high ductility (i.e., >1,500 megapascals [MPa] ultimate tensile strength; >1,200 MPa yield strength; and >25% elongation) and high strength and exceptional ductility (i.e., >1,200 MPa ultimate tensile strength; >800 MPa yield strength; and >30% elongation).
- Gap: The ICME model will predict the microstructural constituents needed to meet the target mechanical properties; however, process development (e.g., melting, rolling, intermediate heat treatments, and finishing) may be needed to produce sheet steel with the predicted microstructure. The project will leverage the expertise of steel industry project participants to guide process development using laboratory size heats to develop a process that can achieve the predicted microstructure.

Introduction

The program's goal is to successfully demonstrate the applicability of ICME for development and deployment of 3GAHSS for immediate weight reduction in passenger vehicles. The ICME approach used in this project will accelerate development and widespread deployment of 3GAHSS through modeling of multiscale metallurgical, thermal, and mechanical processes in coil sheet development to automotive part and assembly manufacturing and, ultimately, in vehicle performance. By integrating a suite of comprehensive, science-based computational models at different length scales in the ICME environment, this project will demonstrate to end users in the automotive and steel industries that immediate cost-effective weight savings can be achieved with 3GAHSS and that the ICME framework will support a reduced development to deployment lead time in all

lightweight materials systems. The product of this proposed effort will be a simulation toolset and computational infrastructure composed of material models and associated validation data at different length scales, along with the software and application programming interfaces developed by the project team.

The project faces three distinct challenges: (1) to develop an ICME model, (2) to develop viable 3GAHSS sheet, and (3) to optimize an automotive design concept for a material that does not yet exist. Figure III-9 illustrates the relative values for the QP980 steel and the two DOE targets for 3GAHSS. Although the manufacturing of 3GAHSS is not a deliverable of this program, DOE proposed two 3GAHSS grades with the mechanical properties listed in Table III-3 as targets for the program: neither of these materials exists in the commercial domain; therefore, they were initially unavailable to the project. The project began the task of adapting existing material models for steel by selecting an advanced high-strength steel grade, QP980, which has mechanical properties on the cusp of the 3GAHSS envelope. The QP980, with its mixed ferrite, martensite, and metastable retained austenite microstructure will (1) facilitate identification of relevant constitutive parameters for each length scale material model, (2) provide a means to validate these models, and (3) help define the microstructural elements that will be needed for 3GAHSS.

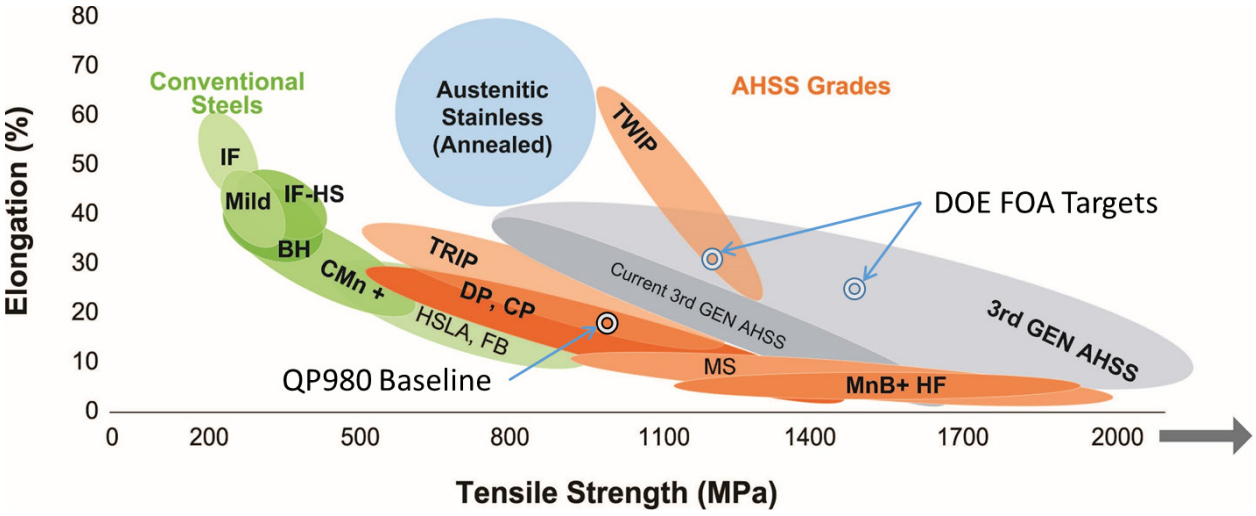

Figure III-9: 3GAHSS mechanical properties with baseline QP980 Steel and DOE FOA 3GAHSS targets (background image courtesy of SMDI and World AutoSteel).

Table III-3: 3GAHSS types specified in FOA.

Ferrous Sheet Metal Type	Yield Strength (MPa)	Tensile Strength (MPa)	Total Elongation (Uniaxial Strain to Failure)	Uniform Elongation
High-Strength, Exceptional Elongation	≥800	≥1,200	≥30%	≥20%
Exceptional Strength, High Ductility	≥1,200	≥1,500	≥25%	≥8%

A baseline sub-assembly from a 2008 model year production sedan was identified to demonstrate the potential benefits of 3GAHSS in reducing automotive component and assembly weight. The baseline assembly will be fully characterized in terms of weight, cost, and performance criteria. An iterative design optimization process of gauge and shape optimization will be applied to the baseline assembly by substituting 3GAHSS for advanced high-strength steel and developing a 3GAHSS design that can meet the proposed weight savings target listed in Table III-4. Coupled with design optimization are forming modeling and simulation, fracture modeling and simulation, and technical cost modeling to assess the manufacturability, performance, and cost of the different design iterations, with the goal of achieving the cost targets listed in Table III-4 without compromising component and assembly performance.

Table III-4: DOE FOA weight and cost targets.

Vehicle System	System Definition	Weight Reduction Target	Cost per Pound of Weight Saved ($/lb saved)
Body	Body-In-White, Closures, Windows, Fenders, and Bumpers	≥35%	≤3.18/lb

Work to integrate the material, forming, fracture, and cost models with design optimization will span the entire length of the program. The primary project deliverable includes an ICME model and user guide to enable users to run the model. The objective is to create an ICME model capable of predicting part and assembly properties from the sheet properties and process history within 15% accuracy at all length scales that will enable the baseline structure to meet the specified weight and cost targets.

The challenges of this program require significant academic and cross-industry expertise and regular communication and collaboration between these parties to make the integration component of the project successful. The project is highly leveraged with expertise from the participants shown in Table III-5, supporting the entire lifecycle of material, process, and product development. Prior collaboration between these project participants through the United States Automotive Materials Partnership and A/SP provides a unique and successful foundation for addressing the technical challenges of this program.

Table III-5: Project participants.

Universities/National Laboratories	Industry	Consortiums
Brown University	FCA US LLC	A/SP
Clemson University	Ford Motor Company	United States Automotive Material Partnership
Colorado School of Mines	General Motors Company	
PNNL	ArcelorMittal	
Ohio State University	AK Steel	
University of Illinois Urbana-Champagne	Nucor Steel Corporation	
	U.S. Steel	

Approach

The project has been structured with the following seven tasks:

- Task 1: Project Management and Planning
- Task 2: Model Development and Model-Level Validation
- Task 3: Forming: Component-Scale Performance Prediction and Validation
- Task 4: Assembly
- Task 5: Design Optimization
- Task 6: Integration
- Task 7: Technical Cost Modeling

Development, calibration and validation of an ICME 3GAHSS model is a simultaneous six-stage process as follows:

1. The first stage is calibration and assembly of material and forming models based on a baseline steel with mechanical properties close to that of 3GAHSS. This project selected QP980 as the baseline steel, which has properties just outside of the tensile strength/elongation space that defines 3GAHSS (see Figure III-9).
2. The second stage is to produce steels with mechanical properties that meet the definition of 3GAHSS in order to further develop and calibrate the material and forming models for 3GAHSS.
3. The third stage is to calibrate the material and forming models for 3GAHSS and assemble them into a rudimentary ICME model.
4. The fourth stage is to use the ICME model to predict the microstructures needed for two 3GAHSS steels specified in the DOE FOA; an exceptional strength, high ductility steel (i.e., 1,500 MPa tensile strength and 25% total elongation) and a high-strength, exceptional ductility steel (i.e., 1,200 MPa tensile strength and 30% total elongation).
5. The fifth stage is to validate the ICME model predictions by producing the two predicted 3GAHSS steels and verifying that the steels have the mechanical properties specified in the FOA.
6. Lastly, the project has to demonstrate the mass savings potential of the 3GAHSS by optimizing the design of a minimum of four advanced high-strength steel components in a 2006 model year or later a baseline assembly. The optimized design must achieve a 35% or greater mass savings at no more than $3.18 per pound weight saved. This project selected the side structure from a 2008 model year production vehicle as the baseline assembly.

The project deliverables include an ICME model, a user guide, and an associated material database.

Results and Discussion

FY 2013 Report (February 1, 2013 to September 30, 2013)

The first year of the program developed the framework for assembling the length scale material models; identified the steel pathways, chemistries, and processing recipes for making a 3GAHSS sheet into the DOE mechanical property targets; and coordinated testing needed to further develop material, form models, and prepare for the validation phase in subsequent years.

QP980 steel was identified as the baseline material for initial 3GAHSS model development. Under Task 2, the experimentalist at Brown University and Clemson University began characterizing the QP980 steel and provided test results to the modelers at the University of Illinois at Urbana-Champaign, MSU, and PNNL. A key accomplishment during this period was development of 3D RVEs, which should improve the accuracy of the CPM because 3D RVEs can better account for material anisotropy than two-dimensional RVEs.

Additional steels with mechanical properties within the tensile strength/elongation space were needed for further model development during the second year. Using prior literature studies, CSM identified two pathways (i.e., a quench and partitioning [QP] process and a transformation-induced plasticity [TRIP] process), which were expected produce 3GAHSS with the mechanical properties of the specified DOE FOA 3GAHSS steels (see Table III-3). CSM proposed steel chemistries and processing recipes, which were approved by the steel expert team as reported in Project Milestone #1. The team then began evaluating laboratories to produce 3GAHSS sheet using the approved recipes.

During Task 4, A/SP outlined the process for assembling the material models and integrating these models with forming simulation, fracture simulation, design optimization, and technical cost modeling. LSTC, which began work toward the end of the first project year, started preparing an ICME user interface using LS-OPT, a

software system capable of integrating computer models. Concurrently, LSTC worked with MSU and PNNL to identify the input and output variables for both the CPM and SVM in preparation for assembly into an ICME model.

Under Task 5, EDAG and A/SP identified the 2008 model year side structure sub-assembly from a production donor vehicle as the baseline assembly for which to demonstrate the potential of 3GAHSS materials to lightweight automotive components and assemblies without compromising vehicle performance (i.e., Project Milestone #7). To eliminate joining as a variable in design optimization, the team decided to apply spot welding with adhesive bonding for all joints in the baseline and optimized designs, which, if unchanged by the end of the program, will satisfy Project Milestone #6. A technical cost model was created and applied to the baseline assembly and will be applied to the optimized design for a cost comparison when complete (Project Milestone #11).

FY 2014 Report (October 1, 2013 to September 30, 2014)

During the second year, the project initially focused on experimentation, creating 3GAHSS steels, material and forming model development, and characterizing performance of the baseline side structure assembly against defined load cases. Toward the end of the second year, the project began calibrating material models and assembling the models within a previously defined ICME infrastructure.

Task 2 continued to characterize the baseline QP980 steel. Data derived from experimentation were used to refine and calibrate the material models and the CPM and SVM models. The ABAQUS-based, user-defined material model and solid finite element material models were translated into LS-DYNA in preparation for assembly in Task 4. The SVM was a finite element-based model originally constructed for solid elements. To enable the model's use in performance modeling, the team adapted the model for shell elements.

Also under Task 2, the project produced interim 3GAHSS sheet at AK Steel using the 3GAHSS recipes provided by CSM in the first year. The mechanical properties of the two alloys, which were labeled "AK Steel Medium Mn 1" and "AK Steel Q&P 1," were close to the specified DOE FOA mechanical properties of the "exceptional strength, high ductility" and "high-strength, exceptional ductility" 3GAHSS, respectively. The project team then contracted with CMAT to produce 3GAHSS strips using the same recipes as CSM. CMAT could provide wider strips than AK Steel and produce greater quantities, which would be needed for comprehensive material characterization. The purpose of the interim 3GAHSS heats was to further develop the material models and calibrate them for 3GAHSS.

Meanwhile, the Task 3 team identified a component-based forming model that is based on a T-component design. The T-component provided features that would enable simulation of multiple strain paths and fracture and would enable validation of assembled material model output.

As the QP980-based CPM and SVM models matured, the Task 4/6 team began the process of assembling the two models using LS-OPT under the predefined ICME infrastructure. The assembled material model was validated when the predicted uniaxial polycrystalline flow curve for QP980 was found to closely approximate the experimentally derived uniaxial flow curve. This accomplishment was later documented in Milestone #2, "Meso-scale Computational Predictions," delivered on January 30, 2015.

The Task 5 team defined the load cases for the side structure and then assessed the performance of the side structure against the defined load cases, which was documented in National Energy Testing Laboratory Milestone #2 (Baseline Assessment Complete), which was delivered on September 30, 2014.

FY 2015 Report (October 1, 2014 to September 30, 2015)

During this period of performance, the project began producing 3GAHSS steels. Work was still mostly focused on characterizing QP980, but testing of 3GAHSS was ramped up as coupons became available from AK Steel and CMAT. The material models continued to be refined as additional experimental QP980 data were made available; a forming model was developed based on the T-component design culminating in the

design and building of a T-component die for forming model validation; and the two 3GAHSS alloys were substituted into the baseline design, yielding a performance neutral 3GAHSS design (called Iteration 3) that met the mass savings target specified in the DOE FOA. This work is explained in greater detail below.

In June, United States Automotive Materials Partnership signed a Cooperative Research and Development Agreement with the National Institute of Standards and Technology to utilize their dSpace data repository for the curating and storage of project data. The project intends for this repository, which will be made public after project completion, to be the "ICME material database" deliverable specified in the FOA.

CMAT successfully cast, hot rolled, and cold rolled the two recipes developed by CSM and validated by AK Steel. The mechanical properties were similar but slightly different between those made at CMAT and those made at AK Steel (see Table III-6); however, all were within the tensile strength/elongation space that defines 3GAHSS (see Figure III-10). This accomplishment showed that the 3GAHSS recipes were scalable from AK Steel's 50-lb heats to CMAT's 450-lb heats. Furthermore, CMAT's processing equipment was closer to production equipment, suggesting the potential that these alloys could be manufactured on a commercial scale. Only one-third of the cast ingots had been processed at CMAT during the remainder expected in the following quarter. Characterization will progress into the next fiscal year.

Table III-6: Summary of AK Steel and CMAT 3GAHSS mechanical properties.

Steel Alloy	Yield Strength MPa	Ultimate Tensile Strength (MPa)	Tensile Elongation	Uniform Elongation
High-Strength, Exceptional Ductility	≥800	≥1,200	≥30%	≥20%
AK Steel Medium Mn 1	750	1,200	37	34
CMAT Medium Mn 2	693	1,042	35%	
Exceptional Strength, High Ductility	≥1,200	≥1,500	≥25%	≥8%
AK Steel Q&P 1	830	1,432	17%	
CMAT Q&P 2	1,218	1,538	19%	15%
	Color Code	Target	Below Target	Met Target

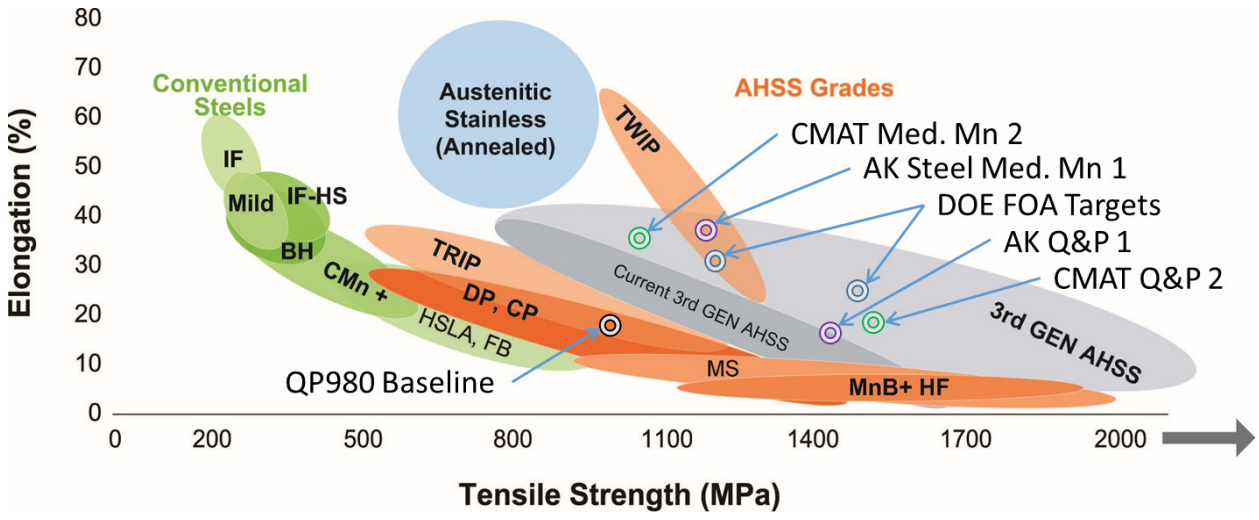

Figure III-10: 3GAHSS mechanical properties with baseline QP980 steel and DOE FOA 3GAHSS targets (background image courtesy of SMDI and World AutoSteel).

Brown University and MSU worked together to create 3D RVEs for the 3GAHSS. In July, MSU was trained in the use of DREAM 3D, which enables a simplified means of constructing 3D RVEs compared to the process used in the first and second year of the program to design a 3D RVE for QP980. As of this report, a 3D RVE had been constructed for the AK Steel Medium Mn 1 steel, which was the first iteration of the TRIP recipe from CSM. A 3D RVE for the AK Steel Q&P 1 steel is expected in the following quarter.

In August, the MSU principal investigator and his team transferred to Ohio State University (OSU). All incomplete work was transferred from MSU to OSU. There is no expected impact on the timing of the project deliverables or milestones.

During this period, PNNL, Clemson University, and General Motors successfully combined DIC with high-energy x-ray diffraction testing to measure the in-situ transformation of retained austenite to martensite as a function of strain for three materials: QP980, CMAT medium Mn 2, and CMAT Q&P 2. Figure III-11 and Figure III-12 show the retained austenite volume fraction as a function of strain for the QP980 baseline steel and CMAT medium Mn 2 steel. The ability to predict phase transformations as a function of strain in a multiphase steel is a first and is expected to dramatically improve the predictive capability of the 3GAHSS ICME model. The work on QP980 has been integrated into the assembled material models, and validation of the modified assembled models will be done through forming trials in Task 3.

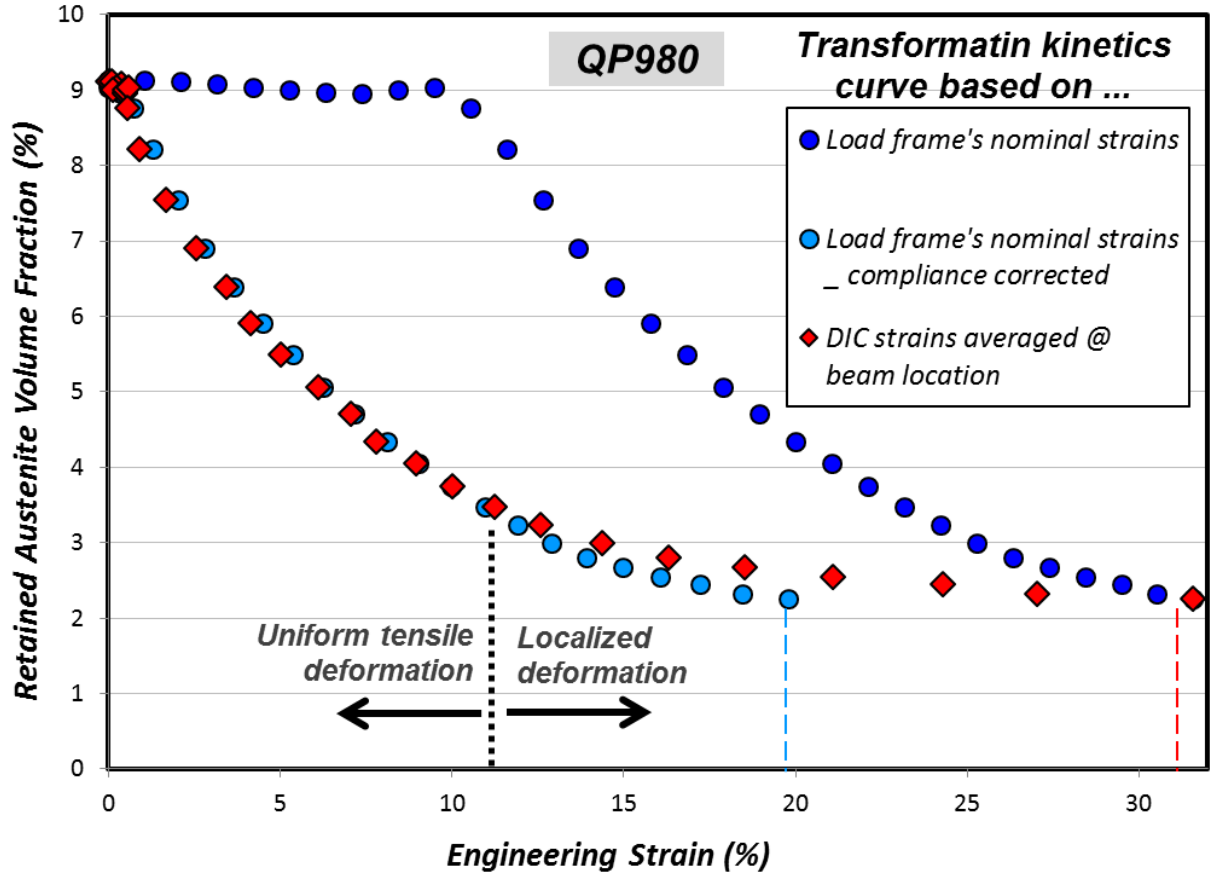

Figure III-11: Retained austenite volume fraction measurements with DIC in-situ of tensile deformation and high-energy x-ray diffraction - QP980.

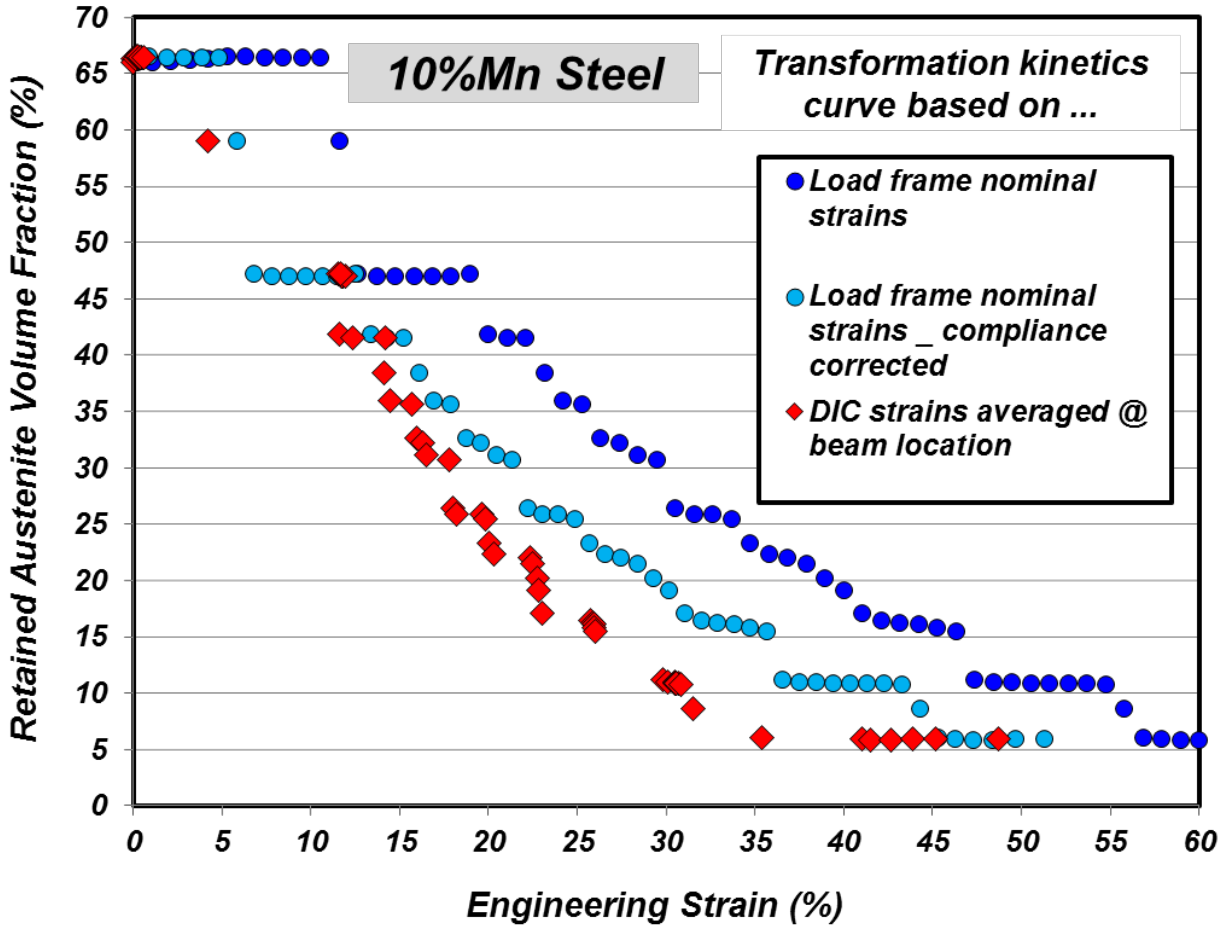

Figure III-12: Retained austenite volume fraction measurements with DIC in-situ of tensile deformation and high-energy x-ray diffraction - CMAT medium Mn 2.

The Task 4 team integrated the modified assembled material models with the T-component forming model. In theory, this preliminary ICME model should be able to predict as-formed component properties. Validation of the preliminary ICME model will be done through forming trials in Task 3.

The Task 3 team (i.e., A/SP, AK Steel, and Ford Motor Company) designed and built a forming die (Figure III-13) based on the T-component design. The die will be used for forming trials that will assist in the development of the forming model, validation of the forming model, and validation of the modified assembled material models. Two T-component QP980 blanks have been gridded, formed, and strain mapped. In the following quarter, the Task 3 team will identify areas of interest with respect to strain and strain paths, measure the amount of retained austenite remaining, and compare the results against model predictions. The work will either validate the modified assembled material models or will be useful in further development and calibration of the models.

Additionally, the Task 3 team has performed a number of T-component forming simulations to determine the blank geometries and features for two scenarios, a best-case scenario, and a worst-case scenario. The best-case scenario is expected to produce T-components that meet intended dimensions without cracks, whereas the worst-case scenario is expected to induce failure in the T-component. These two scenarios will enable the Task 3 Team to validate the integrated material and forming models, starting with the baseline material, which when successful will satisfy Milestone #4 (Initial Forming Model).

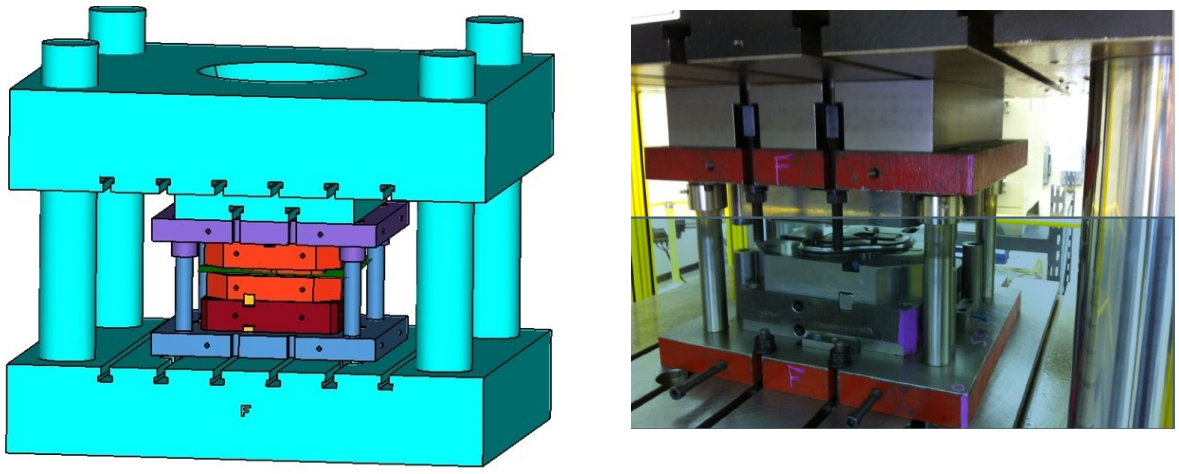

Figure III-13: T-component die schematic and installed at AK Steel.

The Task 5 team began preparations for design optimization by conducting a sensitivity analysis to determine each individual side structure component's contribution to assembly stiffness. This analysis has assisted the design team in identifying those components that can be reduced in gauge and those that might need to be increased in gauge to enable gauge reduction in other components. Upon completion of the sensitivity analysis, the team began substituting the two 3GAHSS materials into the side structure assembly and generated a 3GAHSS design (that was labeled "Iteration 3;" see Figure III-14) that had the same performance as the baseline design. However, it achieved a 35.8% mass savings (exceeded the FOA target) with an approximately 10% and 20% reduction, respectively, in torsional and bending stiffness. Current work is focused on gauge and design optimization to recover bending and torsional stiffness while maintaining mass savings.

Figure III-14: Iteration 3 of the 3GAHSS side structure design showing the components for which the two 3GAHSS alloys were substituted, which yielded a 35.8% mass savings over the baseline design. The outer panels were not changed due to surface finish requirements.

During this period, the material models will continue to evolve, which will require adjustments in the model assembly. LSTC will adapt the model's assembly and refine the user interface accordingly. Successful validation of the modified assembled model through forming trials should satisfy Milestone #3(Macroscopic Constitutive Models) and will mean that the model is sufficiently advanced to enable prediction of mechanical properties as a function of microstructure.

Technology Transfer Path

The primary deliverable of this program is an integrated computer model with a user guide. The software will include a high-level description of the integrated models, along with a description of input variables, output variables, state variables, and relational databases implemented within the final software deliverable. The user's manual will provide an overall description of the user implementation approach for the software.

During development of the ICME model, the project will be developing test methodologies for evaluating and characterizing 3GAHSS (such as nano-hardness testing, micro-pillar, bulge testing, sheet tension-compression, and measurement of austenite-to-martensite transformation with strain). If the results from these tests can be correlated to macroscopic bulk materials properties testing, then these tests are expected to be adopted for future work and, potentially, for industry standardization.

Additionally, if the individual length scale material models show a high degree of accuracy, these models will be adopted by industry and academia for expansion and refinement to cover additional steel processing paths. Primary users of the technology are engaged in this project, which is expected to speed the implementation of results and lessons learned.

Conclusion

The project is currently on schedule to meet all project milestones and deliverables. The project has a number of notable accomplishments this fiscal year, which include making two 3GAHSS alloys with mechanical properties near the DOE FOA targets, successful assembly and calibration of the material models to the baseline QP980 steel, integration of material and forming models, design and building of a T-component die for material and forming model validation, and development of a 3GAHSS side structure design that achieved the 35% mass savings target. These accomplishments were made possible by significant communication and collaboration between project participants.

Work during the next fiscal year will focus on characterization of the two 3GAHSS, calibration of the developing ICME model using two interim 3GAHSS alloys, and gauge and shape optimization of the 3GAHSS side structure design to recover stiffness without sacrificing mass savings. The project will continue to emphasize the need for frequent communication between project participants and participation in project coordination and integration team meetings to ensure effective interaction between tasks for delivery of a comprehensive 3GAHSS ICME model upon project completion.

References

None.

Bibliography

Abu-Farha, F.; Alturk, J.; Hu, S.; Mates, W.; Luecke, L.; Zhang, J.; Carsley, J.; Ming, C.; and Hector Jr., L., 2015, "A Quantitative Comparison between Deformation Measurements with Different Digital Image Correlation Systems: Are we Reading the Same Strains?" presented at the 2015 Society of Automotive Engineers World Congress.

Choi, K. S.; Zhu, Z.; Sun, X.; DeMoor, E.; Taylor, M. D.; Speer, J. G.; and Matlock, D. K., 2015, "Determination of carbon distribution in quenched and partitioned microstructures using nanoscale secondary ion mass spectroscopy," *Scripta Materialia*, 104, pp. 79-82.

Choi, K. S.; Hu, X.; Sun, X.; Taylor, M. D.; DeMoor, E.; Speer, J. G.; and Matlock, D. K., 2015, "Development of Q&P steels with improved performance based on microstructure-based finite element modeling method," presented in *ICME 2015.*

Choi, K. S.; Zhu, Z.; Sun, X.; DeMoor, E.; Taylor, M.; Speer, J.; and Matlock, D., 2015, " Determination of carbon distribution in a quenched and partitioned steel using nanoscale secondary ion mass spectroscopy and electron backscatter diffraction," presented at the *International Conference on Secondary Ion Mass Spectrometry*.

Hector, Jr., L., 2014, "Integrated Computational Materials Engineering (ICME) Approach to Development of Lightweight 3GAHSS Vehicle Assembly," presented at the *A/SP Technology Days*.

Hector, Jr., L., 2015, "Integrated Computational Materials Engineering (ICME) of Generation Three Advanced High Strength Steels," presented at the *TMS Third World Congress on Integrated Computational Materials Engineerin*g.

Hu, J.; Abu-Farha, F.; Hall, J.; and Hector Jr., L., 2015, "Investigation of Temperature Effects on the Tensile Deformation Characteristics of a Quenched and Partitioned Steel using Digital Image Correlation," presented at the *2015 TMS Annual Exhibition*.

Hu, J. and Abu-Farha, F., 2015, "A Comparison between Different Digital Image Correlation based Techniques for Determining the Forming Limits of Sheet Metals," presented at the *2015 Society of Automotive Engineers World Congress*.

Hu, J. and Abu-Farha, F., 2015, "Adiabatic Heating and Its Effects on Material Deformation during Stamping of Quenched and Partitioned Steel," presented at the *2015 Society of Automotive Engineers World Congress*.

Hu, J. and Abu-Farha, F., 2015, "On the Use of Digital Image Correlation for Studying Deformation and Failure of Lightweight Materials at Various Temperatures and Rates," presented at the *2015 Society of Automotive Engineers World Congress*.

Hu, J. and Abu-Farha, F., 2015, "Developing the Forming Limit Curves for QP980 Steel Sheets," presented at the *2015 Society of Automotive Engineers World Congress*.

Hu, J.; Zhang, N.; and Abu-Farha, F., 2015, "Revealing Dynamic Banding during High Temperature Deformation of Lightweight Materials using Digital Image Correlation," presented at the *Society of Experimental Mechanics 2015 Annual Conference*.

Matlock, D.; Thomas, L. S.; Taylor, M. D.; De Moor, E.; and Speer, J., 2015, "Microstructural Developments Leading to New Advanced High Strength Sheet Steels: A Historical Assessment of Critical Metallographic Observations," The 2015 IMS Henry Clifton Sorby Award Lecture. The abstract citation is *Microsc. Microanal.,* 21 (Suppl 3), pp. 5-6.

Mates, S. and Abu-Farha, F., 2015, "Dynamic Tensile Behavior of a Quenched and Partitioned High Strength Steel using a Kolsky Bar," presented at the *Society of Experimental Mechanics 2015 Annual Conference*.

Poling, W.; Savic, V.; Hector, Jr., L. G.; Sachdev, A. K.; Hu, X.; Devaraj, A.; Sun, X.; and Abu-Farha, F., 2015, "Combined Synchrotron X-ray Diffraction and Digital Image Correlation Technique for Measurement of Austenite Transformation with Strain in TRIP-assisted Steels," prepared for the *Society of Automotive Engineers*.

Rana, R.; Gibbs, P. J.; De Moor, E.; Speer, J.; and Matlock, D., 2014,"A Composite Modeling Analysis of the Deformation Behavior of Medium Manganese Steels," *Steel Research International, Special Issue: High Manganese Steels*, 86(10), pp. 1139-1150.

Rana, R.; Gibbs, P. J.; De Moor, E.; Speer, J.; and Matlock, D., 2015, "A Composite Modeling Analysis of the Deformation Behavior of Medium Manganese Steels," *Steel Research International*, 85, currently available on-line DOI: 10.1002/srin.201400577.

Rana, R.; De Moor, E.; Speer, J.; and Matlock, D., 2015, "Austenite Stability Controlled Mechanical Behavior of a Medium Manganese Transformation Induced Plasticity Steels," presented at *International Conference on Frontiers in Materials Processing, Applications, Research & Technology (FiMPART'15)*.

Shen, Y. F.; Qiu, L. N.; Sun, X.; Zuo, L.; Liaw, P. K.; and Raabe, D., 2015, "Effects of retained austenite volume fraction, morphology, and carbon content on strength and ductility of nanostructured TRIP-assisted steels", *Materials Science and Engineering A*, 636, pp 551-564.

Stander, N.; Basudhar, A.; Basu, U.; Gandikota, I.; Savic, V.; Sun, X.; Choi, K.S.; Hu, X.; Pourboghrat, F.; Park, T.; Mapar, A.; Kumar, S.; Ghassemi-Armaki, H.; Abu-Farha, F.; and Chen, M., 2015, "Multi-scale

parameter identification using LS-DYNA and LS-OPT," *Proceedings of the 10th European LS-DYNA Conference*.

Thomas, G., 2015, "ICME 3GAHSS Lab Heat Results Supporting DOE Targets," presented at the *Great Designs in Steel,* Laurel Manor Conference Center, Livonia, Michigan.

III.3. Industrial Scale-Up of Low-Cost Zero-Emissions Magnesium by Electrolysis – INFINIUM, Inc.

Project Details

Adam C. Powell, IV, Principal Investigator
INFINIUM, Inc.
3 Huron Drive
Natick, MA 01760
Phone: 781-898-3430
E-mail: apowell@infiniummetals.com

Aaron Yocum, Project Officer
National Energy Technology Laboratory
3610 Collins Ferry Road
Morgantown, WV 26507
Phone: 304-285-4852
E-mail: Aaron.Yocum@netl.doe.gov

William Joost, Technology Area Development Manager
U.S. Department of Energy
1000 Independence Avenue, SW
Washington, DC 20585
Phone: 202-687-6020
E-mail: william.joost@ee.doe.gov

Contractor: INFINIUM, Inc.
Contract No.: DE-EE0005547

Executive Summary

Direct electrolysis of magnesium oxide (MgO) has been a dream of the magnesium (Mg) industry for decades. Today's electrolysis plants use carbochlorination or hydrochlorination with chloride dehydration to convert low-cost MgO to pure anhydrous magnesium chloride ($MgCl_2$) and electrolyze that to produce Mg metal and chlorine gas (Cl_2) [1]. Direct MgO electrolysis would eliminate the anhydrous $MgCl_2$ production step, which is energy and capital intensive and can produce harmful dioxin and furan emissions. MgO electrolysis also eliminates the need to contain or compress chlorine gas, which often escapes as a pollutant. MgO electrolysis also uses less energy due to the lower formation enthalpy of MgO versus $MgCl_2$.

The INFINIUM MagGen™ system performs this direct MgO electrolysis. This process dissolves MgO in a molten salt, then applies a direct current potential across the salt, producing Mg at the cathode and oxygen gas at the solid electrolyte-sheathed anode interface. The solid electrolyte separates the Mg and oxygen products, preventing back reaction between them. The anode is protected from the harsh molten salt environment, which enables using a variety of inert anode materials such as liquid metals and oxide conductors that are used as solid fuel cell cathodes. Zirconia is a very selective solid electrolyte, such that the oxygen by-product is much more pure than that produced by conventional inert anodes without zirconia protection, such as nickel ferrite.

The overarching objective of this project is to bring the MagGen™ primary Mg production system from a large laboratory demonstration scale to the threshold of industrial production. This energy efficient process produces high-purity Mg directly from low-cost, domestically produced industrial MgO in a single step.

This year, with U.S. Department of Energy input and approval, INFINIUM shifted the near-term goal to production of Mg-rare earth master alloys, particularly alloys with neodymium (Nd). These alloys are used to produce cast alloys such as AE44 that are used in the Chevrolet Corvette engine cradle, WE43, and rolled

stock (sheet) alloys such as ZEK100. These high-value alloys were selected because they provide a value-added niche for initial deployment of this technology in order to prove out production at a small scale, with an eventual goal of deployment for large-scale commodity Mg production.

The success of this project will prepare the technology for the process' industrial implementation by reducing costs, energy use, and emissions associated with Mg production. The resulting low-cost Mg supply will help vehicle manufacturers realize their goals of reduced weight and increased vehicle efficiency. Improved vehicle recyclability may also result by increasing the value of post-consumer automotive scrap metal.

Toward those ends, this project's tasks during this period were as follows:

1. **Project Management and Reporting**
2. **Design, Build, and Test Prototypes** – Produce fully featured prototypes designed to demonstrate all aspects of the process one with a focus on maximum possible run time and the other at increasing scale
3. **Anode Optimization and Manufacturing** – Optimize zirconia tube composition and structure for this novel application and develop other components, including low-cost charge transfer material and current collector
4. **Make and Test Parts from the Recipient Mg** – Manufacture representative automotive parts from the alloyed Mg product
5. **Mg Plant Cost, Energy, Greenhouse Gas, and Other Emissions Modeling** – Characterize these aspects of the process relative to current practices in automotive materials and Mg competitors.

Accomplishments

- Ran our Alpha 4.0 system for 1,968 hours continuously. This included one electrolysis run with an average current efficiency of 90%.
- Developed and successfully demonstrated a process and completed planning to produce Mg-Nd master alloy for alloying into Mg-rare earth die casting alloy.
- Identified molten salt and oxide feed compositions, anode and cathode materials and geometries, and electrolysis parameters for direct co-deposition of Mg-Nd master alloy.
- Identified suppliers for each component of Mg-rare earth die casting alloy, for Mg-Nd separation, and for storage of pure Mg for alloy production.
- Built and began operating two new furnaces and four new cell designs for producing Mg master alloy and rare earth metal.
- Began manufacturing 1-in. and 1.25-in. outer diameter closed-end zirconia tubes as anode sheaths for the process.
- Tested three different materials for displacing elements to reduce the amount of silver required for electrolysis and fabricated thimbles from the materials.
- Operated the Mg-Nd master alloy electrolysis process at a production rate that will meet the 500-lb goal by the end of the project.

Future Directions

- Follow our plan to increase production of the Mg-Nd master alloy and complete production of a total of 500 lb (227 kilogram [kg]), Mg basis.
- Using that master alloy, produce about 600 lb of Mg die casting alloy containing Nd.
- Produce and test representative automotive parts using this Mg die casting alloy.

Technology Assessment

- Target: Production of a sufficient quantity of Mg for automotive test part casting and testing.
- Gap: Need to expand Mg production rate.
- Target: Achieve profitable economics for Mg and/or Mg alloy production.
- Gap: Need to expand scale to achieve break even in Mg alloy production economics.

Introduction

Mg is an important material for long-term vehicle lightweighting, because it is easily die cast and exhibits significantly higher stiffness/weight than aluminum. Indeed, the Vehma International-Ford Motor Company Multi-Material Lightweight Vehicle Project's Mach II design achieves a 50% vehicle weight reduction versus a 2005 Ford Taurus, in large part, by using more than 50% Mg by weight in the chassis and body-in-white, chassis, closures, and subframes [2].

Unfortunately, the energy use and carbon emissions associated with Mg primary production are both very high (much higher than for aluminum and certainly for steel). In addition, China's produces 85% of the world's Mg, which leads to supply risk. These conditions prevent Mg's widespread adoption in motor vehicles today.

This project is developing a new method called MagGen™ for energy-efficient and low-emissions production of high-purity Mg directly from MgO, which is abundant, low-cost, and produced domestically. Production process by-products include high-purity oxygen gas and waste heat. Both are available for other uses. The primary project objective is to expand the MagGen technology from large laboratory demonstration to the threshold of industrial production.

A secondary project objective is to develop application of this technology to direct production of Mg alloys. To do so will open up higher-value product options to enable short-term profitability of Mg production using this technology.

Approach

INFINIUM has taken a three-pronged approach to technology scale-up. First, techno-economic modeling identified key areas of cost, energy consumption, and emissions; their uncertainty and risk; and the potential for their reduction. Second, several electrolysis cell prototypes run metal production experiments using the zirconia solid electrolyte and/or a proprietary anode. Third, the electrode technology was further developed for production, including new anode and cathode designs and scales.

This year, three new cells were added to the alpha and beta electrolysis cell prototypes: one small cell for early stage experiments and two in new furnaces called gamma and delta. Based on the goal of making Mg-Nd alloys, the small cell ran low-cost electrolysis experiments for factor space exploration. The gamma cell performed neodymium oxide reduction to metal for use as a reactive cathode. Delta has been the initial prototype Mg-Nd master alloy production cell.

As a milestone toward commercialization, this project's goal is to produce 500 lb of Mg from MgO. INFINIUM's final product will be a die casting alloy using the produced Mg, currently planned as WE43, which the project partner will make from our master alloy and other inputs. Project partner Magna-Cosma will die cast that metal into vehicle parts for testing for comparison with Mg made by other technology.

Although early in the year, the project planned to electrowin Mg into a reactive Nd cathode; however, plans were changed instead to directly electrowin both Mg and Nd together as an alloy at an inert cathode [3]. Figure III-15 shows the flow sheet used to make the die casting alloy. The project will produce enough master alloy to

reach the goal of 500 lb of Mg. This will be sent to our project partner, who will distill out most of the Mg, blending some with master alloy. They will then add other inputs to produce the final Mg die casting alloy.

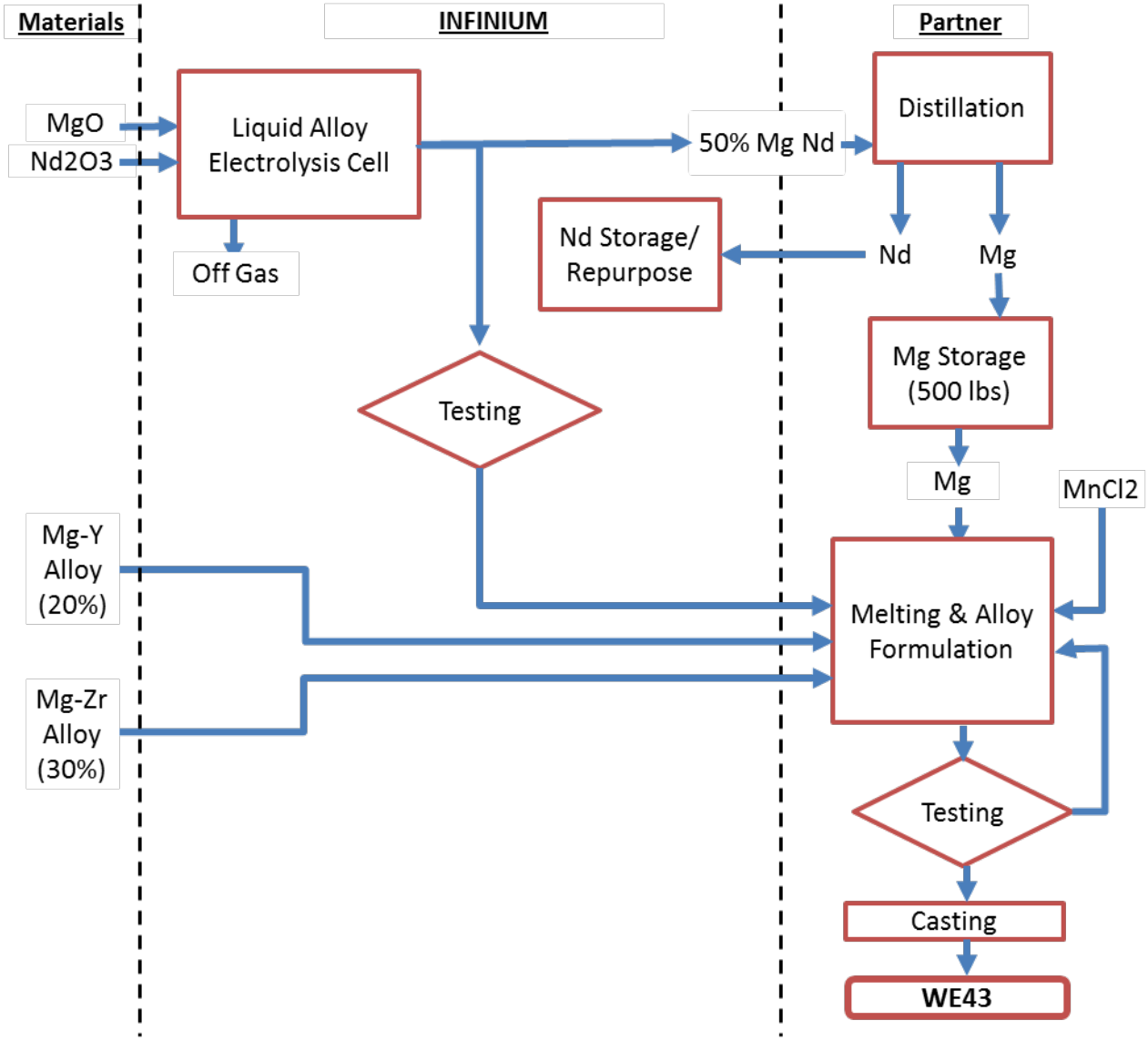

Figure III-15: Flow sheet of Mg die casting alloy production for this project.

Results and Discussion

Zirconia Tube Production

INFINIUM manufactured 1-in. and 1.25-in. outer diameter closed-end zirconia tubes as anode sheaths for the process. The equipment was procured, allowing horizontally firing these larger tube sizes. Ten tubes in these sizes were produced. The ceramics team maintains a record of 100% yield: every green part that went in for firing came out and passed inspection successfully.

Three different porous materials were also tested for displacing elements to reduce the amount of silver required for electrolysis while allowing by-product oxygen gas to pass through. Thimbles were fabricated from the materials, small amounts of silver were placed in those thimbles, and they were heated to 1000 to 1200°C

to melt the silver. Microscopy showed excellent compatibility with liquid silver. Silver did not penetrate into the pores for all three materials.

Figure III-16: Slip casting a 1-in. outer diameter tube.

Pure Mg Vapor Production

The Alpha prototype furnace produces and condenses Mg vapor from MgO at 1150 to 1200°C. This furnace recorded the longest zirconia tube lifetime to date in a 1,968-hour run that operated at about 90% current efficiency. This tube lifetime reached the threshold, where the modeled zirconia tube cost was equivalent to the cost of commercial off-the-shelf graphite anodes.

Magnesium Master Alloy Electrolysis Development

INFINIUM conducted master alloy electrolysis development in four stages. First, a molten fluoride salt composition that is compatible with electrolysis was identified. Second, MgO electrolysis into a liquid Nd cathode was attempted. Third, Mg-Nd alloy was successfully co-deposited from a mixed oxide in the molten salt. Lastly, scale-up production of the Mg-Nd master alloy began. Several electrode configurations, component configurations, and materials were tested in a 10-L capacity cell.

Molten fluoride salt testing began by testing Nd metal compatibility with molten salt compositions. Nd metal was added to a molten salt bath and the mass loss of Nd metal over time due to the reaction was measured:

$$2\ Nd + 3\ MgO \rightarrow Nd_2O_3 + 3\ Mg \quad (1)$$

In three experiments, the Nd metal mass decreased by about 40%, then reached equilibrium with the molten salt.

Nd-Mg metal was then used as the cathode for an MgO electrolysis experiment. Voltage increased in steps from 3 to 5 V. Current and oxygen production rate increased as shown in Figure III-17. This experiment passed 16.8 A-hours of charge and produced 1.6 grams of oxygen, indicating a current efficiency of about 30%.

During this time, INFINIUM built a new cell, labeled gamma, for producing Nd for use as a reactive cathode material. The gamma cell produced about 2 kg of Nd metal. Its use was ceased due to a project approach change. Figure III-18 shows the gamma cell.

After commissioning and starting electrolysis runs in the gamma cell, INFINIUM conducted 12 more experiments on Mg-Nd alloy co-deposition from mixed oxides in the molten fluoride salt. These experiments

varied fluoride salt composition, cathode material, electrolysis voltage, and temperature. At the end of this campaign, we collected sufficient information to select the molten salt and oxide feed compositions, anode and cathode materials and geometries, temperature, and electrolysis parameters required for process scale-up.

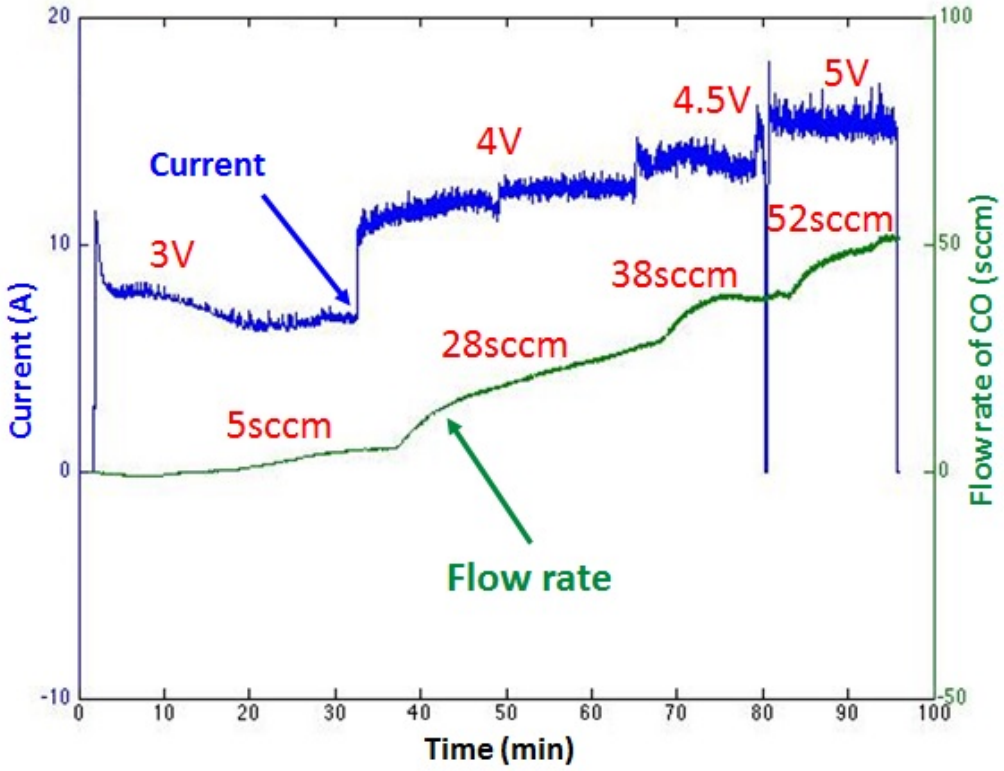

Figure III-17: Current and oxygen flow rate versus time in MgO electrolysis with Nd-Mg alloy cathode.

Figure III-18: Gamma (left) and delta (right) electrolysis cells for Nd and Mg alloy production.

At this point, INFINIUM commissioned a new cell named delta (shown in Figure III-18). The delta cell crucible had approximately a 10-L capacity and its lid had four ports for interchangeable anodes, cathodes, feed or withdrawal apparatus, and/or view ports. This cell ran 14 electrolysis runs over 6 weeks and reached a maximum production rate of about 25 g per hour.

Early experiments used a refractory material to separate the anode and cathode regions. The material swelled in the salt and eventually failed over about a month at temperature. That material was replaced with a new one, whose dam geometry also remained stable for about 1 month. Beyond that, using a metallic separator at the cathode is planned, which draws metal into a small region to facilitate harvesting.

The delta furnace experiments showed that the current efficiency is a strong function of molten salt composition. In 11 of the 14 electrolysis runs, only MgO was added to the molten salt bath, which resulted in a gradual decline in the Nd/Mg ratio. This resulted in an increase, then decrease, in current efficiency. The current efficiency reached its maximum when the product was about 55 weight % Mg.

As of October 30, 2015, INFINIUM had produced a total of 3.9 kg of Mg-Nd alloy. Design and procurement of new components for the delta furnace have begun, which will triple its current and production rate. Two or more 24-L crucibles are planned to be built. This will allow running at a considerably higher throughput to produce at least 500 lb of master alloy (Mg basis) in the coming months. Finally, suppliers for each component of the Mg-Nd die casting alloy have been identified, as well as a partner for Mg-Nd separation and storage of pure Mg for alloy production.

Technology Transfer Path

During the short term, the technology transfer plan involves scaling up the low-cost production of Mg-rare earth master alloy. This is a very important market segment that provides material for high-performance Mg alloys. Rare earth metals have several important effects on Mg, including improved high-temperature tensile and creep strength, reduced corrosion, and reduced flammability. For example, the Corvette engine cradle used AE44 with 4 weight % rare earth metals because of these advantages. Moving forward, ZEK100 alloy sheet is being considered for automotive closures; this will require Mg-Nd master alloys priced at $100 to 200 per kg.

Beyond this high-value market, the developed INFINIUM technology for producing master alloys will require modifications to cost-effectively produce pure Mg for general parts made of aluminum-zinc, aluminum-manganese, and other non-rare earth alloys. This is because at very high Mg fractions, current efficiency in this process decreases dramatically. This issue has barred Mg from using low-cost oxide electrolysis similar to the Hall-Héroult cell, which is used for smelting aluminum.

INFINIUM is developing a new technology to overcome this limitation. This technology is in the planning stage and is outside the scope of the current DOE contract. In the meantime, a great deal can be learnt as the current process is operated at increasing scale to serve the master alloy market.

Conclusion

INFINIUM has nearly completed this project, and has reached some important milestones during the past year. The lifetime of zirconia tubes as anodes has continued to be extended. The project was pivoted to use technology to efficiently generate a new high-margin alloy system that both improves the transition to market and also increases operating efficiency. Dozens of experiments have been run to characterize operation for this new alloy system. The developed technology is close to commercial readiness and will continue to advance as it is used to produce 500 lb of Mg in future efforts.

References

1. Kippouros, G. and Sadoway, D., 2001, “A thermochemical analysis of the production of anhydrous $MgCl_2$,” *J. Light Metals*, 1, pp. 111–117, DOI: 10.1016/51471-5317(01)00004-9.

2. Skszek, T., Wagner, D., Conklin, J., and Zaluzek, M., 2015, "Multi-Material Lightweight Vehicles," presentation at *DOE Vehicle Technologies Office Annual Merit Review*.
3. Soare, V., Gurgu, C., Burada, M., Østvold, T. and Kontoyannis, C., 2006, "Production of a Mg-Nd Alloy by Direct Electrolysis from an Oxyfluoride Melt," *Can. Metall. Quart.*, 45, pp. 153-160, DOI: 10.1179/cmq.2006.45.2.153.

Bibliography

Derezinski, S and Powell, A., 2015, "Scale-Up of Magnesium Production by Fully Stabilized Zirconia Electrolysis," *DOE Vehicle Technologies Office Annual Merit Review*, Arlington, Virginia.

Guan, X.; Su, S.; Pal, U. B.; and Powell, A. C., 2014, "Periodic Shorting of SOM Cell to Remove Soluble Magnesium in Molten Flux and Improve Faradaic Efficiency," *Metall. Mater. Trans.*, 45B, pp. 2138-2144.

Guan, X.; Pal, U.; and Su, S., 2015, "A Method for Improving Faraday Efficiency of Magnesium Production Employing Solid Oxide Membrane (SOM) Based Electrochemical Cells," presented at the *TMS Annual Meeting High Temperature Electrochemistry Symposium*, Orlando, Florida.

Pal, U., 2015, "Green Technology for Metals Production," *TMS Annual Meeting Extraction and Processing Division Distinguished Lecture*, Orlando, Florida.

III.4. High-Strength Electroformed Nanostructured Aluminum for Lightweight Automotive Applications – Xtalic Corporation

Project Details

Shiyun Ruan, Principal Investigator
Xtalic Corporation
260 Cedar Hill Street
Marlborough, MA 01752
Phone: 508-485-9730
E-mail: sruan@xtalic.com

William Joost, Technology Area Development Manager
U.S. Department of Energy
1000 Independence Avenue, SW
Washington, DC 20585
Phone: 202-287-6020
E-mail: william.joost@ee.doe.gov

Executive Summary

The overall project goal is to electroform high-strength nanostructured aluminum alloys (nano-Al) for lightweight automotive applications. The main goals of this 4-year program include (1) build a pilot-scale continuous manufacturing system, (2) electroform materials with properties exceeding U.S. Department of Energy (DOE) targets (i.e., strength >600MPa and ductility >8%), (3) build and test nano-Al vehicle components, and (4) demonstrate economic feasibility for large-scale use. For Fiscal Year (FY) 2015, the engineering design of our electroforming system was completed, methods were developed to analyze various electrolytic bath components, good process control and consistencywas demonstrated, and the properties of nano-Al alloys were validated.

Accomplishments

- Developed methods for analyzing an electrolytic bath (FY 2015).
- Validated mechanical properties of nano-Al (ultimate tensile strength > 600 MPa and ductility > 8%) (FY 2015).
- Completed engineering design of nano-Al sheet electroforming system (FY 2015).

Future Directions

- Build and test nano-Al sheet electroforming system.
- Optimize sheet fabrication rate and bath lifetime.
- Fabricate and test nano-Al sheets, optimize properties, and downselect preferred alloy composition.
- Develop post-fabrication steps (e.g., stamping and joining).
- Fabricate, test, and optimize prototype components.
- Develop and refine economic cost model.

Technology Assessment

- Target: Validate nano-Al sheet manufacturing process on industrial scale.
- Gap: The nano-Al electrolytic bath chemistry and process are unique. The existing process for copper electroplating systems needs to be adapted for Al.
- Target: Materials need to meet full specifications required for target application.

- Gap: Properties such as sheet formability and joining have not been evaluated for nano-Al.
- Target: Integrate nano-Al material into the vehicle component manufacturing process.
- Gap: Potential concerns regarding post-fabrication steps, such as spring-back during stamping and joining methods, need to be addressed.
- Target: Achieve target cost of $2/lb of weight saved.
- Gap: Economic cost model and detailed cost analysis needs to be developed to evaluate the feasibility of commercialization.

Introduction

Xtalic's electrodeposition process is a transformative, disruptive technology that has produced nano-Al sheet materials that dramatically outperform traditional high-strength Al (Figure III-19a), and achieve weight-normalized properties not otherwise available in engineering metals (Figure III-19b) [1,2]. These new materials can enable weight reductions of 50% or more in strength critical applications.

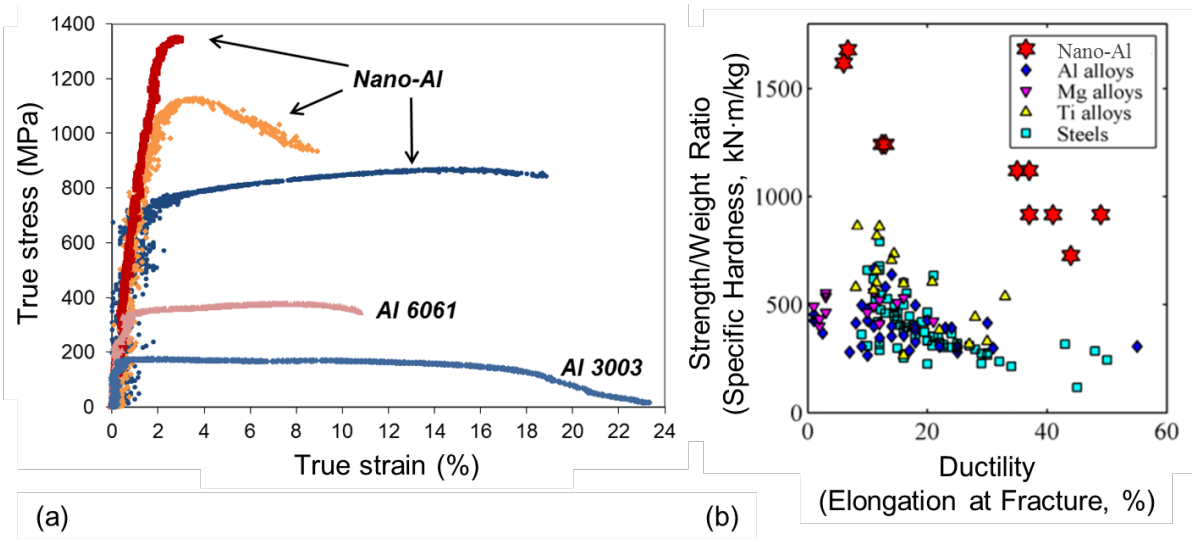

Figure III-19: Properties of nano-Al alloys: (a) stress versus strain in comparison with a typical 6xxx Al alloy, and (b) weight-normalized strength versus ductility in comparison with traditional structural metals.

The objectives of this project are to develop a commercial process for manufacturing high-strength nano-Al sheet and demonstrating use of nano-Al in a prototype automotive component. The expected outcomes are (1) a commercial-grade process for fabricating nano-Al sheet, (2) confirmation that nano-Al materials properties are maintained when produced by the new process, (3) integration of the new alloy material into specific vehicle components, and (4) economic validation that the new material and process are cost competitive for vehicle components.

Approach

The tasks associated with achieving the four main outcomes listed in the previous section include (1) design and build a pilot-scale electroforming system for nano-Al sheets, (2) fabricate nano-Al sheets from the new electroforming system, test, and optimize sheet properties, (3) develop and optimize post-fabrication steps to transform nano-Al sheets into vehicle component parts, and (4) develop and refine an economic model to

identify cost drivers and assess commercial viability. Table III-7 provides an overview of the tasks that will be performed systematically over the course of the 4-year program.

Table III-7: Overview of tasks performed over the course of the 4-year program.

Tasks	Year 1	Year 2	Year 3	Year 4
Optimize process output and consistency				
Develop nano-Al sheet electroforming system				
Go/no-go: Engineering feasibility of design				
Build and validate pilot line				
Go/no-go: Fabricate nano-Al sheet (6-in. x 6 in.) from pilot line				
Fabricate alloys, optimize properties, downselect				
Fabricate preferred alloy(s), test against full specs				
Go/no-go: Economic viability of nano-Al sheet production				
Fabricate, test prototype entry point component(s)				
Economic modeling				
Management and reporting				

During FY 2015 (i.e., budget period 1), our main focus areas included designing the sheet electroforming system and optimizing the process output and consistency. Table III-8 summarizes the planned tasks and milestones for budget period 1.

Table III-8: List of tasks and milestone for budget period 1.

Tasks	Q1	Q2	Q3	Q4
Design nano-Al sheet electroforming system				
• Milestone 1: Design rotating mandrel apparatus				
• Milestone 2: Design mechanisms to detach sheet				
• Specify dimensions of tank and equipment				
• Design termination unit for rinsing and drying				
Optimize process output and consistency				
• Optimize bath and maximize plating rate				
• Milestone 3: Develop methods to analyze bath				
• Milestone 4: Fabricate samples, validate properties				
• Develop methods to maintain bath within specs				
Economic modeling				
• Preliminary cost model				
Go/no-go decision: Engineering feasibility of design				

Results and Discussion

Electroforming System Design

During FY 2015, the engineering design of the nano-Al sheet electroforming system was completed. The sheet electroforming system comprises two modules: one for foil initiation and sheet detachmen, and another for sheet thickening. Each of these modules was designed to fit into one glovebox unit. The ancillary equipment includes rectifiers with suitable amperage and power capacity to enable fabrication of nano-Al sheets (6-in. x 6-in.) at high plating rates (i.e., 250 µm/hour). The system also includes fluid handling equipment and pumps that are capable of generating and maintaining high fluid flow rate and that are compatible with our plating chemistry.

Figure III-20 shows the engineering drawings of the foil initiation and sheet detachment module enclosed within a glovebox unit: (a) front view and (b) side view. A belt tension mechanism is used to initiate nano-Al foil growth onto a suitable substrate material (e.g., stainless steel or titanium) and a strip roll mechanism is used to detach the nano-Al alloy from the substrate to create a free-standing nano-Al sheet.

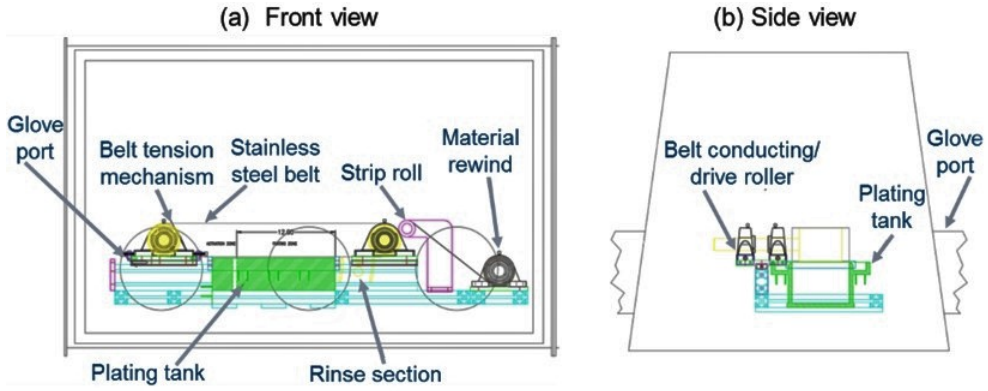

Figure III-20: (a) Front and (b) side views of the initiation and detachment module, where nano-Al foil growth is initiated onto a substrate using a belt tension mechanism and a strip roll is used to detach the nano-Al alloy from the substrate to form a freestanding nano-Al sheet.

Figure III-21 shows the engineering drawings of the sheet thickening module enclosed within one glovebox unit: (a) front view and (b) side view. Freestanding nano-Al sheet is fed into the module in a vertical orientation. As the sheet traverses along the thickening module, double-sided sheet thickening occurs. The final thickness of the sheet primarily depends on the applied current density and waveform, as well as the length of the thickening module and the speed of motion. The final product is rinsed as it exits the thickening tank. Our thickening module is designed to enable optimization of cathode-to-anode spacing. Figure III-22 shows detailed drawings of the thickening tank, where anode carrier brackets are incorporated to enable adjustable anode gap.

With completion of the engineering design, we will proceed with building the new nano-Al sheet electroforming system during budget period 2.

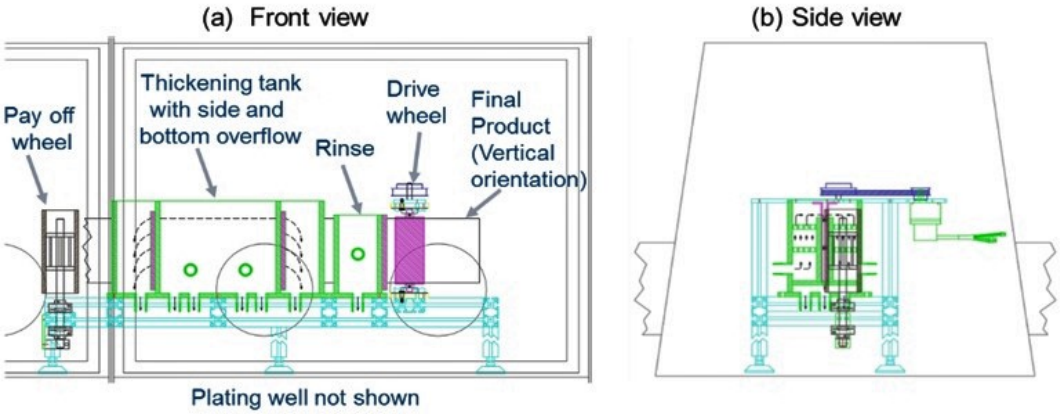

Figure III-21: (a) Front and (b) side views of the thickening module. The final sheet thickness is primarily governed by the applied current density and waveform, as well as the length of the module.

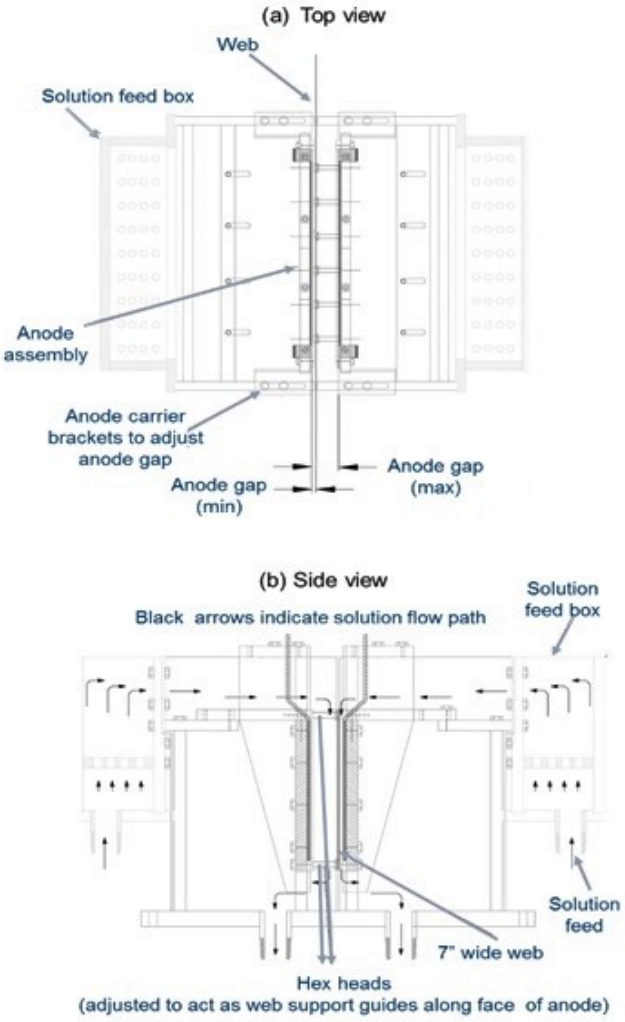

Figure III-22: (a) Top and (b) side views of the thickening tank, where anode carrier brackets are included to enable adjustable anode gap.

Optimize Process Output and Consistency

During FY 2015, significant progress was made toward optimizing the process consistency and output. We developed methods for analyzing various bath components, demonstrating good process control, fabricating nano-Al sheets, and evaluating their properties.

Bath Analysis

Prior to the starting this project, we developed methods for measuring and replenishing the Al and manganese (Mn) constituents in our electroplating bath. Developing methods for analyzing additive and co-solvent concentration is one of our tasks for this DOE program. In FY 2015, the ability to use infrared spectroscopy to quantify co-solvent and additive concentrations with high accuracy was demonstrated. Figure III-23(a) and Figure III-23(b) illustrate spectra that were obtained with known concentrations of the co-solvent and additive, respectively. The intensities of the characteristic peaks changed depending on the co-solvent and additive concentrations. Through construction of calibration curves from these known standards, the concentrations of these organic components can be accurately determined. Figure III-23(c) and Figure III-23(d) show an excellent agreement (nearly a 1:1 relationship) between the known and measured concentrations of various electrolytes. These results show that methods for analyzing critical bath components have been successfully developed.

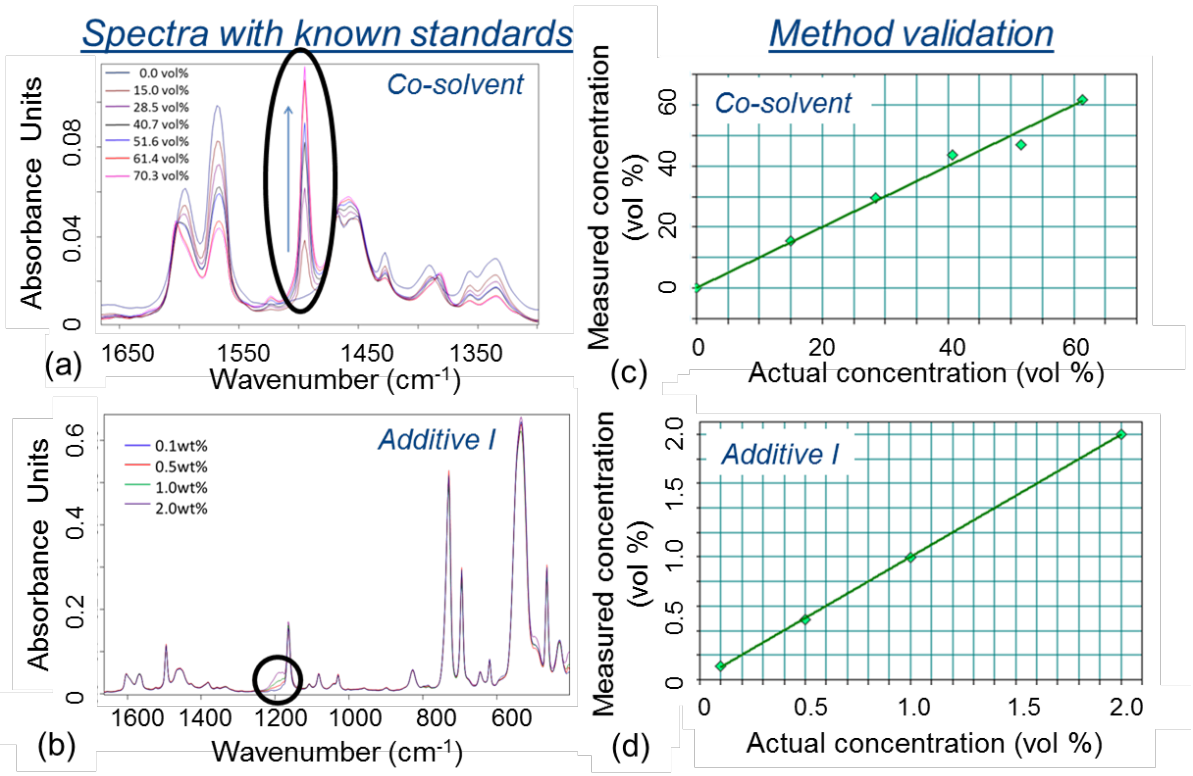

Figure III-23: Infrared spectra obtained from known standards containing various amounts of (a) co-solvent and (b) additive. An excellent agreement is observed between the actual and measured concentrations of electrolytes, as shown in Figure III-23(c) and Figure III-23(d).

Process Consistency

During FY 2015, good process control was demonstrated during a bath aging study (250 amp-hours per liter). By removing aliquots of electrolyte at specific bath age intervals, quantifying the bath metal content using atomic absorption spectroscopy, and replenishing the bath composition using liquid Mn concentrate, the ability to maintain bath and alloy compositions within specifications over 250 A-hour/L of bath age was

demonstrated. The results in Figure III-24 show that we were able to maintain the bath Mn content within ±0.1g/kg and the alloy Mn content within ±1.0 at.%. These results underscore the ability to measure and maintain the bath metal content; these methods will be used in our pilot-scale electroforming system in the upcoming years.

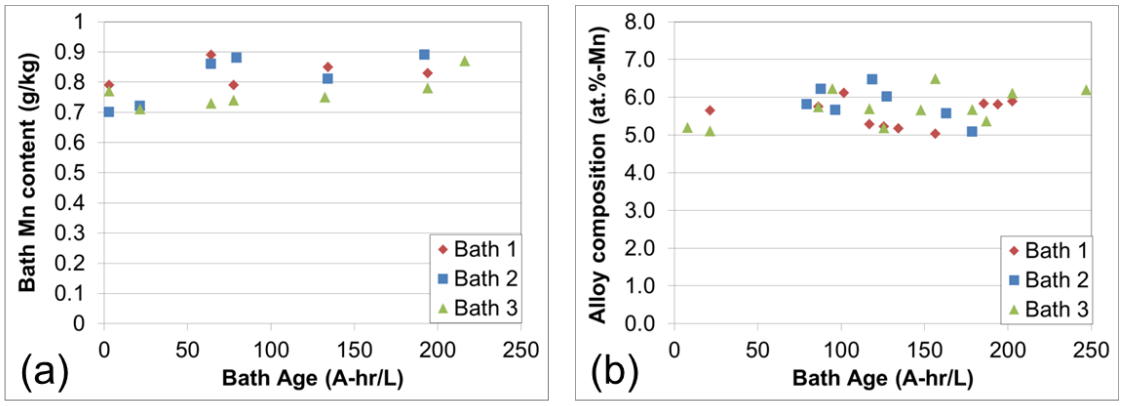

Figure III-24: Plot of (a) bath and (b) alloy Mn content versus bath age, demonstrating good process control during the bath aging study.

Sample Fabrication and Property Evaluation

In parallel to optimizing methods for fabricating freestanding nano-Al sheets, we fabricated composite sheets and evaluated their properties in FY 2015. We electrodeposited nano-Al alloys directly onto pure Al substrates. Figure III-25 shows the cross-section image of a representative composite sheet.

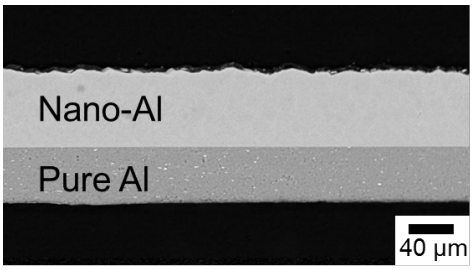

Figure III-25: Cross-sectional view of a composite sheet comprising nano-Al plated directly onto a pure aluminum substrate.

Figure III-26 illustrates stress-strain curves of the composites, as well as the pure Al substrate. The effects of increasing the volume fraction of nano-Al on the tensile properties of the composites are shown in Figure III-26(a), and the effects of increasing Mn content in composites that comprise approximately 50 vol% of nano-Al are illustrated in Figure III-26(b). Figure III-26 clearly shows that nano-Al enhances both the strength and ductility of the substrate layer and that these results are reproducible.

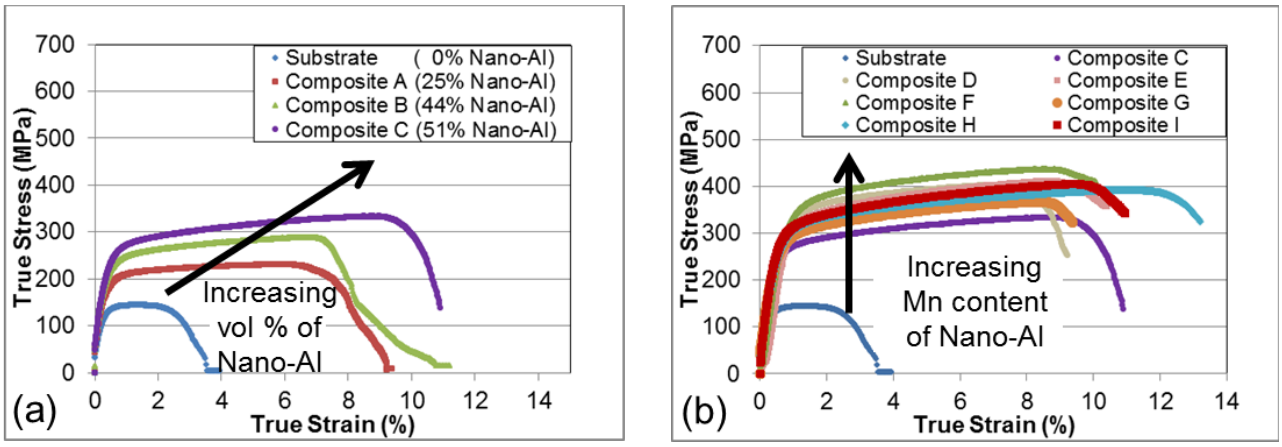

Figure III-26: True stress versus true strain of substrate material and composites that comprise (a) increasing volume fractions of nano-Al and (b) increasing amounts of Mn in nano-Al.

Technology Transfer Path

Xtalic's business model is to work with manufacturing partners to produce its nano-crystalline electrodeposited metal products by providing manufacturing process design specifications and onsite engineering support and raw materials to its manufacturing partners. If the DOE-funded project is successful, Xtalic will work with Tri-Arrows Aluminum, Inc. or another manufacturing partner to fabricate, install, and operate the nano-Al sheet line.

Because the nano-Al electroforming process is very electricity intensive, economics drive the process toward operation in the United States. The equipment footprint is approximately 10 x 40 ft and takes approximately six people per shift to operate. Therefore, a new manufacturing line for nano-Al will create 25 to 30 U.S. manufacturing jobs; we anticipate multiple manufacturing lines as the new technology is being adopted.

Xtalic is actively working with top-tier automotive OEM suppliers to identify suitable entry-point applications. For this project, we are collaborating with Fiat Chrysler Automobiles US, LLC to fabricate and test prototype component parts. This project is the first step in the process of technology development within Fiat Chrysler Automobiles US, LLC. Throughout the duration of this project, Fiat Chrysler Automobiles US, LLC will monitor technical progress and experimental results, as well as economic analysis to evaluate the technology's potential to meet their product performance requirements and economic goals for future vehicle applications. Fiat Chrysler Automobiles US, LLC will determine the technology's suitability to proceed to the next phase of their internal technology development stage-gate process.

Successful completion of this project and subsequent development phases will enable Fiat Chrysler Automobiles US, LLC to migrate the technology into the Chrysler development system, which is a robust gate-based process used to design and develop production vehicles that integrate the technology with the company objectives and supply base. The gates ensure all requirements are completed to deliver high quality vehicles to customers.

Conclusion

During FY 2015, we completed the engineering design of our electroforming system, developed methods for analyzing various bath components, demonstrated good process control and consistency, and validated the properties of nano-Al alloys. We have successfully accomplished all milestones and completed our deliverable for budget period 1.

The process control methods that we developed and optimized during FY 2015 will be adopted and adapted to ensure the electroplating bath and nano-Al sheets remain within specifications.

References

1. S. Ruan and C. A. Schuh, 2009,"Electrodeposited Alloys and Methods of Making Same Using Power Pulses," U.S. Patent Application No. 12/579,062, filed October 14, 2009.
2. S. Ruan, W. Paw, H. Martin, C. A. Schuh, and A. Lund, 2013, "Systems and methods for electrodepositing aluminum alloys," U.S. Patent Application No. 13/830,531, filed March 14, 2013.

Bibliography

S. Ruan, 2015, "High-Strength Electroformed Nanostructured Aluminum for Lightweight Automotive Applications," Department of Energy Vehicle Technologies Program Annual Merit Review, June 10, 2015.

III.5. Development of Low-Cost, High-Strength Automotive Aluminum Sheet – Alcoa

Project Details

Russell Long, Principal Investigator
100 Technical Drive
Alcoa Center, PA 15069
Phone: 724-337-5420
E-mail: russell.long@alcoa.com

Phil Hollinshead, Principal Investigator
100 Technical Drive
Alcoa Center, PA 15069
Phone: 724-337-2625
E-mail: Phillip.hollinshead@alcoa.com

Charles Alsup, Project Manager
National Energy Technology Laboratory
3610 Collins Ferry Road
Morgantown, WV 26507
Phone: 304-285-5432
E-mail: Charles.alsup@netl.doe.gov

William Joost, Technology Area Development Manager
U.S. Department of Energy
1000 Independence Avenue, SW
Washington, DC 20585
Phone: 202-287-6020
E-mail: William.Joost@ee.doe.gov

Contractor: Alcoa
Contract No.: DE-EE0006847

Executive Summary

The goal of the project is to develop an automotive high-strength 7xxx aluminum alloy and demonstrate its ability to replace an ultra-high-strength component with significant weight savings at a cost of $2 per pound saved.

Alcoa, in partnership with Oak Ridge National Laboratory (ORNL) and our industrial partners Honda R&D Americas, Inc. (Honda) and Cosma, leads this project to productively reduce weight in vehicles in a cost-effective manner. This effort to increase the strength of 7xxx material while reducing the costs can only be successfully performed by a team that includes a Tier 1 automotive supplier (i.e., Cosma), an original equipment manufacturer (OEM) (i.e., Honda), and an aluminum producer. Honda will provide requirements for the component in the vehicle and Cosma will develop warm forming tooling and procedures for forming the baseline component. ORNL will develop the method required to use tailor-welded blanks to further reduce material usage.

The proposed alloy developments will initially be done on laboratory-scale and then full-scale trials at Alcoa. Once the full-scale trial material is available, full-scale forming trials will be conducted with and without tailor

welded blanks. The material will be evaluated for strength, formability, and corrosion based on stringent Honda requirements.

Accomplishments

- Produced 18 experimental compositions using direct chill ingot casting. Following casting and homogenization, alloys were rolled into sheet with a target thickness of 2.5 mm. Following heat treatment and quench, multiple aging treatments were applied, with each followed by simulated warm forming exposures of specific temperatures and times. All samples were then given a simulated paint bake cycle (Fiscal Year [FY] 2015).
- A similar set of trials were conducted using the Alcoa Micromill™ process to test the feasibility of using a continuous cast flowpath. Thirteen compositions were chosen to evaluate the best path of reaching the specifications. Again, after sheet materials were produced, they were heat treated, quenched, and aged. All samples were subjected to simulated warm forming conditions and a paint bake cycle. An initial full scale Alcoa Micromill™ trial was also conducted (FY 2015).
- Produced 7055 production material at the desired 2.5-mm thickness. This material will be used for early forming evaluations and for tooling development (FY 2015).
- All ingot-based and Micromill™-produced materials were tested following a warm forming simulation and paint bake treatment. These mechanical properties are being used to select composition for the next year full-scale trials. Corrosion testing is underway on a subset of these experimental materials. Forming characterization is also underway on a subset of the experimental alloys (FY 2015).
- An initial design of the demonstration part has been developed. This design will be modified following forming simulations conducted using the mechanical properties of selected experimental alloys (FY 2015).

Future Directions

- Continue testing the most promising compositions for forming characteristics.
- Complete forming simulation of the demonstration part using material property data developed for the most promising materials from the alloy development phase.
- Develop tooling design modifications and incorporate them into the tooling design before tooling release.
- Begin tooling and oven fabrication for full-scale trials.

Technology Assessment

- Target: Achieve the 600-MPa ultimate tensile strength and 8% elongation targets following warm forming simulation and paint bake cycles on several ingot cast and Micromill™-produced experimental alloys.
- Gap: The 600-MPa ultimate tensile strength is beyond the capability of nearly all 7xxx alloys, especially in the overaged tempers normally specified for improved corrosion performance. The corrosion test requirements are an important factor in alloy and temper selection.
- Gap: The formability of the material is increased with higher forming temperatures; however, the higher temperatures can overage the material, resulting in lower strengths. This requires a good understanding of the part geometry and the material forming characteristics at various temperatures and times.

- Target: Produce sound tailor-welded blanks on sample materials using friction stir welding and successfully form the parts without weld fracture.
- Gap: Formability of the experimental alloys at forming temperatures is not yet understood and including the weld is another area for forming evaluation.

Introduction

The goal of the project is to develop an automotive, high-strength, 7xxx aluminum alloy and demonstrate its ability to replace an ultra-high-strength component with significant weight savings at a cost of $2 per pound saved.

The initial phase is based on alloy development to reach the stated targets. Corrosion and forming requirements are being developed by Honda and Cosma, respectively. Alloy development trials will target the properties stated, as well as the added corrosion and formability requirements.

The team has also defined a demonstration part that includes critical features in current production of the hot stamped steel component. This part geometry will be evaluated in forming simulations using the material properties developed during the alloy development phase. The demonstration part design will be modified based on the forming simulation while maintaining the strength and stiffness requirements needed in the end product.

ORNL is also evaluating the feasibility and productivity of using tailor-welded blanks with friction stir welding in these experimental alloys.

Approach

The first year of the contract provided definition of the detailed requirements. These specifications were targeted during the alloy development phase. Once the initial literature review was completed, target alloy compositions were defined. These new alloys were then produced at a laboratory scale.

For the direct chill casting method, multiple laboratory-scale ingots (i.e., roughly 150 mm x 400 mm x 1500 mm) were produced for each of the 18 desired compositions. These ingots were then homogenized and rolled into sheet with a target thickness of 2.5 mm. Following solution heat treatment and quench, multiple aging treatments were applied with typical warm forming temperatures and times. These materials were then tested against the original specification targets.

A similar set of trials was conducted using the Alcoa Micromill™ process. Thirteen compositions were chosen to evaluate the best path of reaching the specifications. Again, after the sheet materials were produced, they were heat treated, quenched, and aged. A subset of the sample materials was then subjected to typical warm forming temperatures and times and a typical paint bake cycle. A full-scale Alcoa Micromill™ trial was also conducted. These materials were then tested against the original specification targets.

These alloy development trials will be used to define a material that can be produced during the second year of the contract at full scale. A demonstration part has been developed by Honda and Cosma to include all critical features of the current production ultra-high-strength steel part (Figure III-27).

The forming tooling will be designed and built to form this part at elevated temperatures during the second year. A warm forming oven that can heat a single blank with rapid heat up times will also be built as part of the project. The initial forming trials will be conducted late during year two, with more trials, including tailor-welded blanks of the experimental alloy, in year three. The addition of tailor-welded blanks will improve material utilization and reduce cost.

The feasibility of using friction stir welding on these materials is included in the project, along with the cost evaluations.

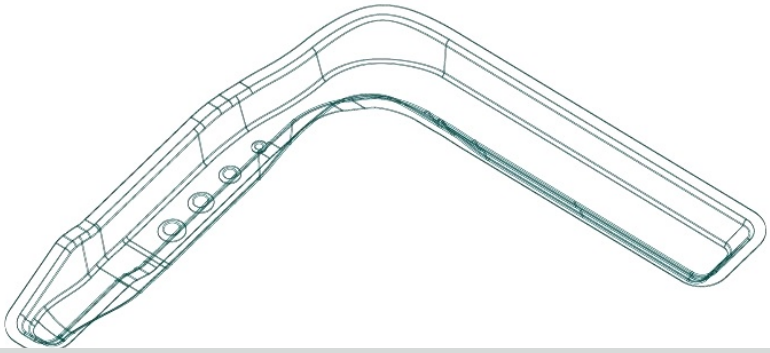

Figure III-27: Demonstration part geometry

Results and Discussion

The plan for FY 2015, which is the first year of the contract, was to conduct alloy development trials. Using both a direct chill ingot cast approach and a continuous casting approach, alloys were produced that would meet material properties in the vehicle (after warm forming and paint bake cycles) defined by DOE and that could be formed at a maximum temperature of 225°C.

Several experimental alloys using the direct chill casting process can reach the U.S. Department of Energy targets, including the simulated warm forming temperature cycle and paint bake cycle. All experimental alloys exceeded the strength of plant processed 7055-T76, which is the highest strength 7xxx that is commercially available. The alloys processed using the Alcoa Micromill™ process were slightly lower strength. This is preliminary data from a full-scale Alcoa Micromill™ production trial. Further work is being undertaken to increase the strengths. The measured mechanical properties of some alloys are shown in Figure III-28.

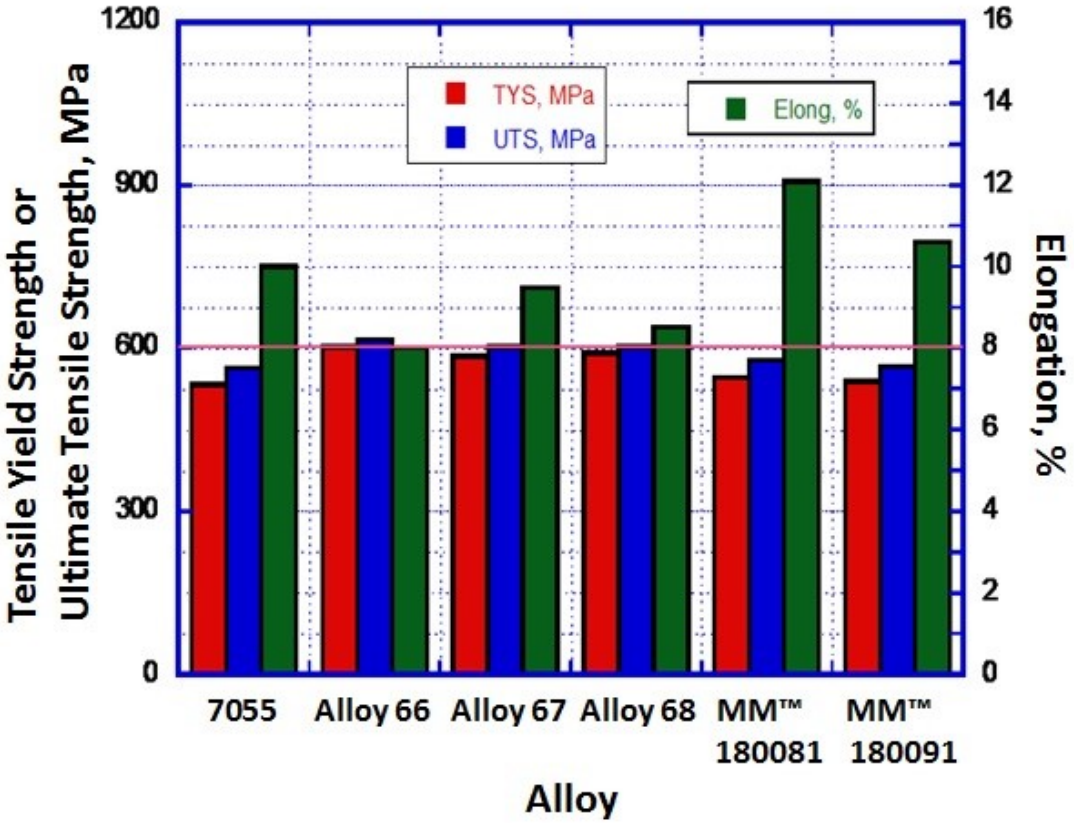

Figure III-28: Experimental alloy tensile properties – L orientation, warm formed for 30 seconds at 227°C + paint bake cycle.

These property measurements were conducted at a specific warm forming time and temperature followed by the paint bake cycle. We have also evaluated the impact of several different warm forming cycles with and without the paint bake cycle. These results are shown in Figure III-29. The experimental alloys show less reduction in strength after the various warm forming cycles when compared to 7055. The impact of the different warm forming times and temperature has been used in developing the furnace specification. The furnace must have a rapid heat-up rate to prevent reductions in properties. We have labeled this as warm forming time, but it should be thought of as time versus temperature during the forming operation.

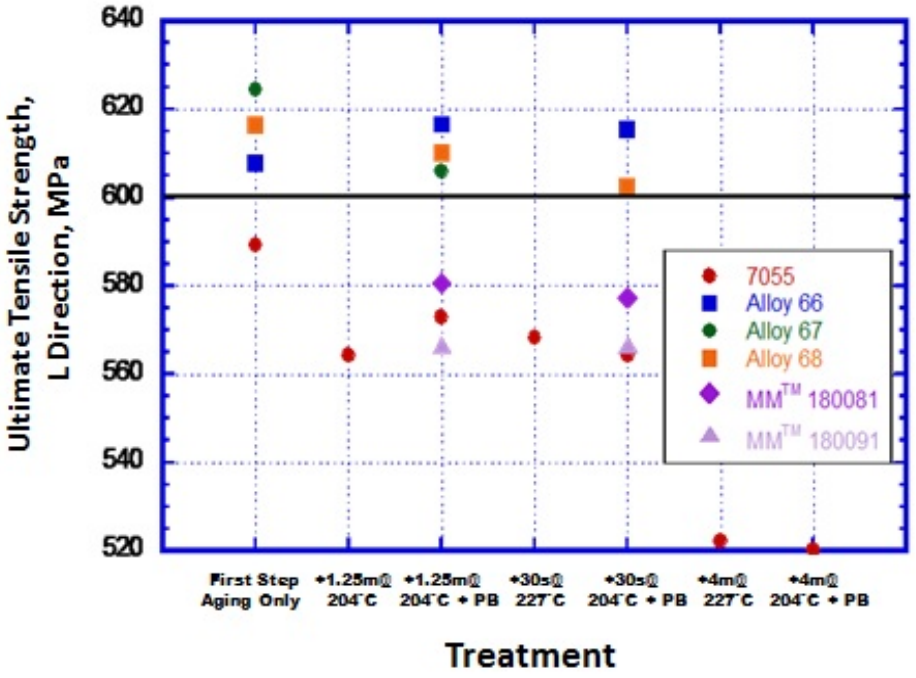

Figure III-29: Impact of warm forming temperature and time on ultimate tensile strength.

All of the promising experimental alloys have also been evaluated based on several different corrosion tests. These samples were all tested uncoated. This testing includes an evaluation of exfoliation using American Society for Testing and Materials Standard G34, "Test Method for Exfoliation Corrosion Susceptibility." These results are shown in Table III-9. The EA and EB ratings (ASTM G34 ratings for slight exfoliation and moderate exfoliation, respectively) obtained for the experimental direct chill cast alloys are considered acceptable in this case. These samples are still being evaluated to understand if the corrosion behavior is exfoliation or pitting. The Alcoa Micromill™ material only showed pitting after the full four-week test. All experimental alloys performed better than 7075-T6, which has much lower strengths. These alloys were also evaluated using ASTM G85-A2 MASTMAASIS (Modified ASTM Acetic Acid Salt Intermittent Spray Test). The ASTM G85-A2 test was selected because it correlates well with automotive exposures [1]. Results for this test are shown in Table III-10. All experimental alloys passed this 4-week test cycle with only pitting observed. The stress corrosion cracking test on experimental alloys is ongoing.

Forming characterization tests are also being conducted on several compositions. The team will select several experimental alloys for a full-scale production trial once the ongoing corrosion testing, forming characterization, and forming simulation of the demonstration part is completed. The material from this full-scale trial will be used for forming trials of the demonstration part.

Table III-9: ASTM G34 results for experimental alloys.

Description (Alloy, Temper, etc.)	Average Depth (mils)	Maximum Depth (mils)	Visual Ratings	
			24 hr	48 hr
0.125" 7075-T651	4.0	4.0	EB	EC
7055 – 1.25m@240C	1.7	2.0	EA	EA
7055 – 30s@227C	1.3	2.0	EA	EA
7055 – 4m@227C	1.3	2.0	EA	EA
Alloy 66 – 1.25m@204C	2.0	2.0	EB	EB
Alloy 66 – 30s@227C	3.0	4.0	EB	EB
Alloy 67 – 1.25m@204C	2.7	3.0	EB	EB
Alloy 67 – 30s@227C	1.3	2.0	EB	EB
Alloy 68 – 1.25m@204C	2.0	2.0	EB	EB
Alloy 68 – 30s@204C	2.3	3.0	EB	EB
MM™ 180081 – 1.25m@204C	-	-	P	P
MM™ 180091 – 1.25m@204C	-	-	P	P

Note: EA - slight exfoliation; EB - moderate exfoliation; EC - severe exfoliation; P - pitting

Table III-10: ASTM G85-A2 results for experimental alloys.

Description (Alloy, Temper, etc.)	Visual Ratings			
	1 week	2 weeks	3 weeks	4 weeks
0.125" 7075-T651	EA	EA	EB	EB
0.375" 2024-T3	EB	EC	EC	EC
7055 – 1.25m@204C	P	P	P	P
7055 – 30s@227C	P	P	P	P
7055 – 4m@227C	P	P	P	P
Alloy 66 – 1.25m@204C	P	P	P	P
Alloy 66 – 30s@227C	P	P	P	P
Alloy 67 – 1.25m@204C	P	P	P	P
Alloy 67 – 30s@227C	P	P	P	P
Alloy 68 – 1.25m@204C	P	P	P	P
Alloy 68 – 30s@204C	P	P	P	P
MM™ 180081 – 1.25m@204C	P	P	P	P
MM™ 180091 – 1.25m@204C	P	P	P	P

Note: EA - slight exfoliation; EB - moderate exfoliation; EC - severe exfoliation; P - pitting

Technology Transfer Path

The project is based on an existing ultra-high-strength door ring in Honda vehicles. This is a state-of-the-art use of hot stamped steel. The project will demonstrate weight reduction, production method, and cost implications of converting this component to high-strength aluminum. The new alloy will be produced at Alcoa's existing production facilities. The forming trials will be conducted at Cosma, who is the current production supplier of hot stamped steel components. Both Alcoa and Cosma are committed to production of high-strength aluminum components. This project serves as a means of developing the part requirements with Honda and the information needed to demonstrate the feasibility of this approach. Alcoa will produce the experimental alloy for supply to the automotive industry once the strength, formability, and cost feasibility is demonstrated.

Conclusion

During the first year of the project, high-strength aluminum sheet requirements were defined to produce an automotive body-in-white safety cage component with significant weight savings over the incumbent part. More than two dozen experimental alloys were produced to meet these specifications. These experimental alloy strengths were characterized following a simulated warm forming cycle and paint bake cycle. Several candidate alloys were identified as reaching the specifications. These alloys have undergone corrosion testing and forming characterizations. Additional, longer-term corrosion testing is ongoing. Once forming simulations are complete on the demonstration part and corrosion tests are complete, alloys will be selected for a full-scale trial. This trial material will be made at a production location and will be used for forming trials to demonstrate the ability to produce the target part.

References

1. F. Bovard; K. Smith; G. Courval; D. McCune; et al., 2010, "Cosmetic Corrosion Test for Aluminum Autobody Panels: Final Report," *SAE Int. J. Passeng. Cars – Mech. Syst.*, 3 (1); pp. 544-553, doi:10.4271/2010-01-0726.

III.6. Advancing Properties, Processes, and Enabling Tools for Lightweight Metals– Pacific Northwest National Laboratory

Project Details

Yuri Hovanski, Field Technical Monitor
Pacific Northwest National Laboratory (PNNL)
902 Battelle Boulevard
Richland, WA 99352
Phone: 509-375-3940
E-mail: yuri.hovanski@pnnl.gov

William Joost, Technology Area Development Manager
U.S. Department of Energy
1000 Independence Avenue, SW
Washington, DC 2058
Phone: 202-287-6020
E-mail: William.joost@ee.doe.gov

Contractor: PNNL
Contract No.: DE-AC05-00OR22725 and DE-AC06-76RL01830

Executive Summary

The Advancing Properties, Processes, and Enabling Tools for Lightweight Metals Project consists of five tasks that are focused on research and development activities advancing the basic mechanical properties, manufacturability, and cost of lightweight materials toward the levels needed for increased implementation in automotive applications. The specific tasks include the following:

- Non-rare earth high-performance wrought magnesium (Mg) alloys
- Microstructure-based ductility prediction for complex Mg castings
- Self-pierce riveting process simulation, analyses, and development for Mg joints
- High strength, dissimilar alloy aluminum (Al) tailor-welded blanks (TWBs)
- Enhancing sheared edge stretchability of advanced high-strength steel (AHSS)/ultra-high-strength steel (UHSS).

The following sections outline specific task work conducted at PNNL in the areas of predictive engineering, process development, and enabling technologies for lightweight metals. Each task supports one or more goals within the project agreement as outlined in the following subsections.

Activity and Developments

Non-Rare Earth High-Performance Wrought Magnesium Alloys

Project Details

Curt A. Lavender, Principal Investigator
PNNL
902 Battelle Boulevard
Richland, WA 99352
Phone: 509-372-6770
E-mail: curt.lavendar@pnnl.gov

Tim Skszek, Principal Investigator
Magna Cosma International
1807 East Maple Road
Troy, MI 48083
Phone: 248-689-5512
E-mail: tim.skszek@cosmaeng.com

Accomplishments

- High shear extrusion of four non-rare earth Mg alloys.
- Detailed characterization of the microstructure variation in the as-extruded non-rare earth Mg alloy tubes.
- A more detailed explanation of the high energy absorbing characteristics of the tubes and the contribution of texture.

Future Directions

- Provide characterization data that includes texture to the phi-model visco-plastic self-consistent plasticity model to better quantify the role of texture and grain on the yield strength symmetry of the shear-extruded alloys
- Provide data from shear extrusion for use in the next (scale-up) phase of this work.

Technology Assessment

- Target: Develop high energy–absorption Mg alloys that do not contain rare earth elements and that can replace Al extrusions at a mass savings of 20% (based on density).
- Target: Use inverse process modeling to develop a low-cost process for producing the microstructures required for high performance at a low cost, making Mg extrusion viable for automotive applications.
- Gap: Currently produced Mg alloys that possess high-strength and ductility (energy absorption) use rare earth elements, which increase cost and are of limited supply, resulting in reluctance of the automotive industry to use Mg extrusions.
- Gap: The cost to produce high-performance Mg extrusion has prevented use in automotive applications.

Introduction

The application of Mg alloys in bumper beams, crush tips, and intrusion beams has been demonstrated to result in significant vehicle weight savings. However, to increase the structural use of Mg alloys, development of cost-effective bulk metal forming methods are necessary. In this regard, extrusion, which is typically used to produce cylindrical bars or hollow tubes or even complex cross-sections at a fairly rapid speed, is an important metal forming method to investigate. Several researchers have studied the role of different process variables during extrusion of Mg alloys. In all of the above-mentioned studies, extrusion experiments were conducted at elevated temperatures, because Mg alloys suffer from limited room-temperature ductility due to limited slip systems. In order to control the grain size of the extruded material, the feed rates are kept very low or need to be followed by severe plastic deformation processes to refine the grain size. The purpose of this project is to develop and demonstrate low-cost wrought Mg alloys that do not rely on rare earth alloying elements for their strength, ductility, and energy absorption properties. A novel low-cost processing method, in conjunction with Mg alloys containing rare earth alternatives, will be developed to produce the microstructure and properties needed for automotive applications at rates that are cost effective for the automobile industry.

Approach

The project is being performed in three phases. During the first phase, the project team produced high-performance alloys using rare earth additions to develop high-energy-absorbing microstructures that were used as model systems for non-rare earth alloys. The second phase of the project involves developing the microstructure found in Phase 1 to produce high-performance alloys without rare earth additions. During the second phase, at least one alloy will be selected and processed for evaluation by Magna Cosma International for use in automotive applications that require additional formability (such as bending or hydroforming). The third phase of the project will use an inverse process modeling method to develop a cost-effective processing approach to producing the alloy with the energy absorbing properties.

The following technical steps were planned and executed over the past 2 years, along with the steps forward:

- Produced rare earth-Mg alloy extrusions and performed mechanical tests comparing quasi-static tension and compression results to the Al alloy AA6061 and the conventional Mg alloy AZ31.
- Evaluated the energy absorption capability of the rare earth-Mg alloy via impact tests and compared to AA6061 and AZ31.
- Experimentally evaluate the deformation mechanisms of the rare earth alloys using interrupted strain tests in tension and compression at room-temperature.
- Develop a continuum-level model to predict microstructure evolution and mechanical deformation behavior of Mg alloys during processing. Validate using experimental data.
- Select up to three alloys from the previous task, consolidate the materials by extrusion, and evaluate the non-rare earth alloys for strength and energy absorption characterization at both quasi-static and elevated strain-rate tension tests.
- Produce sufficient material to provide partner Magna Cosma International with tubular extrusions that can be formed into shapes (such as crush tips and roof structural support beams) for testing and comparison to conventional materials.
- Develop the “Model Alloy” by implementing a statistical continuum mechanics model embedded with crystal plasticity. Use the model to predict grain size, dispersion, and textural effects.
- Use experimental data, crystal plasticity, inverse process path modeling, and laboratory trials to develop the necessary process to create the desired microstructure using an optimum low-cost, high-shear processing route.

- Prototype and demonstrate a small system that will produce extruded shapes by fracturing the coarse intermetallics and developing the strain needed for fine grain size (as predicted by the inverse modeling) and provide the driving force for subsequent extrusion.
- Magna Cosma International will evaluate extrusions produced by the system for formability. Billets produced by the process will be extruded at PNNL and subjected to formability tests using warm gas-pressure forming.

Results and Discussion

For the present work, the starting material was in the form of an extruded AZ31, ZK60-T5 (ZK60) rod, 76.2 mm in diameter and 3.5 m in length, obtained from MetalMart International Inc., California, USA and Mg-2 wt% Si (Mg-2Si) and Mg-7wt% Si (Mg-7Si) alloy were book cast to 30 mm in thickness. These materials were machined down to form pucks 31.75 mm in diameter and 18 mm in height with a center hole approximately 6 mm in diameter to accommodate the mandrel. A graphite puck of similar inner and outer diameters and about 2 mm in height was placed between the machined billet and the base plate to eliminate any bonding between the ram and the base plate during the extrusion process. The assembly containing the ram chamber, backing plate, mandrel, billet, and graphite puck was rigidly clamped down to the friction stir welding (FSW) machine bed. The ram was clamped to the overhead rotating spindle and carefully positioned atop the assembly such that the centerline of the mandrel and the ram were aligned. After final alignment, the ram was lowered to bring the ram face in contact with the billet located inside the chamber/container. A schematic of the process is presented in Figure III-30. The area on the billet that undergoes severe plastic deformation (SPD) and, thus forms the tube, has been marked as well. The current indirection extrusion trial used a spindle rotation of 500 revolutions per minute (RPM), and an axial feed rate of 0.06 mm/s for the ZK60 alloy and 0.6 millimeters per second (mm/s) feed rate for the Mg-2Si alloy. This resulted in an extrusion ratio of 47:1 and extrusion rates of 3 mm/s and 30 mm/s, respectively.

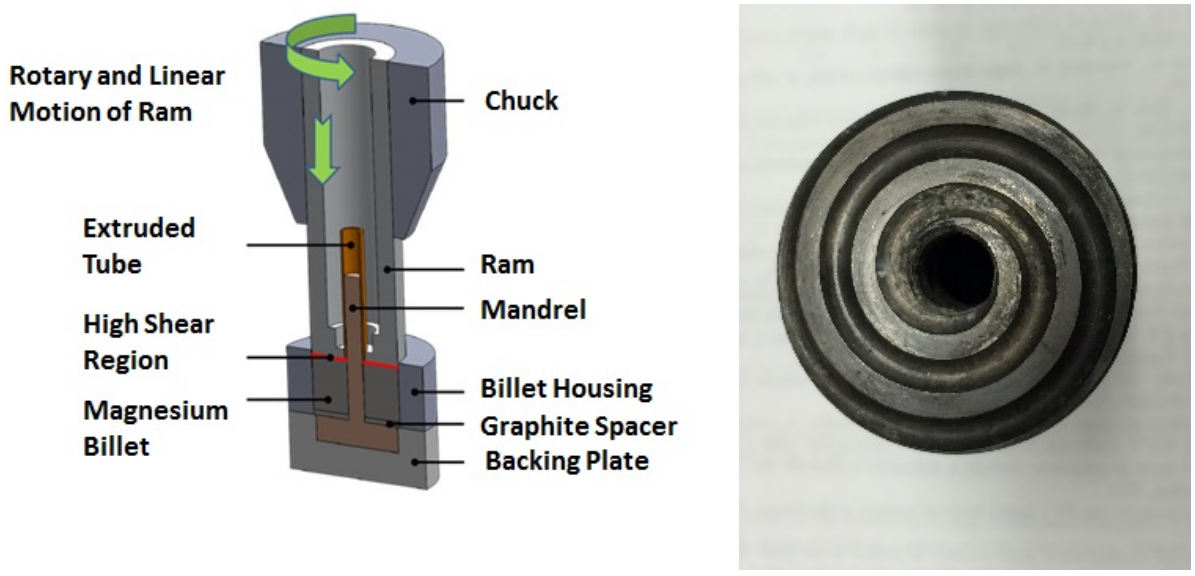

Figure III-30: (a) Shows the diagram of the shear-assisted indirect extrusion process and (b) shows the scrolls on the face of the ram that assists in heating and flow of material.

Determining Texture Development for Shear-Assisted Indirect Extrusion

Figure III-31 shows the microstructure and texture of the billet interiors of the AZ31, Mg-2%Si, Mg-7%Si, and ZK60 specimens, represented in orientation maps and pole figures. Figure III-34a shows that the AZ31 billet has a heterogeneous microstructure, with areas of fine grains and large elongated grains. The average grain diameter was found to be 11.36±11.5 µm. The AZ31 billet shows a partly developed $\{10\bar{1}0\}$ fiber aligned with the extrusion direction. The average grain diameter of the cast Mg-2%Si billet interior (Figure III-34b) was found to be greater than 1 mm. The texture of both of the Mg-Si billets was found to be fairly random. The average grain diameter of the Mg-7%Si was found to be much smaller than the Mg-2%Si alloy at 24.12±7.4 µm. Chinese script and blocky Mg_2Si precipitates are clearly visible as areas of "no data" in the Mg-7%Si billet (Figure III-34c). Note that in order to clearly resolve the precipitates in the Mg-7%Si billet, the CI filter was increased to 0.4. The ZK60 billet shows severely elongated grains in line with the extruded direction divided by areas of fine grains. Like the AZ31 billet, the average grain diameter of the ZK60 billet was found to be highly variable at 9.64±9.38 µm. Also like the AZ31 billet, the texture of the ZK60 billet is a $\{10\bar{1}0\}$ fiber, aligned with the extrusion direction, though the $\{10\bar{1}0\}$ fiber of the ZK60 billet is more developed than the AZ31 billet.

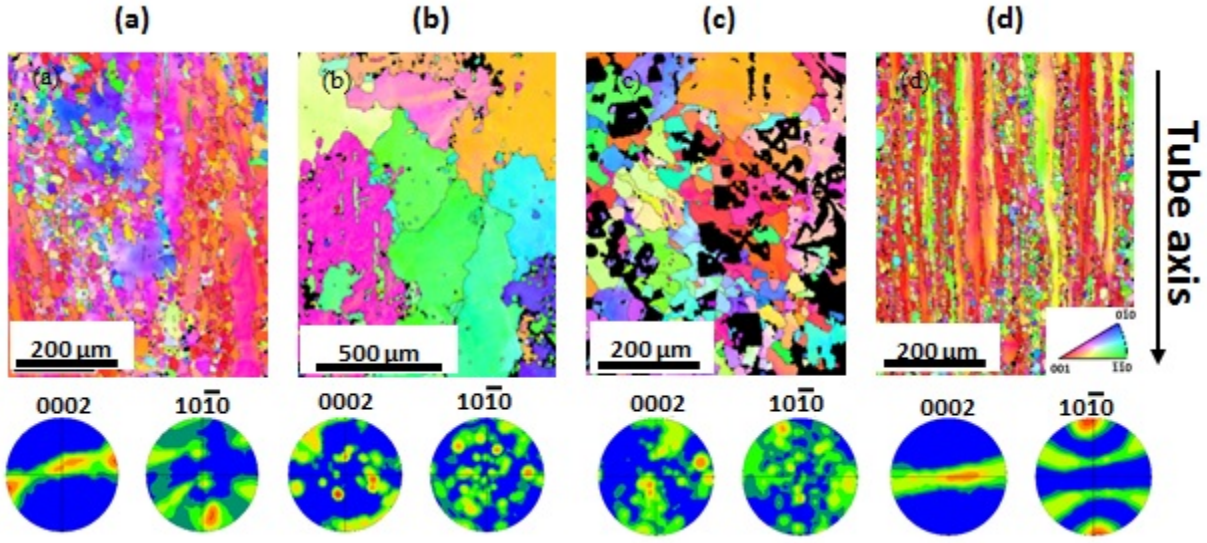

Figure III-31: Orientation maps and pole figures of the (a) AZ31, (b) Mg-2%Si, (c) Mg-7%Si, and (d) ZK60 billet interiors.

The microstructure and texture of the AZ31, Mg-2%Si, Mg-7%Si, and ZK60 tubes are shown in Figure III-32. The shear-assisted indirect extrusion process significantly refined the microstructures of these specimens, producing tubes with equiaxed grains and average grain diameters of 5.52±0.44, 3.95±0.32 µm, 4.33±0.57 µm and 3.30±0.26 µm, respectively. In all four alloys, the grains appear mostly equiaxed with only some minor elongation of the grains in the Mg-7%Si and ZK60 alloys. Similar to the data collected from the billet, the core image filter of the Mg-7%Si tube data was increased to 0.4 in an attempt to detect the presence of precipitates in the tube. No large Chinese script or blocky Mg2Si precipitates are inherently apparent in Figure III-32c, though some areas of "no data" are present at the grain boundaries. If these are indeed precipitates, the shear-assisted indirect extrusion process apparently broke up the large precipitates; a more thorough study would be needed to fully understand the process's effect on the precipitates. The pole figures of the tubes show that the c-axis of the hexagonal close-packed (HCP) crystals has been aligned approximately 45 degrees to the tube-axis, although all but the Mg-2%Si tube appear to have some rotation into the observed plane.

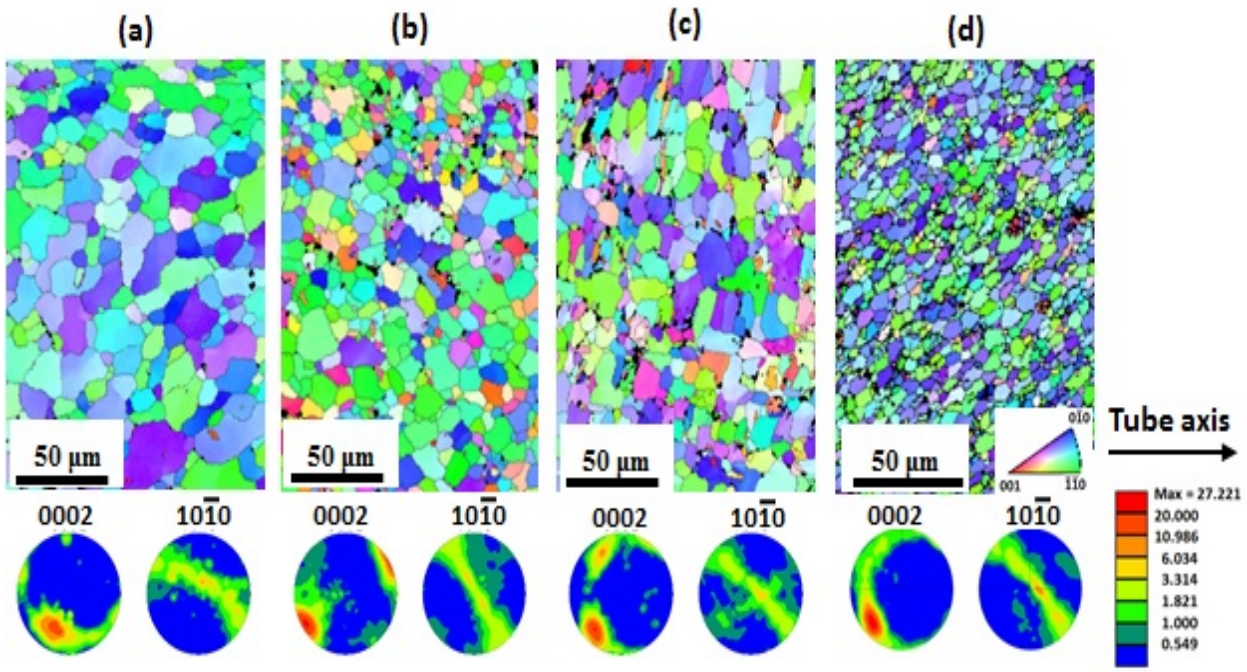

Figure III-32: Orientation map and pole figures of the (a) AZ31, (b) Mg-2%Si, (c) Mg-7%Si, and (d) ZK60 tubes.

The average grain diameter and percent recrystallization (%RX) of the AZ31, Mg-2%Si, and Mg-7%Si tubes as a function of distance from the billet are shown in Figure III-33. The %RX was measured using the orientation data collected by electron backscatter diffraction, where grains with a grain orienting spread less than 1.5 degrees were defined as recrystallized grains. The area fraction of these grains was then used to represent the percent of recrystallized grains. This shows that although heat generated during the shear-assisted indirect extrusion process led to some recrystallization in the tubes, a fine grain size is retained along the tube length. The fact that the %RX decreases with distance from the billet surface, most notably in the Mg-2%Si and Mg-7%Si tubes, shows that recrystallization increases with processing. This suggests that the material that initially formed the tube was formed at a lower temperature than the material that formed the latter part of the tube. The tool temperature time profiles in Figure III-34 show that the temperature during processing initially increased to a peak temperature and then cooled during further processing. However, at 500 RPM and a feed rate of 0.06 mm/s (red curve in Figure III-34), the processing conditions for the AZ31 alloy, the temperature showed a rapid increase, followed by a decrease in the change in temperature as a function of time before reaching a peak temp. It is possible that this change in slope of the temperature versus time curve may correspond to initiation of material flow. As the samples cut from the tube specimen were taken from approximately the first 10 mm of tube, the increase in %RX may be explained by the temperature increase following the initial flow of material. If further analysis of a longer section of tube was performed, it is expected that a peak in %RX and a corresponding peak in tool temperature would be found. It is also expected that, following these peaks, a steady-state condition of %RX and temperature would exist for the remainder of the tube.

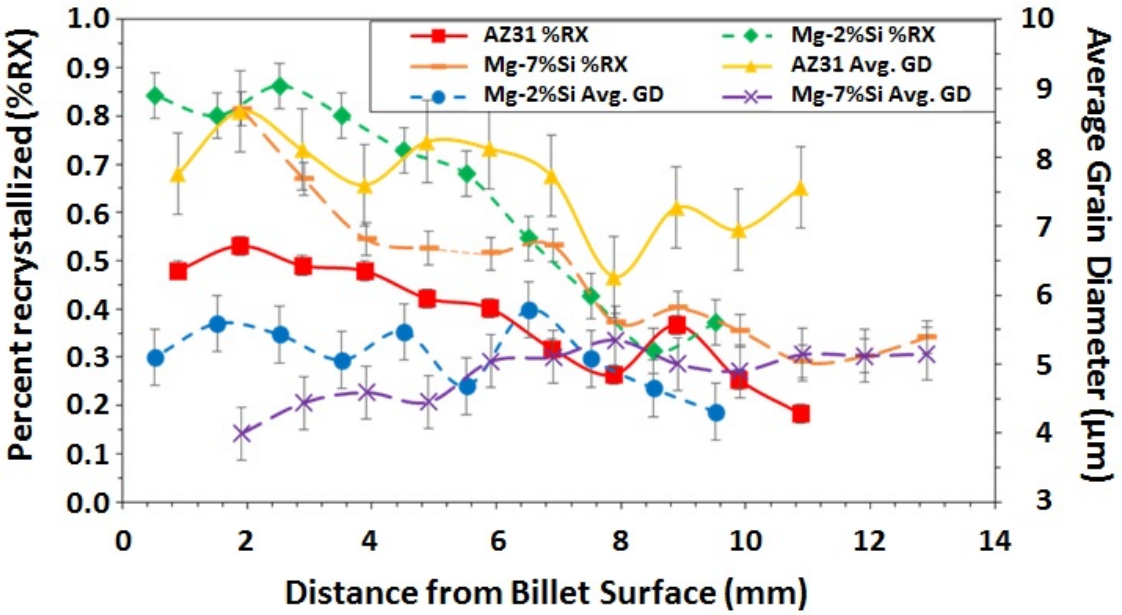

f

Figure III-33: Percent recrystallized (%RX) and average grain diameter as a function of distance from billet surface for the AZ31, Mg-2%Si, and Mg-7%Si tubes.

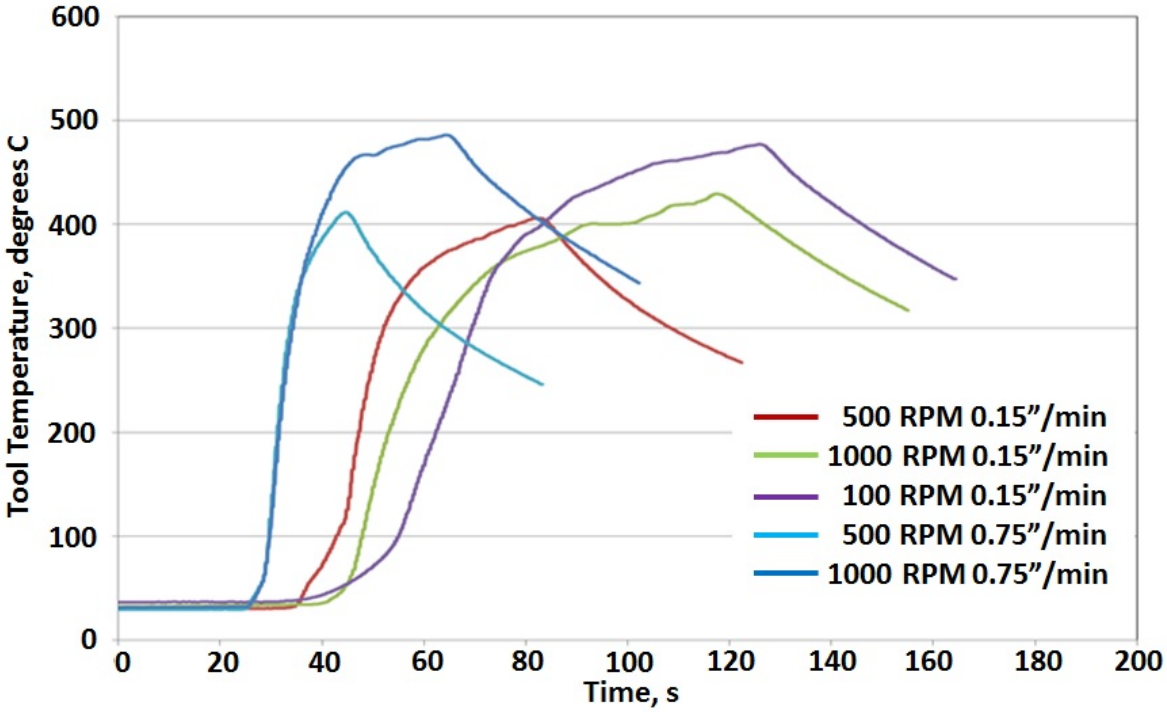

Figure III-34: Tool temperature as a function of time during shear-assisted indirect extrusion processing for various tool RPMs and feed rates.

Material Flow

Even though the previous figures and analysis show that the SAIE process has the capability to transform the microstructure of different Mg alloys into tubes with microstructures suitable for use in automotive applications, the fundamental understanding of the process needs further investigation. Figure III-35 shows the billet-to-surface interface of the AZ31 specimen. In this figure, orientation maps have been overlaid on the secondary electron images to reveal the microstructural evolution in the billet-to-tube interface. Here it can be seen that the SAIE process results in a drastic change in the orientation of the grains near the tube stem and where the billet-face meets the ram. Though the shape of this SPD zone is fairly suggestive of the material flow directions, a more quantitative method of measuring the material flow during the SAIE process was developed.

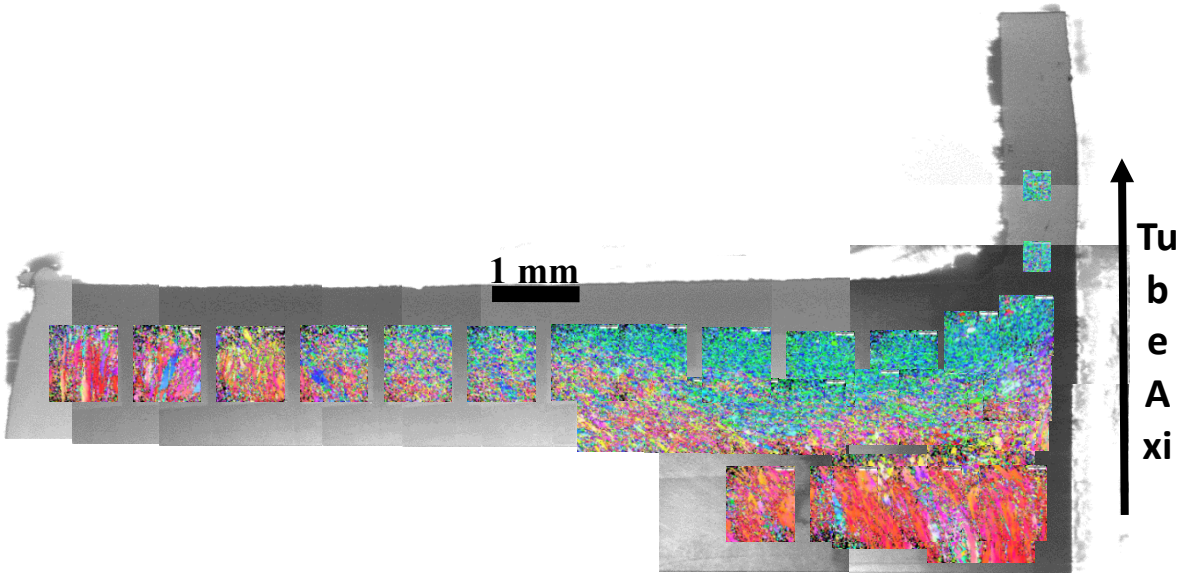

Figure III-35: AZ31 billet-to-tube interface and stem where an orientation map has been overlaid on the secondary electron images.

As the material is expected to deform by shear during processing, the orientation of the shear direction (SD) and shear plane are predictive of the material flow directions. Beausir et al. [1] used a persistent parameter to calculate the fibers that result from simple shear deformation of HCP materials. These fibers were used to calculate the orientation distribution functions shown in Figure III-36. Here the fibers have been labeled using Beausir et al.'s notation. In Beausir et al.'s approach, the Cartesian reference system was fixed to the unit cell of the HCP crystal so that the axis parallel to the shear direction, x1, was parallel to the $[10\bar{1}0]$ direction, x2 was parallel to the $[1\bar{2}1\bar{0}]$ direction, and the radial axis, x3, was parallel to the [0001] direction; orientation imaging microscopy (OIM) analysis assigns x1 parallel to the $[1\bar{2}1\bar{0}]$ direction and shear plane normal, x2, parallel to the $[10\bar{1}0]$ direction. This made it necessary to include a 30-degree shift about the Euler angle, $\phi 2$, before calculating the textures in OIM analysis. As the persistence parameter used by Beausir et al. was dependent on the relative activity of the slip systems of the HCP crystal, what is shown in Figure III-36 represents a situation where all systems are equally active. Since Mg predominately deformed via basal slip, the simple shear deformation of Mg is expected to result in the development of the B fiber. In addition, torsion tests performed by Beausir et al. have shown that the AZ71 alloy develops the B fiber when deformed by shear. This analysis neglects the textural effects of twinning when calculating shear textures. However, as little or no twinning was observed in the SPD zone of the billets or the tubes, it is believed that the twinning's effects to the final texture are expected to be minimal. Therefore, the texture of the SPD zone of the SAIE billets is predicted to be a B-fiber and that the orientation of the B-fiber will be representative of the material flow direction.

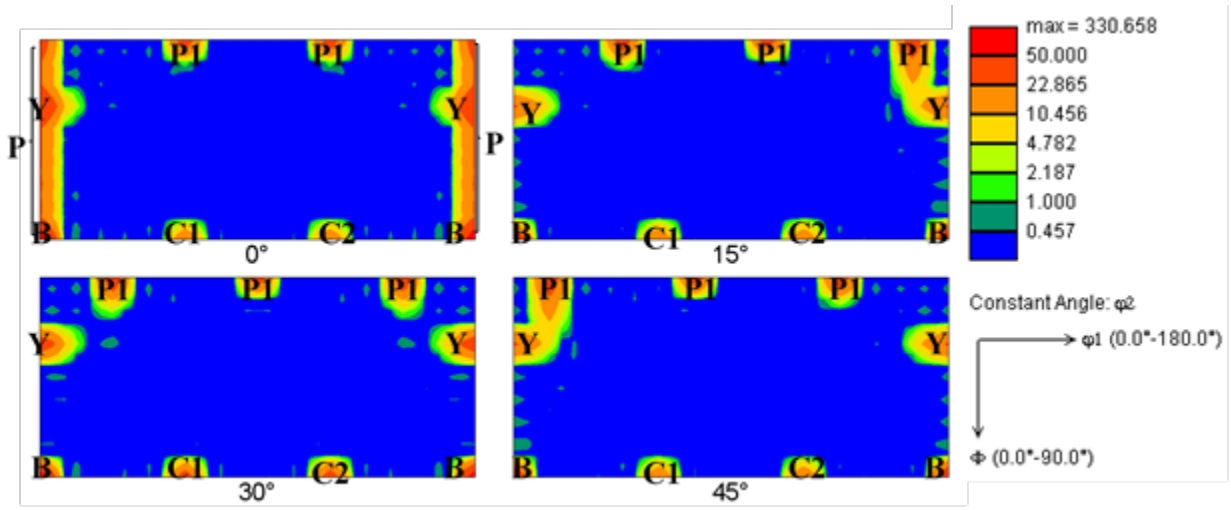

Figure III-36: Orientation distribution function of calculated simple shear HCP texture.

The method used for measuring material flow directions is illustrated in Figure III-37. In Figure III-37a, the texture of the Mg-2%Si tube is represented by orientation distribution functions and pole figures. Figure III-37b shows the texture of the Mg-2%Si tube following rotations to match the calculated B fiber shown in Figure III-37c. The rotations necessary to achieve this agreement are representative of the orientation of the SD and shear plane normal (SPN). A similar method has been previously used to predict material flow direction during FSW of steel. This approach was applied to every electron backscatter diffraction scan of the billet-to-tube interface where a strong B-fiber was found. Even though the orientation distribution functions and pole figures used in this approach were often calculated from less than 10,000 grains, they represent the micro-texture of a particular area in the SPD zone, which can be used to measure the orientation of the SD and SPN in that area.

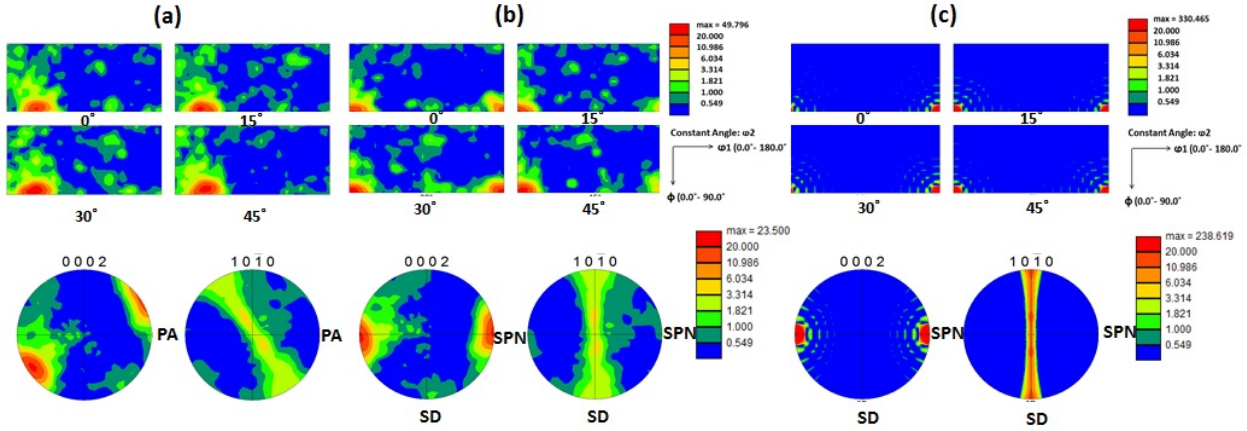

Figure III-37: Orientation distribution functions and pole figures of the (a) Mg-2%Si tube, (b) Mg-2%Si tube rotated into the shear orientation, and (c) the B fiber of the calculated simple shear HCP texture.

The shear plane in the shear zone of all four alloys was found to be independent of the distance from the tube inner wall and only varied ±10 degrees from parallel to the observed plane. The SD was found to increase with distance from the inner wall. These results are summarized for ZK60 in Figure III-38. Here the orientation of the SD is measured in degrees from parallel to the tube axis. This shows that the SD rotates from near perpendicular to the tube axis toward parallel to tube-axis as the material approaches the tube. This suggests that the material is initially pushed by the ram scrolls perpendicular to the tube-axis or, in some cases, slightly down and into the billet. Then, the material flows up toward the tube as it nears the tube stem. This is

illustrated in Figure III-38 for the ZK60 billet. However, the SD did not become fully parallel to the tube-axis before forming the tube in any of the alloys. This created the texture observed in the tubes and suggests that the processing parameters, especially tool rotation speed and scroll geometry, influenced orientation of the B-fiber in the final tubes. Further work will investigate the effects of different processing parameters on the texture of the tube.

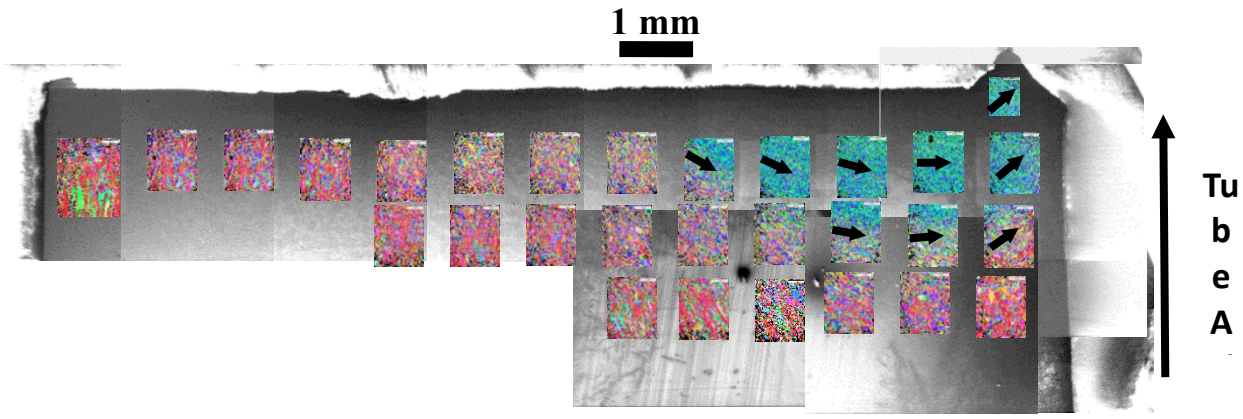

Figure III-38: ZK60 billet to pipe interface and stem where an orientation map has been overlaid on the secondary electron images. Arrow indicates calculated SD with respect to tube axis.

Technology Transfer Path

The technology transfer for this project will occur late in Phase 2 and during Phase 3. The initial phase will be focused on laboratory development and understanding the Mg alloys from a mechanistic standpoint. After the alloy is understood, the technology transfer will occur in two ways: (1) produce and deliver tubes to Magna Cosma for evaluation and (2) Magnesium Electron North America (MENA). MENA has already contributed alloy feedstock for the high-shear extrusion processing and has played an active role in alloy selection.

Magna Cosma and MENA are cost-sharing partners in the project and Georgia Institute of Technology and Washington State University have been sub-contracted for research support.

Conclusion

In this work, a novel extrusion technique, shear-assisted indirect extrusion, was used to produce a tube from four different Mg alloy billets. The texture of the billet-to-tube interface was used to predict the material flow during processing. The conclusions from the study are as follows:

1. The SAIE process successfully produced a 127 mm-long, 7.45 mm-diameter tube from AZ31, Mg-2%Si, Mg-7%Si, and ZK60 billets.
2. The process pressure during extrusion was significantly less than that of conventional indirect extrusion.
3. The microstructures and textures of the produced tubes meet the microstructural requirements for reducing the yield anisotropy, such that the tubes may be suitable for use in automotive applications.
4. The SAIE process appears to have broken up and dispersed the large Chinese script precipitates seen in the Mg-7%Si billet.
5. During processing, the material on the surface of the billet is pushed inward by the scrolls on the ram face, and then the material flows upward to form the tube.
6. The shear direction of the material that forms the tube was not parallel to the tube-axis. This created the texture seen in the tubes that meets the textual requirements for reducing yield anisotropy.

Microstructure-Based Ductility Prediction for Complex Magnesium Castings

Project Details

Xin Sun, Principal Investigator
Pacific Northwest National Laboratory
902 Battelle Boulevard
P.O. Box 999
Richland, WA 99352
Phone: 509-372-6489
E-mail: xin.sun@pnnl.gov

Mei Li, Industry Partner
Ford Motor Company
1 American Road
P.O. Box 6248
Dearborn, MI 48126-2798
Phone: 313-206-4219
E-mail: mli9@ford.com

John Allison, Industry Partner
University of Michigan
4901 Evergreen Road
Dearborn, MI 48128
Phone: 734-615-5150
E-mail: johnea@umich.edu

Accomplishments

- Conducted nanoindentation on AM40, AM50, AM60, and AM70 samples. Extracted elastic material properties from experimental data. Determined statistical distribution of plastic material parameters using finite element (FE) modeling of the nanoindentation experiments (FY 2015).
- Expanded computational tools for generating microstructure geometries to include the presence of externally solidified cells (ESCs) with and without beta phase (FY 2015).
- Conducted FE analyses on microstructure geometry samples with material parameters from nanoindentation experiments to quantify the impact of geometry features and parameter ranges on intrinsic ductility (FY 2015).
- Performed computerized tomography (CT) scans on as-cast samples prior to tensile testing to visualize the three-dimensional (3D) pore distributions within the samples (FY 2015).
- Developed a methodology for generating extrinsic FE models based on actual pore distributions captured from CT scans (FY 2015).
- Validated the developed extrinsic modeling method against the experimental results in terms of ductility and fracture locations of the samples (FY 2015).

Future Directions

- Dissemination of project findings through publications in peer-reviewed journals.

Technology Assessment

- Target: Develop a ductility prediction method for high-pressure die casting with potential for less than 10% error.
- Gap: Conventional computational techniques (e.g., homogenization, continuum damage mechanics, and crystal plasticity) and some phenomenological approaches have no (or quite limited) capability to predict ductility.

Introduction

Mg castings have found increasing applications in lightweight vehicles because Mg and its alloys are the lightest metallic structural materials. However, a critical technical hindrance to wider applications of Mg castings in vehicles is the limited ductility of Mg. It is well established that, among various factors, microstructural features such as the properties and distributions of porosity, brittle eutectic phases, and grain size can significantly influence the ductility of Mg castings. However, these microstructural features vary from specific alloy to alloy, among different casting processes, and among different locations on a single casting [2,3]. Although some commercial casting software or material models are available for Mg casting research, their predictive capability typically stops short of predicting the location-dependent stress versus strain behavior, particularly ductility. The purpose of this project was to develop an empirical casting process simulation tool and a mechanistically based ductility prediction capability in order to provide a modeling framework that can be used in future alloy design and casting process optimization.

Approach

The factors limiting the ductility of Mg castings can generally be categorized into two types: intrinsic and extrinsic. We have adopted two complementary modeling approaches (i.e., intrinsic/extrinsic modeling) for investigating the influence of various microstructure-level features on the strength and ductility of Mg castings [4-6].

In FY 2015, for the intrinsic modeling tasks, characterization of the 2.5-mm cast plates and nanoindentation experiments was used to quantify geometric features and material parameters for intrinsic models. Analyses of the intrinsic models were then used to evaluate the influence of these features and parameters on the matrix ductility limit to be passed upscale to extrinsic models. For the extrinsic modeling tasks, a high-resolution CT scan was performed on as-cast samples prior to tensile testing in order to visualize the 3D pore distributions within the samples and to characterize their distribution features. An extrinsic modeling method was then developed that generates 3D FE models based on the obtained actual pore distribution data from the sample gauge area. Modeling results were also validated against experimental results in terms of ductility and fracture location.

Results and Discussion

For intrinsic modeling, previous exploratory work was conducted to extract plastic material parameters from FE modeling of nanoindentation experiments. Young's modulus and hardness are directly extracted from nanoindentation experiments. A methodology for FE modeling of the nanoindentation experiment was refined to determine hardening parameters for each indent. This combination of modeling and experiments was used to determine elastic and plastic material parameters for each alloy under consideration. Figure III-39 shows the application of nanoindentation tests in Mg castings for extracting the material properties of the alpha phase.

The capability for generating intrinsic microstructure geometries was expanded to include the presence of ESCs with and without a beta phase present. ESCs were observed in the core regions of the castings. The average areas of individual ESCs and the overall area fraction of ESCs were measured by the University of

Michigan. These measurements were used to generate statistically equivalent microstructure geometries. Figure III-40 shows example microstructure geometries with different microstructural features. Individual cell material parameters were sampled from the statistical distribution of properties generated from the modeling and nanoindentation efforts. FE simulations were conducted to determine the effects of geometric features and distributions of material parameters on the matrix ductility limit and variability. Figure III-41 compares intrinsic stress-strain responses between different models with various geometric features and material parameters. As shown in Figure III-41, intrinsic ductility may vary significantly, depending on an alloy's microstructural features. It was observed that the developed multiphase modeling methodology can be used to predict a reasonable range of intrinsic ductility that can be passed up to the extrinsic models that consider casting defects and pores.

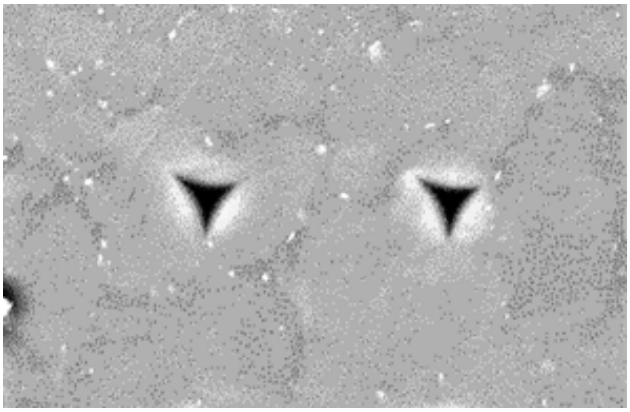

(a)

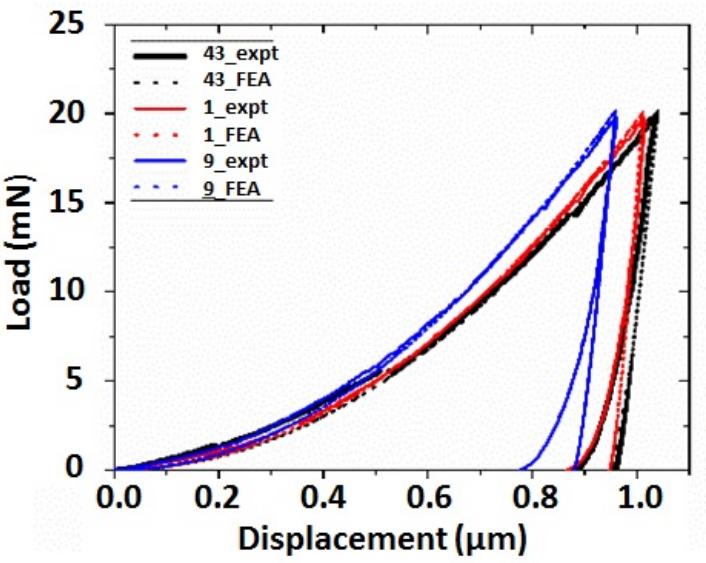

(b)

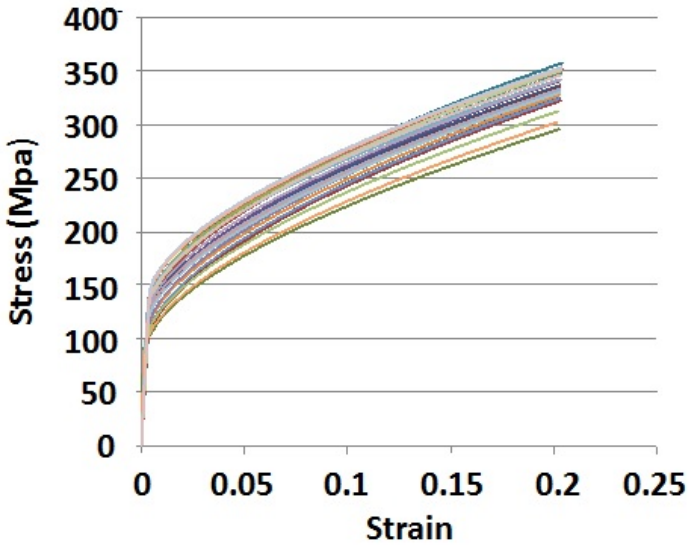

(c)

Figure III-39: (a) Nanoindentation test on Mg Casting, (b) comparison of load-displacement curves between the FE modeling and experiments, and (c) distribution of stress-strain curves for the alpha phase of the sample, extracted from 200 indents.

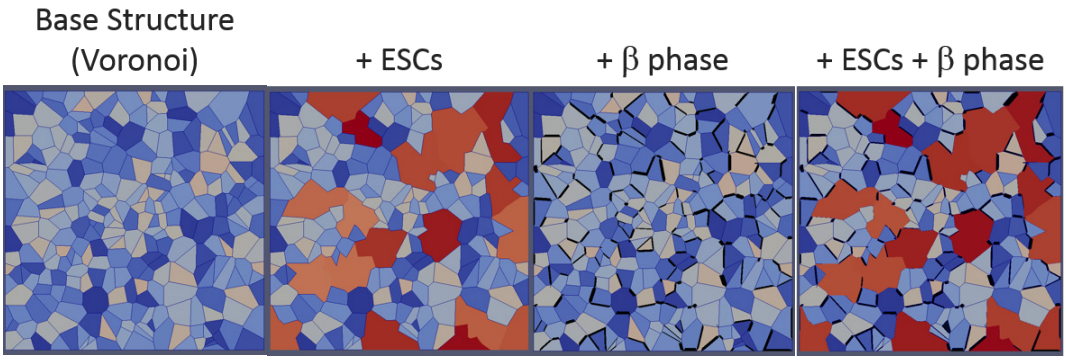

Figure III-40: Examples of modeled microstructure geometries, including different combinations of key microstructural features.

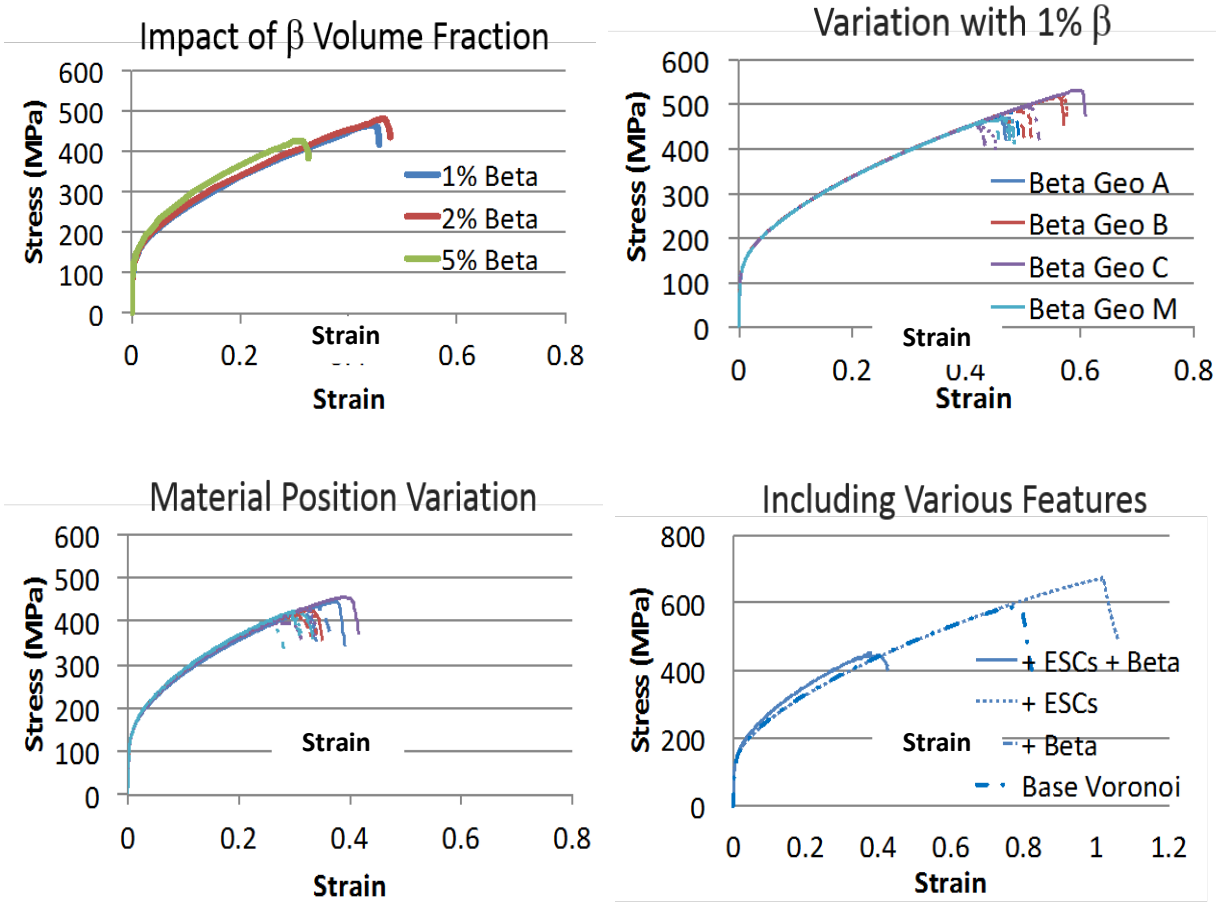

Figure III-41: Comparison of intrinsic stress-strain responses between the models with various geometric features and material parameters.

Figure III-42(a) shows a special metal die used to produce several different sizes of round and flat tensile samples for examining the effects of cast skin on the mechanical properties of high-pressure die-cast Mg alloys [7]. As-cast tensile samples, designated F3, were CT scanned to obtain the pore distributions within the samples. CT data from some selected samples were then used to generate 3D microstructure-based FE models. Figure III-42(b) and Figure III-42(c) show the CT images of the cross sections of the selected samples and the corresponding 3D FE models generated based on the CT data, respectively. The generated 3D models appear to capture the overall pore distribution features within the samples. Here, the input properties for the matrix material of the samples were determined by fitting the simulation result to the experimental result from one sample (#2). Figure III-43 compares the simulation results of the samples with their experimental results in terms of ductility and fracture location. The figure indicates that the current extrinsic models, which considered only the porosity captured from CT, can predict the ductility and fracture locations of tensile samples from Mg castings. This finding may support the premise that the porosity is a dominant factor influencing the ductility of Mg materials cast under the same conditions.

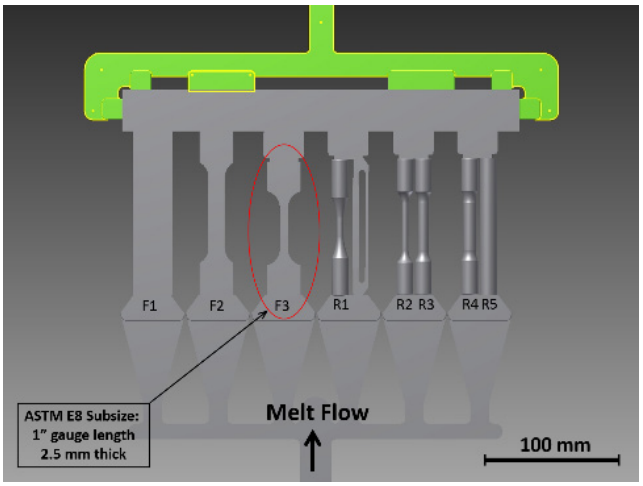

(a)

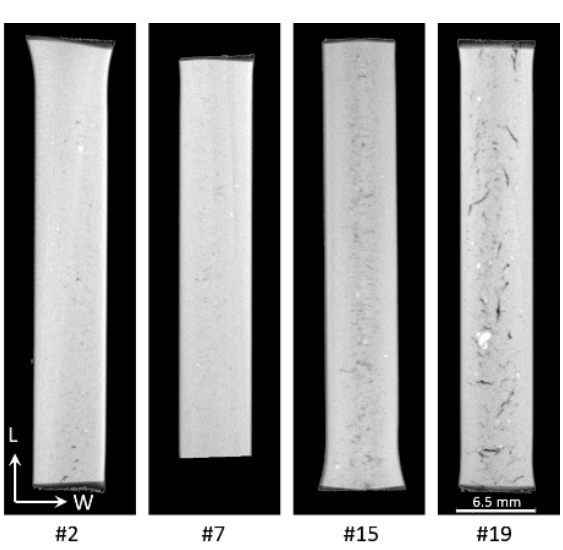

(b)

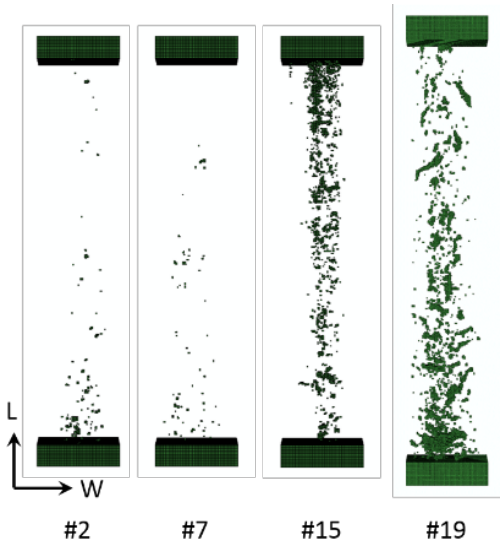

(c)

Figure III-42: (a) Die geometry for generation of as-cast sample, (b) CT images showing cross sections of selected samples, and (c) 3D FE models generated based on CT data.

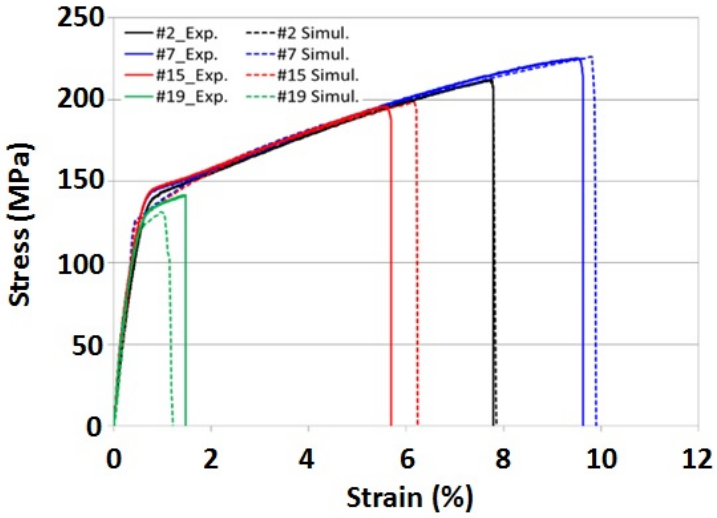

(a)

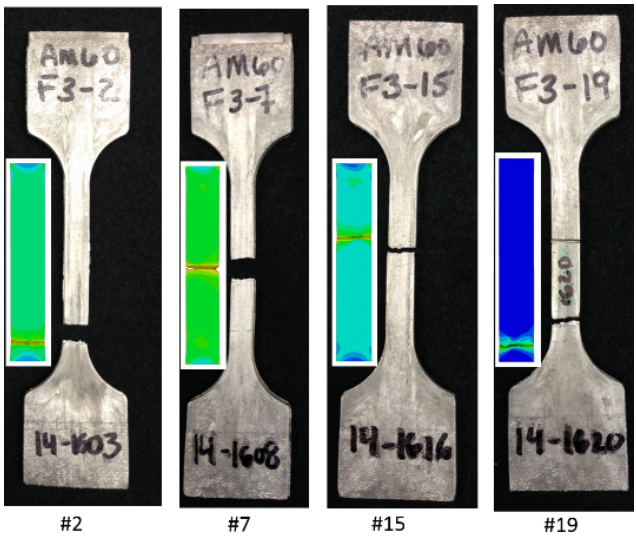

(b)

Figure III-43: Comparison of (a) stress-strain curves and (b) fracture locations from experiments and simulations.

Technology Transfer Path

The deliverables from this project have already been transferred to Ford and will be transferred to other OEMs casting producers through scientific publications. Industry can use the modeling methodology and results to improve performance and reduce the number of prototypes needed to validate a casting design, thereby saving time and cost.

Conclusions

Intrinsic models were expanded to include additional key geometry features and use alloy-specific material parameter distributions. The expanded intrinsic modeling method predicts reasonable ranges of intrinsic properties/ductility that can be used as input properties for the matrix material in the larger-length-scale extrinsic modeling. With its validation against experimental results, the developed 3D extrinsic modeling

method can be combined with synthetic microstructures and used to investigate the influence of various aspects of pore sizes/distributions and intrinsic properties on the ductility/fracture of Mg castings. The influence of intrinsic properties can also be examined with respect to aspects such as differences in intrinsic properties between the cast skin region and core region, inhomogeneous distribution of intrinsic properties, and others.

Self-Pierce Riveting Process Simulation, Analyses, and Development for Magnesium Joints

Project Details

Elizabeth Stephens, Principal Investigator
Pacific Northwest National Laboratory
902 Battelle Boulevard
P.O. Box 999
Richland, WA 99352
Phone: 509-375-6836
E-mail: elizabeth.stephens@pnnl.gov

Xin Sun, Co-Principal Investigator
Pacific Northwest National Laboratory
902 Battelle Boulevard
P.O. Box 999
Richland, WA 99352
Phone: 509-372-6489
E-mail: xin.sun@pnnl.gov

Eric Nyberg, Co-Principal Investigator
Pacific Northwest National Laboratory
902 Battelle Boulevard
P.O. Box 999
Richland, WA 99352
Phone: 509-375-2103
E-mail: eric.nyberg@pnnl.gov

Siva Ramasamy, Principal Investigator
Stanley Engineered Fastening
49201 Gratiot Avenue
Chesterfield, Michigan 48051
Phone: 586-949-0550
E-mail: siva.ramasamy@sbdinc.com

Accomplishments

- Completed the joint performance and fatigue evaluations for AZ31B Mg SPR joints (FY 2015).
- Validated modeling tool simulation results with experimental data from the joining process (FY 2015).
- Created induction-heated 7075 Al to AZ31B Mg SPR joints (FY 2015).
- Explored alternate rivet materials via the modeling tool (FY 2015).
- Completed project final report and recommendations for successful Mg SPR joining (FY 2015).

Future Directions

- Because of completion of the project, further research and interests will be explored by Stanley Engineered Fastening (Stanley). Interests include exploring automation of the induction heating system and furthering research in Mg castings, dissimilar metals, and alternate rivet materials.

Technology Assessment

- Target: Create Mg SPR joints of similar and dissimilar materials under the guidance of SPR modeling tools established by PNNL with no tail-side cracking.
- Target: Produce Mg SPR joints with a minimum target joint strength of 1.5 kN of lap shear strength per millimeter of substrate thickness.
- Gap: Mg alloys have low ductility at room temperature and, when conventional SPR processing is used with Mg, rivet tail end cracking occurs.
- Gap: Cracks in the SPR joint can be detrimental to joint performance in terms of static and fatigue strength and corrosion performance.

Introduction

Because of increased pressure from government agencies and consumer advocate groups to produce safer, more durable, fuel-efficient vehicles, automotive OEMs are investigating Mg for use in major structural sections of vehicles. Mg components offer a potential weight reduction of approximately 50% when substituted for the higher-density or lower-strength steel materials conventionally deployed in vehicles. Historically, poor joining methods for Mg components have limited their application in vehicles. Over the years, a variety of joining technologies have been introduced into the automotive industry to achieve lightweight vehicle goals. SPR is potentially a viable method for joining similar and dissimilar metals involving Mg. SPR is a low-energy-consumption joining process with relatively low initial capital equipment cost. Because SPR is a mechanical joining process, the joint formation process involves large plastic deformation at the rivet tail end to ensure a mechanical interlock between the rivet material and the bottom sheet material. However, Mg alloys have low ductility at room temperature; thus, conventional SPR processing typically causes rivet tail end cracking. These cracks can be detrimental to rivet performance in terms of static strength, fatigue strength, and corrosion performance.

Approach

This project was focused on developing and enabling the SPR process for joining Mg components in new vehicle applications to reduce vehicle weight through efforts established in a Cooperative Research and Development Agreement between PNNL and Stanley. This project aimed to eliminate or substantially address key technical barriers to using SPRs in Mg-joining applications by using an integrated modeling and experimental approach. Barriers include tail-side cracking of Mg sheet or castings due to the lack of ductility at room temperature; lack of desired joint properties, including corrosion at the joint; and lack of acceptable processing parameter windows. Further, the project explored alternative/nonconventional rivet metals similar to the materials being joined to minimize the galvanic potential in the joint and that may further promote joining of Mg. Initial work focused on development of a numerical tool used to build reliable Mg riveting process parameters through modeling and provide guidance in the development of joining process windows.

Phase 1 focused on experimental validation of the modeling tool previously developed for Mg SPR joining using conventional rivet materials and geometries. This phase experimentally validated the predicted results from the modeling tool to provide actual joint performance data (e.g., joint strength, fatigue strength, and corrosion performance) for the joint combinations evaluated. Phase 2 focused on optimizing Mg SPR joints using the established modeling tool to investigate alternate rivet materials, investigate dissimilar metal joining, and optimize rivet geometry (i.e., shape and length) and die design to promote joint integrity and performance.

Results and Discussion

In FY 2015, efforts focused on optimization and characterization of the AZ31B Mg SPR joint, exploration of alternate rivet materials via the modeling tool, exploration of dissimilar metal joining, validation of modeling tool simulations, and final project wrap-up between PNNL and Stanley. The following highlights the results achieved this fiscal year. The rivet geometry and die design were optimized and select processing conditions were applied to 2 mm-to-2 mm and 1 mm-to-2 mm AZ31B SPR lap shear coupons to assess the joint and fatigue strengths of the induction-heated joints. The target joining temperature was 250ºC for the final joints characterized and they were processed within the target cycle time of 3 seconds.

Figure III-44 compares the previous lap shear strength results for 2 mm-to-2 mm joints made at varying elevated temperatures ranging from 250 to 300°C via the induction heating system with the final 2 mm-to-2 mm joints created at 250ºC. All specimens exceeded the target joint strength of 3.5 kN. Previously, the mean joint strength observed was 5.7 kN, with a maximum of 6.2 kN and a minimum of 4.8 kN observed (Figure III-44a). Variation of strengths observed was due to the varying rivets and die geometries selected for processing. In Figure III-44b, the mean joint strength observed was 6.9 kN, with a maximum of 7.2 kN and a minimum of 6.6 kN. Optimization of rivet and die design and the heating process led to more repeatable results with improved strengths (i.e., about a 20% increase).

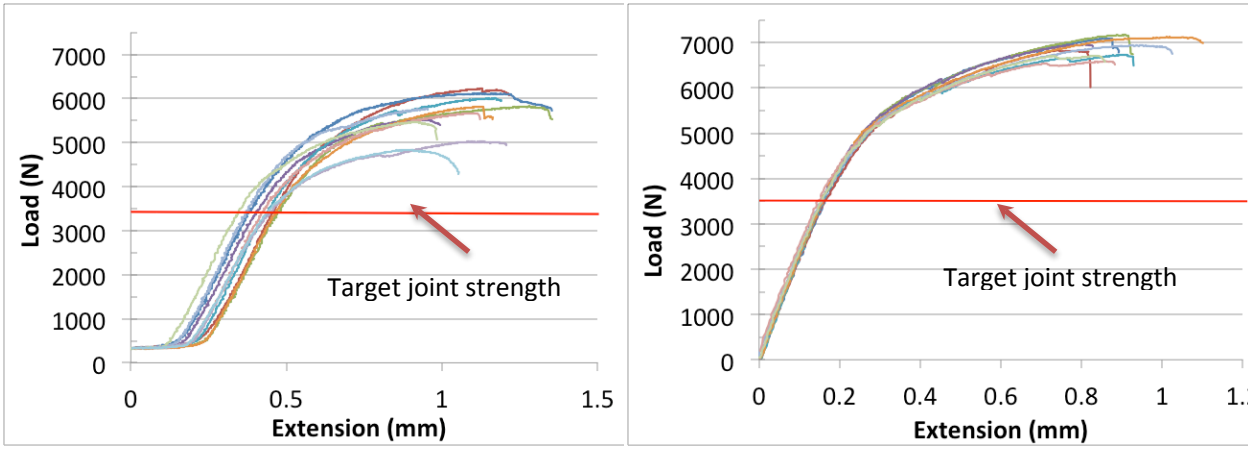

Figure III-44: Comparison of lap shear strength results of AZ31 Mg SPR joints created at elevated temperatures, with an induction heating system (a) before optimization and (b) after optimization of the rivet and die design and processing parameters

Vickers microhardness tests were also performed to assess the integrity of the AZ31B Mg sheet after joining. Hardness measurements of the final AZ31B Mg joint indicated no detrimental strength effects of the alloy sheet arising from the heating process. Hardness uniformity was observed in the Mg sheets surrounding the rivet (illustrated in Figure III-45). The average hardness observed in the sheets was a Vickers Pyramid Number of 81.5 HV, with increased values observed approaching the rivet interface that ranged from 90 to 100 HV.

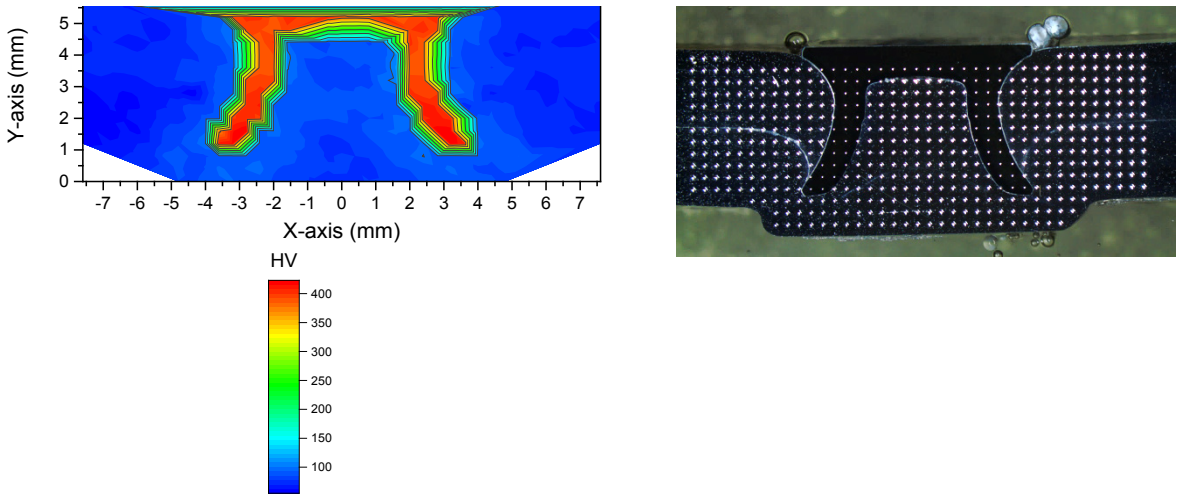

Figure III-45: Vickers microhardness results of the AZ31B SPR joint showing (a) the hardness profile map and (b) the corresponding cross section evaluated.

Fatigue evaluations with a stress ratio of R = 0.1 were performed on the AZ31B Mg SPR joints under lap shear loading for both Mg sheet configurations. Figure III-46 illustrates the fatigue test results and results of 2 mm-to-2 mm 5182-O Al SPR joints for comparative purposes. Increased fatigue performance was observed in the 2-mm joint configurations in comparison to the 1 mm to 2 mm. When comparing the 2-mm Mg joints to the 2-mm Al joints, similar behavior was observed. At low cycles, the 5182-O Al SPR joint had slightly improved fatigue performance; however, at higher cycles, the AZ31B had slightly improved fatigue performance.

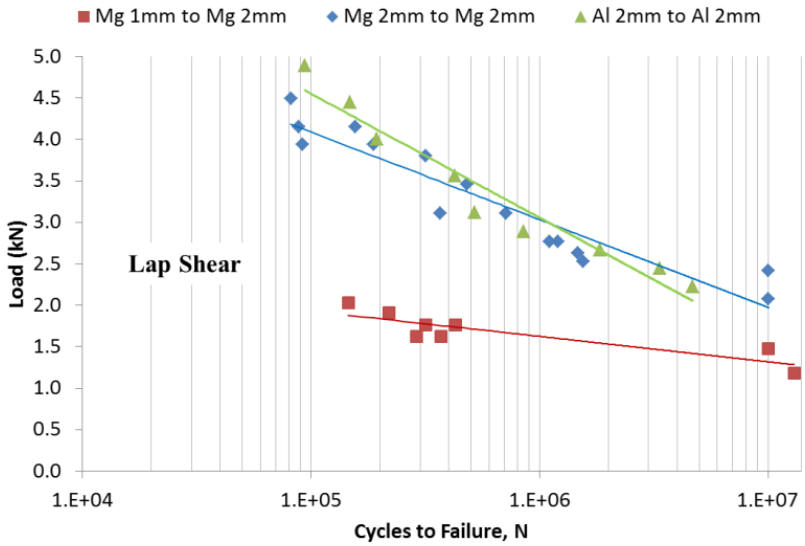

Figure III-46: Fatigue test results of AZ31B Mg and 5182-O Al SPR joints under lap shear loading.

In FY 2015, modeling efforts continued on improving the previously developed SPR finite element model (FEM) through validation with actual riveted joints and utilizing the modeling tool to explore alternate rivet

materials. Simulations of the SPR process used Stanley's rivet and die geometries with the thermomechanical FEM. As another validation of the model, the team compared the predicted joint geometry (i.e., interlock shape) to an actual SPR joint created using the same die and rivet geometries to join 7075-T6 Al to AZ31B sheets (2-mm thick each) as part of the dissimilar metal joining investigation.

Figure III-47 shows a comparison between the simulation and actual dissimilar metal SPR joint created at 250ºC. Fair agreement is shown between the experiment and the model. More flaring of the rivet tip is observed in the simulation than in the actual joint. The model prediction suggests that the 7075 Al top sheet, which is stronger than the Mg, causes a more pronounced deformation and thickening of the rivet before it penetrates into the Mg bottom sheet. In addition, differences observed may be attributed to an artifact of the model, in which element deletion occurs when the fracture criteria are met, when in reality the Al material is dragged into the pierced bottom sheet.

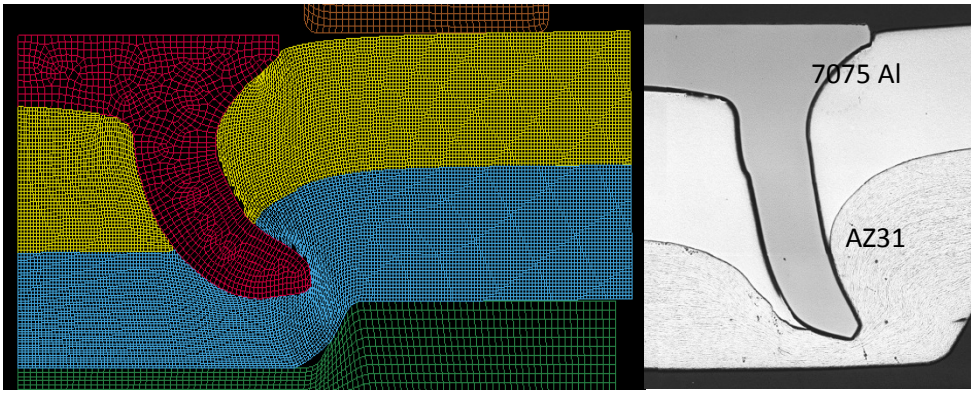

Figure III-47: Results of 2 mm-to-2 mm Al-to-Mg sheet SPR joints at 250ºC comparing the cross section of the FEM-predicted shape (left) with the actual joint (right).

Figure III-48 shows the preliminary lap shear joint strength of the dissimilar metal Al to Mg SPR joints. Target joint strengths are achievable. However, variations in strength were observed, which may be attributed to the thermal instability of the 7075 Al alloy.

Previously, the force versus rivet displacement during joining was simulated to aid in validation of the model. In FY 2015, experimental data during the joining process was gathered to validate these simulated results. Figure III-49 represents the simulated force versus rivet-head displacement curve along with the experimental data gathered during SPR joining of 7075 Al to AZ31B Mg. Good agreement between the simulation and experimental data is observed. A slight deviation between measurements and the prediction is observed at about 4.5-mm vertical displacement. This may be attributed to an artifact of the model, where the top sheet is split before the rivet comes in contact with the bottom sheet.

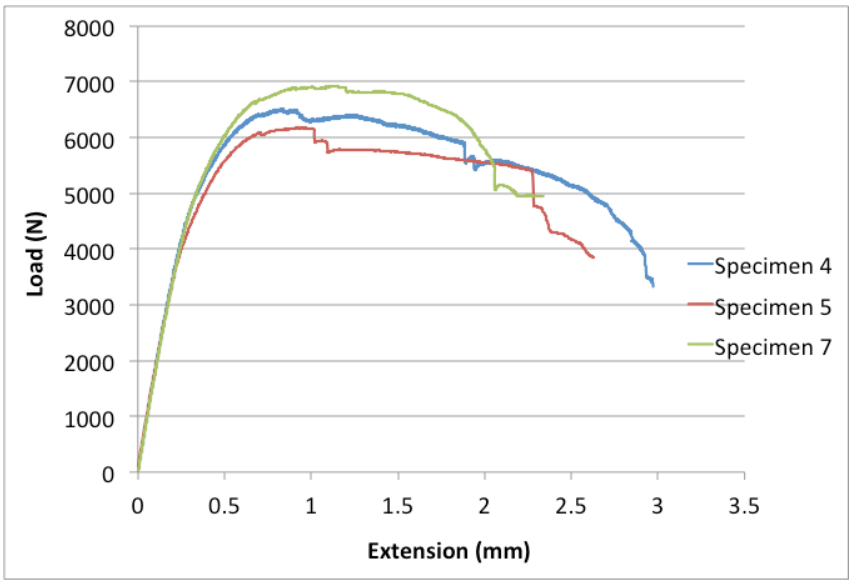

Figure III-48: Preliminary joint strength results of 2 mm-to-2 mm 7075Al to AZ31B SPR joints under lap shear loading. The joints were created via induction heating.

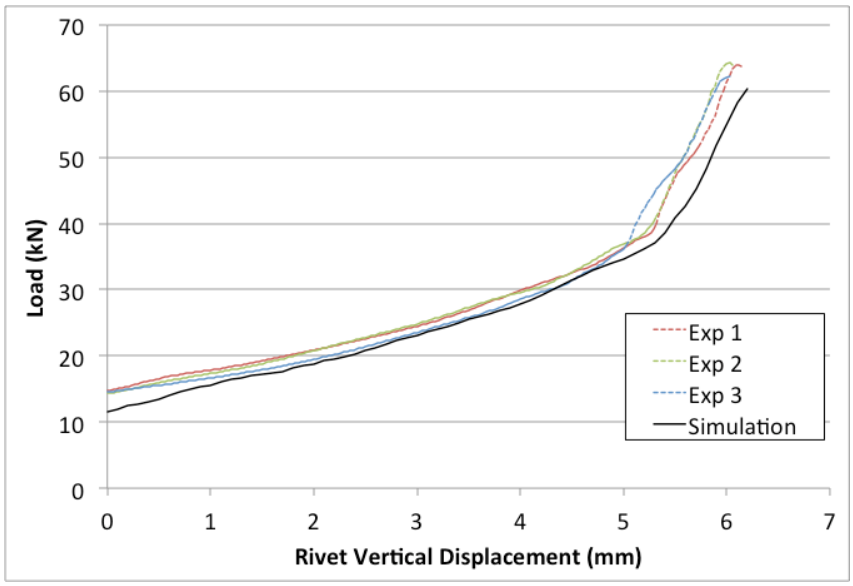

Figure III-49: Comparison of the simulated force versus rivet-head displacement curve during SPR joining at elevated temperature with actual experimental data. Results shown are for 7075 Al to AZ31 Mg SPR joints created via induction heating.

Simulations of the lap shear strength tests were performed to assess and explore the performance of 2 mm-to-2 mm Mg SPR joints created with alternate rivet materials. The SPR joining process was first simulated, then the die and sheet holder were removed and adequate boundary conditions applied on the remaining parts to simulate lap shear. Simulations of Mg joined sheets using different SPR rivet materials (such as carbon steel and varying Al [7075-T6 and 5182-O]) were performed. Figure III-50 shows the predicted joint strengths under lap shear loading. The predicted joint strength for Mg SPR joints created with carbon steel rivets is about 30% greater than the equivalent joint created with 5182-O Al rivets. However, the predicted joint strength is lower than the equivalent joint created with 7075-T6 Al rivets.

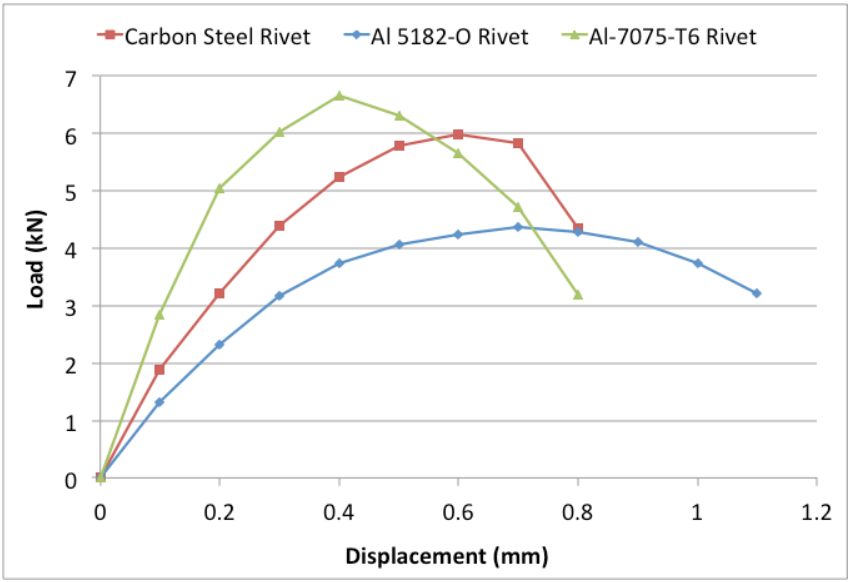

Figure III-50: A Comparison of the predicted joint strength results of 2 mm-to-2 mm AZ31B Mg SPR joints created with varying rivet materials (such as carbon and Al).

Technology Transfer Path

Technology transfer occurred throughout the project via close collaboration between PNNL and Stanley. The technology transfer approach included development of process equipment and processing parameters necessary to achieve successful Mg SPR joints and transferring of the modeling tool to Stanley.

Conclusion

In FY 2015, the project concluded, successfully optimized and created AZ31B SPR joints via induction heating at 250ºC, and characterized performance of the joint. Under lap shear loading conditions, a mean joint strength ofbout 6.9 kN was observed, which was approximately 20% greater than previously reported results. The fatigue performance of 2-mm Mg SPR joints is similar to that of 2-mm 5182-O Al SPR joints. In addition, continued improvement of the modeling tool was performed through experimental validation. Good agreement was observed between predicted and experimental results for 2mm-to-2 mm 7075 Al and AZ31B Mg SPR joints during joining. Fair agreement between predicted results and actual joints created was observed. Alternate rivet materials were also explored using the modeling tool, which predicted that increased strengths under lap shear loading will occur with use of 7075-T6 Al rivets in comparison to carbon steel rivets for equivalent Mg SPR joints.

High-Strength, Dissimilar Alloy Aluminum Tailor-Welded Blanks

Project Details

Yuri Hovanski, Principal Investigator
Pacific Northwest National Laboratory
902 Battelle Boulevard
Richland, WA 99352
Phone: 509-375-3940
E-mail: yuri.hovanski@pnnl.gov

Accomplishments

- Completed a series of bead-on-plate welds on 2-mm thick AA7075-T6, AA6022-T4, AA6022-F, and AA5182-O alloys across a wide range of welding speeds (1 to 6 m/min) with in situ temperature measurement inside the FSW tool (FY 2015).
- Compiled datasets on the effects of welding speed on transient tool temperatures and resulting weld macro and microstructure and hardness in the nugget and the heat affected zone (HAZ) (FY 2015).
- Developed a welding parameter set to produce dissimilar thickness/dissimilar material FSW joints between (a) AA7075-T6 (2 mm) and AA5182-O (1.1 mm), (b) 6022-T4 (2 mm) and AA5182-O (1.1 mm), and (c) AA7085-T6 (2 mm) and AA5182-O (1.1 mm). Tensile tests along the length of the welds showed fractures away from the weld region for all of the above cases (FY 2015).
- Validated formability simulation model for limiting dome height (LDH) tests on dissimilar thickness sheet (AA5182 and AA6022) with experimental LDH tests in tapered machined samples (FY 2015).

Future Directions

- Establish repeatability of the developed weld parameter set for dissimilar alloy/dissimilar thickness FSW and expand the welding window to achieve higher welding speed for high volume production.
- Develop parameter window, tooling, and fixturing needs for curvilinear high-speed FSW in both similar and dissimilar alloy combinations.
- Develop material coefficients, including Barlat coefficients, for weld regions in association with General Motors and Alcoa for similar and dissimilar alloy FSW.
- Develop a formability model to include weld properties in combinations of similar and dissimilar alloys (results from above bullet point) to be ready for model validation of actual parts joined.
- Determine the influence of tool durability, tool material selections, and coatings on weld quality, process repeatability, and production readiness.
- Supplier will validate process parameters, demonstrating near-term deployability for high-volume production.

Technology Assessment

- Target: Achieve FSW speeds for dissimilar Al TWBs in excess of 3 m/min with repeatable quality and surface finish.
- Gap: While similar alloy Al TWBs have been demonstrated to be weldable above 3 m/min, the process needs to be developed to go beyond 3 m/min in dissimilar materials because of the inherent problem of different high-temperature flow stresses of dissimilar materials.
- Target: Develop high-speed welding parameters such that the soft zone typically present in the HAZ in precipitation hardening alloys is shifted to the recrystallized region in the nugget.

- Gap: A mostly unexplored range of welding speed in the industry is being used and is required to obtain defect free, repeatable welds at high welding speed.
- Target: Develop material constitutive coefficients, including Barlat coefficients, for welded regions to serve as input to the formability model.
- Gap: While Barlat coefficients have been established for base materials in the past, this will be the first attempt to obtain coefficients for a non-homogeneous welded region.
- Target: Demonstration of a formability model in prototypically sized welded part that demonstrates predictability.
- Gap: Current modeling practices do not take into account non-homogeneous weld properties; thus, the modeling effort needs to be fully verified with full-size component testing.

Introduction

This work is focused on development of high-strength, high-speed FSW in dissimilar Al alloy combinations in linear and curvilinear geometries. The alloy combinations include work hardenable alloys (5XXX series) capable of deep drawing and precipitation hardenable alloys (6XXX, 7XXX) that can be hardened after joining and forming to yield high strength for application in body skin and structural supports. This work will shed light on the effects of high welding speed on resulting weld properties that have not been explored yet and find ways to exploit the high-speed FSW to enhance strength and ductility.

The work will develop the material coefficients required to support formability modeling of dissimilar alloy combinations with different hardening mechanisms (i.e., strain hardening in 5XXX and precipitation hardening and HAZ degradation due to coarsening in 6XXX and 7XXX). The resulting material coefficients will, in turn, be used to develop a formability model capable of simulating combinations of dissimilar alloy and dissimilar thickness TWBs. Ultimately, the formability model will be validated against the formability performance of actual welds made at a supplier facility.

Approach

In order to develop FSW for a high-strength dissimilar alloy combination, the work scope is divided into four main task areas. The first task is concerned with obtaining relationships between the weld parameters, material, and weld properties. This includes base metal characterization, including strength, ductility, orientational homogeneity, and Barlat coefficients supporting finite element analysis modeling, comparative analysis of weld properties, and reporting. Characterization of welds, both “bead on plate” and dissimilar alloy combinations, to understand functional relationships of welding parameters on resulting properties will also be performed in this task.

The second task is primarily focused on developing high-speed parameter sets to produce sound welds in dissimilar alloy combinations for 5XXX to 6XXX and 7XXX in similar or dissimilar thickness combinations. In addition, tooling, transitional weld parameters, and fixtures will be developed to support curvilinear, high-speed FSW.

The third task pertains to production readiness and deployability, including study of FSW repeatability and tool durability. This task will begin in FY 2016.

The fourth task concerns weld formability modeling and validation, including development of material coefficients and simulation of sheet formability in dissimilar material, dissimilar thickness TWBs.

Results and Discussion

The effects of welding speed on temperature attained in the material during the process can provide important information related to resulting weld properties. A comprehensive set of temperature versus welding speed datasets extracted from a series of bead-on-plate welds in three different materials of interest across a wide range of welding speeds is shown in Figure III-51. As welding speed increases, the temperature attained by the weld nugget gradually decreases. Given that most FSW made on aluminum sheets reported in literature are made at speeds lower than 1 m/min, this set of data and the resulting weld properties can provide a unique opportunity to understand the effects of rapid thermal transients.

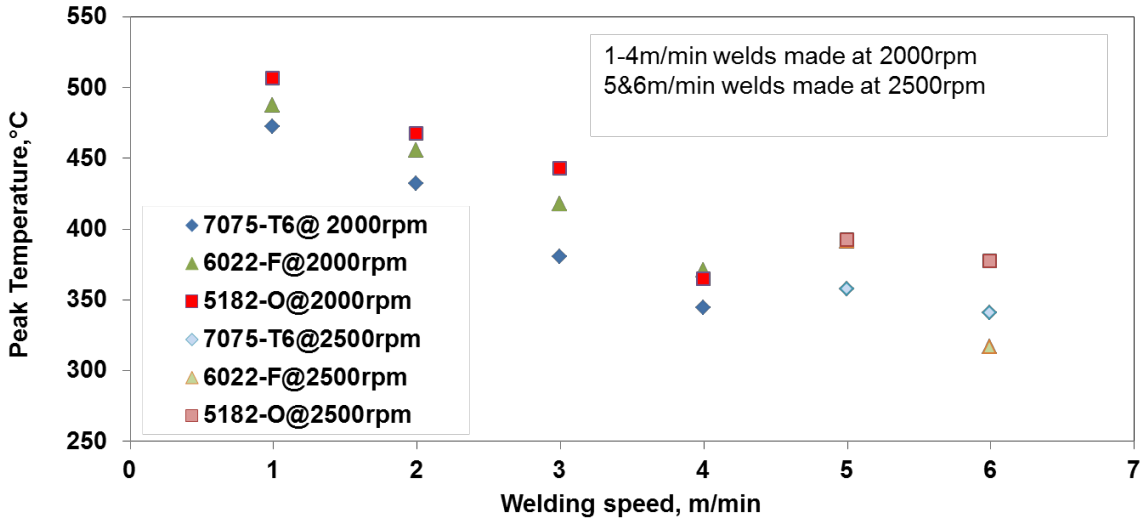

Figure III-51: Peak tool temperature versus welding speed obtained from bead-on-plate welds.

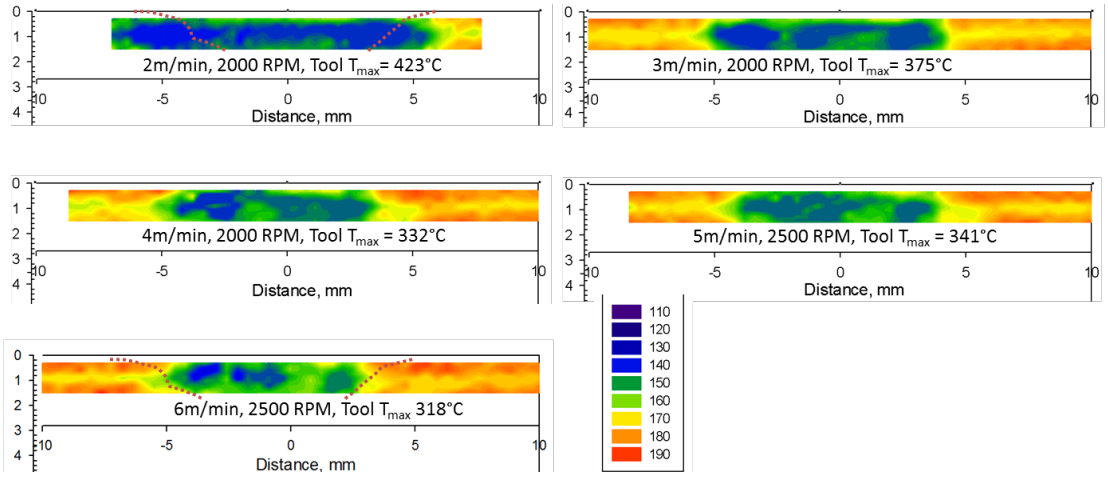

Figure III-52: Full-field microhardness maps for bead-on-plate welds made in 2-mm thick AA7075-T6 for a range of welding speeds.

The full-field hardness plots for a range of welding speeds from 2 to 6 m/min for AA7075 (2-mm thick) shown in Figure III-52 provides an overview of variation in a weld property with change in weld thermal history caused by change in welding speed. The extent of the soft zone is gradually reduced as the welding speed increases from 2 to 6 m/min, owing to reduced exposure of time at temperature for precipitate coarsening and

dissolution in the matrix. In addition, at higher welding speeds (i.e., viz. 4, 5, and 6 m/min), the relatively small soft zone is concentrated inside the recrystallized weld nugget rather than in the HAZ, where the soft zone is typically located.

In addition to full-field hardness testing, grain structure characterization in the weld nugget, the thermomechanically affected zone, and the HAZ was carried out. Grain mapping for different sets of welding parameters allows correlation with measured tool temperature and effects of parameter sets on grain sizes. For instance, the average grain size of the weld corresponding to welds made at 3 m/min is significantly smaller than that made at 1 m/min. This can be directly related to the peak temperature measured in the tool during welding (Figure III-53).

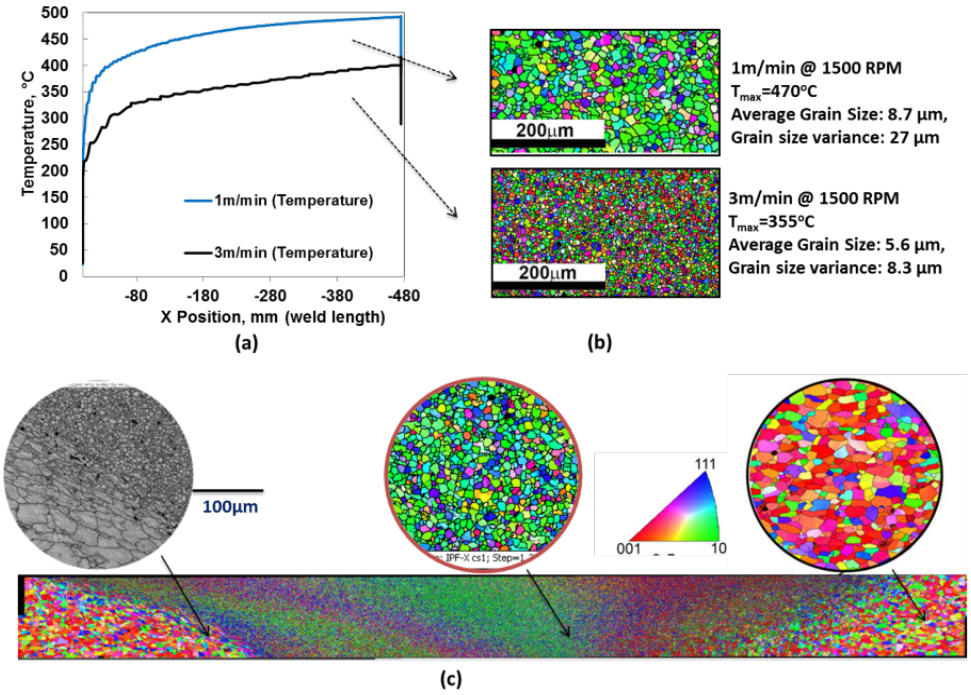

Figure III-53: (a) Tool temperature versus weld position for two different welding speeds. (b) OIM pictures showing nugget grain structure for the corresponding two welds. (c) Full-field OIM of weld cross section showing different weld regions.

Aside from the fundamental weld characterization discussed above, progress was also made on developing weld parameter windows to produce sound welds between dissimilar thickness, dissimilar alloy combinations. Specifically, welding parameter sets were developed for (a) AA7075-T6 (2 mm) and AA5182-O (1.1 mm), (b) 6022-T4 (2 mm) and AA5182-O (1.1 mm), and (c) AA7085-T6 (2 mm) and AA5182-O (1.1 mm). Figure III-54 shows the stress versus strain curves for welded specimens extracted along the length of the weld in comparison to the 5182-O dataset. For all welded samples, fracture occurred outside the weld in the thin sheet base metal. Figure III-54 clearly shows the fracture strength of the joint is similar to that of the base metal 5182-O. Similar results were obtained from material combinations (b) and (c) above.

Commercial finite element software ABAQUS™ was used to numerically model sheet deformation under a hemispherical die with a goal of simulating the LDH test. After a through validation and input of appropriate material coefficients (anticipated in FY 2016), this model will ultimately be developed to predict sheet deformation behavior of stamped, dissimilar-alloy TWB joints at a supplier site. The first step of validation was completed this year by comparing the simulation results with experimental LDH results obtained from machined different thickness sheets.

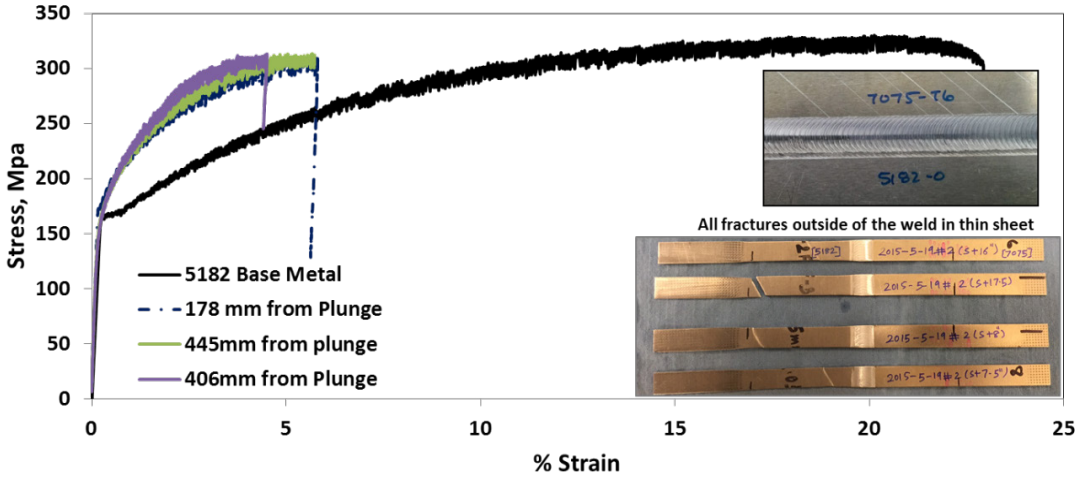

Figure III-54: Stress versus strain plots for welds made between AA7075-T6 (2 mm thick) and AA5182-O (1.1 mm) along the length of the weld. A corresponding plot for AA582-O base metal is shown for comparison. Fracture samples and a close-up of the weld crown are shown in the inset.

Figure III-55 shows experimental versus predicted dome heights for differentially machined AA6022 sheets. Two distinct failure criteria were used: (1) global limit strain and (2) an existing formability limit diagram (FLD). The experimental results match well with FLD criteria, owing to the higher allowable biaxial strain compared to a global limit strain. The two geometric approaches (i.e., step and taper) shown in Figure III-55 yielded very similar results. This outcome provides a basis for moving forward to establish a comprehensive deformation modeling tool once appropriate material coefficients are obtained for the weld region.

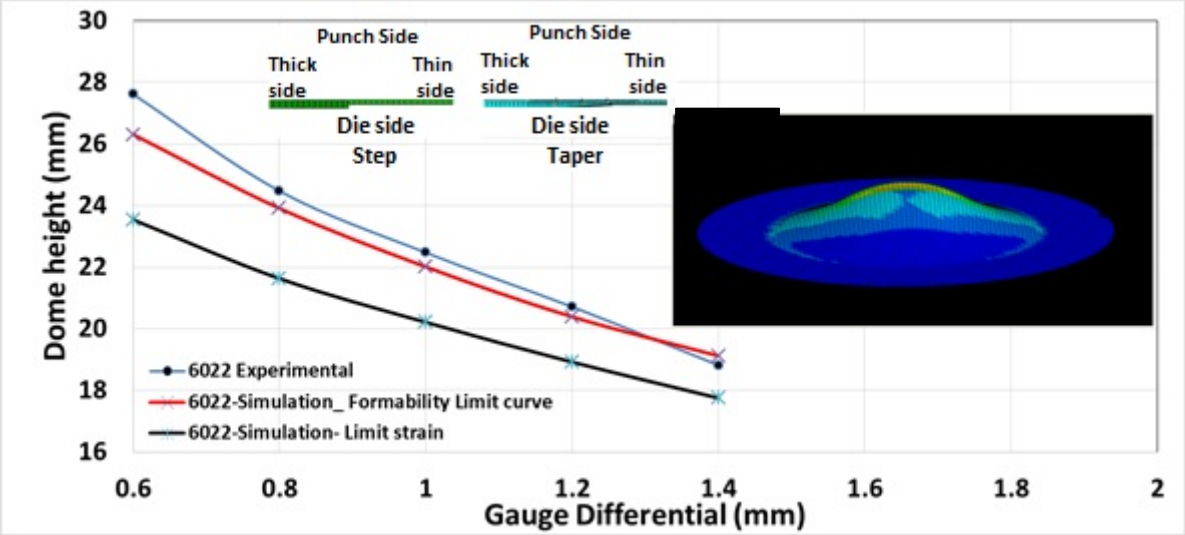

Figure III-55: Experimentally measured dome height and predicted dome heights from numerical models for various sheet thickness ratios versus simulation. The step and taper approaches of geometric simulation are shown above the curve. Inset: a representative strain map obtained from a model showing strain localization outside the weld line.

Technology Transfer Path

Technology transfer of the project will be made directly through the project participants General Motors, TWB LLC, and Alcoa, who will be the implementers of the technology. TWB, a tier 1 supplier to the automotive industry, will be able to use the joining technology developed during the project to address a wide cross section of the automotive industry by implementing TWB technology for Al alloys, which can be used to reduce vehicle mass.

Conclusions

As a continued effort to enable the automotive supply chain to adopt FSW of TWB Al into mainstream production lines, the initiation of this project allowed stakeholders to be involved in making key decisions in developing dissimilar material TWBs. Early in FY 2015, decisions were made regarding materials and gauges of interest and desired outcomes. All industrial partners contributed significant in-kind efforts over FY 2015, including materials, material properties by Alcoa, and an experimental formability study by General Motors. Having completed base material characterization for all materials of interest, the project quickly moved to obtaining a dataset for weld process parameters and resulting weld properties and functional relationships thereof for three different types of Al alloys over a large range of welding speeds. Aside from fundamental weld characterization, progress was also made on developing weld parameter windows to produce sound welds that performed well in tensile tests between dissimilar thicknesses, dissimilar alloy combinations. A numerical formability model was developed and validated against monolithic differential gauge experimental results.

Enhancing Sheared Edge Stretchability of Advanced and Ultra-High-Strength Steels through Integrated Manufacturing Process Simulations

Project Details

Xin Sun, Principal Investigator
Pacific Northwest National Laboratory
902 Battelle Boulevard
Richland, WA 99352
Phone: 509-372-6489
E-mail: xin.sun@pnnl.gov

Constantin Chiriac and Raj Sohmshetty, Industrial Collaborators
Ford Motor Corporation
2101 Village Road
Dearborn, MI 48121
Phone: 313-390-0839
E-mail: cchiriac@ford.com, rsohmshe@ford.com

Ming Shi and Brandon Hance, Industrial Collaborators
U.S. Steel
5850 New King Court
Troy, MI 48098
Phone: 248-267-2610
E-mail: mfshi@uss.com, bhance@uss.com

Kavesary (KS) Raghaven and Yu-wei Wang, Industrial Collaborators
AK Steel
705 Curtis Street
Middletown, OH 45043
Phone: 513-425-2922
E-mail: kaversary.raghaven@aksteel.com, yu-wei.wang@aksteel.com

Accomplishments

- Performed mechanical and microstructural examination of DP980 steels produced by U.S. Steel (UDP980) and AK Steel (ADP980) (FY 2015).
- Performed accumulated rolling and tension tests for ADP980 to obtain the flow stresses for large strains (FY 2015).
- Phase properties of the two DP980 steels were determined by in-situ high-energy x-ray diffraction (HEXRD) tensile tests and elasto-plastic self-consistent crystal plasticity modeling (FY 2015).
- Performed trimming tests of the two DP980 steels and cross-sectional examinations have been performed on the UDP980 steel (FY 2015).
- A macro trimming model has been set up and some initial trimming simulations have been performed for parametric studies (FY 2015).

Future Directions

- Accumulated rolling and tension tests will be performed for UDP980.
- Edge fracture and damage will be examined by metallography and three-dimensional HEXRD tomography.

- A macro-micro approach will be applied to the trimming simulations and predicted edge fracture and damage will be compared with experimental results.
- Tensile stretchability studies will be performed on previously trimmed parts.

Technology Assessment

- Target: Enhance sheared edge stretchability of AHSS/UHSS by creating a predictive framework linking microstructural features to ultimate edge stretchability.
- Gap: The most commonly observed failure mode for AHSS/UHSS is edge splitting and the contributions of various microstructural features and process parameters to edge stretchability are not well understood.

Introduction

More and more advanced high-strength steels are being developed and introduced into vehicle structures for weight reduction and crash performance improvement. During cold stamping of AHSS/UHSS parts, the most commonly observed failure mode is edge splitting; sheared edge stretchability appears to depend on a combination of factors, including edge stretching mode, edge shearing/trimming conditions, and initial sheet properties defined by the microstructure. For the same steel, different edge or hole preparation methods yield different formability results. For different dual phase steels within the same strength family (i.e., DP980), the same hole preparation method also yields different hole expansion ratios. Therefore, the contributions of these various factors to AHSS/UHSS edge stretchability are not well understood due to the complex interactions of these factors during edge preparation and subsequent forming operations.

In addition to the above-mentioned factors in edge preparation methods and material intrinsic microstructures, the term “edge stretchability” also has different definitions and associated measurements. While the traditional way of defining edge stretchability is through a hole expansion test with a conical or flat punch, recent edge stretchability studies with tensile half–dog-bone samples show that the hole expansion test yields significantly higher strain values, especially at smaller clearances.

The edge damage caused by a piercing operation is generally accepted as depending on the microstructure of the material and the difference in the edge stretching limit between different dual-phase steels of the same ultimate tensile strength (UTS) level could be due to the different degrees of edge damage induced by the hole piercing operation. But quantitative and predictive capabilities linking the microstructure characteristics to the sheared edge stretchability under different loading modes (i.e., tensile stretching or hole expansion) are not available. Although there is much experimental data reported in open literature on measured edge stretchability values for various steels with specific edge preparation methods and sample designs, data are typically only valid for the specific material under the specific combination of edge preparation and stretching conditions due to lack of fundamental understanding of the effects of microstructure on sheared edge stretchability. There is a keen interest from steel producers for more fundamental understanding on the key microstructure features influencing the macroscopic properties (i.e., tensile properties, hole expansion ratio, and localized formability of AHSS/UHSS) in their steel development processes. On the other hand, automotive original OEMs urgently need a quantitative and predictive understanding on whether a specific type of macroscopic test result can be used to infer the in-die behaviors of these steels such that robust manufacturing processes can be established for the new generations of AHSS/UHSS.

Approach

During this project, a combined experimental and modeling approach is used to develop a quantitative understanding and a predictive capability about the effects of microstructural features on sheared edge fracture and stretchability for AHSS/UHSS sheet steels with UTS of 980 MPa. We will develop experimentally

validated predictive capabilities at different length scales: (1) microstructure-based property predictions for AHSS/UHSS at the meso-scale; (2) integrated shearing and edge stretchability simulations at the macroscopic scale; and (3) various multiscale characterization techniques for quantifying edge stretchability. Ford will provide tools for making half–dog-bone tensile stretchability samples, perform shearing experiments, and analyze the effects of shearing process conditions on the quality of sheared edges; U.S. Steel and AK Steel will provide sheet materials and perform rolling experiments to evaluate material properties at high strain levels, hole expansion-based stretchability testing, and characterization of shear-affected zone hardness profile after trimming. Oakland University will provide coupon- and microstructure-level characterization capabilities.

Results and Discussion

U.S. Steel and AK Steel have provided two DP980 sheets to Oakland University for shearing and tension experiments. The two steels are hereafter designated as UDP980 and ADP980, where U stands for U.S. Steel and A for AK Steel. The UDP980 is non-coated, while the ADP980 is galvanized. Scanning electron microscopy microstructural examinations performed at AK Steel and U.S. Steel show that the two steels are rather different in grain sizes of the martensite and ferrite phases (Figure III-56). The average grain size in ADP980 is about one-third of that of the UDP980 steels, although they are similar in UTS. This may explain why the amount of uniform elongation in UDP980 is much smaller than that of ADP980 (Figure III-57).

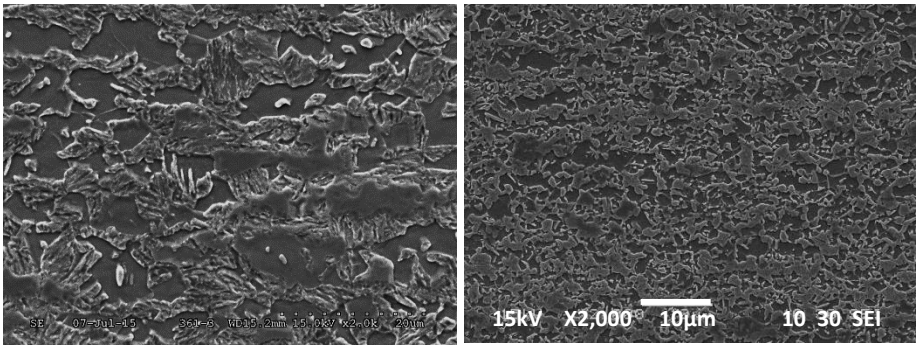

(a) UDP980 (b) ADP980

Figure III-56: 2000× scanning electron microscope microstructure at the longitudinal section rolling direction x normal direction of the two DP 980 steels.

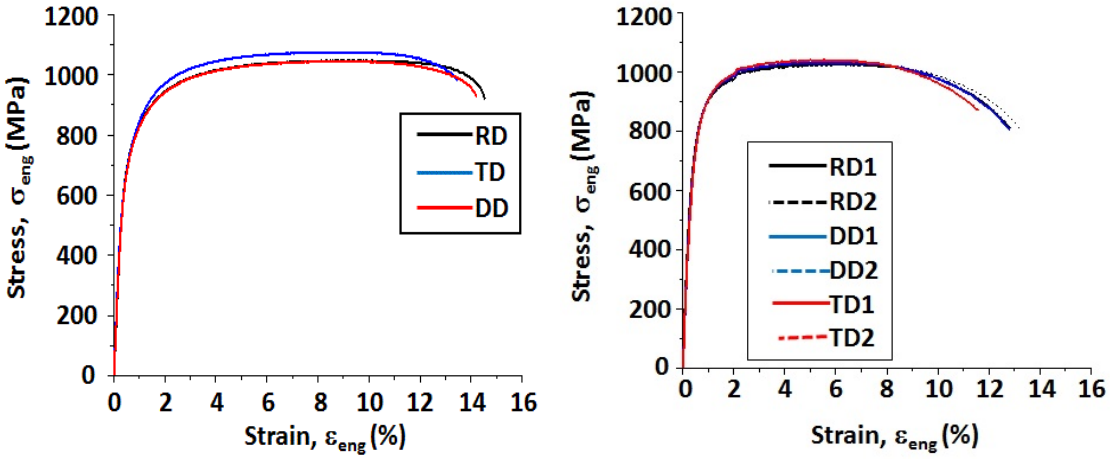

(a) (b)

Figure III-57: Engineering stress-strain curves of the two DP980 steels.

Optical microscopy performed at PNNL of the UDP980 steel (Figure III-58) shows that there are banded microstructures in the L (long cross section: rolling direction x normal direction) and T (transverse cross section: transverse direction x normal direction) cross sections; no banding is found on the P (planar cross section: rolling direction x transverse direction) sections. The banding is more prominent at the L section.

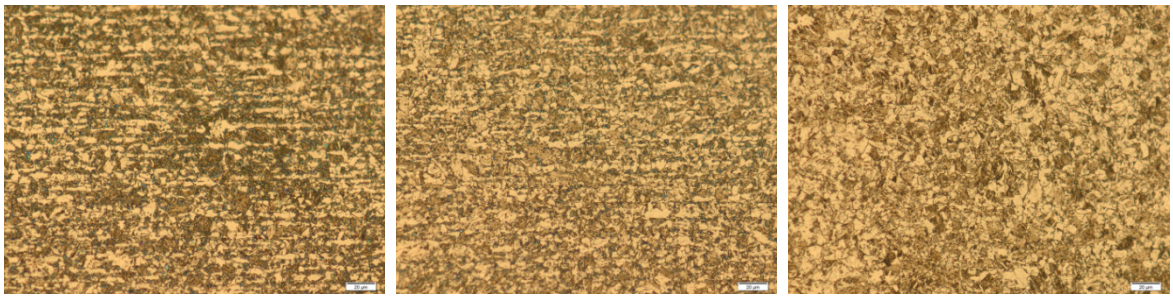

(a) L section (b) T section (c) P section

Figure III-58: 500× optical micrographs of the UDP980 at the L, T, and P sections.

Trimming experiments have been performed on both ADP980 and UDP980. The burr heights measured along the edges of trimmed sheets show very large variation between the two steels. There is almost zero burr for all clearances of the ADP980 steel. The same is observed for UDP980 for clearances 4%, 10%, 16.7%, and 30%, while the normalized burr height at 20% is around 2.7% and that at 40% clearance is 8.1%. The standard deviation for 40% clearance of the UDP980 steel is large, indicating the edge variability is large for this case. These results are summarized in Figure III-59(a). The large edge variation maybe due to the heterogeneous microstructure observed in this steel. The burr heights of both materials seem to be much smaller than those observed for Al alloys reported previously. The cross-sectional examinations of trimmed edges of UDP980 have been completed, while those for ADP980 steel are still under way.

Accumulated rolling and tension tests have been performed on AK DP980 steel with a 1.5-mm initial thickness to obtained stress-strain curves at large strains and serve as input for the steel trimming model. The sheet was rolled incrementally to thicknesses of 1.4, 1.3, to 0.3 mm and the samples were cut for sheets after each reduction for tensile tests. All experiments were performed at AK Steel. The tensile test results of sheets after each rolling reduction are shown in Figure III-59(b). In this figure, the accumulated strain (i.e., the rolling strain plus the tensile strain) is used for the horizontal axis. Figure III-59(b) shows that a power-law fitting [the green curve in Figure III-59(b)] works very well for the stress (σ) versus accumulated strain (ε) relationship:

$$\sigma = 1574.4\varepsilon^{0.1348} \quad (1)$$

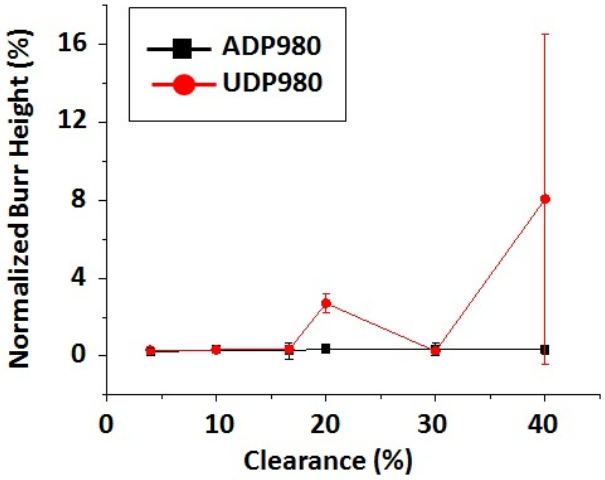

(a)

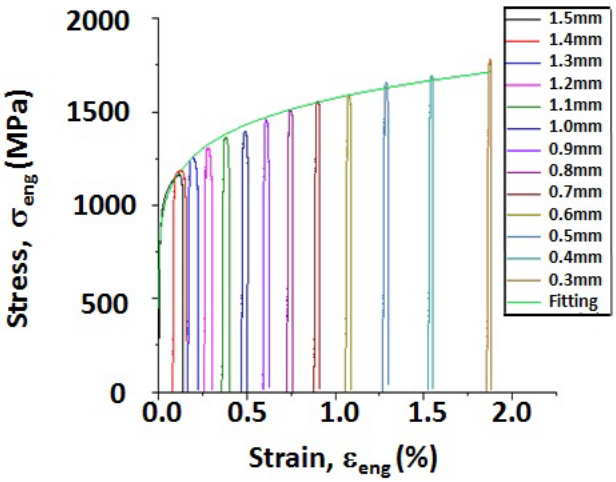

(b)

Figure III-59: (a) Normalized burr height as a function of trimming clearance for the ADP980 and UDP980 steels; (b) stress-strain curves of sheets cold rolled to different thicknesses and a power-law fitting.

The results of power-law–fitted stress-strain curves are used in the two-dimensional plane-strain trimming model previously developed [8]. The simulated results will be compared with experimental observations in terms of burr geometry. Because no experimental results are available for fracture parameters for the DP980 material examined, parametric studies were performed first to identify the correct fracture parameters by comparing the simulations with experimental sheared-edge characteristics. The accumulated damage criterion is utilized and the Johnson-Cook model used to represent the fracture strain [8]:

$$D = \int_0^{\varepsilon_p} \frac{d\varepsilon_p}{\bar{\varepsilon}_f}, \tag{2}$$

where $\bar{\varepsilon}_f = A_0 + Ae^{-B\eta}$.

Figure III-60 shows examples of simulations of two sets of parameters: (a) Case 1, $A_0 = 0.3$, $A = 4.77$ [9] and $B = 5.11$, (b) Case 2, $A_0 = 0$, $A = 0.5$ and $B = 0.5$. It appears that neither case has captured the experimentally observed burr geometry correctly. Further studies are currently under way.

In addition to the modeling and experimental accomplishments mentioned here, the macro-micro [10] and micro-macro-scale bridging approaches are also being developed and examined to study trimming-induced edge damage. For the microstructure-based micro-models, the properties of individual phases are necessary. Building on previous work [11], the phase properties for ADP980 have been characterized with in-situ HEXRD tensile tests coupled with elastic-plastic self-consistent crystal plasticity (EPSCCP) models. The results of individual phase properties determined for the ADP980 steel are shown in Figure III-61, where the property for martensite is represented by the blue line and that for ferrite represented by the red line. The average stress calculated by the EPSCCP models (the green line) is comparable to those obtained experimentally from the in-situ HEXRD test (the purple line) and to those obtained by AK Steel (the light blue line) using ASTM standard samples. Similar work on UDP980 steel will be performed in October 2015 at the Advanced Photon Source.

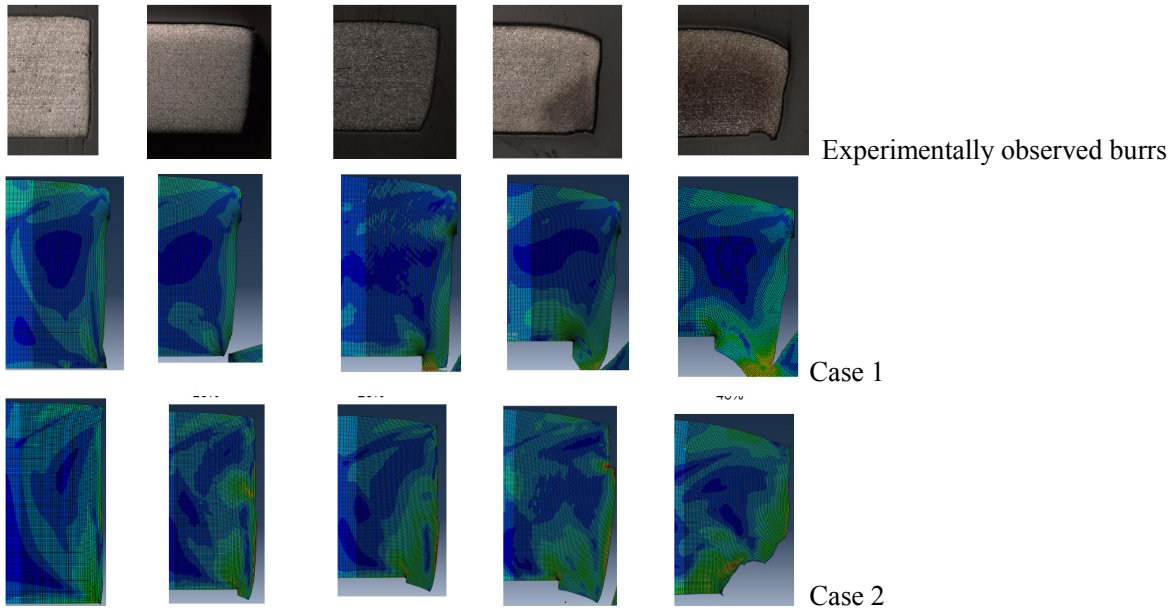

Figure III-60: Preliminary results of fracture strain parametric studies in comparison with experimentally observed sheared edge geometry for UDP980.

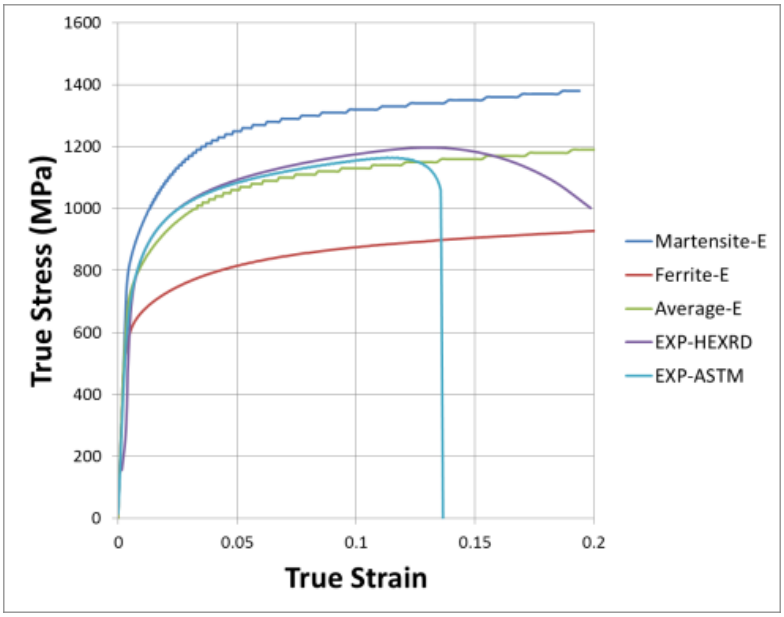

Figure III-61: Phase properties of individual phases obtained from HEXRD/EPSCCP and the average stress-strain curve in comparison with experimental results.

Technology Transfer Path

The findings and knowledge from this project have been continuously transferred to Ford and the two steel companies in the form of bi-weekly progress review meetings and other presentations. Additional technology transfer to other OEMs and steel producers will be carried out through scientific publications and conference presentations. Industry can use the results obtained in this study to improve the edge stretchability of dual-phase steels and reduce the development time and cost needed for new steels.

Conclusions

The obtained phase properties obtained this year will be applied to the microstructure-based micro-models. Once the trimming model is completed and the predicted trimmed-edge geometry and damage are validated, the integrated modeling framework developed previously [12,13] will be applied to study stretchability and compared with experimental observations. In addition, the modeling results will help optimization of trimming operation parameters, which will improve the forming properties of trimmed sheet.

Project Conclusions

The Advancing Properties, Processes, and Enabling Tools for Lightweight Metals Project is focused on research and development activities for advancing the basic mechanical properties, manufacturability, and cost of lightweight materials toward levels needed for increased implementation in automotive applications. This project includes five different tasks with unique scope and leadership that each addresses an aspect of the materials challenges limiting implementation of lightweight metals solutions in current or planned automotive applications. The following highlights summarize the accomplishments of the tasks in this project during FY 2015:

- Non-Rare Earth High-Performance Wrought Magnesium Alloys: Performed high shear extrusion of four non-rare earth Mg alloys. Detailed characterization of microstructure variation in the as-extruded non-rare earth Mg alloy tubes. Provided a more detailed explanation of the high–energy-absorbing characteristics of the tubes and the contribution of texture.
- Microstructure-Based Ductility Prediction for Complex Magnesium Castings: Conducted nanoindentation on AM40, AM50, AM60, and AM70 samples. Extracted elastic material properties from experimental data. Determined statistical distribution of plastic material parameters using FE modeling of the nanoindentation experiments. Expanded computational tools for generating microstructure geometries to include the presence of ESCs with and without beta phase. Conducted FE analyses on microstructure geometry samples with material parameters from nanoindentation experiments to quantify the impact of geometry features and parameter ranges on intrinsic ductility. Performed computerized tomography (CT) scans on as-cast samples prior to tensile testing to visualize the 3D pore distributions within the samples. Developed a methodology for generating extrinsic FE models based on actual pore distributions captured from CT scans. Validated the developed extrinsic modeling method against the experimental results in terms of ductility and fracture locations of the samples.
- Self-Pierce Riveting Process Simulation, Analyses, and Development for Magnesium Joints: Completed the joint performance and fatigue evaluations for AZ31B Mg SPR joints. Validated the modeling tool simulation results with experimental data from during the joining process and created induction-heated 7075 Al to AZ31B Mg SPR joints. Explored alternate rivet materials via the modeling tool. Completed task final report and recommendations for successful Mg SPR joining.
- High-Strength, Dissimilar Alloy Aluminum Tailor-Welded Blanks: Completed a series of bead-on-plate welds on 2-mm thick AA7075-T6, AA6022-T4, AA6022-F, and AA5182-O alloys across a wide range of welding speeds (1 to 6 m/min) with in situ temperature measurement inside the FSW tool. Compiled datasets on the effects of welding speed on transient tool temperatures and resulting weld macro and microstructure and hardness in the nugget and the HAZ. Developed a welding parameter set to produce dissimilar thickness/dissimilar material FSW joints between (a) AA7075-T6 (2 mm) and AA5182-O (1.1 mm), (b) 6022-T4 (2 mm) and AA5182-O (1.1 mm), and (c) AA7085-T6 (2 mm) and AA5182-O (1.1 mm). Tensile tests along the length of the welds showed fractures away from the weld region for all above cases. Validated formability simulation model for LDH tests on dissimilar thickness sheet (AA5182 and AA6022) with experimental LDH tests in tapered machined samples.

- Enhancing Sheared Edge Stretchability of Advanced and Ultra-High-Strength Steels: Performed mechanical and microstructural examination of DP980 steels produced by U.S. Steel (UDP980) and AK Steel (ADP980). Performed accumulated rolling and tension tests for ADP980 to obtain the flow stresses for large strains. Determined phase properties of the two DP980 steels by in-situ HEXRD tensile tests and elasto-plastic self-consistent crystal plasticity modeling. Performed trimming tests of the two DP980 steels and cross-sectional examinations on the UDP980 steel. Established a macro trimming model and performed some initial trimming simulations for parametric studies.

References

1. B. Beausir; L. S. Toth; and K. W. Neale, 2007, "Ideal orientations and persistence characteristics of hexagonal close packed crystals in simple shear," *Acta Materialia* 55; pp 2695–2705.
2. G. Chadha; J. E. Allison; and J. W. Jones, 2007, "The role of microstructure on ductility of die-cast AM50 and AM60 magnesium alloys," *Metallurgical and Materials Transactions A* 38; pp. 286-297.
3. J. Song; S. M. Xiong; M. Li; and J. E. Allison, 2009, "The correlation between microstructure and mechanical properties of high-pressure die-cast AM50 alloy," *Journal of Alloys and Compounds* 447; pp. 863-869.
4. K. Choi; D. Li; X. Sun; M. Li; and J. Allison, 2013, "Effects of Pore Distributions on Ductility of Thin-Walled High Pressure Die-Cast Magnesium," SAE Technical Paper 2013-01-0644.
5. X. Sun; K. S. Choi; and D. S. Li, 2013, "Predicting the influence of pore characteristics on ductility of thin-walled high pressure die casting magnesium," *Materials Science and Engineering A* 572; pp. 45-55.
6. E. I. Barker; K. S. Choi; X. Sun; E. Deda; J. Allison; M. Li; J. Forsmark; J. Zindel; and L. Godlewski, 2014, "Microstructure based modeling of β phase influence on mechanical response of cast AM series Mg alloys," *Computational Materials Science* 92; pp. 353-361.
7. J. Forsmark; Z. Dowling; K. Gibson; C. Mueller; L. Godlewski; and J. Zindel, 2015, "An investigation of the effects of cast skin on the mechanical properties of an AM60 die-cast magnesium alloy," *SAE International Journal of Materials and Manufacturing* 8; pp. 714-721.
8. X. H. Hu; K. S. Choi; X. Sun; and S. F. Golovashchenko, 2014, "Edge Fracture Prediction of Traditional and Advanced Trimming Processes for AA6111-T4 Sheets," *Journal of Manufacturing Science and Engineering* 136(2): 021016.
9. S. Dey; T. Børvik; O. S. Hopperstad; J. R. Leinum; and M. Langseth, 2004, "The Effect of Target Strength on the Perforation of Steel Plates using Three Different Projectile Nose Shapes," *International Journal of Impact Engineering* 30(8-9); pp. 1005.
10. X. M. Hu; M. Jain; P. D. Wu; D. S. Wilkinson; and R. K. Mishra, 2010, "A Macro–Micro-Multi-Level Modeling Scheme to Study the Effect of Particle Distribution on Wrap-Bendability of AA5754 Sheet Alloys," *Journal of Materials Processing Technology* 210(9); pp. 1232.
11. X. H. Hu; K. S. Choi; X. Sun; Y. Ren; and Y. D. Wang, 2015, "Determining individual phase flow properties in a Quench and Partitioning steel with in-situ high energy X-ray diffraction and multi-phase elasto-plastic self-consistent method," accepted *Metallurgical and Materials Transactions A-Physical Metallurgy and Materials Science*.
12. X. H. Hu; X. Sun; and S. F. Golovashchenko, 2014, "Predicting Tensile Stretchability of Trimmed AA6111-T4 Sheets," *Computational Materials Science* 85; pp. 409.
13. X. H. Hu; X. Sun; and S. F. Golovashchenko, 2016, "An Integrated Finite Element-Based Simulation Framework: From Hole Piercing to Hole Expansion," *Finite Elements in Analysis and Design* 109; pp. 1.

Bibliography

E. I. Barker; K. S. Choi; X. Sun; and G. Cheng, 2015, "Intrinsic Microstructure Modeling for Mechanistic-Based Ductility Prediction for Cast Mg Alloys," presented at the *TMS 2015 144th Annual Meeting and Exhibition, March 15-19, 2015*, Orlando, FL.

E. I. Barker; K. S. Choi; G. Cheng; and X. Sun, 2015, "Intrinsic and Extrinsic Scale Modeling of Cast Mg," presented at the *PRISMS Workshop 2015*, September 1, 2015, Ann Arbor, MI.

K. S. Choi, E. I. Barker, and X. Sun, 2015, "Effects of Porosity on the Ductility of Thin-Walled High Pressure Die Casting Magnesium," presented at the *TMS 2015 144th Annual Meeting and Exhibition*, March 15-19, 2015, Orlando, FL.

K. S. Choi; E. I. Barker; G. Cheng; X. Sun; J. H. Forsmark; and M. Li, 2016, "Predicting Stress vs. Strain Behaviors of Thin-Walled High Pressure Die Cast Magnesium Alloy with Actual Pore Distribution," to be presented at the *SAE 2016 World Congress*, April 12-14, 2016, Detroit, MI.

Y. Hovanski; J. Carsley; B. Carlson; S. Hartfield-Wunsch; B. Landino; and M. Eisenmenger, 2015, "Aluminum Tailor Welded Blanks – Preparing for High Volume Production," presented by Yuri Hovanski (invited speaker) at the *TMS 2015 144th Annual Meeting & Exhibition*, Orlando, FL on March 17, 2015; PNNL-SA-108776, Pacific Northwest National Laboratory, Richland, WA.

Y. Hovanski; J. Carsley; B. Carlson; S. Hartfield-Wunsch; M. Eisenmenger; T. Luzanski; D. Marshall; B. Landino; P. Upadhyay; and A. Soulami, 2015, "Enabling High Volume Production of Aluminum Tailor Welded Blanks," *The 4th International Conference on Scientific and Technical Advances on Friction Stir Welding and Processing,* October 1-2, 2015, Ordizia, Spain; PNNL-SA-112243, Pacific Northwest National Laboratory, Richland, WA.

Y. Hovanski; P. Upadhyay; A. Soulami; B. Carlson; J. Carsley; S. Hartfield-Wunsch; M. Eisenmenger; T. Luzanski; D. Marshall; and B. Landino, 2015, "Aluminum Tailor Welded Blanks – Preparing for High Volume Production," presented by Yuri Hovanski (invited speaker) at the *Advanced Materials & Processes Conference (AeroMat) and Exhibition 2015*, Long Beach, CA on May 12, 2015; PNNL-SA-110463, Pacific Northwest National Laboratory, Richland, WA.

Y. Hovanski; P. Upadhyay; A. Soulami; J. Carsley; B. Carlson; S. Hartfield-Wunsch; M. Eisenmenger; T. Luzanski; and B. Landino, 2015, "Post-weld Formability of Aluminum Tailor Welded Blanks," presented at *MS&T 2015*, Columbus, OH, October 5, 2015; PNNL-SA-109255; Pacific Northwest National Laboratory, Richland, WA.

Y. Hovanski; P. Upadhyay; B. Carlson; R. Szymanski; T. Luzanski; and D. Marshall, 2015, "FSW of Aluminum Tailor Welded Blanks across Machine Platforms," presented at the *Friction Stir Welding and Processing VIII, March 15-19, 2015, Orlando, FL*; R. S. Mishra et al. (eds.); pp. 99-103, John Wiley & Sons, Inc., Hoboken, NJ; doi:10.1002/9781119093343.ch17.

Y. Hovanski; P. Upadhyay; J. Carsley; T. Luzanski; B. Carlson; M. Eisenmenger; A. Soulami; D. Marshall; B. Landino; and S. Hartfield-Wunsch, 2015, "High-Speed Friction-Stir Welding to Enable Aluminum Tailor-Welded Blanks," *Journal of the Minerals, Metals and Materials Society* 67(5); pp. 1045-1053; doi:10.1007/s11837-015-1384-x.

E. A. Nyberg; E. V. Stephens; A. Soulami; S. Ramasamy; and R. Belknap, 2015, "Magnesium Alloy Sheet Self-Pierce Riveting (SPR) Development," presented at the *10th International Conference on Magnesium Alloys and Their Applications*, October 11-16, 2015, Jeju, Korea.

S. Ramasamy and R. Belknap, 2015, "Self-Pierce Riveting Process Simulation, Analyses, and Development for Magnesium Joints Internal Program Review," presented at Stanley Engineered Fastening.

A. Soulami; E. V. Stephens; E. A. Nyberg; X. Sun; S. Ramasamy; and R. Belknap, 2015, "Effect of Processing Parameters on Heat-Assisted Self-Piercing Riveting of Mg Alloys," submitted to *Science and Technology of Welding and Joining,* PNNL-SA-113443, Pacific Northwest National Laboratory, Richland, WA.

E. V. Stephens; A. Soulami; E. A. Nyberg; and X. Sun, 2015, "2015 DOE Vehicle Technologies Program Review SPR Process Simulation, Analyses, and Development for Mg Joints," presented at the *DOE Vehicle Technologies Annual Merit Review*, June 8-12, 2015, Arlington, VA.

E. V. Stephens; A. Soulami; E. A. Nyberg; and X. Sun, 2015, "Self-Pierce Riveting Process Simulation, Analyses, and Development for Magnesium Joints," presented at the *Lightweight Materials Portfolio Review*, Richland, WA.

E. V. Stephens; A. Soulami; E. A. Nyberg; and X. Sun, 2015, "Self-Pierce Riveting Process Simulation, Analyses, and Development for Magnesium Joints Project Review," presented to Stanley Engineered Fastening.

X. Sun; K. S. Choi; E. I. Barker; M. Li; J. Forsmark; J. Allison; and E. Deda, 2015, "Predicting Ductility of Thin Walled High Pressure Die Casting Magnesium with an ICME Approach," presented at the *SAE 2015 World Congress*, April 20-22, 2015, Detroit, MI.

III.7. Multimaterial Enabling—Oak Ridge National Laboratory

Project Details

C. David Warren, Field Technical Monitor
Oak Ridge National Laboratory
1 Bethel Valley Road
Oak Ridge, TN 37831
Phone: 865-574-9693
E-mail: warrencd@ornl.gov

William Joost, Technology Area Development Manager
U.S. Department of Energy
1000 Independence Avenue, SW
Washington, DC 20585
Phone: 202-287-6020
E-mail: william.joost@ee.doe.gov\\

Contractor: Oak Ridge National Laboratory
Contract No.: DE-AC05-00OR22725

Executive Summary

This project consists of three separate tasks. The first is to develop an understanding of the protective film formation in magnesium (Mg) alloys and how that film changes upon exposure to automotive service environments. The second task involves the development and commercialization of a rapid, in-line, nondestructive evaluation method for inspecting spot welds in an automotive production environment that saves production costs. The third task is related to the development of a novel method for mitigating weld fatigue in advanced high-strength steels due to microstructural changes.

Activity and Developments

Understanding Protective Film Formation by Magnesium Alloys in Automotive Applications

Project Details

Michael P. Brady, Principal Investigator
ORNL
1 Bethel Valley Road
Oak Ridge, TN 37831
Phone: 865-574-5153
E-mail: Bradymp@ornl.gov

Bruce Davis, Partner
Magnesium Elektron North America (MENA)
1001 College Street
P.O. Box 258
Madison, IL 62060
Phone: 618-709-5023.
E-mail: Bruce.Davis@Magnesium-ElektronUSA.com

Accomplishments

- Completed an advanced characterization study of as-conversion coated and conversion coated + e-coated metal-coating interface structures. Substrate alloy composition is influenced by the as-conversion coated structure, which was modified both compositionally and morphologically by subsequent e-coating (Fiscal Year [FY] 2015).
- Demonstrated via deuterium oxide (D_2O) exposure studies that the addition of zirconium (Zr) and neodymium (Nd) to Mg alloys significantly enhances uptake of hydrogen into the alloy on aqueous exposure, whereas aluminum (Al) additions do not (FY 2015).
- Completed isotopic tracer study of aqueous film formation growth on Mg alloys in the presence of salt species, which was shown to result in a transition to an outward elemental oxygen (O) film growth mechanism (FY 2015).
- Successfully completed and published a $D_2{}^{16}O$ and $H_2{}^{18}O$ isotopic tracer study for aqueous film formation growth mechanism by commercial Mg alloys AZ31B and E717 relative to ultrahigh purity (UHP) Mg. This is the first isotopic tracer study of Mg corrosion ever reported (FY 2014).
- Demonstrated small angle neutron scattering (SANS) as a new tool for providing insights into Mg corrosion. SANS was found to be sensitive to formation of nanoporous, filamentous magnesium hydroxide ($Mg(OH)_2$) that results from accelerated corrosion of Mg alloys in salt solutions. The SANS data indicated extremely high surface areas in the $Mg(OH)_2$ corrosion product, which has implications for understanding film growth and breakdown (FY 2014).
- Successfully completed advanced transmission electron microscope (TEM) characterization study of ambient immersed aqueous film formation as a function of exposure time (4 to 48 hours) and alloy type (AZ31B, Elektron 717 (E717), and UHP Mg) elucidating nanoscale film segregation tendencies of Al, rare earth (RE), zinc (Zn), and zirconium (Zr) alloy additions (FY 2013).
- First successful demonstration of secondary ion mass spectrometry (SIMS)/$D_2{}^{16}O$ and $H_2{}^{18}O$ isotopic tracer studies for film formation by Mg alloys under immersed aqueous and air + steam exposure

conditions, providing new insights into film growth mechanism and relative penetration of H and O species (FY 2013).

Future Directions

- Project completed. A new project will employ similar fundamental advanced characterization corrosion studies and expand the test matrix to include AZ91 and WE43 alloys for comparison of higher alloy addition levels and second-phase microstructure on corrosion film, hydrogen uptake, and coating formation compared with previous work on AZ31B and E717.
- Publication of findings related to salt tracer and hydrogen uptake studies from the FY 2015 results. Attempts will also be made to identify the speciation of enhanced hydrogen uptake observed for Zr and Nd-containing Mg alloys via evaluation of additional advanced characterization techniques (e.g., nanosims imaging and neutron techniques).

Technology Assessment

- Target: Gain improved understanding of protective film formation by Mg alloys and conversion coatings as a function of alloy chemistry and impurities, microstructure, and exposure conditions.
- Target: Provide a fundamental basis for designing and optimizing new Mg alloys and/or conversion coating processes to improve corrosion resistance under automotive relevant conditions.
- Gap: The lack of corrosion prevention strategies is a key limiting factor to more widespread use of Mg alloys in automotive applications.
- Gap: Alloying has been shown to modify surface film performance; however, a detailed understanding of how and why is currently lacking. This understanding is needed to develop improved alloys and surface treatments/coatings to permit more widespread adoption of Mg alloys.

Introduction

Mg alloys are of great interest to automotive manufacturers due to their attractive combination of low density, good strength, amenability to casting, and ease of recycling. A major obstacle to the widespread adoption of Mg alloys is susceptibility to corrosion [1–3]. Surface treatments and/or coatings are needed for many applications [3]; these treatments and coatings can result in increased cost and can be a source of component durability issues. The inability of Mg alloys to establish a continuous and fully protective surface film under many exposure conditions is a key factor underlying their susceptibility to corrosive attack. Alloying and/or conversion coatings have been shown to modify surface film performance; however, a detailed understanding of how and why is currently lacking. This understanding is needed to develop improved alloys and surface treatments and/or coatings to permit more widespread adoption of Mg alloys.

The goal of this effort is to develop an improved understanding of how alloy composition, microstructure, and exposure conditions affect the establishment, continuity, nature, and growth of protective films on Mg alloys. To accomplish this goal, this project has employed advanced characterization techniques not previously widely applied to Mg surface film formation to provide new insights into film formation. This project is a systematic study of aqueous film formation and its evolution with time on two representative Mg alloy classes relative to UHP Mg as a control. Alloy AZ31B was studied as representative of the Mg-Al-Zn alloy class and alloy Elektron 717 (also known as ZE10A, referred to as E717 for simplicity) was studied as representative of the RE and Zr-alloyed class of Mg alloys. These results will then serve as baseline information for evaluation of more corrosive environments (e.g., salt species); modified alloy compositions; and conversion coatings. The study of both bare, untreated Mg alloy surfaces and conversion-coated surfaces is being pursued. The corrosion of Mg alloys has been the subject of intense research activity, with significant gains in mechanistic understanding in recent years for both pure Mg and Mg alloys. These studies have identified the inability of

Mg alloys to establish a continuous and fully protective surface film under many exposure conditions as a key factor underlying their susceptibility to corrosive attack. Deliverables on this project are related to application, development, and suitability assessment of advanced characterization techniques to provide new insights into Mg alloy corrosion.

Approach

The ambient corrosion of Mg differs from many corrosion-resistant structural alloy classes because protective surface films can become quite thick (i.e., on the order of tens to hundreds of nanometers rather than the few nanometers typically encountered in stainless steels [4–6]. As a result, corrosion resistance is influenced not only by classical thin film electrochemical passivity considerations, but also by thermodynamic and kinetic considerations typically encountered in thick film, high-temperature alloy oxidation phenomena.

The experimental approach adopted merges ambient and high-temperature corrosion study approaches, leveraging extensive and unique expertise in these areas at MENA and at ORNL. ORNL has world-class characterization capabilities to more fully probe and understand the chemical, morphological, and structural features of the surface films formed on Mg alloys and conversion coatings as a function of alloy composition, microstructure, and exposure condition.

A major goal of the project is to assess which advanced characterization techniques are most amenable for providing new insights into film formation on Mg alloys. This is a key activity because Mg alloys are notoriously difficult to work with. Sample procedure techniques are being developed and not all proposed characterization approaches have proven effective. Advanced characterization approaches to be investigated include (1) development of ex situ focused ion beam sample preparation and TEM of film/surface layer cross sections; (2) SIMS $D_2{}^{16}O$ and $H_2{}^{18}O$ (^{18}O water) tracer studies of Mg alloys/coatings under immersion aqueous and gaseous vapor exposure conditions to gain insight into the growth aspects of the surface films; (3) ex situ neutron scattering techniques (e.g., small angle and inelastic) to characterize Mg alloy surface film nanoporosity and hydrogen species incorporation as a function of alloy composition and exposure condition; and (4) atom probe tomography (APT) techniques to provide 3D quantification of chemistry at the atomic scale in the bulk Mg alloy and the alloy in the vicinity of the alloy-surface layer interface to characterize corrosion-driven alloy clustering or precipitation phenomena.

Advanced TEM sample preparation techniques were successfully developed in FY 2012 and applied in FY 2013 through 2015 to Mg alloy aqueous film formation as a function of exposure time, alloying, and the absence or presence of salt. SIMS isotopic tracer techniques were successfully developed and demonstrated in FY 2013 and applied in FY 2014 through 2015 for understanding the effects of alloying additions on the aqueous and humid air film formation growth mechanism of Mg, with and without salt species present and hydrogen uptake tendencies. In FY 2014, SANS and TEM characterization was successfully applied to the formation of nonprotective, nanoporous $Mg(OH)_2$ corrosion products formed by Mg alloys in salt solutions. SANS data for coated Mg alloys were pursued in FY 2015 in an effort to quantify nanoporous coating defects. Initial attempts at applying APT techniques to Mg corrosion films were not successful due to sample preparation complications, but APT techniques remain a key area of study for improved understanding of Mg corrosion.

Results and Discussion

Work in FY 2015 focused on three main Mg corrosion activities for which select highlight results are presented: (1) SIMS isotopic tracer aqueous film growth tracer studies in the presence of salt; (2) studies of hydrogen uptake in aqueous exposures as a function of Al, Nd, and Zr alloying additions to Mg; and (3) studies of the effect of substrate composition on conversion coating formation as-conversion coated and after subsequent e-coating.

SIMS isotopic tracer studies of the effect of sodium chloride (NaCl) on the aqueous film growth mechanism for AZ31B and E717 were completed. The exposure sequence was based on 4 h D_2O + 20 h ^{18}O water with 0.01 wt.% NaCl and the inverse 4 h ^{18}O water + 20 h D_2O water with 0.01 wt.% NaCl. The AZ31B and E717 materials were from the same alloy batches as the pure water tracer film growth study previously conducted under this project [7]. Figure III-62 shows example SIMS data for the 4 h D_2O + 20 h ^{18}O water ± 0.01 wt.% NaCl exposures sequence for E717 (^{18}O fraction shown). The E717 alloy exhibited an intermediate peak in the ^{18}O fraction curves for the sample tracer sequence that included 0.01 wt.% NaCl in the second step, compared to a smooth profile suggestive of inward O-dominated growth in pure water (no salt). The intermediate peak is suggestive of a transition to a mixed inward/outward growth mechanism in the presence of NaCl. A similar intermediate peak in the ^{18}O fraction plot was also observed for AZ31B. (deuterium [D] fraction plots were also obtained for both alloys and suggested inward penetration of D, both with and without salt present). Analysis of the films for a salt tracer set of AZ31B and E717 by x-ray photoelectron spectroscopy (XPS) and cross-section TEM were consistent with the change in growth mechanism indicated by the SIMS tracer data. The film structure by XPS indicated a complex mixed Mg oxide (MgO)–$Mg(OH)_2$ film structure, with MgO and $Mg(OH)_2$ enriched at the surface, followed by decreasing and then increasing MgO content with depth. This finding is consistent with formation of a primarily MgO–based film in the first salt free 4-h water exposure, followed by transition to outward growth with enhanced $Mg(OH)_2$ formation in the second step of the sequential exposure when 0.01% NaCl was introduced. Cross-section TEM analysis and surface scanning electron microscopic (SEM) imaging of the filamentous $Mg(OH)_2$ (Figure III-63, shown for E717) confirmed the SIMS tracer and XPS results, revealing a duplex film structure of outer filamentous $Mg(OH)_2$ overlying an inward protruding nodular and irregular mixed MgO base film, likely also containing $Mg(OH)_2$. Elemental mapping also indicated that Na penetrated to the metal-film interface at the inward nodular-metal interface.

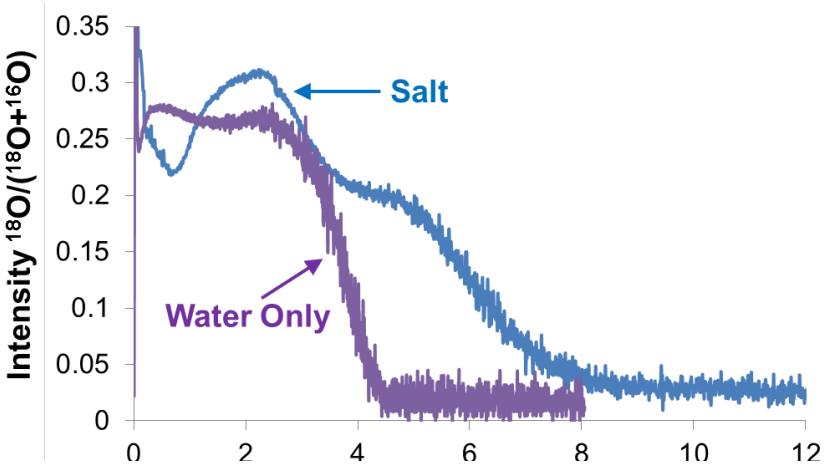

Figure III-62: Fraction $^{18}O/(^{18}O+^{16}O)$ SIMS data (counts per second versus sputtering depth) for alloy E717. Water-only exposure was 4 h D_2O + 20 h ^{18}O water [7]. Salt exposure was 4 h D_2O + 20 h ^{18}O water with 0.01 wt.% NaCl. Zero sputtering time corresponds to the film surface.

SIMS isotopic tracer studies performed in FY 2013 through 2014 indicated that hydrogen species penetrated throughout the hydroxide/oxide film and into the underlying metal on room temperature aqueous exposure, particularly for the Zr and Nd-containing E717 alloy [7,8]. Much less hydrogen penetration beyond the film and into the underlying metal was observed for AZ31B and pure Mg [7]. This effect was further studied in FY 2015 via repeat exposures of AZ31B; E717; commercial purity and UHP Mg; and a cast model alloy set series of Mg-0.4Zr, Mg-0.4Zr-1Zn, Mg-0.4Zr-0.3Nd, Mg-0.4Zr-1Zn-0.3Nd, Mg-0.4Zr-0.3Ce, Mg-0.4Zr-1Zn-0.3Ce, Mg-0.19Zr, Mg-0.14Nd, and Mg-2.1Al. Select data from this study for commercial purity Mg, Mg-2.1Al, Mg-0.14Nd, and Mg-0.19 Zr are shown in Figure III-64. Compared to as-polished condition, exposure for 30 min and 4 h in D_2O resulted in enhanced D levels for all alloys. However, the D levels were far higher in the Mg-0.14Nd and Mg-0.19Zr alloys. Work in this area will continue under the new project in FY 2016, including attempts at gaining a better understanding of the speciation form of hydrogen introduced into the underlying alloy by aqueous exposure.

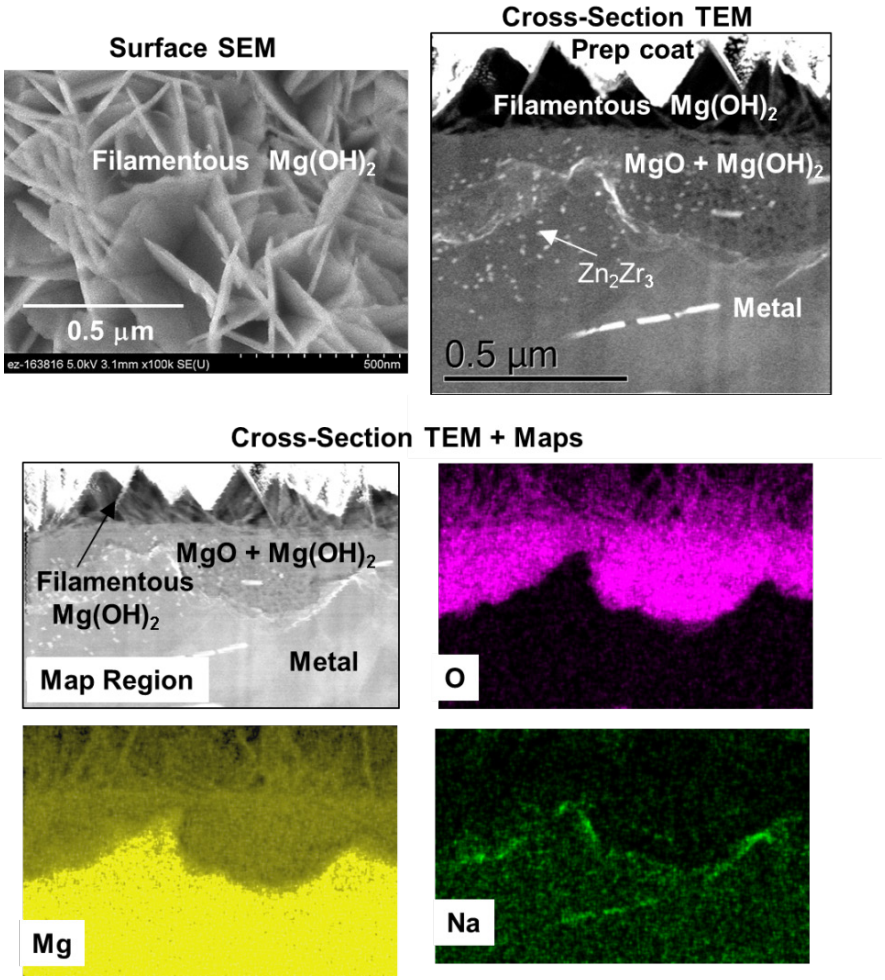

Figure III-63: Surface SEM, cross-section TEM images, and elemental maps for alloy E717 after salt tracer study exposure of 4 h D_2O + 20 h ^{18}O water + 0.01 wt.% NaCl.

The coating evaluation test matrix is shown in Figure III-65. This evaluation focused on AZ31B and E717 substrates, with conversion coatings, electro-ceramic coatings (in conjunction with Henkel Corporation), and e-coatings. The goal of this work was to approach coating formation on AZ31B and E717 from a film growth perspective (i.e., conversion coating, in particular, is a form of controlled film growth via the corrosion reaction of the alloy substrate with the coating solution). Coatings were characterized by XPS, SEM, TEM, and SANS, with insight into corrosion behavior from potentiodynamic and electrochemical impedance spectroscopy techniques in saturated $Mg(OH)_2$ + 1 wt.% NaCl (findings to be published in [9]).

The substrate alloy played a role in the resulting conversion coating chemistry, with aluminum from the AZ31B substrate alloy and Zr from the E717 substrate alloy migrating into the conversion-coated surface [9]. Of particular relevance, it was observed that e-coating the conversion-coated alloys increased porosity and modified chemistry at the metal-coating interface initially formed during conversion coating by dispersal of fluorine (F), titanium (Ti), Zr, chromium (Cr) additive from the conversion coatings [9]. However, although the same e-coating parameters were used on all samples, the impact on the metal-coating interface structure varied with the conversion coating/alloy substrate combination. An example of TEM analysis of the metal coating interface is shown in Figure III-66 for E717 as-conversion coated and after e-coating. The combinations that best retained the original conversion-coated structure and chemistry appeared to correlate with more consistent and better corrosion protection by the coatings on evaluation under aggressive conditions in salt solution [9].

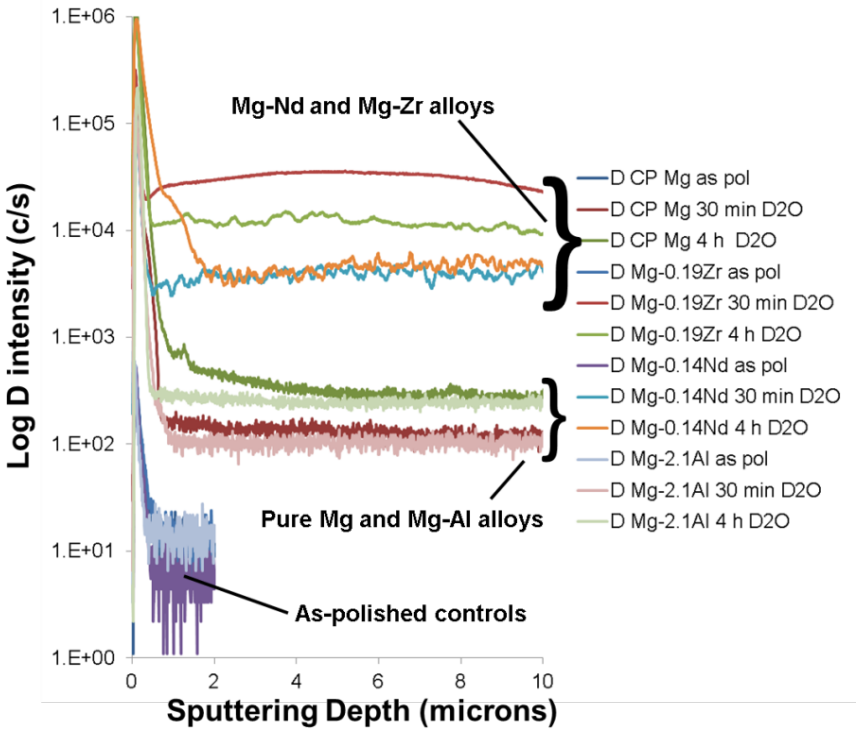

Figure III-64: Master plot of select SIMS tracer data for as-polished, 30-min immersion in D_2O and 4-h immersion in D_2O for commercial purity Mg and cast model alloys Mg-0.14Nd, Mg-0.19Zr, and Mg-2.1Al wt.%.

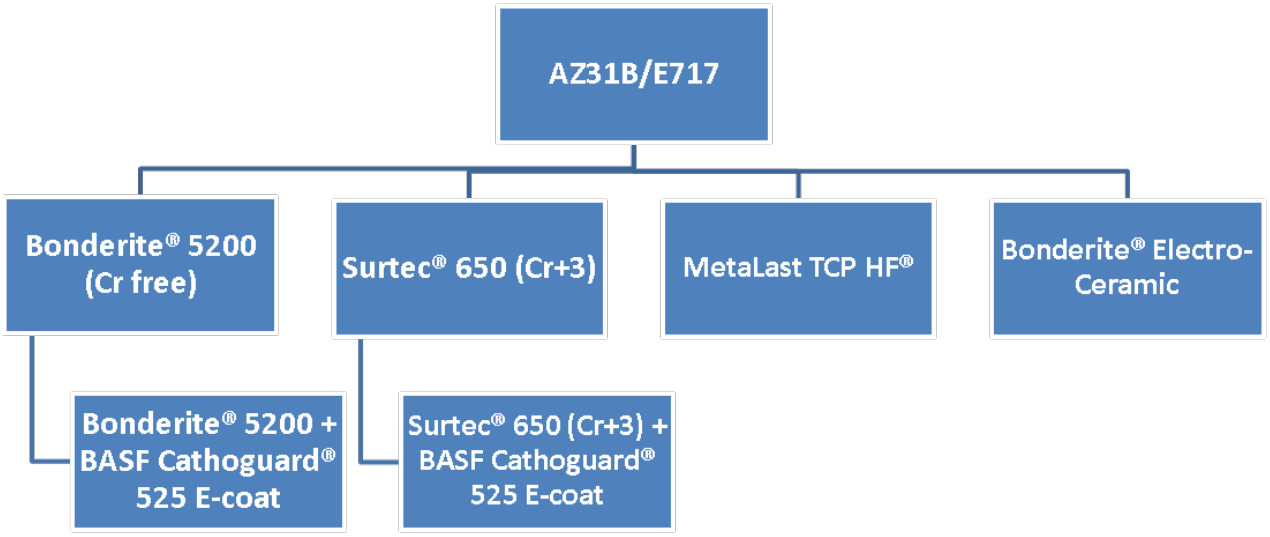

Figure III-65: Coating evaluation test matrix.

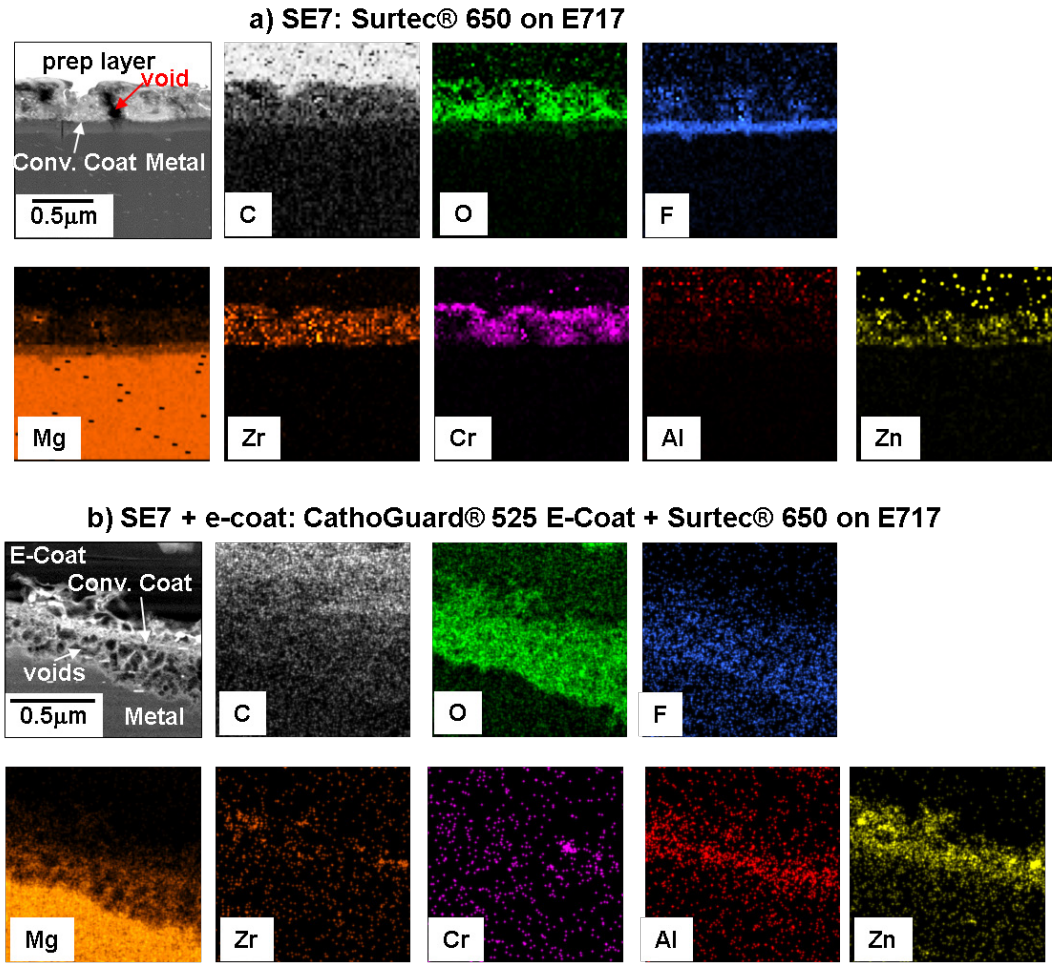

Figure III-66: Cross-section dark field TEM images and corresponding elemental maps for (a) as-conversion coated Surtec® 650 on E717 and (b) the coating-substrate interfacial region after subsequent application of the CathoGuard ® 525 e-coat [9].

Technology Transfer Path

Basic understanding of the film formation on Mg alloys and its behavior in different environments will provide insight into how to design new Mg alloys and conversion coatings that will be more corrosion resistant under automotive relevant conditions. The current gap in basic understanding of the film formation mechanics, kinetics, and correlation with alloy chemistry and microstructure limits achievement of improved corrosion resistance that would permit more widespread use of Mg alloys in automotive applications. A partnership with MENA, a leading Mg alloy producer, augmented by collaborations initiated mid-project with the coating company Henkel Corporation, provides a direct path toward incorporating insights from this effort into practice.

Conclusions

This project evaluated advanced characterization approaches for gaining a better fundamental understanding of film growth on bare and coated Mg alloys. Cross-section TEM with sample preparation by focused ion beam techniques has proven particularly useful in understanding film/coating structure and chemistry. Application of the SIMS isotopic tracer study approach to Mg corrosion is a key outcome of this project, with feasibility established for aqueous conditions with and without salt species and elevated temperature humid air oxidation.

Given the formation of oxide-hydroxide films by Mg, tracers incorporating both O-18 and D can provide unique insights not achievable by other techniques. The observation of enhanced hydrogen uptake into the underlying Mg alloy with additions of Zr and Nd as a result of aqueous exposure was quite unexpected. These results are potentially relevant to Mg alloy design from a hydrogen embrittlement and stress corrosion cracking perspective, as well as functional use of Mg alloys (such as in batteries or hydrogen storage). Although further work is needed, advanced characterization of substrate alloy-coating interfaces suggests substrate alloy design to optimize synergy between alloy composition and subsequent conversion coating chemistry and structure. This characterization allows possible modification of e-coating parameters to avoid degradation of the initially formed conversion coating surface as potential paths forward to more corrosion-resistant protection schemes for Mg alloys.

Online Weld Nondestructive Examination with Infrared Thermography

Project Details

Zhili Feng, Principal Investigator
ORNL
1 Bethel Valley Road
Oak Ridge, TN 37831
Phone: 865-576-3797
E-mail: fengz@ornl.gov

Accomplishments

- Completed the new infrared (IR) nondestructive examination (NDE) prototype system and software development and testing (FY 2015).
- Licensed the technology to industry (FY 2015).
- Assisting APLAIR Manufacturing Systems (APLAIR) to identify low-cost hardware suitable to production applications and to transfer the original LabVIEW-based software to more efficient code (FY 2015).

Future Directions

- Continue to work with industrial partner to transfer the prototype system to a commercial product.

Technology Assessment

- Target: Develop a system that can meet or exceed the inspection cycle time requirements dictated by the mass production assembly line environment, including (1) collection time less than 2 to 3 seconds for online inspection, (2) collection time less than 5 to 10 seconds for offline inspection, and (3) data analysis and decision making time less than 1 to 2 seconds.
- Target: The prototype spot weld quality inspection system based on IR thermography can detect a stuck weld, weld nugget size (up to 0.2-mm resolution), and surface indentation (up to 0.1-mm resolution) in both two layer (2T) and three layer (3T) stackup configurations.
- Gap: Currently, there is no combination of IR image acquisition, analysis algorithms, and hardware that is capable of determining weld quality within the targeted time period and with the necessary quality and resolution.

Introduction

The development of resistance spot welding for advanced high-strength steels (AHSSs) is critical for enabling the broader implementation of AHSSs in vehicle structures for lightweighting and crashworthiness. For example, boron steel, with a strength of 1,500 MPa (i.e., five times that of mild steels common to vehicle structures), has been successfully implemented in mass production commercial vehicles [10]. Lotus estimated a 16% weight reduction for body-in-white (BIW) by using an AHSS-intensive automotive body structure [11]. Variations in welding conditions, part "fit-up," and other production conditions inevitably occur in the complex, high-volume BIW assembly process. These variations can result in out-of-tolerance joints that impair the quality and performance of vehicles. Increasing use of AHSSs and other lightweight metals is expected to pose even more stringent requirements on joint quality. Reliable quality inspection techniques are crucial for achieving and ensuring high-quality joints on the assembly line. For it to be successfully adopted by the automotive industry, any new quality inspection technology needs to be low cost, fast, and highly accurate.

During FY 2011 through 2014, a prototype system and data analysis algorithm was developed to demonstrate the feasibility for both real-time (i.e., online) and post-weld (i.e., offline) inspection applications. The system was extensively tested in the laboratory. A wide range of weld coupons made with different steel grades, coatings, thickness, and stackup configurations was produced. Welds with varying attributes (e.g., nugget size and indentation depth) were intentionally made by carefully controlling the welding parameters. Tests showed the system was able to positively quantify the weld nugget size, shape, and thickness and to identify welding defects, including lack-of-fusion and excessive indentation. A field demonstration was performed for automobile original equipment manufacturers (OEMs) in Detroit in 2013; this demonstration immediately attracted great attention. Automobile OEMs and their part suppliers are interested in working further with ORNL to put the system in production lines.

In FY 2015, this technology was licensed by APLAIR, a Tennessee-based company. ORNL is assisting APLAIR to further transfer the technology and prototype system from the laboratory to a commercial product.

Approach

Our new infrared-based NDE technology is capable of both real-time online (i.e., during welding) and post-weld online/offline (i.e., after welding) inspections. The system mainly consists of an IR camera and a computer program with proprietary thermal imaging analysis algorithms integrated into existing production lines (Figure III-67).

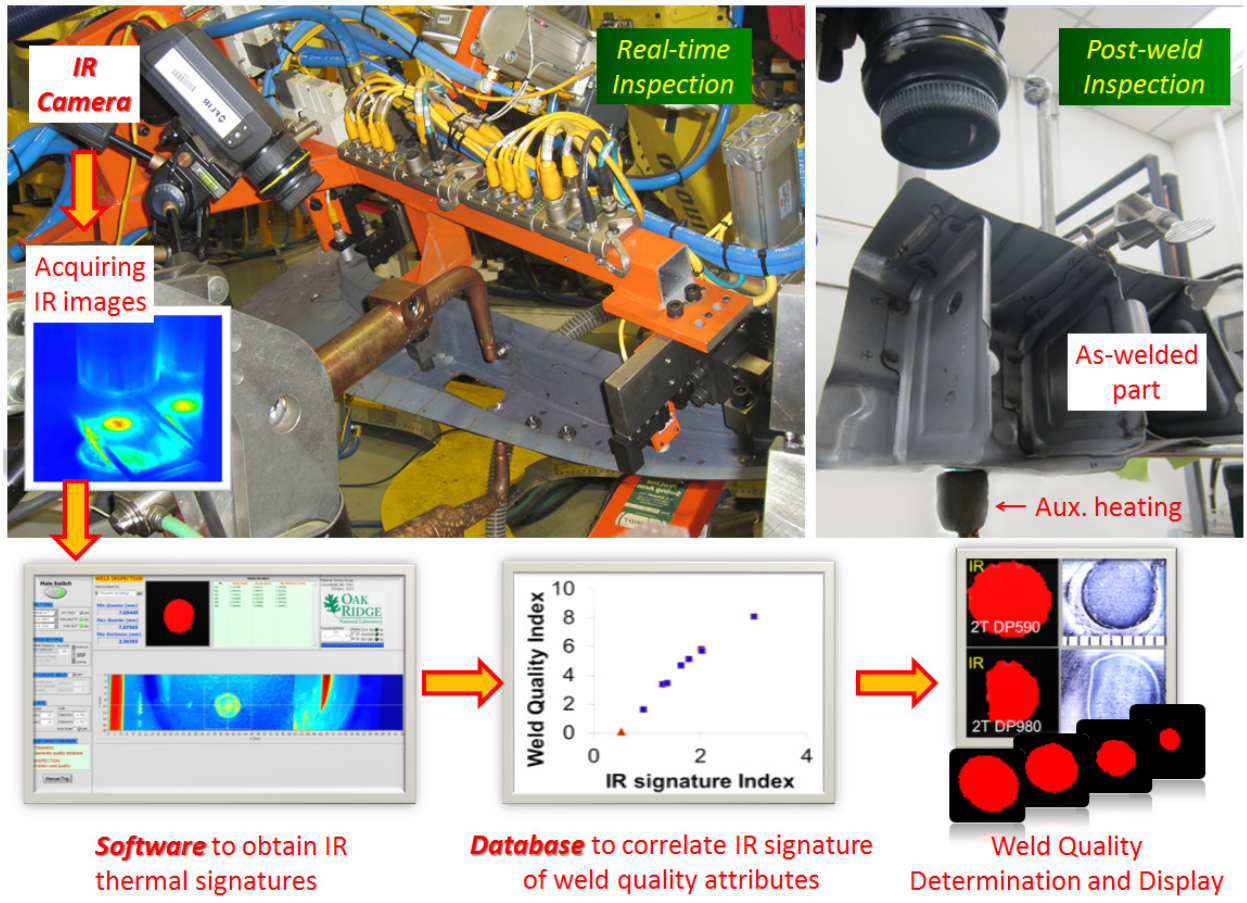

Figure III-67: IR NDE weld system consisting of IR camera, copyrighted computer program with proprietary thermal imaging analysis algorithms, and weld quality database.

For real-time inspection (Figure III-68), the heat flow generated from the welding process (with temperatures exceeding 1000°C) is monitored by the IR camera. For post-weld inspection (Figure III-69), a novel auxiliary heating device is applied to locally heat the weld region, resulting in temperature changes on the order of 10°C and the transmitted heat flow is monitored. Compared with the flash lamp–based heating method attempted by others, which results in a temperature change on the order of 0.01 to 0.1°C, our technology's greater temperature change, coupled with our copyrighted thermal image analysis software, effectively solves the major technical challenge that has hindered past attempts at IR-based weld inspection: the influence of unavoidable surface variations that render prediction of weld size unreliable in high-volume automotive body assembly production environments.

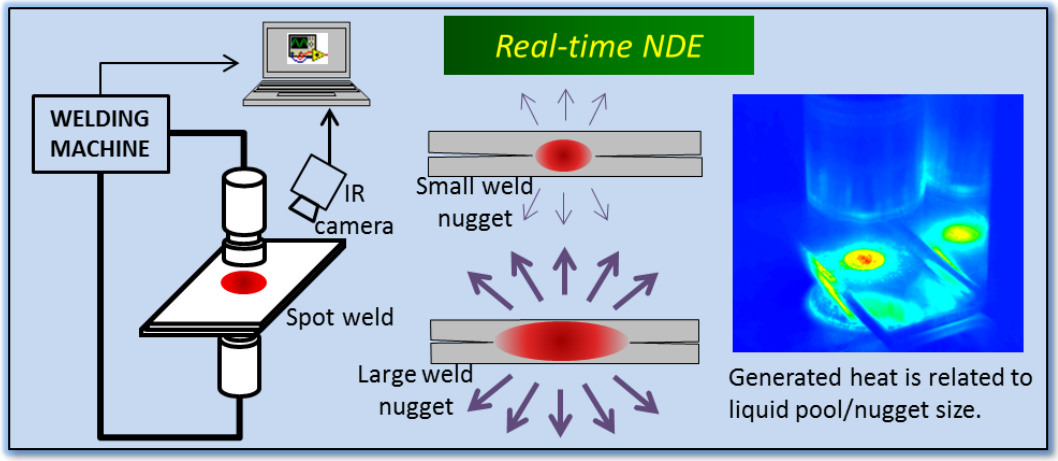

Figure III-68: Schematic setup and principle of real-time IR NDE.

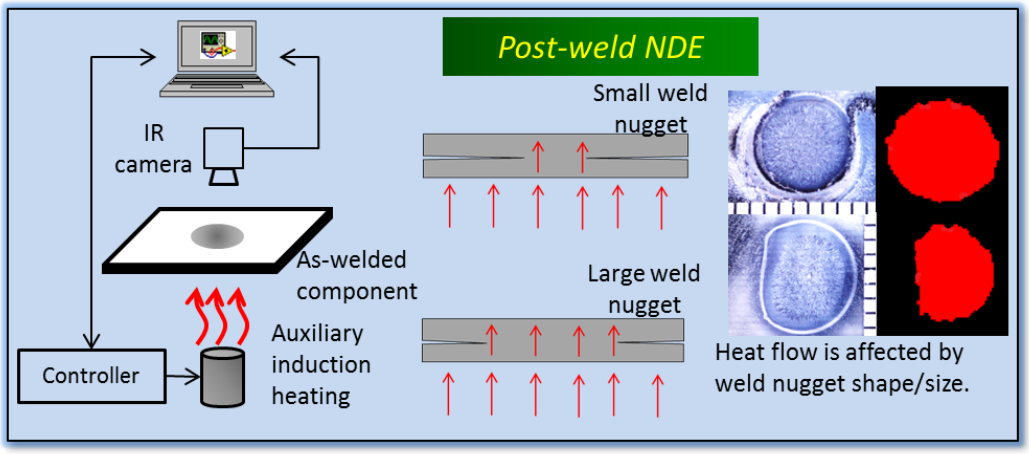

Figure III-69: Schematic setup and principle of post-weld IR NDE.

From the principles of IR thermography, we discovered a set of unique "thermal signatures," extracted from IR thermal images that positively correlate to weld quality with a high degree of confidence. A weld quality database implemented with such correlations has been established. A robust, computational software for analyzing IR images, extracting thermal signatures, and linking to the database nearly instantly has been copyrighted.

During inspection, the system automatically collects and processes thermal images of the spot welds, compares them with the weld quality database, and immediately outputs a quantitative measurement of weld quality information. The inspection cycle is 1 to 2 seconds, which is fast enough to measure each weld made during

the welding operation and to provide industry with a low-cost and nondestructive method for monitoring welds in real time.

Technology Transfer Path

Since 2013, our IR NDE prototype system has been demonstrated to major auto OEMs (i.e., GM, Ford, Chrysler, and Honda), their part suppliers (i.e., COSMA); and instrument manufacturers. They all showed keen interest in our new technology. In FY 2015, this technology was licensed by APLAIR. APLAIR plans to have a commercial product within 2 years. Figure III-70 is the photo taken during the license signing ceremony.

Figure III-70: ORNL's IR NDE technology licensed to APLAIR.

Conclusion

ORNL has successfully developed an online nondestructive spot weld quality inspection/monitoring technology that is based on IR thermography. The primary technological advantages of the technology are that it is capable of both real-time and post-weld inspections and IR is highly reliable in the extremely demanding high-volume auto-body assembly environment. With it, every weld or at least every critical weld can be measured without damaging the part. Automakers now have an efficient method for sending immediate feedback to the production lines to correct potential weld quality issues, potentially saving the U.S. automotive industry hundreds of millions of dollars per year. Our new technology is a key enabler for the automakers' adoption of advanced high-strength, lightweight auto-body materials, which are more difficult to weld and inspect but will improve fuel efficiency and safety of the vehicle fleet. Because resistance spot welding is the primary auto-body assembly process for automotive companies worldwide, our new NDE technology has the potential for revolutionizing the welding and assembly of automotive body structures.

Improving Fatigue Performance of Advanced High-Strength Steel Welds

Project Details

Zhili Feng, Principal Investigator
ORNL
1 Bethel Valley Road
Oak Ridge, TN 37831
Phone: 865-576-3797
E-mail: fengz@ornl.gov

Benda Yan and Sriram Sadagopan, Principal Investigators
ArcelorMittal USA
3300 Dickey Road
East Chicago, IN 46312
Phone: 219-399-6922
E-mail: benda.yan@arcelormittal.com

Contributors:
ORNL: Xinghua Yu, Don Erdman, Yanli Wang, Wei Zhang, Dongxiao Qiao, and Stan David
ArcelorMittal: Wenkao Hou and Steve Kelly; ESAB: Wesley Wang
Colorado School of Mines: Zhifeng Wang, Zhenzhen Yu, Sindu Thomas, and Stephen Liu

Accomplishments

- Demonstrated the feasibility of alternating weld distortion in thin gauge steel sheet metals by means of low transformation temperature (LTT) weld wires (FY 2015).
- Confirmed reduced residual weld stresses in the LTT welds through means of a high-energy synchrotron experiment (FY 2014).
- Successfully demonstrated a new weld filler metal design approach and concept that could effectively control stresses in the high-stress concentration region of short stitch welds commonly used in autobody structures. Preliminary fatigue testing confirmed three to five times weld fatigue improvement (FY 2013).
- Successfully developed a mechanical stress management approach and demonstrated that such an approach improves the weld fatigue life between 5 to 10 times at the high-cycle fatigue testing range, which is more relevant to the durability of autobody structures (FY 2013).
- Completed initial fatigue testing of baseline welds fabricated with both conventional weld wire and LTT weld wires to generate the applied stress magnitude against cyclic stress to cycles to failure (S-N) curves (FY 2012).
- Completed initial development of the weld thermal-metallurgical-mechanical model to gain an understanding of the effect of low-temperature phase transformation on formation of compressive weld residual stress at the fatigue cracking initiation region (FY 2012).
- Developed a new weld fatigue testing specimen configuration that is essential to maintaining the weld's residual stress field that is representative of actual welded automotive body structures (FY 2011).
- Completed a comprehensive survey of open literature to collect the published chemistry of LTT weld wires; down-selected and produced three different types of baseline LTT weld wires (FY 2011).

Future Directions

- Implement commercialization of the weld fatigue life improvement technology developed in this project.

Technology Assessment

- Target: Develop robust in-process weld fatigue life improvement technologies that can be used to join AHSS auto-body structural components with cost penalties acceptable to the auto industry.
- Gap: Weld fatigue strength in the as-welded condition does not increase in proportion to the yield/tensile strength of AHSS. The insensitivity of weld fatigue strength to steel static strength is a major barrier for lightweighting through down-gauging for chassis and other load-bearing components.
- Gap: Today's weld fatigue improvement techniques are mostly post-weld based. The added steps are cost prohibitive in the high-volume mass production automotive environment; large variability exists in the fatigue life achieved by the post-weld-based techniques.

Introduction

Under a Cooperative Research and Development Agreement (CRADA), ORNL and ArcelorMittal USA are working together to develop the technical basis and demonstrate the viability of innovative technologies that can substantially improve the weld fatigue strength and durability of autobody structures. Durability is one of the primary metrics in designing and engineering automotive body structures. Fatigue performance of welded joints is critical to the durability of body structure because the likeliest locations for fatigue failure are often at welds. Recent studies by the Auto/Steel Partnership Sheet Metal Fatigue Committee, the U.S. Department of Energy's Lightweighting Materials Program, and others have clearly revealed that, unlike base metal fatigue strength, weld fatigue strength of AHSS is largely insensitive to base metal composition, microstructure, and strength under typical welding conditions used in BIW [12–16]. The lack of inherent weld fatigue strength advantage of AHSSs over conventional steels is a major barrier for vehicle weight reduction through down-gauging, because down-gauging leads to increases in stresses, thereby reducing durability under the same dynamic road-loading conditions. In addition to AHSSs, a recent comparative study reveals that other lightweight alloys (such as Al and Mg alloys) may not offer improved weld fatigue strengths on a "specific weight" basis [17]. Therefore, solutions for improving the fatigue strength of welds are critical to BIW lightweighting.

Approach

Instead of using post-welding techniques to improve the weld fatigue strength, this project focuses on developing in-process weld technology as part of the welding operation. The overall goal of the project is to develop effective ways of controlling and mitigating the key factors governing the fatigue life of AHSS welds, including weld residual stress, weld profile, and weld microstructure/chemistry. The joint research also fully utilizes state-of-the-art integrated computational welding engineering, neutron/synchrotron and other advanced residual stress measurement techniques, and fatigue testing and microstructure analysis capability at ORNL and ArcelorMittal Global R&D to perform research and development for this project.

Two specific in-process approaches were further developed during this project. Issues of both a technical and economic nature unique to the automotive body structural welding environment have been identified and will be addressed. Per CRADA policy, specific details of the approaches will be released to the public at a later time.

Results and Discussion

The project was successfully completed. The feasibility of improving the effective weld fatigue life by means of two different in-process weld residual stress mitigation approaches was demonstrated. (1) A new metal weld design was demonstrated that could effectively control stresses in the high-stress concentration region of the short-stitch weld commonly used in autobody structures. Fatigue testing confirmed a three to five times weld fatigue improvement under high-cycle testing conditions (Figure III-71). (2) A thermomechanical stress management approach improves the weld fatigue life five and ten times the high-cycle fatigue testing range, which is more relevant to the durability of autobody structures (Figure III-72).

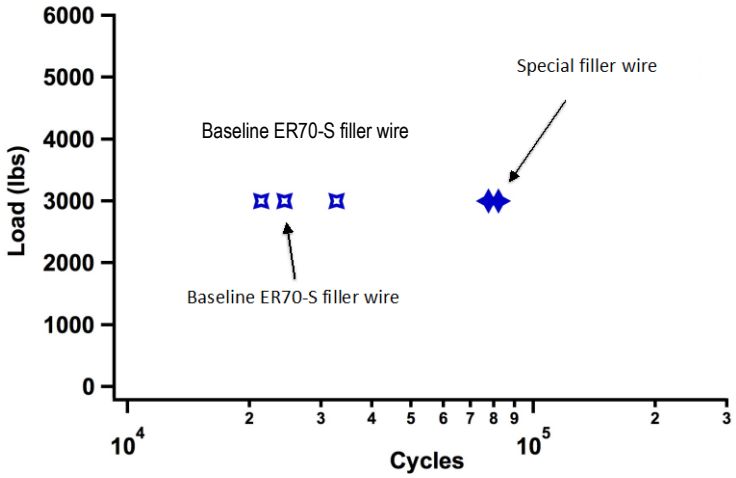

Figure III-71: Comparison of the weld fatigue lives of baseline an ER70 weld versus the new filler wire developed in this project.

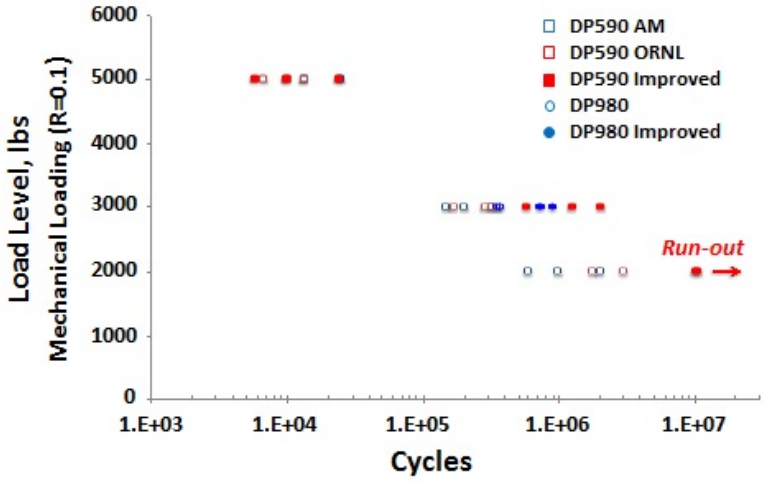

Figure III-72: Improvement of weld fatigue lives through innovative thermomechanical stress management.

The changes in weld residual stresses via LTT wire showed drastic dimensional changes of the thin gauge steel sheet materials. This is illustrated in Figure III-73. In this particular case, two stitch bead-on-plate welds were deposited on a 2-mm thick low carbon steel sheet. Compared to the standard reference ER70S-3 weld wire, the welded steel sheet exhibited complete reversal of the distortion direction. In the case of reference ER70S-3 weld wire, the middle section of the steel sheet was bent downward for about 10 mm. In contrast, the weld

made with the new LTT wire bent the steel sheet upward for about 15 mm. Such a drastic change in the distortion from the new LTT wire suggests the possibility of control weld distortion by further refinement of LTT weld wire.

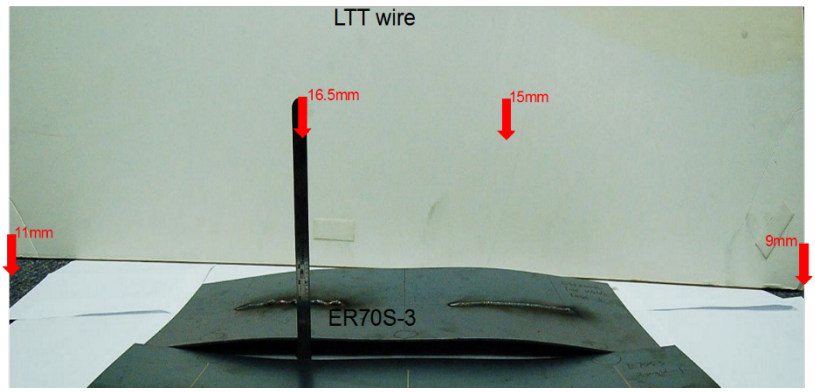

Figure III-73: Reversal of distortion mode with the use of LTT wire.

Finally, the concept of LTT has been extended to mitigate hydrogen embrittlement (hydrogen-induced cracking) in welding of high-strength steels through a collaborative research and development effort with the U.S. Army. The effectiveness of using a new LTT weld wire to mitigate hydrogen embrittlement of armored high-strength steel has been demonstrated as shown in Figure III-74. The effectiveness of ORNL's LTT weld wire to mitigate hydrogen-induced cracking is clearly demonstrated in welding of high-strength armored steels (Military Detail Specification (MIL-DTL)-12560 and MIL-DTL-46100). The widely used commercial high-strength steel weld wire ER100-S requires preheating to temperatures of 100 and 150°C to eliminate hydrogen-induced cracking in the two armored steels. In contrast, the new weld wire developed by ORNL in partnership with the U.S. Army (patent pending) did not require any preheating prior to welding to eliminate hydrogen-induced cracking. Potential application of the LTT weld wires developed during this project has generated a lot of interest in the automotive industry.

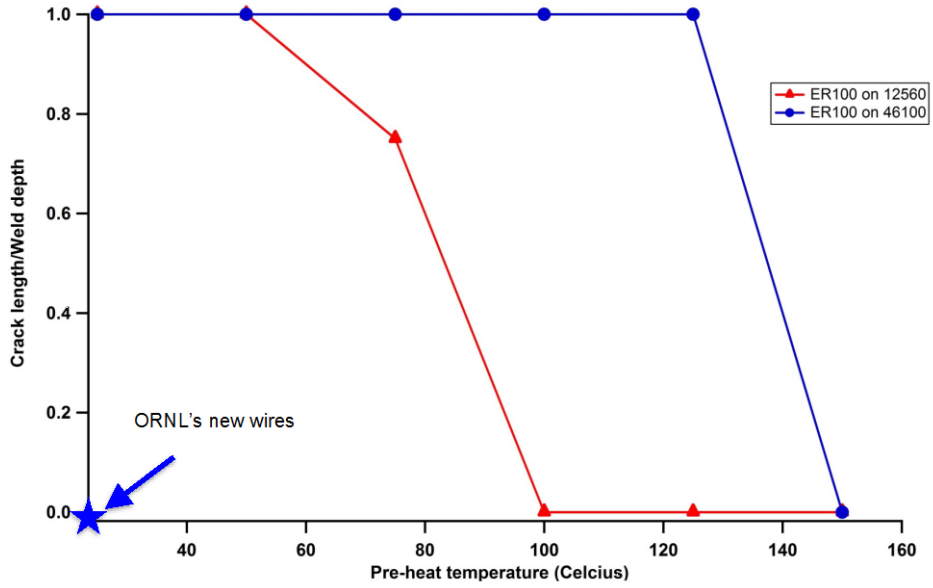

Figure III-74: Y-groove testing results show the effectiveness of ORNL's new LTT weld wire to mitigate hydrogen-induced cracking in welding high-strength armored steels.

Technology Transfer Path

The primary technology transfer path is to work closely with the project's industry partners (i.e., a major steel supplier and a major welding consumables manufacturer) that have business interests and marketing capability for quickly commercializing the technology developed during this project. In addition, we plan to disseminate the findings and results from the project to automotive OEMs and other interested parties through extensive communication channels that we have established over the years.

Conclusions

Weld fatigue life has been identified as one of the key technology barriers to widespread use of lightweight materials (AHSS and Al and Mg alloys) for autobody structure lightweighting. The technology developed during this project is expected to provide the automotive industry with cost-effective and practical solutions.

Significant technical progress has been achieved during this project. Weld fatigue life improvements on the order of three to five times and five to ten times through innovative thermomechanical stress management were demonstrated using the two novel approaches developed in this project to control and mitigate weld residual stresses. The changes of weld residual stresses could also drastically change the welding-induced distortion in thin sheet steels used for autobody structural components. The potential of LTT weld wires developed by ORNL in collaboration with the U.S. Army has been demonstrated to mitigate hydrogen-induced cracking in welding of high-strength steels.

Project Conclusions

The Mg corrosion project has furthered understanding of how protective films on Mg alloys form and how they behave when subjected to aqueous, salt-containing environments. A new inline, real-time tool has been developed for nondestructive inspection of spot welds and that system is in the process of being commercialized. A new weld filler wire technology has been developed to mitigate the effects of fatigue loading in advanced high-strength steels demonstrating up to ten times improvement in weld fatigue life.

References

1. G. L. Song and A. Atrens, 2007; "Corrosion mechanisms of magnesium alloys," *Advanced Engineering Materials,* 9 (3); pp. 177–83.
2. G. L. Song, 2005, "Recent progress in corrosion and protection of magnesium alloy," *Advanced Engineering Materials,* 7 (7); pp. 563–86.
3. J. E. Gray and B. Luan, 2002, "Protective coatings on magnesium and its alloys—a critical review," *Journal of Alloys and Compounds,* 336 (1–2); pp. 88–113.
4. A. Seyeux et al., 2009, "ToF-SIMS depth profile of the surface film on pure magnesium formed by immersion in pure water and the identification of magnesium hydride," *Corrosion Science,* 51 (9); pp. 1883–86.
5. N. Hara et al., 2007, "Formation and breakdown of surface films on magnesium and its alloys in aqueous solutions," *Corrosion Science,* 49 (1); pp. 166–75.
6. J. H. Nordlien et al. 1997, "A TEM investigation of naturally formed oxide films on pure magnesium," *Corrosion Science,* 39 (8); pp. 1397–1414.
7. M. P. Brady et al., 2014, "Tracer film growth study of hydrogen and oxygen from the corrosion of magnesium in water," *Journal of the Electrochemical Society,* 161 (9); pp. C395–C404.
8. K. A. Unocic et al., 2014, "Transmission Electron Microscopy Study of Aqueous Film Formation and Evolution on Magnesium Alloys," *Journal of the Electrochemical Society,* 161 (6); pp. C302–C311.

9. M. P. Brady et al., "Advanced Characterization Study of Commercial Conversion and Electro-Deposition Coating Structures on Magnesium Alloys AZ31B and ZE10A," to be submitted.
10. B. O'Hara and P. Shafer, 2010, "2011 Honda Odyssey Body Development: Concept, Styling, Weight Reduction, and Safety," presented at the *International Automotive Body Congress (IABC)*, November 2010.
11. Lotus Engineering, Inc., 2010, *An Assessment of Mass Reduction Opportunities for a 2017–2020 Model Year Vehicle Program*, March 2010.
12. J. Bonnen and R. M. Iyengar, 2006, "Fatigue of Spot Welds in Low-Carbon, High-Strength Low-Alloy, and Advanced High-Strength Steels and Fatigue of Fusion Welds in Advanced High-Strength Steels," *2006 International Automotive Body Congress;* pp. 19–30.
13. B. Yan; S. H. Lalam; and H. Zhu, 2005, "Performance Evaluation of GMAW Welds for Four Advanced High-Strength Steels," *SAE International Paper No. 2005-01-0904*.
14. R. M. Iyengar et al., 2008, "Fatigue of Spot-Welded Sheet Steel Joints: Physics, Mechanics and Process Variability," *Great Designs in Steel,* April 9, 2008.
15. Z. Feng; J. Chiang; M. Kuo; C. Jiang; and Y. Sang, 2008, "A New Perspective on Fatigue Performance of Advanced High-Strength Steel GMAW Joints," *Sheet Metal Welding Conference XIII*.
16. Z. Feng; Y. Sang; C. Jiang; J. Chiang; and M. Kuo, 2009, "Fatigue Performance of Advanced High-Strength Steels (AHSS) GMAW Joints," *SEA 2009 World Congress*, Paper No. 09M-0256.
17. R. J. Moat et al., 2011, "Design of weld fillers for mitigation of residual stresses in ferritic and austenitic steel welds," *Science and Technology of Welding and Joining*, 16; pp. 279–84.

Bibliography

M. P. Brady; M. Fayek; H. H. Elsentriecy; K. A. Unocic; L. M. Anovitz; J. R. Keiser; G. L. Song; and B. Davis, 2014, "Tracer Film Growth Study of Hydrogen and Oxygen from the Corrosion of Magnesium in Water," *Journal of the Electrochemical Society,* 161 (9); pp. C395–C404.

M. P. Brady; M. Fayek; H. M. Meyer; D. N. Leonard; H. H. Elsentriecy; K. A. Unocic; L. M. Anovitz; E. Cakmak; J. R. Keiser; G. L. Song; and B. Davis, 2015, "Tracer study of oxygen and hydrogen uptake by Mg alloys in air with water vapour," *Scripta Materialia,* 106; pp. 38–41.

M. P. Brady; D. N. Leonard;H. M. Meyer; J. K. Thomson; K. A. Unocic; H. H. Elsentriecy; G. L. Song; K. Mitchen; and B. Davis, "Advanced Characterization Study of Commercial Conversion and Electro-Deposition Coating Structures on Magnesium Alloys AZ31B and ZE10A," to be submitted.

M. P. Brady; G. Rother; L. M. Anovitz; K. C. Littrell; K. A. Unocic; H. H. Elsentriecy; G. L. Song; J. K. Thomson; N. C. Gallego; and B. Davis, 2015, "Film Breakdown and Nano-Porous $Mg(OH)_2$ Formation from Corrosion of Magnesium Alloys in Salt Solutions," *Journal of the Electrochemical Society* 162 (4); pp. C140–C149.

J. Chen; Z. Feng; H. Wang; and W. Zhang, 2011, "Non-destructive Inspections of Welds and Joints Using Infrared Imaging and Post-Weld Heating," ORNL patent application, May 2011.

J. Chen; Z. Feng; and C. D. Warren, 2014, "Nondestructive Inspection of RSW of AHHS by Infrared Technology," *International Symposium on Advances in Resistance Welding*, Atlanta.

J. Chen; Z. Feng; and W. Zhang, 2012, "A Non-destructive and Real-time Inspection System for Monitoring Resistance Spot Welding Using Infrared Thermography," ORNL patent application, August 2012.

J. Chen; Z. Feng; and W. Zhang, 2013, "An Online Infrared-based Resistance Spot Weld Inspection System," presentation to *SAE 2013 World Congress*.

J. Chen; Z. Feng; and W. Zhang; 2014, software, "IR Spot Weld Inspect," Copyright Number 50000074.

J. Chen; W. Zhang; and Z. Feng, 2012, "Resistance Spot Welding On-line Inspection System Based on Infrared Thermography," presentation to *FABTECH 2012*.

J. Chen; W. Zhang; Z. Yu; and Z. Feng, 2012, "Automated Spot Weld Inspection using Infrared Thermography," proceedings of *9th International Conference on Trends in Welding Research*, Chicago.

J. Chen; W. Zhang; Z. Yu; H. Wang; and Z. Feng, 2012, "Automated Spot Weld Inspection using Infrared Thermography," presented at the *9th International Conference on Trends in Welding Research*, Chicago.

Z. Feng; Z. Yu; S. David; and D. Tzelepis, 2015, "High-Strength Weld Wire for Hydrogen Embrittlement Control," U.S. Patent Application.

D. Qiao et al., 2012, "The Effect of Martensitic Phase Transformation on Weld Residual Stress Distribution in Steel Sheet Lap Joint—A Computational Study," proceedings of the *9th International Conference on Trends in Welding Research*, Chicago.

G. L. Song et al., 2014, "Advanced Characterization of Mg Alloy Surface Films," invited presentation at *CORROSION 2014*, NACE, San Antonio, Texas, March 9 through 13, 2014.

G. L. Song et al., 2014, "Film Evolution on Mg Alloys," presented at *Materials Science & Technology 2014*, Pittsburgh, October 12 through 16, 2014.

K. A. Unocic et al., 2013, "Characterization of Film Formation on Commercial and Model Magnesium Alloys," poster presented *at 2013 TMS Annual Meeting*, San Antonio, Tex., March 4, 2013.

K. A. Unocic; H. H. Elsentriecy; M. P. Brady; H. M. Meyer; G. L. Song; M. Fayek; R. A. Meisner; and B. Davis, 2014, "Transmission Electron Microscopy Study of Aqueous Film Formation and Evolution on Magnesium Alloys," *Journal of the Electrochemical Society* 161 (6): pp. C302–C311.

Z. Wang; Z. Yu; and Z. Feng, 2015, "Effect of Low Transformation Temperature Welding Consumables on the Weld Microstructure and Mechanical Properties," *2015 AWS Annual Convention*, Chicago.

Z. Wang; Z. Yu; Z. Feng; and S. Liu, 2014, "Effect of Low Transformation Temperature Welding Consumables on Mechanical Properties of Lap Joints," *2014 AWS Annual Convention*, Atlanta.

III.8. In Situ Investigation of Microstructural Evolution During Solidification and Heat Treatment in a Die-Cast Magnesium Alloy – Pacific Northwest National Laboratory

Project Details

Aashish Rohatgi, Principal Investigator
Pacific Northwest National Laboratory (PNNL)
902 Battelle Boulevard
Richland, WA 99352
Phone: 509-372-6047
E-mail: aashish.rohatgi@pnnl.gov

Nigel D. Browning, Principal Investigator
PNNL
902 Battelle Boulevard
Richland, WA 99352
Phone: 509-375-7569
E-mail: nigel.browning@pnnl.gov

William Joost, Technology Area Development Manager
U.S. Department of Energy
1000 Independence Avenue, SW
Washington, DC 20585
Phone: 202-287-6020
E-mail: William.joost@ee.doe.gov

Contractor: PNNL
Contract No.: DE-AC05-00OR22725 & DE-AC06-76RL01830

Executive Summary

The goal of this project is to understand the microstructural evolution in the AZ91 (i.e., 9 weight percent [wt%] aluminum [Al] and 1 wt% zinc [Zn]) magnesium (Mg) alloy under non-equilibrium solidification conditions of die casting and during subsequent heat treatment. The two primary objectives of this work are to (1) understand the solidification kinetics of AZ91 melt at high cooling rates and (2) understand the kinetics of phase evolution of β-$Mg_{17}Al_{12}$ and α-Mg during heat treatment. The purpose of the first objective is to understand the nucleation and growth kinetics of the dendrites ($Mg_{17}Al_{12}$) and eutectic under non-equilibrium high-rate cooling (i.e., about 100 to 1000°C/s), as experienced by the molten AZ91 Mg alloy during high-pressure die casting (HPDC). The purpose of the second objective is to understand the kinetics of phase evolution when casting, comprising a non-equilibrium microstructure, is heat-treated between 150 and 300°C.

During Fiscal Year (FY) 2015, the three primary activities were (1) solidification modeling of AZ91 using ProCAST modeling software, (2) electron microscopy analysis of microstructural evolution in Mg-9 wt% Al films during heat treatment, and (3) atomistic modeling of the Mg-Al system. In activity (1), phase evolution and macro-level thermophysical characteristics during solidification of AZ91 were investigated in the cooling rate range of 100 to 1000°C/s using ProCAST modeling software. The results showed that solidification behavior of AZ91 can be modeled assuming a single set of thermophysical properties, and the predicted secondary dendrite arm spacing (SDAS) was in good agreement with published SDAS values in the literature. In activity (2), microstructural evolution in Mg-9 wt% Al thin films following heat treatment between 150 and 300°C was analyzed using transmission electron microscope (TEM) and electron energy loss spectroscopy (EELS) techniques. The resulting activation energy for α-grain growth in the thin-film geometry samples was found to be significantly lower than the literature values reported for bulk samples. Finally, in activity (3), a

self-learning kinetic Monte Carlo (SLKMC) method was used to determine vacancy formation energies and activation energy barriers for vacancy-atom exchange processes in the Mg-Al system. The diffusivity of Al in the Mg lattice was calculated in the in-plane and out-of-plane directions and found to be of the same order of magnitude as published in the literature.

Accomplishments

- Investigated the alloy phase evolution and macro-level thermophysical characteristics across a cooling rate range of 1 to 1000°C/s (FY 2015).
- Simulated solidification of molten AZ91 in ProCAST and predicted the SDAS for cooling rates of 1, 100, and 1000°C/s (FY 2015).
- Heat treated Mg-Al films at 150°C, 200°C, and 300°C for three different times each and determined the grain-size and distribution of $Mg_{17}Al_{12}$ precipitates (FY 2015).
- Determined the grain-growth exponent and activation energy for grain-growth in Mg-Al thin films (FY 2015).
- Established a combination of EELS and precession electron diffraction (PED) techniques to determine the composition and phase identification in multiphase, nanocrystalline Mg-Al thin films (FY 2015).
- Developed a new, on-lattice, SLKMC code, named atomistic-kinetic simulations of microstructural evolution (AKSOME). This code was used to investigate the diffusion kinetics of vacancy and Al-atom diffusion as function of Al concentration, and to understand Al segregation in Mg-Al alloys (FY 2015).
- Used SLKMC simulation to extract activation barrier and diffusion prefactors for Al diffusion in Mg. Using 56 nearest neighbors in a Mg-Al system, identified all Al-vacancy exchange processes and obtained their activation energies (FY 2015).

Future Directions

- Analyze grain-growth and precipitate formation in Mg-Al-Zn thin films.
- Perform in situ solidification experiments and determine the kinetics of phase formation under high cooling rates.
- Determine Al and vacancy diffusivities as a function of Al concentration (0.1, 1.0, and 8 wt%) and temperature (300 K, 400 K, and 500 K).
- Analyze evolution of Al clusters in a Mg lattice at 150°C to understand nucleation and growth of $Mg_{17}Al_{12}$ precipitates.

Technology Assessment

- Target: Quantify the nucleation and growth kinetics during solidification in molten AZ91 Mg alloy at high cooling rates (approximately 100 to 1000°C/s).
- Gap: Traditional analytical techniques cannot image the microstructural evolution in situ during solidification of molten metals at high cooling rates. Thus, existing research is restricted to post-solidification analysis or to in situ analysis at cooling rates much lower than 100°C/s.
- Target: Develop solidification models that can predict the non-equilibrium microstructures developed in AZ91 Mg alloy during die casting.
- Gap: Microstructural evolution data during solidification of Mg alloys at high cooling rates is not available to validate existing models. Hence, solidification models cannot accurately predict the non-equilibrium as-cast microstructure that is formed during die casting of Mg alloys.

Introduction

Mg has the potential to provide 60 to 75% mass savings relative to steel or cast iron and HPDC can be used to economically produce large, thin-walled Mg castings to replace steel subsystems [1]. Mg castings can take advantage of mass-saving potential for automotive applications because castings do not have to overcome the limited room-temperature formability of Mg, which is an aspect that has hindered the widespread use of Mg sheets in automotive applications.

High cooling rates during HPDC lead to formation of a non-equilibrium microstructure comprising β-$Mg_{17}Al_{12}$ precipitates and inhomogeneous α-Mg-Al solid-solution. However, the kinetics of the solidification process during HPDC are not well understood because the associated high cooling rates (i.e., approximately 100 to 1000°C/s) make it virtually impossible for traditional analytical techniques to image the microstructural evolution in situ during solidification of molten metals. Thus, existing research on in situ solidification analysis is restricted to cooling rates up to about 40°C/s using differential scanning calorimetry. Alternatively, post-solidification analysis can be used for rapidly cooled samples but without detailed understanding of the solidification history. Further, current solidification models are limited mainly to mold filling, thermal, and stress analyses; however, they lack the ability to extensively predict the post-solidification microstructure. This limitation is due to the inadequacy of the current modeling techniques to model non-equilibrium phase transformation, diffusion, and other processes. In this work, we propose to perform in situ melting and solidification experiments inside a dynamic TEM to address the above knowledge gap. This information will feed into the commercially available solidification modeling software, ProCAST (process casting evaluation software from ESI North America), to help enable its use for predicting HPDC microstructures in Mg alloys.

Once cast, high-pressure die castings are generally not heat treated to avoid blister formation caused by the presence of porosity. Although alloy development and process improvement efforts are ongoing to reduce/eliminate porosity and enable heat treatment to improve the mechanical performance of die castings, post-solidification heat treatment investigations have been limited to sand/gravity castings, where the casting is solutionized and then aged. For example, the T6 treatment for AZ91 involves solution treating at 413°C for 16 to 24 hours, followed by cooling/quenching and artificially aging at 168°C for 16 hours [2]. The significant time spent at elevated temperatures during such heat treatments can lead to undesirable grain growth, thus lowering strength and negating precipitation strengthening resulting from T6 treatment [3]. Alternately, a T5 heat treatment may be performed where the casting is aged at 168°C for 16 hours without solutionization [2]. However, the full potential of precipitation strengthening is not realized due to the absence of the solutionization step. Further, precipitation during T5 heat treatment occurs from an as-cast, non-equilibrium microstructure. Therefore, if high-strength Mg alloys and their heat treatments are to be developed, an understanding of phenomena such as grain growth and precipitation in an initial non-equilibrium microstructure are crucial. In this project, non-equilibrium microstructures were generated via sputtering (i.e., thin films of Mg-Al and Mg-Al-Zn were fabricated via magnetron sputtering and subsequently heat treated inside a TEM to investigate the kinetics of microstructure evolution). The results pertaining to heat treatment of only the Mg-Al system are presented in this report.

In AZ91, solute diffusion kinetics mediated by vacancy diffusion are important in controlling the kinetics of $Mg_{17}Al_{12}$ precipitation. Modeling of diffusion in alloys is particularly challenging because this phenomenon consists largely of an interplay of the ensemble of thermally activated atomic jumps, which are dependent on local atomic arrangement and occurring at time scales of microseconds or longer. While the time scales reached by ab initio and classical molecular dynamics are too short, it is possible to study the precipitation kinetics spanning time scales of minutes to hours using the kinetic Monte Carlo (KMC) method of Clouet and Soisson et al. [4,5]. This work focuses on development and implementation of the SLKMC method of Trushin et al. [6] to study vacancy diffusion in the Mg-Al alloy. The understanding gained from atomistic simulations is expected to be helpful in designing compositions and thermal treatments aimed at controlling the size, spatial distribution, and morphology of precipitates at the nanoscale.

Approach

Solidification Modeling

This task was performed by our industrial collaborator, ESI North America. Using the nominal chemistry for AZ91, ProCAST software was used to model the solidification paths corresponding to equilibrium solidification (lever rule), Scheil method (i.e., non-equilibrium and no back diffusion), and several cooling rates (0.0001 to 1000°C/s) in between. The influence of cooling rate on microstructural features was evaluated by simulating solidification in a simple cylindrical geometry (i.e., 13-mm diameter × 15-mm high).

In Situ Heat Treatment

Mg-Al alloy thin films of about 60-nm thickness and a target composition of Mg-9 wt% Al were deposited by magnetron sputtering. The thin films were deposited on a 25-nm amorphous silicon nitride (Si_3N_4) TEM support membrane with a viewing area of 30 × 400 μm. The heat treatments were carried out at 150°C, 200°C, and 300°C for times between 5 and 190 minutes. The test temperature was indicated by the vendor-provided, heating-stage controls and was reached in about 90 seconds; cooling to room temperature (at the end of the heat treatment) was achieved in about 120 seconds. Each heat treatment was conducted on a fresh, as-sputtered thin film sample. TEM analysis of heat-treated films was performed, after cooling, in an aberration-corrected, monochromated FEI Titan 80-300 TEM operated at 300 kV and a JEOL ARM200CF at 200 kV. EELS analysis was performed with a high-resolution Gatan Imaging Filter. The Zn L3 edge at 1020 eV, the Mg K1 edge at 1305 eV, and the Al K1 edge at 1560 eV were used for EELS.

For the purpose of grain growth analysis, grain size measurements in the thin films were performed on bright-field (BF) images using the linear intercept method described in ASTM E112 and on at least two micrographs per heat treat condition taken at 36k× magnification. Horizontal parallel lines were drawn across the TEM image of a heat-treated film to obtain several hundred intercepts in each case. The size of the $Mg_{17}Al_{12}$ β-precipitates was measured in the EELS relative composition maps at the largest diameter for every individual precipitate.

Atomistic Modeling

An SLKMC method was used to determine vacancy formation energies and activation energy barriers for vacancy atom exchange processes in the Mg-Al system. In SLKMC, a pattern-recognition scheme [6-9] is used to generate a unique tag for each unique arrangement of neighboring atoms around an atom. All identified diffusion processes the atom can perform, along with their activation barriers, are attached to the unique tag and stored in a database for future use, thus avoiding redundant calculations. The climbing image nudge-elastic band (CI-NEB) [10] method module within the large-scale atomic/molecular massively parallel simulator (LAMMPS) [11] was used to calculate the local Al environment-dependent energy barriers for the vacancy hops. Simulations were performed using an orthorhombic cell of 511 Mg atoms with one vacancy and periodic boundary conditions. The original parameters for Mg-Al modified embedded atom method (MEAM) potential taken from reference [12] were adjusted to get material parameters of pure Mg and Al, Al in Mg, Mg in Al, and $Mg_{17}Al_{12}$ close to first principles and experimental values available in literature.

Results and Discussion

Solidification Modeling

Figure III-75 shows the predicted volume fraction of the α-Mg-Al phase during the solidification of molten AZ91 as a function of cooling rates from 0.0001 to 1000°C/s. Thus, under equilibrium cooling (curve marked "lever rule"), molten AZ91 solidifies to 100% α-Mg-Al at about490°C. However, under non-equilibrium cooling (e.g., curves marked "Scheil" and various cooling rates), the solidus temperature is shifted below the equilibrium such that at 437°C, the fraction of α-Mg-Al formed is less than 1 and the remainder liquid forms

the α-β eutectic (indicated by the vertical step in the curves near the end of solidification). For the cooling rates between 100 to 1000°C/s, Figure III-75 shows the minimal difference in the solidification paths and phase fractions and, thus, a single set of thermophysical properties can be assumed for cooling rates between 100 and 1000°C/s.

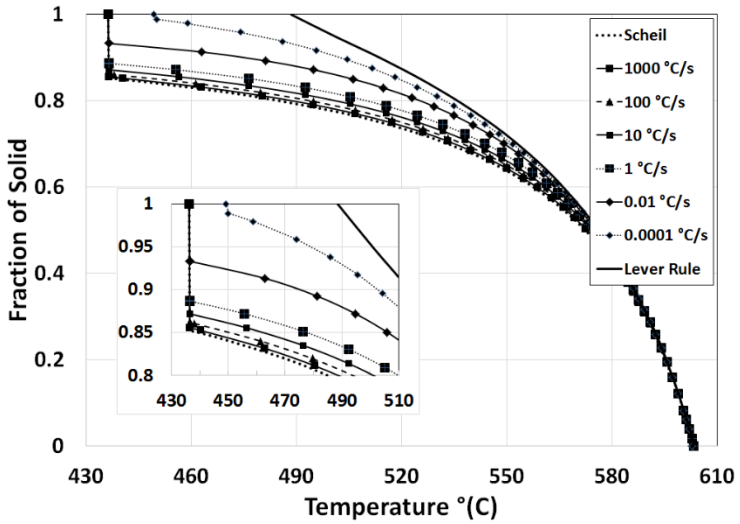

Figure III-75: Predicted fraction of α-Mg-Al during solidification of AZ91 as a function of cooling rates. The inset shows a magnified view near the end of solidification.

Figure III-76 shows the predicted SDAS in AZ91 when it is cooled from 700°C at the indicated cooling rates. The simulations predict a SDAS of about 57, 12, and 6 microns at cooling rates of 1, 100, and 1000°C/s, respectively. Although these initial predictions have not been "calibrated" with experiments, they are in good agreement with the literature [13].

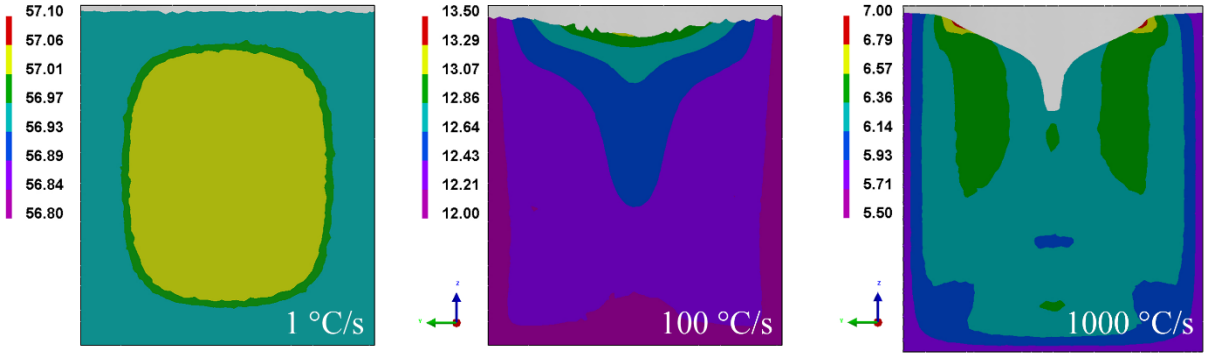

Figure III-76: Predicted SDAS (in microns) in a 13-mm diameter × 15-mm high volume of AZ91 at the indicated cooling rates.

In Situ Heat-Treatment

Grain growth in the binary Mg-9 wt% Al films was analyzed using the following relation:

$$D^n - {D_0}^n = K \cdot t, \tag{1}$$

where D is the average grain-size at a given time t, D_0 is the average grain-size at time $t = 0$, K is a constant, and n is often referred to as the grain growth exponent. The activation energy Q for grain growth can then be determined from an Arrhenius plot of $\ln K$ vs. $\frac{1}{T}$:

$$K = K_0 \exp\left(-\frac{Q}{RT}\right) \Rightarrow \ln K = \ln K_0 - \frac{Q}{RT}\ , \qquad (2)$$

where R is the gas constant, K_0 is a constant, and T is the absolute temperature. For a given heat treating temperature, the term, $D^n - {D_0}^n$ was determined for integer values of n with $2 \leq n \leq 15$. In each case, an adjusted R-squared was determined to find the best linear fit and the corresponding n was identified as the grain-growth exponent. To account for the columnar grains in this study, the initial average grain size $\overline{D_0}$, as measured with the linear intercept method, was adjusted to represent an equiaxed grain of the same volume.

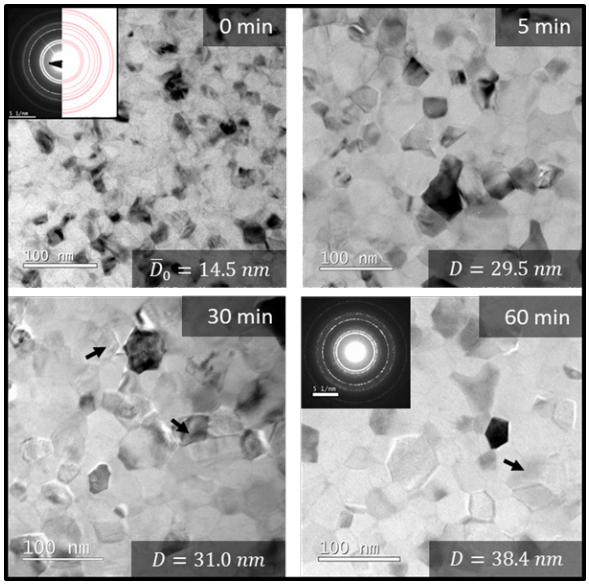

Figure III-77: TEM BF images of Mg-9 wt% Al film heat treated at 150°C. The inset in the image for *t* = 0 shows the experimental (Mg-9 wt% Al) and a simulated diffraction pattern of Mg. The scale bar in the diffraction pattern inset is 5 1/nm.

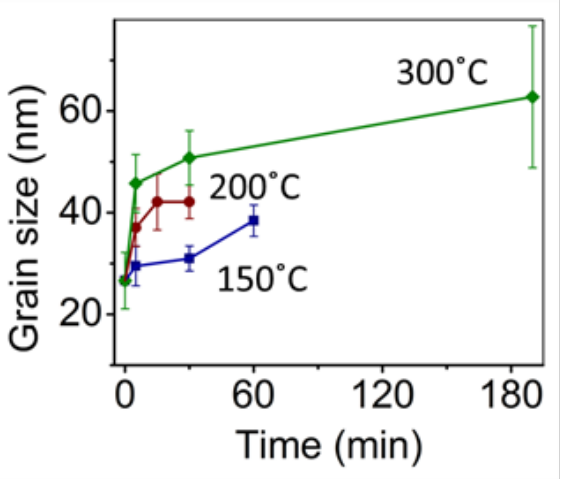

Figure III-78: Grain size evolution in Mg-9wt% Al during isothermal heat treatment.

Figure III-77 is an example of a sequence of TEM BF images that show grain growth in a Mg-9 wt% Al thin film after isothermal heat treatment at 150°C for 0, 5, 30, and 60 minutes. Figure III-78 summarizes the grain size evolution as a function of time at different heat treating temperatures. Following the procedure described above, the grain growth exponent n was determined to be 7 ±2, with the resulting activation energy Q = 31.1 ± 13.4 kJ/mol. This value of activation energy is lower than the 92 kJ/mol value for core diffusion in

Mg reported in [14], as well as lower than the 115-kJ/mol value reported as the apparent activation energy for grain growth in AZ31B (with micron-sized grains) in [15]. An explanation for the low activation energy for grain growth in the present work, relative to reported values for bulk, is the strong effect of surface diffusion in the thin film, as has also been reported for Cu and Ag films [16,17].

While the grain structure of the nanocrystalline films was clearly revealed by the BF contrast (Figure III-77), the β-phase could not be distinguished from the α-phase in BF TEM images, owing to their similar morphology. Instead, the EELS and PED techniques were found suitable to distinguish the individual phases based on their composition and diffraction patterns, respectively. For example, in the EELS technique, β-$Mg_{17}Al_{12}$ phase was identified based on the relative Al% (see Figure III-79): $Mg_{17}Al_{12}$ corresponds to about 41 at% Al, while the as-sputtered film contained about 8 at% (or 9 wt%) Al. Thus, precipitation of $Mg_{17}Al_{12}$ from a supersaturated Mg-9 wt% Al corresponds to a five-fold local enrichment in Al. It is hypothesized that the solute drag effect of Al solute atoms and the pinning effect of $Mg_{17}Al_{12}$ precipitates are responsible for the high value of the growth exponent (relative to a value of 2, as described by Burke and Turnbull [18] in the original equation).

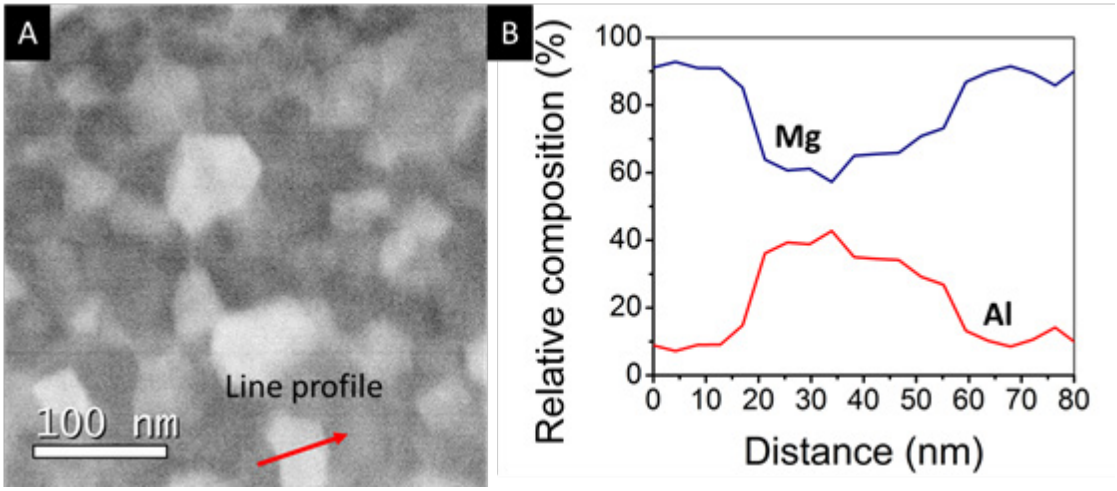

Figure III-79: (A) Scanning TEM annular dark-field image of Mg-9 wt% Al thin film heat treated at 300°C for 5 minutes. (B) Relative composition in at% as quantified by EELS technique.

Atomistic Modeling

All simulations were carried out using a simulation cell size of 128 × 128 × 128 lattice points in the *x*, *y* and *z* directions with periodic boundary conditions in all directions. This corresponds to a system size of 411 × 356 × 665 $Å^3$. Note that the basis of each lattice point is 2; therefore, the number of atoms in the simulation cell is equal to 2^{22} (= 128 × 128 × 128 × 2). Mg lattice constants in our calculations are taken as a = 3.21 Å and c/a = 1.621. A single vacancy and an Al atom are introduced in the simulation box and SLKMC simulations are performed at various temperatures to determine the effective activation energies and diffusion prefactors. The pre-exponential factor for vacancy hops is taken as $2 \times 10^{13} s^{-1}$.

Table III-11 shows the effective activation energies and diffusion prefactors for diffusion of an Al atom in an Mg lattice (within basal plane, out-of-basal plane, and total diffusion) obtained from SLKMC simulations along with values obtained from 8-frequency model [19], diffusion couple [20], and Boltzmann-Matano [21] experiments. Table III-11 shows that the effective activation energies obtained from SLKMC simulations are in qualitative agreement with the published model and experimental values (i.e., the activation energy for diffusion within the basal plane is lower than for diffusion along the c-axis).

Table III-11: Effective activation energies and prefactors for Al atom diffusion in pure Mg matrix obtained using SLKMC simulations (this work), 8-frequency model, and experiments

Orientation	Effective Activation Energy (eV)				Effective Prefactor (Å²/s)			
	SLKMC	8-freq. [a]	Expt. [b]	Expt. [c]	SLKMC	8-freq. [a]	Expt. [b]	Expt. [c]
Basal Plane	1.46	1.42	1.60 ± 0.04	—	1.12×10^{15}	4.24×10^{14}	4.86×10^{17}	—
C-axis	1.53	1.48	1.65 ± 0.03	—	2.63×10^{15}	7.17×10^{14}	9.51×10^{17}	—
Total	1.47	—	—	1.44 ± 0.15	1.62×10^{15}	—		6.25×10^{15} ± 5.37×10^{16}

freq. = frequency; Expt. = Experiment

[a] Ganeshan et al. 2011 [19]; [b] Das et al. 2013 [20]; [c] Kammerer et al. 2014 [21].

When comparing effective prefactors for Al diffusion, Table III-11 shows the SLKMC values to be slightly higher than those obtained from the 8-frequency model [19]. In a recent work, Allnatt et al. show that to fully consider the anisotropy of a hexagonal close-packed lattice, 13 independent atom vacancy exchange frequencies are needed [22]. However, unlike the 8-frequency model, closed form expressions to calculate correlation factors do not exist for the 13-frequency model. On the other hand in KMC simulation, the anisotropy of a hexagonal close-packed lattice is naturally included.

When comparing the SLKMC values with the experimental results [20,21], Table III-11 shows a good agreement for the effective activation energy. The effective prefactor from SLKMC is of the same order of magnitude as obtained using the Boltzmann-Matano method in reference [21] and two orders of magnitude smaller than that obtained from the diffusion couple method in reference [20]. It should be noted that the standard deviation bar in the Boltzmann-Matano value is an order of magnitude greater than the value of the prefactor itself. Further, Brennan et al. [23] reported that prefactors obtained from diffusion couple experiments of Karmmerer et al. [21] tend to overestimate impurity diffusion coefficients. Therefore, there does not seem to be a consensus over the value of prefactor for Al diffusion in the Mg lattice. Irrespective, the accuracy of the effective activation energies and prefactors for Al-atom diffusion, obtained from KMC simulations, can be improved by using density functional theory calculated activation energies and prefactors for vacancy atom/solute exchange processes that were identified in the current SLKMC simulations.

Technology Transfer Path

ESI will use the results and knowledge developed in this work to identify modifications that may be necessary in their solidification modeling code, ProCAST, for predicting microstructures in die-cast Mg alloys. These validated and commercially available microstructural codes will allow automotive original equipment manufacturers to reduce time for casting trials and speed up implementation of Mg alloy castings in production vehicles.

Conclusion

Solidification of molten AZ91 was modeled as a function of cooling rates from 0.0001 to 1000°C/s. The results show that the solidification path and phase fractions exhibit minimal difference for cooling rates between 100 and 1000°C/s, thus a single set of thermophysical properties can be assumed in this range of cooling rates.

Solidification of molten AZ91 was modeled and the SDAS was predicted to be about 12 and 6 microns at cooling rates of 100 and 1000°C/s, respectively. These “uncalibrated” values are in good agreement with those published in the literature.

Binary Mg-9 wt% Al alloy thin films were heat treated at 150°C, 200°C, and 300°C for times between 5 and 190 minutes. The resulting grain growth of α-phase was analyzed using the equation proposed by Burke and Turnbull [18]. The activation energy for grain growth was calculated to be 31.1 ± 13.4 kJ/mol, which is lower than that reported for bulk Mg with micron-scale grains. The lower activation energy value in the present work is attributed to the strong effect of surface diffusion typically associated with the thin-film geometry.

The solute drag effect of Al solute atoms and the pinning effect of $Mg_{17}Al_{12}$ precipitates are believed to be responsible for the high value of the growth exponent 7 ±2. However, the β-$Mg_{17}Al_{12}$ phase was indistinguishable from the α-phase in the BF TEM images, owing to their similar morphology. The EELS technique was found suitable to distinguish the β-$Mg_{17}Al_{12}$ phase based on comparing the Al% within the β grain and the surrounding α grains.

Diffusion of an Al atom in the Mg matrix was modeled using an on-lattice SLKMC method. The diffusivity of an Al atom was found to be faster within the basal plane than out of the basal plane and is in agreement with the behavior reported in theoretical and experimental studies.

The effective activation energies for Al atom diffusion in Mg, obtained from SLKMC simulations, are in qualitative agreement with the published model and experimental values. The SLKMC calculated effective prefactors are slightly higher than those obtained from the 8-frequency model of Ganeshan et al. 2011 [19] but smaller than the experimentally determined values of Kammerer et al. and Das et al. 2013) [20,21]. However, there is significant scatter in experimentally determined prefactors and the reason for differences between the model and experimental values needs further investigation.

References

1. W. F. Powers, 2000, "Automotive Materials in the 21st Century," *Advanced Materials and Processes,* 157; pp. 38-41.
2. M. M. Avedesian and H. Baker, 1999, *ASM Speciality Handbook: Magnesium and Magnesium Alloys*. ASM International, New York; pp. 79.
3. X. J. Wang; S. M. Zhu; M. A. Easton; M. A. Gibson; and G. Savage, 2014, "Heat treatment of vacuum high pressure die cast magnesium alloy AZ91," *International Journal of Cast Metals Research,* 27; pp. 161-166.
4. E. Clouet and F. Soisson, 2010, "Atomic simulation of diffusional phase transformation," *C.R. Phys,*. 11; pp. 226.
5. F. Soisson; A. Barbu; and G. Martin, 1996, "Monte Carlo simulation of copper precipitation in dilute iron-copper alloys during thermal aging and under electron irradiation," *Acta. Mater.* 44; pp. 3789.
6. O. Trushin; A. Karim; A. Kara; and T. S. Rahman, 2005, "Self-learning kinetic Monte Carlo method: Application to Cu (111)," *Phys. Rev. B.,* 72; pp. 115401.
7. S. I. Shah; G. Nandipati; A. Kara; and T. S. Rahman, 2012, "Extended pattern recognition scheme for self-learning kinetic Monte Carlo simulations," *J. Phys: Condens. Mater.,* 24; pp. 354004.
8. G. Nandipati; S. I. Shah; A. Kara; and T. S. Rahman, 2012, "Off-lattice pattern recognition scheme for kinetic Monte Carlo simulation," *J. Comput. Phys.,* 231; pp. 3548.
9. A. Kara; O. Trushin; H. Yildirim; and T. S. Rahman, 2009, "Off-lattice self-learning kinetic Monte Carlo: Application to 2D cluster diffusion on the FCC (111) surface," *J. Phys: Condens. Mater.,* 21; pp. 084213.
10. G. Henkelman; B. P. Uberuaga; and H. Jonsson, 2000, "A climbing image nudged elastic band method for finding saddle points and minimum energy paths," *J. Chem. Phys.,* 113; pp. 9901.
11. P. Plimpton, 1995, "Fast Parallel Algorithms for Short-Range Molecular Dynamics," *J. Comput. Phys.,* 117; pp. 1.

12. Y.-M. Kim; N. J. Kim; and B.-J. Lee, 2009, "Atomistic modeling of pure Mg and Mg-Al systems," *Calphad,* 33; pp. 650.
13. C. H. Cáceres; C. J. Davidson; J. R. Griffiths; and C. L .Newton, 2002, "Effects of solidification rate and aging on the microstructure and mechanical properties of AZ91 alloy," *Materials Science & Engineering,* A325; pp. 344-355.
14. H. J. Frost and M. F. Ashby, 1983, "Deformation Mechanism Maps," Pergamon Press, Oxford; pp. 44.
15. J. J. Bhattacharyya; S. R. Agnew; and G. Muralidharan, 2015, "Texture enhancement during grain growth of magnesium alloy AZ31B," *Acta Materialia,* 86; pp. 80.
16. R. Dannenberg; E. Stach; J. R. Groza; and B. J. Dresser, 2000, "TEM annealing study of normal grain growth in silver thin films," *Thin Solid Films,* 379; pp. 133-138.
17. S. Simoes; R. Calinas; M. T. Vieira; M. F. Vieira; and P. J. Ferreira, 2010, "*In situ* TEM study of grain growth in nanocrystalline copper thin films," *Nanotechnology,* 21, pp. 145701.
18. J. E. Burke and D. Turnbull, 1952, "Recrystallization and grain growth," *Progress in Metal Physics,* 3; pp. 220-292.
19. S. Ganeshan; L. G. Hector Jr.; and Z. K. Liu, 2011, "First-principles calculation of impurity diffusion coefficients in dilute Mg alloys using the 8-frequency model," *Acta. Mater.,* 59; pp. 3214.
20. S. K. Das; Y. M. Kim; T. K. Ha; R. Gauvin; and I.-H. Jung, 2013, "Anisotropic Diffusion Behavior of Al in Mg: Diffusion Couple Study Using Mg Single Crystal," *Metall. and Mater. Trans. A,* 44; pp. 2593.
21. C. C. Kammerer; S. N. Kulkarni; R. J. Warmack; and Y. H. Sohn, 2014, "Interdiffusion and impurity diffusion in polycrystalline Mg solid solution with Al or Zn," *J. Alloys and Compound,* 617; pp. 968.
22. A. R. Allnatt; I. V. Belova; and G. E. Murch, 2014, "Diffusion kinetics in dilute binary alloys with the h.c.p. crystal structure," *Phil. Mag.,* 22; pp. 2487.
23. S. Brennan; A. P. Warren; K. R. Coffey; N. Kulkarni; P. Todd; M. Kilmove; and Y. H. Sohn, 2012, "Aluminum Impurity Diffusion in Magnesium," *J. Phase Equilib. Diffus.,* 33; pp. 121.

Bibliography

K. Kruska; A. Rohatgi; R. S. Vemuri; J. E. Evans; L. Kovarik; P. Abellan; L. R. Parent; B. L. Mehdi; and N. D. Browning, 2015, "Dynamical TEM investigation of solidification kinetics in an AZ91 Mg alloy," *ASCI Symposium*, Pullman, Wasington, May 20 through 22, 2015 (poster).

K. Kruska; A. Rohatgi; R. S. Vemuri; L. Kovarik; and N. D. Browning, 2015, "Microstructural Evolution in Mg-Al Thin Films during Early-Stage Heat-Treatment Inside the TEM," *Electron Microscopy for Biological, Environmental, and Energy Research 2015*, Richland, Washington, July 29 through 30, 2015 (poster).

K. Kruska; A. Rohatgi; R. S. Vemuri; L. Kovarik; T. H. Moser; J. E. Evans; and N. D. Browning, "Quantification and analysis of the early stages of grain-growth in nanocrystalline Mg-9 wt.% Al thin films during heat-treatment," journal manuscript in preparation.

K. Kruska; D. J. Edwards; R. S. Vemuri; L. Kovarik; A. Rohatgi; and N. D. Browning, 2015, "A Precession Electron Diffraction and EELS Study of Beta-phase Evolution in Nano-crystalline Mg-9 wt.% Al Thin Films during Heat Treatment," *Microscopy & Microanalysis 2015*, Portland, Oregon, August 2 through 6, 2015, (presentation).

G. Nandipati; N. Govind; A. Andersen; and A. Rohatgi, "Self-learning kinetic Monte Carlo Simulations of Al diffusion in pure Mg," *J. Phys: Condens. Mater*., under review.

G. Nandipati; N. Govind; A. Andersen; and A. Rohatgi, "Self-learning kinetic Monte Carlo Simulations of concentration dependent atomic diffusion in MgAl alloy," journal manuscript in preparation.

III.9. Corrosivity and Passivity of Metastable Magnesium Alloys—Oak Ridge National Laboratory

Project Details

Guang-Ling Song, Principal Investigator (report prepared by M. P. Brady)
Oak Ridge National Laboratory (ORNL)
1 Bethel Valley Road
Oak Ridge, TN 37831
Phone: 865-574-5153
E-mail: bradymp@ornl.gov

Aaron Yocum, Project Officer
National Energy Technology Laboratory
3610 Collins Ferry Road
Morgantown, WV 26507-0880
Phone: 304-285-4852
E-mail: aaron.yocum@netl.doe.gov

William Joost, Technology Area Development Manager
U.S. Department of Energy
1000 Independence Avenue, SW
Washington, DC 20585
Phone: 202-287-6020
E-mail: William.Joost@ee.doe.gov

Contractor: ORNL
Contract No.: 0793-1594

Executive Summary

The purpose of this project was to investigate the possibility of forming a passive film on magnesium (Mg) alloys through adding strong passivating elements in metastable Mg solid solution. The project manufactured and compared the behavior of ingot and magnetron-sputtered pure Mg relative to magnetron-sputtered magnesium-titanium (Mg-Ti) and magnesium-chromium (Mg-Cr) alloys. A transition to passive-like behavior was observed for both Mg-Ti and Mg-Cr; however, the transition only occurred if the level of Ti or Cr exceeded that of the Mg (in atomic percent).

Accomplishments

- A set of 24 sputtered Mg-Cr alloy library samples was successfully manufactured by project collaborator Montana State University (Fiscal Year [FY] 2015).
- Completed electrochemical evaluation and screening level characterization of the Mg-Cr library by x-ray photoelectron spectroscopy (XPS) and scanning electron microscopy (SEM)/energy-dispersive x-ray spectroscopy (EDS), which suggested a transition to passive behavior for Mg-Cr compositions with Cr greater than 50 at.% (FY 2015).
- Magnetron-sputtered pure Mg and a set of 24 magnetron-sputtered Mg-Ti alloy library samples were successfully manufactured by project collaborator Montana State University and evaluated by electrochemical methods to identify key composition regions of interest for potential passivity transition (FY 2014).

- Completed electrochemical evaluation, XPS, and SEM/transmission electron microscopy(TEM) characterization of select Mg-Ti alloys from the library study set, which indicated a transition to passive-like behavior for Mg-Ti compositions with Ti greater than 50 at.% (FY 2014).
- Investigated and characterized the anodic surface film formed on pure Mg ingot and sputtered pure Mg, which provided benchmarks for understanding the corrosion behavior of the metastable sputtered Mg alloys (FY 2014).

Future Directions

- Completed project in FY 2015. Wrap up of final project publications and presentations.

Technology Assessment

- Target: Gain an understanding of the effect of strong passivating alloying elements such as Ti and Cr in Mg solid solution on Mg passivity and corrosivity.
- Gap: There is very limited knowledge of producing and characterizing corrosion behavior of magnetron-sputtered Mg-X (X = Ti, Cr, etc.) alloys, which permit metastable solid solution extension well beyond equilibrium solution levels of additions. If Mg can become passive by alloying with these strong passivating elements, then insight into the development of corrosion-resistant Mg alloys or coatings can be gained from this knowledge.

Introduction

Significant efforts have been undertaken to understand corrosion behavior [1] and improve corrosion performance [2] of Mg alloys. The corrosivity of numerous Mg alloys has been investigated through casting, forming, and heat treating. However, virtually none of the previously studied alloying systems is adequately corrosion resistant for automotive applications [3,4], thus penetration of this market by lightweight Mg alloys has been limited [5].

Surface alloying offers a promising potential to dramatically enhance corrosion resistance without significantly altering a material's bulk properties and density. To create a corrosion-resistant surface layer, it is important to know which alloying elements can significantly improve Mg corrosion resistance.

It is well known that passivated metals have very low corrosion rates. An example is stainless steel, which is produced by the addition of Cr as a passivating element. It may be possible to obtain a corrosion-resistant Mg alloy through alloying with passivating elements such as Cr, Ti, Al, and Ni. The matrix phase, which is weakly corrosion resistant and preferentially attacked by corrosion, is a critical factor in Mg alloy corrosion. Passivating the matrix phase through alloying with a strong passivating element would be a significant step toward improvement in overall corrosion resistance of Mg alloys. Some existing research has indicated that amorphous Mg alloys containing Ni, yttrium, or neodymium show a distinct passive region when anodically polarized in a chloride-containing solution [6]. Passivation can significantly shift the corrosion potential in the noble direction and dramatically inhibit anodic dissolution. A passivated Mg alloy would have a low galvanic corrosion rate. Therefore, even if it were in contact with cathodic metals, the galvanic corrosion damage would not be significant. Mitigation of galvanic corrosion based on the natural passivation behavior of Mg alloys would be reliable because a naturally formed passive film could self-heal if damaged.

There is a lack of fundamental knowledge of surface films on Mg alloys. Corrosivity or passivity is closely associated with formation and dissolution of surface films on Mg alloys. However, the influence of the alloying elements on film composition and stability has not been systematically studied and the potential effects of substrate metallurgical defects on film properties and protectiveness have not been carefully addressed. This gap has been narrowed in this study.

Approach

The following steps were undertaken during this project.

1. Magnetron-sputtered pure Mg and Mg-X (X = Ti, Cr) alloys were successfully produced on inert quartz substrates by project partner Montana State University, with the resultant structures consistent with metastable single-phase alloys over broad Mg-X composition ranges.
2. Corrosion studies in solution [0.1 wt. % sodium chloride (NaCl) + saturated magnesium hydroxide ($Mg(OH_2)$, pH~11] and electrochemical techniques (including polarization curve and AC impedance measurements) were used to characterize the effect of X alloying on corrosivity and passivity.
3. Characterization techniques, including x-ray diffraction, SEM/TEM, and XPS, were used to assess the chemistry and structure of select initially sputtered Mg-X alloys and subsequent surface films formed on exposure to NaCl solutions.

Results and Discussion

Study findings under this program for pure Mg and sputtered Mg-Ti alloy corrosion behavior are reported in [7-9]. Select key findings from these publications are summarized in this report. Magnetron sputtering was used to manufacture a compositional library spread of Mg-X alloys (X = Ti, Cr) on inert quartz substrates for evaluation of corrosion behavior (Figure III-80). Based on corrosion studies of the sputtered Mg-Ti library in saturated $Mg(OH)_2$ + 0.1 wt % NaCl, select sputtered Mg-Ti compositions were manufactured and studied after electrochemical assessment and/or immersion exposures. XPS analysis indicated that the sputtered alloys also contained C and O in addition to Mg and Ti (i.e., about 5 to 10 at. % O + C total except for Ti-rich alloys, which XPS suggested contained up to about 15 to 20 at. % O and C) [9]. For a simplified nomenclature, only the Mg and Ti levels (in atomic percent) are used to identify the alloys. It should be noted that XPS analysis of a nominally pure Ti metal sheet suggested that argon-ion sputter profiling in XPS likely creates surface carbide and oxide as clean Ti getters some of the residual gas in the XPS analysis chamber, yielding estimates of about 10 to 20 at. % O + C in the Ti sheet metal. Therefore, XPS analysis may overestimate the amount of O and C impurities present in the sputtered Mg-Ti alloys, especially for Ti-rich compositions [9].

Figure III-81 shows electrochemical data for pure Mg ($Mg_{93}Ti_0$), Mg $_{68}Ti_{19}$, $Mg_{52}Ti_{38}$, and $Mg_{28}Ti_{51}$ [8, 9]. The sputtered $Mg_{93}Ti_0$ had an open circuit potential (OCP) further negative than −1.8 V and high anodic current densities. Addition of Ti into Mg positively shifted the OCP and reduced the anodic current densities. Best behavior was exhibited when the Ti level exceeded that of the Mg level, with more noble OCP and lowest anodic current densities for the $Mg_{28}Ti_{51}$ alloy.

Figure III-82 through Figure III-84 [8,9] show cross-section TEM and corresponding element maps of $Mg_{93}Ti_0$, $Mg_{68}Ti_{19}$, and $Mg_{52}Ti_{38}$ sputtered alloys after 5 hours of immersion at OCP in saturated $Mg(OH)_2$ + 0.1 wt % NaCl. The pure Mg alloy ($Mg_{93}Ti_0$) formed a thick, uniform, continuous magnesium oxide-rich layer (Figure III-82). Increase in Ti content to $Mg_{68}Ti_{19}$ (Figure III-83) resulted in a transition to non-uniform corrosion attack, with nodular-like magnesium oxide base penetration into the alloy. However, further increase in Ti level to $Mg_{52}Ti_{38}$ yielded reduced corrosive attack over much of the surface, with only a thin surface oxide region evident for the region imaged in TEM oxygen mapping. However, SEM analysis did indicate that the $Mg_{52}Ti_{38}$ alloy had regions of greater corrosion attack in addition to the thin protective oxide regions such as those imaged in TEM (Figure III-84). This finding suggests borderline protective behavior at this composition range. Only when the composition was increased to $Mg_{28}Ti_{51}$ was a thin protective surface formed over the entire sample under these exposure conditions. Analysis by XPS confirmed these trends and indicated a substantial presence of oxidized Ti in the surface film formed on $Mg_{28}Ti_{51}$ [8,9].

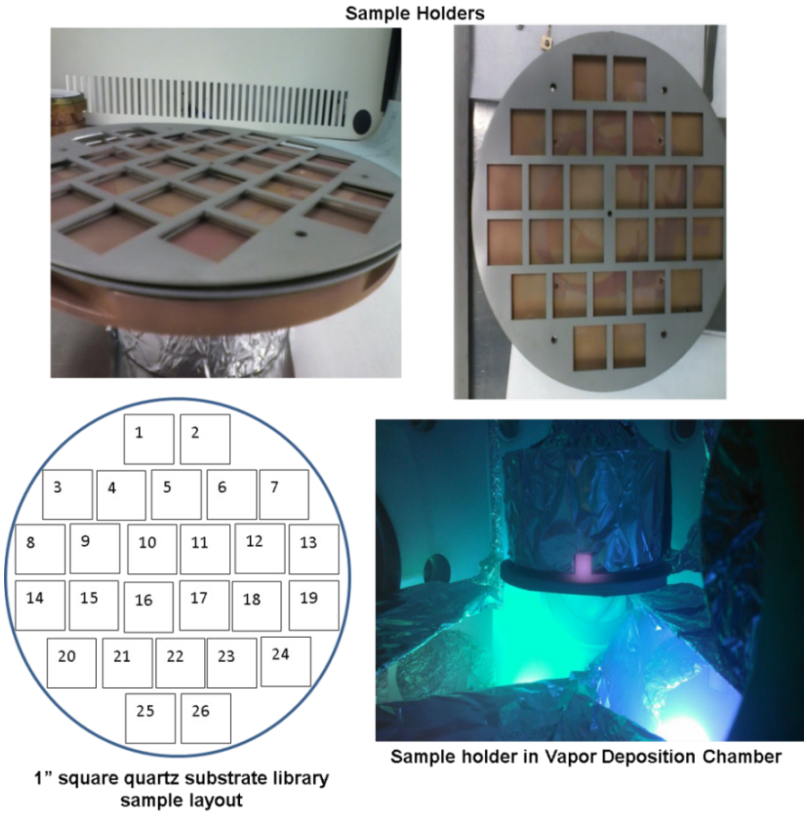

Figure III-80: Magnetron sputtering of Mg-X alloys sample holder and composition library arrangement (courtesy Montana State University). Shown specifically for the Mg-Ti set (Mg-Cr processed in a similar manner).

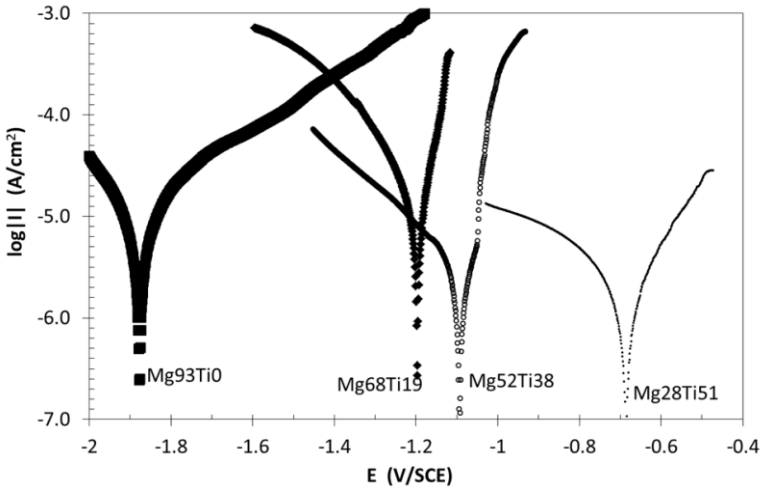

Figure III-81: Polarization curves for select magnetron-sputtered Mg-Ti alloys in saturated $Mg(OH)_2$ + 0.1 wt % NaCl solution [8, 9].

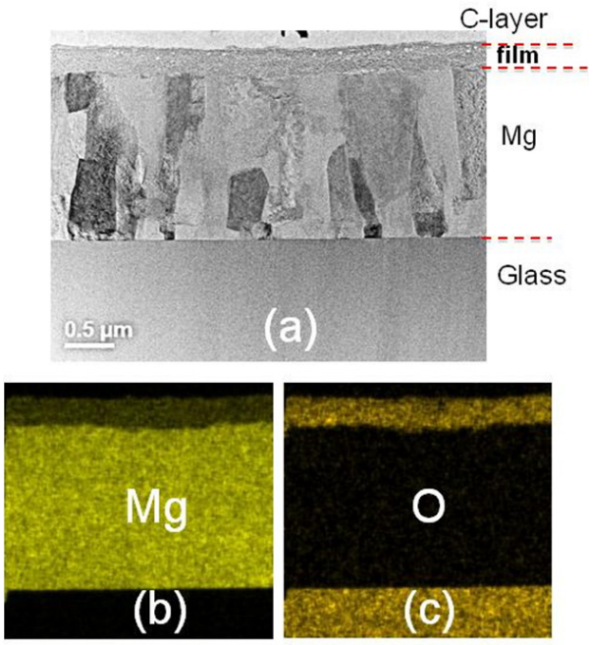

Figure III-82: Bright field scanning TEM image of the cross section for the magnetron-sputtered Mg-Ti alloy $Mg_{93}Ti_0$ after 5 hours of immersion in saturated $Mg(OH)_2$ + 0.1 wt % NaCl (a) and EDS elemental maps for Mg (b) and O (c) [8, 9].

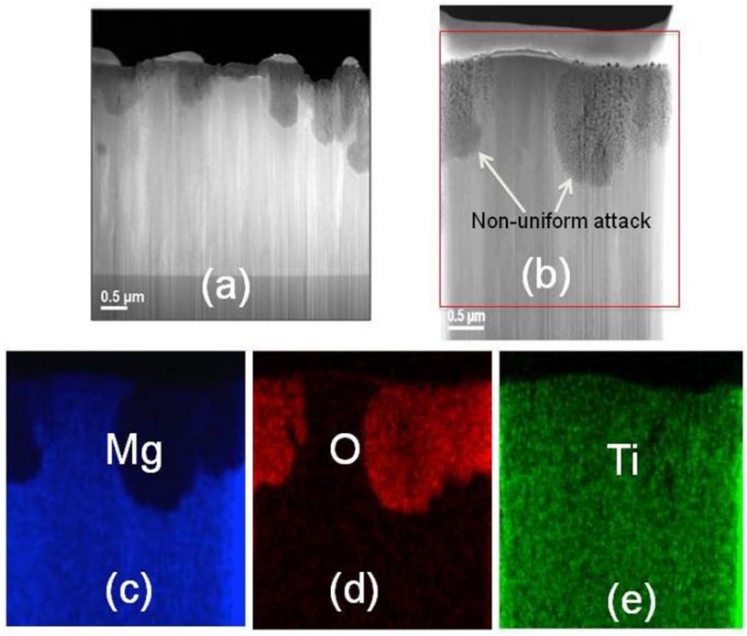

Figure III-83: Bright field scanning TEM images of the cross section for the magnetron-sputtered $Mg_{68}Ti_{19}$ alloy after 5 hours of immersion in saturated $Mg(OH)_2$ + 0.1 wt % NaCl [(a) and (b)] and EDS elemental maps for Mg (c), O (d), and Ti (e) [8, 9].

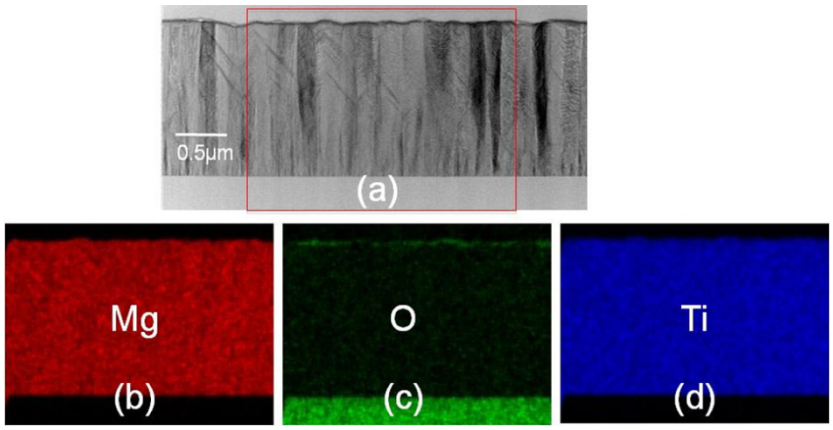

Figure III-84: Bright field scanning TEM image of the cross section of the magnetron-sputtered Mg-Ti alloy $Mg_{52}Ti_{38}$ after 5 hours of immersion in saturated $Mg(OH)_2$ + 0.1 wt % NaCl (a) and EDS elemental maps for Mg (b), O (c), and Ti (d) [8, 9].

Figure III-85 shows select electrochemical data for the magnetron-sputtered Mg-Cr compositional library sample set in saturated $Mg(OH)_2$ + 0.1 wt % NaCl. The Mg-Cr library samples contain a spread in composition over a given test sample. Estimates of Cr levels in atomic percent per library sample were made by EDS and XPS (estimate did not include O, C, and other impurities).

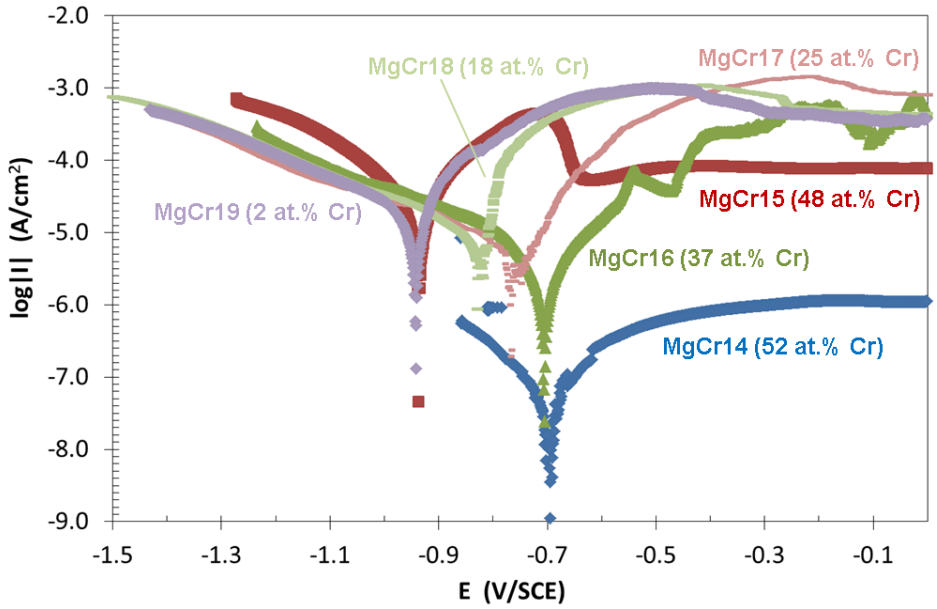

Figure III-85: Polarization curves for select magnetron-sputtered Mg-Cr composition library alloys in saturated $Mg(OH)_2$ + 0.1 wt % NaCl solution.

These composition levels at the library sample stage are considered semi-quantitative. The polarization curves (Figure III-85) of the sputtered Mg-Cr library composition alloys show that samples $MgCr_{14}$ (52 at. % Cr) and $MgCr_{15}$ (48 at. % Cr) have a clear passive region in the curve, with very low current densities exhibited by the Mg_{14} (52 at. % Cr) sample. In contrast, the $MgCr_{17}$ (25 at. % Cr) and $MgCr_{18}$ (18 at. % Cr) library alloys do not show such passive regions, rather they were actively dissolved in their anodic regions. The $MgCr_{16}$ (37 at. % Cr) appears to be in a composition transition region from active to passive, because there are several breakdown points on the anodic polarization curve. These trends were confirmed by 1-day immersion of select low and high Cr samples in saturated $Mg(OH)_2$ + 0.1 wt % NaCl.

Figure III-86 shows an overview plot of the key magnetron sputtered Mg-Cr library samples and select sputtered Mg-Ti alloys. For the evaluated conditions, the Mg-Cr alloys appear to have a more stable passivation region when the Cr content is in excess of the Mg content in the Mg-Cr system than do the Mg-Ti alloys when the Ti content is in excess of the Mg level in the Mg-Ti system.

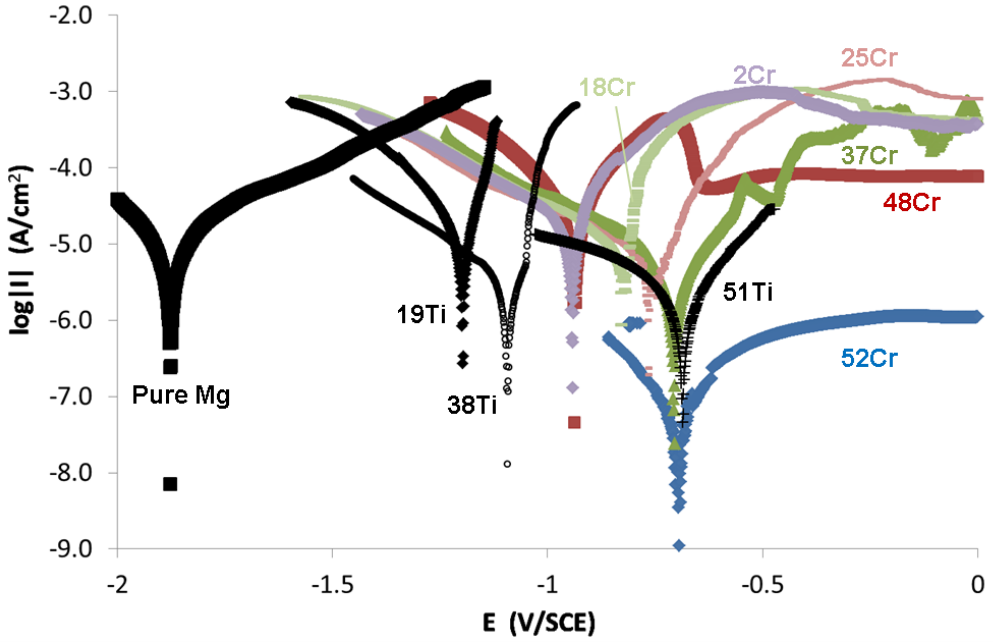

Figure III-86: Polarization curves for select magnetron-sputtered Mg-Cr composition library alloys (Figure III-85) and magnetron sputtered Mg-Ti alloys (Figure III-81) in saturated $Mg(OH)_2$ + 0.1 wt % NaCl solution.

Technology Transfer Path

The results and analyses in this project provide new primary insight into the effects of alloying on the potential for passivity in Mg alloys. Passive-like transitions were only observed at high levels of Ti or Cr, effectively shifting the alloy to Ti- or Cr-base. This is of limited utility for Mg alloy design, with the possible exception of new classes of complex, multi-element, high entropy alloys [10] for which such insights may prove beneficial. The findings may also provide guidance for coating approaches that enrich the local surface of an Mg alloy in Cr or Ti because both elements are commonly used in conversion coating strategies.

Conclusions

1. Magnetron sputtering can be used to produce metastable, single-phase solid solution Mg-X alloys (X = Ti, Cr) over a wide composition range, extending into the X-rich metastable solid solution composition range well in excess of the equilibrium phase stability regions.
2. Minor amounts of Ti or Cr in metastable Mg solid solution alloys cannot effectively inhibit the anodic dissolution of Mg.
3. Transition to passive-like behavior can be obtained with alloying of Ti or Cr to Mg, but only when the Ti/Cr level exceeds the Mg level (atomic percent). In general, the passivation effects of Cr additions appear to be more effective than Ti additions for yielding corrosion resistance in dilute salt solutions.

References

1. G.-L. Song, ed., 2011, *Corrosion of Magnesium Alloys,* Cambridge, UK: Woodhead Publishing.
2. G.-L. Song, ed., 2013, *Corrosion Prevention of Magnesium Alloys,* Cambridge, UK: Woodhead Publishing.
3. G. Song and A. Atrens, 1999, "Corrosion Mechanisms of Magnesium Alloys," *Adv. Eng. Mater.,* 1(1); pp. 11–33.
4. X. Gu; Y. Zheng; Y. Cheng; S. Zhong; and T. Xi, 2009, "In Vitro Corrosion and Biocompatibility of Binary Magnesium Alloys," *Biomaterials,* 30; pp. 484–498.
5. G.-L. Song, 2010, "Corrosion Behavior and Mitigation Strategy of Magnesium Alloys," H. Dong, ed., *Surface Engineering of Light Alloys: Aluminum, Magnesium and Titanium Alloys,* CRC Press/Woodhead Publishing; pp. 23-35.
6. H. Yao; Y. Li; and A. Wee, 2003, "Corrosion Behavior of Melt-Spun $Mg_{65}Ni_{20}Nd_{15}$ and $Mg_{65}Cu_{25}Y_{10}$ Metallic Glasses," *Electrochim. Acta,* 48; pp. 2641–2650.
7. G.-L. Song and K. A. Unocic, 2015, "The Anodic Surface Film and Hydrogen Evolution on Mg," *Corros. Sci.,* 98; pp. 758–765.
8. G.-L. Song, 2014, "Corrosivity and Passivity of Metastable Mg Alloys—Oak Ridge National Laboratory, Chapter III.22," *FY 2014 Annual Progress Report—Lightweight Materials R&D,* DOE/EE 1164, Washington, D.C., U.S. Department of Energy; pp. 136–144.
9. G.-L. Song; K. A. Unocic; H. M. Meyer III; E. Cakmak; M. P. Brady; P. E. Gannon; P. Himmer; and Q. Andrews, "The Corrosivity and Passivity of Sputtered Mg-Ti Alloys" (forthcoming).
10. I. Toda-Caraballo and P. E. J. Rivera-Diaz-del-Castillo, 2015, "Modelling and Design of Magnesium and High Entropy Alloys through Combining Statistical and Physical Models," *JOM,* 67(1); pp. 108–117.

Bibliography

G.-L. Song, 2014, "Corrosion and Protection of Mg Alloys," invited seminar, presented at the University of Brno, Czech Republic, April 12, 2014.

G.-L. Song, "The Surface Films and Their Possible Roles for Mg Corrosion," paper and presentation for *Magnesium Technology, 2016 TMS Annual Meeting and Exhibition,* February 14 through 18, 2016 (forthcoming).

G.-L. Song and K. A. Unocic, 2015, "The Anodic Surface Film and Hydrogen Evolution on Mg," *Corros. Sci.,* 98; pp. 758–765.

G.-L. Song; K. A. Unocic; H. M. Meyer III; E. Cakmak; M. P. Brady; P. E. Gannon; P. Himmer; and Q. Andrews, "The Corrosivity and Passivity of Sputtered Mg-Ti Alloys," *Corros. Sci.* (forthcoming).

III.10. Dealloying, Microstructure, and the Corrosion/Protection of Cast Magnesium Alloys – Arizona State University

Project Details

Karl Sieradzki, Principal Investigator
Ira A. Fulton School of Engineering
Arizona State University
501 E. Tyler Mall
P.O. Box 876106
Tempe, AZ 85287
Phone: 480-965-8990
E-mail: karl.sieradzki@asu.edu

Aaron Yocum, Project Officer
National Energy Technology Laboratory
3610 Collins Ferry Road
P.O. Box 880
Morgantown, WV 26507-0880
Phone: 304-285-4852
E-mail: Aaron.yocum@netl.doe.gov

William Joost, Technology Area Development Manager
U.S. Department of Energy
1000 Independence Avenue, SW
Washington, DC 20585
Phone: 202-287-6020
E-mail: william.joost@ee.doe.gov

Contractor: Arizona State University
Contract No.: DE-EE0006436

Executive Summary

The purpose of this project is to develop an understanding of micro-galvanic effects that control corrosion behavior in cast magnesium (Mg) alloys. Progress has been made on both the experimental and computational aspects of the project. The full immersion-free corrosion behavior of AZ91D, AZ31B, and AM60, as well as model single-phase magnesium-aluminum alloys (Mg-Al) and synthetic Mg-Al alloys, were characterized. Potentiostatic dissolution experiments were performed in an ionic liquid (iL) electrolyte for AZ91D and α-phase Mg in order to elucidate the anodic dissolution behaviors of these alloys. Rotation disk electrodes (RDE) were utilized in accelerated corrosion testing in aqueous chloride to evaluate the long-term Al redistribution behavior in AZ91D and α-phase Mg. These tests revealed that Al in solid solution redistributes in the form of platelets that can cover a large percent of the corroding surface. For each of these test protocols, both energy dispersive spectroscopy and lithium (Li) underpotential deposition (UPD) were used to assess the time-dependent surface concentration of Al. Atmospheric corrosion tests were performed in order to determine the time-dependent changes in contact angle and pH within a 5-microliter drop of the electrolyte. We observed large decreases in the contact angle with times over 20 hours, indicating that corrosion product layers enhance wetting of water on Mg alloy surfaces. Increases of electrolyte pH from 6 to 10 occurred within only a few seconds. This result has important implications for the kinetic Monte Carlo (KMC) simulations we are developing that are aimed at modeling corrosion behavior of Mg alloys, because we can consider that virtually the entire corrosion process occurs in an electrolyte with a pH range of 9 to 10. Inductively coupled plasma mass spectroscopy (ICP-MS) studies are underway to determine the kinetics of oxide dissolution and these results will be incorporated into the KMC simulations.

Accomplishments

- Further development of the Li UPD Al assay protocol using oriented Al single crystals for model development (Fiscal Year [FY] 2015).
- Characterized general corrosion behavior of commercial alloys AZ31B, AM60B, AZ91D, and individual samples of the common components found in commercial Mg-Al alloys, including solid-solution α-phase Mg-Al with various concentrations and $Mg_{17}Al_{12}$ β phase and manganese-aluminide compounds (FY 2015).
- Characterized the potentiostatic anodic dissolution behavior of AZ91D, AM60, AZ31B, α-phase Mg in choline-chloride:urea (CC-urea) (FY 2015).
- Accelerated corrosion tests in aqueous chloride were performed using RDE in order to access the diffusion boundary layer effects and long-term Al redistribution behavior for alloys AZ91D and α-phase Mg-Al containing 5 atomic percentage (at%) Al (FY 2015).
- Characterized aluminum redistribution behavior using scanning electron microscopy, energy dispersive spectroscopy (EDS) and Li UPD assays following RDE accelerated corrosion testing of alloy AZ91D and Mg containing 5 at% Al in solid solution (α-phase) (FY 2015).
- Atmospheric corrosion behaviors of Mg alloys were characterized for the time-dependent changes in contact angles and pH evolution within a 5-microliter drop of electrolyte (FY 2015).
- Compiled data using coupled ICP-MS to determine the kinetics of oxide dissolution for incorporation into the KMC simulations (FY 2015).
- A modified embedded atom method (MEAM) potential for the Mg-Al corrosion simulations was selected [1].

Future Directions

- Continue atmospheric corrosion testing with pH indicators to more thoroughly evaluate pH and wetting angle changes on phase evolution and Al redistribution of commercial Mg-Al alloys and α-phase Mg.
- Continue characterization of anodic dissolution behaviors of real Mg-Al alloys, model α-phase Mg, and synthetic alloys in CC-urea.
- Continue with ICP-MS analysis to determine the kinetics of MgO and Al_2O_3 chemical dissolution in aqueous chloride for incorporation into the KMC simulations.
- Perform KMC simulations incorporating embedded atom (EAM) potentials to ascertain the anodic dissolution behavior of Mg-Al alloys.
- Develop and test hydrophobic coatings using aprotic hydrophobic iLs.
- Develop and test stainless-like Mg alloys identified using KMC simulations.

Technology Assessment

- Target: Fabricate synthetic Mg-Al alloys based on the relative length scales of real alloys and validate their electrochemical behavior within 10% accuracy.
- Gap: Standard photolithographic techniques have not been designed for the Mg system, including interference from its native oxide.
- Target: Develop an Al assay protocol within 5% accuracy to ascertain the electrochemical surface area (ECSA) of Al on corroded Mg-Al alloys due to redistribution and enrichment.

- Gap: Conventional compositional techniques (such as EDS) probe not only the electrochemically active Al on the surface, but also a significant amount of bulk due to the large interaction volume of the electron beam.
- Gap: Limited experimental results exist on the crystallographic dependence of Li UPD shifts for Al.
- Target: Clarify the anodic dissolution behaviors of commercial Mg-Al alloys in terms of the time-dependent surface concentrations of the components in iLs containing less than 1 parts per million oxygen and 100 parts per million water.
- Gap: A limited selection of iLs exist that have a large enough electrochemical potential window to allow for anodic dissolution/deposition of Mg without simultaneous breakdown of the solvent.
- Gap: Anodic dissolution behaviors of components in Mg-Al alloys are not well known or understood due mainly to the competing cathodic process of water reduction.
- Target: Determine the effect of microstructural composition (i.e., 2 to 8 at% Al) and length scales (i.e., 1 to 100 microns [μm]) on the local time-dependent pH evolution under full immersion conditions in aqueous chloride.
- Gap: Standard glass electrodes have inadequate sensitivity over the relevant length scales in Mg-Al alloys.
- Gap: Conventional scanning electrochemical microscopy (SECM) may lack resolution to ascertain local pH changes over relevant length scales in most Mg-Al alloys due to dynamic surface topography during corrosion.
- Target: Determine the effect of microstructural composition (i.e., 2 to 8 at% Al) and length scales (i.e., 1 to 100 μm) on the local time-dependent pH evolution under atmospheric corrosion conditions.
- Gap: Conventional pH measurement techniques are not well suited for this because they affect wetting behavior.
- Target: Characterize (morphology) and measure (to within 5%) the time-dependent compositional changes occurring on corroding Mg-Al alloy surfaces using accelerated corrosion test techniques that simulate atmospheric corrosion processes.
- Gap: Typical atmospheric corrosion testing is performed over several years, which makes alloy evaluation of corrosion behavior a lengthy process.
- Target: Develop and validate KMC code that simulates time-dependent electrochemical dissolution behaviors, including pH-dependent chemical dissolution and Al redistribution during corrosion of Mg-Al solid solutions to within 10% accuracy compared to experimental results.
- Gap: Selection of the EAM potential must be chosen from existing potentials in the literature based on convenience of analytical forms and the speed at which they will allow the KMC simulations to run.
- Target: Develop hydrophobic coatings for corrosion protection of Mg-Al alloys.
- Gap: Coatings that provide passive blocking layers often lack self-healing capabilities and suffer from the potential of pinhole formation.

Introduction

The objective of this project is to develop an improved understanding of micro-galvanic corrosion behavior in advanced automotive cast Mg alloys. By expanding on scientific knowledge in the field of study, this project will help identify paths toward development of corrosion-resistant Mg alloys and coatings. Iterative experimental and computational efforts are being performed in order to elucidate the effects of composition

and phase distribution (e.g., the spatial length scales of β phase and α/β eutectic) on the corrosion behavior of cast Mg-Al alloys in aqueous environments and in iL,s where the absence of water and oxygen will prevent interference from corresponding reduction reactions.

Approach

This project utilizes three general approaches for the study of Mg-Al corrosion behavior: (1) artificial/synthetic and model Mg alloys, (2) iL electrolytes, and (3) KMC simulations, which model the time-dependent effects and spatial redistribution of alloying elements during corrosion. During this first FY of the project (i.e., FY 2014), major headway was made with the first two approaches, including synthesis and testing of synthetic alloys using photolithography and initial corrosion studies in non-aqueous iL electrolytes. In addition, a new Li UPD protocol was developed for assaying the electrochemical surface area of Al that evolves on corroding Mg alloy surfaces. During the second year of this program (FY 2015), we have continued to make advances in our understanding of alterations in surface composition occurring during corrosion of these alloys and elucidating anodic dissolution behaviors of alloy components in iL electrolytes. Our advances in understanding the surface compositional changes that can occur in aqueous chloride stems from our use of a RDE, which serves to alter the thickness of the diffusion boundary layer, thus accelerating corrosion processes. Additionally, we have studied various aspects of atmospheric corrosion, including time-dependent contact angles/wetting and pH evolution within a 5-microliter drop of the electrolyte. In order to develop kinetic data that will serve as input to our KMC simulations, we have been using ICP-MS to measure the kinetics of chemical dissolution of $MgO/Mg(OH)_2$ and Al_2O_3.

Results and Discussion

As a general characterization of the corrosion behavior of Mg-Al alloys, the corrosion potential of nine systems in aqueous chloride was monitored for 20 hours. These systems include commercial alloys (i.e., AZ91D, AZ31B, and AM60); component phases (i.e., α-Mg and β-Mg); and elemental Mg, Al, and two synthetic alloys. The "microstructure" of the synthetic alloy surfaces is composed of 7.3-μm diameter Al discs, 100- nm in thickness, located on the corners and edges of a square 50-μm two-dimensional lattice occupying 5% of the surface area. This pattern is deposited onto 99.95% Mg (referred to herein as the *primary synthetic alloy*) and a α-Mg-5 at%Al solid-solution alloy (referred to herein as *synthetic AZ91D*). Because of the sensitivity of the sample surface, no sample preparation was performed on the sample surface prior to corrosion. Other than synthetic alloys, samples were prepared by sanding the surface to U.S. 1200 grit/European grade P4000, followed by a methanol rinse and drying in a nitrogen gas flow. In conjunction with potential monitoring, linear sweep voltammetry was used to define cathodic and anodic behaviors in this electrolyte. Figure III-87 shows results for samples immediately following immersion in the electrolyte and 20 hours after immersion. Polarization data (versus silver ion/silver chloride [$Ag^+/AgCl$] reference electrode) are given for (a) commercial alloys, (b) component phases, and (c) synthetic alloys over 20-hours in 3.5% NaCl. Solid lines indicate data obtained within the first minute of immersion; dotted lines indicate data obtained after 20 hours of immersion.

Significant positive shifts in corrosion potentials, E_{corr}, were observed for all systems except the α-phase Mg-5 at% Al alloy and AM60. The greatest shift is seen within the first hour, after which the potential achieves quasi-steady-state behavior. The linear sweep voltammetry data are summarized in Table III-12. The increased corrosion potentials are indicative of an increase in cathodic dissolution current that arises from increases in both the surface area of cathodes and likely accumulation of noble-metal clusters on the surface that serve to activate water reduction.

The changes in corrosion potential observed over 20 hours result from changes in the surface composition of the alloys. Examination of the cathodic branches of the 1-minute (immediately following immersion) polarization curves of the commercial alloys shows inflection branches indicative of localized corrosion pitting. Following 20 hours of immersion, similar features were observed for AZ31B and AZ91D; notably, pitting is absent in AM60.

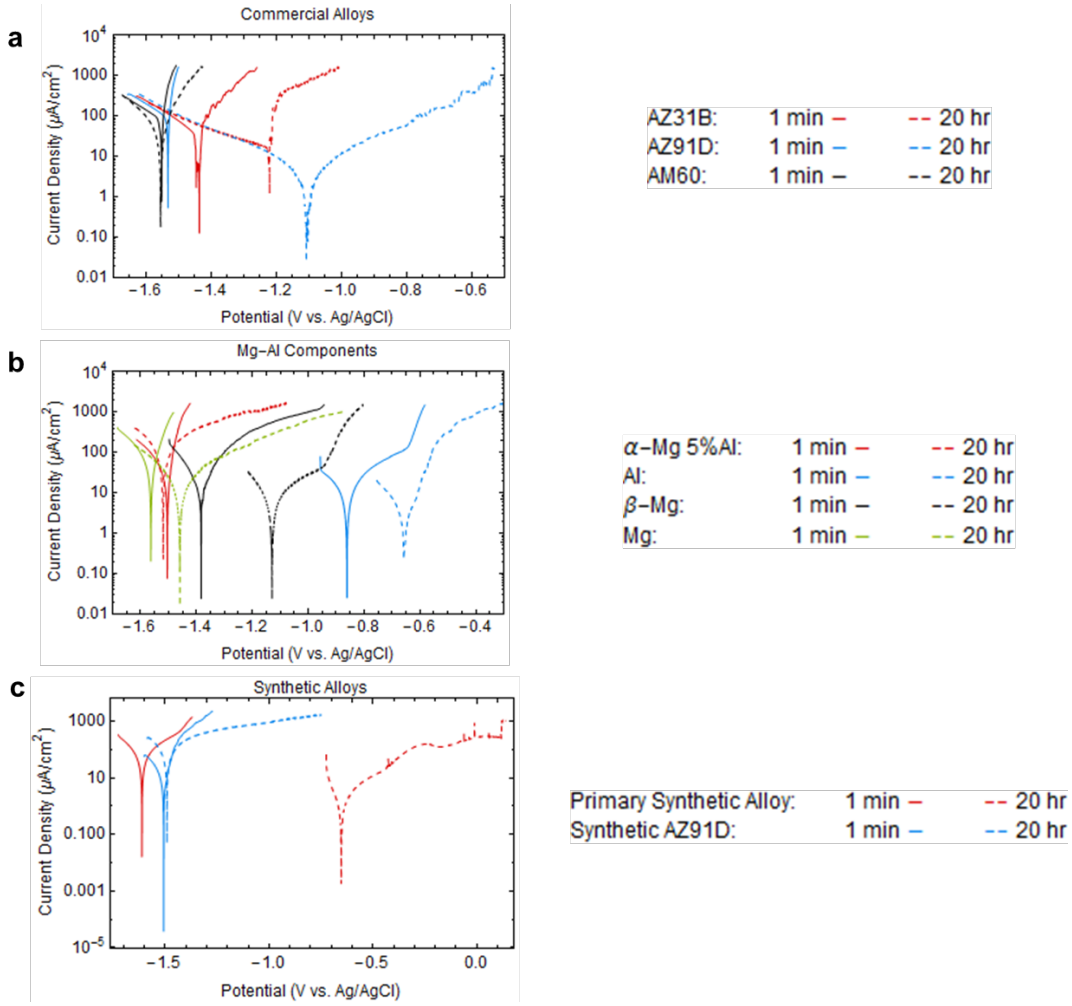

Figure III-87: Polarization data (versus Ag^+/AgCl reference electrode) for (a) commercial alloys, (b) component phases, and (c) synthetic alloys over 20 hours in 3.5% NaCl. Solid lines indicate data obtained within the first minute of immersion; dotted lines indicate data obtained after 20 hours of immersion.

Table III-12: Summary of general corrosion data, showing the shift in corrosion potential (ΔV).

Corrosion Potential, V versus Ag/AgCl; 3.5% NaCl			
Sample	**1 minute**	**20 hours**	**ΔV**
AZ31B	-1.44	-1.22	0.215
AZ91D	-1.53	-1.11	0.425
AM60	-1.55	-1.56	-0.004
Mg-5at%Al	-1.50	-1.52	-0.015
Al	-0.86	-0.66	0.205
βMg	-1.38	-1.13	0.254
Mg	-1.56	-1.46	0.104
Primary Synthetic Alloy	-1.61	-0.65	0.959
Synthetic AZ91D	-1.51	-1.49	-0.016

The large positive shift in E_{corr} for AZ91D is accompanied by a significant decrease in the corrosion current density, i_{corr}, from about 20 microamp per square centimeter ($\mu A/cm^2$), immediately following immersion to about 5 $\mu A/cm^2$ after 20 hours. While a similar positive shift occurred for AZ31B, this was accompanied by a doubling of i_{corr} to about 10 $\mu A/cm^2$. There is nothing remarkable in the polarization behavior of the component phases, except for the anodic branch of the β-phase. While there is a 0.5-volt (V) difference in E_{corr} between this phase and elemental Al, the shapes of the polarization curves are remarkably similar. The anodic branches of these curves display an inflection that corresponds to pitting in elemental Al and pitting and dealloying of Al from the $Mg_{17}Al_{12}$ β-phase.

Accelerated free corrosion testing in aqueous 3.5% NaCl was conducted on α-phase Mg containing 5 at% Al in solid solution and AZ91D using RDEs. Samples were prepared by sanding down to 1200 grit/p4000, followed by a methanol rinse and drying under nitrogen gas flow. A thin layer of Parafilm was wrapped around the side of the sample to prevent leakage within the sample holder and to maintain the laminar flow created by sample rotation. Following experiment completion, samples were rinsed with water and dried using a nitrogen gas stream. Tests were conducted for varying free-corrosion times and rotation speeds of 0 revolutions per minute (rpm) and 1,600 rpm, for which the diffusion layer boundary thicknesses are about 100 µm and 12 µm, respectively. Figure III-88 shows scanning electron microscope (SEM) images for the results of morphology and composition evolution obtained for α-Mg 5 at%Al.

The evolution of platelets was observed over 20 hours of free corrosion at 1,600 rpm that cover a large percent of the electrode surface area. The average composition of platelets is about 6.5 at% Al; however, the platelets were likely thin enough. Therefore, EDS is underestimating this owing to the influence of the Mg-rich substrate. We are in the process of using Li UPD to assess the electrochemically active surface area of Al. Samples displaying this platelet morphology were further characterized by measuring anodic polarization curves in 3.5% NaCl. This was followed by a free corrosion treatment for 20 hours at 0 rpm, measurement of subsequent corrosion behavior, and SEM examination. Figure III-89a shows the anodic behavior of these samples initiates at about 0.2 V (versus Ag/AgCl) and displays a dissolution wave at about +0.10 V. The voltage at which dissolution behavior initiates is about 1 V more positive than that observed for the behavior of any real alloys following 20 hours of corrosion (Figure III-87). After 20 hours of free corrosion, E_{corr} decreases to about -0.45 V. Figure III-89b shows an image (compare to Figure III-88d) of the sample surface following the 20-hour, 0-rpm free corrosion treatment. We observed a significant decrease in the EDS-determined Al surface concentration from 6.5 to 0.16%.

AZ91D samples treated at 1,600 rpm also showed significant increases in the Al surface over 20 hours. Figure III-90 provides SEM results showing pitting attack (Figure III-90b), substrate cracking (Figure III-90c), and significant pit development that evolved into general corrosion attack (Figure III-90d), with corrosion debris and evolution of Al nanowires within the debris. Crack formation within the substrate was apparent after 1 hour at submicron-length scales. After 4 hours, these cracks ranged in size from submicron to tens of microns. We suggest that the likely cause of cracking is the large difference in molar volume between Mg and MgO, resulting in a Pilling-Bedworth ratio of 0.8. Thus, the oxide is in tension causing crack formation as the oxide thickens. The Al nanowires that can be seen in Figure III-90f are similar in nature to those formed by anodic dissolution in α-Mg in the CC-urea iL that we reported on in the FY 2014 annual report and as described below similar to that found for AZ31B, AZ91D, and AM 60 (see Figure III-95).

AZ91D samples treated at 1,600 rpm also showed significant increases in the Al surface over 20 hours. Figure III-91 shows Li UPD assays for the Al surface coverage for varying treatment times. The observed enrichment in Al is consistent with the images shown in Figure III-90f, as well as a positive shift in the corrosion potential and a reduced value of the corrosion current density. Over 20 hours, the Al surface concentration increases from 0.5 to 2.5%.

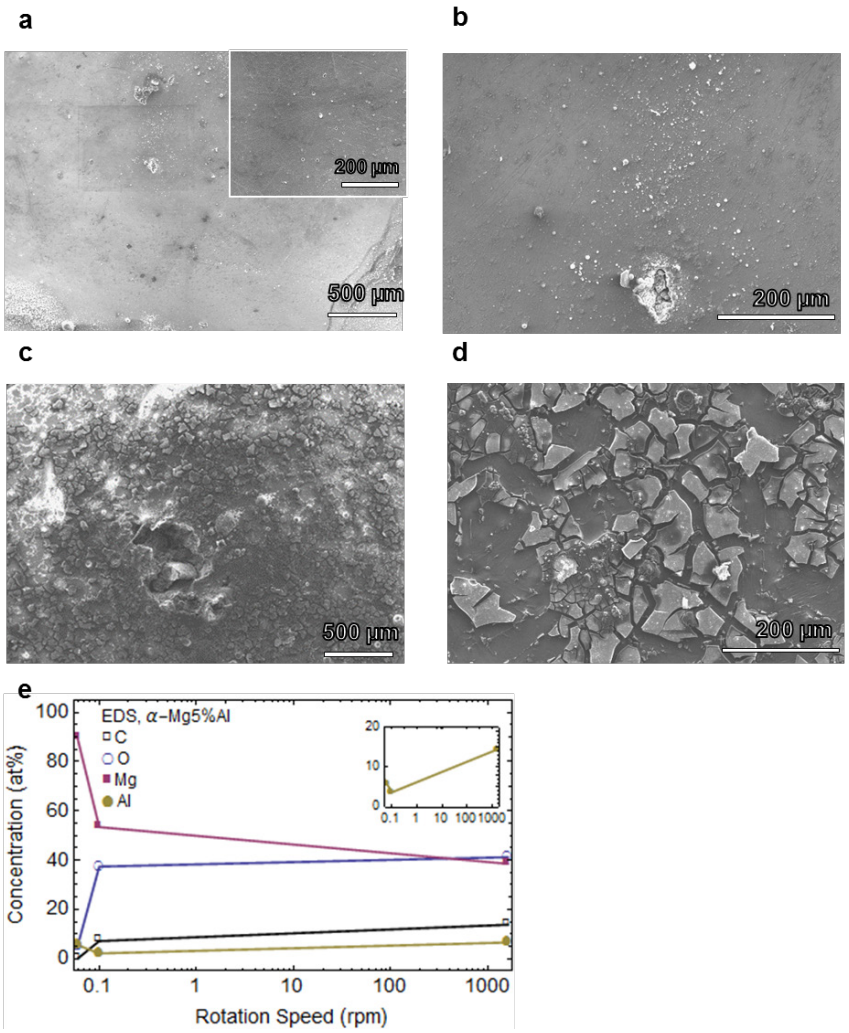

Figure III-88: SEM images of α-Mg 5 at%Al after 20 hours of free-corrosion in aqueous chloride. Low magnification images of the surface at (a) 0 rpm and (b) 1,600 rpm. The inset of (a) shows the uncorroded surface. Higher magnification images of the surface at (c) 0 rpm and (d) 1,600 rpm with the average Al content obtained by EDS are indicated in the images. (e) shows compositional data from EDS. The inset of (e) shows the Al concentration normalized to Mg + Al.

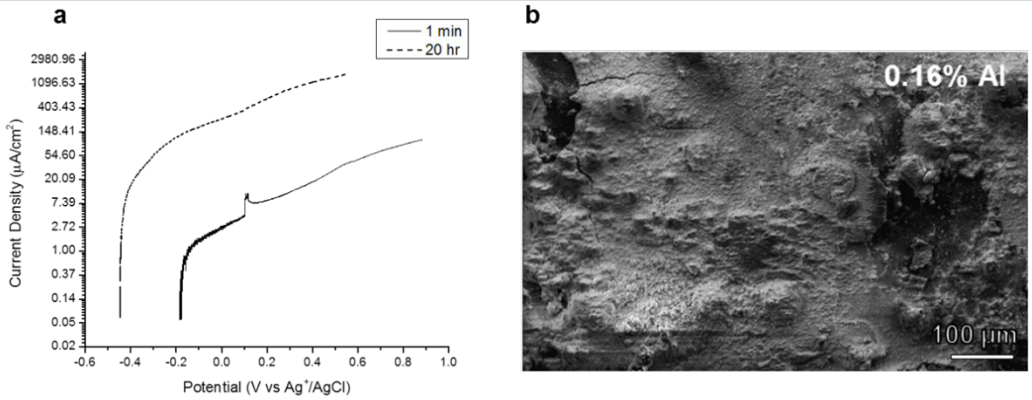

Figure III-89: (a) Anodic polarization behavior of the sample shown in Figure III-88d and following 20 hours of free-corrosion in 3.5% NaCl at 0 rpm. (b) Image of sample following the 20-hour corrosion treatment. Compare this image to that in Figure III-88d. Currently, we are investigating the origin of the +0.1-V stripping wave and expect to report a detailed analysis of this in the near future.

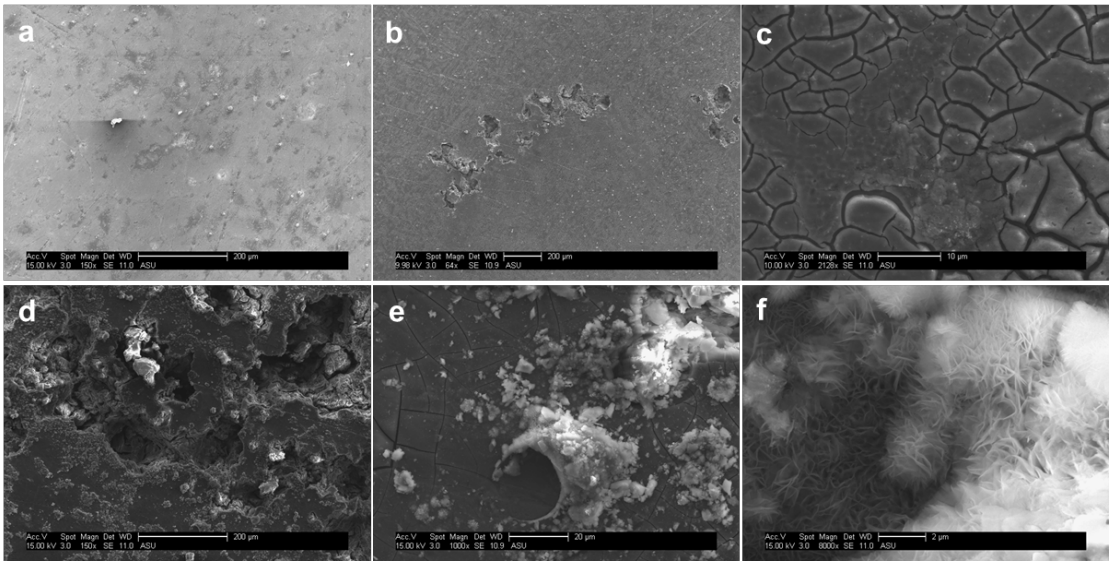

Figure III-90: Scanning electron micrographs showing the morphology evolution following free-corrosion of AZ91D RDE samples at 1,600 rpm in 3.5% NaCl (a) 1 minute, (b) 5 minutes, (c) 1 hour, (d) 4 hours, (e) 8 hours, and (f) 20 hours at an increasing level of magnification.

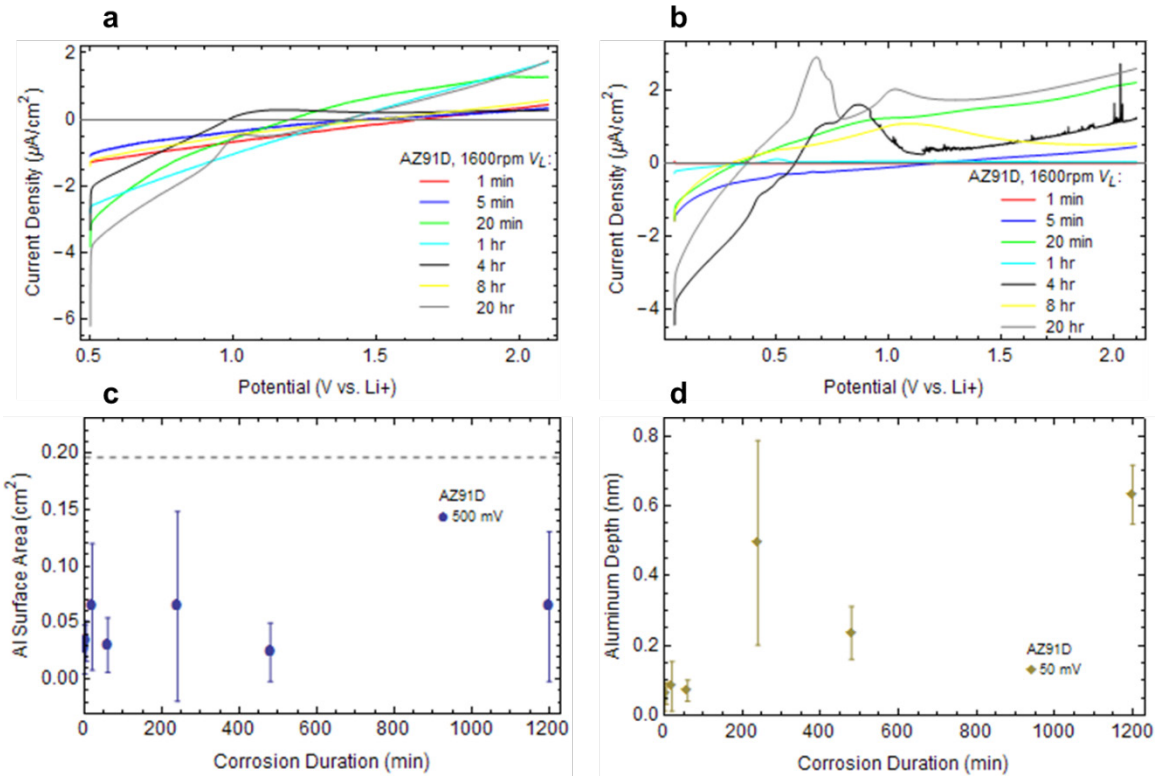

Figure III-91: Li UPD assay for Al following RDE free-corrosion of AZ91D at 1,600 rpm in 3.5% NaCl. Li UPD anodic stripping curves at lower potential limits (a) 500 millivolts (mV) and (b) 50 mV. Li stripping charge densities converted to (c) surface area and (d) depth of Al coverage. The dashed line in Figure III-91c indicates the Al assay measured using the calibration sample. The error bars correspond to the standard deviation found for five sample assays.

The anodic polarization behavior of the commercial alloys (AZ91D, AM60, and AZ31B) and the component phases (Mg, Al, and α-Mg 5%Al) in CC-urea at 150°C is shown in Figure III-92. Samples were prepared by sanding up to a 1200 grit/p4000, followed by methanol rinse and drying under nitrogen gas flow. The samples

were then placed in an argon glove box. To minimize the oxide layer thickness, a brief 600-grit sanding was performed. For all samples, a sequential series of five anodic sweeps from a lower potential limit of -600 mV to an upper potential limit of +600 mV versus Al was performed.

Figure III-92f shows that Al does not dissolve in CC-urea within this potential range, while Figure III-92e shows that Mg is highly reactive. Interestingly, AZ91D and AZ31B activate at about -0.6 V versus Al and show higher values of current density then elemental Mg. We attribute this behavior to the comparatively high concentration of zinc in these alloys. Figure III-92d shows that the α-Mg-5%Al alloy does not show significant dissolution until about -300 mV, which is significantly higher in potential than observed in the commercial alloys containing relatively high concentrations of zinc. The AM60 alloy shows almost an order of magnitude lower current density within the range of potential explored.

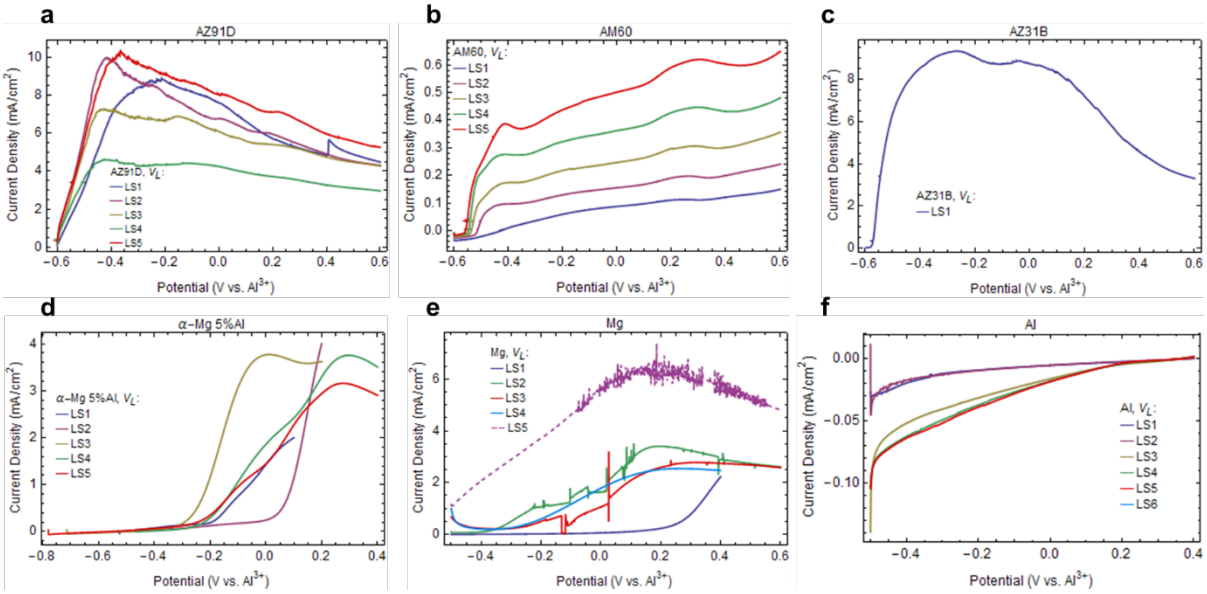

Figure III-92: Anodic dissolution polarization behavior of commercial alloys and component phases in CC-urea at 150°C (a) AZ91D, (b) AM60, (c) AZ31B, (d) a-Mg 5at%Al, (e) elemental Mg and (f) elemental Al.

The surface composition evolution in CC-urea at 150°C was examined with Li UPD at a fixed dissolution potential of -220 mV versus Al for both the commercial alloys and component phases. Samples were sanded down to a 1200 grit/p4000, followed by methanol rinse and drying via nitrogen gas flow, and placed in an argon glove box. Additional sanding (i.e., 600 grit) was used in the argon environment to minimize the oxide layer thickness. Samples then underwent a 1-M propylene carbonate rinse at 150°C to remove electrolyte from the corroded surface and were placed in a 1-M $LiClO_4$ in PC cell for the Li UPD Al assay. Representative results of Li stripping waves for α-Mg 5%Al and AZ91D are shown in Figure III-93; Figure III-94 summarizes the results for the commercial alloys and component phases.

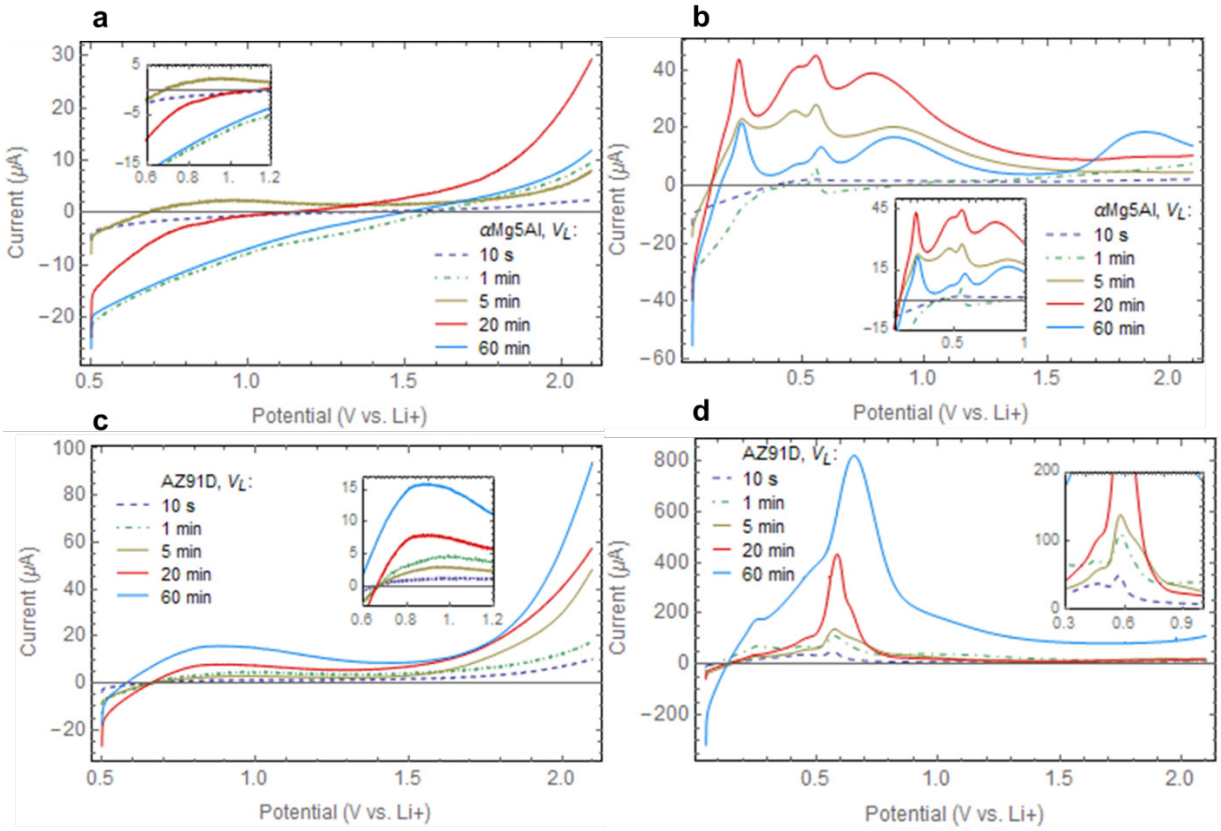

Figure III-93: Li UPD stripping curves following potentiostatic dissolution in CC-urea at -220 mV versus Al for the indicated times (see legend): (a, b) α-Mg 5%Al and (c,d) AZ91D. Anodic stripping curves were obtained at 5 mV/s in 1.0 M $LiClO_4$ in propylene carbonate following a 600-second hold for lower potential limits: (a,c) 500 mV and (b,d) 50 mV.

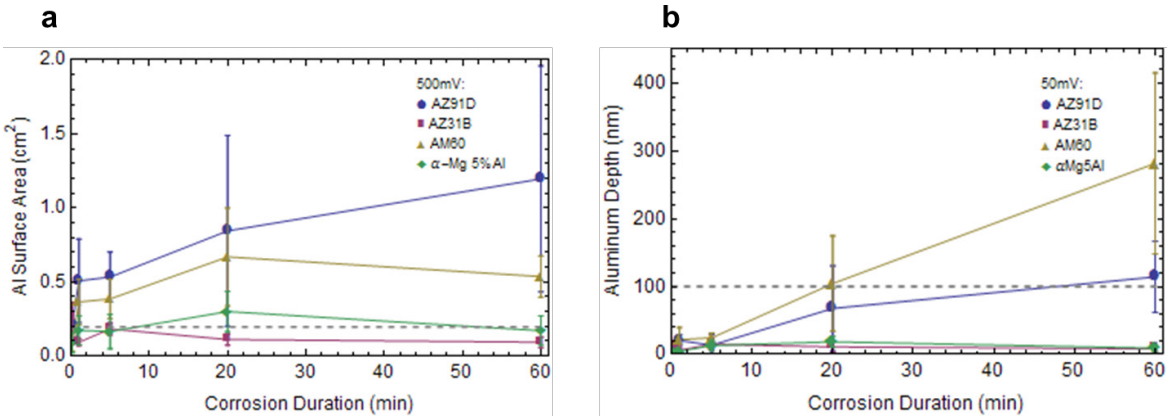

Figure III-944: (a) Equivalent Al surface area and (b) estimated depth for commercial alloys and component phases versus dissolution time in CC-urea at 150°C. Anodic charge density calculated from Li UPD stripping waves for the indicated lower potential limits (see legend). The grey dashed lines indicate the equivalent signal of a planar Al film of 100-nm in thickness. The error bars correspond to the standard deviation for five sample assays.

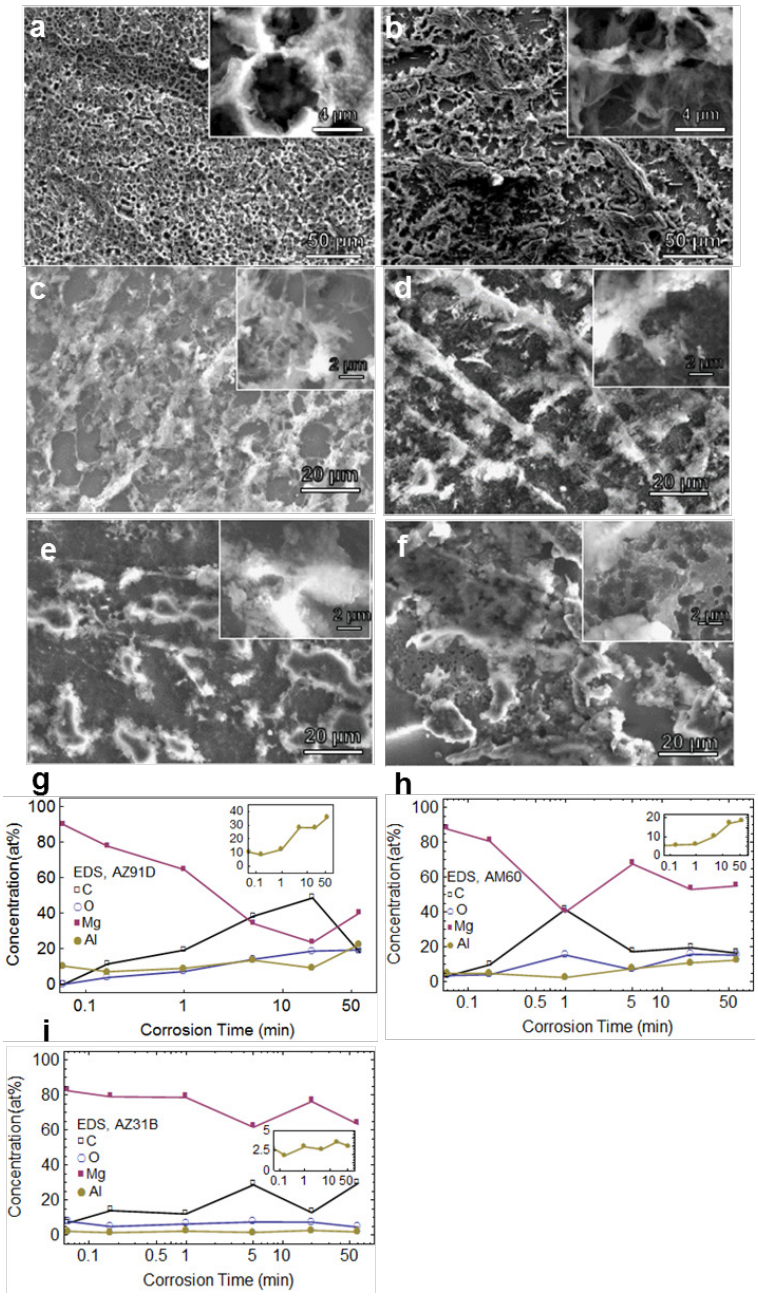

Figure III-95: SEM images of commercial alloy surface morphologies following potentiostatic dissolution in CC-urea for the indicated times at -220 mV versus AL wire. Top panel: AZ91D for (a) 20 minutes, (b) 60 minutes; middle panel: AM60, (c) 20 minutes, (d) 60 minutes; bottom panel AZ31B, (e) 20 minutes, (f) 60 minutes. The corresponding insets show higher magnification images. Plots (g), (h), and (i) are the corresponding EDS compositional data. These insets show the Al concentration normalized to Al+Mg.

The increased surface area of Al that evolved upon anodic dissolution of the alloys in the CC-urea iL can be understood by examining the corresponding morphologies. All experiments were performed in an argon glove box. Samples were prepared by sanding the surface down to a 1200 grit/p4000, followed by a methanol rinse and drying under nitrogen gas flow. Once samples were within the argon gas environment, additional sanding (i.e., 600 grit) was performed to minimize the thickness of the air-formed oxide. A potential of -220 mV (versus an Al wire quasi-reference electrode) was applied for times, ranging from 1 to 60 minutes. Following dissolution treatments, the electrolyte was rinsed from the surface in 1-M propylene carbonate at 150°C. SEM

micrographs and EDS composition analysis for the as-treated commercial alloys are shown in Figure III-95. As previously observed for the single-phase α-Mg 5at%Al alloy, development of highly porous surface morphologies becomes readily apparent for AZ91D and AZ31B following dissolution for 20 minutes or longer. This includes development of Al nanowire-like structures within surface ridges.

Both the micrographs and EDS results lend qualitative support to the Li UPD assays (Figure III-93 and Figure III-94) and the potentiostatic dissolution data. AM60 shows only about 2.5% surface coverage of Al following 60 minutes of dissolution in the iL, while AZ91D and AZ31B show 40% and 20%, respectively. This should be interpreted as an *equivalent* surface coverage as these high values result from high surface area Al-rich nanostructures that evolve on these corroding surfaces.

To begin characterization of atmospheric corrosion behavior of Mg-Al alloys, contact angle measurements for commercial alloys (i.e., AZ91D, AZ31B, and AM60) and component systems (i.e., Al, Mg, and α-Mg 5%Al) were performed as a function of free-corrosion duration. Samples were prepared by sanding down to 1200 grit/p4000, followed by a methanol rinse and drying via nitrogen gas flow. Parafilm was used to secure five samples to the bottom of a plastic sample dish containing five holes of 0.397-cm diameter that provided an exposed surface area of 0.124 cm^2. Samples underwent free corrosion in 30 mL of 3.5% NaCl for variable durations (i.e., 5 minutes, 20 minutes, 1 hour, 4 hours, and 20 hours). Following completion, samples were dried under nitrogen gas flow and allowed to dehydrate in a desiccator overnight. A Nikon D3200 camera with lens extension tube set was used to image a 5-µL drop of 3.5% NaCl on the sample surface. Image J software was then used to measure the contact angle.

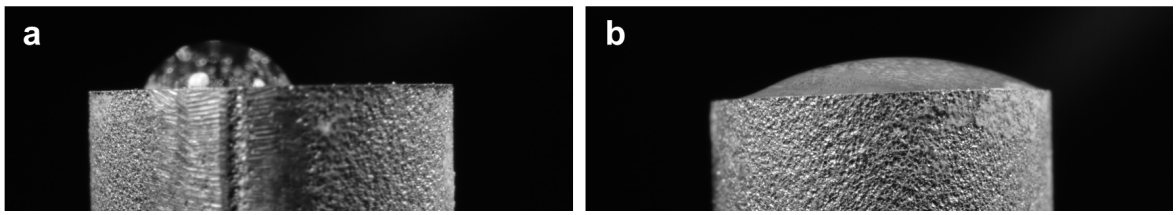

Figure III-96: Contact angle images of 3.5% NaCl on AZ91D (a) uncorroded and (b) following 20 houra of aqueous corrosion in 3.5% NaCl.

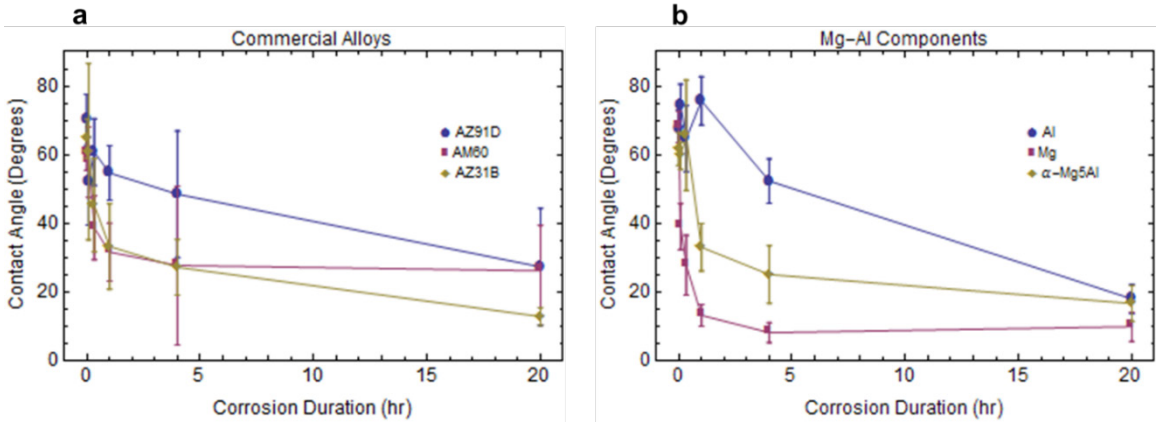

Figure III-97: Time-dependent contact angle of a 5 µL of 3.5% NaCl on the indicated sample surfaces (a) commercial alloys and (b) component phases.

Figure III-96 shows representative images for wetting of uncorroded AZ91D and following 20 hours of free corrosion. One can qualitatively observe the decrease in contact angle. Figure III-97 shows the exponential-like decrease in wetting angle with increasing corrosion time for the commercial alloys and component phases. These results are summarized in Table III-13. Interestingly, all alloys and component phases show a significant decrease in the contact angle with corrosion time. These results will aid in coating evaluation, because contact angle is one parameter that should enter into coating design. Ideally, one would

like to design a coating that displays large contact angles (greater than 90 degrees) to minimize wetting in atmospheric corrosion. Figure III-97 shows the exponential decrease in wetting angle with increasing corrosion time for commercial alloys and component phases.

Table III-13: Summary of time-dependent change in contact angle as a function of free-corrosion time in aqueous chloride for commercial alloys and component phases.

Average Contact Angle (degrees)						
Sample	**Uncorroded**	**5 minutes**	**2 minutes**	**1 hour**	**4 hours**	**20 hours**
Al	68	74	65	76	52	18
Mg	68	39	28	13	8	10
αMg-5at%Al	62	60	66	33	25	17
AM60	60	58	39	32	28	26
AZ31B	65	61	45	33	27	13
AZ91D	70	52	61	55	48	27

Atmospheric corrosion studies are best performed in the field with test samples exposed over several years. We cannot hope to repeat such measurements in the laboratory over significantly shorter periods of time. Importantly, many such studies already exist in relevant literature, including a recent manuscript [2]. They report field test results over a 3-year time period performed in urban and marine environments for 10 Mg alloys that included AZ91D, AM60, and AZ31B. They observed many of the morphology features, including pitting and cracking, that we observed in our accelerated corrosion testing using RDEs. The main conclusions from their study were as follows:

- Of the 10 Mg alloys examined, AZ91D showed the best corrosion resistance in marine and urban environments.
- The higher the Al content within grains (i.e., solid solution Al), the higher the corrosion resistance.
- Generally, atmospheric corrosion rates increased with exposure time over the three 3 years of the study. This behavior was attributed to the increasing number of cracks within the corrosion product layer.

We find it a bit concerning that for all alloys examined, atmospheric corrosion rates increased with exposure time. However, this result would seem to support our rather aggressive approach to accelerated corrosion testing, which employs RDEs.

As another part of our atmospheric corrosion studies, we studied the time-dependence of pH evolution within a drop of aqueous electrolyte on the surface of Mg-Al alloys. To preserve the integrity of the interactions and wetting between the droplet and bulk surface, dye indicators were used to monitor the pH. Four different dye indicators were chosen for this experiment: Bromocresol Purple, Phenol Red, Phenolphthalein, and Alizarine Yellow R. The properties of these are summarized in Table III-14 below. Controls were developed by adding a dye indicator to a suitable buffer solution in 0.5-pH increments, beginning below the activation pH range and ending above the activation pH range. Images were then taken of each control on the surface of the sanded (4000 p) AZ91D using a Nikon D3200 camera with the lens extension tube set (Figure III-98).

Table III-14: Summary of pH indication behaviors and color shifts.

Dye Indicator	pH Range of Indicator Dyes		
	pH Activation Range		Color Change
	Low	High	
Bromocresol Purple	5.2	6.8	Yellow to blue
Phenol Red	6.4	8.2	Yellow to red
Phenolphthalein	8.3	10.0	Colorless to fuchsia
Alizarine Yellow R	10.2	12.0	Yellow to red

Figure III-98: Control images of dye indicators in buffered solutions on AZ91D at the indicated pH levels: (a) bromocresol purple, (b) phenol red, (c) phenolphthalein, and (d) alizarine yellow R.

Initial experiments were performed by adding dye indicator to 3.5% NaCl and observing the color change of a drop on the surface of samples. Because the color changes were too rapid for clear observation, these experiments were repeated with dye indicator added to ultra-pure water. Images were taken every 0.25 seconds for the first two seconds, followed by one image per second for a total duration of 5 seconds. Owing to the near-neutral pH of ultrapure water, little observable effect is present in bromocresol purple, indicating that the pH immediately exceeds 7.0 upon contact with the surface. As shown in Figure III-99 and Figure III-100, time-dependent pH increases were observable in pH ranges between 8.5 and10. These images also clearly show the movement of pH fronts. This type of data will be used in the future to estimate corrosion rates to be input into KMC simulations. Images taken with alizarine yellow R show no strong signs of complete activation to a red color, indicating the pH was limited to values approximately 10. For all indicators, Mg showed the fastest activation, followed by αMg-5%Al.

Figure III-99: Sequential time images (0.00, 0.25, 0.50, 0.75, and 1.00 seconds) of phenol Red color in ultra-pure water for (a) AM60, (b) AZ91D, (c) AZ31B, (d) α-Mg5at%Al, and (e) Mg. The bottom row of images corresponds to the control images for phenol red.

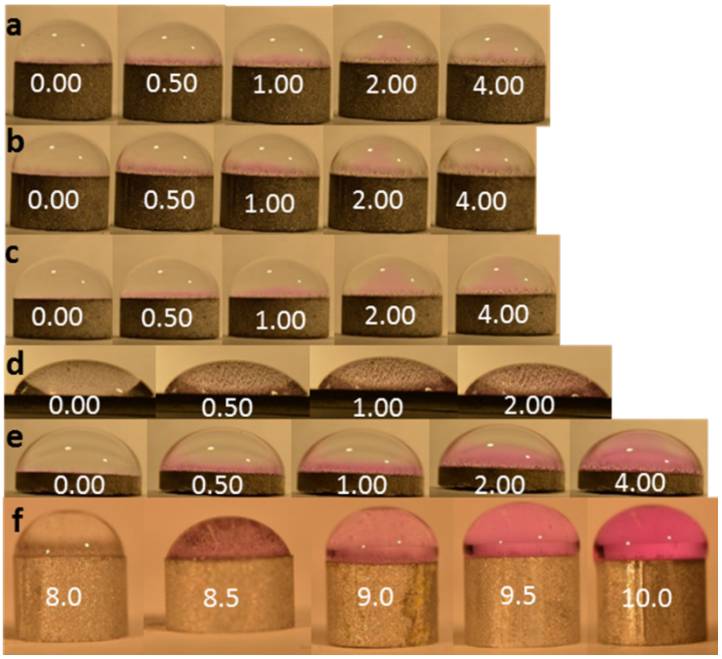

Figure III-100: Phenolphthalein in ultra-pure water for the indicated times (seconds) on (a) AM60, (b) AZ91D, (c) AZ31B, (d) α-Mg5at%Al, and (e) Mg. The bottom row of images corresponds to the control images for phenolphthalein.

The extremely rapid changes observed in pure water and water-containing chloride demonstrates that under atmospheric corrosion conditions pH 9 through 10 electrolytes evolve on these corroding surfaces within several seconds. This has significant implications for our KMC studies because pH evolution will likely not have to be considered in modeling the corrosion behavior of Mg alloys.

To study reaction kinetics of Mg and Al dissolution, ICP-MS was used to record Mg and Al concentrations in 3.5% NaCl as a function of time. Al, Mg, AM60, AZ91D, and α-Mg 5%Al were freely corroded in 10 mL of 3.5% NaCl for 20-minute, 80-minute, 180-minute, 240-minute, 4-hour, and 20-hour durations in 30-mL glass vials. All glassware was acid cleaned using nitric acid, followed by sulfuric acid and an ultra-pure water rinse. Samples were prepared by sanding down to 1200 grit/p4000, followed by a methanol rinse and drying via nitrogen gas flow. Kapton tape was used to provide an exposed surface area of 0.124 cm^2. To study Al dissolution kinetics, Al was corroded in both 3.5% NaCl and 3.5% NaCl + pH 9 buffer solution. Owing to the fact that the studied Mg-Al alloys display self-buffering pH levels between 9 and 10 in aqueous chloride, a pH 9 chloride electrolyte was used to study the Al reaction kinetics occurring at these elevated pH levels.

The ICP-MS results are summarized in Figure III-101. As expected, the Mg concentration, in parts per billion (ppb), generally increases with increasing corrosion time. However, the Al concentration displays extreme fluctuations over time. This is suggestive of either re-deposition of Al on to the surface or possible contamination in this set of experiments. However, the Al in pH 9 chloride solution showed consistent trends, with a very gradual increase in Al concentration over time, as expected. To continue these studies, a new procedure has been identified to limit contamination issues. This includes replacement of glassware with acid-cleaned plastic containers and use of a new ultra-pure water source.

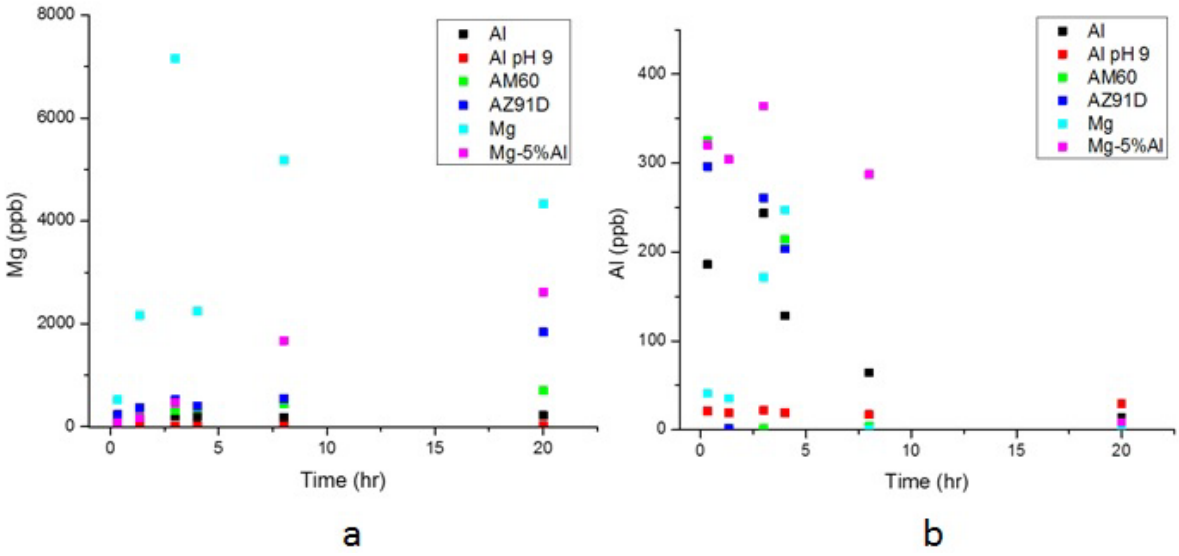

Figure III-101: ICP-MS determination of the evolution of (a) Mg and (b) Al in 10 mL of 3.5% NaCl over 20 hours of free-corrosion in 3.5% NaCl.

The EAM potential for Mg that we decided to use is described in references [1] and [3].

The most difficult part of setting up the KMC simulations involves determination of appropriate rate expressions for the chemical dissolution of the oxides/hydroxides. The thermodynamic route for Mg dissolution involves the following sequence of steps:

$$Mg = Mg^{2+} + 2e^{-} \qquad E = \text{-.263 V (normal hydrogen electrode (NHE))} \tag{1}$$

$$Mg + H_2O = MgO + 2H^{+} + 2e^{-} \qquad E = \text{-1.86 -0.059 V (NHE)} \tag{2}$$

$$Mg^{2+} + H_2O = Mg(OH)_2 \qquad \textit{Hydration} \tag{3}$$

$$Mg^{2+} + H_2O = MgO + 2H^{+} \qquad \log\left[Mg^{2+}\right] = 16.95 - 2pH$$

(4)

$$Mg(OH)_{2\ solid} + 2Cl^- = Mg^{2+} + 2Cl^- + 2OH^- \quad (5)$$

Reaction 1 dominates in acid and near-neutral pH; however, at about pH 8, Mg oxidation occurs via formation of the oxide. Also at pH 8 and higher, Mg cations in solution react with water forming the oxide/hydroxide. If there is chloride present in the range of 30 millimoles per liter, then reaction (5) dominates dissolution because $MgCl_2$ is highly soluble and the hydroxide is insoluble. A theoretical form for the kinetics of the chemical dissolution of the hydroxide forming the soluble chloride is given by the Nernst-Brunner equation [4]:

$$\frac{dC}{dt} = \frac{DA}{Vh}(C_s - C) \quad (6)$$

where D is the diffusion coefficient, A the surface area of the dissolving hydroxide, V the volume of electrolyte, h the thickness of the diffusion boundary layer, C the concentration of $MgCl_2$, and C_s the saturation concentration. Taking D to be 10^{-6} cm^2s^{-1}, V = Ah, h = 100 x 10^{-4} cm, we obtain a rate constant of $0.01s^{-1}$. We can see that from this large rate, constant chemical dissolution will always be rapid for small volume electrolyte layers (as in atmospheric corrosion) and will only slow up as C approaches C_s. Our aim is to fit the ICP-MS data to an equation similar in form to the Nernst-Brunner equation.

Technology Transfer Path

Technology produced by this program will be disseminated to the automotive engineering community by development of a website from which our detailed raw data, reports, source code for KMC simulations, and literature publications can be downloaded. The raw data, which is typically unavailable in research publications, will be made available through this site. Future journal publications will contain a citation indicating the location of this site. In addition, the KMC source code and additional relevant information will be recorded in the National Institute of Standards and Technology Materials Genome Initiative repository.

Conclusion

During the second fiscal year of the project, significant headway has been made toward development of a better understanding of the corrosion behavior in advanced automotive cast Mg alloys. Aqueous corrosion studies have demonstrated that Al in solid solution will accumulate at the surface of corroding alloys in the form of high surface area Al-rich nanostructures that can serve to significantly increase corrosion rates. Anodic dissolution experiments in iL electrolytes demonstrate that new phases form on Mg alloy surfaces during dissolution with morphologies similar to that obtained during free corrosion of theses alloys in aqueous chloride. Quantitative estimates of the equivalent area fraction of Al surface coverage was possible using a new Li UPD assay protocol developed during this program. Atmospheric corrosion experiments examined time-dependent contact angles and pH evolution within a drop of electrolyte sitting on Mg alloy surfaces. For all alloys examined, there was an exponential decrease in the contact angle over a 20-hour period. Importantly, for all alloys examined, pH within the drop increased from a near neutral value to 9.5 to 10 within only a few seconds. This indicates that one can model the atmospheric corrosion of these alloys by assuming a constant value of pH; this has important implications for the KMC simulations under development.

References

1. M. Baskes and R. Johnson, 1994, “Modified embedded atom potentials for hcp metals,” *Modelling Simul. Mater. Sci Eng*., 2; pp. 147-163.
2. J. Liao and M. Hotta, 2015, “Atmospheric corrosion behavior of field-exposed magnesium alloys: Influences of chemical composition and microstructure,” *Corrosion Science*, 100; pp. 353-364.

3. S. Lillard; G. Wang; and Baskes, 2006, "The Role of Metallic Bonding in the Crystallographic Pitting," *J. Electrochem. Soc*., 153; pp. B358-B364.
4. A. Dokoumetzidis and P. A. Macheras, 2006, "Century of dissolution research: From Noyes and Whitney to the Biopharmaceutics Classification System," *Intl. J. of Pharmaceutics*, 321; pp. 1-11.

Bibliography

A. Wingersky; A. Handler; J. Fisher; A. Weiss; and K. Sieradzki, 2015, "Dealloying of Magnesium Alloys," *Fall 2015 Meeting of the Electrochemical Society*, Phoenix, Arizona, October 15, 2015.

III.11. A Systematic Multiscale Modeling and Experimental Approach to Protect Grain Boundaries in Magnesium Alloys from Corrosion – Center for Advanced Vehicular Systems – Mississippi State University

Project Details

Mark F. Horstemeyer, Principal Investigator
Center for Advanced Vehicular Systems
Mississippi State University (MSU)
206 Carpenter Building
P.O. Box ME
Mississippi State, MS 39762
Phone: 662-325-7308
E-mail: mfhorst@cavs.msstate.edu

Santanu Chaudhuri, Co-Principal Investigator
Illinois Applied Research Institute
Computational Science and Engineering
University of Illinois at Urbana-Champaign
2100 S Oak Street
Champaign IL 61822
Phone: 509-944-1296
E-mail: santc@illinois.edu

William Joost, Technology Area Development Manager
U.S. Department of Energy
1000 Independence Avenue, SW
Washington, DC 20585
Phone: 202-287-6020
E-mail: william.joost@ee.doe.gov

Contractor: MSU
Contract No.: DE-EE0006440

Executive Summary

The goal of the proposed multiscale modeling research is to establish fundamental structure-property relationships in cast magnesium (Mg) alloys by investigating critical grain boundary phenomena (intergranular failure) during corrosion coupled with experimental electrochemical studies. This endeavor has led to an experimentally validated physically based internal state variable (ISV) model developed from lower-length scale information to be used in the finite element analysis of structural components.

Accomplishments

- Lower-length scale simulations were accomplished during previous research efforts and that information was used to inform the macroscale ISV corrosion model.
- The macroscale ISV corrosion model was finalized and calibrated to Mg with different amounts of aluminum (Al) (0%, 2%, 4%, and 6% by weight [wt.%]).

Future Directions

- Introduce the ISV corrosion model into industry for practical engineering usage.

Technology Assessment

- The technology of the ISV corrosion model is now ready for engineering practice. The model has been developed, implemented, and calibrated.

Introduction

Aging of materials in corrosive environments has become a principal cause for the reduced reliability and durability of engineered systems [1-4]. Mg alloys are getting increasing attention from automotive and aerospace industries due to their specific high strength–to-weight ratio [5]. However, Mg alloys' service lives are significantly reduced when exposed to the ambient external environment, because of their high corrosion rate [6]. Developing an accurate constitutive model that accounts for damage progression effects from mechanical loading and corrosion is necessary for understanding this behavior.

ISV theory is a constitutive material model that captures the history effect of materials and is widely used in the continuum damage mechanics field [7]. Coleman and Curtin [8] first developed the ISV theory framework. They used the Clausius-Duhem inequality to restrict the response functions. Later, Gurson [9] developed yield criteria for ductile materials, including damage evolution and plasticity. Bammann [10] employed the Cocks and Ashby [11] creep void growth rule into the ISV formulism to account for large deformation kinematics. Voyiadjis [12-14] extended the ISV damage model by coupling kinematics, kinetics, and thermodynamics into the damage rate equations. By including damage as an ISV variable, different forms of damage rules can be easily incorporated into the constitutive framework. Horstemeyer [15,16] enriched the ISV damage model by accounting for the microstructure features and dividing the damage progression into void nucleation, growth, and coalescence. ISV theory has made big achievements during the past decades to capture damage evolution for materials subjected to mechanical loadings. The corrosion process can also induce damage, reduce material strength, enhance inelastic flow, and reduce the elastic moduli. However, ISV theory was not widely applied to capture damages caused by corrosion. Walton [17] developed a corrosion model based on ISV theory by using an extended multiplicative decomposition of the deformation gradient that accounts for corrosion effects. Walton's ISV corrosion model captures macroscale damages (e.g., general corrosion, pit nucleation, pit growth, pit coalescence, and intergranular corrosion).

It is well known that corrosion is highly dependent on alloying elements and microstructural features. Many grain boundaries and grain orientations may be modified during the manufacturing process. Some impurity elements and second phase may segregate from the matrix, whereby modifying the material's corrosion stability. However, there is no clear knowledge about how doping and material engineering can be used to favorably alter corrosion rates in promising Mg alloys. The multiscale modeling technique provides a powerful approach for accurately modeling corrosion effects by considering doping effects and material microstructure-property relationships.

The following sections explain the multiscale ISV inelasticity model for corrosion that was developed in this project. This model adds corrosion ISVs to the Bammann [10,18,19] and Horstemeyer [15,20] thermomechanical plasticity model. The developed model also relates different corrosion mechanisms (e.g., general corrosion, pitting corrosion, and intergranular/filiform corrosion) to materials' microstructural features based on the corrosion framework of Walton [17]. For the ISV constitutive corrosion model part, a macroscale corrosion damage model is explained first. Because the nature behind the corrosion damage was actually the anodic and cathodic reactions occurring on the material surfaces, the Butler-Volmer equation was applied to bridge the macroscale corrosion damage to the mesoscale electrochemical kinetics. The mesoscale electrochemical kinetics behaviors can be predicted by bridging Butler-Volmer equation to materials'

microstructural features and nanoscale electrochemical activation energy. Second, the lower-length scale first principles simulations of corrosion are also presented.

Approach

ISV corrosion model development was built on the framework proposed by Walton [17], which in turn was built on the Bammann [10, 18, 19] and Horstemeyer [15, 20] frameworks. The kinematics and thermodynamic formulations can be found in Walton [17]; therefore, these aspects are not discussed in this report. Instead, an abbreviated version of the new macroscale damage formulation is presented. The full version of the new macroscale damage formulation can be found in Song [21].

Macroscale Corrosion Damage

The damage parameter ϕ is used throughout kinematic development and in the plastic flow rule. In this section, a physical and phenomenological-based model was developed to capture corrosion damage evolution. The total corrosion ϕ_{total} damage is defined as

$$\phi_{total} = \phi_{gc} + \phi_{pc} + \phi_{ic} \tag{1}$$

where ϕ_{gc} is the general corrosion damage, ϕ_{pc} is the localized pitting corrosion damage, and ϕ_{ic} is the intergranular corrosion damage. For different Mg alloys, types of second-phase particles, base materials' chemical composition, and microstructure features will affect each type of corrosion damage differently. In addition, filiform corrosion may substitute intergranular corrosion occurring on the surface. In this situation, the ϕ_{ic} can be changed to ϕ_{fc} in Equation (1). The associated damage rate equation is obtained as the following form

$$\dot{\phi}_{total} = \dot{\phi}_{gc} + \dot{\phi}_{pc} + \dot{\phi}_{ic} \tag{2}$$

Horstemeyer [15] developed an equation that accounts for relative pitting corrosion damage

$$\phi_{pc} = \eta_p \nu_p c_p \tag{3}$$

where η_p represents pit nucleation related to the pit number density; ν_p represents pit growth related to the pit in-plane area, pit depth, and pit volume; and c_p is the pit coalescence term related to the nearest neighbor distance (NND) between pits.

Macroscale General Corrosion Rate

General corrosion is defined as corrosion that attacks an exposed surface uniformly without inducing appreciable localization. General corrosion can be obtained by measuring the mass change or thickness change of the specimen. Faraday's Law [22] proposed that the mass loss of an electrode during electrolysis is directly proportional to the quantity of electricity transferred at that electrode

$$m = \frac{QM}{Fz} \tag{4}$$

where m is the mass change of an electrode in grams, Q is the total electric charge passed through the substance, F is the Faraday constant, M is the molar mass of the substance, and z is the valency number of ions of the substance ($z = 2$ for Mg). A modified form of Faraday's law was proposed for the general corrosion rate $\dot{\phi}_{gc}$

$$\dot{\phi}_{gc} = C_1\left(C_2 + \phi_{gc}\right)\frac{M}{Fz} \tag{5}$$

where C_1 and C_2 are parameters that are determined by the material properties.

Macroscale Pitting Corrosion

Pitting corrosion is extremely localized corrosion that results in creation of small holes in the metal. Pitting corrosion is usually defined as an autocatalytic process [23]. Spatial separation of the cathodic and anodic half-reactions generates a potential gradient and promotes electromigration of aggressive anions into the pits, causing pit nucleation, growth, and coalescence.

Pits are susceptible to nucleate at impurities, inclusions, grain boundaries, and/or surface defect/flaw regions, because these inhomogeneous sites can facilitate breakdown of passive films [24]. The pit nucleation rate can be written as

$$\dot{\eta}_p = \begin{cases} C_3(C_4 - \eta) & \text{if } t < t_c \\ C_5(C_6 - \eta) & \text{if } t \geq t_c \end{cases} \tag{6}$$

where $C_3 - C_6$ are material parameters that are as a function of second phase/particle volume fraction, particle size, temperature, and pH level. t_c is the transition time from pit nucleation dominated to pit coalescence or general corrosion dominated.

The pit growth rate and stability of the active corrosion are dependent on material composition, aggressive electrolyte concentration, formation and dissolution of corrosion film, and the potential inside the pit [24,25].

The pit growth equation is expressed as the following form

$$\dot{v}_p = \begin{cases} C_7(C_8 - v) & \text{if } t < t_c \\ C_9(C_{10} - v) & \text{if } t \geq t_c \end{cases} \tag{7}$$

where C_7 and C_8 are material parameters that change as a function of temperature, pH level, and materials microstructural characteristics. v is the average pit volume on the specimen surfaces. It is important to note that v can also be the average in-plane pit area if the pit area was measured instead of the pit volume.

In real-world situations, pits will interact with neighboring pits and coalesce into larger pits. The coalescence rate $\dot{C}$ relates electrochemical interaction forces between pits. Walton [17] proposed a pit coalescence model based on the Coulomb's Law and Maxwell's stress. The original form of Coulomb's Law is

$$F_c = \frac{k_e q_1 q_2}{r^2} \tag{8}$$

where F_c is the electrostatic interaction force between pits, k_e is Coulomb's constant ($k_e = 8.987 \times 10^9\ \mathrm{Nm^2/C^2}$), and q_1 and q_2 are point charges. r is the separation distance between two neighboring pits, defined as the NND for corrosion pits. Combining Coulomb's Law and Maxwell stress resulted in the following pitting coalescence rate equation:

$$\dot{c}_p = \frac{k_e q_1 q_2}{\varepsilon_0 \pi \left[\overline{N\dot{N}D}(t)\right]^4} \tag{9}$$

$$\overline{N\dot{N}D} = \begin{cases} C_{11}(C_{12} - NND) & \text{if } t < t_c \\ C_{13}(C_{14} - NND) & \text{if } t \geq t_c \end{cases} \tag{10}$$

In this equation, ε_0 is the electric constant (8.854×10-12 F/m) and $C_{11} - C_{14}$ are material parameters.

Macroscale Intergranular Corrosion

Intergranular corrosion is the localized attack along grain boundaries or regions adjacent to the grain boundaries [26]. This form of corrosion is mainly induced by uneven distribution of the chemical composition

in the alloy, because impurities or second phases tend to form on the grain boundaries. This chemical composition segregation results in formation of galvanic cells along grain boundaries. The intergranular corrosion rate ϕ_{ic} is formulated as the following form

$$\dot{\phi}_{ic} = \begin{cases} C_{15}(C_{16} - \phi_{ic})\left(\frac{MO}{MO_0}\right)^{z_{ic}} & \text{if } t < t_c \\ C_{17}(C_{18} - \phi_{ic})\left(\frac{MO}{MO_0}\right)^{z_{ic}} & \text{if } t \geq t_c \end{cases} \quad (11)$$

where $C_{15} - C_{18}$ are material parameters and $(MO/MO_0)^{z_{ic}}$ is a is grain misorientation factor that represents galvanic cells formed. The grain misorientation factor describes distribution of crystallographic orientation and is obtained from electron backscatter diffraction/pole figure results.

Mesoscale Electrochemical Kinetics

The Butler-Volmer equation describes the kinetics for electrochemical reactions and is controlled by transfer of charge across the interface [27,28]. The Butler-Volmer equation links four very important parameters together: Faradaic current, electrode potential, concentration of reactant, and concentration of product.

$$i = i_{corr}\left\{\exp\left(\frac{\alpha_a n F_R}{RT}\Delta E\right) - \exp\left(-\frac{\alpha_c n F_R}{RT}\Delta E\right)\right\} \quad (12)$$

$$\Delta E = \left(E - E_{eq}\right) \quad (13)$$

The first term represents the anodic partial current density. The second term is the cathodic partial current density [29]. Where i is the electrode current density, i_{corr} is the exchange corrosion current density, ΔE is the overpotential, E is the electrode potential, and E_{eq} is the equilibrium/reversible potential. From the above relationships, the net current (i) is positive when the electrode is polarized anodically and negative when the electrode is polarized cathodically; n is the number of electrons involved in the electron reaction; F_R is the Faraday constant; and R is the universal gas constant. α_a and α_c are the so-called anodic and cathodic charge transfer coefficients. The values of α_a and α_c do not necessarily sum to unity, but they are related by

$$\alpha_a + \alpha_c = \upsilon^{-1} \quad (14)$$

where υ is the stoichiometric number or the number of times the rate-determining step must occur for overall reaction to occur once.

When the anodic polarization potential is greater than the equilibrium potential ($\eta_a > 50$ mV), the first term of Equation (12) dominates the second term. In this case, the Butler-Volmer equation can be simplified to

$$i = i_0 \exp\left(\frac{\alpha_a n F_R}{RT}\Delta E\right) \quad (15)$$

Equation (15) can be rearranged to get the Tafel equation [30] as

$$\eta_a = \beta_a \log\left(\frac{i}{i_0}\right) \quad (16)$$

where β_a is the anodic Tafel slope. β_a can be associated with α_a in the following way:

$$\beta_a = \frac{2.3RT}{\alpha_a n F_R} \quad (17)$$

A similar equation is obtained for cathodic activation polarization

$$\eta_c = -\beta_c \log\frac{|i|}{i_0} \tag{18}$$

where β_c is the cathodic Tafel slope and it relates to α_c by

$$\beta_c = \frac{2.3RT}{\alpha_c n F_R} \tag{19}$$

According to the Stern-Geary equation [31], the exchange corrosion current can be determined by a small polarization from the corrosion potential

$$i_{corr} = \frac{\beta_a \beta_c}{(\beta_a + \beta_c) + 2.3R_p} \tag{20}$$

where R_p is the polarization resistance and can be defined as the slope of the linear polarization curve at the corrosion potential. For our model, we regard R_p as a material property and it does not change over exposure time. Note that the unit of R_p is $\Omega\ \mathrm{cm}^{-2}$. When substituting Equations (17 and 19) into Equation (20), it results in

$$i_{corr} = \frac{RT}{nF(\alpha_a + \alpha_c)R_p} \tag{21}$$

Substituting the exchange current Equation (21) into the Butler-Volmer equation Equation (15), the corrosion current formula can be changed to the following form:

$$i = \frac{RT}{nF(\alpha_a + \alpha_c)R_p} \exp\left(\frac{\alpha_a n F_R}{RT}\Delta E\right) \tag{22}$$

The corrosion current density, i, determined from the electrochemical kinetic part of the equation is used to quantify the corrosion rate occurring on the surface. The rate of material loss, r ($\mathrm{g\ h}^{-1}$), is associated with the exchange corrosion current density, i_{corr} ($\mathrm{A\ cm}^{-2}$), by:

$$r = i\frac{M}{nF} \tag{23}$$

The corrosion current, i, is the sum of general corrosion current, i_{gc}, and pitting corrosion current, i_{pc}.

Microstructural Analysis

For multi-phase Mg alloys, macroscale corrosion damages are affected by three important factors: (1) the chemical composition of each phase, (2) the fraction of each phase in the material, and (3) the microstructural distribution of second phases in the material. For cast Mg-Al alloys, the eutectic α phase usually formed along dendritic arms or grain boundaries. This phase contained a higher level of Al in the solid solution. The β phase usually precipitates within the eutectic α phase, with the increase of Al content in material. The β phase precipitates more continuously along the grain boundaries and forms a finer lamellar arrangement.
Figure III-102 shows distribution of the α, eutectic α, and β phases in the Mg-6Al alloy. Because the eutectic α phase and β phase have lower corrosion rates than the α phase, they can improve the material's overall corrosion resistance. On the other hand, because the eutectic α phase and β phase have more positive electrochemical potential, they can act as effective cathodic sites for matrixing α phase and accelerating the dissolution rate of the α phase [32]. Therefore, in order to capture the corrosion behavior of Mg alloys accurately, we need to consider both corrosion resistance improvement and anodic dissolution acceleration affected by the second phases.

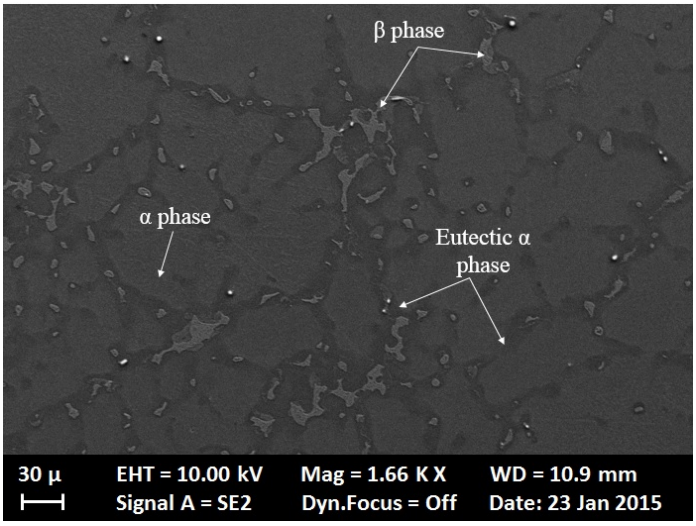

Figure III-102: The distribution of α, eutectic α, and β phases in the Mg-6Al alloy.

Liu [33] quantified the eutectic α phase and β phase ($Mg_{17}Al_{12}$) for Mg-Al alloys (Mg-0.5 weight percent [wt.%] Al, Mg-1 wt.% Al, Mg-2 wt.% Al, Mg-4 wt.% Al, Mg-6 wt.% Al, Mg-9 wt.% Al, and Mg-12 wt.% Al). This research determined that the volume fraction and size of both phases increased with addition of Al content and almost followed a linear relationship. The microstructure for the same Mg alloys can differ due to the different manufacturing process used (e.g. cooling rate and heat treatment). The casted Mg-Al alloys for this study were prepared with the same casting procedure. Their microstructure features can be associated with Al weight percentage,ξ, by the following form:

$$GS(\xi) = 370599\xi^2 - 37012\xi + 1025.8, \quad D_{Eu\,\alpha}(\xi) = 358.21\xi + 1.0318, \quad \delta_{Eu\,\alpha}(\xi) = 6903\xi + 7.6459 \tag{24}$$

$$NND_{Eu\,\alpha}(\xi) = 114.25\xi + 38.285, \quad f_{Eu\,\alpha}(\xi) = -3.407\xi + 0.4044 \tag{25}$$

$$P_{Eu\,\alpha}(\xi) = 25.012\xi^2 + 0.0993\xi + 0.002, \quad P_{matrix}(\xi) = 0.5007, \quad D_{\beta}(\xi) = 1944\xi^2 - 20.223\xi - 0.0921, \quad \delta_{\beta}(\xi) = 41518\xi^2 - 446.9\xi - 443.926 \tag{26}$$

$$NND_{\beta}(\xi) = -436.13\xi + 39.707, \quad f_{\beta}(\xi) = 7.3 \times 10^{-6} \exp 145.3\xi, \quad E(\xi) = 1.667\xi + 1.663 \tag{27}$$

where $GS(\xi)$ is the grain size (µm), $D_{Eu\,\alpha}(\xi)$ is the particle size/phase size (µm) of the eutectic α phase, $\delta_{Eu\,\alpha}(\xi)$ is the number density (mm^{-2}) of the eutectic α phase, $NND_{Eu\,\alpha}(\xi)$ is the NND (µm) of the eutectic α phase, and $f_{Eu\,\alpha}(\xi)$ is the area fraction of the eutectic α phase in the material. $P_{Eu\,\alpha}(\xi)$ is the Al content (wt.%) in the eutectic α phase and $P_{matrix}(\xi)$ is the Al content (wt.%) in the matrix material. $D_{\beta}(\xi)$, $\delta_{\beta}(\xi)$, $NND_{\beta}(\xi)$, and $f_{\beta}(\xi)$ are the particle size (µm) of the β phase, particle number density (mm^{-2}) of β phase, NND (µm) between the β phase particles, and area fraction of the β phase, respectively. $E(\xi)$ is the electrochemical potential value of Mg-Al solution phase. Song [21] explains the link between the microstructure specific equations in Equations (24 through 27) and the corrosion equations.

Results and Discussion

The microstructural features (i.e., particle size, particle number density, NND, Al content in each phase, grain size, and second phase area fraction) were quantified for the casted pure Mg, Mg-2% Al, and Mg-6% Al alloys. Then the microstructural characteristics and electrochemical potential of each phase were inputted into

the multiscale ISV corrosion model, and the predicted corrosion process (i.e., general, pitting, and intergranular corrosion) were compared with experimental data as shown in Figure III-103 through Figure III-105. Good agreement was found between model validation results and experimental data.

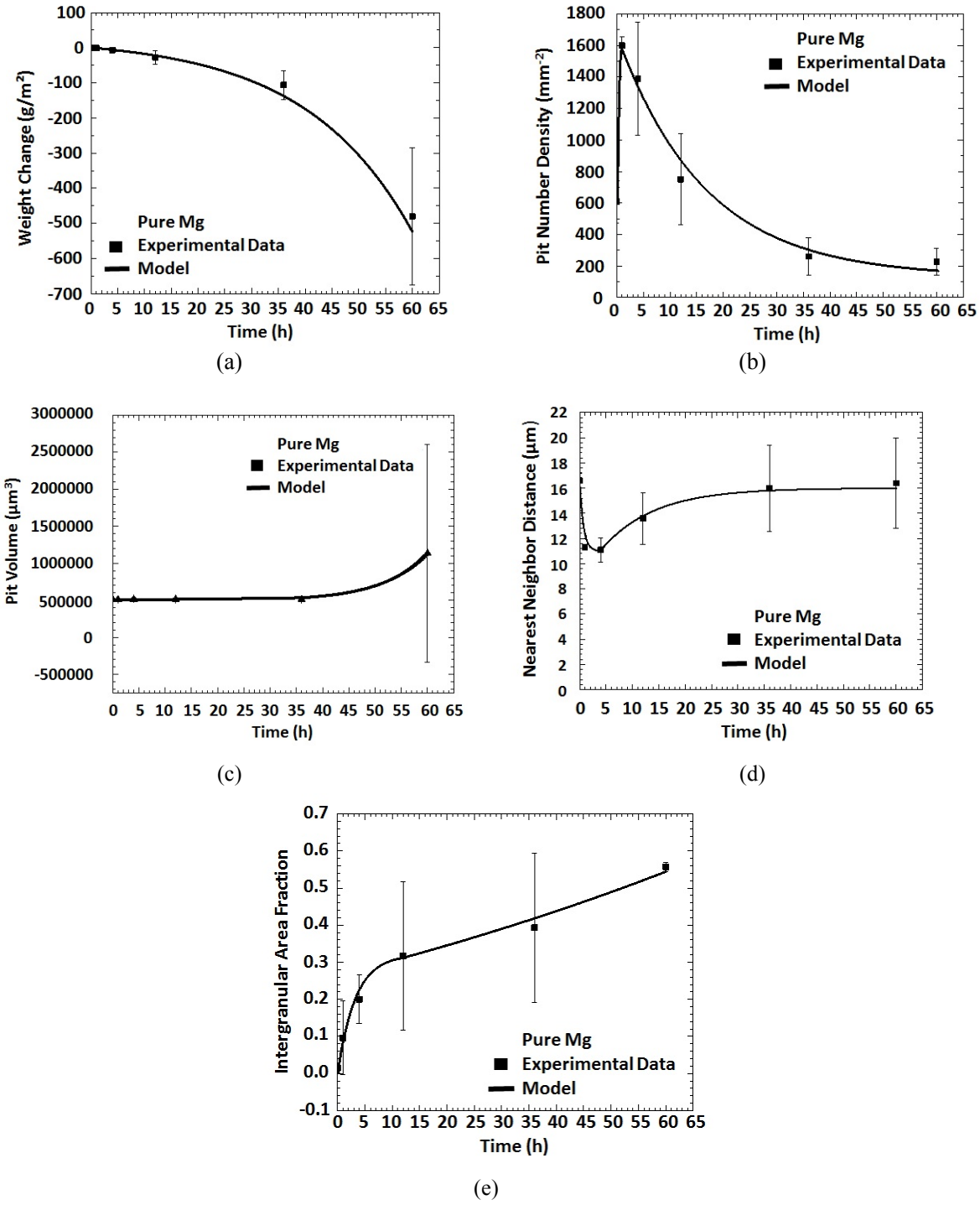

Figure III-103: Comparison between the proposed theoretical damage framework and the corrosion experimental data of Pure Mg (3.5 wt.% sodium chloride (NaCl) immersion environment). Experimental data versus the model for (a) change in mass, (b) pit number density, (c) pit volume, (d) pit nearest neighbor distance, (e) intergranular corrosion area fraction. The error bars indicate one standard deviation in each direction.

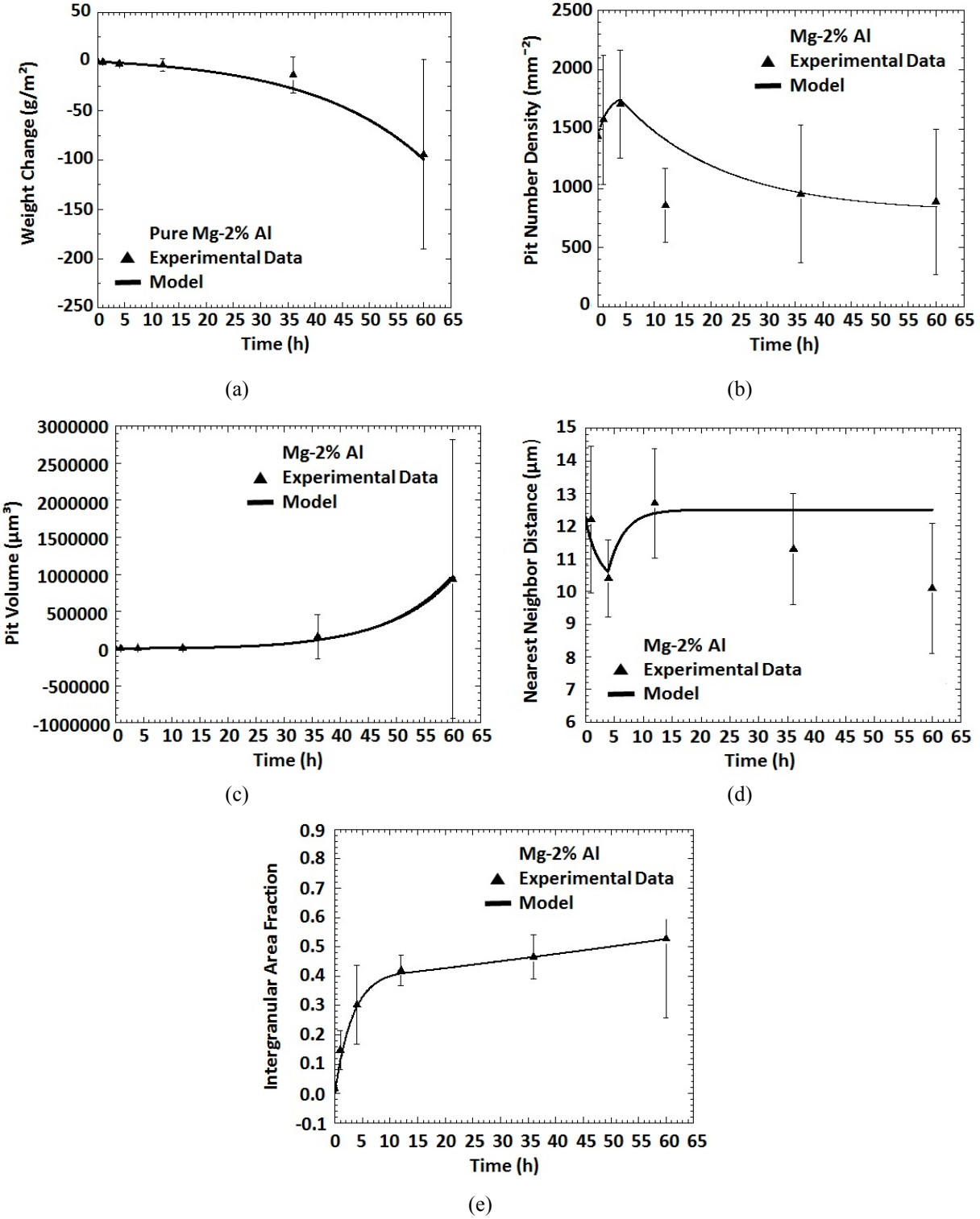

Figure III-104: Comparison between the proposed theoretical damage framework and the corrosion experimental data of Mg-2% Al alloy (3.5 wt.% NaCl immersion environment). Experimental data versus the model for (a) change in mass, (b) pit number density, (c) pit volume, (d) pit nearest neighbor distance, and (e) intergranular corrosion area fraction. The error bars indicate one standard deviation in each direction.

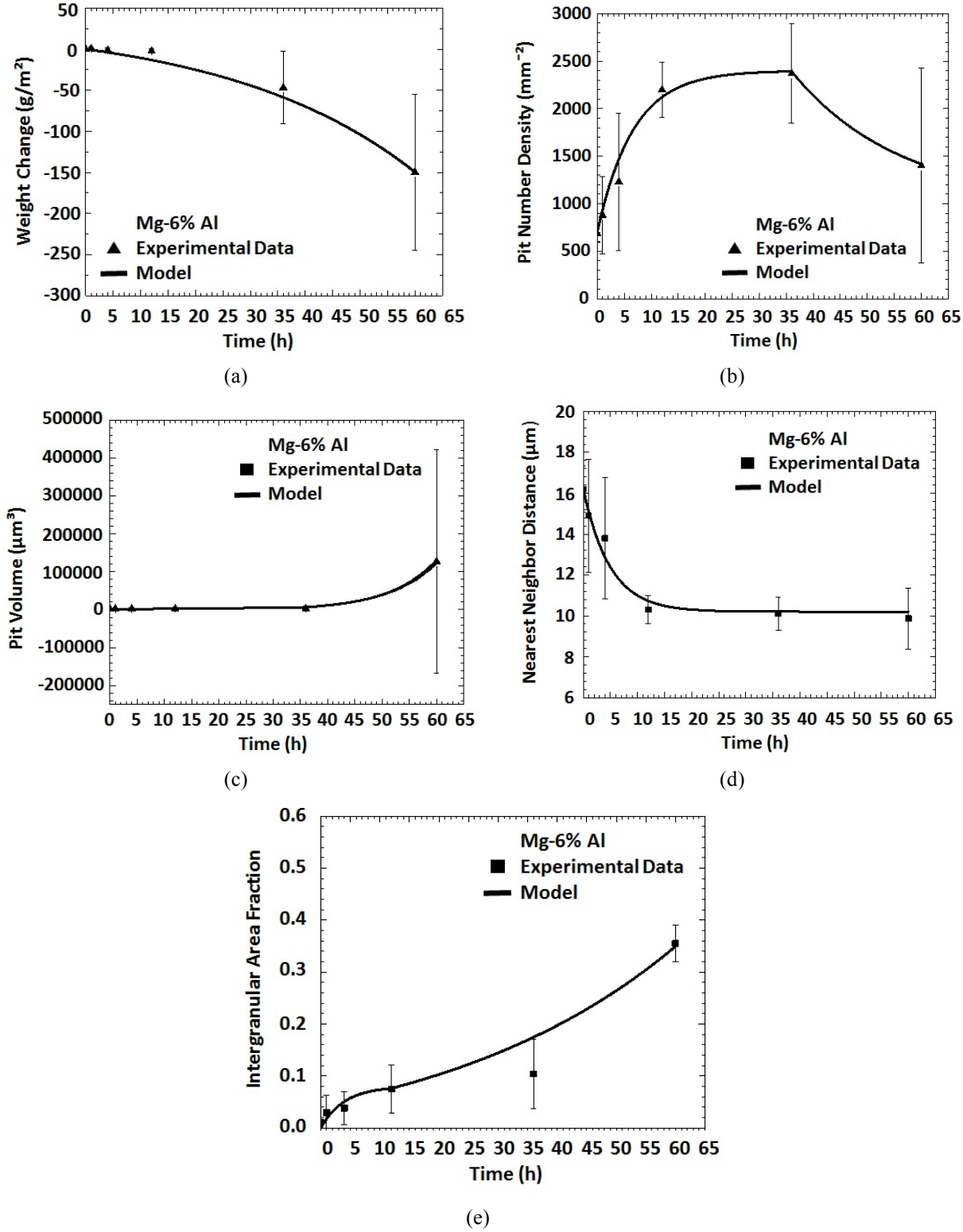

Figure III-105: Comparison between the proposed theoretical damage framework and corrosion experimental data of Mg-6% Al (3.5 wt.% NaCl immersion environment). Experimental data versus the model for (a) change in mass, (b) pit number density, (c) pit volume, (d) pit nearest neighbor distance, and (e) intergranular corrosion area fraction. The error bars indicate one standard deviation in each direction.

Technology Transfer Path

The simulation and experimental results (e.g., intellectual capital, such as information, data, models, and tools) of the fully developed and validated model will enable vehicle manufacturers, component suppliers, the materials science community, and researchers in the field of Mg alloys to better understand corrosion processes and develop products that minimize their effects.

Conclusion

A multiscale corrosion constitutive model that joins the damage and mechanical effects for Mg alloys was developed. The kinematics, thermodynamics, and kinetics were included in formulation of the internal state variables to account for different corrosion damage mechanisms (e.g., general corrosion, pitting corrosion, and intergranular corrosion). Macroscale corrosion damage is bridged to the mesoscale electrochemical kinetics based on the Butler-Volmer equation, which is further bridged to materials' microstructural properties. The model's theoretical framework can be implemented to a finite element code for engineering analysis. The model can also be extended to include other kinds of damage that occurs in the engineering field.

References

1. M. Rodríguez, 2014, "Anticipated Degradation Modes of Metallic Engineered Barriers for High-Level Nuclear Waste Repositories," *JOM,* 66; pp. 503-525.
2. M. Caro; K. Woloshun; F. Rubio; S. A. Maloy; and P. Hosemann, 2013, "Heavy Liquid Metal Corrosion of Structural Materials in Advanced Nuclear Systems," *JOM,* 65; pp. 1057-1066.
3. T. Perez, 2013, "Corrosion in the Oil and Gas Industry: An Increasing Challenge for Materials," *JOM,* 65; pp. 1033-1042.
4. B. Gordon, 2013, "Corrosion and Corrosion Control in Light Water Reactors," *JOM,* 65; pp. 1043-1056.
5. S. A. Khan; Y. Miyashita; Y. Mutoh; and Z. B. Sajuri, 2006, "Influence of Mn content on mechanical properties and fatigue behavior of extruded Mg alloys," *Materials Science and Engineering: A,* 420; pp. 315-321.
6. C. A. Walton; H. J. Martin; M. F. Horstemeyer; P. T. Wang, 2012, "Quantification of corrosion mechanisms under immersion and salt-spray environments on an extruded AZ31 magnesium alloy," *Corrosion Science,* 56; pp. 194-208.
7. M. F. Horstemeyer and D. J. Bammann, 2010, "Historical review of internal state variable theory for inelasticity," *International Journal of Plasticity,* 26; pp. 1310-1334.
8. B. D. Coleman and M. E. Gurtin, 1967, "Thermodynamics with Internal State Variables," *The Journal of Chemical Physics,* 47; pp. 597-613.
9. A. L. Gurson, 1977, "Continuum Theory of Ductile Rupture by Void Nucleation and Growth: Part I—Yield Criteria and Flow Rules for Porous Ductile Media," *Journal of Engineering Materials and Technology,* 99; pp. 2-15.
10. D. Bammann; M. Chiesa; M. Horstemeyer; and L. Weingarten, 1993, "Failure in ductile materials using finite element methods," *Structural Crashworthiness and Failure*; pp.1-54.
11. A. C. F. Cocks and M. F. Ashby, 1980, "Intergranular fracture during power-law creep under multiaxial stresses," *Metal Science,* 14; pp. 395-402.
12. G. Z. Voyiadjis and B. Deliktas, 2009, "Formulation of strain gradient plasticity with interface energy in a consistent thermodynamic framework," *International Journal of Plasticity,* 25; pp. 1997-2024.
13. G. Z. Voyiadjis and R. J. Dorgan, 2007, "Framework using functional forms of hardening internal state variables in modeling elasto-plastic-damage behavior," *International Journal of Plasticity,* 23; pp. 1826-1859.

14. G. Z. Voyiadjis and P. I. Kattan, 1992, "A plasticity-damage theory for large deformation of solids I. Theoretical formulation," *International Journal of Engineering Science,* 3; pp. 1089-1108.
15. M. Horstemeyer; J. Lathrop; A. Gokhale; and M. Dighe, 2000, "Modeling stress state dependent damage evolution in a cast Al–Si–Mg aluminum alloy," *Theoretical and Applied Fracture Mechanics,* 33; pp. 31-47.
16. M. F. Horstemeyer and A. M. Gokhale, 1999, "A void–crack nucleation model for ductile metals," *International Journal of Solids and Structures,* 36; pp. 5029-5055.
17. C. A. Walton; M. F. Horstemeyer; H. J. Martin; and D. K. Francis, 2014, "Formulation of a macroscale corrosion damage internal state variable model," *International Journal of Solids and Structures,* 51; pp. 1235-1245.
18. D. J. Bammann, 2001, "A model of crystal plasticity containing a natural length scale," *Mater. Sci. Eng.*; pp. 406–410.
19. D. J. Bammann and G. C. Johnson, 1996, "Modeling large deformation and failure in manufacturing processes," T. Tatsumi; E. Wanatabe; and T. Kambe (eds.), *Theoretical Applied Mechanics*, Philadelphia, PA: Elsevier Science; pp. 359-376.
20. M. F. Horstemeyer, 2012, *Integrated Computational Materials Engineering (ICME) for Metals: Using Multiscale Modeling to Invigorate Engineering Design with Science*, Charlottesville, Virginia: John Wiley & Sons.
21. W. Song, 2015, *Development of a multiscale internal state variable inelasticity-corrosion damage model for magnesium alloys,* Ph.D. Thesis, Mississippi State, Mississippi: MSU, 146 pages; 3716738.
22. R. G. Ehl and A. J. Ihde, 1954, "Faraday's electrochemical laws and the determination of equivalent weights," *Journal of Chemical Education,* 31; p. 226.
23. ASME, 1987, "Corrosion," ASM Handbook, Vol. 13, Novelty, Ohio: ASM International, ASM International; ISBN 0-87170-007-7.
24. L. Zhu, 2002, *Study of Corrosion Pits in Chloride Solution*, Ph.D. Thesis, Champaign, Illinois: University of Illinois, 253 pages; 3044276.
25. P. Ernst and R. C. Newman, 2002, "Pit growth studies in stainless steel foils. I. Introduction and pit growth kinetics," *Corrosion Science,* 44; pp. 927-941.
26. C. S. Tedmon; D. A. Vermilyea; and J. H. Rosolowski, 1971, "Intergranular Corrosion of Austenitic Stainless Steel," *Journal of The Electrochemical Society,* 118; pp. 192-202.
27. J. A. V. Butler, 1924, "Studies in heterogeneous equilibria. Part II. - the kinetic interpretation of the Nernst theory of electromotive force," *Trans. Faraday Soc.,* 19; pp. 729-733.
28. T. Erdey-Grúz and M. Z. Volmer, 1930, "Zur Theorie der Wasserstoffuberspannung," *Physik. Chem. A,* 150; pp. 203-213.
29. A. J. Bard; M. Stratmann; E. Gileadi; M. Urbakh; E. J. Calvo; P. R. Unwin; G. S. Frankel; D. Macdonald; S. Licht; H. J. Schäfer; G. S. Wilson; I. Rubinstein; M. Fujihira; P. Schmuki; F. Scholz; C. J. Pickett; and J. F. Rusling, 2007, "Corrosion and Oxide Films," Chapter V, *Encyclopedia of Electrochemistry*, Charlottesville, Virginia: John Wiley & Sons; 7720 pages.
30. Z. Shi; M. Liu; and A. Atrens, 2010, "Measurement of the corrosion rate of magnesium alloys using Tafel extrapolation," *Corrosion Science*, 52; pp. 579-588.
31. M. Stern and A. L. Geary, 1957, "Electrochemical Polarization: I. A Theoretical Analysis of the Shape of Polarization Curves," *Journal of the Electrochemical Society,* 104; pp. 56-63.
32. G. Song; A. L. Bowles; and D. H. St. John, 2004, "Corrosion resistance of aged die cast magnesium alloy AZ91D," *Materials Science and Engineering: A,* 366; pp. 74-86.
33. M. Liu; P. J. Uggowitzer; A. V. Nagasekhar; P. Schmutz; M. Easton; G. L. Song; and A. Atrens, 2009, "Calculated phase diagrams and the corrosion of die-cast Mg–Al alloys," *Corrosion Science,* 51; pp. 602-619.

Bibliography

D. J. Bammann, 1989, "A damage model for ductile metals," *Nucl. Eng*., 116; pp.355–362.

B. D. Coleman and W. Noll, 1959, "Thermodynamics with internal state variables," *Archive for Rational Mechanics and Analysis,* 4; pp. 97–128.

B. D. Coleman and M. Gurtin, 1967, "Thermodynamics with internal state variables," *Journal of Chemical Physics* 47.

K. B. Deshpande, 2011, "Numerical modeling of micro-galvanic corrosion," *Electrochimica Acta,* 56; pp. 1737-1745.

M. Gurtin, 1981, "An Introduction to Continuum Mechanics," Academic Press, San Diego, California.

D. K. Francis; J. L. Bouvard; Y. Hammi; and M. F. Horstemeyer, 2014, "Formulation of a damage internal state variable model for amorphous glassy polymers," *International Journal of Solids and Structures,* 51; pp. 2765-2776.

M. Malvern, 1969, "Introduction to the Mechanics of a Continuous Medium," Prentice Hall, Inc., Englewood Cliffs, New Jersey.

III.12. High-Throughput Study of Diffusion and Phase Transformation Kinetics of Magnesium-Based Systems for Automotive Cast Magnesium Alloys – The Ohio State University

Project Details

Alan A. Luo, Principal Investigator
Ohio State University
137 Fontana Labs
116 W. 19th Avenue
Columbus, OH 43210
Phone: 614-292-5629
E-mail: luo.445@osu.edu

Ji-Cheng Zhao, Principal Investigator
Ohio State University
286 Watts Hall
116 W. 19th Avenue
Columbus, OH 43210
Phone: 614-292-9462
E-mail: zhao.199@osu.edu

Adrienne Riggi, Project Officer
National Energy Technology Laboratory
3610 Collins Ferry Road
P.O. Box 880
Morgantown, WV 26507-0880
Phone: 304-285-5223
E-mail: Adrienne.riggi@netl.doe.gov

William Joost, Technology Area Development Manager
U.S. Department of Energy
1000 Independence Avenue, SW
Washington, DC 20585
Phone: 202-287-6020
E-mail: william.joost@ee.doe.gov

Contractor: Ohio State University, CompuTherm LLC (Madison, WI)
Contract No.: DE-EE0006450

Executive Summary

The objective of the proposed study is to establish the scientific foundation for kinetic modeling of diffusion, phase precipitation, and casting/solidification in order to accelerate the design and optimization of cast magnesium (Mg) alloys for weight reduction of the U.S. automotive fleet. The team will (1) study diffusion kinetics of six Mg-containing binary systems using high-throughput diffusion multiples to establish reliable diffusivity and mobility databases for the Mg-aluminum (Al)-zinc (Zn)-tin (Sn)-calcium (Ca)-strontium (Sr)-manganese (Mn) system; (2) study precipitation kinetics (i.e., nucleation, growth, and coarsening) using both innovative dual-anneal diffusion multiples and cast model alloys to provide large amounts of kinetic data (including interfacial energy) and microstructure atlases to enable implementation of the Kampmann-Wagner numerical model to simulate phase transformation kinetics of non-spherical/non-cuboidal precipitates in Mg alloys; (3) implement a micromodel to take into account back diffusion in the solid phase in order to predict microstructure and microsegregation in multi-component Mg alloys during dendritic solidification, especially

under high pressure die-casting (HPDC) conditions; and, (4) widely disseminate the data, knowledge and information using the Materials Genome Initiative infrastructure (http://www.mgidata.org), as well as publications and digital data sharing, to enable researchers to identify new pathways/routes to better cast Mg alloys.

Accomplishments

- Liquid-solid diffusion couples of Mg-Al, Zn, Sn, Mn, Sr, Ca, neodymium (Nd), and zirconium (Zr) systems were successfully made. Two diffusion multiples of Mg-Al, Sn, Ca, and Mn systems were prepared. The diffusion profiles were measured using electro probe microanalysis (EPMA) (Fiscal Year [FY] 2015).
- The forward simulation was used to extract diffusivities and results were compared with available literature data. Diffusivities have been determined for Mg-Al and Mg-Sn systems covering both high and low temperatures. Diffusivities for the Mg-Zn system have been determined at high temperatures. Two sets and one set of diffusivities have been extracted for Mg-Ca and Mg-Nd systems, respectively (FY 2015).
- The Mg atomic mobility database was updated using new experimental diffusivities extracted this year (FY 2015).
- Precipitation of the Mg-7Al-2Sn (weight percentage [wt.%]) alloy during the aging process was investigated (FY 2015).
- Phase formation and microsegregation in four directionally solidified Mg-Al-Ca-Sn alloys were characterized (FY 2015).
- The microstructures of AE42 (Mg-4Al-2RE, rare earth (RE) added as misch metal) alloys prepared by three different cooling conditions were investigated (FY 2015).
- A modified Scheil-Gulliver model that takes back diffusion into account was developed and tested on a binary Mg-Al system (FY 2015).

Future Directions

- Extract diffusivities from the profiles of liquid-solid diffusion couples of Mg-Ca and Mg-Nd systems. Develop a method for analyzing the concentration profiles of the Mg-Sr system with very low solubility of Sr in (Mg). Measure the diffusivities of the Mg-Mn and Mg-Zr systems.
- Introduce other alloying elements into Mg-Al-Sn alloys to investigate whether there is further improvement of precipitation strengthening during aging.
- Study the microsegregation of alloying elements in Mg alloys prepared by the conventional casting process.
- Further test the code of the modified Scheil-Gulliver model and extend the simulation to ternary and quaternary Mg alloys.

Technology Assessment

- Target: Establish a diffusivity database of an Mg-Al-Zn-Sn-Ca-Sr-Mn-Nd-Zr system using liquid-solid diffusion couples and diffusion multiples.
- Gap: The solubility of Sr in (Mg) is extremely low, which leads to difficulty in measuring the diffusion profiles. Mn and Zr are prone to oxidation and it is difficult to generate a reliable interface of Mn or Zr and Mg for EPMA. New methods need to be developed to solve these problems.
- Target: Investigate the precipitation of the Mg-Al-Sn alloy during aging through a combination of experiment and simulation to improve the precipitation response of the alloy.

- Gap: The precipitation of rare-earth-free Mg alloys is very sluggish and microalloying needs to be developed to improve precipitation. In addition, transmission electron microscopy (TEM) experiments are needed to generate more quantitative microstructure data for calibrating the simulation.
- Target: Develop a code for simulating the solidification of multi-component Mg alloys.
- Gap: Issues, including undercooling and dendrite arm coarsening, need to be solved. The model should also be improved so that it is applicable to higher order Mg alloys.

Introduction

The lack of diffusivity data for Mg alloys is hindering the computational design of high-performance Mg alloys using the integrated computational materials engineering approach. Compared with Al alloys, the precipitation hardening in rare-earth-free Mg alloys is sluggish and needs to be improved. The Scheil-Gulliver solidification model does not take back diffusion into account and may not be able to accurately predict the microstructure under the casting condition. A modified model taking back diffusion into account should be developed. In FY 2015, solid-liquid diffusion couples and diffusion multiples were made and characterized. The forward simulation [1] was used to extract diffusivities from the diffusion profiles measured by EPMA. Using the CALculation of PHAse Diagrams (CALPHAD) approach [2], the Mg atomic mobility database was updated based on experimental diffusivities obtained this year. The precipitation of Mg-7Al-2Sn during aging was investigated by experiment and simulation. The phase formation and microsegregation in directionally solidified Mg-Al-Ca-Sn alloys were characterized. In addition to directional solidification, Mg alloys from undirectional solidification were investigated and the first target alloy is commercial AE42. The microstructures of the AE42 alloys prepared by different cooling conditions were investigated. The modified Scheil-Gulliver model that considers back diffusion was developed and tested on the Mg-Al binary system.

Approach

Diffusion

Two approaches were used for Mg alloy system diffusion studies (Figure III-106 and Figure III-107). One approach is liquid-solid diffusion couple for high-temperature measurement; the other approach is a diffusion multiple for efficiently extracting diffusivities at low temperatures. The sample preparation process has been described in the last annual progress report and is not repeated here. The concentration profile is measured using EPMA and the forward simulation is used to extract both the interdiffusivity and impurity diffusivity.

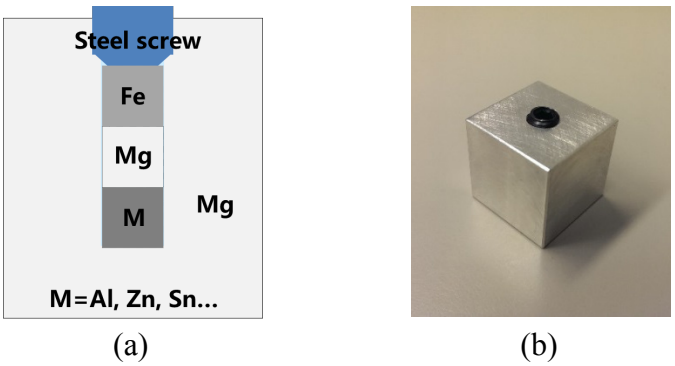

Figure III-106: Liquid-solid diffusion couple: (a) geometry; and (b) assembly.

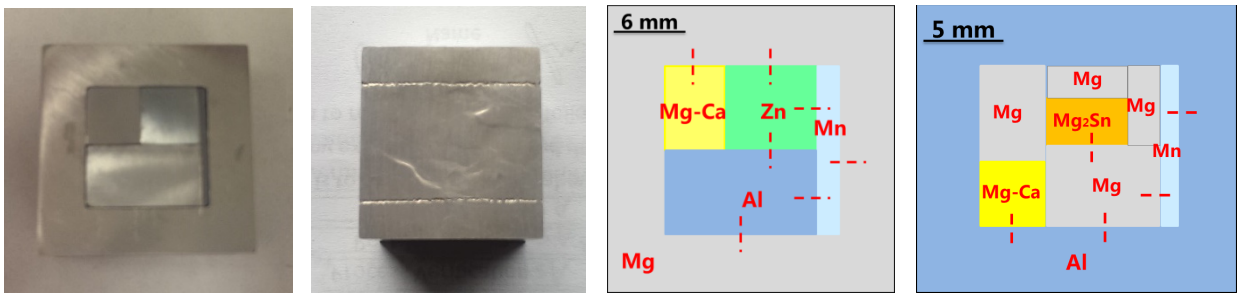

(a) (b) (c) (d)

Figure III-107: (a) Assembly of a diffusion multiple; (b) diffusion multiple after being hot isostatic pressed; (c) design in FY 2014; and (d) design in FY 2015.

The Mg atomic mobility database of the Mg-Al-Zn-Mn-Sn-Ca-Sr-Nd-Zr system was updated based on new diffusivities. The CALPHAD method was used to assess the atomic mobility of each element by using the new data from this work and literature. Empirical methods were used to obtain the unavailable diffusivities for hypothetic atomic mobility parameters.

Precipitation

The as-cast Mg-7Al-2Sn alloys were solution-treated and aged at 200°C for precipitation. The samples were cut into discs, grinded, punched, and polished in a solution of lithium chloride, magnesium perchlorate, 2-butoxy-ethanol, and methanol in a twin jet polishing machine. TEM was used to characterize the microstructure. Convergent beam electron diffraction was used to measure the thickness of the peak-aged sample for calculating the number density of the precipitates. The precipitation model known as the Kampmann-Wagner-numerical model [3] implemented in the PanPrecipitation module of Pandat software [4] was used to simulate the precipitation. The PanMagnesium thermodynamic database and Mg atomic mobility database established in this work were used to generate driving force, phase equilibria, and diffusivity for the simulation.

Solidification

Phase Formation and Microsegregation in Mg-Al-Ca-Sn Alloys

The phase formation and microsegregation of four directionally solidified Mg-Al-Ca-Sn alloys with a cooling rate of 0.4 K/s were measured using scanning electron microscope/energy-dispersive X-ray diffraction spectroscopy (SEM/EDS) and EPMA. Concentrations of Al, Ca, Sn, and Mg on 400 points uniformly distributed in an area covering several primary (Mg) grains were measured by EPMA and data were analyzed to extract microsegregation profiles of Al, Ca, and Sn in primary (Mg).

Solidification of the AE42 Alloy

Three AE42 alloys were prepared under different cooling conditions of HPDC, gravity casting using steel mold, and furnace cooling. Temperatures during solidification in the latter two were measured by thermo-couple and average cooling rates were derived. The microstructures were characterized by X-ray diffraction, SEM/EDS, and TEM.

Modified Scheil-Gulliver model

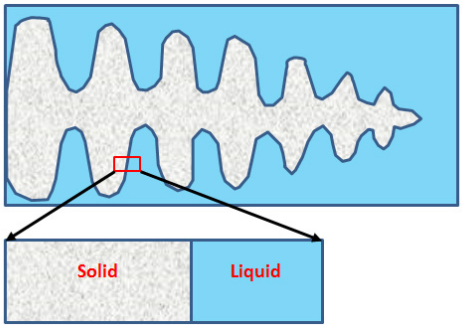

Figure III-108: A schematic diagram of dendrites in the solid and liquid region.

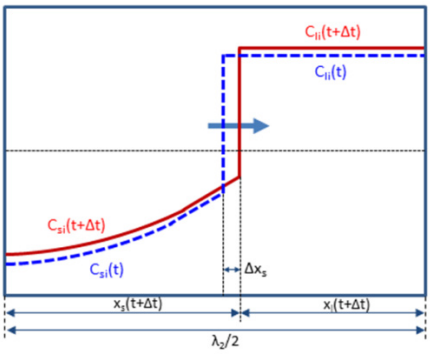

Figure III-109: Concentration distribution at times t and t+Δt.

A similar numerical micro-model developed by Yan [5] is employed; this model is basically a modified Scheil-Gulliver model that incorporates back diffusion, undercooling, and dendrite arm coarsening. The only major simplification of the model is that the geometry of dendrites is assumed to be geometrically similar throughout solidification (i.e., plate, cylinder, or sphere). A one-dimensional morphology is used to describe the growing secondary dendrite arms (Figure III-108). The modeling region is focusing on the small area between two secondary dendrite arms. Figure III-109 shows the schematic concentration distribution at times t and t+Δt using the modified Scheil-Gulliver model considering back diffusion.

Results and Discussion

A large quantity of diffusivities was obtained for the Mg-Al, Zn, Sn, Nd, and Ca systems. Table III-15 shows a summary of progress. Diffusivities have been extracted for Mg-Al and Mg-Sn systems at high and low temperatures. Diffusivities for the Mg-Zn system have been determined at high temperatures. Two sets and one set of diffusivities were extracted for the Mg-Ca and Mg-Nd systems, respectively. Mg-17.4wt.%Nd and Mg-15wt.%Ca alloys were used because pure Nd is not easily available and pure Ca is too reactive. The solubility of Sr in (Mg) is extremely low, which leads to difficulty in accurately measuring the diffusion profile by EPMA. A better method should be developed. The reaction of Mn and Zr with Mg is weak and new diffusion samples need to be designed.

Figure III-110 through Figure III-113 show some representative results. Figure III-110a is the back-scattered electron (BSE) image with an EPMA scanning line across the phase boundary of liquid-solid diffusion couple for Mg-Al system, while Figure III-110b is a typical solid-solid diffusion interface with formation of two Mg-Al compounds. The forward simulation was employed to extract diffusivities from the diffusion profiles measured by EPMA. Figure III-111 presents interdiffusivities and impurity diffusivities for the Mg-Al system from 275 to 600°C. The interdiffusivities have good self-agreement among results from either liquid-solid diffusion couples or diffusion multiples. The Al impurity diffusivities in (Mg) were consistent with most of other studies from experiment or first principle calculations [6-10]. The reliability of the novel liquid-solid diffusion couple approach has been proved.

Diffusivities for the Mg-Sn systems at high and low temperatures are shown in Figure III-112. This is the first time that interdiffusivities of (Mg) in the Mg-Sn system have been measured. The dependence of interdiffusivity on Sn composition is rather weak. The solubilities of Nd and Ca in Mg are very low compared to the above solutes (e.g., Al, Zn, and Sn). Thus, it is reasonable to assume that diffusivity is a constant. The impurity diffusivities of Ca in (Mg) were firstly extracted (Figure III-113). There were no experimental studies on Ca in the literature. Our low-temperature data were lower than the first principle calculation results [9-10]. More measurements on Nd and Ca will be carried out to verify present data and extract new data at other temperatures.

Table III-15: Diffusion samples prepared or analyzed this year.

	System	Heat Treatment
Liquid-solid diffusion couples for high-temperature experiments	Mg-Zn	450°C 8 hours 500°C 6 hours 550°C 6 hours
	Mg-Al	450°C 8 hours 500°C 6 hours 550°C 6 hours 600°C 4 hours
	Mg-Sn	500°C 30 hours 550°C 24 hours 600°C 4 hours
	Mg-Nd	630°C 10 hours
	Mg-Sr	630°C 10 hours 600°C 16 hours
	Mg-Ca	630°C 12 hours
	Mg-Mn	500°C 192 hours 550°C 96 hours 630°C 10 hours
	Mg-Zr	630°C 10 hours
Diffusion multiples for low-temperature experiments	Mg-Al	275°C 1,760 hours 315°C 790 hours 375°C 210 hours 420°C 100 hours
	Mg-Ca	375°C 210 hours 420°C 100 hours
	Mg-Sn	375°C 210 hours 420°C 100 hours

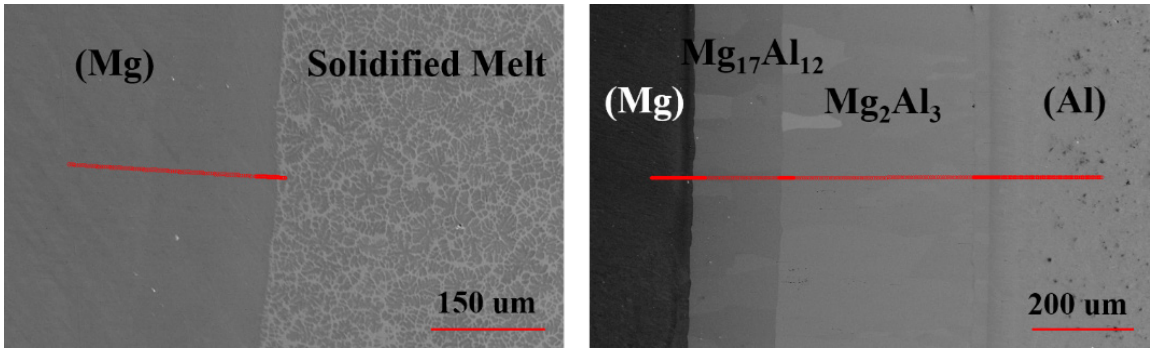

Figure III-110: BSE images with EPMA scanning lines for the Mg-Al system: (a) liquid-solid diffusion couple, 550°C, 6 hours; and (b) Mg-Al system in the diffusion multiple, 420°C, 100 hours.

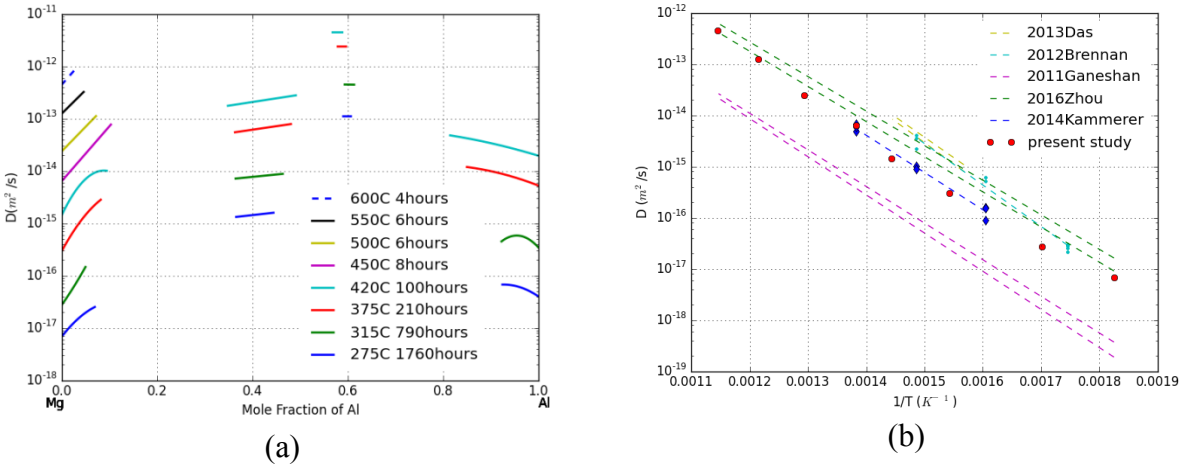

Figure III-111: Diffusivity of the Mg-Al system: (a) interdiffusivity; (b) impurity diffusivity of al in (Mg) from the present work and refs [6-10].

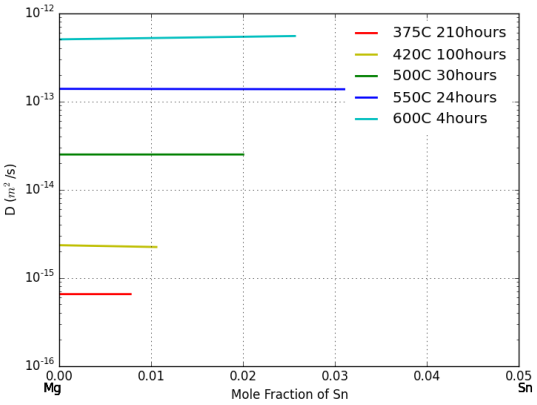

Figure III-112: Interdiffusivity of (Mg) in the Mg-Sn system.

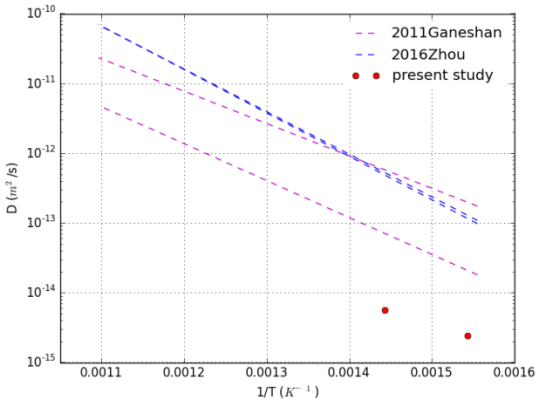

Figure III-113: Impurity diffusivity of Ca in (Mg) from the present work and [9-10].

Update of the Mg Atomic Mobility Database

The atomic mobilities of the elements for Al, Zn, Sn, and Ca in the database were re-optimized based on new diffusivities obtained in FY 2015. Figure III-114 shows the calculated interdiffusivities of (Mg) in the Mg-Zn system can reproduce experimental data in this work and literature [8]. Figure III-115 shows the calculated impurity diffusivities of the elements in Mg. The database is continuously being updated according to the new experimental data.

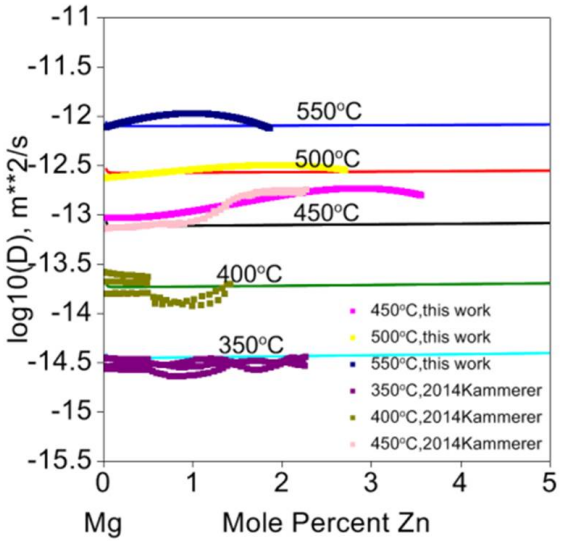

Figure III-114: Calculated interdiffusivities of (Mg) in the Mg-Zn system with date from this work and literature [8].

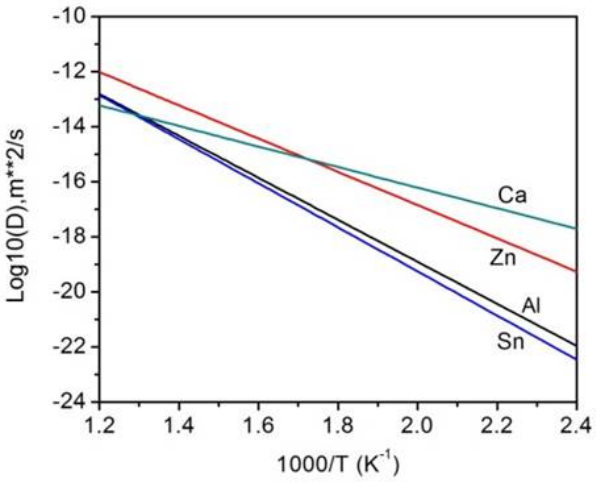

Figure III-115: Calculated impurity diffusivities of the elements in Mg.

Precipitation

Figure III-116 shows the bright field TEM images of Mg-7Al-2Sn alloys at 200ºC for 10, 30, and 72 hours. The number of precipitates is growing as time increases; coarsening already happens at 72 hours.
Figure III-117 shows the high-angle annular dark field-scanning transmission electron microscope (HAADF-STEM) image of the sample aged for 30 hours, where the Mg_2Sn and $Mg_{17}Al_{12}$ precipitates can be distinguished by the contrast. According to the image, the precipitation of Mg_2Sn is comparable with that of $Mg_{17}Al_{12}$ based on counting the numbers of Mg_2Sn and $Mg_{17}Al_{12}$ precipitates in the Mg-7Al-2Sn alloy aged at 200ºC for 30 hours. Convergent beam electron diffraction was used to measure the foil thickness for calculating the number density. As shown in Figure III-118, a previous simulation by directly combining the parameters from the simulations on Mg-Al and Mg-Sn binary alloys shows the number density of $Mg_{17}Al_{12}$ is close to experimental data. However, the number density of Mg_2Sn is underestimated, which means the parameter for Mg_2Sn should be adjusted. The result indicates the precipitation of Mg_2Sn is enhanced significantly in the ternary alloy. According to the simulation on the Mg-Sn binary alloy and the TEM analysis shown in Figure III-119, the precipitation of Mg_2Sn in the binary alloy is very sluggish. By comparison, the result demonstrates that Al can accelerate precipitation of Mg_2Sn in the ternary alloy.

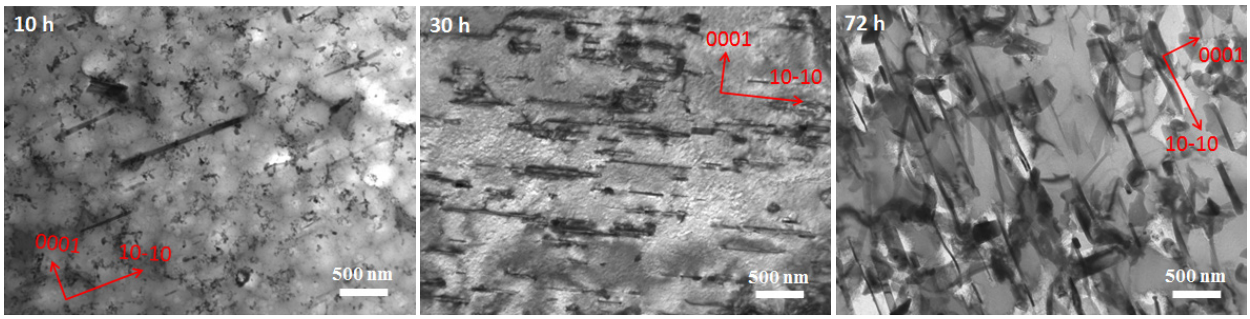

Figure III-116: Bright field TEM images of aged Mg-7Al-2Sn alloys at 200ºC for 10, 30, and 72 hours with the beam direction close to <11-20>.

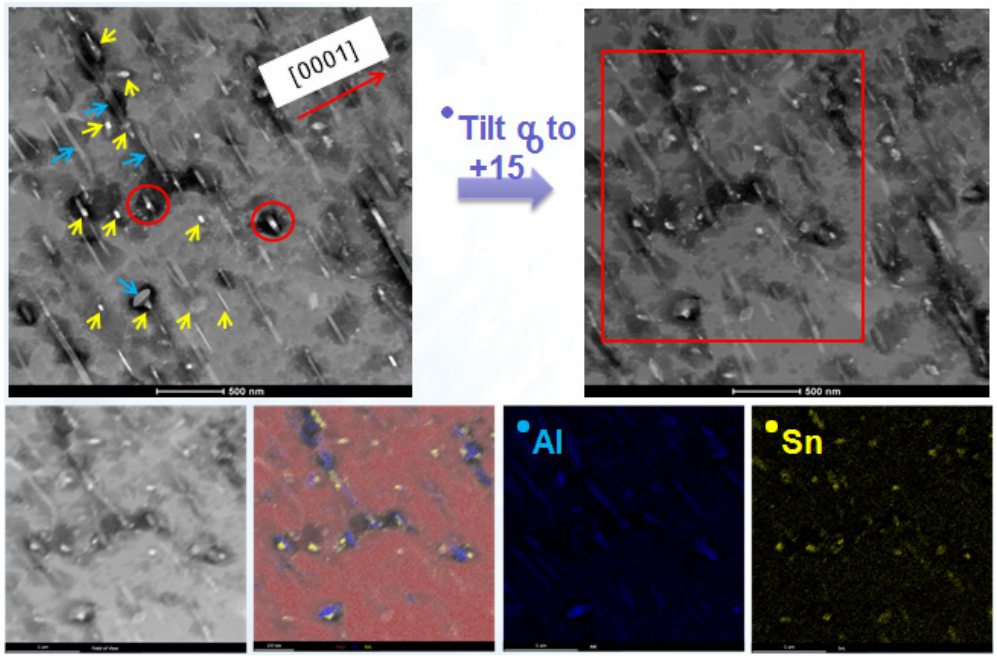

Figure III-117: HAADF-STEM image taken with beam direction ~ <11-20> (aged for 30 hours).

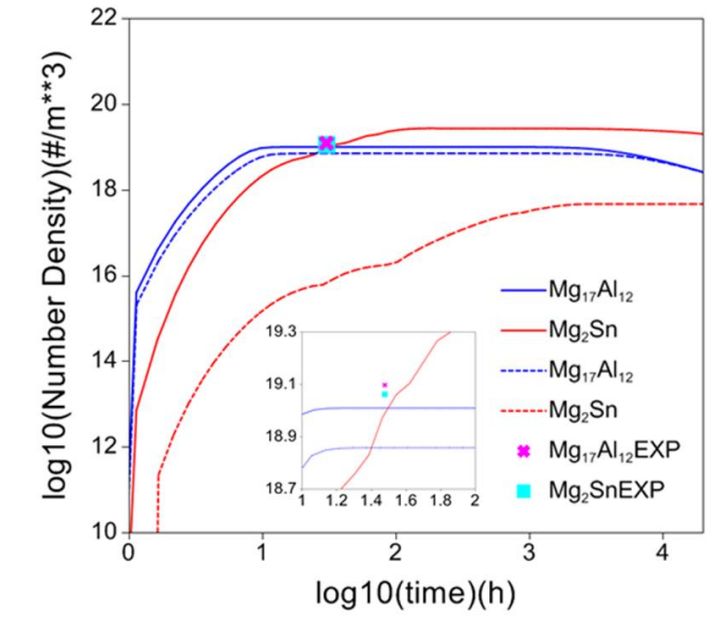

z

Figure III-118: Simulation of the precipitation of the $Mg_{17}Al_{12}$ and Mg_2Sn in Mg-7Al-2Sn alloys during aging at 200°C. The dash line shows the previous simulation by directly combing parameters from the simulations on Mg-Al and Mg-Sn alloys, while solid lines are from present simulations.

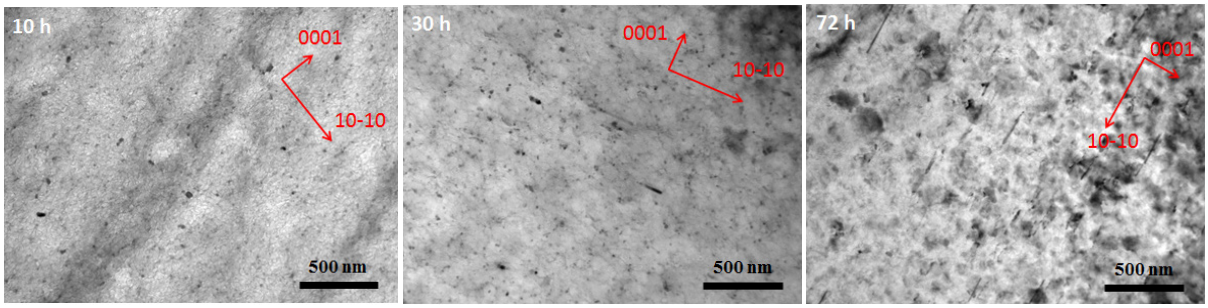

Figure III-119: Bright field TEM images of aged Mg-2Sn alloys at 200ºC for 10, 30, and 72 hours with the beam direction close to <11-20>.

Solidification

Phase Formation and Microsegregation in Mg-Al-Ca-Sn Alloys

The Mg-Al-Ca-Sn alloys were characterized by SEM/EDS and EPMA to get phase formation and microsegregation. Results were compared with the Scheil-Gulliver simulation. Figure III-120 shows the microstructure of Mg-7.3Al-1.47Ca-0.79Sn and Figure III-121 presents the solidification paths from the Scheil-Gulliver and equilibrium simulations. The phase formation agrees with the Scheil-Gulliver simulation. The primary phase is (Mg), followed by formation of CaMgSn in the early stage. Ternary compound AlCaMg and $Mg_{17}Al_{12}$ form by eutectic reactions in the later stage. Figure III-122 shows the concentration distributions of Al, Ca, and Sn in primary (Mg). In Figue 17a, the concentration of Al is higher than that of the Scheil-Gulliver simulation. Distribution of Ca is somewhat uniform in Figure III-122b. In Figure III-122c, the microsegregation of Sn deviates from simulation. It should be mentioned that in the early stage of the growth of (Mg), another compound CaMgSn will also grow simultaneously, which may influence redistribution of Ca and Sn.

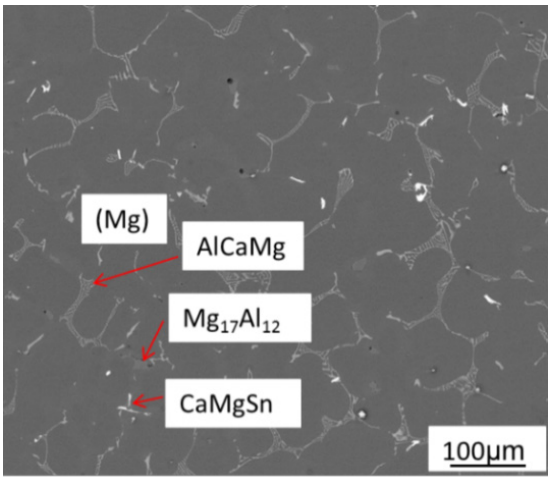

Figure III-120: Bright field TEM images of aged Mg-2Sn alloys at 200ºC for 10, 30, and 72 hours with the beam direction close to <11-20>.

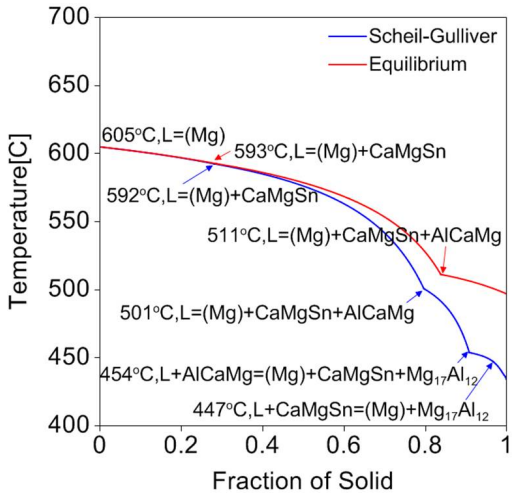

Figure III-121: Solidification paths from Scheil-Gulliver and equilibrium simulations for the Mg-7.3Al-1.47Ca-0.79Sn alloy.

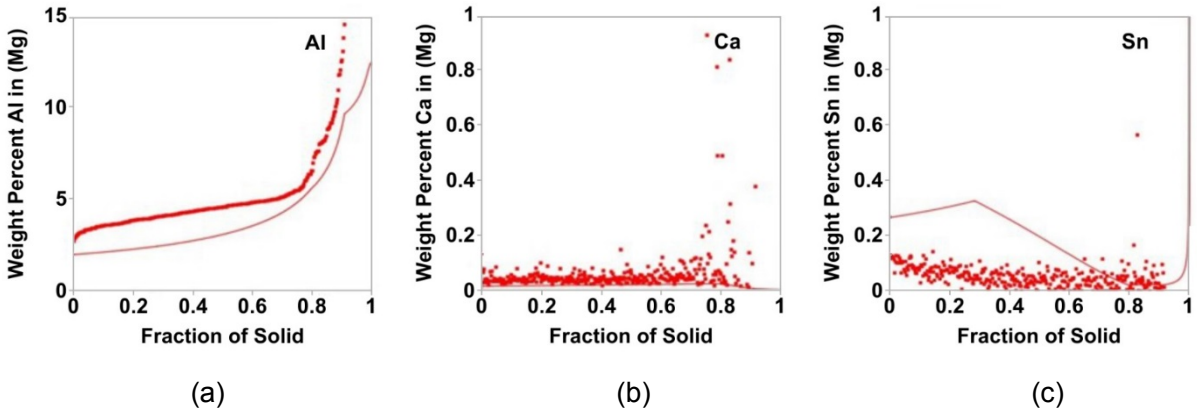

Figure III-122: Distributions of the alloying elements in primary (Mg) with the Scheil-Gulliver simulations for the Mg-7.3Al-1.47Ca-0.79Sn alloy: (a) Al, (b) Ca, and (c) Sn.

Solidification of AE42 Alloys

According to the combination of the analysis, including x-ray diffraction, SEM/EDS, and TEM, the dominant intermetallics in the alloys with high cooling rates (i.e., HPDC and steel mold casting) is lamellar $Al_{11}RE_3$ and particulate Al_2RE is the minor phase. In the sample prepared by furnace cooling, the amount of Al_2RE phase is increased significantly and comparable with that of $Al_{11}RE_3$, which means high cooling rate favors the formation of $Al_{11}RE_3$ and decreases the Al_2RE. In addition, the high cooling rate refines the microstructure. The eutectic structure consisted of $Mg_{17}Al_{12}$ and (Mg) phase was observed by SEM/EDS in the sample prepared by furnace cooling (Figure III-123a). The structure was cut by focus ion beam and further confirmed by TEM analysis (Figure III-124). By carefully adjusting the brightness and contrast in the SEM/EDS analysis, the $Mg_{17}Al_{12}$ was also observed in the sample prepared by steel mold casting and confirmed by EDS analysis (Figure III-123b). The $Mg_{17}Al_{12}$ phase in the sample prepared by HPDC was not observed, which does not agree with the Scheil-Guiliver simulation (Figure III-125). Analysis of the discrepancy indicates that more Al can be trapped in (Mg) during the HPDC process.

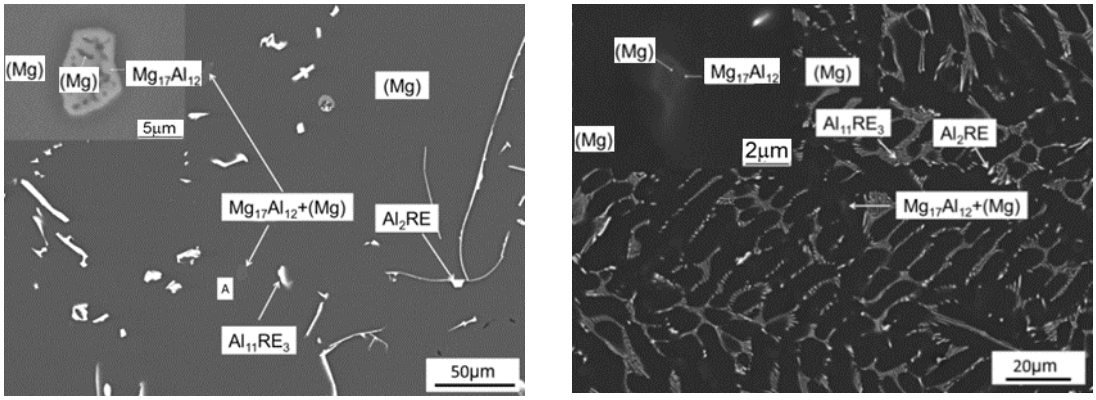

Figure III-123: BSE images of the AE42 samples: (a) furnace cooling and (b) steel mold casting.

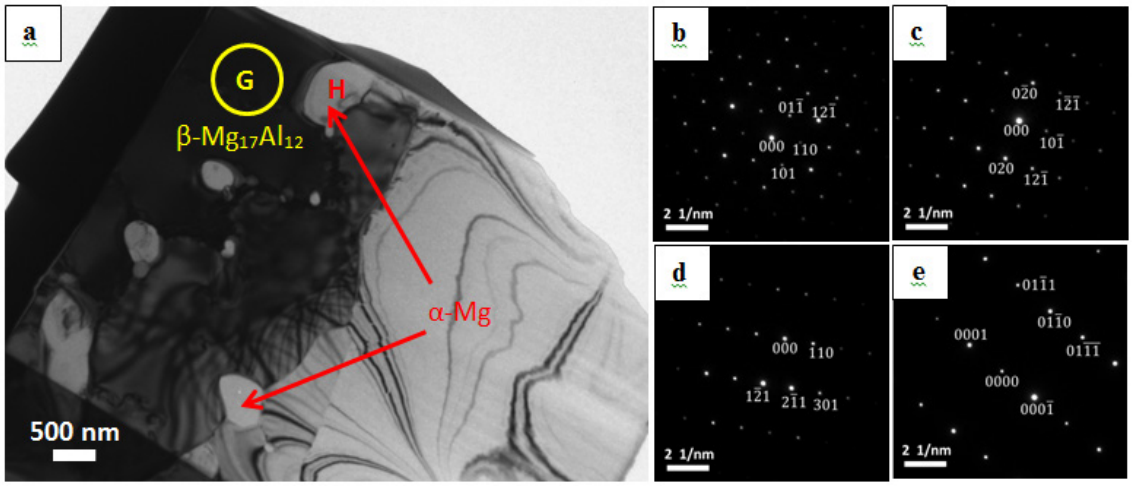

Figure III-124: (a) TEM image of $Mg_{17}Al_{12}$; (b)(c)(d) are three different diffraction patterns of area G circled in (a) (B=<1̄11>, <011>, <311>, respectively); (e) is the diffraction patterns of area H marked in (a)

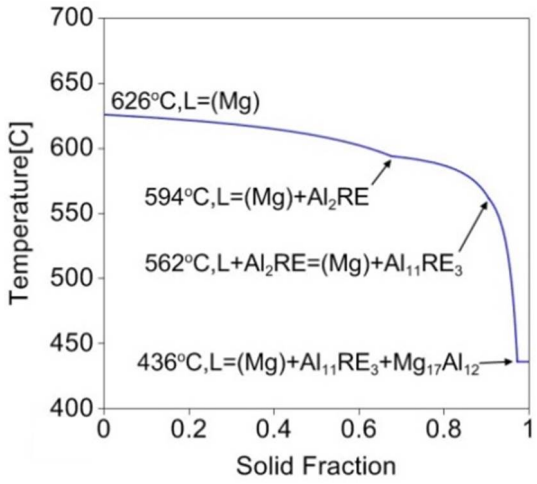

Figure III-125: Calculated solidification path of the AE42 alloy. The calculation is based on composition of Mg-4Al-2Ce.

Modified Scheil-Gulliver Model

Project partner CompuTherm LLC is testing the modified Scheil-Gulliver model, taking back diffusion into account. Currently, the testing on binary systems shows reasonable results. As shown in Figure III-126a, the calculated solidification paths under different cooling rates for Al-6.7wt.% Mg alloy agree with available experimental data. Figure III-126b shows results for the Mg-4Al alloy. As the cooling rate is increased, the solidification path gets closer to the Scheil-Gulliver simulation.

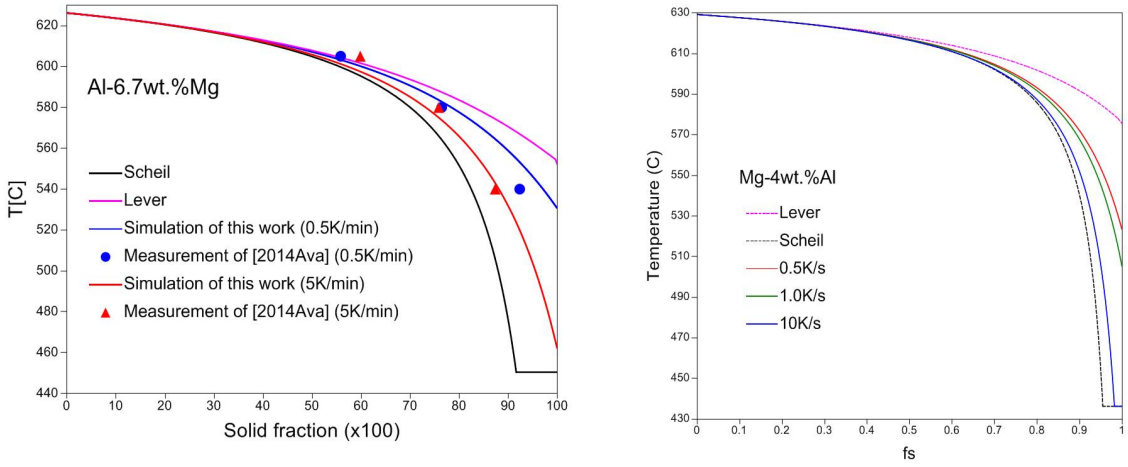

(a) (b)

Figure III-126: Simulated solidification paths under different cooling rates: (a) Al-6.7wt.%Mg with experimental data and (b) Mg-4 wt.%Al.

Technology Transfer Path

The diffusivities obtained from this work significantly improve the Mg alloys diffusivity database, which is rather inadequate due to scarcity of literature data. These data can assist design of high-performance Mg alloys using an integrated computational materials engineering approach.

The study of precipitation of the Mg-7Al-2Sn alloy indicates that the precipitation of Mg_2Sn can be enhanced, which means the mechanical properties of as-cast Mg-7Al-2Sn can be improved by aging.

The microsegregation experiment on directionally solidified Mg-Al-Ca-Sn samples provides microsegregation information of the alloying element in (Mg), which is inadequate for Mg alloys. The investigation of the AE42 alloy demonstrates the advantage of the HPDC process. The modified Scheil-Gulliver model can be used to predict a more accurate solidification path and microsegregation for practical use.

Conclusions

Large quantities of diffusivities were extracted by experiment and forward simulation. These data significantly improve the current Mg alloys diffusivity database. The Mg atomic mobility database was updated based on present experimental work.

The precipitation of the Mg-7Al-2Sn alloy during aging was investigated and results show that Mg_2Sn precipitation can be improved in the ternary alloy. Other elements that can improve the precipitation of the Mg-Al-Sn alloys will be investigated during future research.

Microsegregations in directionally solidified Mg-Al-Ca-Sn alloys were characterized to provide microsegregation information of alloying elements in (Mg). Besides directional solidification, the undirectional solidifications of the AE42 alloy prepared by different cooling conditions were investigated and results demonstrate that HPDC cannot only refine the microstructure, but also dissolve more (Al) in (Mg). The modified Scheil-Gulliver model has been successfully tested on the binary Mg-Al system and will be extended to multicomponent Mg alloys.

References

1. Q. Zhang and J. C. Zhao, 2013, "Extracting interdiffusion coefficients from binary diffusion couples using traditional methods and a forward-simulation method," *Intermetallics* 34; pp. 132-141.
2. N. Saunders and A. P. Miodownik, 1998, *CALPHAD (Calculation of Phase Diagrams): A Comprehensive Guide*, Elsevier.
3. R. Kampmann and R.Wagner, 1983, "Kinetics of precipitation in metastable binary alloys-theory and application to Cu-1.9 at % Ti and Ni-14 at % Al," in *Decomposition of Alloys: the early stages, Proceedings of the 2nd Acta-ScriptaMetallurgica Conference,* P. Haasen; V. Gerold; and R. Wagner (eds.), Pergamon Press; pp. 91-103.
4. W. Cao et al., 2009, "PANDAT software with PanEngine, PanOptimizer and PanPrecipitation for multi-component phase diagram calculation and materials property simulation," *CALPHAD*, 33(2); pp. 328-342.
5. X. Yan, 2001, "Thermodynamic and Solidification Modeling Coupled with Experimental Investigation of the Multicomponent Aluminum Alloys," PhD thesis, University of Wisconsin-Madison.
6. S. Brennan et al.,2012, "Aluminum impurity diffusion in magnesium," *Journal of phase equilibria and diffusion,* 33; pp. 121-125.
7. S. Das et al., 2013, "Anisotropic diffusion behavior of Al in Mg: diffusion couple study using Mg single crystal," *Metallurgical and Materials Transactions*, 44; pp. 2539-2547.
8. C. Kammerer et al., 2014, "Interdiffusion and impurity diffusion in polycrystalline Mg solid solution with Al or Zn," *Journal of Alloys and Compounds*, 617; pp. 968-974.
9. S. Ganeshan et al., 2011, "First-principles calculations of impurity diffusion coefficients in dilute Mg alloys using the 8-frequency model," *Acta Materialia,* 59; pp. 3214-3228.
10. B. Zhou et al., 2016, "Diffusion coefficients of alloying elements in dilute Mg alloys: A comprehensive first-principles study," *Acta Materialia*, 103: pp. 573-586.

Bibliography

A. A. Luo; W. Sun; W. Zhong; and J. C. Zhao, 2015, "Computational Thermodynamics and Kinetics for Magnesium Alloy Development," *Advanced Materials and Processes*, 173(1); pp. 26-30.

W. H. Sun; C. Zhang; A. D. Klarner; W. Cao; and A. A. Luo, 2015, "Simulation of concurrent precipitation of two strengthening phases in magnesium alloys," *Magnesium Technology*, V. Michele and V. Manuel et al. (eds.), *TMS*; pp. 289-293.

W. Sun; C. Zhang; A. D. Klarner; W. Cao; and A. A. Luo, 2015, "Simulation of Concurrent Precipitation of Two Strengthening Phases in Magnesium Alloys," *Magnesium Technology 2015, TMS 2015 144th Annual Meeting & Exhibition*, March 15 through 19, 2015, Orlando, Florida.

W. Sun; C. Zhang; W. Zhong; A. A. Luo; J. C. Zhao, 2015, "Investigation of Microstructure and Microsegregation during Solidification of Mg Alloys," *MS&T2015*, October 4 through 8, 2015, Columbus, Ohio.

W. Zhong; W. Sun; J. C. Zhao; and A. A. Luo, 2015, "Establishment of Mg Diffusivity Database Using Diffusion-Multiple and CALPHAD Approaches," *Computational Thermodynamics and Kinetics, TMS 2015 144th Annual Meeting & Exhibition*, March 15 through 19, 2015, Orlando, Florida.

W. Zhong; W. Sun; J. C. Zhao; and A. A. Luo, 2015, "Establish a Mg Diffusivity Database using Diffusion Multiples and Liquid-Solid Diffusion Couples," *MS&T2015*, October 4 through 8, 2015, Columbus, Ohio.

III.13. Phase Transformation Kinetics and Alloy Microsegregation in High-Pressure Die Cast Magnesium Alloys –University of Michigan

Project Details

John E. Allison, Principal Investigator
University of Michigan (UM)
500 South State Street
Ann Arbor, MI 48109
Phone: 734-971-3989
E-mail: johnea@umich.edu

Aaron Yocum, Project Officer
National Energy Technology Laboratory
3610 Collins Ferry Road
P.O. Box 880
Morgantown, WV 26507-0880
Phone: 304-285-4852
E-mail: aaron.yocum@netl.doe.gov

William Joost, Technology Area Development Manager
U.S. Department of Energy
1000 Independence Avenue, SW
Washington, DC 20585
Phone: 202-287-6020
E-mail: william.joost@ee.doe.gov

Contractor: UM
Contract No.: DE-EE0006434

Executive Summary

High-pressure die casting (HPDC) is the predominant manufacturing method for magnesium (Mg) alloy automotive components; however, the phase transformation kinetics that occur in this process are, at best, poorly understood. Cooling rates during solidification in HPDC are far from equilibrium and have not been the subject of significant quantitative research. Improved understanding of microstructural kinetics and alloy segregation are required to refine industrial processes and to develop new alloy systems. Improvements in this understanding will be accomplished by combining systematic and quantitative experiments and state-of-the-art modeling and simulation.

The primary objectives of this project are as follows:

- To conduct a systematic, quantitative study of phase transformation kinetics and microsegregation in HPDC Mg alloys under conditions that occur in automotive component production.
- To conduct a systematic, quantitative study of phase transformation kinetics and changes in microsegregation during solution treatment and aging of super vacuum die cast (SVDC) Mg alloys.
- To develop physics-based phase transformation kinetics micro-models that quantitatively capture microstructural evolution and microsegregation during HPDC and heat treatment of Mg alloys.
- To transfer this knowledge to industry and the wider research community through these micro-models and through experimental data that will be stored in the National Institute of Standards and

Technology (NIST)/U.S. Department of Energy (DOE) Office of Energy Efficiency and Renewable Energy (EERE) Advanced Automotive Cast Magnesium Alloys Repository (accessed January 6, 2016: https://materialsdata.nist.gov/dspace/xmlui/handle/11256/4) and in a new repository (i.e., The Materials Commons).

To accomplish the above goals, a systematic and comprehensive experimental study is being combined with computational modeling and simulation.

UM is conducting all experimental characterization of microstructures and microsegregation in materials. Microstructure and chemical compositions of as-cast HPDC Mg alloys are being quantitatively and systematically characterized using a combination of methods, including electron probe microanalysis (EPMA), optical, scanning electron microscopy (SEM), and transmission electron microscopy (TEM). This comprehensive characterization has been initiated in AM60 and AZ91 cast at Tsinghua University and in AM40, AM50, AM60, and AM70 plates provided by the Ford Research and Innovation Center at MagTech Corporation. These initial results have shown that while Scheil solidification kinetics appear to describe the aluminum (Al) segregation profile at mid-thickness in 2.5 and 5.0-mm plates, Scheil models do not describe the microsegregation that occurs during rapid solidification at the edge of the plate. Continued characterization will provide new insights in understanding phase transformation kinetics during high cooling rate solidification, micro-segregation of different alloying elements, and the impact of casting parameters like cooling rate and casting thickness on as-cast microstructure and microstructure evolution during subsequent heat treatment processes. Ford Motor Company and Professor Shoumei Xiong of Tsinghua University in Beijing China are providing support to this project by supplying HPDC/SVDC Mg plates and complex-shaped castings.

Based on quantitative experimental results, a solidification micro-model is being developed in close collaboration with Dr. Mei Li at Ford Motor Company to predict evolution of the primary microstructure features of as-cast HPDC Mg alloys. Micro-models will also be developed to predict dissolution of eutectic phases and redistribution of alloying elements during solution treatment and precipitation of strengthening phases during aging. These micro-models will be validated using quantitative results obtained on complex-shaped HPDC/SVDC casting of AM50 and AZ91.

Experimental data and models will be made available to the technical community via the NIST DOE-EERE Advanced Automotive Cast Magnesium Alloys Repository and the Materials Commons (i.e., a new knowledge repository under development within the UM Center for PRedictive Integrated Structural Materials Science [PRISMS] funded by DOE Basic Energy Sciences [BES]).

This project is planned to span 4 years and will be conducted in one phase consisting of six tasks.

Accomplishments

- Produced plates of ternary Mg alloys AM60B, AM70, and AZ91 using a super vacuum HPDC technique (Fiscal Year [FY] 2014).
- Completed initial precision MagmaSoft HPDC simulation of the SVDC casting conditions and geometry (FY 2014).
- Established reliable and consistent EPMA and metallographic procedures on the above ternary alloys (FY 2014).
- Developed a Monte Carlo “Forward Model” simulation of microsegregation behavior as measured by EPMA in HPDC Mg Alloys (FY 2014).
- Characterized microsegregation behavior in HPDC AM60B (of two plate thicknesses), AM70, and AZ91, as well as in Mg-9 Al produced under different casting conditions (FY 2014).
- Characterized microsegregation behavior in HPDC AM40, AM50, AM60, and AM70 (of two plate thicknesses) (FY 2015).

- Completed quantitative characterization of beta-phase area fraction in HPDC AM60B (FY 2014).
- Completed electron backscatter diffraction (EBSD) characterization of HPDC AM60B (of two plate thicknesses) and AZ91 as-cast microstructure (FY 2014).
- Completed EBSD characterization of HPDC Al-Mg (AM) series alloys (of two plate thickness) (FY 2015).
- Began characterization of externally solidified crystals in HPDC AM series alloys (FY 2015).
- Began to develop micro-model to predict microsegregation as a function of solidification front velocity (FY 2015).
- Determined that macrosegregation of Al exists in the as-cast plates and persists through solution treatment (FY 2015).

Future Directions

- Complete SVDC of Mg-Al binaries and Mg-Al-Mn, Mg-Al-Zn, Mg-Al-Ca, and Mg-Al-Sr ternaries.
- Complete phase transformation and microsegregation characterization of binaries and Mn and Zn ternaries.
- Complete phase transformation and microsegregation characterization of Ca and Sr ternaries and in complex casting of AM50 and AZ91.
- Complete study of precipitation kinetics and of eutectic phase transformation and microsegregation during heat treatment in selected binary and ternary alloys.
- Complete micro-model for Mg-Al binaries and Mg-Al-Mn, Mg-Al-Zn, Mg-Al-Ca, and Mg-Al-Sr ternaries for HPDC and heat treatment conditions.
- Incorporate experimental data for Mg-Al binaries and Mg-Al-Mn, Mg-Al-Zn, Mg-Al-Ca, and Mg-Al-Sr ternaries into the Materials Commons and release to public.
- Incorporate micro-model into the NIST/DOE-EERE Repository and the Materials Commons and release to public.

Technology Assessment

- Target: Improved predictive capabilities for HPDC Mg alloy microstructures and precipitation kinetics.
- Gap: There is a lack of quantitative information on phase transformations and microsegregation in HPDC Mg alloys.

Introduction

HPDC is used to manufacture over 90% of commercial Mg products [1]. This process is fast, economical, and produces complex thin-wall Mg components that cannot be fabricated by other means. The cooling rate involved in HPDC and SVDC are extremely high and range from 10 to 1000°C/s [2,3]. The solidification processes experienced in this region are far from equilibrium conditions. Under such extreme conditions, the solidification kinetics, phase transformations, and redistribution of alloying elements cannot be predicted using equilibrium thermodynamics or typical modifications to predict alloy partitioning (such as those represented by the Scheil model) [4]. There is essentially no systematic, quantitative information on eutectic phase formation or microsegregation in this region. This represents a major and distinct gap in our scientific understanding of this important manufacturing process.

The redistribution of alloying elements during non-equilibrium solidification leads to micro-scale segregation across the dendrite/cell and this micro-scale segregation is strongly dependent on the cooling rate. Although microsegregation has been the subject of a limited number of investigations in Mg alloys [5-11], there is no known microsegregation study for Mg alloys under HPDC conditions in open literature. Previous studies of microsegregation in Mg alloys have been obtained in directionally solidified castings or in samples cast under moderate cooling rate conditions.

Research on heat treatment of die cast Mg alloys has been limited due to the blistering that occurs when entrapped air expands during solution treatment. A new processing technology, SVDC for Al and Mg alloy components [12,13] significantly reduces or eliminates air entrapment, enabling heat treatment of die casting alloys and components. This advanced processing route offers new approaches for alloy development and improved Mg component properties. To-date, studies of the dissolution of eutectic phases and precipitate evolution during heat treatment of die cast alloys has been very limited [14-16] and there has been no systematic investigation of alloying and processing effects.

Precipitation hardening has the potential to be a major strengthening mechanism in heat treatable SVDC Mg alloys; however, SVDC Mg alloys have not yet been the subject of extensive studies. Gradients in alloy microsegregation and eutectic phase transformation that will be exhibited during SVDC will likely have a key influence on development of new alloy systems. In addition, quantitative characterization of precipitation microstructure under different heat treatment conditions is crucial for optimizing the effects of precipitation strengthening and building physics-based strengthening models.

Approach

Manufacture High Pressure Die Cast Plates and Complex-Shaped Castings and Simulation

The alloy compositions to be used in this study are shown in Table III-16. The alloy matrix was selected to include a wide range of compositions that will provide for optimization of current commercial alloys AM50/AM60 and AZ91, as well as pave the way for development of advanced, high-temperature Mg-Al-Ca and Mg-Al-Sr alloys. The castings are being provided by the Ford Research and Innovation Center at MagTech Corporation. These castings will be processed using SVDC casting procedures.

Table III-16: Planned alloy compositions and casting method used in this study.

Alloy Compositions (wt%)					
Mg	Al	Zn	Mn	Ca	Sr
Bal	3				
Bal	5				
Bal	9				
Bal	12				
Bal	9	0.5			
Bal	9	1			
Bal	9	2			
Bal	5		0.5		
Bal	5			3	
Bal	5				3

Die casting process controls linked with precision MagmaSoft HPDC simulation are being used to provide an estimate of the cooling rate as a function of location in casting and casting geometry. The simulations use a fine finite difference mesh (at least 5 to 10 elements through the cross section) and high-fidelity HPDC interfacial heat transfer coefficients for HPDC developed by Li and Allison and co-workers [17-19] to estimate cooling rate as a function of location.

Quantitative Characterization of Phase Transformation Kinetics and Microsegregation in High-Pressure Die Castings

Solidification phase transformation kinetics are being quantified using comprehensive microstructural characterization, including optical metallography and SEM coupled with advanced image analysis. The primary characteristics that are being quantified are eutectic volume fraction and size and alpha grain/cell size as a function of alloy, location, sample thickness, and process condition. Microsegregation profiles of alloying elements (i.e., Al, Mn, Zn, Ca, and Sr) versus solidification fraction are being quantitatively characterized using the EPMA scan method [5-7]. These microsegregation results are being compared with Calphad-based Scheil solidification estimates of alloy partitioning. Phase transformation kinetics and

microsegregation profiles will also be quantified in a complex casting of both AM50 and AZ91 to confirm the experimental findings and to validate the phase transformation kinetics micro-models described below.

Quantitative Characterization of Phase Transformation Kinetics and Microsegregation During Heat Treatment of Super Vacuum Die Castings

This task is to quantitatively characterize phase transformation kinetics and changes in microsegregation profiles during heat treatment of SVDC plates. Eutectic phase dissolution and changes in microsegregation are being characterized as a function of solution treatment time and temperature. Phase transformation kinetics are being quantified using quantitative microstructural characterization, including x-ray diffraction, optical metallography, and SEM. The primary characteristics that are being quantified are changes in eutectic volume fraction and size as a function of alloy, location, sample thickness, and process condition. Solution treatment-induced changes in microsegregation profiles of alloying elements (i.e., Al, Mn, Zn, Ca, and Sr) are being quantitatively characterized using the EPMA method. Precipitate evolution will be characterized in selected alloys using quantitative TEM techniques [15]. Precipitate evolution will be captured in the form of isothermal transformation curves. Beta phase dissolution kinetics and changes in microsegregation profiles will also be quantified in complex castings of AM50 and AZ91 to validate the phase transformation kinetics micro-models.

Develop Physics-Based Phase Transformation Kinetics Micro-Models that Quantitatively Capture Microstructural Evolution and Microsegregation During High-Pressure Die Casting and Heat Treatment

The quantitative and systematic results described above are being used to develop state-of-the-art phase transformation kinetics micro-models for HPDC alloys. A comprehensive solidification kinetics micro-model is being developed that considers solute trapping, dendrite arm coarsening, and dendrite tip undercooling and couples these calculations directly with multicomponent phase diagram computations. Given solidification conditions and alloy compositions, this micro-model will be capable of predicting secondary dendrite arm spacing, types and fractions of various non-equilibrium phases, liquid concentrations, and solute concentration profiles in the primary Mg phase under the extreme high-heat extraction conditions that exist in HPDC and SVDC. A dissolution kinetics micro-model will be developed to account for eutectic phase dissolution and compositional homogenization. In addition, an analytical precipitation kinetics micro-model for predicting precipitate kinetics will also be developed.

Transfer Project Knowledge to Industry and the Research Community through Micro-Models and Experimental Data Housed in the Materials Commons

The information produced during this study is being uploaded to the NIST/DOE EERE Advanced Automotive Cast Magnesium Alloys Repository and the Materials Commons (i.e., a knowledge repository that is under development within the UM-DOE PRISMS Center). Data schemas that are being developed are being done in coordination and consultation with Dr. Carrie Campbell at NIST.

Results and Discussion

The focus this past year has been on characterizing microstructure and microsegregation in a set of HPDC AM series plates provided by the Ford Research and Innovation Center at MagTech Corporation. Four alloys (nominally AM40, AM50, AM60, and AM70) were provided in two thicknesses (i.e., 2.5 and 5 mm). These are the same plates being used for another DOE project titled, “Mechanistic-Based Ductility Prediction for Complex Mg Castings.”

Microstructure Characterization of High-Pressure Die Casting Alloys

Externally solidified crystals (ESCs), which are sometimes referred to as externally solidified grains, form when liquid metal is poured into the shot sleeve prior to injection into the die. ESCs tend to become segregated in the center of the castings (Figure III-127). This is consistent with observations by Laukli [20]. In general, there are very few ESCs at the edge of the casting (particularly in the thinner plates). There tends to be more ESCs in the thicker plates, though the difference is not significant for most conditions. As ESCs solidify outside the mold, the cooling gradient and cooling rate are different for ESCs and for grains formed within the mold (called "in-mold grains"). Characterization of the ESCs is essential for informing our microsegregation simulations and models.

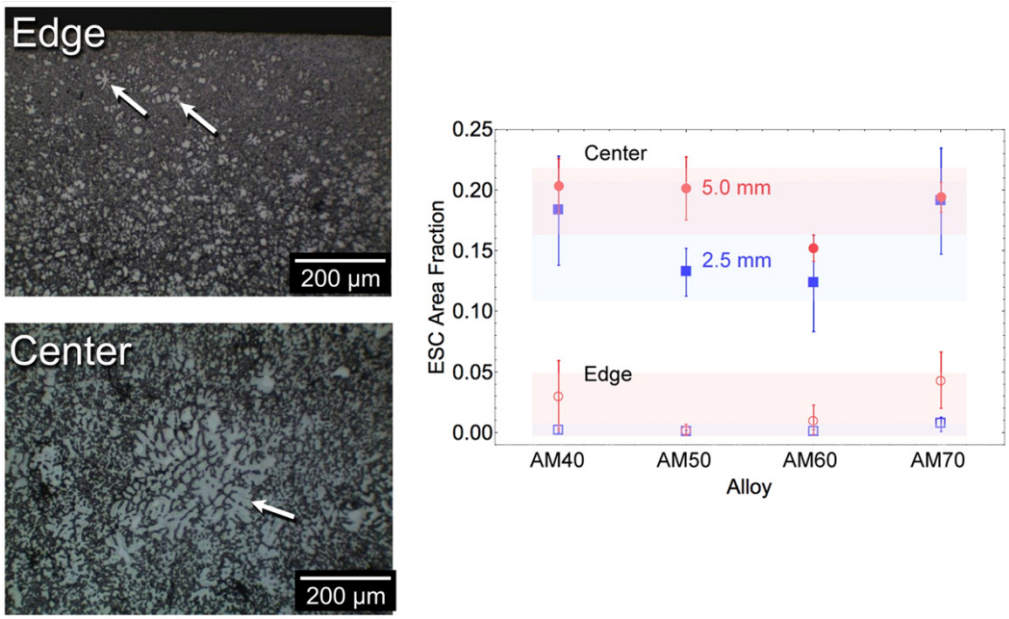

Figure III-127: Optical micrographs illustrating the size and distributions of ESCs at the edge and center of a 2.5-mm thick AM60 plate (left) and a summary of the ESC area fraction as a function of alloy, thickness, and location. Only ESCs greater than40 µm are included in this comparison.

Multiple EBSD maps have been collected for each sample. A set of EBSD maps for the 5.0-mm thick AM70 plate is shown in Figure III-128, as well as the grain size distribution for both plate thicknesses. The grain size distribution is independent of Al content for the AM alloys studied. The grain size distribution at the edge of the thin plates can be described by a lognormal distribution with an average diameter of 8 µm. The grain size distribution in both locations in the 5.0-mm plates and at the center of the 2.5-mm plates is comparable (Figure III-128). In these locations, the sum of two lognormal distributions, the first with an average diameter of approximately 10 µm and the second with an average diameter near 35 µm, better represent the distribution. The peak at the larger grain sizes is due to the presence of ESCs and leads to the shoulder on the right side of the distributions. The discrepancy between the optical and EBSD measurements is a result of both the improved ability to distinguish finer features via EBSD and user bias (large ESCs were avoided when setting up the EBSD scan region). The bimodal nature of these plates is less distinct than in the HPDC plates cast at Tsinghua University [21]. The Tsinghua and Ford plates use different die geometries and different casting conditions, both of which can affect ESC size and distribution [20].

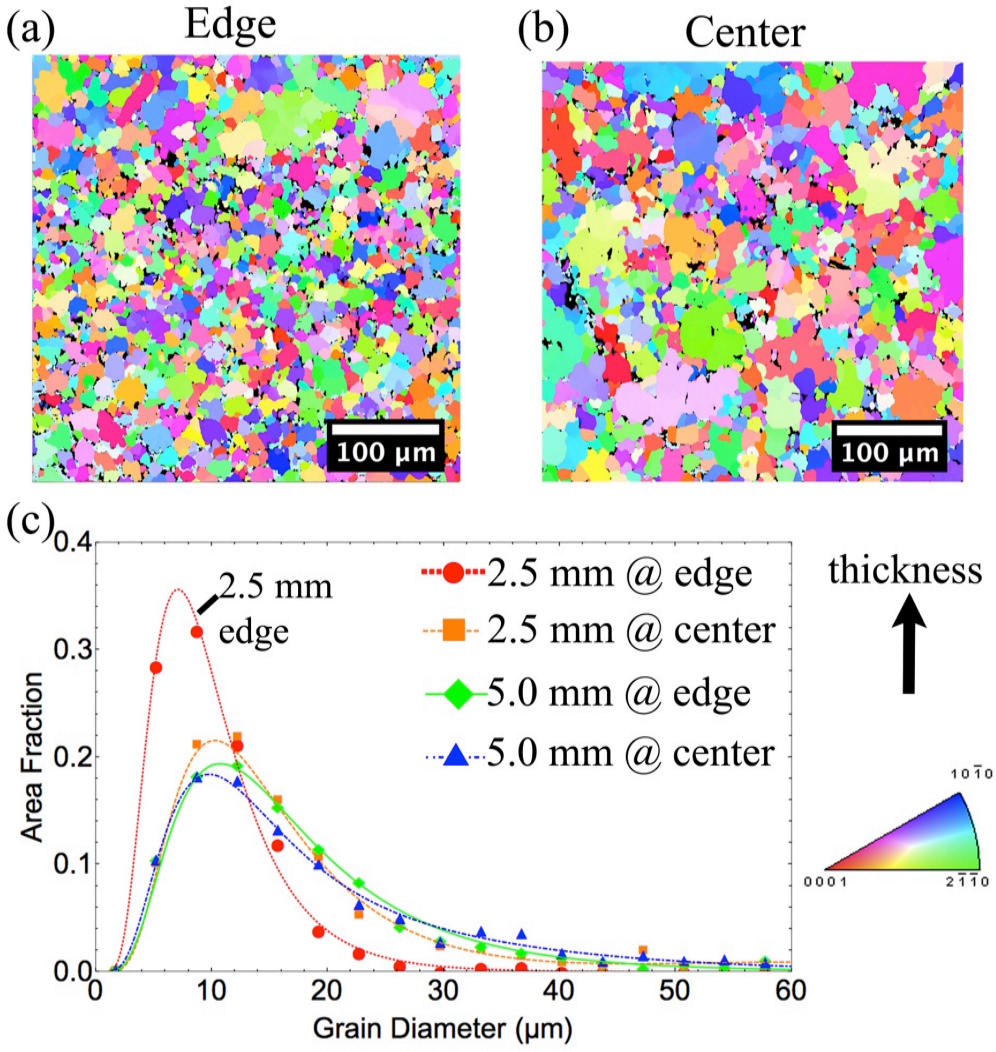

Figure III-128: EBSD inverse pole figure maps at the (a) edge and (b) center of 5.0-mm thick AM70 plates. (c) The grain size distributions at the edge and center for both thickness of the AM70 plate.

Microsegregation Behavior in High-Pressure Die Casting AM Series Alloys

Using the experimental procedures reported last year [21], microsegregation was studied in HPDC AM series alloys of two plate thicknesses. Microsegregation profiles were generated for all four AM series alloys in both plate thickness at the edge, near edge (i.e., 200 to 400 µm from the surface of the casting), and center locations. The number of EPMA point measurements used to reconstruct the profile ranges from 200 to 900.

A summary plot of the microsegregation in the thinner AM70 plates is shown in Figure III-129. At the center location, where the cooling rate is lowest, the EPMA microsegregation profile can be represented adequately with the Scheil model. As the measurement moves closer to the casting surface, agreement between measurement and prediction using the Scheil model is significantly reduced. The average Al concentration at four different times during solidification (i.e., 0, 25, 50, and 75% fraction solid [fs]) is used to summarize the microsegregation profiles, which is illustrated schematically by the boxes on the profile from the center location.

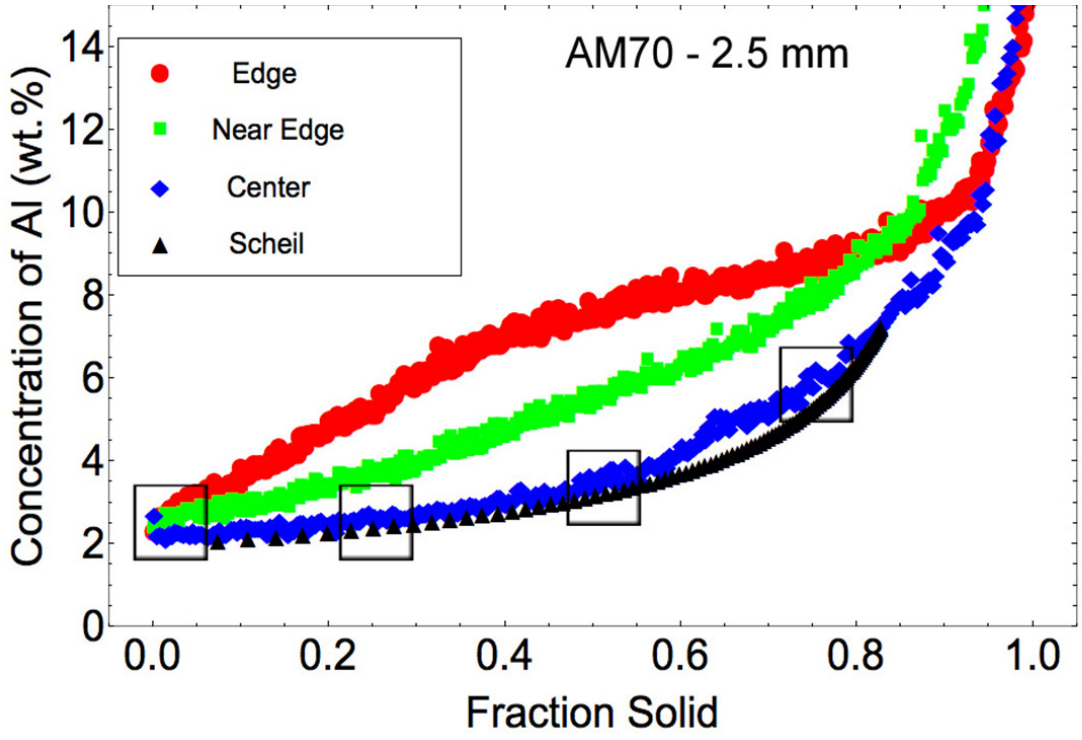

Figure III-129: Summary of microsegregation as a function of location in the 2.5-mm thick AM70 plates.

Microsegregation summary plots for the center and edge locations are shown in Figure III-130. Data points under the label "Tsinghua" are from HPDC AM60 and AZ91 plates provided by Tsinghua University. For clarity, the Tsinghua and Ford AM60 plates are offset slightly from 6 wt.% Al. The red, green, blue, and black lines are linear fits to the Scheil model results for each alloy at 0, 0.25, 0.5, and 0.75 fractions solid, respectively. In the future, these will be replaced by results from the HPDC microsegregation model. As noted earlier, the Scheil model is in good agreement with the microsegregation results at the center location (Figure III-130(a)). At the edge location (Figure III-130(b)), Scheil is only appropriate at the beginning of solidification (fs=0). Microsegregation behavior is largely independent of plate thickness and supplier.

To begin to study changes in micro/macrosegregation during heat treatment, several solution treatments (0.5, 1, 2, 20, and 44 hours at 420ºC) were performed on the 5.0-mm thick AM70 plates. The evolution of microsegregation at the center location is shown in Figure III-131(a). Microsegregation is eliminated after approximately 2 hours; however, macrosegregation, or differences between the locations, persists after 44 hours (Figure III-131(b)). Elimination of macrosegregation would require heat treatment durations that are impractical in an industry setting. As a consequence, in HPDC parts there will be less Al available in the bulk for solid solution strengthening or for aging in the heat-treatable SVDC components.

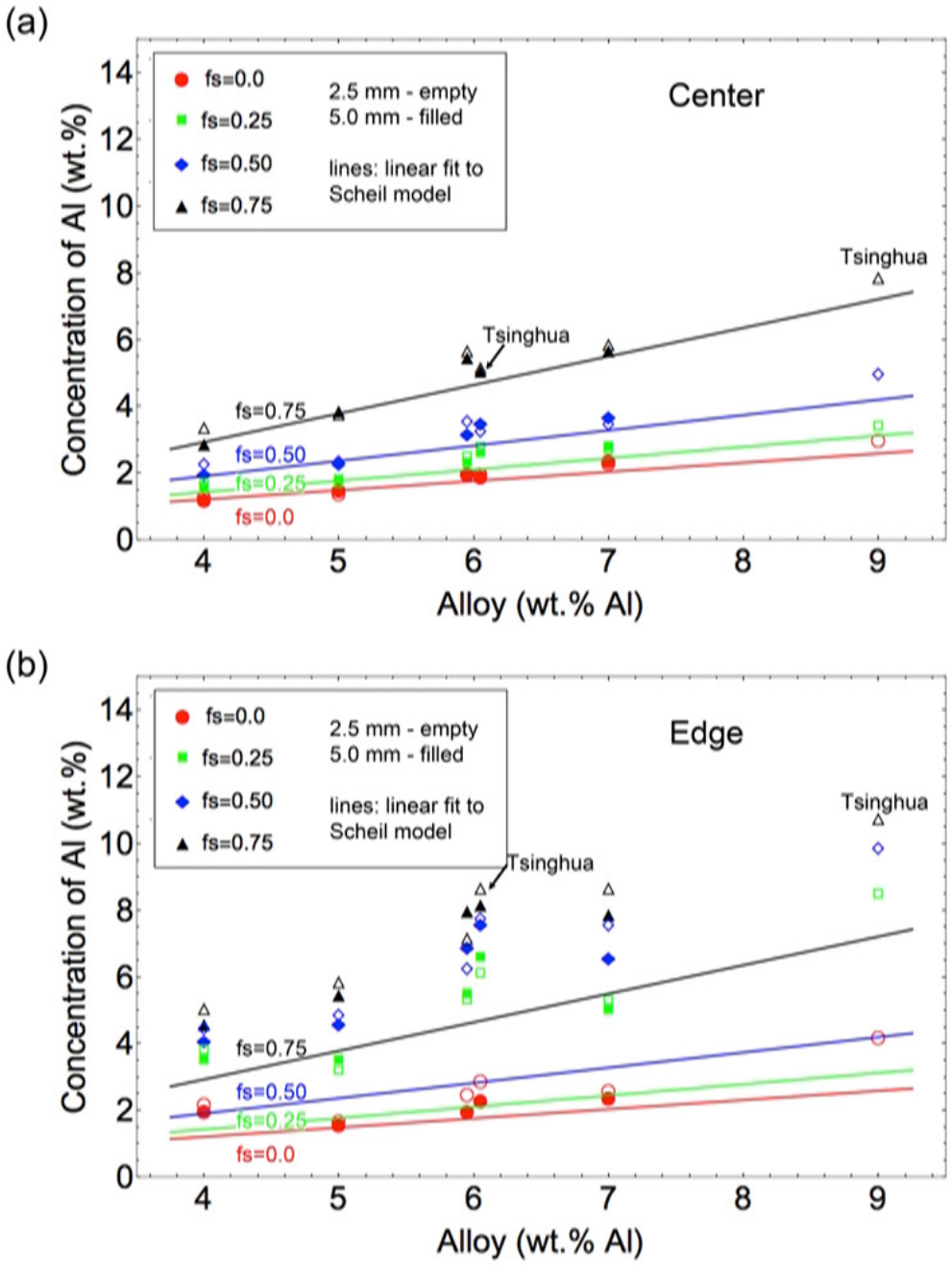

Figure III-130: Summary of microsegregation behavior at the (a) center and (b) edge of the HPDC plates.

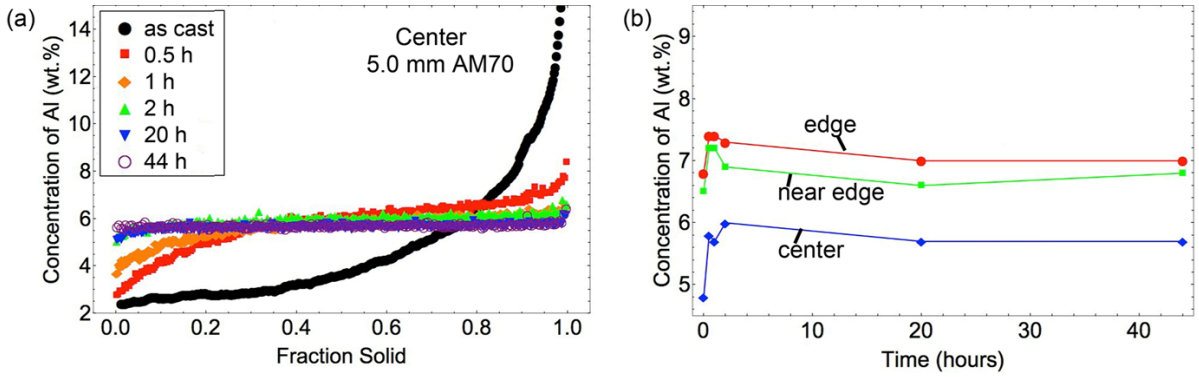

Figure III-131: Evolution of (a) microsegregation at the center and (b) macrosegregation during solution treatment of the 5.0-mm thick AM70 plates.

Electron Probe Microanalysis Forward Model Simulation of Microsegregation behavior in High-Pressure Die Casting Magnesium Alloys

The Monte Carlo simulation model, termed "Forward Model" has been developed to quantitatively evaluate the effect of microstructure parameters and experimental conditions on measured microsegregation behavior. This model has been refined to enable bimodal grain size distributions and grain size-dependent microsegregation profiles. The model is currently a one-dimensional analysis that assumes a circular two-dimensional cell (Figure III-132(a)), where the microsegregation profile can be modeled by an input function (shown as Scheil) from the center to the edge of the grain until it reaches a constant value at the eutectic. The variables of the model are an assumed solidification profile, grain size distribution, the fraction of eutectic, and average solute content. Electron flight simulation modeling indicates that EPMA operating conditions result in an electron interaction volume 4.5 µm in diameter; this value is used to represent the integration length.

Figure III-132(b) shows the apparent microsegregation profile when assuming a uniform grain size. When the grain size is at least an order of magnitude larger than the beam size, the experimental EPMA microsegregation profile matches the input function (Scheil is used here) up to a high solid fraction. As the ratio of the grain size to the beam size decreases, the profile becomes smeared out toward the average Al composition. The bend in the profiles is due to integrating the profile across eutectic; as the grain size decreases, the beam is more likely to hit the eutectic; therefore, the bend shifts into earlier solidification times. The bend becomes less drastic if a grain size distribution is used instead of an assumed uniform grain diameter.

Figure III-132(c) shows comparison between the simulation results and the EPMA-generated profile at the near edge location in the 5.0-mm thick AM70 plates. The grain size distribution shown in Figure III-128 was used. Based on analysis of optical micrographs, the eutectic fraction in this region is approximately 2%. In order to achieve mass balance, as the fraction of eutectic decreases, the partition coefficient must increase. The average Al content at the near edge location is 6.5 wt.% in the AM70 alloys, leading to a partition coefficient of 0.6. The simulated profile matches the experimental profile during the middle of solidification (0.2<fs<0.8), but over predicts the Al concentration at the beginning of solidification (when fs=0, $C_s = k_v C_0 = 0.6 * 6.5 = 3.9$) and under predicts at the end of solidification. Because the ESCs form outside the mold, with a different solidification environment, it is reasonable to assume these large features do not have the same microsegregation profile as the in-mold grains. Using the same modified Scheil model for in-mold grains as in Figure III-132(c) but assuming that the grains larger than 20-µm in diameter follow Scheil ($k = 0.31$), results in an improved agreement between the simulated and experimental profile (Figure III-132(d)). Due to the similarity of the grain diameter and electron beam interaction volume in the HPDC materials, this forward model simulation is an important tool for aiding interpretation of the EPMA results.

Microsegregation Micro-Model

One of the primary objectives of this project is to develop physics-based phase transformation kinetics micro-models that quantitatively capture microstructural evolution and microsegregation during HPDC and heat treatment of Mg alloys. The prediction of microsegregation is based on the work of Kraft et al. [22]. This numerical model will allow for determination of non-equilibrium phase diagrams for high cooling rates, where composition at the solid/liquid interface becomes a function of the solidification front velocity, v. Solidification front velocity can be determined from MagmaSoft HPDC casting simulations by dividing the cooling rate by the thermal gradient. In the 5-mm plate castings, we have solidification front velocities between 10 and 100 mm/s.

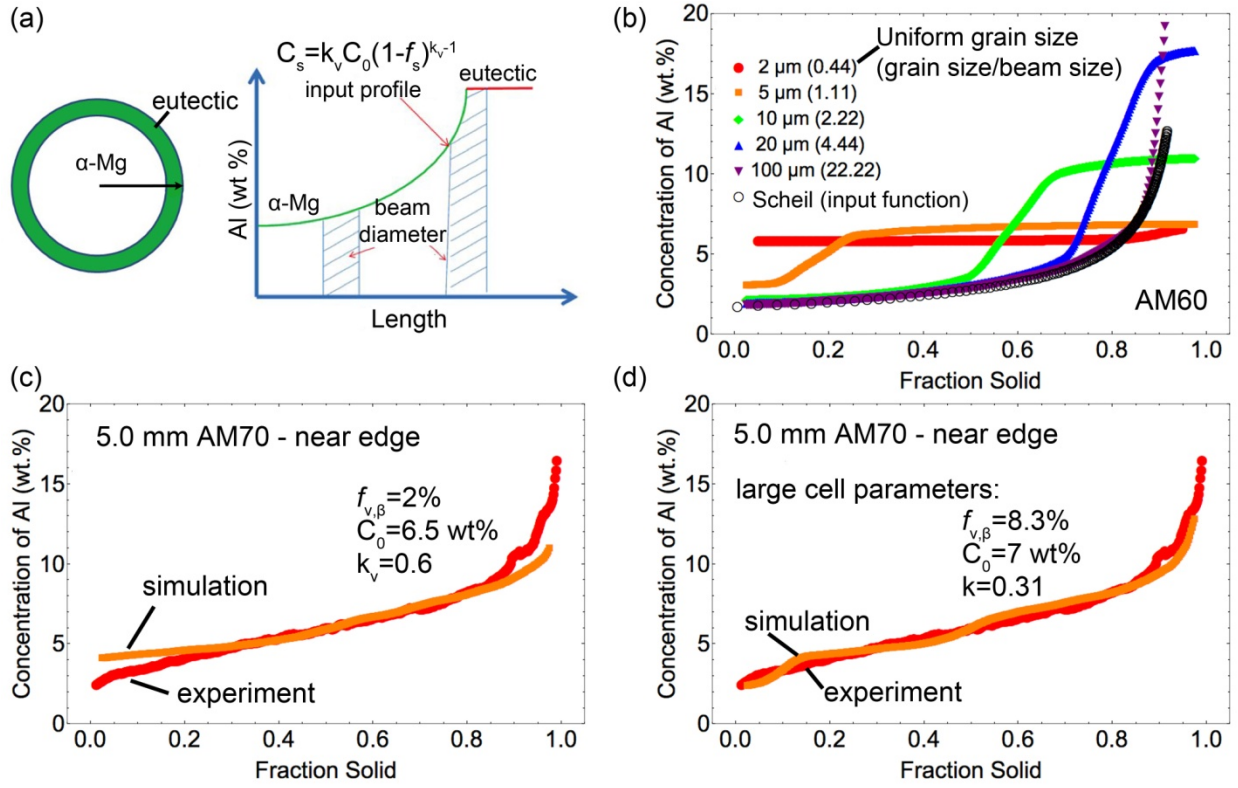

Figure III-132: (a) Illustration of the forward model. (b) Apparent microsegregation profile assuming a uniform grain size. (c) Comparison between simulation and experiment, assuming all cells are described by a modified Scheil profile. (d) Comparison between simulation and experiment, assuming large cells (i.e., >20 μm) follow Scheil, while smaller grains follow the same modified profile used in (c).

The numerical model developed by Kraft builds on modeling by Carrard et al. [23], which describes the interface motion during solidification in dilute Al-Fe, Al-Cu, and Ag-Cu alloys. Equation 1, given by Aziz and Kaplan [24] gives the velocity dependent partition coefficient

$$k_v = \frac{\frac{a_0 v}{D_i} + \kappa_e}{\frac{a_0 v}{D_i} + 1 - (1-k_e)c_{Lv}} \quad (1)$$

as a function of solidification front velocity, v. Where a_0 is a solute trapping parameter, D_i is the diffusion coefficient of the solute at the solid/liquid interface, k_e is the partition coefficient from the equilibrium phase diagram, c_{Lv} is the velocity-dependent liquidus composition, and κ_e is a partitioning parameter given by

$$\kappa_e = k_e \frac{1-c_{Se}}{1-c_{Le}} \quad (2)$$

where c_{Se} and c_{Le} are the solidus and liquidus compositions from the equilibrium phase diagram, respectively. The velocity dependent liquidus composition is given by Equation 3

$$c_{Lv} = c_{Le} - \frac{v}{v_0}\frac{1}{1-k_e}\left(\frac{1-k_e}{1-k_v+[k_v+(1-k_v)\beta]\ln\left({}^{k_v}/_{k_e}\right)}\right) \quad (3)$$

where v_0 is a parameter describing the maximum speed of crystallization, on the order of the speed of sound in metals, and β is used to turn on (β=1) and off (β=0) solute drag. The equilibrium phase diagram for the Mg-Al binary system, as generated by ThermoCalc, has been used to fit polynomial equations for c_{Se} and c_{Le} as a function of Al content and k_e and κ_e as a function of temperature. The unknown parameters are v_0, a_0, and D_i. Initially, a_0/D_i will be combined into a single variable, B, resulting in two unknowns. The coupled equations for k_v and c_{Lv}will be solved for the experimentally determined values of k_v to solve for B and v_0.

Technology Transfer Path

In addition to publications and presentations at national and international conferences, project knowledge, including experimental data and micro-models, will be transferred to industry and the research community through the NIST/DOE-EERE Advanced Automotive Cast Magnesium Alloys Repository and the Materials Commons. The database structure and content used for the Materials Commons is being constructed in coordination with national Materials Genome Initiative repository efforts lead by NIST. Discussions with key repository experts at NIST (i.e., Dr. C. Campbell) and elsewhere have already commenced. This will ensure information developed during this program will be broadly accessible to the technical community. Templates specific to the EPMA data acquisition and analysis and EBSD data collection have been implemented into the Material Commons.

Conclusion

During FY 2015, the focus has been on characterizing microstructure and microsegregation in HPDC AM series alloys. Microstructure characterization has shown that ESCs segregate to the center of the castings and there are very few ESCs at the edge of the thinner plates. The presence of ESCs leads to a broadened, bimodal grain size distribution in the center locations and at the edge of the thicker plates. The distribution of ESCs is being used to develop a more through understanding of EPMA microsegregation profiles.

The results of the forward model Monte Carlo simulation indicate that although the EPMA microsegregation profile may be distorted due to a low grain size to electron interaction volume ratio, it is still possible to extract the true microsegregation behavior. At the near edge location, microsegregation can be described by assigning all in-mold grains (i.e., those less than 20 μm in diameter) a velocity dependent partition coefficient of 0.6, while the large ESCs solidify with a partition coefficient close to that at equilibrium (i.e., 0.31). Higher partition coefficients toward the edge of the casting, where the cooling rate is the highest, lead to more Al trapped in the α-Mg phase and result in an Al-rich skin on HPDC plates. Though microsegregation can be reduced or eliminated through heat treatment at 420ºC for 2 hours, macrosegregation persists through extended solution treatments of up to 44 hours. At mid-thickness the macrosegregation can be adequately described by the Scheil model; however, solute trapping is needed to model microsegregation through the plate thickness.

References

1. S. Slade, 2010, "Magnesium : Bridging Diverse Metal Markets," in *Magnesium Technology,* S. R. Agnew; N. R. Neelameggham; E. A. Nyberg; and W. H. Sillekens (eds.), Wiley; pp. 91–95.
2. H. Gjestland and H. Westengen, 2007, "Advancements in High Pressure Die Casting of Magnesium," *Adv. Eng. Mater., 9;*pp. 769–776.
3. J. S. Kim; M. Isac; and R. I. L. Guthrie, 2004, "Metal-Mold Heat Transfer and Solidification of Magnesium Alloys in Belt Casting Processes," in *Magnesium Technology*, A. A. Luo (ed.), *Metallurgical Society of AIME*; pp. 247–255.
4. D. A. Porter and K. E. Easterling, 1992, *Phase Transformations in Metals and Alloys,* 2nd ed., Nelson Thornes Ltd.: Cheltenham, United Kingdom.
5. D. Mirković and R. Schmid-Fetzer, 2009, "Directional Solidification of Mg-Al Alloys and Microsegregation Study of Mg Alloys AZ31 and AM50: Part I. Methodology," *Metall. Mater. Trans. A*, 40; pp. 958–973.
6. J. R. TerBush; N. D. Saddock; J. W. Jones; and T. M. Pollock, 2010, "Partitioning of Solute to the Primary α-Mg Phase in Creep-Resistant Mg-Al-Ca–Based Cast Alloys," *Metall. Mater. Trans. A*, 41; pp. 2435–2442.
7. X. Zheng; A. A. Luo; C. Zhang; J. Dong; and R. A. Waldo, 2012, "Directional Solidification and Microsegregation in a Magnesium-Aluminum-Calcium Alloy," *Metall. Mater. Trans. A,* 43; pp. 3239-3248.
8. M. I. Khan; A. O. Mostafa; M. Aljarrah; E. Essadiqi; and M. Medraj, 2014, "Influence of Cooling Rate on Microsegregation Behavior of Magnesium Alloys," *J. Mater.,* 2014; pp. 1–18.
9. C. Zhang; D. Ma; K.-S. Wu; H.-B. Cao; G.-P. Cao; S. Kou; Y. A. Chang; and X.-Y. Yan, 2007, "Microstructure and microsegregation in directionally solidified Mg–4Al alloy," *Intermetallics*, 15; pp. 1395–1400.
10. M. Paliwal; D. H. Kang; E. Essadiqi; and I. H. Jung, 2014, "The evolution of as-cast microstructure of ternary Mg-Al-Zn alloys: An experimental and modeling study," *Metall. Mater. Trans. A*, 45; pp. 3596–3608.
11. S. Liu; G. Yang; and W. Jie, 2014, "Microstructure, Microsegregation, and Mechanical Properties of Directional Solidified Mg–3.0Nd–1.5Gd Alloy," *Acta Metall. Sin. (Engl. Lett.),* 27; pp. 1134–1143.
12. K. Sadayappan; W. Kasprzak; Z. Brown; L. Quimet; and A. A. Luo, 2009, "Characterization of Magnesium Automotive Components Produced by Super-Vacuum Die Casting Process," *Mater. Sci. Forum,* 618-619; pp. 381–386.
13. A. A. Luo, 2010, "Advanced casting technologies for lightweight automotive applications," *China Foundry*, 7; pp. 463–469.
14. M. Li; R. Zhang; and J. Allison, 2010, "Modeling Casting and Heat Treatment Effects on Microstructure in Super Vacuum Die Casting (SVDC) AZ91 Magnesium Alloy," in *Magnesium Technology*, S. R. Agnew; N. R. Neelameggham; E. A. Nyberg; and W. H. Sillekens (eds.), Wiley; pp. 623–627.
15. J. Miao; M. Li; and J. E. Allison, 2012, "Microstructure Evolution During Heat Treatment in a Super Vacuum Die Casting AZ91 Alloy," in *Magnesium: Proceedings of the 9th International Conference Magnesium Alloys and Their Applications,* W. J. Poole and K. U. Kainer (eds.), ICMAA2012, Vancouver,Canada; pp. 493–498.
16. J. Wang; M. Li; B. Ghaffari; L.-Q. Chen; J. Miao; and J. Allison, 2012, "A Microstructural Evolution Model for $Mg_{17}Al_{12}$ Precipitates in AZ91," in *Magnesium Technology,* S. N. Mathaudhu; W. H. Sillekens; N. Hort; and N. R. Neelameggham (eds.), Wiley; pp. 163–170.
17. Z.-P. Guo; S.-M. Xiong; B.-C. Liu; M. Li; and J. Allison, 2008, "Effect of Process Parameters, Casting Thickness, and Alloys on the Interfacial Heat-Transfer Coefficient in the High-Pressure Die-Casting Process," *Metall. Mater. Trans. A, 39*; pp. 2896–2905.

18. Z. Guo; S. Xiong; B. Liu; M. Li; and J. Allison, 2008, "Determination of the heat transfer coefficient at metal–die interface of high pressure die casting process of AM50 alloy," *Int. J. Heat Mass Transf*, 51; pp. 6032–6038.
19. S. Li; S. Xiong; B. Liu; M. Li; and J. E. Allison, 2010, "Numerical Simulation of Flow-Induced Air Entrapment Defects in the High Pressure Die Casting Process," in *Magnesium Technology,* S. R. Agnew; N. R. Neelameggham; E. A. Nyberg; and W. H. Sillekens (eds.), Wiley; pp. 613–616.
20. H. I. Laukli, 2004, "High Pressure Die Casting of Aluminium and Magnesium Alloys - Grain Structure and Segregation Characteristics," Norwegian University of Science and Technology.
21. DOE VTO, 2014, "FY 2014 Annual Progress Report - Lightweight Materials R&D," U.S. Department of Energy Vehicle Technologies Office, accessed January 8, 2016, http://energy.gov/sites/prod/files/2015/07/f24/DOE%20VTO%202014%20Materials%20Annual%20report.pdf.
22. T. Kraft; M. Rettenmayr; and H. E. Exner, 1996, "An extended numerical procedure for predicting microstructure and microsegregation of multicomponent alloys," *Model. Simul. Mater. Sci. Eng.,* 4; pp. 161–177.
23. M. Carrard; M. Gremaud; M. Zimmermann; and W. Kurz, 1992, "About the Banded Structure in Rapidly Solidified Dendritic and Eutectic Alloys," *Acta Met. mater.*, 40; pp. 983–996.
24. M. J. Aziz and T. Kaplan, 1988, "Continuous Growth Model for Interface Motion During Alloy Solidification," *Acta Matallurgica*, 36; pp. 2335–2347.

Bibliography

J. E. Allison, 2015, "Phase Transformation Kinetics and Alloy Microsegregation in High Pressure Die Cast Magnesium Alloys," *Annual Performance Review Meeting*, Washington, DC, April 10, 2015.

T. D. Berman and J. E. Allison, "Phase Transformation Kinetics and Alloy Microsegregation in High Pressure Die Cast Magnesium Alloys," *USCAR Materials Tech Team*, February 11, 2015.

IV. Carbon Fiber and Polymer Composites

IV.1. Advanced Oxidative Stabilization of Carbon-fiber Precursors—Oak Ridge National Laboratory

Project Details

Felix L. Paulauskas, Principal Investigator
Oak Ridge National Laboratory (ORNL)
1 Bethel Valley Road
Oak Ridge, TN 37831
Phone: 865-576-3785
E-mail: paulauskasfl@ornl.gov

Truman Bonds, Principal Investigator
RMX Technologies (RMX)
835 Innovation Drive, Suite 200
Knoxville, TN 37932
Phone: 865-777-2741
E-mail: tbonds@rmxtechnologies.net

C. David Warren, Field Technical Monitor
ORNL
1 Bethel Valley Road
Oak Ridge, TN 37831
Phone: 865-574-9693
E-mail: warrencd@ornl.gov

Carol Schutte, Technology Area Development Manager
U.S. Department of Energy
1000 Independence Avenue, SW
Washington, DC 20585-0340
Phone: 202-287-5371
E-mail: carol.schutte@ee.doe.gov

Contractor: ORNL
Contract No.: DE-AC05-00OR22725

Executive Summary

The total manufacturing cost of carbon fiber is one of the single largest obstacles to its incorporation into future automotive systems. According to a cost study, 51% of the cost of producing carbon fiber is attributable to the cost of the precursor, 43% of the cost of carbon fiber is attributable to conversion of the precursor into carbon fiber and activating the surface for resin compatibility, and the remaining 6% of the cost is for spooling and handling [1]. This task deals with the oxidation stage of the conversion process, with development focused on cost and energy reductions.

Fiscal Year (FY) 2015 was the final year of U.S. Department of Energy (DOE)-funded development for advanced oxidation of carbon-fiber precursor. Development is now complete and the technology has been successfully demonstrated to a variety of companies in the carbon-fiber industry. Industry interest is strong, and a subsequent private commercialization effort to scale this technology to production levels is under way.

Accomplishments

- Doubled the capacity of the ReMaxCo Technologies (RMX) large reactor, 1 annual metric ton (aMT) Plasma Oxidation Oven, from two tows to four tows of 20,000+ filaments per tow. Carbonized tows exceeded 250-ksi strength, 25-Msi Modulus, and 1% strain (FY 2015).
- Processed two 20,000+ filament tows continuously for at least 8 hours of continuous operation with no equipment failures or breaks in fiber. Oxidized fiber exceeded a minimum density of 1.35 g/cc (FY 2015).
- Plasma oxidized four 20,000+ filament tows. The mean values of the oxidized mechanical properties did not vary more than ±20% and the density not more than ±3% (FY 2015).
- Processed four simultaneous tows of 48,000+ filaments each to test the exothermic capacity of the large reactor. Density was greater than 1.34 g/cc for all tows and mechanical properties did not vary by more than 20% (FY 2015).
- Completed a process-to-properties correlation on the large reactor in an extension on prior work (FY 2015).
- Processed four simultaneous tows of 48,000+ filaments each and demonstrated that densities exceeding 1.34 grams per cubic centimeter (g/cc) can be achieved, fiber mechanical properties will not vary by more than 30%, and fiber densities will not vary by more than 6% (FY 2015).

Future Directions

- DOE-funded work is complete. Privately funded commercialization work has already begun.

Technology Assessment

- Target: Develop higher throughput (about three times faster) oxidation of carbon fiber, thus lowering the manufacturing costs of carbon fiber and increasing the material throughput and production rate.
- Gap: Conventional oxidation methods require 80 to 120 minutes, thus limiting carbon-fiber production rates. Faster oxidation could reduce the cost per pound for downstream processes such as carbonization, surface treatment, and sizing for manufacturing carbon fiber because mass throughput rates would be increased.
- Gap: Conventional oxidation methods are rate-limiting and mass-throughput–limiting steps due to the long residence times required. Increasing the mass throughput would decrease the cost per pound attributable to oxidative stabilization for carbon fiber.
- Gap: The advanced oxidative stabilization process has been successfully demonstrated in the laboratory but has not yet been demonstrated while integrated with other parts of the carbon-fiber conversion process or at speeds and reliability levels required for industrial adoption of the technology.

Introduction

The purpose of this project was to develop a plasma processing technique to rapidly and inexpensively oxidize polyacrylonitrile (PAN) precursor fibers. Conventional oxidation is a slow thermal process that typically consumes more than 80% of the processing time in a conventional carbon-fiber conversion line. A rapid oxidation process could dramatically increase the conversion line throughput and appreciably lower the fiber cost. Atmospheric pressure plasma is a new technology that is relatively inexpensive to implement in industrial processes [2]. The oxidation residence time must be greatly reduced to effect fast conversion and match the speed of the advanced carbonization technology. This project has been developing an atmospheric plasma

oxidation technology that could be used in line with conventional conversion equipment or integrated with other advanced fiber conversion processes to produce lower cost carbon fiber with properties suitable for use by the automotive industry. Critical technical criteria include (1) DOE programmatic goals (i.e., ≥25-Msi tensile modulus, ≥250-ksi tensile strength, and ≥1.0% ultimate elongation in the finished fiber); (2) uniform properties over the length of the fiber tow; (3) repeatable and controllable processing; and (4) significant unit cost reduction compared with conventional processing. All of these goals have been met and the project is concluded.

Approach

The researchers investigated PAN precursor fiber oxidation using non-thermal plasma at atmospheric pressure. As illustrated in Figure IV-1, conventional oxidative stabilization produces core-shell geometry with a distinct interphase between the (slowly growing) fully oxidized shell and the (shrinking) stabilized inner core. Plasma processing enhances oxygen diffusion and chemistry in the PAN oxidation process, accelerating the oxidized layer growth rate and oxidizing the fiber more uniformly, with a considerably less pronounced interface between the two regions. Previous work has shown that this approach can reduce the required residence time for complete oxidation. The overall project approach was to develop and validate the plasma processing process up to the 1-aMT scale (i.e., large reactor). In addition to the DOE-funded work discussed in this report, the large reactor has been successfully demonstrated to industry using industry precursors. A preproduction-scale prototype unit is currently being designed and built with private funds by RMX.

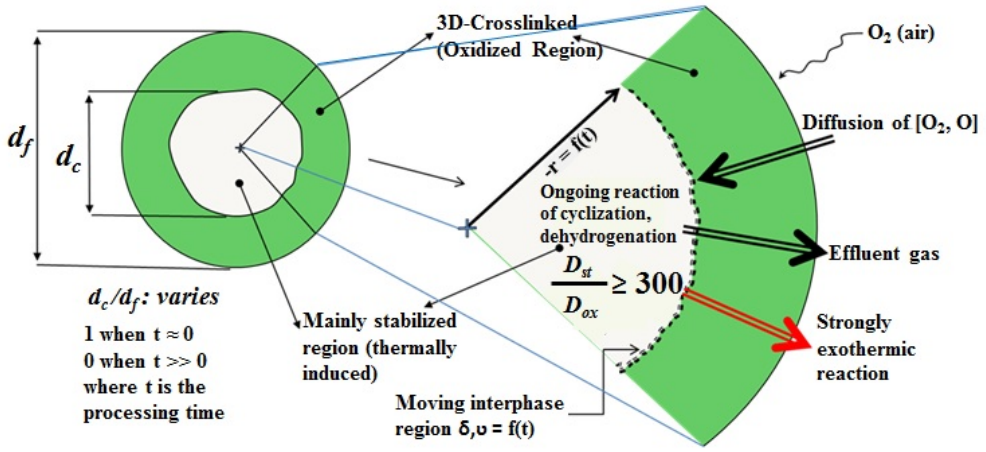

Figure IV-1: Single filament cross section during conventional oxidative stabilization process [3–5].

Results and Discussion

With the 1-aMT large reactor fully operational, testing during this period was focused on optimization to maximize mechanical properties for both oxidized PAN fiber and carbonized PAN fiber. All testing was performed with commodity-grade BlueStar 24k precursor. As testing progressed, significant hardware and configuration changes were implemented, as well as the test parameters themselves, to optimize the oxidation process.

The ultimate goal of the research team is to demonstrate that plasma oxidation can produce oxidized and carbonized fiber with mechanical properties *as good as or better than* **any** conventionally processed fiber. However, oxidation and carbonization are two completely different processes; therefore, this goal is being approached in two steps. The first step is to exceed the conventional oxidized fiber properties. This has been achieved and is shown in the results below. The second step is to exceed conventional carbonized fiber properties. This is achieved through a combination of optimization of oxidization conditions and optimization of carbonization conditions.

A major contributor to the tensile strength of both oxidized PAN fiber (OPF) and carbon fiber is the stretch parameter during both oxidation and carbonization. With the large reactor, stretch can be independently controlled for each of the four processing "zones." Oxidation was performed at three different stretch conditions for each four-tow run for the first stage of tensile strength optimization. All other oxidation conditions were held constant. The oxidization residence time was 30 minutes. This set of runs produced 12 tows (each a minimum of 100 ft in length) of oxidized PAN fiber that were submitted to ORNL for conventional carbonization and mechanical testing. The oxidation work at RMX was completed and ORNL began carbonization at various conditions, generating hundreds of samples for mechanical property analysis. In addition, differential scanning calorimetry was performed on the oxidized samples to determine the degree of stabilization.

During this testing, the large reactor was regularly in operation a minimum of 6 hours a day for several weeks. During this time, no downtime was experienced due to equipment failures. In fact, because full-scale operations began in the summer of 2014, the plasma subsystem has proven to be extremely reliable and robust under a variety of conditions that would be experienced in a production environment.

Table IV-1 shows sample organization/identification. Stretch condition 1 has the lowest applied stretch, while condition 3 has the highest. The four fiber positions are right to left (A to D), as if looking at the entrance of the oven, centered and spaced about 1.5 in. apart center-to-center, and so encompass about 6 to 7 in. of processing width. The maximum processing width of the oven is 8 in.

Table IV-1: OPF sample pool identification, corresponding stretch conditions, and oven positions.[a]

OPF Sample Number	Stretch Condition	Oven Position	Density (g/cc)
Conventional Baseline	NA	NA	1.38
MTR20075A	1	A	1.38
MTR20075B	1	B	1.36
MTR20075C	1	C	1.38
MTR20075D	1	D	1.37
Mean	1		1.37
Variation from Mean	1		<±1%
MTR20077A	2	A	1.38
MTR20077B	2	B	1.38
MTR20077C	2	C	1.38
MTR20077D	2	D	1.39
Mean	2		1.38
Variation from Mean	2		<±1%
MTR20078A	3	A	1.38
MTR20078B	3	B	1.38
MTR20078C	3	C	1.39
MTR20078D	3	D	1.39
Mean	3		1.39
Variation from Mean	3		<±1%

[a]Density values are from undried pycnometry using helium. Exact stretch conditions are export controlled and are not shown.
Note that the variation of density across the multiple tows was minimal and well below program requirements.

Differential Scanning Calorimetry of Oxidized Polyacrylonitrile Fiber

Differential scanning calorimetry (DSC) analysis was performed on selected samples from this pool. DSC yields information on the residual exothermic energy retained in the fiber, which is inversely proportional to the degree of processing. As shown in Figure IV-2 through Figure IV-4, all results fell within the typical limits of conventional oxidation performed at ORNL (80 minutes residence time). Precursor results are shown for comparison.

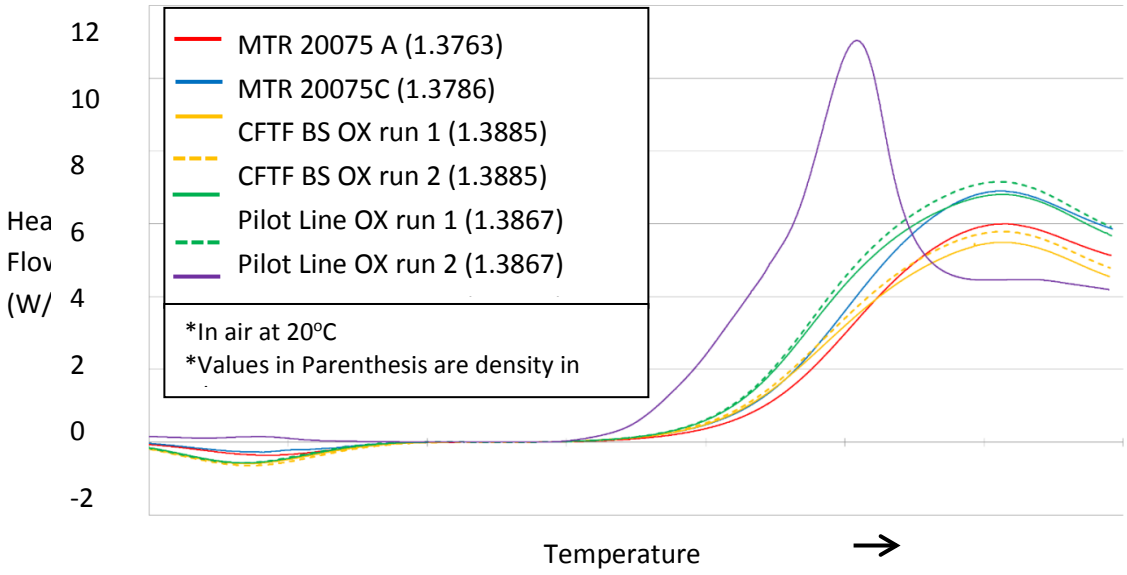

Figure IV-2: DSC results for MTR20075 select OPF samples and comparison to conventionally processed OPF.

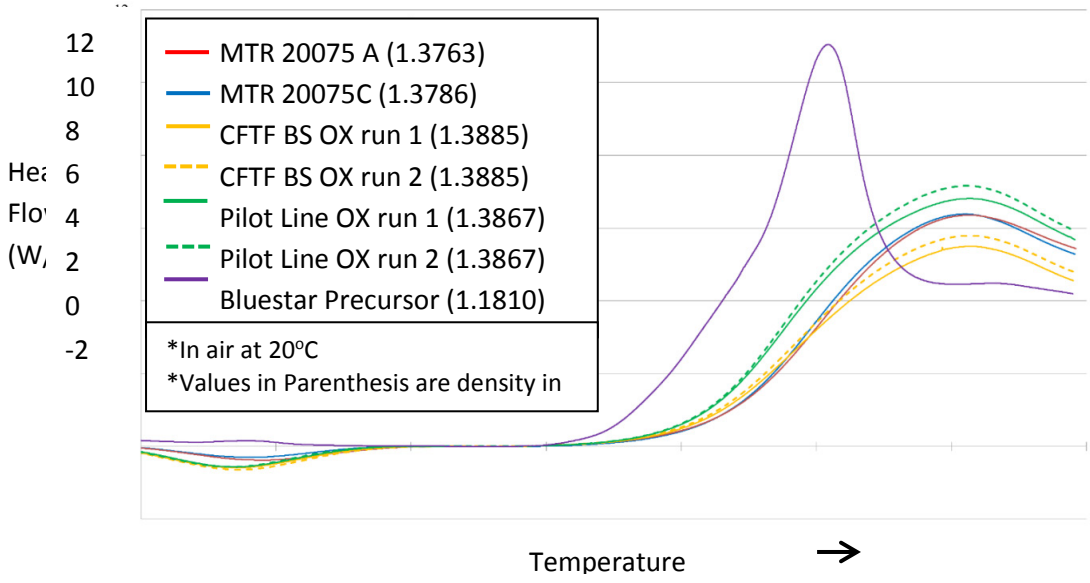

Figure IV-3: DSC results for MTR20077 select OPF samples and comparison to conventionally processed OPF.

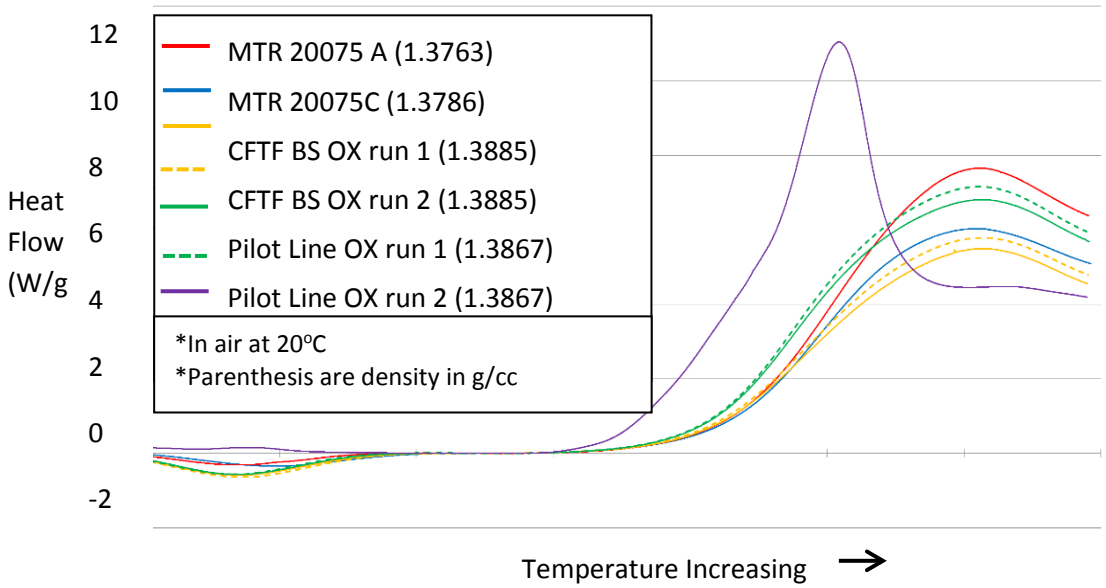

Figure IV-4: DSC results for MTR20078 select OPF samples and comparison to conventionally processed OPF.

Mechanical Analysis

All density measurements were made through undried pycnometry at ORNL. All mechanical property analysis was performed using single-filament tensile measuring equipment at ORNL. To determine force/area ratings from raw force results from measurement, the filament diameter must be measured. This was determined through both optical microscopy and gravimetric calculation from pycnometry. However, in this report, the optically determined diameter is used for consistency as the basis for all fiber property calculations.

BlueStar 24k precursor was used exclusively in all plasma oxidation testing and subsequent processing and testing. Nevertheless, all tables include information from other PAN fiber types for reference purposes. Mechanical properties of the virgin precursor, oxidized fiber, and carbonized fiber are shown in Table IV-2.

Table IV-2: Reference information concerning PAN precursor mechanical properties (as delivered by manufacturer).

Type	Size	Diameter (µm)	Tensile Strength (ksi)	Modulus (Msi)	Strain (%)
BlueStar	24k	13.5	63.8	1.4	15.5
Textile[a]	26k	11.7	66.7	1.3	14.5
Commodity[b]	50k	11.7	73.5	1.5	11.2
Aerospace	3k	12.9	76.6	1.7	10.5

[a]Textile is Fisipe F886B and is continues to be so throughout this document.

[b]Commodity is Courtaulds precursor and OPF data from [3] and Fortifil 511 carbon-fiber data from [4]. Bluestar is the same facility that used to be known as Akzo Nobel and Acordis, which produced the Fortafil precursor.

Oxidized Polyacrylonitrile Fiber Mechanical Properties

The mechanical properties of the OPF samples were determined through single filament testing performed at ORNL. Figure IV-5 gives a comparison of the average properties per stretch condition (results from the four samples for each stretch condition were averaged). Table IV-3 gives the full results. The two important metrics

of tensile strength and modulus were met or exceeded for oxidized fiber properties. Based on these data, the obvious next step is to further increase overall stretch during oxidation.

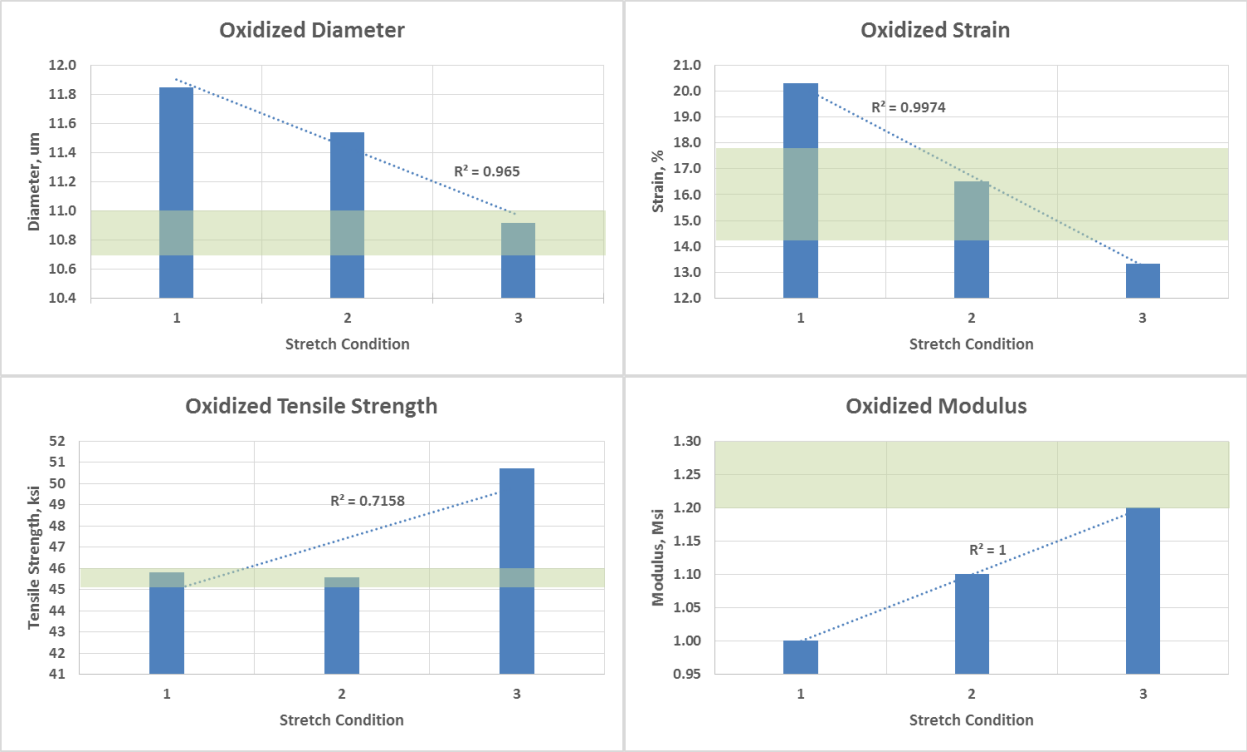

Figure IV-5: Average OPF mechanical properties versus stretch condition. The higher stretch condition number indicates higher overall stretch. The highlighted sections are conventional ranges as shown in the first row of Table IV-3. (R2 is the correlation coefficient of the linear regression line. It is a measure of how good the linear fit is to the data, with 1 being a perfect correlation.)

Table IV-3: Summary of OPF mechanical properties.[a]

Stretch	Sample	Tensile Strength (ksi)	Modulus (Msi)	Strain (%)	Diameter (µm)
	BlueStar	45.3 to 46.0	1.2 to 1.3	14.3 to 17.7	10.7 to 11
	Textile[b]	60.1	0.9	13.0	12.9
	Commodity[c]	47.5	1.9	25.0	9.7
	Aerospace	43.7	1.4	13.0	11.8
1	MTR20075A	45.7	1.0	19.1	12.8
1	MTR20075B	42.8	1.0	20.0	11.7
1	MTR20075C	47.3	1.0	20.6	11.5
1	MTR20075D	47.4	1.0	21.6	11.5
1	Mean	45.8	1.0	20.3	11.9
1	Standard Deviation	2.2	0.0	1.0	0.6
1	Variation from Mean	-7/+3%	0%	-6/+6%	-4/+8%
2	MTR20077A	42.3	1.2	13.9	11.7
2	MTR20077B	48.8	1.1	15.8	11.9
2	MTR20077C	45.7	1.0	19.4	11.2
2	MTR20077D	45.5	1.1	17.0	10.7

Stretch	Sample	Tensile Strength (ksi)	Modulus (Msi)	Strain (%)	Diameter (µm)
2	Mean	45.6	1.1	16.5	11.5
2	Standard Deviation	2.7	0.1	2.3	0.3
2	Variation from Mean	-7/+7%	-9/+9%	-16/+18%	-7/+3%
3	MTR20078A	50.2	1.2	13.9	10.7
3	MTR20078B	51.3	1.2	12.2	11.8
3	MTR20078C	50.7	1.2	13.6	10.5
3	MTR20078D	50.7	1.2	13.6	10.7
3	Mean	50.7	1.2	13.3	10.9
3	Standard Deviation	0.5	0.0	0.8	0.6
3	Variation from Mean	-1/+1%	0%	-8/+5%	-4/+8%

[a]Yellow cells indicate data for conventional processing.

[b]Textile is Fisipe F886B.

[c]Commodity is Courtaulds precursor and OPF data from [3] and Fortifil 511 carbon-fiber data from [4]. This fiber source is related to the Akzo Nobel/Acordis/BlueStar progression of companies.

Carbonized Fiber Mechanical Properties

Two carbonization conditions (conventional) were selected for inclusion in Table IV-4. All carbonization on this project is conventional. Multiple carbonization conditions were used per oxidized sample; only two per oxidized sample were selected for presentation in Table IV-4. The hyphenated numbers attached to the sample numbers (e.g., "-2" in MTR20075a-2, which is the first sample in the table) denote carbonization condition. For reference, conventional numbers of other carbon fiber types are shown. While carbon fiber manufacturers present "brochure" data for their fibers, the test methods are not always revealed. Therefore, other data measured at the ORNL Carbon Fiber Technology Facility are presented for direct comparison to our results. These two sets of data are delineated by the terms "brochure" and "measured."

Table IV-4: Summary of select carbon fiber mechanical properties.[a]

Stretch Condition	Sample[b]	Tensile Strength (ksi)	Modulus (Msi)	Strain (%)	Diameter (µm)
	BlueStar 24k (measured)	*528.5*	*28.2*	*1.7*	*7.3*
	Zoltek Panex 35 (brochure)	600.0	35.0	1.5	7.2
	Zoltek Panex 35 (measured)	386.3	23.5	1.5	8.6
	Aerospace (brochure)	820.0	40.0	1.9	5.2
	Aerospace (measured)	667.0	32.5	1.8	5.6
	Textile (measured)	409.1	25.5	1.5	6.4
	Commodity (brochure)	550.0	33.5	1.6	6.0
	Commodity (measured)	402.3	24.6	1.5	7.0
1	MTR20075A-2	351.5	26.7	1.2	7.3
1	MTR20075A-3	328.4	29.8	1.0	7.2
1	MTR20075B-2	372.5	30.1	1.2	6.9
1	MTR20075B-3	417.9	29.9	1.3	6.4
1	MTR20075C-3	402.6	25.1	1.5	7.4
1	MTR20075C-5	358.5	26.9	1.2	7.0
1	MTR20075D-1	*NA*			
1	MTR20075D-2				
1	Mean	371.9	28.1	1.2	7.0
1	Max	417.9	29.9	1.3	6.4

Stretch Condition	Sample[b]	Tensile Strength (ksi)	Modulus (Msi)	Strain (%)	Diameter (µm)
1	Maximum versus Conventional	-21%	+6%		
2	MTR20077A-1	390.2	28.1	1.3	6.9
2	MTR20077A-2	399.4	28.0	1.3	7.1
2	MTR20077B-1	366.9	27.5	1.2	7.4
2	MTR20077B-2	346.6	27.8	1.2	7.2
2	MTR20077C-1	251.0	21.1	1.1	7.9
2	MTR20077C-2	*NA*			
2	MTR20077D-2	381.1	28.0	1.3	6.9
2	MTR20077D-3	396.6	26.1	1.4	6.9
2	Mean	361.7	26.7	1.3	7.2
2	Max	399.4	28.1	1.4	6.9
2	Max vs. Conv.	-24%	0%		
3	MTR20078A-7	353.1	24.8	1.3	6.8
3	MTR20078A-11	357.9	25.7	1.3	6.8
3	MTR20078B-1	*NA*			
3	MTR20078B-2				
3	MTR20078C-1	335.9	26.5	1.2	6.8
3	MTR20078C-5	352.5	28.4	1.2	6.6
3	MTR20078D-1	443.4	28.5	1.4	6.6
3	MTR20078D-4	453.0	26.5	1.5	6.6
3	Mean	382.6	26.7	1.3	6.7
3	Max	453.0	28.5	1.4	6.6
3	Maximum versus Conventional	-14%	+1%		

[a]Yellow-highlighted cells indicate conventional processing conditions.

[b]Textile = Fisipe F886B; Commodity = Courtaulds precursor and OPF data from [3] and Fortifil 511 carbon-fiber data from [4]. This fiber source is related to the Akzo Nobel/Acordis/BlueStar progression of companies; brochure = information from carbon fiber manufacturers, where the test methods were not always known; and measured = ORNL/Carbon Fiber Technology Facility data measured under known conditions, for comparison with the results. Hyphenated numbers following the sample ID number (e.g., the 7 and 11 following MTR20078A) denote carbonization condition.

Mechanical properties of the carbonized fiber vary widely. Even though BlueStar is a known precursor due to the plasma oxidation process, the oxidized fiber was treated as an "unknown" OPF; therefore, a parametric investigation (subjected to different carbonization conditions) was undertaken to determine the optimal carbonization conditions. As a result, some of the numbers in Table IV-4 are not reliable, which can happen when the limits of the parameter space are explored. Note that all but one of the carbonized results in the table surpass the DOE minimum requirements of 250 ksi and 25 Msi. All data are based on optical microscopy diameters, except for "brochure" data on the conventional fiber, which are most likely full tow testing, which generally yields better results than single filament testing.

All results presented in Figure IV-6 through Figure IV-9 and Table IV-5 are for 24k BlueStar commodity-grade precursor. Conventional references are from work performed at ORNL with the same precursor. Mechanical properties are based on optical microscopy. This round of testing looked at three different stretch conditions (other conditions held constant) during plasma oxidation, with four times 24k tow processing for each condition. Then conventional carbonization was performed at ORNL under a variety of conditions to determine the best carbonization conditions. The following data capture all oxidation and carbonization results, not just the optimal cases.

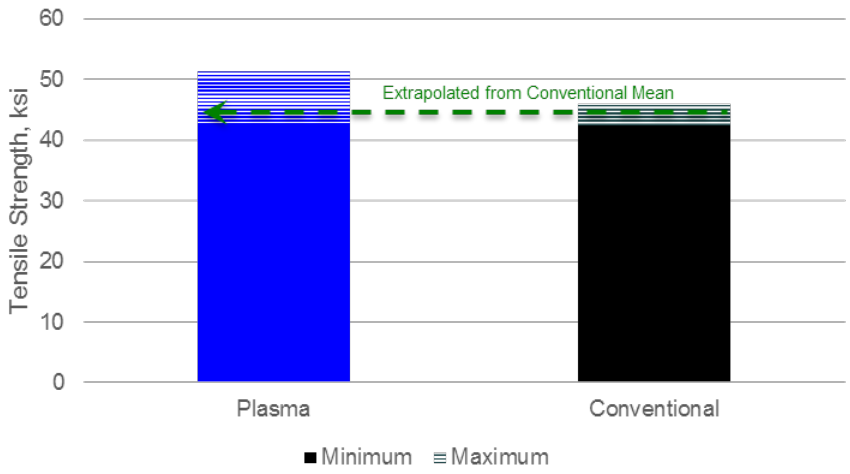

Figure IV-6: Tensile strength of plasma-oxidized fiber versus conventionally oxidized fiber. The dotted section captures the minimum and maximum values. The green dashed arrow projects the average conventional results to plasma results.

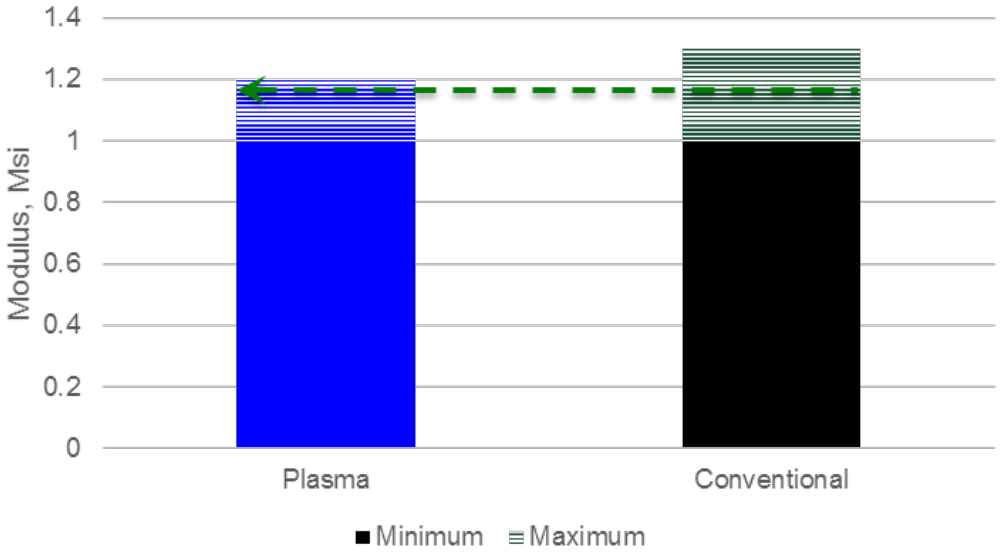

Figure IV-7: Modulus of plasma-oxidized fiber versus conventionally oxidized fiber. The dotted section captures the minimum and maximum values. The green dashed arrow projects the average conventional results to plasma results.

Table IV-5: Four-tow processing variation of oxidized properties across tows for the three stretch conditions.[a]

Parameter	Requirement[a]	Condition 1	Condition 2	Condition 3
Density Mean, g/cc	—	1.3518	1.3528	1.3594
Density Variation about the Mean, %	≤±3.0	+0.8/-1.1	+0.9/-1.4	+0.4/-0.4
Tensile Strength Mean, ksi	—	45.80	45.93	50.73
Tensile Variation about the Mean, %	≤±20	+3.5/-6.6	+6.3/-4.8	+1.1/-1.0
Modulus Mean, Msi	—	1.00	1.10	1.20
Modulus Variation about the Mean, %	≤±20	~0	+9.1/-9.1	~0

Parameter	Requirement[a]	Condition 1	Condition 2	Condition 3
Strain Mean, %	—	20.31	16.83	13.34
Strain Variation about the Mean, %	≤±20	+6.1/-6.0	+15.1/-10.1	+4.3/-8.7

[a]Requirement = Milestone M3 requirement: "Plasma oxidize four 20,000+ filament tows. Variability across all tows will be analyzed. The mean values of the oxidized mechanical properties should not vary more than ±20%, and the density should not vary more than ±3%."

Note: Actual stretch conditions are not presented here due to export control restrictions. The variation results are presented as the maximum and minimum above and below the mean value of all results for that run. Specifically, represented as m/w, m = the maximum value above the mean of all values, while the w represents the maximum value below the mean of all values. The same representation exists for all variation results presented in this report.

Figure IV-8 and Figure IV-9 summarize the results for the successful completion of milestone M1: Capacity Test 1: "Double the capacity of the 1 aMT plasma oxidation from two tows to four tows of 20,000+ filaments per tow. Carbonized tows must meet 250 ksi strength and 25 Msi modulus."

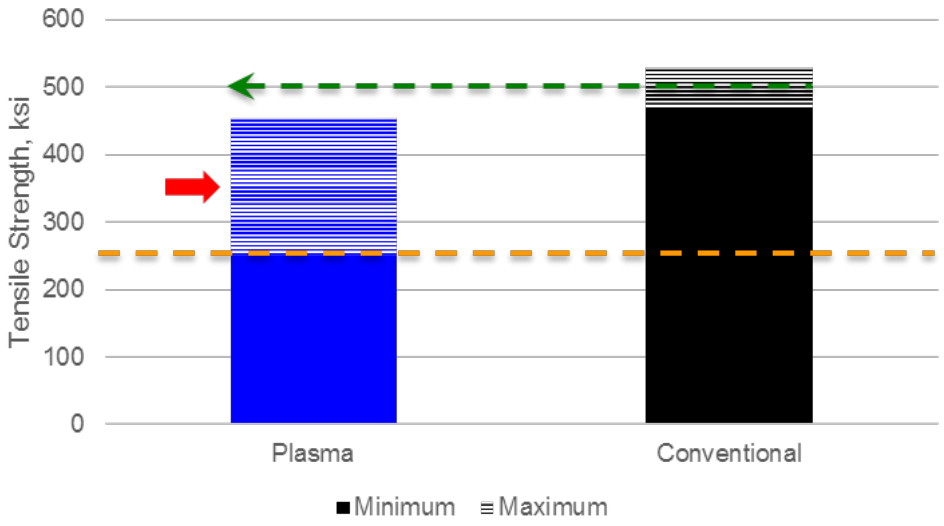

Figure IV-8: Tensile strength of plasma-oxidized, conventionally carbonized fiber versus conventionally-oxidized/carbonized fiber. The green dashed arrow projects the average conventional results to plasma results. The orange dashed line denotes the DOE program minimum. The red arrow points out the large variation in this parameter, which is due to the wide variation of carbonization conditions explored at ORNL.

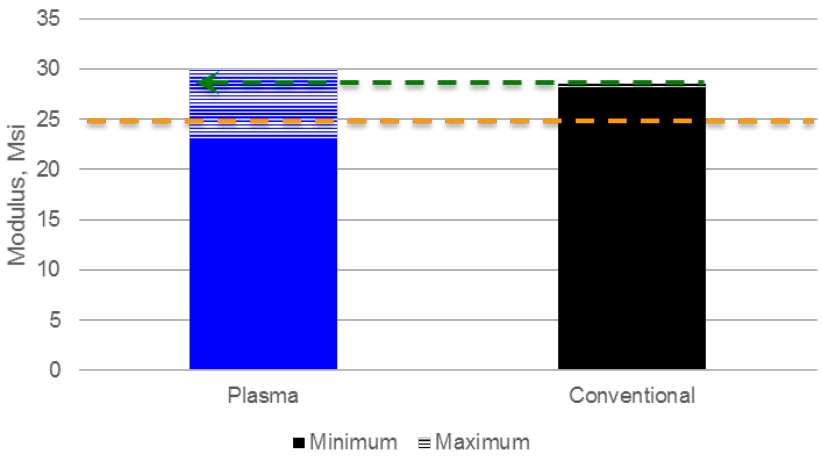

Figure IV-9: Modulus of plasma-oxidized, conventionally carbonized fiber versus conventionally oxidized/carbonized fiber. The green dashed arrow projects the average conventional results to plasma results. The orange dashed line denotes the DOE program minimum.

Table IV-6: Four-tow processing variation of carbonized properties across tows for the three stretch conditions.

Parameter	Condition 1	Condition 2	Condition 3
Tensile Strength Mean (ksi)	399.10	353.48	387.80
Tensile Strength (%)	+4.7/-5.6	+13.0/-29.0	+16.8/-9.1
Modulus Mean (Msi)	27.53	25.68	26.87
Modulus (%)	+8.6/-8.8	+9.1/-17.8	+5.7/-4.3
Strain Mean (%)	1.34	1.27	1.32
Strain (%)	+9.4/-6.2	+11.2/-13.2	+15.9/-12.1

Note: Actual stretch conditions are not presented here due to export control restrictions.

It is important to note that the data presented in Table IV-6 do not represent the best case for achieving carbon fiber mechanical properties. These data represent an average of the entire explored range of carbonization process conditions, good and bad. For variation, there was no specified milestone requirement for carbonized values.

Table IV-7: Individual mechanical property results of plasma-oxidized, conventionally carbonized fiber.

Stretch Condition	Sample	Density (g/cc)	Diameter (µm)	Tensile Strength (ksi)	Modulus (Msi)	Strain (%)
Note: These are select samples from a pool of more than 45 sample results.	*DOE Program Goal*			*250*	*25*	*1*
	Conventional 1	*1.80*	*7.02*	*467.3*	*28.6*	*1.48*
	Conventional 2	*1.80*	*7.27*	*528.5*	*28.2*	*1.69*
1	MTR20075A-1	1.79	7.18	376.8	27.6	1.26
1	MTR20075A-3	1.78	7.15	328.4	29.8	1.04

Stretch Condition	Sample	Density (g/cc)	Diameter (µm)	Tensile Strength (ksi)	Modulus (Msi)	Strain (%)
1	MTR20075B-3	1.78	6.37	417.9	29.9	1.30
1	MTR20075C-3	1.80	7.35	402.6	25.1	1.47
2	MTR20077A-2	1.79	7.07	399.4	28.0	1.32
2	MTR20077B-1	1.78	7.43	366.9	27.5	1.24
2	MTR20077C-1	1.78	7.91	251.0	21.1	1.10
2	MTR20077D-3	1.79	6.87	396.6	26.1	1.41
3	MTR20078A-11	1.80	6.83	357.9	25.7	1.27
3	MTR20078C-5	1.79	6.64	352.5	28.4	1.16
3	MTR20078D-1	1.80	6.56	443.4	28.5	1.41
3	MTR20078D-4	1.80	6.63	453.0	26.5	1.53

During the testing reflected in Table IV-7's results for carbonized fiber, the milestone M2 of robustness was completed: "Process two 20,000+ filament tows continuously for at least 8 h of continuous operation with no equipment failures or breaks in fiber. Oxidized fiber will have a minimum density of 1.35 g/cc." Three tows of BlueStar 24k were processed simultaneously for nearly 9 hours with no breakages or equipment failures. All oxidized fiber densities before carbonization were between 1.36 and 1.37 g/cc (above the minimum of 1.35 g/cc).

All results presented in Table IV-8 and Table IV-9 are for 24k BlueStar commodity-grade precursor. Conventional references are from work performed at ORNL with the same precursor. Fiber diameters for mechanical property calculations are based on optical microscopy. This round of testing looked at variation in the mechanical properties of four tow positions that were simultaneously oxidized in the 1–MT carbon fiber/year plasma oxidation oven. Densities are reported in Table IV-8. Mechanical properties are shown in Table IV-9. All values demonstrate that milestone metrics were surpassed. Results were from one run with four simultaneous tows. Four 35-in. samples were pulled from the run, with eight shorter samples pulled from these larger samples for density measurements at RMX and ORNL and mechanical property measurements at ORNL.

Table IV-8: Oxidized fiber densities.[a]

Position	Density	Variation from Mean (%)
A	1.3876	+0.4
B	1.3864	+0.3
C	1.3767	-0.4
D	1.3782	-0.3
Mean	1.3822	—

[a]Measured by pycnometer (with helium) at ORNL. Note: Milestone requirement is ±3% maximum.

Energy consumption data are part of the common data collected with the LabVIEW-based control system used at RMX on the RMX large reactor. A summary comparison of unit energy consumption is shown in Table IV-10. "Unit energy consumption" is defined as the amount of energy, in kilowatt-hours (kWh), required to oxidize 1 kg of OPF. Conventional values obtained from industry range from 17 to 26 kWh/kg of OPF.

Table IV-9: Mechanical properties of oxidized polyacrylonitrile fiber.

Samples/Entries	Values Based On Optical Measurements							
Tow ID	Diameter by Optical Microscopy (µm)	Deviation for Diameter (µm)	Peak Stress (ksi)	Deviation for Peak Stress (ksi)	Modulus (Msi)	Deviation for Modulus (Msi)	Strain at Peak Stress (%)	Deviation for Strain (%)
130 A (Blue Star 24k)	12.57	0.91	33.1	3.3	0.81	0.09	19.21	4.74
130 B (Blue Star 24k)	12.64	0.73	34.3	6	0.95	0.12	18.63	5.14
130 C (Blue Star 24k)	12.35	0.55	35.8	5.3	0.9	0.13	19.36	4.83
130 D (Blue Star 24k)	13.08	0.49	34.6	6.7	0.88	0.1	21.42	6.68
AVERAGE	**12.66**	**0.67**	**34.45**	**5.33**	**0.89**	**0.11**	**19.66**	**5.35**
STANDARD DEVIATION	**0.31**	**0.19**	**1.11**	**1.47**	**0.06**	**0.02**	**1.22**	**0.90**
Data Range from Mean (%)	−2.45/+3.32		−3.92/+3.92		−8.99/+6.74		−5.24/+8.95	
MILESTONE Requirements (%)	<20		<20		<20		<20	

Table IV-10: Summary of unit energy consumption.

Oxidation Rate Increase	Density (g/cc)	Unit Energy Consumption (kWh/kg OPF)		Precursor
		1 ton/year	1,500 tons/year[a]	
2.7X	1.36	44.8	2.7	2 x BlueStar 24k
2.7X	1.37	33.5	2.0	3 x BlueStar 24k
2.7X	1.37	27.0	1.6	4 x BlueStar 24k

[a]Estimated using scaling law provided by industry.

Note: Conventional values obtained from industry range from 17 to 26 kWh/kg of OPF.

After this, we stopped work with the 24k and switched to four tows of 48k precursor. To generate the necessary data, several feet per tow of oxidized material were collected at intervals from the multiple runs conducted over the past several months. The samples have not been carbonized (i.e., carbonization was out of the scope of this milestone). The oxidation processing time for these fibers was 30 minutes. Some stretch and relaxation was applied on the four tows, but not optimized. It is important to note that the mechanical properties of the fibers obtained during this work match those of the oxidized fibers obtained from commodity-grade precursors conventionally oxidized at ORNL.

The RMX large reactor was used to oxidize four simultaneous tows of commodity grade (BlueStar) PAN 48k precursor. Oxidized fiber densities in the range of 1.35 to 1.38 g/cc were measured (all samples were dried before density measurement). The resulting mechanical properties, based on individual filament tests, are shown in Table IV-11 through Table IV-15. On runs 153 and 154 at different temperatures (single variable), milestone targets were reached with a minimum fiber density of 1.34 g/cc for each tow, while deviation of the mechanical properties did not exceed 30% and fiber densities of tows did not vary more than 6%. On run 154,

milestone targets were reached with a minimum fiber density of 1.34 g/cc for each tow, while deviation of the mechanical properties did not exceed 20% between the four tows.

A data analysis report was completed and submitted as a separate document for milestone M5 completion: "Analyze and correlate process parameters to fiber properties and determine relationships between them." This correlation is necessary for further scale-up to the demonstration level. Energy balance analysis will also be undertaken.

Each chart reports the data collected and calculated for a batch of four tows at one specific process condition. Each tow is labeled as follows: RRR L T# (where RRR = Run #; L = tow name (A, B, C, or D); T# = reference number for the hottest temperature the four tows experienced during a specific run). Percentages were calculated as a variation FROM the "AVERAGE" to "the lowest/ highest" value of the four tows.

Table IV-11: Summary of results for Milestone 4: Process four simultaneous tows of 48,000+ filaments each to test exothermic capacity of plasma oxidation oven. Tows should exceed 1.34-g/cc density and mechanical properties not vary by more than 20%)

Samples	Values Based on Optical Measurements				Values Based on Pycnometer Measurements			
Tow ID	Diameter by Optical Microscopy (microns)	Peak Stress (ksi)	Modulus (Msi)	Strain at Peak Stress (%)	Pycnometer Density (g/cc)	Pyconometer Diameter (microns)	Peak Stress (ksi)	Modulus (Msi)
154 A T2	11.53	36.2	1.04	20.3	1.37	10.90	40.5	1.16
154 B T2	12.65	36.9	0.99	18.6	1.37	10.93	49.4	1.33
154 C T2	11.89	38.1	0.98	20.8	1.38	10.90	45.4	1.17
154 D T2	11.92	40.8	1.09	20.8	1.35	11.27	45.7	1.22
Average	12.00	38.0	1.03	20.13	1.37	11.00	45.2	1.22
Standard Deviation	0.47	2.02	0.05	1.04	0.01	0.18	3.7	0.08
Data Range from Mean (%)	-3.9/ 5.44%	-4.74/ 7.37%	-4.39/ 6.34%	-7.58/ 3.35%	-1.28/ 3.35%	-0.92/ 2.45%	-10.46/ 9.26%	-4.55/ 8.78%
Milestone Requirement	<20%	<20%	<20%	<20%	<3%	<20%	<20%	<20%

Table IV-12: Summary of results for Milestone 6: Process four simultaneous tows of 48,000+ filaments each and demonstrate that densities exceeding 1.34 g/cc can be achieved, fiber mechanical properties will not vary by more than 30%, and fiber densities will not vary by more than 6%.

Samples	Values Based on Optical Measurements				Values Based on Pycnometer Measurements			
Tow ID	Diameter by Optical Microscopy (microns)	Peak Stress(ksi)	Modulus (Msi)	Strain at Peak Stress (%)	Pycnometer Density (g/cc)	Pyconometer Diameter (microns)	Peak Stress (ksi)	Modulus (Msi)
153 A T1	12.33	36.4	1.04	22.8	1.36	11.42	42.4	1.21
153 B T1	12.43	41.5	1.09	20.8	1.35	11.27	50.5	1.33
153 C T1	12.11	38.5	1.09	22.1	1.36	11.32	44.1	1.25
153 D T1	13.22	38.0	1.00	20.4	1.35	11.30	52.0	1.37
Average	12.52	38.6	1.06	21.53	1.36	11.33	47.2	1.29
Standard Deviation	0.48	2.13	0.04	1.12	0.01	0.06	4.7	0.07
Data Range from Mean (%)	-3.29/ 5.57%	-5.70/ 7.51%	-5.21/ 3.32%	-5.23/ 5.92%	-0.37/ 0.37%	-0.49/ 0.81%	-10.18/ 10.01%	-5.91/ 6.15%
Milestone Requirement	<30%	<30%	<30%	<30%	<6%	<30%	<30%	<30%

Table IV-13: Summary of results for Milestone 6: Process four simultaneous tows of 48,000+ filaments each and demonstrate that densities exceeding 1.34 g/cc can be achieved, fiber mechanical properties will not vary by more than 30%, and fiber densities will not vary by more than 6%.

Samples	Values Based on Optical Measurements				Values Based on Pycnometer Measurements			
Tow ID	Diameter by Optical Microscopy (microns)	Peak Stress (ksi)	Modulus (Msi)	Strain at Peak Stress (%)	Pycnometer Density (g/cc)	Pyconometer Diameter (microns)	Peak Stress (ksi)	Modulus (Msi)
154 A T1	12.87	38.1	1.21	20.3	1.35	10.89	53.2	1.69
154 B T1	12.27	38.4	1.30	19.7	1.36	10.94	48.3	1.63
154 C T1	12.27	35.6	1.17	21.2	1.36	10.94	44.8	1.47
154 D T1	13.16	38.4	1.24	20.9	1.36	10.94	55.5	1.79
Average	12.64	37.63	1.23	20.53	1.36	10.93	50.5	1.65
Standard Deviation	0.45	1.36	0.05	0.67	0.01	0.03	4.8	0.13
Data Range from Mean (%)	-2.95/ 4.09%	-5.38/ 2.06%	-4.88/ 5.69%	-4.02/ 3.29%	-0.55/0.18%	-0.36/ 0.15%	-11.23/ 10.09%	-10.65/ 8.87%
Milestone Requirement	<30%	<30%	<30%	<30%	<6%	<30%	<30%	<30%

Table IV-14: Summary of results for Milestone 6: Process four simultaneous tows of 48,000+ filaments each and demonstrate that densities exceeding 1.34 g/cc can be achieved, fiber mechanical properties will not vary by more than 30%, and fiber densities will not vary by more than 6%.

Samples	Values Based on Optical Measurements				Values Based on Pycnometer Measurements			
Tow ID	Diameter by Optical Microscopy (microns)	Peak Stress (ksi)	Modulus (Msi)	Strain at Peak Stress (%)	Pycnometer Density (g/cc)	Pyconometer Diameter (microns)	Peak Stress (ksi)	Modulus (Msi)
154 A T2	11.53	36.2	1.04	20.3	1.37	10.90	40.5	1.16
154 B T2	12.65	36.9	0.99	18.6	1.37	10.93	49.4	1.33
154 C T2	11.89	38.1	0.98	20.8	1.38	10.90	45.4	1.17
154 D T2	11.92	40.8	1.09	20.8	1.35	11.27	45.7	1.22
Average	12.00	38.0	1.03	20.13	1.37	11.00	45.2	1.22
Standard Deviation	0.47	2.02	0.05	1.04	0.01	0.18	3.7	0.08
Data Range from Mean (%)	-3.90/5.44%	-4.74/ 7.37%	-4.39/ 6.34%	-7.58/ 3.35%	-1.28/0.91%	-0.92/2.45%	-10.46/ 9.26%	-4.55/ 8.78%
Milestone Requirement	<30%	<30%	<30%	<30%	<6%	<30%	<30%	<30%

Table IV-15: Summary of results for Milestone 6: Process four simultaneous tows of 48,000+ filaments each and demonstrate that densities exceeding 1.34 g/cc can be achieved, fiber mechanical properties will not vary by more than 30%, and fiber densities will not vary by more than 6%.

Samples	Values Based on Optical Measurements				Values Based on Pycnometer Measurements			
Tow ID	Diameter by Optical Microscopy (microns)	Peak Stress (ksi)	Modulus (Msi)	Strain at Peak Stress (%)	Pycnometer Density (g/cc)	Pyconometer Diameter (microns)	Peak Stress (ksi)	Modulus (Msi)
154 A T3	11.92	38.4	1.33	21.9	1.38	10.91	45.9	1.59
154 B T3	11.53	39.6	1.17	22.9	1.38	10.79	45.2	1.34
154 C T3	12.12	37.5	1.29	19.8	1.38	10.69	48.2	1.66
154 D T3	12.20	36.8	1.17	20.4	1.38	10.72	47.7	1.52
Average	11.94	38.08	1.24	21.25	1.38	10.78	46.7	1.52
Standard Deviation	0.30	1.21	0.08	1.41	0.00	0.10	1.4	0.14
Data Range from Mean (%)	-3.45/2.16%	-3.35/ 4.01%	-5.65/ 7.26%	-6.82/ 7.76%	-0.30/0.28%	-0.78/1.21%	-3.29/ 3.09%	-12.40/ 8.72%
Milestone Requirement	<30%	<30%	<30%	<30%	<6%	<30%	<30%	<30%

Technology Transfer Path

RMX is negotiating to license ORNL's rights to the intellectual property covering plasma oxidation. (RMX already has rights to this intellectual property through co-invention.) RMX and its subsidiary, 4M Industrial Oxidation, have already begun scaling up this technology to the 175-aMT level with their industry partner, C.A. Litzler, with the goal of demonstrating the technology at this scale to industry.

Conclusion

All milestones for this project were successfully completed in FY 2015, as indicated in Table IV-16.

Table IV-16: FY 2015 milestone completion table.

Advanced Oxidation				
Milestone	**Due Date**	**Type**	**Milestone**	**Decision Criteria**
M1	12/31/2014	Quarterly Regular	Capacity Test 1: Double the capacity of the 1-ton/year plasma oxidation from 2 tows to 4 tows of 20,000+ filaments per tow. Carbonized tows must meet 250-KSI strength and 25-Msi modulus.	Carbonized tows must meet 250-ksi strength and 25-Msi modulus.
M2	3/31/2015	Quarterly Regular	Robustness test: Process two 20,000+ filament tows continuously for at least 8 hours of continuous operation with no equipment failures or breaks in fiber. Oxidized fiber will have a minimum density of 1.35 g/cc.	Oxidized fiber will have a minimum density of 1.35 g/cc.
M3	6/30/2015	Quarterly Regular	Variability test: Plasma oxidize four 20,000+ filament tows. Variability across all tows will be analyzed. The mean values of the oxidized mechanical properties should not vary more than ±20% and the density not vary more than ±3%.	±20% and the density not vary more than ±3%.
M4	9/30/2015	Annual Stretch	Capacity Test 2: Process four simultaneous tows of 48,000+ filaments each to test the exothermic capacity of a plasma oxidation oven. Tows should exceed 1.34-g/cc density and mechanical properties not vary by more than 20%.	Tows should exceed 1.34-g/cc density and mechanical properties not vary by more than 20%.
M5	9/30/2015	Annual Regular	Process correlation: Analyze and correlate process parameters to fiber properties and determine relationships between them. This correlation is necessary for further scale-up to demonstration level. Energy balance analysis will also be undertaken.	Report delivery.
M6	9/20/2015	Go/No-Go Decision Point	Process four simultaneous tows of 48,000+ filaments each and demonstrate that densities exceeding 1.34 g/cc can be achieved, fiber mechanical properties will not vary by more than 30%, and fiber densities will not vary by more than 6%.	Fiber mechanical property variation less than or equal to 30% and fiber density variation less than or equal to 6%.
M7	12/31/2015	Annual Regular	Final report	

Technology development is sufficiently complete at the 1-aMT level to begin scaling up to a larger pilot line scale; therefore, industry demonstrations producing significant quantities of fiber-proving economies–of-scale

can be performed. This will be a private-led collaboration between several partners involved at every step of the carbon-fiber supply chain.

References

1. B. Friedfeld, 2007, "Cost Assessment of Lignin-and PAN-Based Precursor for Low-Cost Carbon Fiber," presented at the *Automotive Composites Consortium,* January 17, 2007.
2. J. R. Roth, 2001, "Applications to Nonthermal Plasma Processing," *Industrial Plasma Engineering*, Vol. 2, Philadelphia: Institute of Physics Publishing, Chapter 15.
3. F. L. Paulauskas, 2010, "Advanced Oxidation and Stabilization of PAN-Based Carbon Precursor Fibers," presented at the *2010 DOE Annual Merit Review,* June 9, 2010.
4. F. L. Paulauskas, 2004, "Temperature-Dependent Dielectric Measurements of Polyacrylonitrile Fibers," presented at *SAMPE 2004*, May 16 through 20, 2004.
5. S. M. White; J. E. Spruiell; and F. L. Paulauskas, 2004, "Fundamental Studies of Stabilization of Polyacrylonitrile Precursor, Part 1: Effects of Thermal and Environmental Treatments," presented at *SAMPE 2004*, May 16 through 20, 2004.

Bibliography

F. L. Paulauskas and T. A. Bonds, 2015, "Advanced Oxidation and Stabilization of PAN-Based Carbon Precursor Fibers," presented at the *2015 U.S. Department of Energy Hydrogen and Fuel Cells Program and Vehicle Technologies Office Annual Merit Review and Peer Evaluation Meeting,* June 11, 2015.

IV.2. Carbon-fiber Technology Facility—Oak Ridge National Laboratory

Project Details

Ronald Ott, Principal Investigator
Oak Ridge National Laboratory
P.O. Box 2008
Oak Ridge, TN 37830-6186
Phone: 865-574-5172
E-mail: ottr@ornl.gov

Carol Schutte,Technology Area Development Manager
U.S. Department of Energy
1000 Independence Avenue, SW
Washington, DC 20585-0340
Phone: 202-586-5371
E-mail: carol.schutte@ee.doe.gov

Contractor: Oak Ridge National Laboratory
Contract No.: DE-AC05-00OR22725

Executive Summary

In March 2009, the U.S. Department of Energy's (DOE's) Office of Energy Efficiency and Renewable Energy (EERE) issued a competitive call for proposals to construct and operate a highly flexible, highly instrumented, low-cost carbon-fiber technology facility for demonstrating and evaluating new low-cost manufacturing technologies at a pilot scale. Oak Ridge National Laboratory (ORNL) responded to the call and was awarded the project. Construction of the Carbon-Fiber Technology Facility (CFTF) began in March 2011 and the facility was commissioned for operations in March 2013.

The CFTF offers a unique, highly flexible, highly instrumented carbon fiber line for demonstrating advanced technology scale-up and for producing market development volumes of prototypical carbon fibers. The CFTF's unique capabilities, including the flexibility to process a range of feedstocks and product forms, are unmatched anywhere in the world. Designed to bridge what has been called the "valley of death" between laboratory research and commercial-scale deployment of low-cost carbon-fiber (LCCF) technologies, CFTF fills a critical need for supporting industrial competitiveness in the manufacture of carbon fiber in this nation. The objective of this project is to accomplish the safe and reliable operation of CFTF and to further DOE's objectives for large-scale commercialization of LCCFs. The CFTF supports EERE's efforts toward transitioning technologies to industry, specifically with respect to cost-effective carbon fiber for composite materials in high-volume energy applications.

Activities funded under this project include development of the process science for converting alternative precursor material into carbon fiber, production of sufficient quantities of carbon fiber from lower cost precursor materials to place LCCF in the hands of industry partners for the development of prototypical composite applications, and establishment of a skilled workforce and a training system that can be leveraged to assist industry in the development of a skilled carbon fiber and composites workforce. No information in any section of this report is export controlled.

Accomplishments

- Increased the modulus of the Kaltex textile-based polyacrylonitrile (PAN) carbon fiber to 41 Msi from 33.6 Msi in 2014, with tensile strength of 423 ksi versus 511 ksi in 2014 and greater than 1% strain. This puts the carbon fiber into the intermediate modulus (IM) range and exceeds automotive industry values (provided by USDRIVE) and DOE critical technical requirements for a modulus of 25 Msi, a

tensile strength of 250 ksi, and strain greater than 1.0% for carbon-fiber composite structural applications [1] (Fiscal Year [FY] 2015).

- Achieved high-volume throughput with the large tow Kaltex fibers, demonstrating processing of up to four (4×) bands. This is equivalent to doubling the CFTF throughput (i.e., 25 tons/year to 50 tons/year). Trials with additional bands have been attempted, but further development work is required for increased volume (FY 2015).
- An initial parametric study was performed to isolate the impact of low-temperature (LT) versus High-temperature (HT) carbonization furnace dwell times on the modulus of the Kaltex fibers. It was shown that for given temperature profiles, increasing dwell times increased the modulus. However, increased dwell time increases cost; therefore, a balance must be determined based on the desired modulus versus cost. This would also have an impact on capital investment because the required LT and HT dwell times impact furnace length (FY 2015).
- Dralon® textile-based PAN dry-spun fibers were processed at CFTF with average strength values of 204 ksi (standard deviation 45.36 ksi) and 247.2 ksi (standard deviation 44.2 ksi) from two different lots with modulus values of 27.55 Msi (standard deviation 0.97 Msi) and 30.7 Msi (standard deviation 2.1 Msi), respectively. This fiber shows promise as a precursor material and conversion protocols need to be developed once the fiber becomes manageable (FY 2015).
- CFTF ran a 2-week nonstop baseline run with standard 24-K industrial grade (BlueStar) commercial PAN precursor to demonstrate process consistency and equipment reliability in a long continuous run. During this trial, 1,293 lb of carbon fiber was produced with an average tensile strength of 517 ksi (standard deviation 37.9) and tensile modulus of 34.1 Msi (standard deviation 0.4). The carbon-fiber scrap rate was 2.1% of total carbon fiber produced. The start-up and shutdown precursor waste rate was 11% of total precursor compared to the industry average of 15% consumed (FY 2015).
- A precursor prestretch simulation was performed by stretching textile PAN (Kaltex) in an oxidation oven, collecting the prestretched fiber, and processing it through the normal conversion process. The initial simulation showed that mechanical properties were unaffected by prestretching vs. oxidative stretching, but the line speed could be increased by 20% in the trial. Based on increased line speed, a prestretch station offers value to the conversion process. Additional trials are needed to engineer the equipment specifications of the prestretch station (FY 2015).
- 650 visitors representing 110 companies toured CFTF. ORNL is currently in discussions with one manufacturer to process their material in CFTF (FY 2015).
- CFTF produced 15,165.2 kg of carbon fiber and 12,407.2 kg was transferred to outside companies and research organizations for further research (FY 2015).

Future Directions

- Develop economically attractive (as defined by suppliers) processing conditions for alternative precursor materials to establish multiple sources of precursors. Manufacturers of LCCF will need/require multiple sources of precursor material to not be locked into one supplier, thus reducing risk.
- Increase the number of bands of the large tow format Kaltex material to determine the maximum number of bands capable of being processed at CFTF; monitor and report power consumption to correlate with mass throughput.
- Establish lot-to-lot Kaltex precursor variability through mechanical properties, linear density, and chemical and microstructural analysis to establish variability of the textile manufacturing process.
- Identify patterns and relationships among discrete process steps and inputs through advanced analytics applied to historical process data and optimize the factors that prove to have the greatest effect on yield.

- Support all EERE's low cost carbon fiber development activities.

Technology Assessment

- Target: Scale up alternative low-cost precursors and precursor-specific processing technologies for manufacture of LCCFs. Alternative materials include multiple sources of textile acrylic fiber and lignin for functional applications.
- Gap: The availability of alternative precursors (such as textile acrylic fiber) may be a challenge due to the small quantities, relative to the needs of the textile industry, required by CFTF.
- Target: Increase the number of Kaltex textile fiber bands to successfully increase the volume of fiber to three times throughput.
- Gap: Equipment limitations may limit determination of the ultimate number of bands able to be successfully processed.

Introduction

The goal of CFTF is to provide the advanced carbon fiber research, development, and demonstration capability necessary to achieve commercialization of LCCF technologies to support a wide range of clean energy initiatives. CFTF serves as a multi-industry, multi-participant technology demonstration and deployment facility easily accessed by key research and development and industry partners. The main objectives are to translate the science of carbon fiber manufacturing to a scalable, cost-effective, and energy-efficient manufacturing process; demonstrate and deploy a skilled workforce development model; and enable commercialization of LCCF and composites for a broad range of industrial clean energy applications. Key strategies to be implemented by the project are to (1) develop and implement the process science for th conversion of alternative precursor materials into LCCF, (2) produce and disseminate quantities of LCCF to industrial partners for evaluation in composite components, and (3) develop a skilled workforce for the carbon fiber and composites industries and transition technology by being a user facility to help industry scale up their precursors.

Approach

CFTF is open for tours; therefore, industry and others can see the technology and process science being developed to produce LCCF with industry-appropriate mechanical properties from alternative precursor materials. Currently, there is no commercial manufacturer of this particular LCCF; therefore, CFTF plans to produce enough of it for industry to evaluate, thus showcasing the quality of the LCCF on a multitude of end user platforms. This is intended to produce industry demand for the technology. CFTF staff members continue to hold discussions with industrial partners that are interested in scaling the processes being developed at CFTF. The financial investment for industry to scale the technology is significant and is not quickly decided upon. One CFTF mission is to transition this technology to industry for scaling, but numerous technical challenges remain that must be overcome to further reduce the risk for industry to implement the technology. These technical challenges are being addressed at CFTF in collaboration with industry in order to reduce implementation risks. Some of these challenges are handling the large tow, increasing throughput, splicing and splitting the large tow, and developing appropriate sizing for LCCF for specific composite applications. CFTF continues to be a training ground for technical staff in the production of carbon fiber. Multiple tools have been developed to establish a training program for future carbon fiber production facilities.

Results and Discussion

Tow Splitting

Tow splitting trials have been run in the following locations on the line:

- Before oxidation on raw tow out of Drive 1: This location proved to be problematic due to the heavy intermingling of the raw tow. The splitter apparatus created rough regions in the tow that burned out in the first oxidation oven. This was not a viable option for splitting the large tow.
- Exit of Zone 4 before the LT furnace (Figure IV-10): This location was much better than the first area, but it created fuzz in the bands that had to be manually removed very frequently. A different design of splitter will be tried here.
- Sizing bath: The fiber is wet and lubricated here. This area shows promise, but some filament sections are crossed over, causing breakage and loose ends in winding. We are working to understand the cause and correct the crossed over filaments upstream.

Immediately before winding (Figure IV-11).The fiber was sized and dried at this point in the line. The splitter apparatuses used in this area tended to break or cut the crossed over filaments, causing loose ends on the spools, which is unacceptable. Again, more work is needed upstream to understand and correct the crossed over filaments.

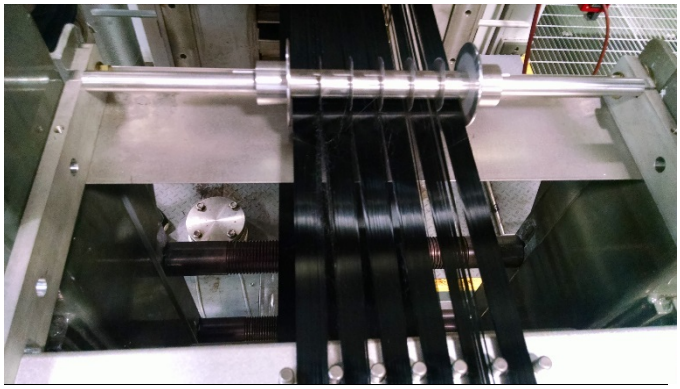

Figure IV-10: Tow splitting trial at exit of oxidation oven in Zone 4.

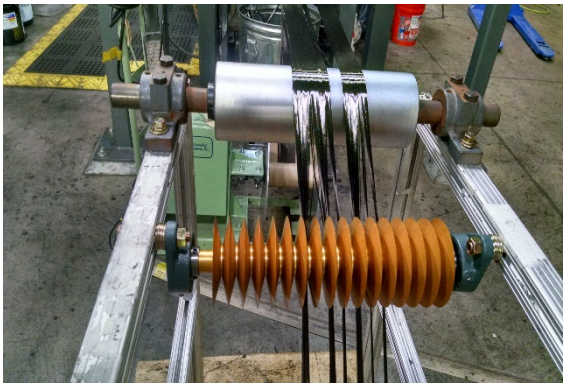

Figure IV-11: Tow splitting trial before winding station.

In addition to splitting efforts in the conversion process, Kaltex is working to split the tows for carbon fiber production without increasing cost. Kaltex is implementing key aspects of splitting the tow at the spinnerets and has provided initial split tows to CFTF. CFTF ran these initial split tows for the first time in September 2015 and was successful in getting the fiber through the oxidation ovens, LT furnace, HT furnace, and surface treatment. Samples were collected and tested. More work needs to be done to optimize fiber quality through temperature and stretch profile changes and more development work at Kaltex is needed. This split tow precursor shows a lot of potential. Thermoplastic sizing/resin systems are being evaluated to allow the fiber to be manufactured into tapes rather than split into dry tows, with any loose edges contained by the sizing/resin.

Two-Week Baseline Run

CFTF ran a 2-week nonstop baseline run with a standard 24-K industrial grade (BlueStar) commercial PAN precursor. The purpose of this 2-week baseline run was to demonstrate process consistency and equipment reliability of the carbon fiber line in a long continuous run. This required in situ splicing of feed material bobbins. The trial lasted for 332 hours with a throughput rate of 4 kg per hour. During this trial, 1,293 lb of carbon fiber was produced with an average tensile strength of 517 ksi (standard deviation 37.9) and tensile modulus of 34.1 Msi (standard deviation 0.4). The carbon fiber scrap rate was 2.1% of total carbon fiber

produced. The startup and shutdown precursor waste rate was 11% of total precursor consumed. Table IV-17 gives a summary for this run and the resulting properties of the products by lot number.

Several observations were made during this run. There was a clear pattern that showed operating with the drive nip rolls down improved the tensile strength and tensile modulus versus operating the drives with the nip rolls raised. More analysis is needed to understand this phenomenon. In addition, higher carbon fiber mechanical properties were achieved with the makeup air fans set at 1,800 cfm versus 3,000 cfm. This trial demonstrated that the CFTF carbon fiber conversion line and technicians are capable of performing at the stated engineering specifications of the equipment.

Table IV-17: CFTF 2-week continuous production run (2/22/15 through 3/8/15) summary and results.

CFTF B24 2-Week Continuous Production Run 2/22/2015 through 3/8/2015 Lot Numbers PEO241150203 through PU0241150301					
Precursor		**Carbon Fiber**		**Production Hours/Rates**	
Precursor Input after Zone 4 to Begin Production (kg)	3,036.62	Carbon Fiber Tubes (kg)	1,267.03	Total Hours from Z4 to Begin Production	332.5
Startup Precursor Waste (kg)	235.68	Waste Carbon Fiber (kg)	26.48	Total Hours "Off Series"	8.4
Shutdown Precursor Waste (kg)	101.63	Total Carbon Fiber Produced (kg)	1,293.51	Total Carbon Fiber Production Hours	324.1
Total Precursor Waste (kg)	337.31			Precursor Throughput (kg/hour)	8.1
				Carbon Fiber Production Rate (kg/hour)	4.0

Lot Analysis Information	Tensile Strength (ksi)	Tensile Modulus (msi)	Elongation (%)	Linear Density with Size (g/m)	Sizing (%)	Density (g/cc)
PEO241150203	500.0	34.1	1.47	1.52	1.09	1.750
STD	48.8	0.4	0.14	0.03	0.23	0.003
PUO241150301	534.8	34.1	1.57	1.49	0.94	1.752
STD	27.0	0.4	0.08	0.06	0.23	0.007

Dralon® Precursor Processing

Dralon®-supplied, dry-spun PAN fibers were processed at CFTF and the research team had great difficulty in getting the fiber out of the bale and into the machine. The tow would tear and kink before even entering the first oxidation oven. Dralon® has been made aware of this and is in the process of evaluating multiple solutions about how the fiber is sized to render it at least minimally transportable through the system. Despite these difficulties CFTF was able to process small amounts of the fiber through the system. This is a remarkable development because just getting a new precursor through the system the first time typically takes weeks. After carbonization, some melting of the fibers occurred during this first run. This is not an unexpected development and some modification of processing conditions will likely remedy this problem.

CFTF staff performed mechanical tensile testing on "broomstraw" samples (American Society for Testing and Materials Method D4018) [2] of the small amount of fiber they were able to get through the system. A single sample achieved 320-ksi strength; however, average strength values for each lot were between 200 and 250 ksi. Modulus values were around 30 Msi, which indicates that the appropriate graphene structure is being developed. Densities were typically below 1.78 g/cc. Typical carbon fibers have densities of 1.79 to 1.82 g/cc.

The results of this initial processing of Dralon® are (1) sizing for the precursor must be modified to enable processing of fiber continuously through the system to develop the conversion protocol; (2) the property values achieved (i.e., strength, modulus, and density) show potential for using this material as a precursor, but data are very limited and preliminary; (3) the conversion protocol needs to be developed once the fiber becomes manageable; and (4) fiber fusing must be eliminated, which must be done by Dralon® because it involves the chemistry of the precursor and/or the chemistry of the sizing.

High Volume

CFTF was successful in simultaneously processing four large tows (Figure IV-12) of Kaltex through the oxidation ovens, LT furnace, HT furnace, and surface treatment area and collecting carbon-fiber samples for testing on each of the four tows. The initial trial run showed no decrease in resultant carbon-fiber mechanical properties and an unexpected reduction in power draw in the oxidation ovens. This run configuration doubles the nameplate capacity throughput of the CFTF carbon fiber line from 25 to 50 tons/year. More material handling equipment development needs to be completed to run four simultaneous large tows consistently; however, this volume increase is feasible with the textile PAN polymer formulation. This will be a significant, cost-lowering technology breakthrough over the current state of the industry once all trials and necessary equipment adjustments have been made.

Figure IV-12: Four bands of large tow Kaltex fibers entering the oxidation ovens

Prestretch

One of the primary differences between textile PAN and carbon-fiber precursor PAN is the amount of drawing or stretching the fiber experiences in the spinning operation. Carbon-fiber precursors are drawn more than 10 times in the spinning process. By contrast, textile PAN fibers (such as those manufactured by Kaltex® and Dralon®) are drawn only about three times. Drawing is important for alignment of carbon in the molecular chain. Proper alignment of the carbon is necessary for producing optimal mechanical properties in the resultant carbon fiber. Therefore, textile PAN must be drawn further in or before the oxidation step of the conversion process to both improve mechanical properties of the carbon fiber and facilitate faster line speeds.

For these reasons, a prestretch station could be beneficial to achieving the highest possible mechanical properties from low-cost textile PAN precursors and other alternative precursors. A simulation trial was performed to determine whether a prestretch station would improve the mechanical properties of the resultant carbon fiber or facilitate faster line speeds. This simulation was performed by stretching textile PAN (Kaltex) in an oxidation oven, collecting the prestretched fiber, and processing it through the normal conversion process. The initial simulation showed that the mechanical properties were unaffected by the prestretching versus oxidative stretching, but the line speed was increased by 20% during the trial. Based on the increased line speed, a prestretch station offers value to the conversion process. Additional trials are needed to engineer the equipment specifications of the prestretch station.

Parametric Study

The first in a series of parametric studies was performed to evaluate the impact of processing conditions/parameters on the economics and mechanical performance of the carbon fiber. Evaluation of the dwell time within the LT and HT carbonization furnaces was selected for this first study. Although, the LT and HT dwell times are not the most sensitive parameters impacting cost, they are very easy to isolate with respect to other process parameters and they do have a significant impact on mechanical performance, specifically the tensile modulus.

Figure IV-13 shows that with an increased dwell time in the LT and HT furnaces for the given temperature profiles in the furnaces, the modulus increases with increased dwell time for throughputs greater than 4 kg/hour. This will have an impact on operating cost and capital cost based on the performance level of the desired carbon fiber.

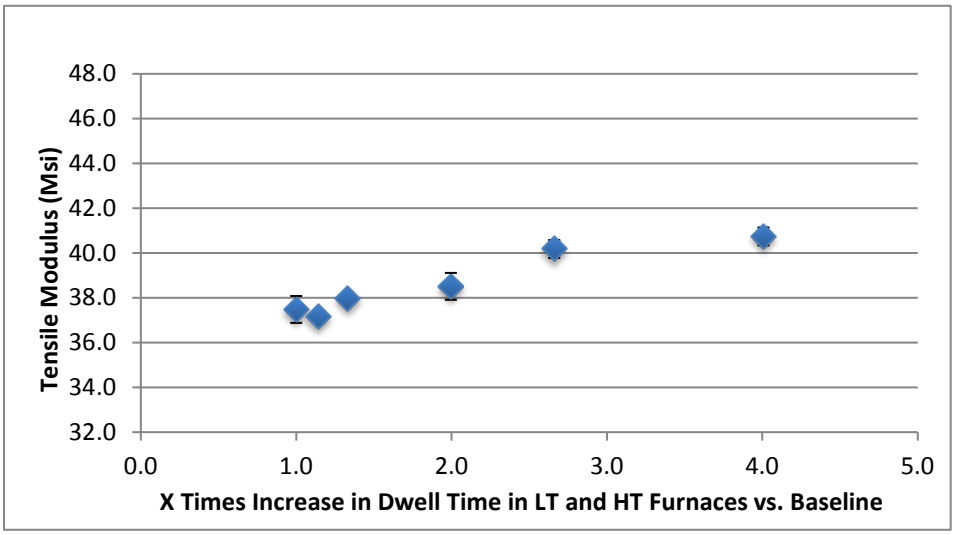

Figure IV-13: Modulus versus LT and HT dwell time for two tows of the Kaltex precursor.

Intermediate Modulus

Efforts are ongoing for increasing the modulus of the Kaltex fiber into the IM regime (greater than or equal to 40 Msi). This effort will exceed the original industry requirements and is also a direct result of feedback from the automotive industry indicating that stiffness is preferred over strength [1]. IM carbon fiber is within a different price market from industry-grade carbon fiber. This work will be able to provide about 50% cost reduction compared to industry-grade carbon fiber and also provides a modulus equivalent to IM grade fiber. The Kaltex fiber can be modified to have an IM, but with strength values that are lower than commercially available IM carbon fiber. CFTF has explored multiple methods for increasing the modulus of the Kaltex fiber while maintaining the tensile strength, achieving a modulus of 41 Msi and a tensile strength of 423 ksi for a particular set of processing conditions. Once the optimal set of conditions is determined, validation runs need to be conducted to show consistent, low variations in performance data for the specific set of processing conditions.

Technology Transfer Path

CFTF staff is in the process of submitting an invention disclosure to capture the unique combination of materials and processing conditions that are being used to produce the high-volume IM carbon fiber: “Method of Producing Carbon Fibers from Multipurpose Commercial Fibers.” Technology transfer also occurs when the CFTF is used by industry to evaluate scale-up of their precursors.

Kaltex, the producer of the textile PAN, has shown significant interest in commercializing LCCFs being developed at CFTF. Earlier during the fiscal year, the CFTF staff was invited to be part of a meeting held at Faurecia’s North American headquarters to discuss a commercialization strategy. The following companies participated in the meeting and each has shown interest in LCCFs: Kaltex, BST Nano Carbon, Caterpillar, Asahi Kasei (AK) Plastics, Laystitch, Chomarat, and Baden Aniline and Soda Factory (BASF). At this meeting, Kaltex showed interest in scaling the technology, either by themselves or in some form of a business arrangement with other end user companies. Since that meeting, Kaltex’s interest in scaling the technology has increased so they are pursuing loan opportunities (one is through the DOE Loan Program).

Several other groups have shown interest in scaling the technology and are in discussions with material suppliers, end users, and loan institutions.

Conclusion

CFTF has been focused on addressing technical challenges that impact the cost per unit volume of carbon fiber. Cost analyses show that the approach CFTF is taking with commodity-grade textile PAN at a high volume should reduce the cost of industrial-grade carbon fiber by approximately 50%. Significant advancements have been made in this area and increases the performance of the Kaltex-based carbon fiber. In order to impact the cost per unit volume of carbon fiber, there has been a doubling of volume of the textile-based carbon fiber that has a significant impact on reducing operational cost per unit volume of carbon fiber. Also, with the increased modulus (which is the desire of the end users), the textile-based carbon fiber is able to provide a unique set of mechanical performance that does not exist on the market today at any cost. The automotive industry acknowledges that stiffness is a need and that they are able to give up some level of strength based on cost. The textile-based carbon fiber with low 400s ksi tensile strength and greater than a 40-Msi modulus and high-volume processing capability has tremendous potential for meeting the performance and cost metrics for the automotive sector.

References

1. S. Baker, 2016, "Low Cost Carbon Fiber from Renewable Resources,"" presented at the *2010 DOE Annual Merit Review*, Washington, DC on June 7-11, 2010 ORNL, accessed January 4, 2016, https://www1.eere.energy.gov/vehiclesandfuels/pdfs/merit_review_2010/lightweight_materials/lm005_baker_2010_o.pdf and private communications with industries including BST Nano, Faurecia, Fiat Chrysler Automobiles, and Honda,.
2. ASTM Standard D 4018-11, "Standard Test Methods for Properties of Continuous Filament Carbon and Graphite Fiber Tows," ASTM International, West Conshohocken, PA, 2011, DOI: 10.1520/D4018-11; www.astm.org.

Bibliography

Presentations

C. Jackson, 2014, "Manufacturing of Low-Cost Carbon Fiber from Unmodified Textile PAN Fiber," presented at the *Composites World 2014 Conference*, La Jolla, CA.

C. Jackson, 2015, "ORNL Carbon Fiber Technology Facility," presented at the *USCAR Materials Tech Team Meeting*, Southfield, Michigan.

R. Ott, 2014, "Carbon Fiber Technology Facility Update," presented to the Oak Ridge Carbon Fiber and Composites Consortium," Knoxville, Tennesssee.

R. Ott, 2015, "ORNL Manufacturing Demonstration Facility and Carbon Fiber Technology Facility," presented at the American Carbon Society Workshop, Oak Ridge, Tennessee.

Patents/Invention Disclosures

R. Chambers; J. Crabtree; and C. Jackson, 2015, "Method of Measuring Density of Oxidized and Carbonized Fibers In-Situ," Invention Disclosure 201503593, September 2015.

C. Jackson, 2015, "Method of Producing Carbon Fibers from Multipurpose Commercial Fibers," Invention Disclosure 201503583,(September 2015).

C. Jackson, 2014, "Modular Line Configuration for Carbon Fiber Conversion," Invention Disclosure 201403438, (December 2014).

IV.3. Predictive Engineering Tools for Injection-Molded Long Carbon-Fiber Thermoplastic Composites—Oak Ridge National Laboratory

Project Details

Vlastimil Kunc, Principal Investigator
Oak Ridge National Laboratory
1 Bethel Valley Road
Oak Ridge, TN 37831
Phone: 865-919-4595
E-mail: kuncv@ornl.gov

C. David Warren, Principal Investigator
Oak Ridge National Laboratory
1 Bethel Valley Road
Oak Ridge, TN 37831
Phone: 865-574-9693
E-mail: warrencd@ornl.gov

Aaron Yocum, Contract Manager
National Energy Technology Laboratory
3610 Collins Ferry Road
Morgantown, WV 26507-0880
Phone: 304-285-4852
E-mail: aaron.yocum@netl.doe.gov

Carol Schutte, Technology Area Development Manager
U.S. Department of Energy
1000 Independence Avenue, SW
Washington, DC 20585
Phone: 202-287-5371
E-mail: carol.schutte@ee.doe.gov

Contractor: Oak Ridge National Laboratory
Contract No.: DE-AC05-00OR22725

Executive Summary

The objective of this project is to validate three-dimensional (3D) models for long carbon-fiber-reinforced, thermoplastic, injection-molded composites. Advanced characterization techniques are being used to generate a database of experimental results for carbon-fiber orientation and carbon-fiber length distribution within a component. Computational models validated using a part with features representative of an automotive component and the database of results will be made available to the general public via the World Wide Web. Additionally, this predictive technology will be used to create a demonstration part that will lead to production implementation of a separate part by Ford Motor Company.

Oak Ridge National Laboratory (ORNL) is mainly responsible for generating and distributing experimental data with proven measurement techniques and coordinating the project. Ford Motor Company is responsible for system specification and weight-reduction analysis. BASF and PlastiComp are preparing and supplying materials for the project and will assist with part molding. Minco and BASF are responsible for molding the final part. The University of Illinois jointly assists by supporting model integration with Virginia Polytechnic

Institute. Moldex3D North America is responsible for implementation and commercialization of validated models.

Accomplishments

- Established acceptable temperatures for fiber-length sample pyrolysis in atmosphere and in nitrogen (Fiscal Year [FY] 2014).
- Qualified molding machines intended for plaque molding and complex part molding by performing fiber length distribution (FLD) measurements on purges (FY 2014).
- Produced material for molding trial: polypropylene (PP) with 20% and 40% carbon fiber and polyamide (PA) with 20% and 40% carbon fiber (FY 2014).
- Established target molding parameters and molded plaque samples with all materials under target (FY 2014).
- Performed rheology measurements with cone and capillary rheometers and established model input rheology data for PP materials (FY 2014).
- Performed preliminary flow analysis for the complex part (FY 2014).
- BASF-modified injection molding screw to achieve greater fiber lengths (FY 2015).
- Molded end-gated plaques with four materials with combinations of slow/fast fill speed and low/high back pressure (FY 2015).
- Molded complex parts with four materials with selected combinations of slow/fast fill speed and low/high back pressure (FY 2105).
- Performed fiber-length measurements at three locations for each plaque type (FY 2015).
- Performed fiber orientation measurements at three locations for each plaque, with five replicates performed at a central location (FY 2015).
- Completed a plaque mold filling simulation using Moldex3D software and compared fiber orientation and fiber length to experimental data (FY 2015).
- Completed measurements of FLD in the complex part to be reported after predictions are released by the team (FY 2105).
- Completed physical preparation of all fiber orientation samples for fiber orientation measurements in the complex part (FY 2015).
- Completed tensile and flexural stiffness predictions using experimental and predicted fiber orientation for plaque molded under the base condition: PA 40% carbon fiber, slow fill speed, and low back pressure (FY 2015).

Future Directions

- Complete flow simulation for the complex part.
- Report comparison of flow simulations and experimental measurements for the complex part.

Technology Assessment

- Target: Validate carbon-fiber length to 15% of model prediction on flat plaques using the reduced-order fiber breakage model.
- Target: Validate carbon-fiber length to 15% of prediction for the complex part using the reduced-order fiber breakage model.

- Target: Validate carbon-fiber orientation to 15% of prediction for the complex part using the fiber orientation model.
- Gap: A reduced-order fiber breakage model is not available in a commercial code. A reduced-order model is not validated for injection-molded carbon-fiber–reinforced thermoplastics.
- Gap: Fiber orientation and length models are not validated in commercial codes for injection-molded carbon-fiber–reinforced thermoplastics.
- Gap: An experimental dataset for validation of fiber orientation and fiber-length models, specifically for carbon fiber, is not available for parts with complex geometries.

Introduction

The objective of this project is to implement and validate computational tools for predicting fiber orientation distribution (FOD) and FLD in injection-molded, long carbon-fiber, thermoplastic composites for automotive applications. Validation for a complex part with realistic features was conducted and experimental results are being made available to the public. The intent is to validate prediction tools on an actual 3D automotive part using a long carbon-fiber thermoplastic material, resulting in weight savings at an acceptable cost.

The preliminary design indicates a potential for more than 50% weight reduction resulting from both part consolidation and material substitution. Ford Motor Company, with the support of this project team, has committed to bringing the technology toward production implementation with an integrated long carbon-fiber injection-molded thermoplastic system. In FY 2015, the team performed plaque and complex part molding trials, fiber length and fiber orientation measurements, Moldex3D and Moldflow software simulations, and stiffness predictions.

Approach

In FY 2015, the team molded plaques and complex parts with qualified equipment. The molding trial for the complex part was delayed while BASF modified the injection molding screw on the all service plastic molding (ASPM) equipment to achieve longer average fiber lengths. Plaques and complex parts were molded with four material compositions: PP with 20% and 40% carbon fiber and PA with 20% and 40% carbon fiber (C). Molding was performed in a combination of fast/slow fill speed and high/low back pressure. The conditions were held as close as possible for the different machines used for the plaque and complex part molding trials.

Fiber orientation and fiber length measurements were performed using previously reported techniques [1–4]. The techniques for plaque measurements are standard; however, modifications were made to account for the complex geometry part. Experimental data on the plaques are provided for three locations along the flow length. Because we encountered unexpected orientation states, additional replicate measurements were performed for the central location. For the complex part, the team agreed on feature-based validation, where the effect of a gate, rib, hole, change in thickness, and change in direction on fiber length and orientation is evaluated. Experimental results and approaches are detailed in this report. With most of the experimental work completed, predictions for complex parts can be finalized before the experimental results for the complex part are released for comparison.

Results and Discussion

The team performed purge trials with PlastiComp and ASPN equipment to qualify molders in the spring of 2014. Fiber length measurements have shown that a significant amount of fibers in the purge samples were long; however, there was a notable difference in FLD when measured on the PlastiComp sample compared to the ASPN sample. Based on this, the industry team members decided that modifying the screw design for the

ASPN injection molding press was necessary to produce parts with desirable properties, despite delays caused by such modification. BASF designed and procured a modified 105-mm diameter screw during the summer and fall months of 2014.

PA (PA6,6) and PP pellets of 12-mm length were pultruded at PlastiComp with 20% and 40% carbon fiber. These pellets were then used for plaque molding at PlastiComp, complex part molding at ASPN, and rheology measurements at Virginia Tech.

Table IV-18 shows the materials and processing conditions used for both plaque and complex part molding trials. The processing conditions (i.e., screw zone temperatures, mold temperatures, back pressure, screw speed, and fill speeds) were kept as close as possible for both molding trials; therefore, the results measured on plaques could be used for prediction of part results.

Table IV-18: Matrix of materials and processing conditions for plaque and complex part molding trials.[a]

Designation	Polymer	Fiber Loading [%]	Fill Speed	Back Pressure
PA20SL	PP	20	Slow	Low
PA20FH	PP	20	Fast	High
PA40SL	PP	40	Slow	Low
PA40FH	PP	40	Fast	High
PA20SL	PA	20	Slow	Low
PA20FH	PA	20	Fast	High
PA40SL	PA	40	Slow	Low
PA40FH	PA	40	Fast	High

[a]Sample labeling key: PA = polyamide, PP = polypropylene, 20 or 40 = 20% or 40% carbon-fiber content, S or F = slow or fast fill speed, L or H = low or high back pressure.

Figure IV-14 shows the 300-ton injection molding press used for plaque molding at PlastiComp. Figure IV-15 shows the 950-ton press used for seat back part molding at ASPN. The plaque and part tools are shown in Figure IV-16 and Figure IV-17. Figure IV-18 and Figure IV-19 show examples of a molded edge-gated plaque and a seat back part. Figure IV-20 shows a purge from the second trial before measurement, with Table IV-19 confirming that the screw design modification resulted in an increase of average weight-based fiber length from 4.44 to 5.06 mm.

Figure IV-14: PlastiComp 300-ton injection molding press.

Figure IV-15: ASPN 950-ton injection molding press.

Figure IV-16: PlastiComp edge-gated plaque tool.

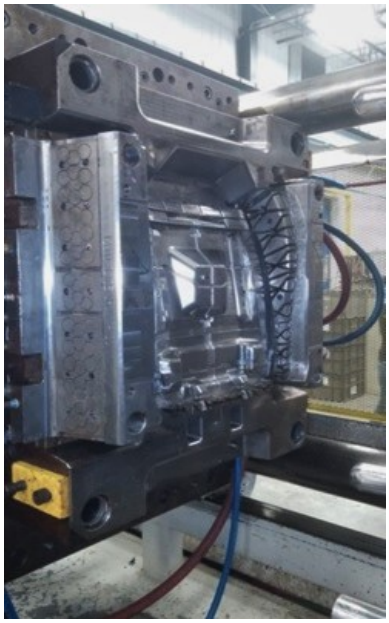

Figure IV-17: BASF seat back tool.

Figure IV-18: Molded edge-gated plaque.

Figure IV-19: Molded seat back part.

Figure IV-20: Purge sample from a molding trial with a new screw.

Table IV-19: Fiber length measurement results for purge samples.[a]

	Specimen Description	Fibers	Ln (mm)	Lw (mm)
1	PlastiComp	2,185	4.06	7.33
2	ASPN old screw	2,134	1.69	4.44
3	ASPN new screw	2,065	2.58	5.06

[a]Ln = number-averaged fiber length; Lw = weight-averaged fiber length.

After confirming that the screw modification achieved the desired FLD improvement, the team agreed on features and locations to be measured for model validation. The features include a gate, change in thickness, ribs, holes, and change in direction (Figure IV-21). The particular measurement locations were selected based on initial flow simulations predicting weld lines. The objective was to select locations not containing weld lines to establish the effect of part features on the polymer flow and resulting changes in FLD and FOD. Figure IV-21 also shows one of the exploratory pyrolysis trials performed to perfect the procedure for FLD measurement in a complex part.

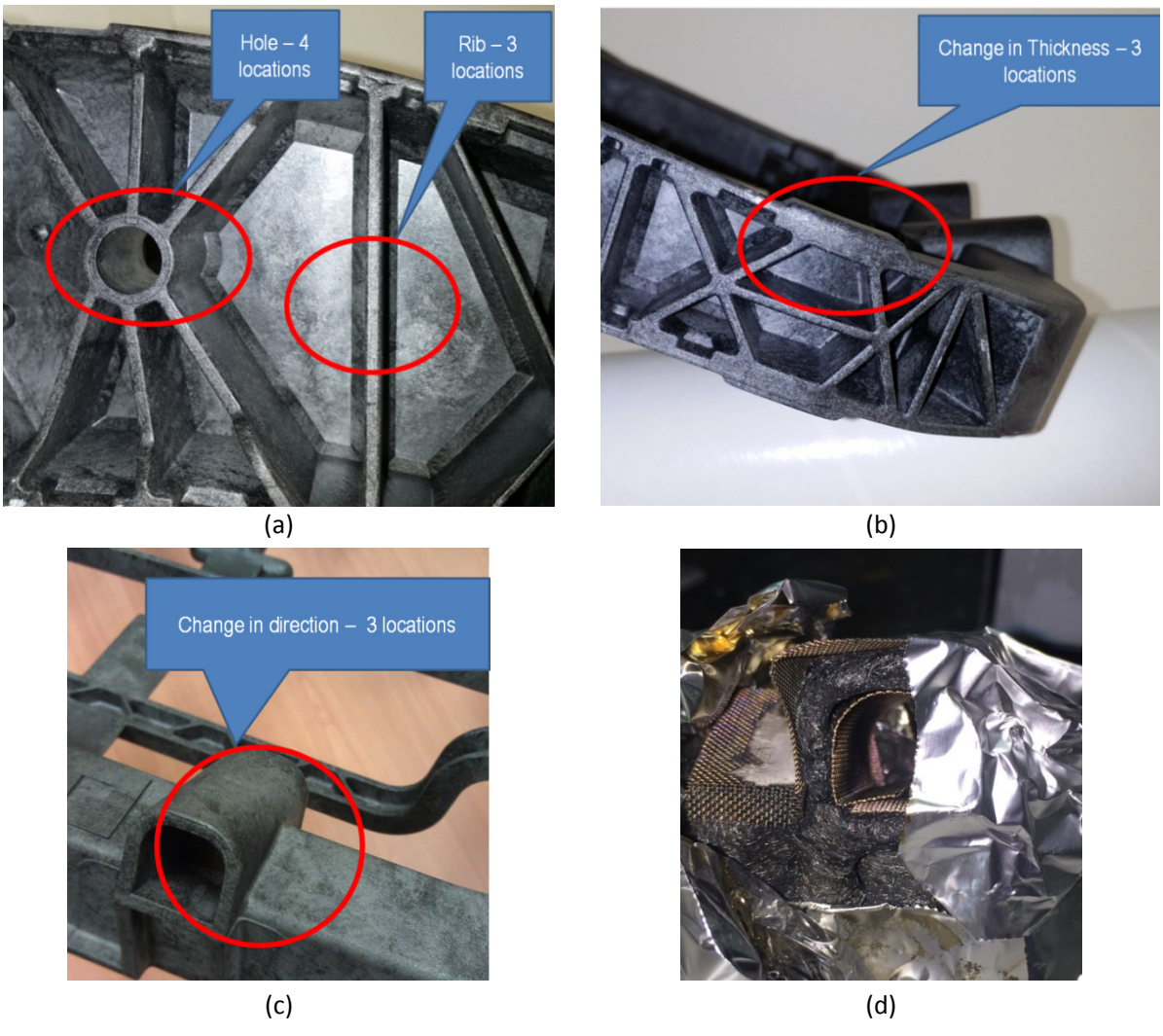

Figure IV-21: Hole and rib sample locations (a), change in thickness sample location (b), change in direction sample location (c), and pyrolized sample (d).

During this reporting period, all FLD and FOD measurements have been completed for plaques. These measurements have been disseminated among the team and used for establishing model parameters in Moldex3D software that will be used later for blind prediction of flow within a complex part. FLD measurement for the seat back is under way, with several measurements completed. Physical samples for FOD measurement are being prepared for optical measurement.

Plaque Fiber Length and Orientation Distribution Measurement

Plaque measurements have been performed at three locations along the flow length. Figure IV-22 provides the distances from the gate along the centerline for the measurement locations.

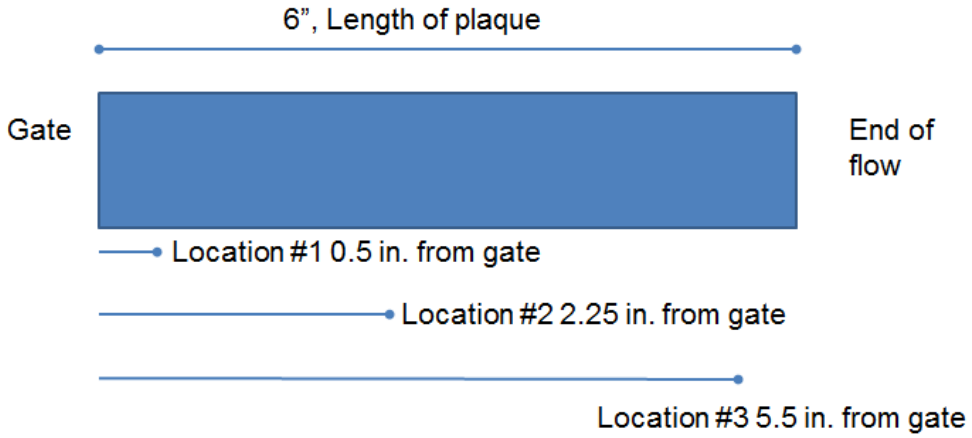

Figure IV-22: Sampling locations along the centerline of the plaque.

The project team shares measurement techniques and results during regular biweekly teleconferences. This venue serves as an informal technology transfer mechanism for the project partners and as a useful technical check of results in case of unexpected results. Figure IV-23 shows carbon fibers independently isolated by Ford and ORNL, confirming the presence of long-fiber bundles and short-fiber fragments.

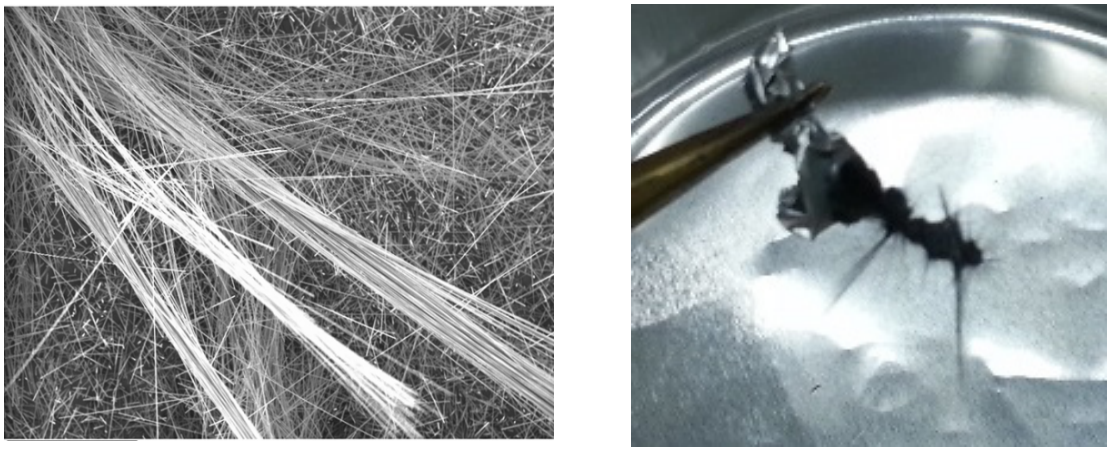

(a) (b)

Figure IV-23: Scanning electron microscope image of fibers obtained by Ford (a) and isolated fiber sample from ORNL (b). Both samples indicate the presence of long fibers and short fragments in the molded material.

Experimental measurements begin with sample isolation. FOD samples are then mounted, polished and etched, and imaged with a microscope [3,4]. FLD samples are pyrolized twice with a previously developed procedure

[1] and dispersed for imaging. For seat back samples, the team agreed on the features and locations to be measured.

Figure IV-24 shows an end-gated plaque and isolated FOD and FLD samples for all plaque types. Three locations along the flow length were isolated for each combination of material and processing conditions selected for measurement.

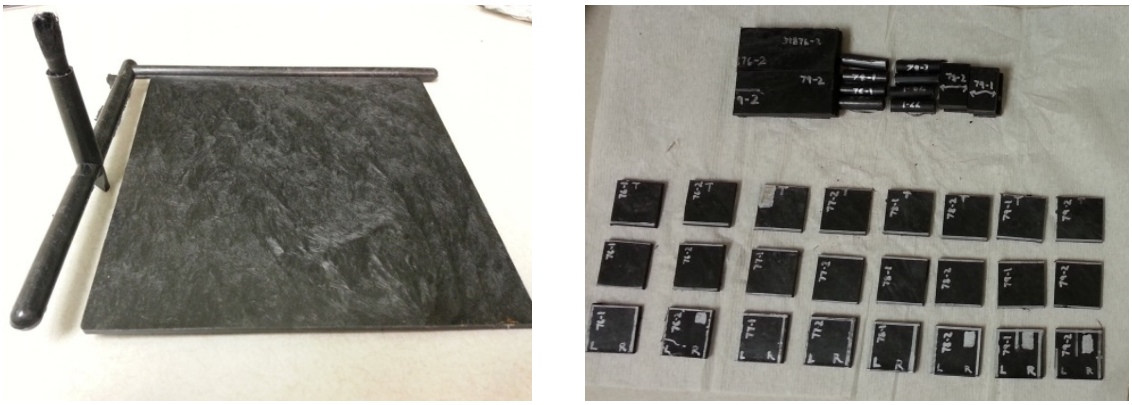

(a) (b)

Figure IV-24: End-gated plaque (a) and isolated FLD and FOD samples (b).

Figure IV-25 shows mounted FOD samples that were polished and etched before microscope imaging and the fiber plugs selected for FLD measurement. FLD samples undergo a second pyrolysis before dispersion and imaging.

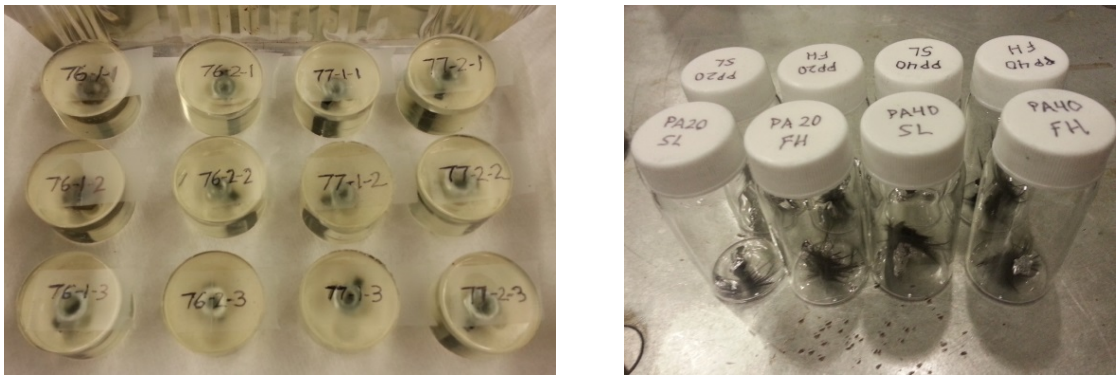

(a) (b)

Figure IV-25: Mounted FOD samples (a) and selected FLD plugs (b).

Figure IV-26 shows an FOD sample being imaged. After multiple trials, we have been able to obtain polishing, etching, and imaging settings for both PP and PA materials, giving us good contrast between fiber, matrix, and shadows for resolving ambiguity in fiber orientation. This optimization of settings was performed with utmost care because identical settings are used for measurement of FOD in the complex part where the ability to resolve fiber orientation ambiguity is critical.

Table IV-20 shows weight-averaged fiber length measurements for all plaques considered in this project. Slow fill speed and low back pressure molded samples exhibit longer average fiber length. Some scatter in the results can be attributed to fiber domains observed in the samples. Figure IV-26 shows a polished cross section of a plaque orientation sample with concentrated fiber domains being apparent as white regions in the image.

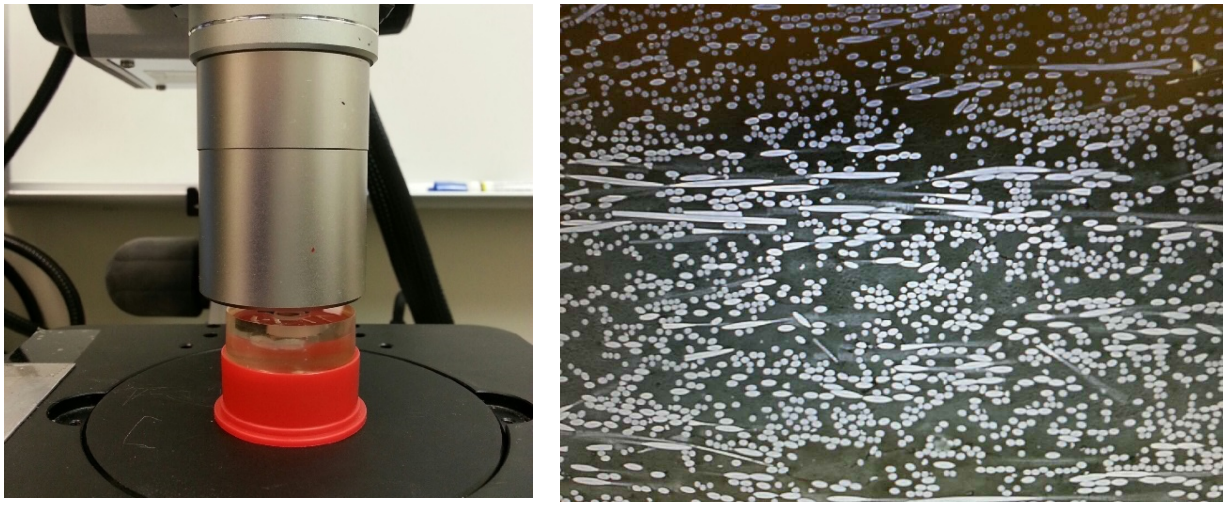

(a) (b)

Figure IV-26: FOD sample being imaged (a) and an example FOD image (b).

Table IV-20: Summary of weight-averaged fiber length measurements for plaques.[a]

Sample	Weight-Averaged Fiber Length
PA20SL_1	2.088
PA20SL_2	2.523
PA20SL_3	2.411
PA40FH_1	1.205
PA40FH_2	1.530
PA40FH_3	1.305
PA40SL_1	2.894
PA40SL_2	4.296
PA40SL_3	4.305
PP20SL_1	2.248
PP20SL_2	1.677
PP20SL_3	2.410
PP40FH_1	3.257
PP40FH_2	1.659
PP40FH_3	1.867
PP40SL_1	1.928
PP40SL_2	1.851
PP40SL_3	4.339

[a]Sample labeling key: PA = polyamide; PP = polypropylene; 20 or 40 = 20% or 40% carbon-fiber content; S or F = slow or fast fill speed; L or H = low or high back pressure; and 1, 2, or 3 = location from Figure IV-14.

The presence of these domains or fiber bundles was suspected to cause not only scatter in the FLD measurements, but also unexpected profiles in the FOD measurements. Therefore, replicate FOD measurements were performed at a single location (Figure IV-27), with the general profile of the FOD being confirmed (Figure IV-28).

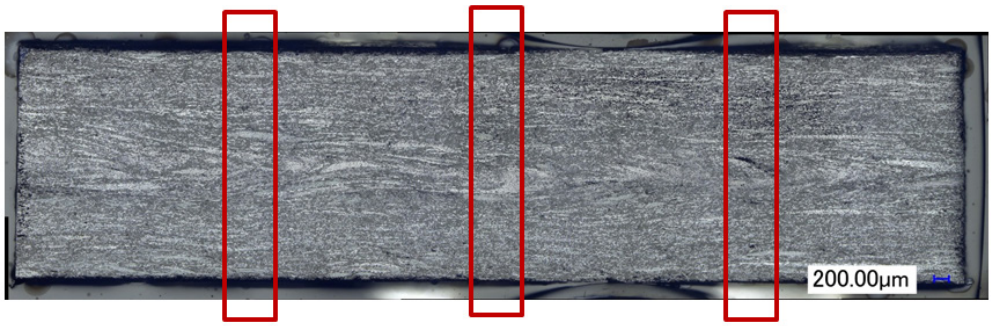

Figure IV-27: Polished cross section of an FOD sample with the locations of three replicate measurements.

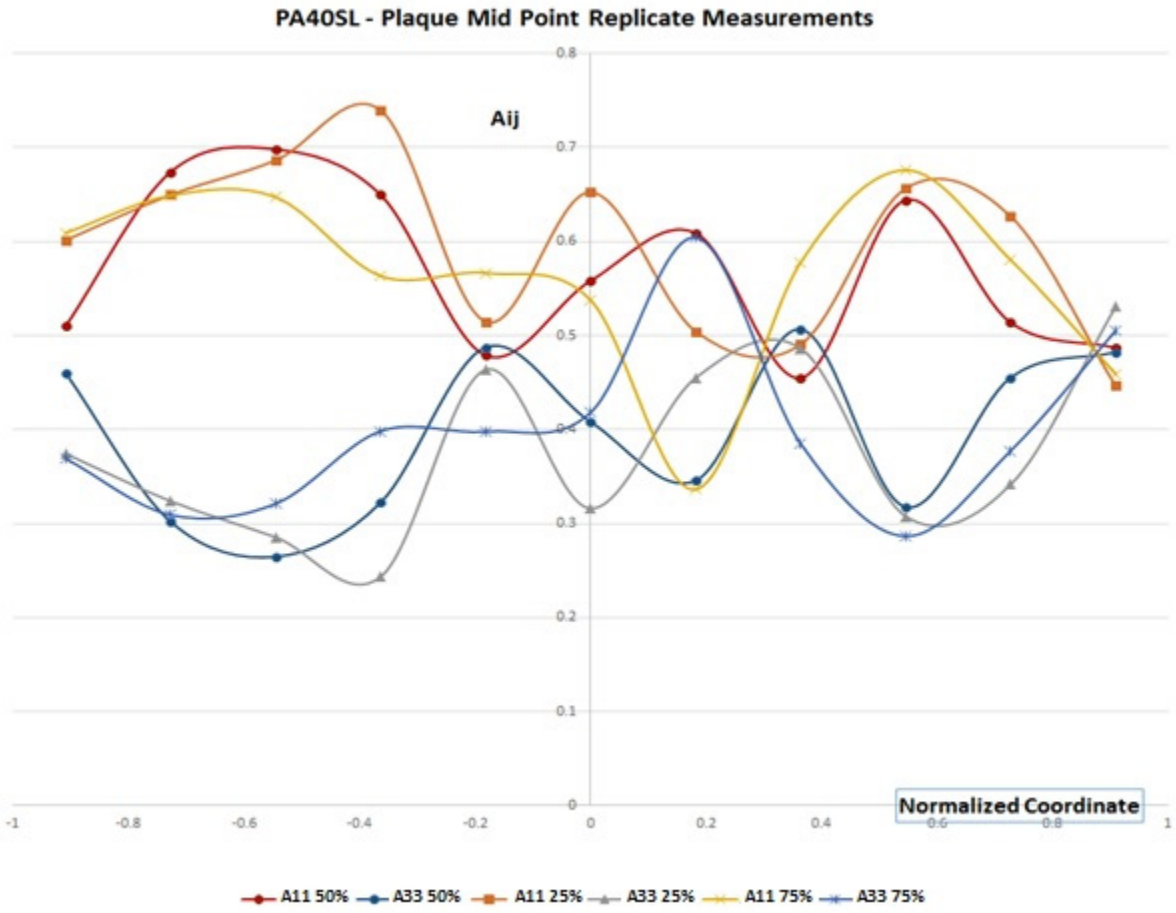

Figure IV-28: Replicate measurements at a single measurement location.

After measurements were verified, the database of results was distributed to the team members for comparison with Moldex3D and Moldflow simulations.

Complex Part Fiber Length and Orientation Distribution Analysis and Experiments

Measurements on the complex part samples began with cutting out relevant features from the parts. The procedure differed for FLD and FOD measurements. All complex part features must be isolated for FLD and FOD measurements. This isolation step was followed by fiber sample isolation, imaging, and measurement. FLD measurements for the complex part were complete. Isolation of FOD features required a careful final cut

near the plane, which was subsequently polished and imaged. Figure IV-29 shows isolated features for FOD measurements. All FOD samples were physically prepared for imaging during FY 2015.

Figure IV-29: Isolated features of the complex part.

Results of FLD and FOD measurements of the complex part samples will be released after predictions using Moldex3D and Moldflow are finalized.

Mold-Filling Simulations Using Moldex3D and Moldflow

The team has been performing validation primarily with Moldex3D software; however, significant effort has been devoted to comparing results between Moldflow and Moldex simulations. Initial simulations suggest that details of simulations (such as mesh density and element) may strongly influence differences in simulation results. Figure IV-30 shows the Moldflow and Moldex3D meshes used for initial simulations.

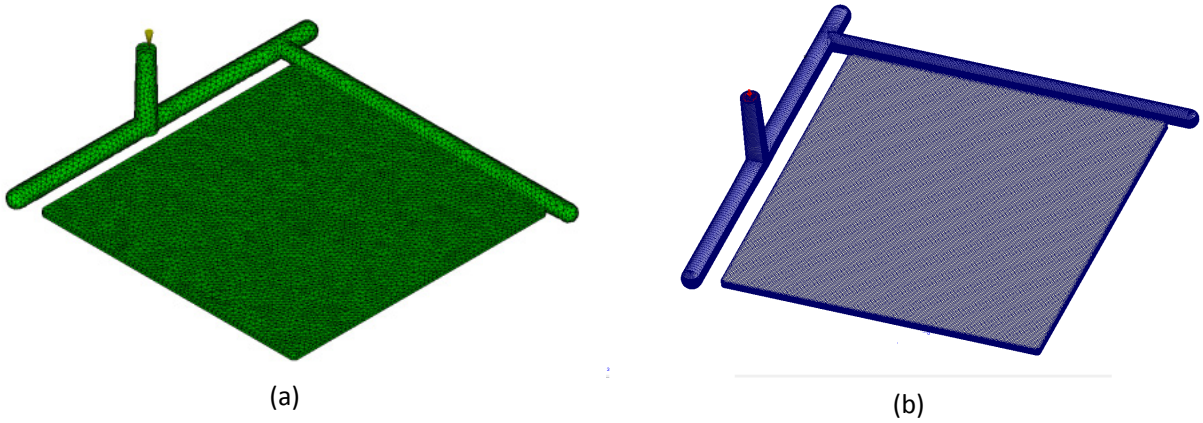

Figure IV-30: Moldflow mesh of plaque (a) and Moldex3D mesh of plaque (b).

A summary of the work done by Moldex3D North America in predicting fiber orientations and fiber lengths in the new test plaque design is given here. These predictions are compared with ORNL experimental data. Figure IV-31 illustrates the ORNL end-gated-plaque injection molding with slow filling for 40 wt % long carbon fiber-nylon66 composites.

For the fiber orientation parameter of the improved anisotropic rotary diffusion model, combined with the retarding/retardant principal rate model [5], parameters $C_I = 0.01$, $C_M = 1.0$ and Alpha = 0.965 are set in Moldex3D. Figure IV-32 through Figure IV-34 present a comparison of ORNL experimental data and Moldex3D predictions for FOD at three locations through the normalized thickness. The thickness-averaged

values of A_{11} and A_{22} are summarized in Table IV-21 and Table IV-22. The overall accuracy assessment for all locations meets the 15% deviation criterion.

Initial long carbon-fiber length and diameter are 13 mm and 7 μm, respectively. In the fiber breakage parameter setting of the Phelps-Tucker model [6], parameters C_D = 30 (drag coefficient), C_B = 0.01(breakage factor), and S = 2.5 (scalar factor) are given. Moldex3D provided a precondition function of screw-induced variation in fiber length (Figure IV-35). Before entering into sprue, the number-averaged fiber length L_n is 0.806 mm and the weight-averaged fiber length L_w is 3.059 mm. Figure IV-36 through Figure IV-38 present FLD through the normalized thickness. In addition, the thickness-averaged Ln and Lw values are summarized in Table IV-23 and Table IV-24, including experimental data, predicted values, and accuracy.

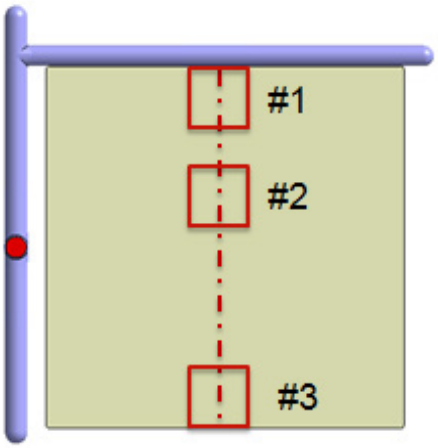

Figure IV-31: Measured points of fiber orientation are taken at three locations on the end-gated plaque.

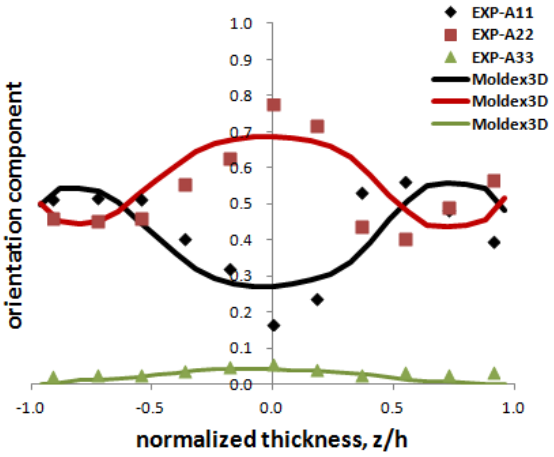

Figure IV-32: Experimental and predictive fiber orientation tensor-component distributions through the normalized thickness at Location 1 (Figure IV-31).

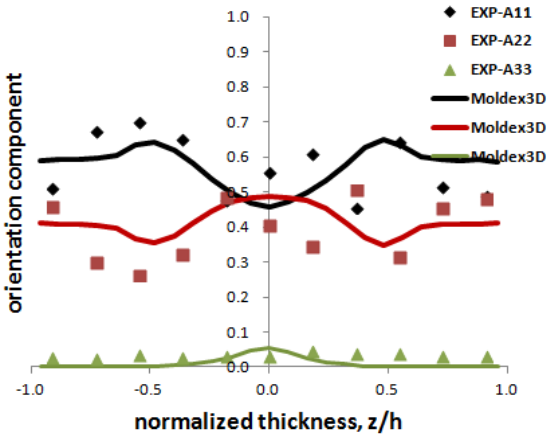

Figure IV-33: Experimental and predictive fiber orientation tensor-component distributions through the normalized thickness at Location 2 (Figure IV-31).

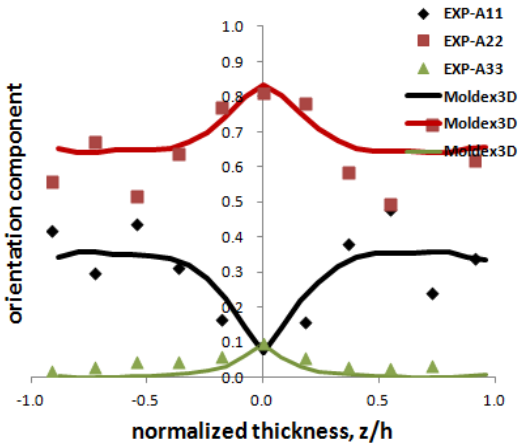

Figure IV-34: Experimental and predictive fiber orientation tensor-component distributions through the normalized thickness at Location 3 (Figure IV-31).

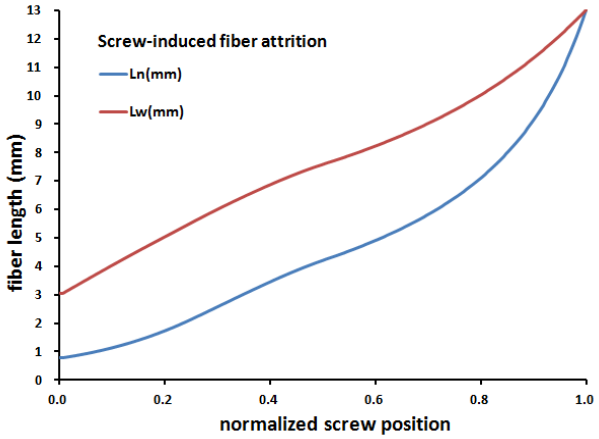

Figure IV-35: Moldex3D precondition of screw-induced variation in fiber length with respect to the normalized screw position.

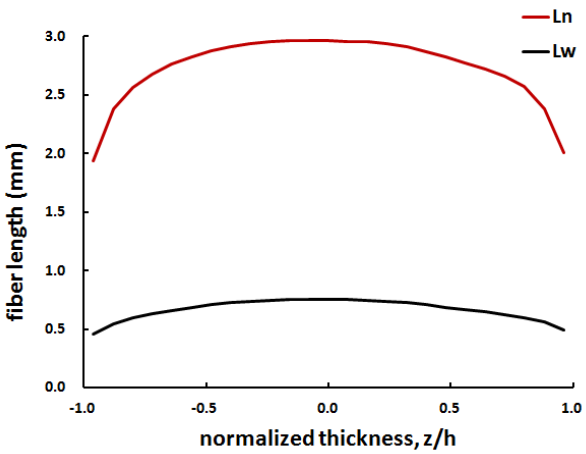

Figure IV-36: Predictive fiber length distribution through the normalized thickness at Location 1 (Figure IV-31).

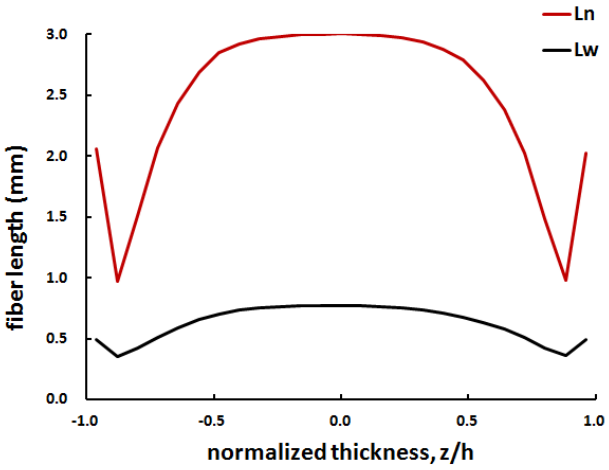

Figure IV-37: Predictive fiber length distribution through the normalized thickness at Location 2 (Figure IV-31).

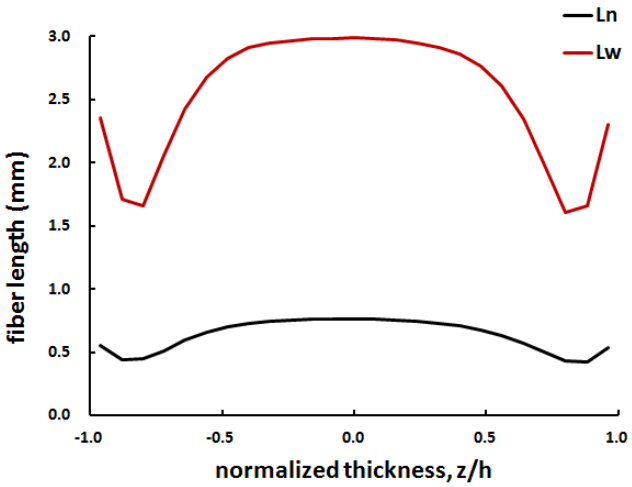

Figure IV-38: Predictive fiber length distribution through the normalized thickness at Location 3 (Figure IV-31).

Table IV-21: Averaged value of flow directional fiber orientation component A_{11} of ORNL experimental data and Moldex3D prediction showing the accuracy of the prediction.

Location	Averaged A_{11} (ORNL Experiment)	Averaged A_{11} (Moldex3D Prediction)	Agreement Within (%)
1	0.424	0.421	0.6
2	0.571	0.574	0.7
3	0.304	0.302	0.6

Table IV-22: Averaged value of cross-flow directional fiber orientation component A_{22} of ORNL experimental data and Moldex3D prediction showing the accuracy of the prediction.

Location	Averaged A_{22} (ORNL Experiment)	Averaged A_{22} (Moldex3D Prediction)	Agreement Within (%)
1	0.542	0.556	2.8
2	0.396	0.415	4.8
3	0.653	0.682	4.5

Table IV-23: Number-averaged fiber length (Ln) of flow directional component of ORNL experimental data and Moldex3D prediction showing the accuracy of the prediction.

Location	Ln (ORNL Experiment)	Ln (Moldex3D Prediction)	Agreement Within (%)
1	0.633	0.668	2.2
2	0.799	0.628	21.4
3	0.993	0.636	36.0

Table IV-24: Weight-averaged fiber length (Lw) of flow directional component of ORNL experimental data and Moldex3D prediction showing the accuracy of the prediction.

Location	Lw (ORNL Experiment)	Lw (Moldex3D Prediction)	Agreement Within (%)
1	2.894	2.730	5.7
2	4.296	2.460	42.7
3	4.305	2.536	41.1

Moldflow trial runs of plaque and seat back part simulations are completed, with filling patterns shown in Figure IV-39 and Figure IV-40. The parameter tuning process, which will follow the process in Moldex3D simulations, is in progress. Fiber length and orientation results will be obtained and compared with Moldex3D results once the parameters for fiber breakage and orientation models are determined.

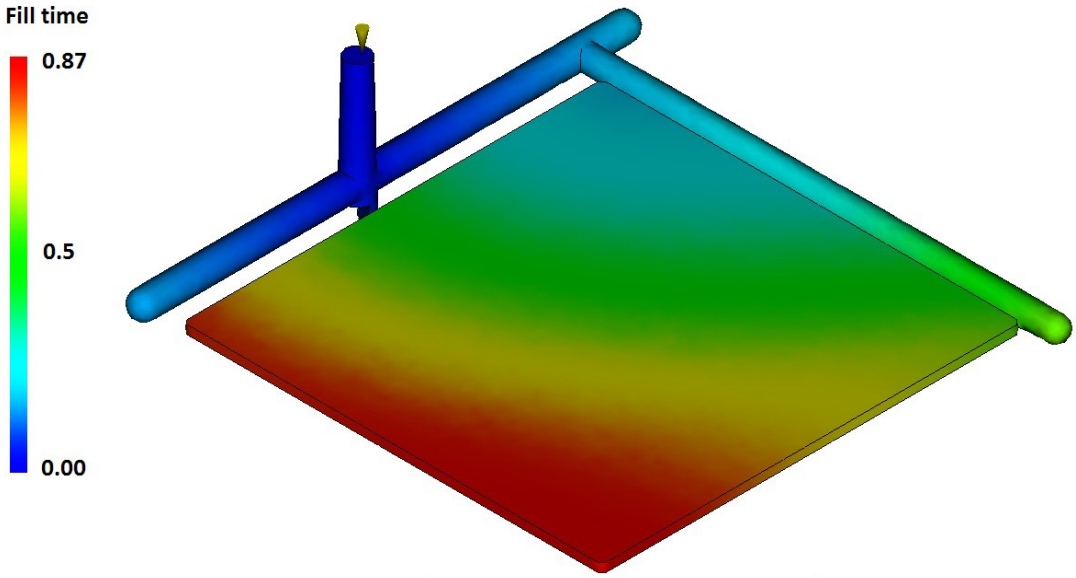

Figure IV-39: Predicted filling pattern for the plaque model in Moldflow.

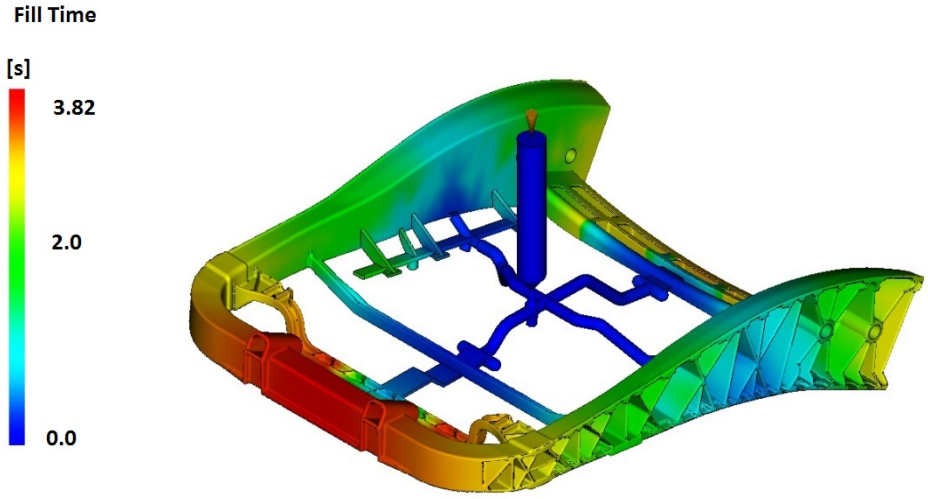

Figure IV-40: Predicted filling pattern for the seat back part in Moldflow.

Stiffness Predictions

Comparison of stiffness estimates using experimental and predicted fiber orientation measurements was performed for base material and processing conditions (i.e., PA resin with 40% carbon fiber molded under slow fill speed and low back pressure). Comparisons were performed at three locations within the plaque (Table IV-25).

Table IV-25: Calculated stiffness from measured and predicted fiber orientation showing the accuracy of the prediction.

Tensile Modulus

Location	E11 [Pa] (Predicted Orientation)	E11 [Pa] (Measured Orientation)	Agreement Within (%)
1	1.58E+10	1.57E+10	1.17
2 (average)	1.44E+10	1.45E+10	0.74
3	1.05E+10	1.58E+10	40.2
	E22 [Pa] (Predicted Orientation)	**E22 [Pa] (Measured Orientation)**	**Agreement Within (%)**
1	1.91E+10	2.06E+10	6.43
2 (average)	2.10E+10	2.06E+10	1.77
3	2.44E+10	2.06E+10	17.2

Flexural Modulus

Location	D11 [Pa m^3] (Predicted Orientation)	D11 [Pa m^3] (Measured Orientation)	Agreement Within (%)
1	4.25E+01	4.96E+01	15.6
2 (average)	4.33E+01	4.40E+01	1.73
3	6.29E+01	5.02E+01	22.6
	D22 [Pa m^3] (Predicted Orientation)	**D22 [Pa m^3] (Measured Orientation)**	**Agreement Within (%)**
1	5.50E+01	5.04E+01	8.85
2 (average)	5.52E+01	5.70E+01	3.19
3	3.49E+01	5.09E+01	37.3

Five replicate fiber orientation measurements were performed at Location 2.

Technology Transfer Path

The fiber orientation and fiber length prediction models validated in this project will be commercially available through Moldex 3D. Experimental data used for validation will be available in a publically accessible format. Additionally, industry participants are performing this project with a production intent.

Conclusion

In FY 2015, BASF modified the injection molding screw on the ASPN equipment to achieve greater fiber lengths; the team molded end-gated plaque and complex part samples with four materials for combinations of slow/fast fill speed and low/high back pressure (FY 2015). The team performed fiber length and fiber orientation measurements at three locations for each plaque type. Mold filling simulations using Moldex3D software were completed and simulated fiber orientation and fiber length were compared to experimental data.

Fiber length measurements were completed for the complex part and fiber orientation experiments are under way. Technical details of fiber length measurements and flow simulations are discussed in this report.

References

1. V. Kunc; B. J. Frame; B. N. Nguyen; C. L.Tucker III; and G. Velez-Garcia, 2007, "Fiber Length Distribution Measurement for Long Glass and Carbon Fiber Reinforced Injection Molded Thermoplastics," presented at *Composites Conference & Exposition*; Society of Plastic Engineers: Troy, Michigan.
2. C. Eberhardt and A. Clarke, 2001, "Fibre-Orientation Measurements in Short-Glass-Fibre Composites. Part I: Automated, High-Angular-Resolution Measurement by Confocal Microscopy," *Compos. Sci. Technol.,* 61(10); pp. 1389–1400.
3. G. M. Velez-Garcia et al., 2012, "Unambiguous Orientation in Short Fiber Composites Over Small Sampling Area in a Center-Gated Disk," *Composites, Part A,* 43(1); pp. 104–113.
4. G. M. Velez-Garcia et al., 2012,"Sample Preparation and Image Acquisition using Optical-Reflective Microscopy in the Measurement of fiber Orientation in Thermoplastic Composites," *J. Microsc.,* 248(1); pp. 23–33.
5. H.-C. Tseng; R.-Y. Chang; C.-H. Hsu, 2013, "Phenomenological Improvements to Predictive Models of Fiber Orientation in Concentrated Suspensions," *J. Rheol.,* (57); pp. 1597.
6. J. H. Phelps; A. I. Abd El-Rahman; V. Kunc; and C. L. Tucker, 2013, "A Model for Fiber Length Attrition in Injection-Molded Long-Fiber Composites," *Composites, Part A,* 51; pp.. 11–21.

Bibliography

None.

IV.4. Predictive Engineering Tools for Injection-Molded, Long-Carbon Fiber Thermoplastic Composites– Pacific Northwest National Laboratory

Project Details

Ba Nghiep Nguyen, Principal Investigator
Pacific Northwest National Laboratory
902 Battelle Boulevard
P.O. 999 – MSIN J4-55
Richland, WA 99352
Phone: 509-375-3634
E-mail: ba.nguyen@pnnl.gov

Leonard S. Fifield, Project Manager
Pacific Northwest National Laboratory
902 Battelle Boulevard
P.O. 999 – MSIN K4-18
Richland, WA 99352
Phone: 509-375-6424
E-mail: leo.fifield@pnnl.gov

Aaron Yocum, Project Officer
National Energy Technology Laboratory
3610 Collins Ferry Road
P.O. Box 880
Morgantown, WV 26507-0880
Phone: 304-285-4852
E-mail: aaron.yocum@netl.doe.gov

Carol Schutte, Technology Area Development Manager
U.S. Department of Energy
1000 Independence Avenue, SW
Washington, DC 20585
Phone: 202-586-1022
E-mail: carol.schutte@ee.doe.gov

Contractor: Pacific Northwest National Laboratory
Contract No.: DE-AC05-00OR22725 & DE-AC06-76RLO1830

Executive Summary

This project aims to integrate, optimize, and validate fiber orientation and length distribution models previously developed and implemented in the Autodesk® Simulation Moldflow® Insight (ASMI) software package for injection-molded, long-carbon fiber (LCF) thermoplastic composites. The project is organized into two phases: Phase 1 demonstrates the ability of the advanced ASMI package to predict fiber orientation and length distributions in LCF/polypropylene (PP) and LCF/polyamide 6,6 (PA66) plaques within 15% of experimental results. Phase 2 will validate the advanced ASMI package by predicting fiber orientation and length distributions within 15% of experimental results for a complex three-dimensional (3D) Toyota automotive part injection molded from LCF/PP and LCF/PA66 materials. Finally, Toyota and Pacific Northwest National Laboratory (PNNL) will estimate weight savings and cost impacts for the vehicle system using ASMI and structural analyses of the complex part.

This report describes the completion of Phase 1 activities and initiation of Phase 2 work performed by the team comprising PNNL; PlastiComp, Inc. (PlastiComp); Purdue University (Purdue); Autodesk, Inc. (Autodesk); Toyota Research Institute North America (Toyota); Magna Exteriors and Interiors Corp. (Magna); University of Illinois; and Virginia Tech. The work includes (a) improving and implementing advanced process models in ASMI for fiber orientation and length prediction, (b) measuring fiber orientation and length for the PlastiComp two-dimensional (2D) plaques selected for the go/no-go decision point, (c) validating ASMI fiber orientation and length predictions against the measured data for these plaques to pass the go/no-go decision point, (d) building tools to mold the complex 3D Toyota parts with and without ribs, (e) molding these parts using the conventional injection molding process and the PlastiComp Pushtrusion® in-line, direct-injection, long-fiber thermoplastic molding process (D-LFT), and (f) performing ASMI molding analyses of the 3D complex parts with and without ribs using actual process parameters to assess mold filling patterns.

Accomplishments

- Autodesk delivered a new research version of ASMI to PNNL for process modeling. This version includes the improved 3D fiber orientation solver and the reduced order model for fiber length distribution (FLD) using the proper orthogonal decomposition (POD) implemented in the mid-plane, dual-domain, and 3D solvers (Fiscal Year [FY] 2015).
- Autodesk implemented an improved fiber-orientation-distribution inlet-profile specification method through the part thickness for 3D meshes and provided an updated ASMI research version to PNNL (FY 2015).
- The University of Illinois assisted Purdue with fiber orientation measurement technique strategies, including interpretation of off-axis cross sections (FY 2015).
- The University of Illinois assisted Autodesk with software implementation of the POD approach for fiber length modeling and with fiber orientation modeling (FY 2015).
- Purdue conducted fiber orientation measurements at selected locations (i.e., named A, B and C) on the PlastiComp plaques adopted for the go/no-go decision point, including the fast-fill 30% by weight (wt%) LCF/PP edge-gated and center-gated plaques, slow-fill 50 wt% LCF/PP edge-gated and center-gated plaques, and fast-fill 50 wt% LCF/PA66 edge-gated and center-gated plaques. Purdue also delivered fiber orientation data to PNNL (FY 2015).
- PNNL used known methods to recover intact carbon fibers from LCF/PP molded materials and developed a new method for recovering intact carbon fibers from LCF/PA66 molded materials. Isolated fibers from the recovery were shipped to Purdue for length distribution analysis (FY 2015).
- Purdue conducted fiber length measurements for the nozzle 30 wt% LCF/PP purge materials and for the selected locations on the PlastiComp plaques adopted for the go/no-go decision point, including the slow-fill 30 wt% LCF/PP and 30 wt% LCF/PA66 edge-gated plaques (FY 2015).
- PNNL performed ASMI mid-plane and 3D analyses of PlastiComp plaques for fiber orientation and length model validations. Tensile and bending stiffness values calculated using the predicted fiber properties were compared with stiffness values calculated using the corresponding measured data provided by Purdue. The 15% accuracy criterion for agreement between stiffness based on ASMI mid-plane simulated and experimentally measured fiber properties, averaged over three locations for each plaque, was met for all but one of the 16 test cases considered in the go/no-go project midpoint decision (FY 2015).
- Magna oversaw the tool build and prepared the molding plan for the complex 3D part (FY 2015).
- PlastiComp hosted a visit by Magna and Toyota on April 23, 2015, to finalize the molding scope and schedule. The plan for molding trials, including selection of molding parameters for both LFT and D-LFT molding of the complex part, was established (FY 2015).

- PlastiComp provided 30 wt% LCF/PP and 30 wt% LCF/PA66 compounded pellets to Magna for molding the 3D complex part (FY 2015).
- Magna performed preliminary molding trials on June 2, 2015, to validate wall thickness, fill profile, tool temperature, and shot size requirements for the complex 3D part. Magna then conducted final molding of the part from the 30 wt% LCF/PP and 30 wt% LCF/PA66 compounds. In total, Magna molded fifty 30 wt% LCF/PP parts with ribs, fifty 30 wt% LCF/PP parts without ribs, fifty 30 wt% LCF/PA66 parts with ribs, and fifty 30 wt% LCF/PA66 parts without ribs. Purge materials from the injection molding nozzle were also extracted for fiber length analysis (FY 2015).
- The University of Illinois advised the team on selection of sampling locations for the complex part (FY 2015).
- Magna cut samples at four selected locations (i.e., named A, B, C, and D) from the molded parts based on a plan discussed with PNNL; the team and shipped these samples to Virginia Tech for fiber orientation and length measurements (FY 2015).
- PlastiComp used the PlastiComp D-LFT Pushtrusion® system to injection mold forty 30 wt% LCF/PP parts with ribs, forty 30 wt% LCF/PP parts without ribs, forty 30 wt% LCF/PA66 parts with ribs, and thirty-five 30 wt% LCF/PA66 parts without ribs. In addition, purge materials from the injection molding nozzle were obtained for fiber length analysis (FY 2015).
- PNNL and Autodesk built ASMI models for the complex parts with and without ribs and performed preliminary analyses of these parts using the actual molding parameters received from Magna and PlastiComp to compare predicted to experimental mold filling patterns (FY 2015).
- PNNL developed a procedure for importing fiber orientation and length results from a 3D ASMI analysis to a 3D ABAQUS® model that enables structural analyses of the complex 3D part for a later weight reduction study.
- Virginia Tech started fiber orientation and length measurements for the samples taken from the complex parts using Virginia Tech's established procedure (FY 2015).
- In a parallel effort to this project, Toyota developed mechanical test setups and built fixtures for three-point bending and torsion tests of the complex parts (FY 2015).

Future Directions

- Virginia Tech will complete fiber orientation and length measurements for samples cut from the complex parts with and without ribs at the selected locations and deliver the measured data to PNNL.
- PNNL will continue ASMI analyses of the complex parts with and without ribs and will compare predicted fiber orientation and length results with measured data using the same method used for plaques to evaluate to the 15% accuracy criterion.
- After successful validation of fiber orientation and length predictions, PNNL will perform bending analysis of the complex parts with ribs.
- At the end of Phase 2, PNNL and Toyota will investigate weight savings and cost impact vis-à-vis program requirements defined in Table 2 of DE-FOA-0000648 (Area of Interest 1) with the assistance of Autodesk.

Technology Assessment

- Target: Demonstrate length distributions of LCFs in molded parts providing weight-average length exceeding 2 mm.
- Gap: Isolating carbon fibers from the resin matrix through heating in air oxidizes the fibers, promotes fiber breakage, and leads to underestimation of fiber length.

- Gap: Incompletely filling the ribs of the parts from LCF/PA66 material due to the high viscosity of PA66 and narrow rib cross sections. Increasing the back pressure or screw rotation could achieve complete filling, but could be detrimental to fiber length retention.

Introduction

The two phases of this project aim to advance predictive engineering (PE) tools to accurately predict fiber orientation and length distribution in injection-molded LCF thermoplastic composites to enable optimum design of automotive structures that meet weight reduction and cost impact requirements as defined in DE-FOA-0000648 (Area of Interest 1, Table 2).

Phase 1 Objective and Scope: Phase 1 integrates, optimizes, and validates the fiber-orientation and length-distribution models previously developed and implemented in the ASMI package for injection-molded LCF/PP and LCF/PA66 plaques. Phase 1 demonstrates the ASMI package as a PE tool that accurately predicts fiber orientation and length distributions within 15% of experimental results.

Phase 2 Objective and Scope: Phase 2 will focus on validating the ASMI package to predict flow-induced fiber orientation and length distribution in a complex, injection-molded, 3D Toyota automotive part (Figure IV-41). The project will compare predicted fiber orientation and length for key locations on the complex LCF/PP and LCF/PA66 parts with experimental results. Agreement within 15% will validate the PE tool. At the end of Phase 2, the team will evaluate the ASMI tool for its effect on weight and cost of the relevant vehicle system.

Upon successful validations of ASMI fiber orientation and length predictions for LCF/PP and LCF/PA66 plaques, the project team was approved to move to Phase 2 of the project on March 19, 2015.

Approach

This project integrates, optimizes, and validates injection-molded, LCF thermoplastic composite PE tools. Figure IV-41 illustrates the technical approach that progresses from compounding LCF/PP and LCF/PA66 materials, to process model improvement and implementation, to molding and modeling LCF/PP and LCF/PA66 plaques. Lessons learned from the plaque study and successful validations of improved process models for fiber orientation and length distributions for these plaques have enabled the project to progress to Phase 2 for molding, modeling, and optimizing the 3D complex part.

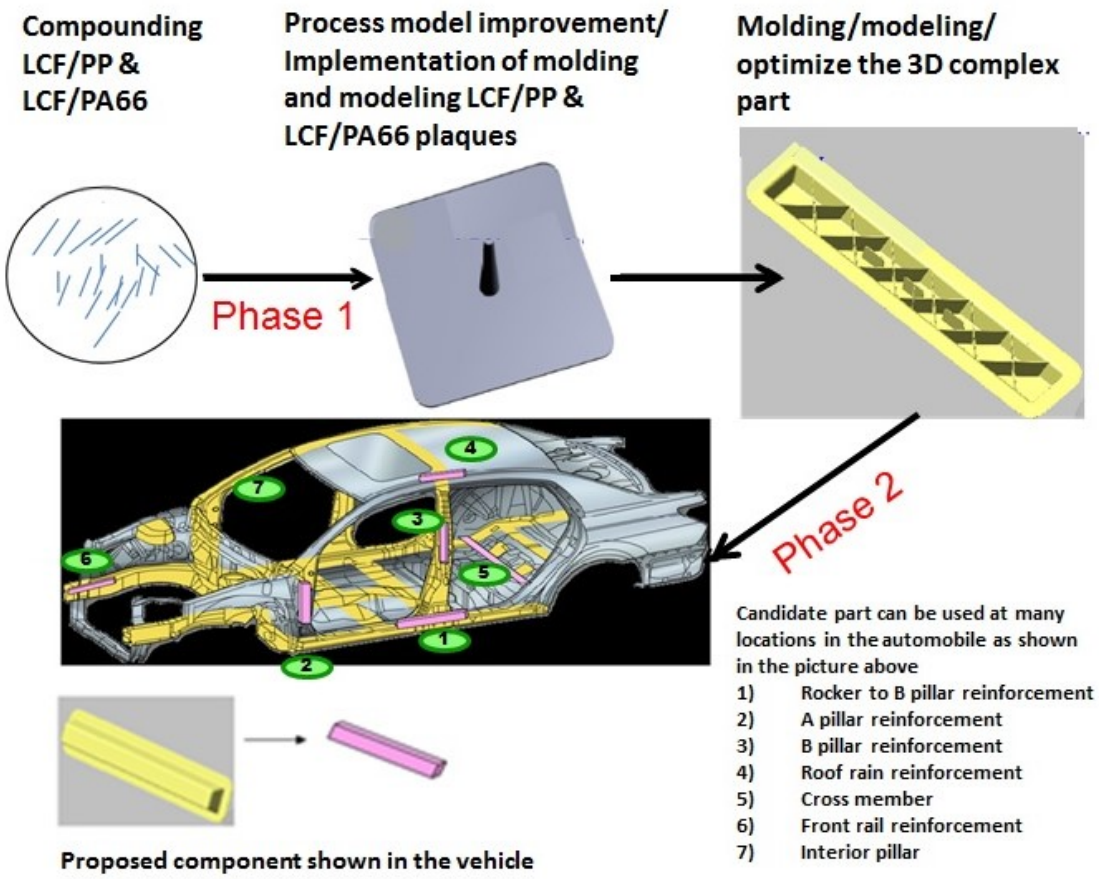

Figure IV-41: Schematic picture illustrating the technical approach for integrating and validating the tools for designing injection-molded LCF thermoplastic automotive structures.

Results and Discussion

Fiber Separation for Length Measurement*:* An important technical challenge for the team in FY 2015 was separation of fibers from the samples for length measurement. To assist Purdue in the fiber length characterization effort, PNNL developed a method for recovering intact carbon fibers from long LCF/PP and LCF/PA66 composites for FLD measurement. In previous attempts to recover carbon fibers from PP and from PA66 composites through heating of the composites in air (i.e., burn-off for resin removal), the diameters of the recovered fibers (i.e., about 5 microns) were smaller than the initial diameters (i.e., 7 microns) and the fiber ends were sharpened. These observations were consistent with oxidative damage to fibers during the heating process for resin removal. The fact that measured fiber lengths were shorter than anticipated was also hypothesized to be due to oxidative damage that resulted in fiber embrittlement and breakage during recovery. To avoid oxidative damage and recover fiber samples with length distributions representative of those in the molded composite, an inert atmosphere heating process was developed for resin removal. The process consists of heating the LCF/PP composite sample in argon at 500°C for 2 hours. Microscopic evaluation of the resultant fibers confirmed that the fiber diameter was maintained, no fiber end sharpening was present, and the resin was cleanly removed (Figure IV-42a). Residual fiber mass further confirmed the complete extent of resin removal within the process.

The inert atmosphere burn-off process does not result in complete removal of PA66 as evidenced by 2 to 3 wt% residual mass, in addition to the fiber mass in the recovered samples and through visible microscopic residue on the fibers. PNNL then developed a solvent method for removal of PA66 from the carbon fibers in

PA66 composites. In the polyamide resin dissolution method, a PA66/carbon-fiber composite sample is wrapped in an envelope of stainless steel mesh and immersed in phenol in a glass bottle. The glass bottle is capped and heated up to 100°C overnight. The solvent is replaced with fresh phenol and the process repeated three times. The enveloped sample is then carefully taken from the bottle of molten phenol (phenol melting point is 40 to 42°C) and washed twice with 60°C ethyl alcohol. The final isolated carbon-fiber sample is dried at 60°C under vacuum for 6 hours. Microscopic evaluation of carbon-fiber samples isolated in this way confirmed complete resin removal and no signs of fiber damage (Figure IV-42b).

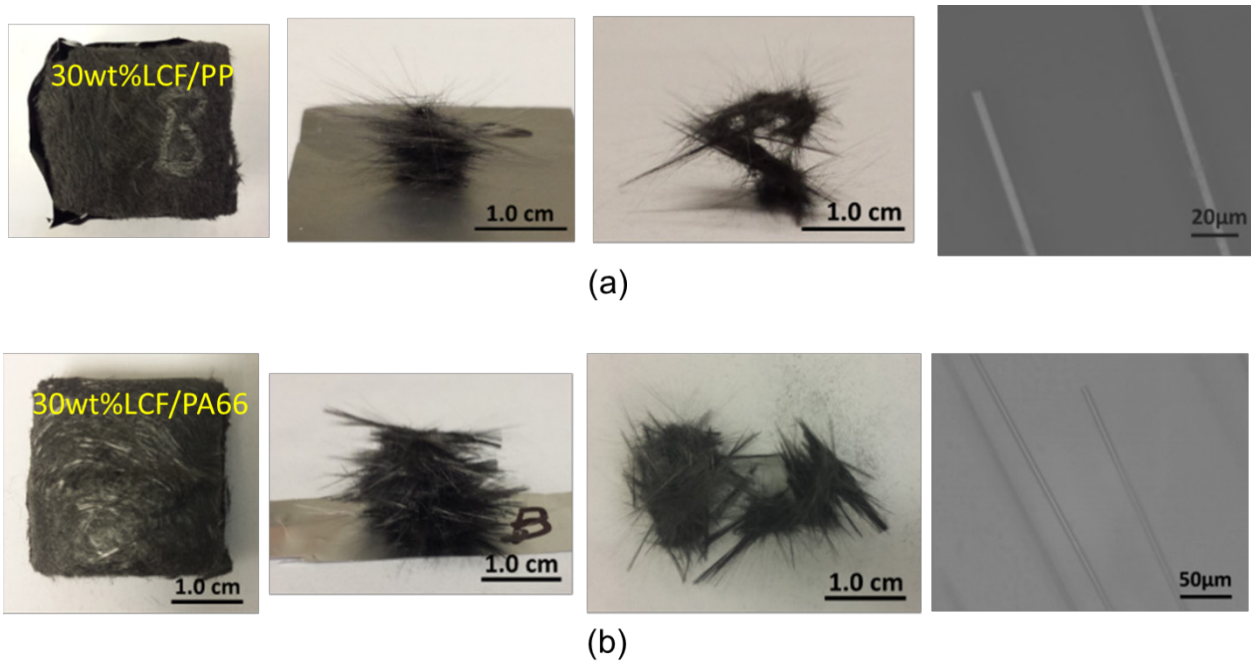

Figure IV-42: PNNL recovered long carbon fibers from (a) PP and (b) PA66 resin matrices and isolated down-selected samples for length analysis by Purdue.

Implementation and Improvements of Process Models in ASMI: Autodesk delivered to PNNL a new research version of ASMI that included the improved 3D fiber orientation solver. Because the inlet orientation condition strongly influences the orientation predicted in the part by the anisotropic rotary diffusion - reduced strain closure (ARD-RSC) model [1], the option to specify the inlet profile, which had already been available in the ASMI mid-plane and dual domain solver, was added in the 3D solver of the ASMI new research version. This option applies the prescribed inlet orientation profile through the thickness direction of the part around the gate. 3D fiber orientation modeling and demonstration of significant improvements in 3D fiber orientation predictions using this new ASMI version are described below. The ARD-RSC model predictions exhibited good agreement with fiber orientation data.

Validation of ASMI Predictions for PlastiComp Plaques*:* PlastiComp molded 30 wt% and 50 wt% LCF/PP and LCF/PA66 center-gated and edge-gated plaques under controlled slow and fast-fill conditions and delivered the plaques to PNNL for the project's Phase 1 activities. A series of plaques was selected for validation of the ASMI fiber orientation and length predictions. PNNL and Autodesk used the research version of ASMI with improved fiber orientation and length models [1-3] to analyze the plaques to validate fiber orientation and length predictions against measured data received from Purdue at selected locations named A, B, and C on plaque center lines [4-6]. Location A is close to the gate, Location B is at the middle of the plaque, and Location C is near the plaque outer edge. Figure IV-43 shows an ASMI 3D mesh for a PlastiComp edge-gated plaque and Locations A, B, and C defined on the plaque where predicted fiber orientation and length distributions were compared to the corresponding measured data to validate the predictions.

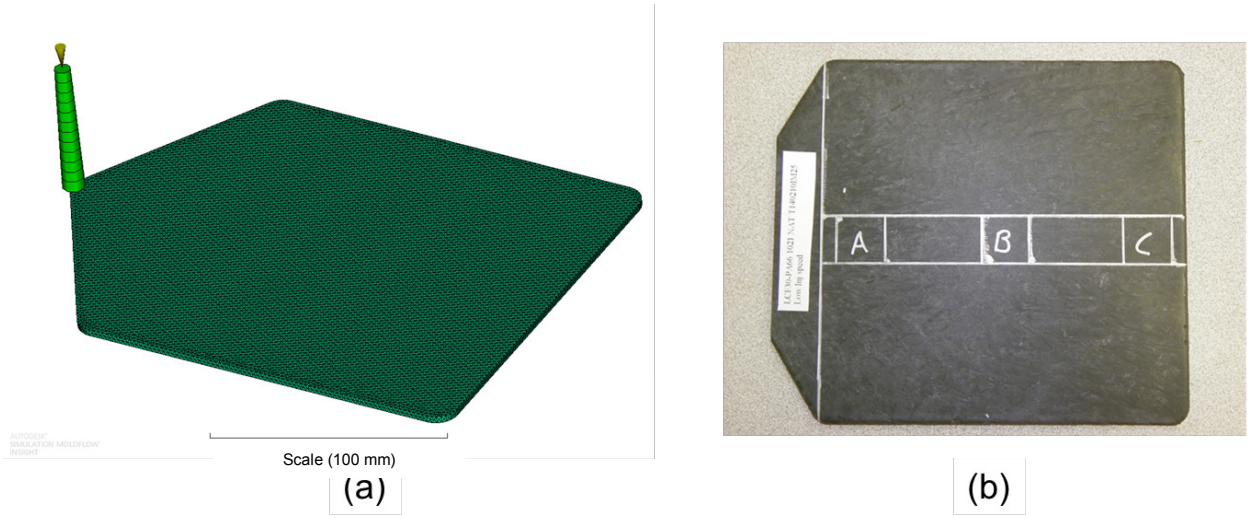

Figure IV-43: (a) A 3D ASMI model for the PlastiComp edge-gated plaque and (b) Locations A, B, and C defined on this plaque where samples were cut out for fiber orientation and length measurements.

Fiber Orientation Predictions*:* Figure IV-44 to Figure IV-46 show the 3D fiber orientation predictions for the flow-direction component A_{11} and cross-flow direction component A_{22} of the fiber orientation tensor for Locations A, B, and C on the slow-fill 50 wt% LCF/PP edge-gated plaque [5]. These figures also display the ASMI mid-plane analysis results and measured fiber orientation data received from Purdue. At Location A, both 3D and mid-plane solutions have reasonable agreement with experimental data. The 3D model predicts similar wide core behavior for fiber alignment as predicted in the mid-plane results, but it has underestimated A_{11} and overestimated A_{22} in the shell layers for Location B. However, the 3D results for Location C are in better agreement with average measured data than the mid-plane solution (Figure IV-46).

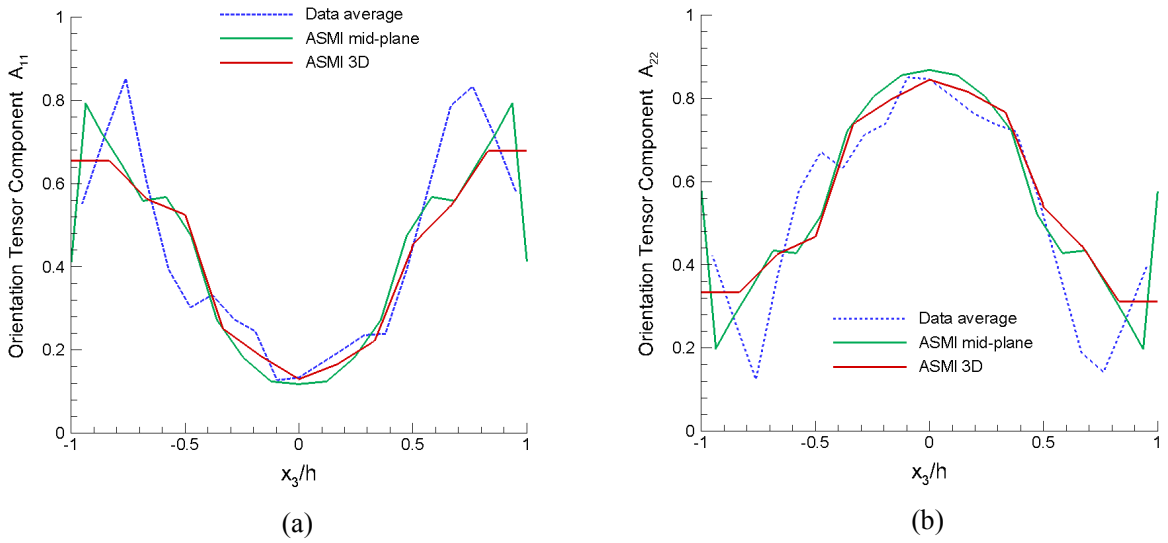

Figure IV-44: Predictions versus measured data for the fiber orientation tensor components: (a) A_{11} and (b) A_{22} for Location A on the slow-fill 50 wt% LCF/PP edge-gated plaque.

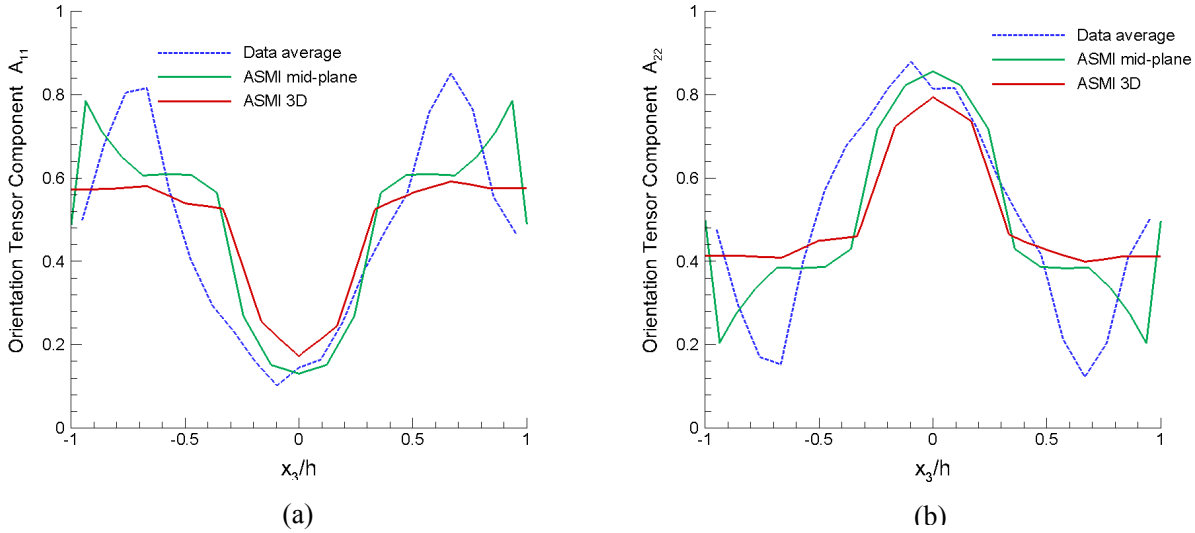

Figure IV-45: Predictions versus measured data for the fiber orientation tensor components: (a) A_{11} and (b) A_{22} for Location B on the slow-fill 50 wt% LCF/PP edge-gated plaque.

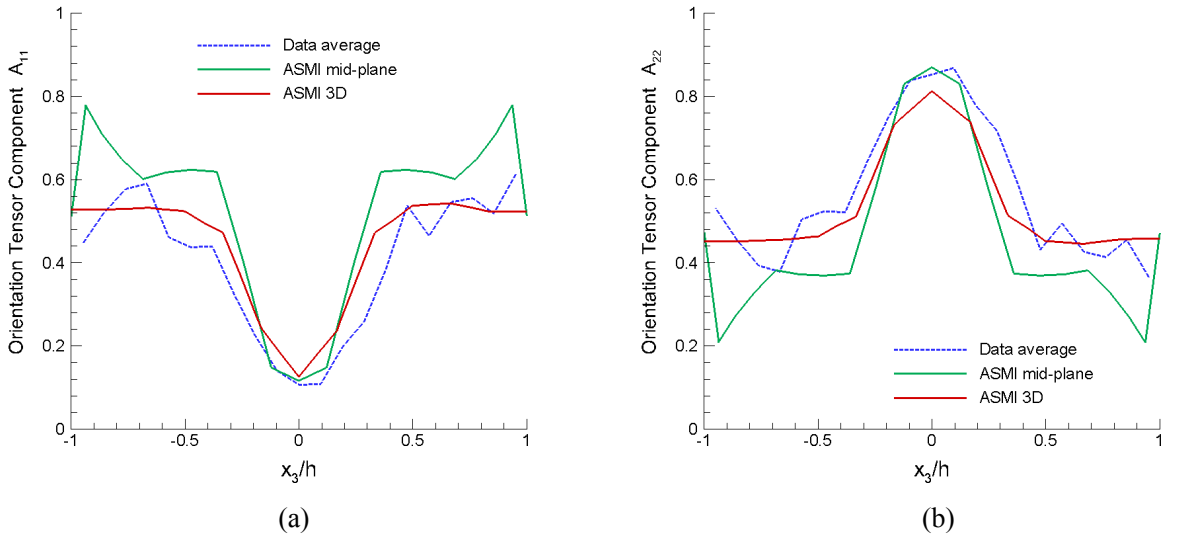

Figure IV-46: Predictions versus measured data for the fiber orientation tensor components: (a) A_{11}, and (b) A_{22} for Location C on the slow-fill 50 wt% LCF/PP edge-gated plaque.

PNNL computed tensile elastic moduli and flexural moduli for the flow and cross-flow directions using predicted and measured fiber orientations to evaluate fiber orientation prediction at selected locations. Typical elastic properties values for the carbon fiber and resin matrix were used in the calculations assuming a mean fiber aspect ratio of 200. Table IV-26 reports tensile and flexural moduli calculated based on predicted and measured fiber orientations for Locations A, B, and C on this plaque. This table compares both mid-plane and 3D solver-produced moduli with corresponding values computed using measured fiber orientation data. The mid-plane results agree with the measured data within 15%, except for some mid-plane predictions for Location C. As shown in Figure IV-46, the predicted mid-plane A_{11} for Location C is above the experimental

curve while the predicted mid-plane A_{22} is below the experimental one. This result led to significant differences in the values of computed moduli for this location. The agreement between the 3D predictions and the measured data in terms of percentage is provided in the far right column of Table IV-26 and indicates that 3D predictions agree well with measured data (i.e., within 15%) for all three locations examined in this example.

Table IV-26: Computed tensile moduli E_{11} and E_{22} and flexural moduli D_{11} and D_{22}, based on measured and predicted fiber orientations at Locations A, B, and C in the slow-fill 50 wt% LCF/PP edge-gated plaque.

Tensile Modulus	E_{11} (Mid-Plane FO) MPa	E_{11} (3D FO) MPa	E_{11} (Measured FO) MPa	Agreement Between 3D and Measured
Location A	30371	29077	28984	0.32%
Location B	34736	30257	31425	3.72%
Location C	35965	26596	24672	7.80%
Tensile Modulus	**E_{22} (Mid-Plane FO) MPa**	**E_{22} (3D FO) MPa**	**E_{22} (Measured FO) MPa**	**Agreement Between 3D and Measured**
Location A	36083	36054	36153	0.27%
Location B	30179	31599	33704	6.25%
Location C	28394	34481	37095	7.05%
Flexural Modulus	**D_{11} (Mid-Plane FO) MPa.mm^3**	**D_{11} (3D FO) MPa.mm^3**	**D_{11} (Measured FO) MPa.mm^3**	**Agreement Between 3D and Measured**
Location A	121362	120868	126761	4.65%
Location B	129217	109921	125239	12.23%
Location C	130646	98981	100300	1.32%
Flexural Modulus	**D_{22} (Mid-Plane FO) MPa.mm^3**	**D_{22} (3D FO) MPa.mm^3**	**D_{22} (Measured FO) MPa.mm^3**	**Agreement Between 3D and Measured**
Location A	78584	71648	70924	1.02%
Location B	69276	78376	70755	10.77%
Location C	66765	86960	88048	1.24%

***Fiber Length Predictions**:* PNNL and Autodesk performed injection molding mid-plane and 3D simulations for the PlastiComp slow-filled 30 wt% LCF/PP and 30 wt% LCF/PA66 edge-gated plaques to predict FLDs in these plaques. In all simulations, FLD data in the injection molding machine nozzle measured by Purdue for each material were applied as the fiber inlet condition at the injection location. Also, for a given

material, the same model parameters were used in mid-plane and 3D analyses. The accuracy in fiber length prediction was determined by comparing calculated principal tensile and flexural moduli computed using predicted versus measured FLDs at Locations A, B, and C for a prescribed fiber orientation distribution. Figure IV-47a, Figure IV-47b, and Figure IV-47c present the predicted FLDs in terms of weight distribution of fibers $w(l)$ versus fiber length compared to FLDs measured by Purdue for Locations A, B, and C on the slow-fill 30 wt% LCF/PPA66 plaque.

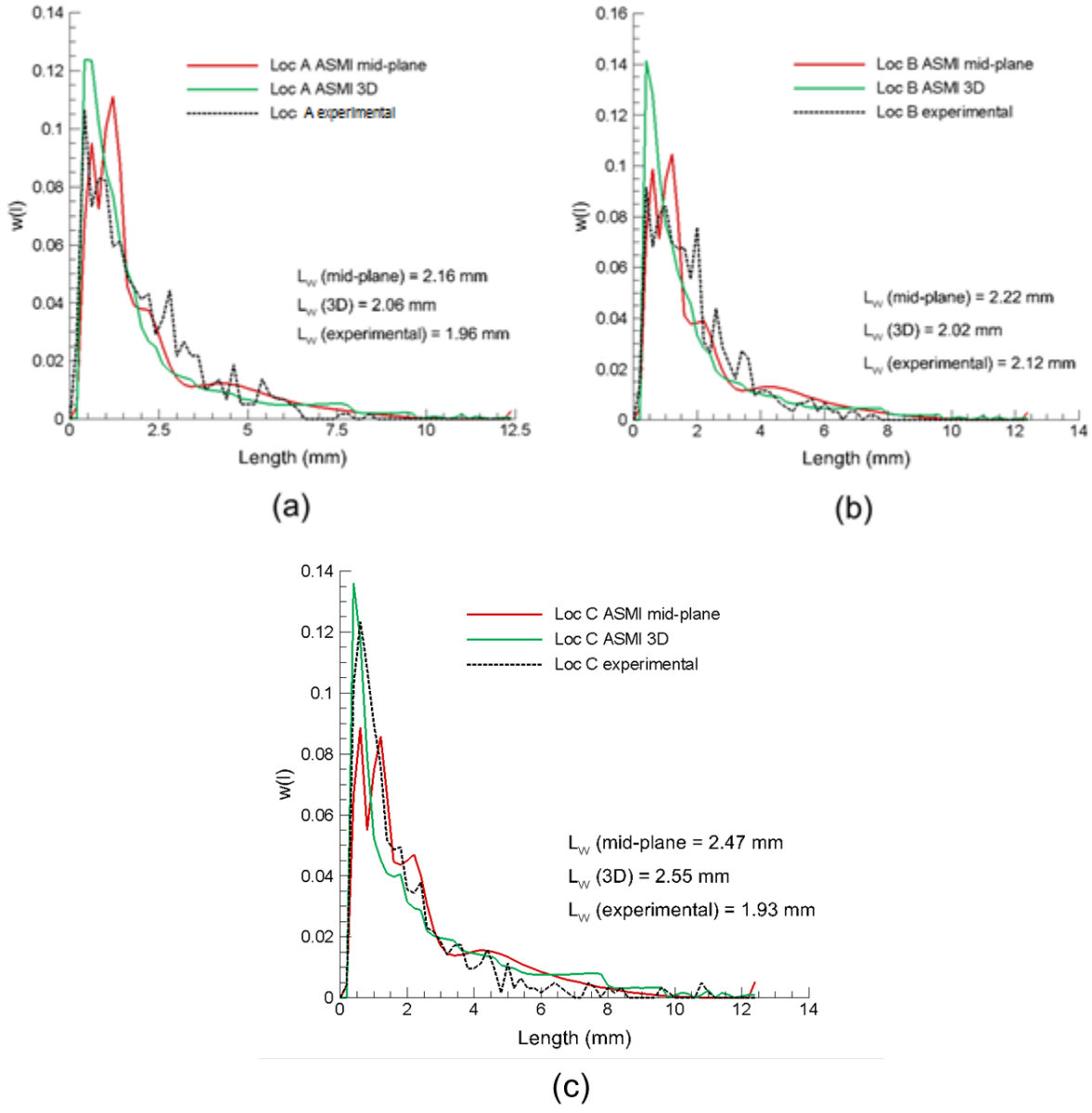

Figure IV-47: Predicted and measured fiber length distributions for (a) Location A, (b) Location B, and (c) Location C on the slow-fill 30 wt% LCF/PA66 plaque. *w(l)* is the weight distribution of fibers as a function of length.

The weight-average lengths resulting from the predicted and measured distributions are also given in these figures. Both mid-plane and 3D ASMI solutions are able to capture the measured length distributions quite well. There is also reasonable agreement between all predicted FLDs and the corresponding weight-average lengths with the experimental results. Table IV-27 provides the tensile and flexural moduli calculated based on the predicted and measured FLDs for Locations A, B, and C on this plaque. Very good agreement of results for

the tensile moduli E_{11} and E_{22} and for the flexural moduli D_{11} and D_{22} are observed for all three locations. The excellent agreement in predicted stiffness performance is not surprising becauses the FLDs achieved represent truly long fibers producing high fiber-aspect-ratio values that bring the elastic moduli near their maximum limits. Modest changes in fiber length in this high-aspect-ratio range have only very little effect on the composite elastic moduli. A sensitivity study on the effect of fiber length on the elastic moduli was reported by Nguyen et al. [5].

Table IV-27: Computed tensile moduli E_{11} and E_{22} and flexural moduli D_{11} and D_{22}, based on measured and predicted FLDs at Locations A, B, and C in the slow-fill 30 wt% LCF/PA66 edge-gated plaque.

Tensile Modulus	E_{11} (Mid-Plane FLD) MPa	E_{11} (3D FLD) MPa	E_{11} (Measured FLD) MPa	Agreement Between Measured and 3D
Location A	22499	22363	22309	0.24%
Location B	25500	25313	25427	0.45%
Location C	26310	26127	26106	0.08%
Tensile Modulus	**E_{22} (Mid-Plane FLD) MPa**	**E_{22} (3D FLD) MPa**	**E_{22} (Measured FLD) MPa**	**Agreement Between Measured and 3D**
Location A	24620	24469	24480	0.04%
Location B	19802	19666	19729	0.32%
Location C	19123	19001	18987	0.07%
Flexural Modulus	**D_{11} (Mid-Plane FLD) MPa.mm^3**	**D_{11} (3D FLD) MPa.mm^3**	**D_{11} (Measured FLD) MPa.mm^3**	**Agreement Between Measured and 3D**
Location A	86813	86293	86085	0.24%
Location B	86750	86137	86511	0.43%
Location C	88210	87622	87556	0.08%
Flexural Modulus	**D_{22} (Mid-Plane FLD) MPa.mm^3**	**D_{22} (3D FLD) MPa.mm^3**	**D_{22} (Measured FLD) MPa.mm^3**	**Agreement Between Measured and 3D**
Location A	56729	56437	56320	0.21%
Location B	53404	53090	53282	0.36%
Location C	51807	51525	51493	0.06%

Conventional LFT Molding of the 3D Complex Parts with and without Ribs*:* Working with Toyota and PlastiComp, Magna injection molded complex 3D parts with and without ribs from the 30 wt% LCF/PP and 30 wt% LCF/PA66 compounds provided by PlastiComp. The molding trials also included producing a series of short-shot fill profiles (Figure IV-48). In total, there were 200 parts molded by Magna. To establish the maximum limits, melt temperatures and tool temperatures were gradually increased until parts began to exhibit flash. The team proceeded to optimize fill speed and pack profile to get the best surface finish and fill of the ribs. The processing trials ran well with very consistent part weights, but there was an issue related to complete

filling of some of the ribs in the 30 wt% LCF/PA66 parts. This was likely due to gas trapped in the thin rib areas; however, strategies for improving rib filling, including increasing plasticizing back pressure or screw rotation speed, were not pursued in an effort to preserve fiber length as much as possible. Venting in the deep ribs to alleviate trapped gas was discussed as another option that could facilitate complete filling of the ribs in a production scenario. The parts without ribs were filled much more easily, because screw rotation speed and plasticizing back pressure were able to be reduced to provide a possibility for achieving longer fiber lengths in the non-ribbed part. Magna retained nozzle purging materials from each of the trials and shipped them to Virginia Tech for fiber length measurement. Magna's molding matrix and process parameters for all parts were reported by Nguyen at al. [6].

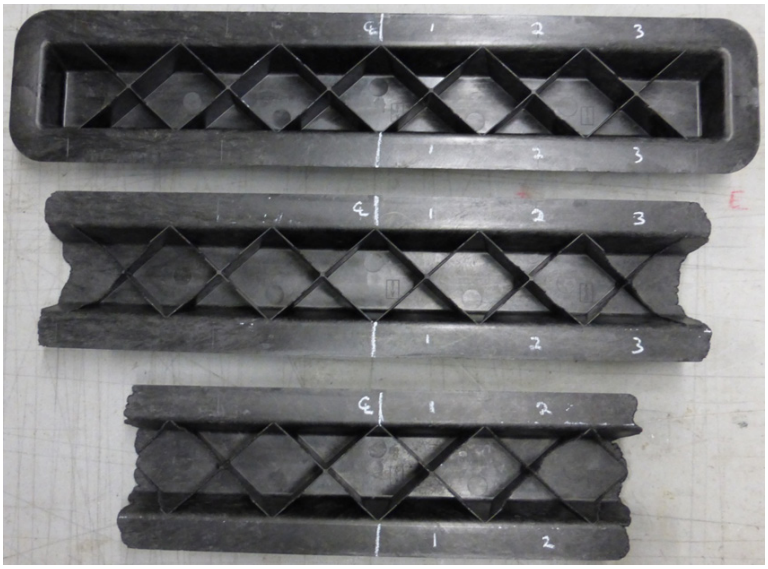

Figure IV-48: Short-shot fill profiles obtained by Magna during LCF thermoplastic molding trials.

Cutting Samples from Molded Parts*:* PNNL established with Magna and the team a plan to cut 8-mm × 12-mm samples from molded parts at judiciously selected locations for fiber orientation and length measurements [5,6]. Validation of ASMI fiber orientation and length predictions will be conducted for complex parts at these selected regions named Locations A, B, C, and D. Location A provides orientation and length data in the immediate gate region. Location B will provide information at a region remote from the gate, but on the same surface as Location A. Location C, on the wall, will allow us to examine fiber orientation and length on another surface. Location D, on a rib, will allow investigation of fiber orientation and length in a typical 3D feature. After molding**,** Magna cut samples from the designated locations and shipped them to Virginia Tech for fiber length and fiber orientation measurements. Location area designations were scribed into the mold for exact location reference on the molded parts.

In-Line Direct Injection Long Fiber Technology Molding (D-LFT) of the 3D Complex Parts with and without Ribs*:* Upon receiving the complex 3D part tools shipped by Magna, PlastiComp applied the PlastiComp D-LFT Pushtrusion system (Figure IV-49) to injection mold 30 wt% LCF/PP and 30 wt% LCF/PA66 parts with ribs and without ribs. Molding trials used standard molding processing conditions to retain optimum fiber lengths. Non-ribbed parts were very well molded from both materials. However, as observed in Magna's moldings, D-LFT molding by PlastiComp also encountered the issue of incomplete filling of the ribs [7]. Incomplete rib filling was more significant for the 30 wt% LCF/PA66 material (Figure IV-50). PlastiComp observed similar mold filling patterns as Magna molding (Figure IV-50), but also observed some poorly wet-out fibers on the surfaces of the D-LFT parts. This issue was most likely due to non-optimal sizing on the carbon fibers and the inability of the Pushtrusion processing to maximize carbon fiber wet-out. Finally, PlastiComp also pursued molding of 50 wt% LCF/PA66 ribbed parts using the

conventional LFT process to determine the effectiveness of molding high LCF loading materials; this was done in case a fiber weight fraction higher than 30% is needed. After molding, PlastiComp shipped the 30 wt% LCF/PP and 30 wt% LCF/PA66 parts to Magna for sample isolation for fiber orientation and length measurements.

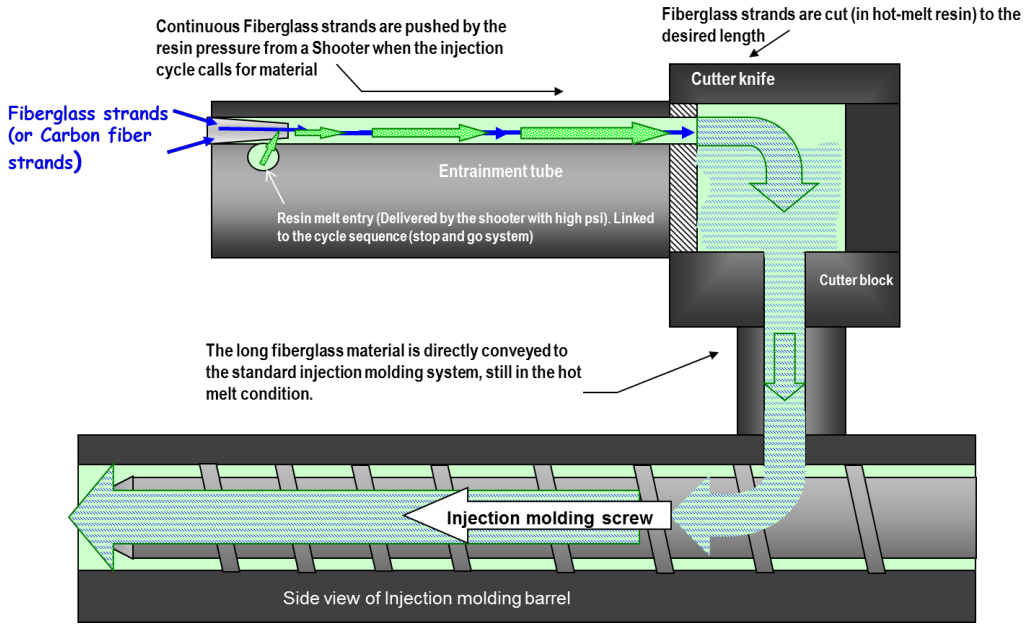

Figure IV-49: PlastiComp D-LFT Pushtrusion system used to injection mold LCF/PP and LCF/PA66 parts with ribs and without ribs.

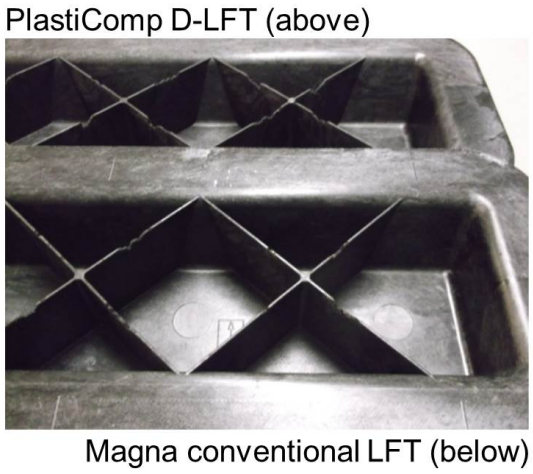

Figure IV-50: D-LFT versus conventional LFT moldings.

***ASMI Models for the 3D Complex Parts**:* Upon receiving the final computer-aided design files and processing data sheets from Magna and PlastiComp for the complex parts with and without ribs, PNNL worked with Autodesk to build ASMI mid-plane and 3D models of these parts for process simulations. ASMI mold filling analyses were conducted to exercise the models, to check mold filling, and to prepare for exporting ASMI results to a corresponding ABAQUS® finite element model for future structural analyses of the parts. Figure IV-51a shows a 3D ASMI finite element mesh of the complex part with ribs. The mesh was finely

discretized for good element aspect ratios for accurate solutions. The predicted mold filling pattern for one example of the Magna short shot series of 30 wt% LCF/PA66 (i.e., 60% fill) is presented in Figure IV-51b, along with the molded part and shows good agreement between the two.

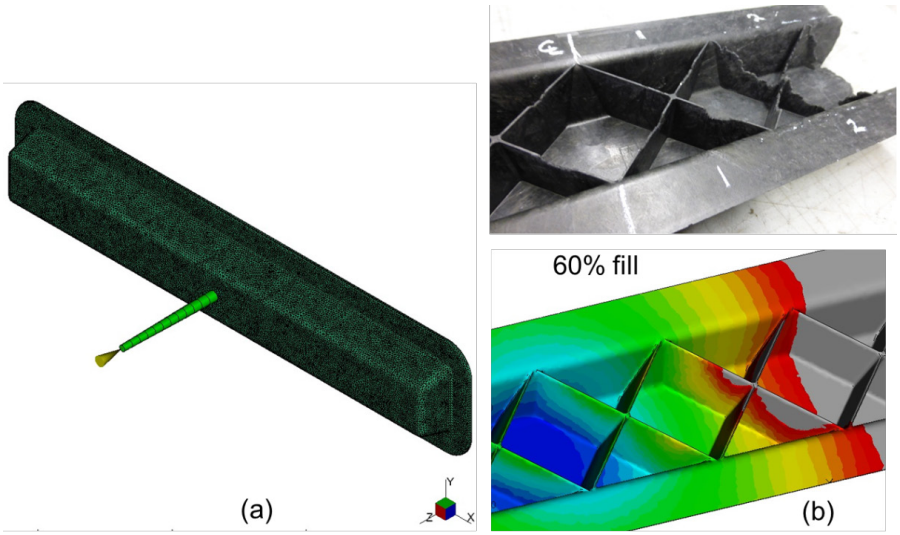

Figure IV-51: (a) A 3D ASMI finite element model for the complex part with ribs; (b) predicted versus experimental mold filling at 60% fill of 30 wt% LCF/PA66.

Building Fixtures for Mechanical Testing and Analysis*:* While mechanical testing is outside the scope of this DOE-funded project, Magna and Toyota did develop mechanical test setups and build fixtures for three-point bending (Figure IV-52a) and torsion (Figure IV-53) tests of the complex parts with ribs in an independent, complimentary effort. Determining the bending and torsion responses of the complex parts supports establishing criteria for the weight reduction study that will be based on part mechanical performance. The approved scope of work requires the design to be based on elastic stiffness; therefore, the linear or nearly linear portions of the load-deflection response to bending and of-the-moment-twist response to torsion of the complex parts will be considered and inform the corresponding predicted responses. While PNNL developed a 3D finite element model of the complex part subjected to three-point bending (Figure IV-52b) that will be analyzed by EMTA-NLA/ABAQUS® [8], Toyota created a finite element model of the same part subjected to torsion that will be analyzed by Digimat and ABAQUS®.

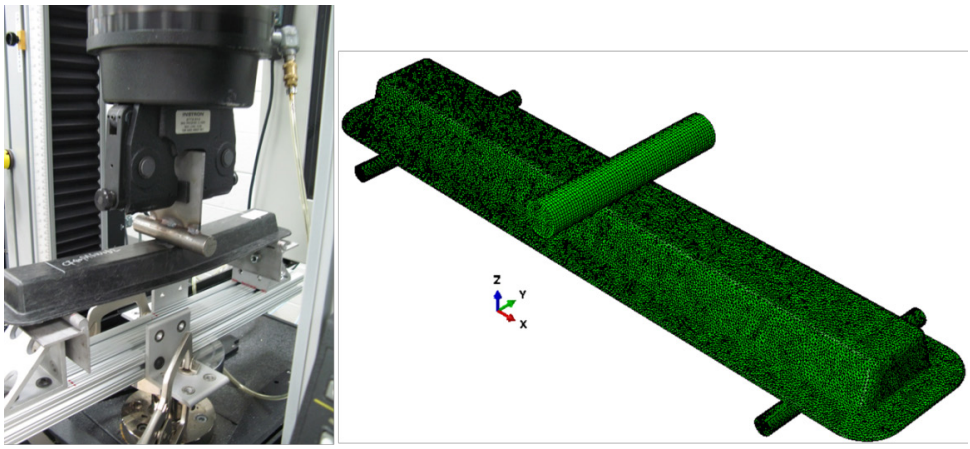

Figure IV-52: (a) Three-point bending test setup and fixtures developed by Toyota; (b) the corresponding 3D finite element model developed at PNNL for analysis.

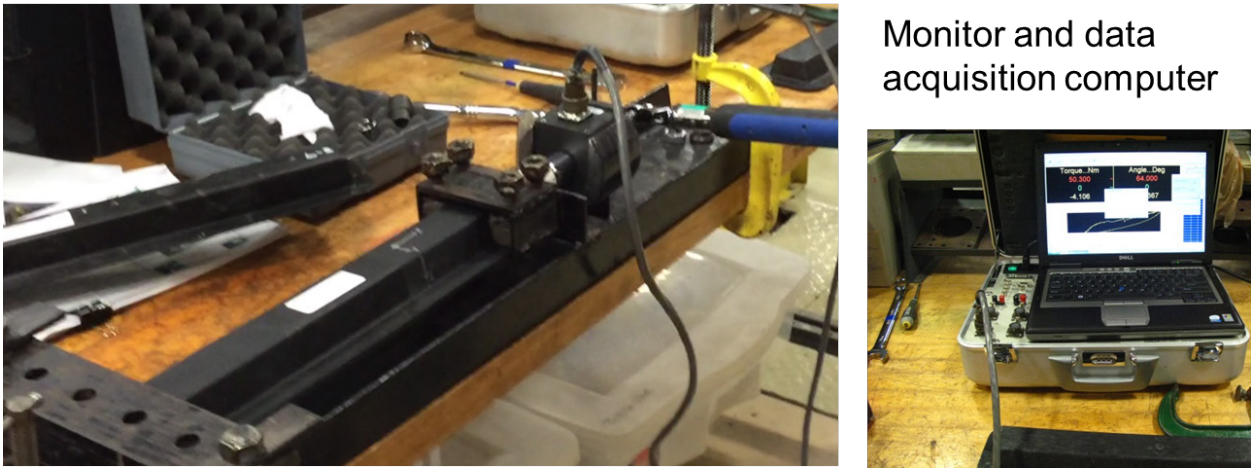

Figure IV-53: Torsion test setup and fixtures developed by Toyota.

Technology Transfer Path

The intensive participation of industrial partners (i.e., Autodesk, PlastiComp, Toyota, and Magna) in this project supports a path for the PE tools and research results to be transferred to U.S. automotive and plastics industries where ASMI is widely used. The advanced PE capability developed here will be available to these industries in the future to help achieve affordable, lightweight vehicle systems.

Conclusion

In FY 2015, the team completed important key steps including (1) improving and implementing process models in ASMI for improved predictions of fiber orientation and fiber length in LCF thermoplastic parts in both mid-plane and 3D modeling, (2) successfully validating ASMI fiber orientation and length for PlastiComp LCF/PP and LCF/PA66 plaques, (3) successfully characterizing fiber orientation and length and demonstrating weight-average LCF lengths exceeding 2 mm, (4) successfully transitioning the project to Phase 2 to validate predictive tools for LCF thermoplastic composites for a complex 3D part, and (5) molding the parts with and without ribs by both the conventional LFT and D-LFT processes. In addition, ASMI finite elements models and models for structural analyses of the complex parts were developed to first validate

ASMI predictions for the parts and, finally, to design the ribbed parts to meet weight and cost reduction targets defined in Table 2 of DE-FOA-0000648 (Area of Interest 1) [9].

References

1. J. H. Phelps and C. L. Tucker, 2009, "An Anisotropic Rotary Diffusion Model for Fiber Orientation in Short- and Long-Fiber Thermoplastics," *J. Non-Newton. Fluid Mech.,* 156(3); pp. 165-176.
2. J. H. Phelps; A. I. Abd El-Rahman; V. Kunc; and C. L. Tucker III, 2013, "A Model for Fiber Length Attrition in Injection-molded Long-fiber Composites," *Composites: Part A,* 51; pp. 11-21.
3. C. L. Tucker III, 2012, "Improved Fiber Length Model for Injection-Molded LFT Composites," Progress Report to the American Chemistry Council, University of Illinois at Urbana-Champaign, Urbana, Illinois.
4. B. N. Nguyen; L. S. Fifield; S. A. Kijewski; M. D. Sangid; J. Wang; X. Jin; F. Costa; C. L. Tucker III; R. N. Mathur; U. N. Gandhi; and S. Mori, 2015a, *Predictive Engineering Tools for Injection-Molded Long-Carbon-Fiber Thermoplastic Composites – FY 2015 First Quarterly Report,* PNNL-24031; PNNL, Richland, Washington.
5. B. N. Nguyen; L. S. Fifield; S. A. Kijewski; M. D. Sangid; J. Wang; X. Jin; F. Costa; C. L. Tucker III; R. N. Mathur; U. N. Gandhi; and S. Mori, 2015b, *Predictive Engineering Tools for Injection-Molded Long-Carbon-Fiber Thermoplastic Composites – FY 2015 Second Quarterly Report*, PNNL-24259; PNNL, Richland, Washington.
6. B. N. Nguyen; L. S. Fifield; S. Mori; U. N. Gandhi; J. Wang; F. Costa; E. J. Wollan; and C. L. Tucker III, 2015c, *Predictive Engineering Tools for Injection-Molded Long-Carbon-Fiber Thermoplastic Composites – FY 2015 Third Quarterly Report,* PNNL-24472; PNNL, Richland, Washington.
7. B. N. Nguyen; L. S. Fifield; E. J. Wollan; D. Roland; S. Mori; U. N. Gandhi; G. Lambert; D. G. Baird; J. Wang; F. Costa; and C. L. Tucker III, 2015d, *Predictive Engineering Tools for Injection-Molded Long-Carbon-Fiber Thermoplastic Composites – FY 2015 Fourth Quarterly Report,* in preparation; PNNL, Richland, Washington.
8. B. N. Nguyen; V. Kunc; X. Jin; C. L. Tucker III; and F. Costa, 2013, "Injection-Molded Long-Fiber Thermoplastic Composites: From Process Modeling to Prediction of Mechanical Properties," in *Proceedings of the 28th Technical Conference of ASC*; Paper #13, edited by C. E. Bakis, *DEStech* Publications, Inc., Lancaster, Pennsylvania.
9. U.S. Department of Energy, National Energy Technology Laboratory, Funding Opportunity Number: DE-FOA-0000648. "Predictive Modeling for Automotive Lightweighting Applications and Advanced Alloy Development for Automotive and Heavy-Duty Engines," Announcement Type: 003, CFDA Number: 81.086 Conservation Research and Development, Issue Date: 05/04/2012.

Bibliography

S. Fifield and B. N. Nguyen, 2015, "Predictive Engineering Tools for Injection-Molded Long-Carbon Fiber Thermoplastic Composites," presented to the *USCAR Materials Technology Team,* June 3, 2015.

J. Wang; B. N. Nguyen; R. Mathur; B. Sharma; M. D. Sangid; F. Costa; X. Jin; C. L. Tucker III; and L. S. Fifield, 2015, "Fiber Orientation in Injection Molded Long Carbon Fiber Thermoplastic Composites," in *Proceedings of the Annual Technical Conference of SPE (SPE-ANTEC)*, Orlando, Florida, March 23 through 25, 2015.

IV.5. Validation of Carbon-Fiber Composite Crash Models Via Automotive Crash Testing– United States Automotive Materials Partnership, LLC

Project Details

Omar Faruque, Principal Investigator
Passive Safety Department
Ford Motor Company Research and Innovation Center
P.O. Box 2053
Dearborn, MI 48121
Phone: 313-322-1044
E-mail: ofaruque@ford.com

Libby Berger, Principal Investigator
Chemical Sciences and Material Systems Lab
General Motors R&D Center
MC 480-106-710
30500 Mound Road
Warren, MI 48090
Phone: 248-930-5018
E-mail: libby.berger@gm.com

Aaron Yocum, Project Manager
National Energy Technology Laboratory
P.O. Box 880
3610 Collins Ferry Road
Morgantown WV 26507-0880
Phone: 304-285-4852
E-mail: aaron.yocum@netl.doe.gov

Carol Schutte, Technology Area Development Manager
U.S. Department of Energy
1000 Independence Avenue, SW
Washington, DC 20585
Phone: 202-287-5371
E-mail: carol.schutte@ee.doe.gov

Contractor: United States Automotive Materials Partnership, LLC (USAMP)
Contract No.: DE-EE0005661

Executive Summary

The objective of this Validation of Material Models (VMM) Project is to validate physics-based crash models for simulating primary load carrying automotive structures made of production-feasible carbon-fiber composites for crash energy management. This will include the two Automotive Composites Consortium (ACC)/United States Automotive Materials Partnership (USAMP)-developed meso-scale models from the University of Michigan (UM) [1-3] and Northwestern University (NU) [4,5], as well as existing composite crash material models in four major commercial crash codes (LS-DYNA [6-10], RADIOSS [11-13], PAM-CRASH [14,15], and ABAQUS [8,16-18]). The models will be used to predict the quasi-static and dynamic crash behavior of a vehicle front end subsystem made of carbon-fiber composites. The project goal is to validate the models for simulating crash of a lightweight carbon-fiber composite front bumper and crush can

(FBCC) system. In order to do this, we are determining the crash behavior of a reference steel FBCC; designing, building, and crash testing a composite FBCC predicted to have equivalent crash behavior; and comparing the predictions with the physical crash tests. The crash performance of the composite FBCC should be equivalent to the steel FBCC under various crash-loading modes. Successful validation of these crash models will allow use of lightweight carbon-fiber composites in automotive structures for significant mass savings.

During Year 3 (i.e., Fiscal Year [FY] 2015), the VMM project's Crash Test team completed all analyses of the four commercial crash code predictions against actual crash test data obtained for the steel FBCCs. The crash energy and peak loads extracted from the steel FBCC tests were used to set targets for driving design of the composite FBCCs. The Design/Computer Aided Engineering (CAE) team has narrowed down the composite crush can and bumper beam concepts to perform detailed design and manufacturability analyses of a C-channel bumper design with internal ribs and a two-piece dodecagonal conical section for the crush cans. These composite components were designed to be compression molded from thermoset epoxy prepreg using woven fabric reinforcements; the bumper incorporates a chopped carbon-fiber sheet molding compound (SMC) for the ribs. The two flanged crush can halves for each side of the vehicle were designed to be joined by adhesive bonding reinforced with rivets. These decisions have been supported by crush testing of simple shapes such as hat-section crush tubes with predictive support from the two academic material models, and at least one of the four commercial codes. Completion of computer-aided design (CAD) was followed by procurement of tooling for fabrication and adhesive joining of the four crush can halves and bumper beam. The Material and Process Systems (MPS) team also began assessment of thermoplastic (TP) laminate materials and vendors for manufacturability evaluations for an unconstrained FBCC package design. The nondestructive evaluation (NDE) team supported these evaluations by providing ultrasonic scans, radiographic images, and computerized thermography (CT) scans and measurements of adhesive applications for the crush tubes prior to drop tower crush testing, as well as proposed NDE methodologies for offline inspection and structural health monitoring of composite FBCCs.

Accomplishments (FY 2015)

- Completed correlation analyses between commercial crash code predictions and crash test data for all six load cases for the baseline steel FBCC crash testing and analyzed results for validity and reproducibility. Compared with predictive modeling results using the selected commercial codes.
- Obtained simple structure test data as calibration material input decks for the various composite crash modeling strategies, including academic models and four commercial computational codes.
- Conducted CAE optimization studies to finalize a composite FBCC design, using the selected two materials: a carbon fiber/epoxy laminate using a 3-k carbon fiber woven into a 2 x 2 twill fabric and a random chopped fiber carbon/vinyl ester SMC.
- Tooling for the FBCC was designed, built, and tool tryout molding trials commenced to develop a stable yield of FBCC components. In addition to the aluminum molding tools, the tooling set includes fiberglass and aluminum preforming tooling and custom fixtures for finish machining, adhesive bonding, dimensional inspection, and NDE.
- NDEs completed multiple method assessments of composite damage areas, adhesive bond-lines, and a 3D printed prototype of the crush can with a section of the bumper beam. The NDE inspection plan of the FBCC system was finalized.

Future Directions (FY 2016)

- Fabricate 50 thermoset FBCC assemblies for crash testing in the six modes, plus another 20 crush cans to be used for development of joining methods and drop tower or sled testing in axial crush.

- Perform inspections, including NDE inspections, of the FBCC components to ensure part quality and assess damage from the crash tests.
- Test composite FBCCs in six crash modes. Compare the results to predictions from the four commercial crash codes. Test composite crush cans in axial crush and compare results to academic and commercial code results.
- Procure fiber Bragg grating (FBG) dynamic strain analyzer and compare its impact detection capabilities to the low-cost microelectromechanical system (MEMS) accelerometers for structural health monitoring (SHM) demonstrations.
- Conduct feasibility evaluation for an alternate FBCC design that incorporates thermoplastic composites.

Technology Assessment

- Target: Assess the validity of material models for crash performance of carbon-fiber composites. Design, fabricate, and crash-test a composite FBCC to provide equivalent crash performance to a steel FBCC, while demonstrating a 33% weight savings over the baseline steel structure.
- Gap: Unvalidated meso-scale material models developed by UM and NWU through past USAMP-ACC support for crash-critical carbon-fiber composite structures.
- Gap: Unknown relationships between meso-scale material models and composite failure modes and properties.
- Gap: Unproven NDE methods for detection of crash damage or durability issues for carbon-fiber composites.
- Gap: SHM strategy has not been tested.
- Gap: Error band for steel and composite FBCCs not established, defaulting to "industry best practice" of $\pm$10%.

Introduction

Several new material models for predicting behavior of carbon-fiber composites were developed by academic collaborators over the last decade under the oversight of ACC and USAMP (sponsored by the U.S. Department of Energy. These included micro-scale and meso-scale models of braided carbon-fabric composite materials, as well as random fiber composites [19-22]. Of these, two models, in particular, UM's representative unit cell (RUC)-based meso-scale material model [1-3] and NWU's micro-plane RUC model [4,5] are promising enough to be used for crash simulation of composite structures. In addition, several engineering design houses and commercial crash software developers have also implemented many advanced constitutive models to characterize highly nonlinear crash response of composite structures in the four major finite element-based commercial crash codes – i.e., LS-DYNA, RADIOSS, ABAQUS and PAM-CRASH. To enable ongoing lightweighting initiatives incorporating advanced materials such as carbon-fiber composites, these models require validation and are the subject of the USAMP VMM project.

Approach

Our approach to validating these models consists of selecting a production steel FBCC, utilizing commercial crash codes to predict the steel FBCC's crash performance under various loads and conditions, crashing it under the same loads, and comparing the crash predictions to the crash results to determine the appropriate targets. These targets will be utilized to design the carbon-fiber composite FBCC and predict its crash behavior

using the commercial codes and UM and NWU material models. The composite FBCC will then be fabricated and experimentally crash tested and predictions will be compared to crash results.

The USAMP Project is organized into seven main tasks to be executed over the 48-month period with the status of all tasks indicated at the end of Year 3 (FY 2015):

Task 1: Project Administration/Management - ongoing

Task 2: Experimental/Analytical Characterization of Crash Performance of a Baseline Steel FBCC – completed

Task 3: Design and Crash Performance Predictions of a Composite FBCC – in progress

Task 4: Manufacture/Assembly of the Composite FBCC – recently begun

Task 5: Crash Test Composite FBCC – begins in Year 4

Task 6: NDE of Composite Structure – in progress

Task 7: Compare Experimental Results with Analytical Predictions – begins in Year 4.

Results and Discussion

Task 1: Project Administration/Management

Members from USAMP companies organized a vertically integrated research and management team that includes leading academic researchers proficient in modeling and crash testing, automotive design/engineering service suppliers, and composite manufacturers. M-Tech International LLC has replaced the National Center for Manufacturing Sciences as USAMP's technology management organization to coordinate project tasks for the remainder of this project.

Task 2: Experimental/Analytical Characterization of Crash Performance of a Baseline Steel FBCC

During FY 2015, post-processing for all six crash test modes was completed for the baseline steel FBCC, during which measurements were analyzed by Wayne State University (WSU) in order to develop design and performance targets for the composite FBCC. Engineered Solutions, Inc. (ESI) completed simulations of all crash load cases using the four commercial codes (i.e., PAM-CRASH, LS-DYNA, ABAQUS, and RADIOSS), and WSU completed their crash test report and protocols for testing composite FBCCs in Task 5. Thereafter, a USAMP original equipment manufacturer (OEM)-led correlation study of steel commercial code predictions and results of physical testing was performed, using the objective International Organization for Standardization (ISO) standard proposal rating metrics for dynamic systems to quantify goodness of fit using measures such as force, displacement, and acceleration versus time histories.

Task 3 Design and Crash Performance Predictions of a Composite FBCC

Task 3.1 Material and Process Systems (MPS)

Adhesive Selection: Dow Automotive joined the MPS team in FY 2015 to help select an appropriate adhesive for the drop tower crush testing of fabricated tubes. Because these tubes are made from hat sections bonded to flat plaques, they will need adhesive joining with both shear and cleavage strength. The MPS team and Dow conducted coupon-level adhesive tests, including lap shear [22], cleavage peel [23], and impact peel [24] on carbon-fiber fabric/epoxy prepreg plaques, with both the quasi-isotropic (QI) and the 0/90 lay-ups.

Figure IV-54 shows the geometry for the cleavage peel test, in which two bonded substrates are pulled apart in cleavage similar to a Mode 1 fracture test. Figure IV-55 shows an impact peel sample in place on the lower support, which will then be impacted from above by a flat plate attached to a load cell. As a result of these tests, the BETAFORCE™ urethane adhesive was selected primarily because of its superior behavior in the two

peel modes. This adhesive was then used to bond the hat sections to the plaques, with the geometry shown in Figure IV-56.

Dow bonded the hats and the plaques together; however, there was an issue with the amount of adhesive used in the bondline and/or the pressure applied during cure. Thus, the width of the bondline was less than anticipated and the thickness was greater than expected, even though glass beads were used to set the bond thickness. This is further described under Task 6.

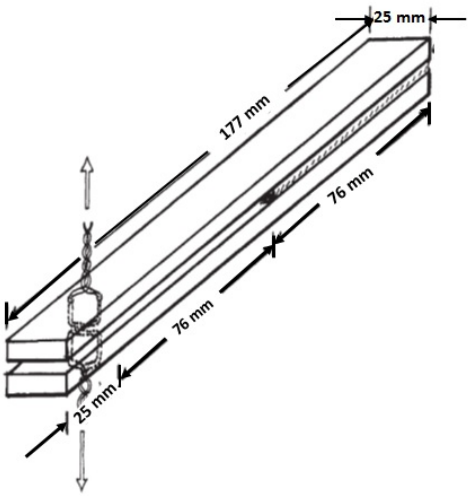

Figure IV-54: Geometry for the cleavage peel test. In this quasi-static test, the bond between the two substrate coupons is pulled to failure in cleavage. Coupon dimensions are in mm.

Figure IV-55: An impact peel sample with carbon-fiber substrate coupons, in place of the wedge of the impact peel test. The sample will be impacted from above with a flat plate that is mounted to a load cell.

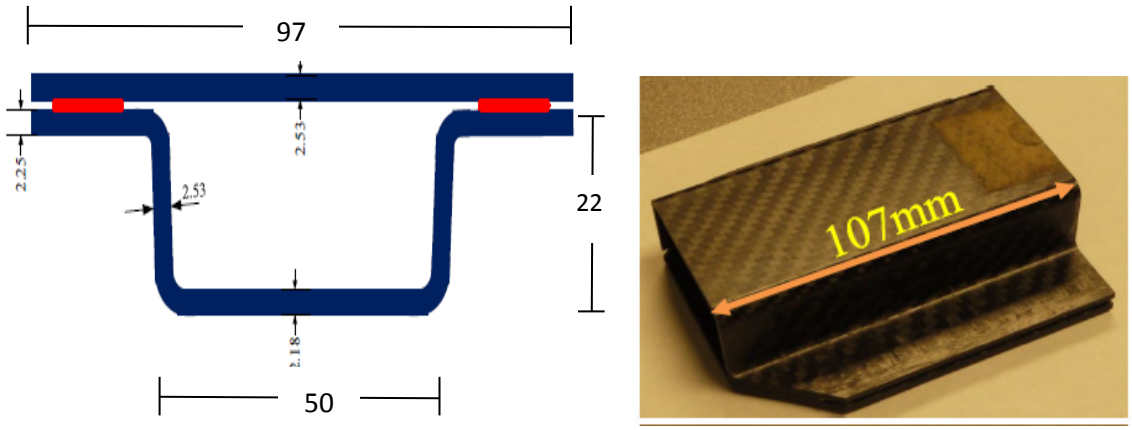

Figure IV-56: Geometry of the bonded crush tube sections. The dimensions of the part are in mm.

To confirm the adhesive assumptions for CAE and continuity of the material assumptions from the earlier developed coupons, hat section samples were fabricated from three different lay-ups after the appropriate fixturing of the parts was developed. These are shown in Figure IV-57:

- Type 1 consisted of cross-ply woven fabric with 8 plies for the plate and 11 plies for the hat section.

- Type 2 consisted of QI woven tube with 0/90/45/-45/0/90/0/-45/45/90/0 lay-up for both the plate and backing plate.
- Type 3 was a combination of both woven and unidirectional with 0/0/0/90/45/90/-45/90/0/0/0 lay-up for the hat section (with the 0/90/45 and -45/90/0 being woven layers), and QI woven material for the backing plate (i.e., Type 2).

Each sample had a chamfered cut on the upper flange to initiate crush at the tip of the section. The tubes were potted into an aluminum block, then tested on the UM drop tower. A flat plate with a mass of 74.5 kg was dropped from a height of 0.98 m. In general, the adhesive held together well, with most samples exhibiting delamination in the bonded flanges, rather than adhesive de-bonding. Figure IV-57 and Figure IV-58 show examples of the failure modes, including crushing, delamination in the plate, and debonding.

Figure IV-57: A 0/90 (Type 1) woven crushed sample.

Figure IV-58: A QI woven (Type 2) crushed sample.

UM then built CAE models of the drop tower simulation, using the material properties derived previously from Delsen test data (in FY 2013) and a second model with UM material properties derived from testing. The force-displacement curves for the Type 1 and Type 2 hat section are shown below in Figure IV-59(a) and Figure IV-59(b) and are compared to two samples of the Type 1 hat section.Table IV-28 shows the summary of force in kilonewtons (kN) and displacement results for the same simulations comparison between the UM and Delsen high strain rate material models.

UM data generate slightly softer properties with higher crush distances; Delsen data provide a closer prediction to the average force and physical test results. These data must that the CAE simulation was based on a drop height of 1.04 m (i.e., 0.06 m higher) than the physical tests, yielding higher impact forces and crush distances than the physical tests. More importantly, although some de-bonding was observed in some specimens, the majority of specimens exhibited delamination and crush in the composite materials. This indicates that the Dow adhesive and bonding method prescribed by the MPS team proved to be quite robust in maintaining bond strength during the axial crush of the can for these loads. Because design loads for the FBCC are approximately double the loads observed by the hat section, the design/CAE team has also recommended the

use of mechanical fasteners (approach to be developed by the MPS team) to further support the adhesive and reduce the chance of de-bonding in the final properties.

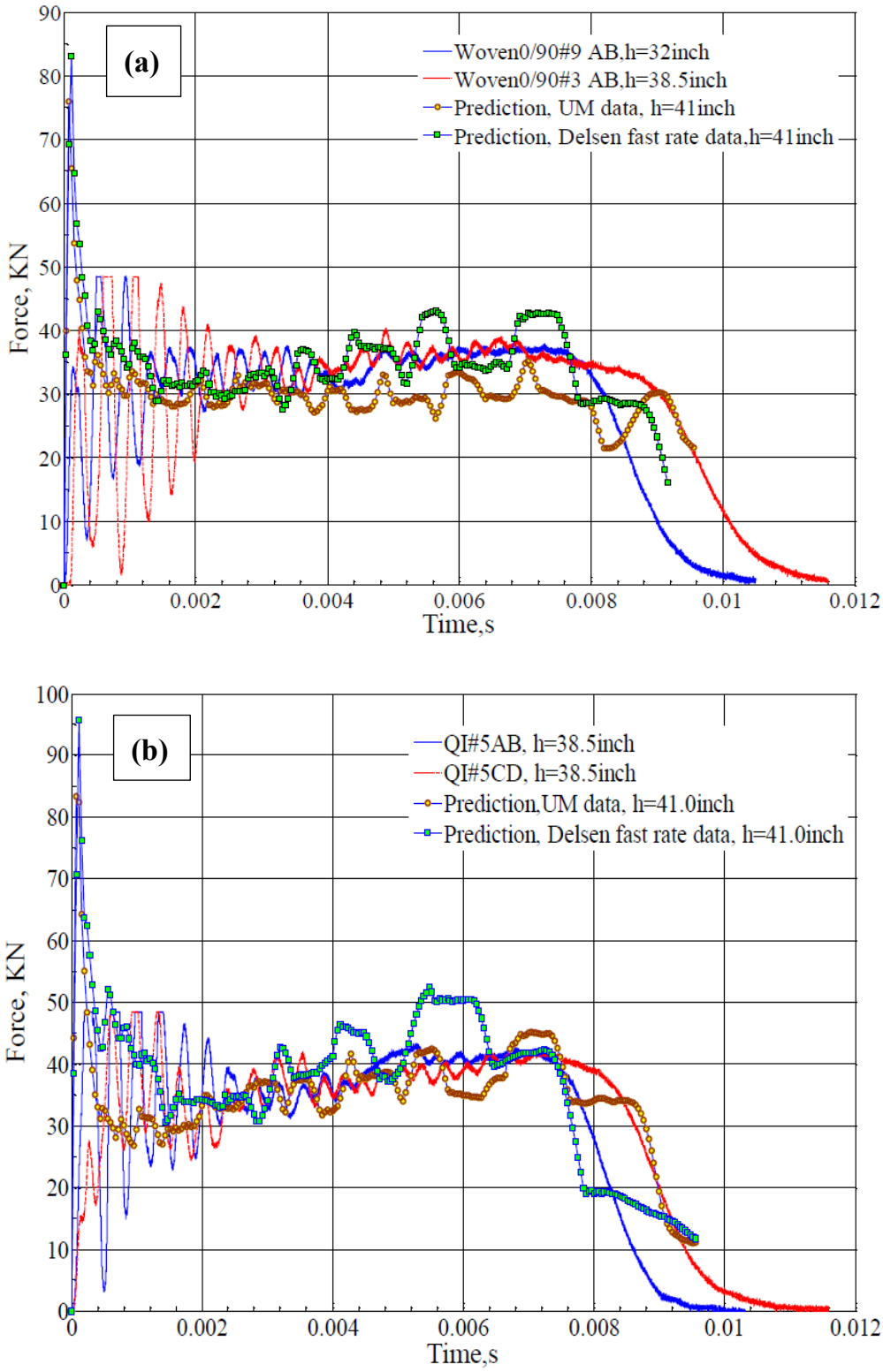

Figure IV-59: CAE results (dotted line) compared to drop tower tests for (a) woven 0/90 (Type 1) and (b) QI woven (Type 2).

Table IV-28: Test data and CAE prediction summary of UM and Delsen material models. (Note that the uni-directional/QI crush results are provided for completeness, although this configuration was not modeled).

Test Results							
Parameter	**QI woven**		**0/90 woven**			**Uni-directional QI**	
Specimen ID	#5 AB	#5 CD	#9 AB	#9 CD	#3 AB	#7 AB	#7 CD
Drop height, inch	38.5	38.5	32	39.5	38.5	38	39.5
Crush distance, mm	18.2	15.5	14.5	16.2	17.7	20.1	16.3
Plateau load, KN	41	41	36	---	36	35	35

Prediction					
UM	**Force**	**Crushing distance**	**Delsen**	**Force**	**Crushing distance**
QI	35KN	22 mm	**QI**	40KN	20 mm
0/90	30KN	29 mm	**0/90**	35KN	24 mm

Task 3.2 Design/CAE Analysis of Composite FBCC

The focus of the Design/CAE Team in Year 3 (FY 2015) was to optimize and release the FBCC design for tooling and to provide final predictions of the FBCC crash load cases using UM and NU RUC-based models and PAM-CRASH composite simulation models. The task report, including predictions from the other three commercial crash software packages, will be available in FY 2016.

Material and Model Characterization Activity: Although the majority of the material characterization work was completed in FY 2014, an effort was made to understand the sensitivity of the material models to other finite element analysis parameters through evaluation on representative hat-section crush tube shapes (as described in the Task 3.1 report). For example, a mesh sensitivity study was conducted to confirm the mesh insensitivity of the material models. A conical crush can impacted by a flat mass of 150 kg at 35 miles per hour (mph) was considered for this purpose (Figure IV-60). The simple geometry allowed investigation of a greater range of mesh sizes. Simulations were run with a 2, 3, and 4-mm mesh for the NWU microplane models. As can be noted from Figure IV-61(a) and Figure IV-61(b), both micro-plane models results were basically independent of the mesh size. A small difference in dissipated energy (always below 3%) was noted and can be ascribed to the effect of element erosion required by analysis codes to solve and run simulations.

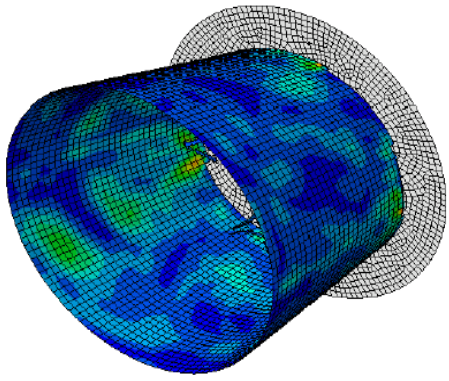

Figure IV-60: Conical crush can geometry for mesh sensitivity study.

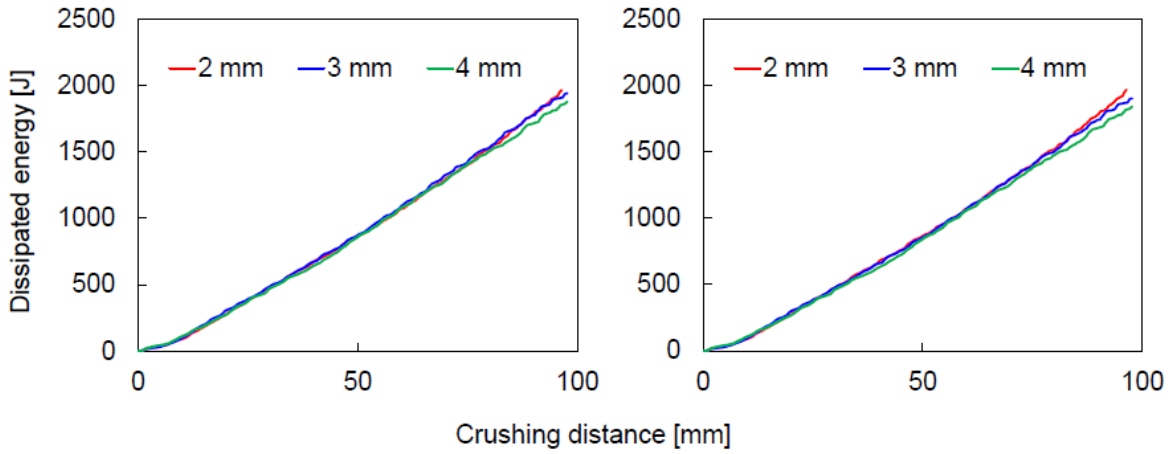

Figure IV-61: Predicted energy dissipated by (a) spectral stiffness micro-plane model and (b) micro-plane triad model for various mesh sizes.

UM provided an assessment of the crush can design with both shell and solid element models in ABAQUS to make the prediction with the RUC material model. Results are presented at the end of this task summary. In general, the solid model exhibited softer behavior than the shell model, with lower energy absorption numbers, but a higher stroke. Important learnings and recommendations are expected once these results are compared to a physical test. Images of the solid model are shown in Figure IV-62 for reference, which also shows the solid elements used to model the rivet in the bond flange.

ESI is preparing to implement the ACC-developed UM RUC material model into an upcoming release of its PAM-CRASH software. This is a significant achievement for the VMM team to facilitate the transfer of developmental academic codes into a commercial application for widespread use. This will foster further development and refinement of the model as it becomes more widely distributed and exercised over a broader range of composite structures, ply configurations, and loading conditions.

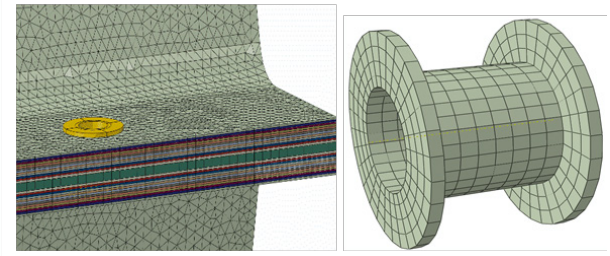

Figure IV-62: SC6R solid element models used to validate RUC model predictions.

Composite FBCC Design Activity: The carbon-fiber composite FBCC design was completed to a satisfactory level to kick-off tooling for both crush can and bumper beam parts. Active participation was provided by Continental Structural Plastics (CSP) and all vendors selected by USAMP for involvement with the tooling design, CAD, prepreg procurement, preform fabrication and molding, post-molding machining, and adhesive joining during these evaluations, which have resulted in an innovative method for joining and reinforcing a composite bumper beam and crush can.

USAMP's collaborative evaluations with the vendors included detailed design-for-manufacturing assessments and virtual validation for each impact load case, including:

- Bumper beam section and layup
- Bumper beam reinforcements and rib patterns
- Optimization of stand-off locations for beam and crush cans

- Optimization of receiver formations in bumper beam for rib formability and joint functional objectives
- Crush can lay-up and fiber orientation
- Design to accommodate manufacturing processes (i.e., draping simulation and run-off areas).

Composite FBCC Design and Performance Summary: Virtual design of the composite FBCC released for tooling had a system weight save of 45% over the steel baseline design, the majority of which came from the crush can and application of intelligent design to leverage the benefits of composites; this allowed integration of additional attachment brackets into the compression molded bumper and crush can parts. The final composite FBCC design was able to reduce the number of parts in the steel FBCC assembly from 9 to 5 parts. Figure IV-63 shows the final composite FBCC design concept. Run-off areas, which facilitate forming and manufacturability of parts, are also shown and are machined off after molding to meet final design geometry.

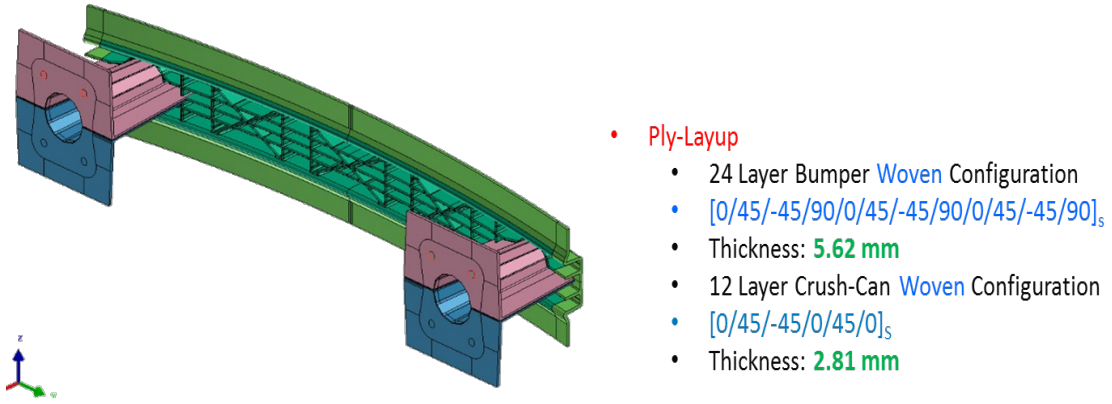

Figure IV-63: Composite FBCC system released for tooling (includes runoffs).

Performance predictions have been completed for impact load case events. In the case of RUC-based meso-scale and micro-plane codes developed by our academic partners, only the crush can itself is assessed for the rigid flat frontal and angular impact load conditions. The full FBCC system (i.e., crush cans and bumpers) will be assessed using commercial codes. Table IV-29 shows the performance summary for the different analyses. The energy targets listed in the table were derived from the steel FBCC as part of the Task 2 FY 2014 (Year 2) activity following the baseline steel FBCC crash testing assessment. The 17.5-kJ energy absorption (per crush can) predicted by PAM-CRASH is within 10% of the 37.8 kJ absorbed by the baseline steel FBCC system-level test and matches the energy absorbed by the steel FBCC predicted in the same software. It was subsequently agreed by the team that this 35-kJ level of energy absorption would be acceptable to release the design. Mass breakdown for FBCC is presented in Table IV-30, with a projected savings of at least 40% over the steel baseline.

Table IV-29: Performance summary of composite FBCC in different analysis codes.

Code	Event	EA Target	Energy Absorption Prediction	Stroke Prediction
PAM-CRASH *MAT131 Multi-Layered Orthotropic	Flat Frontal	About 18.9 kJ (per can)	17.5 kJ	162 mm
	Angular	About 13.4 kJ	13.0 kJ	165 mm
NU Microplane Model	Flat Frontal	About 18.9 kJ (per can)	13.5/13.3 kJ Spectral stiffness microplane model/ microplane triad model	190/204 mm
	Angular	About 13.4 kJ	13.3 to 12.7 kJ Spectral stiffness microplane model/ microplane triad model	204 mm

Code	Event	EA Target	Energy Absorption Prediction	Stroke Prediction
UM RC Model	Flat Frontal	About 18.9 kJ (per can)	12.8/12.6 kJ S3R Shell Element SC6R Solid Element	165/195 mm
	Angular	About 13.4 kJ	11.0/10.0 S3R Shell Element SC6R Solid Element	140/242 mm

Table IV-30: Steel and composite FBCC mass summary.

Component	Total Mass (kG)
Steel	
Steel Bumper	5.3
Steel Crush-Cans	1.8
Front Bracket	0.9
Four Additional Bumper Attachments	0.3
Rear Bracket	2.7
Two Additional Rear Bracket Attachments	0.3
Total Mass	**11.3**
Total Mass without Additional Attachments	**10.7**
Composite	
Bumper 24 Layers	2.8
Crush Cans 12 Layers	1.0
SMC Ribs in Bumper (5 to 7-mm thick)	1.9
SMC Rear (about 3-mm Thick)	0.2
Total Mass	**5.85**
Mass Savings Over Steel	**48.2%**
Mass Savings without Additional Attachments on Steel	**45.5%**

The load-displacement curves for the UM RUC model (both, shell and solid element formulations) are shown in Figure IV-641 and Figure IV-65. The load-displacement curves for the NU microplane model (both spectral stiffness microplane model run in ES3 multiscale-multiphysics analysis of the response of structures [MARS] software and the microplane triad model run in the Abaqus software) are shown in Figure IV-66 and Figure IV-67. To assess the effect of adhesive on crush can performance, these models were also run with and without the adhesive connection. Some minimal variation was observed due to the effect of adhesive in the model. The PAM-CRASH MAT131 results are shown in Figure IV-68 for the New Car Assessment Program (NCAP) and Angular load cases. It is important to note in the Angular load case that even though the composite FBCC load curve is lower than the steel baseline load curve (shown in dark green), the total energy absorption – which is the main objective of the crush can – is similar to the steel FBCC, because the crush mode of the composite can allows a longer stroke and more continuous and efficient energy dissipation. The NU microplane and UM RUC performance predictions are slightly lower than the PAM-CRASH prediction; therefore, the team will try to understand the reason for these differences and conclusively determine which of the codes better correlates to the physical test event in future crash data analysis tasks for FY 2016.

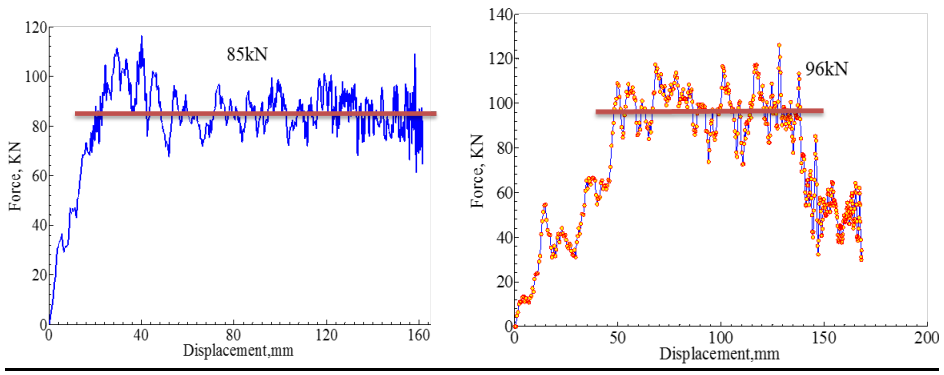

Figure IV-64: Load displacement responses obtained from shell element S3R with the UM RUC model for axial load (left) and angular load (right).

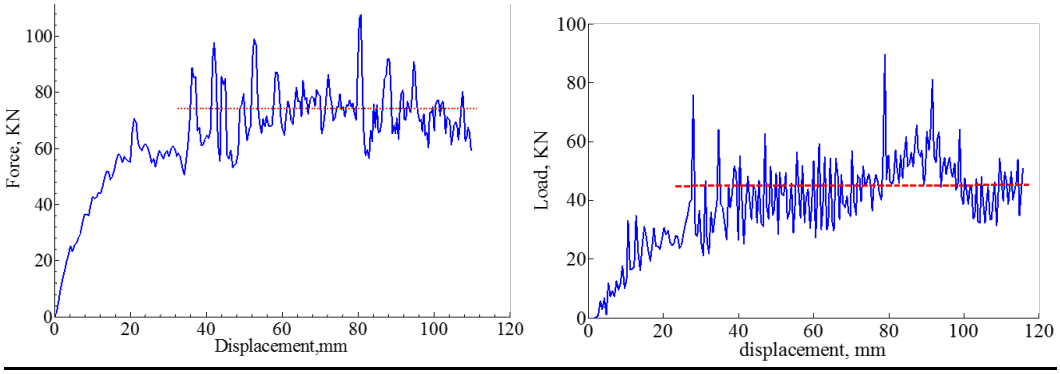

Figure IV-65: Load displacement responses obtained from 'solid' SC6R element with the UM RUC model for axial load (left) and angular load (right).

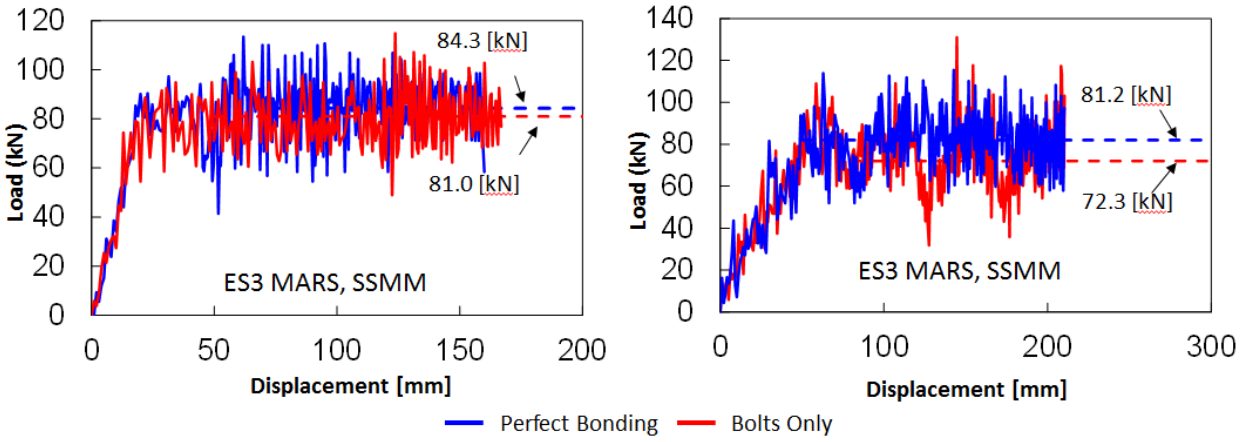

Figure IV-66: Load-displacement responses obtained from the NU spectral stiffness microplane model (SSMM) in ES3 MARS for the flat frontal (left) and angular (right) load case.

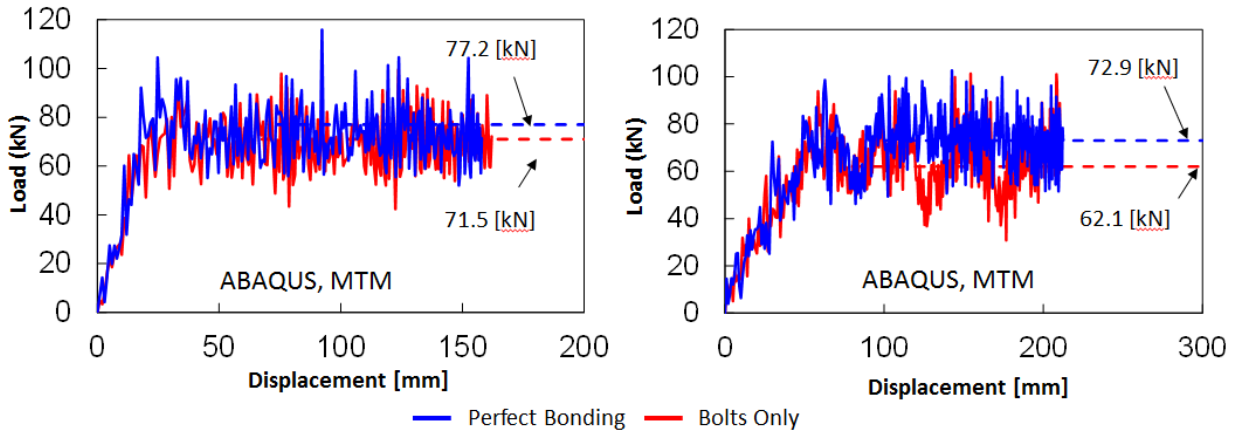

Figure IV-67: Load-displacement responses for the flat frontal (left) and Angular (right) load cases obtained from the NU microplane triad model (MTM) in ABAQUS.

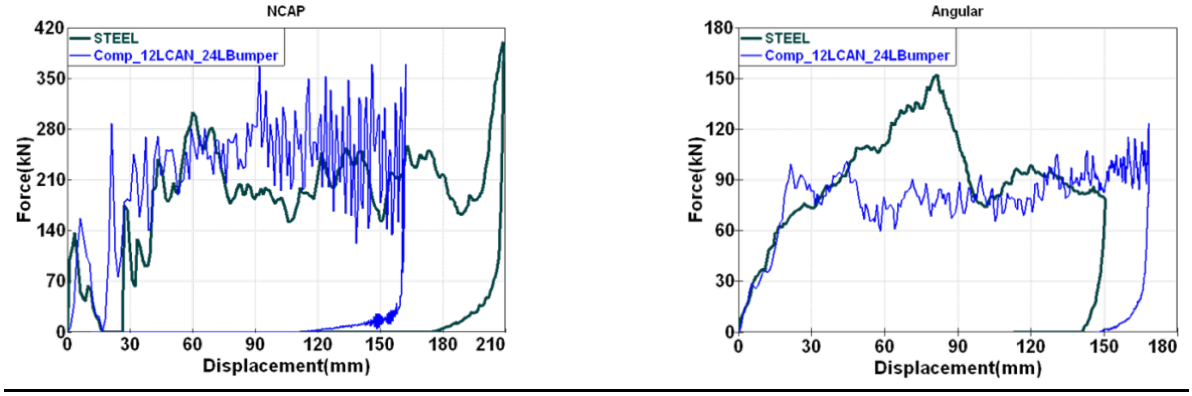

Figure IV-68: Load displacement responses obtained from MAT131 model in PAM-CRASH for the flat frontal (NCAP) load case (left) and Angular load case (right).

Task 4: Manufacture/Assembly of the Composite FBCC

Task 4 began in FY 2015 with collaborative planning for tooling fabrication by representatives from the design/CAE house, fabrication and assembly suppliers, the VMM MPS team, and tooling designers. The MPS team reviewed evolving composite designs for the bumper beam and crush can and solicited feedback on any changes needed based on tooling considerations. Routine discussion topics included appropriate runoff geometries, draft angles, radii, part angle in the tooling, and geometry of the flange attaching the assembly to the vehicle rails (or, in our case, to the test sled). ESI incorporated these issues into their design drawings and eventually incorporated them into the CAD files using an engineering change order process.

While the task focus is on primary tooling for compression molding, secondary tooling is also required, including preforming bucks, tooling and assembly fixtures. Century Tool and Gage Company was contracted for both the primary and secondary tooling. Tooling for the beam and crush cans was delivered. Figure IV-69 shows CAD and photographs of the machined beam tooling. Initial tryout on the preform tooling and molding tooling was completed by the end of Year 3 in September 2015.

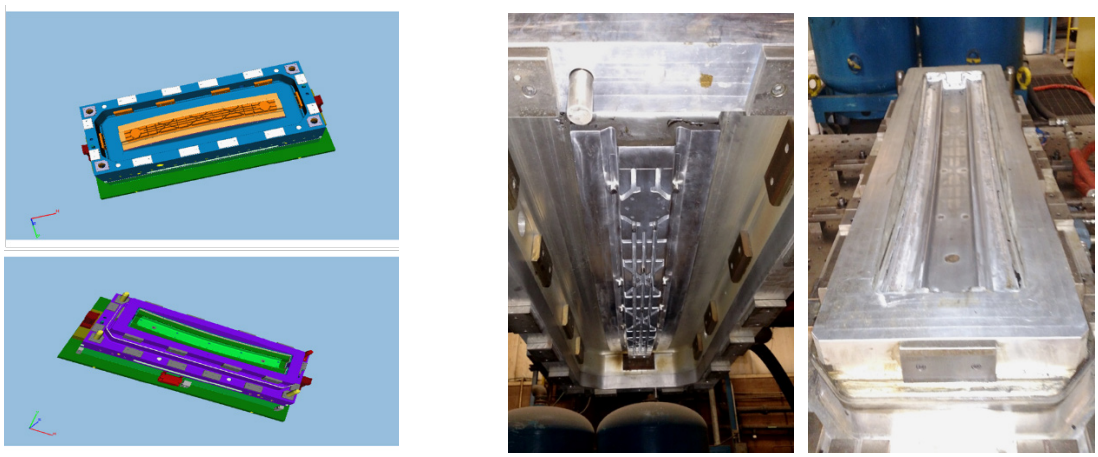

Figure IV-69: The CAD for the beam tooling upper and lower molds (left), and pictures of the machined upper and lower beam tooling (right).

***Preforming*:** Preform nesting and prepreg cutting were done on an automated Gerber Technology cutting table at the CSP facility in North Baltimore, Ohio. After cutting, preform blanks were stored in a freezer until preform molding. Shortly before part molding (hours to a few days), kitted ply parts were preformed in the aluminum preforming tools. A draw bar was used to apply light pressure to the prepreg edges as the ply stack was being deformed, preventing wrinkling. Preforms were then placed onto the preform bucks, with a protective film, and returned to the freezer until molding.

***Mold Tryout for the Crush Cans*:** Initial molding tryout of the crush can tools showed two primary issues. The first was the part stuck on the top surface, while the ejectors were in the lower surface. Usually, this can be controlled by varying the heat differential between the top and bottom of the tools, but this was only marginally effective in this case. Although we did get a few parts that were good enough for development of the joining assembly and NDE processing (Figure IV-70)**,** this was not considered a truly successful molding. Thus, Century Tool and Gage Company in Fenton, Michigan added a set of ejectors to the top surface, with a molding scenario of engaged ejectors at low pressure while the tool was still closed, forcing the part onto the lower surface. The second issue was that the preform did not fit well into the mold. The preforms were about 6 mm too short for the fabric "fingers" to fit well into the front flange. More importantlythe SMC was seen to be pushing the side flanges and the back fingers up into the conical portion of the structure, decreasing their overhang of the surface onto the back flange, and hence not giving as much internal bonding of the fabric and SMC. Thus, Siemens modified the Fibersim preform by adding flaps to the rear flange, which will better position and secure the preforms at the mounting plate radii; they also added 6 mm to the overall length of the preform to assure positioning of the front tabs at the radius.

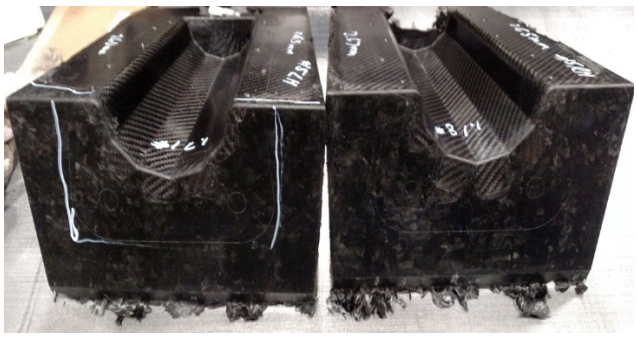

Figure IV-70: Example of as-molded crush can parts from the tool tryout run. Note the molding issues at the top (far end in the right hand part) and the short fabric on the side flanges in the left hand part.

***Mold Tryout for the Beam*:** The beam also had difficulties with initial molding, but did not require rework of the tooling. Instead, by working with the prepreg supplier Cytec, it was determined that the large runoffs used (to ensure fibers do not get caught in the shear edges, thus locking up the tool) were allowing too much resin to bleed out. This essentially starved the part of inter-ply bonding. Cytec was able to suggest a pre-gel procedure that set the edges of the preform and prevented this. The largest molding issues have been worked out; therefore, FBCC production can begin in FY 2016.

***Joining*:** The VMM team engaged Dow Automotive to provide the bonding procedure and parameters for the joining trials of the selected adhesive, based on tests of carbon-fiber composite coupons described in Task 3.1. Dow has provided a step-by-step assembly plan and process flow chart for assembling the crush cans and beam structure into FBCC units, as well as the bonding methodology for applying the primer and adhesives. They have also allocated an area in their Auburn Hills, Michigan, facility for the bonding fixture and other operations (such as assembly, curing, and storage), until the parts are shipped to WSU for crash testing.

***Alternative Design*:** One of USAMP's project goals is to determine what composite design options would be available if there were some flexibility in packaging of the FBCC. For example, composite parts tend to be thicker than metal parts; therfore, when designers attempt to fit a composite part into the same design space used by the metal parts, they are frequently not able to do so. For the VMM project, one key question was whether or not more mass can be saved with better designs if an extra space increment were available. As described in Task 3.2, crash predictions show that composite structures can absorb the required energy in less front overhang space, because the dimension of interest is length instead of thickness. This allows the VMM Project team to investigate other ways for increasing energy absorption, saving mass, or both. Thermoplastic composite materials are commonly thought to have better energy absorption properties than thermosets. Thus, the team is investigating whether or not this common bias holds true for current FBCC designs and rigorous test protocols. Shape Corporation has recently joined the project to investigate this issue by designing and fabricating the thermoplastic crush cans, which will be tested via sled or drop tower. The goal is to the existing tools for the thermoset matrix system to produce thermoplastic crush cans. Because of the tight timing, the team has decided to focus on LS-DYNA for Shape's design optimization and crush simulation studies, which further helps speed up material testing and CAE material card generation.

The MPS team was also interested in using the large tow, low-cost carbon fiber produced at Oak Ridge National Laboratory for at least part of this effort and had been working with BASF to determine a way to make the unidirectional tapes out of this material. However, because of the technical challenge for adapting the large tow size to BASF's existing tape manufacturing process, plus timing required for the project, they have determined that they cannot support this effort at this time. Oak Ridge National Laboratory has proposed alternative partners to work with and the MPS team is currently evaluating these options.

Task 6: NDE of Composite Structure

The NDE team is tasked with development of (1) methods that can verify the build of carbon-fiber composite materials and assemblies and (2) methods that could detect performance-damaging impacts to composites in a passenger vehicle (such as parking lot collisions). Ultrasonic inspection, radiography, computed tomography (CT), and optical surface scans have been selected as the primary NDE inspection methods for ensuring the build quality and assessing FBCC crash damage. For SHM, low-cost accelerometers have been selected as the most promising sensors for automotive applications, but their performance needs to be calibrated using high-performance optical FBG strain sensors.

NDE Characterization Progress: In FY 2015, the NDE capability studies for detecting various kinds of damage were completed. Also, preliminary performance tests for bumper and crush can components were completed. This included adhesive inspections and a CT study on 3D printed prototype versions of the crush can halves and a section of the bumper.

Damage assessment studies have included (1) a standardized compression-after-impact (CAI) test using a hemispherical impactor at energies ranging from below the damage threshold to complete penetration, (2)

four-point flex failure of hat sections, and (3) axial crush damage to adhesively bonded crush tubes composed of hat sections bonded to flat plates. The CAI study was especially conducted to ensure imaging methods have adequate spatial resolution to detect damage that would reduce strength of the composites. On the 2 to 3-mm thick composites tested to date, damage less than 5-mm in diameter has negligible effect on the residual strength of the component.

All methods used have submillimeter resolution in the plane of the composite. Ultrasonic pulse-echo offers the most detailed information. An example of the damage to a hat section in four-point flex is shown in Figure IV-71. Ultrasonic imaging can detect both the lateral extent of damage and identify the plies where delamination occurs.

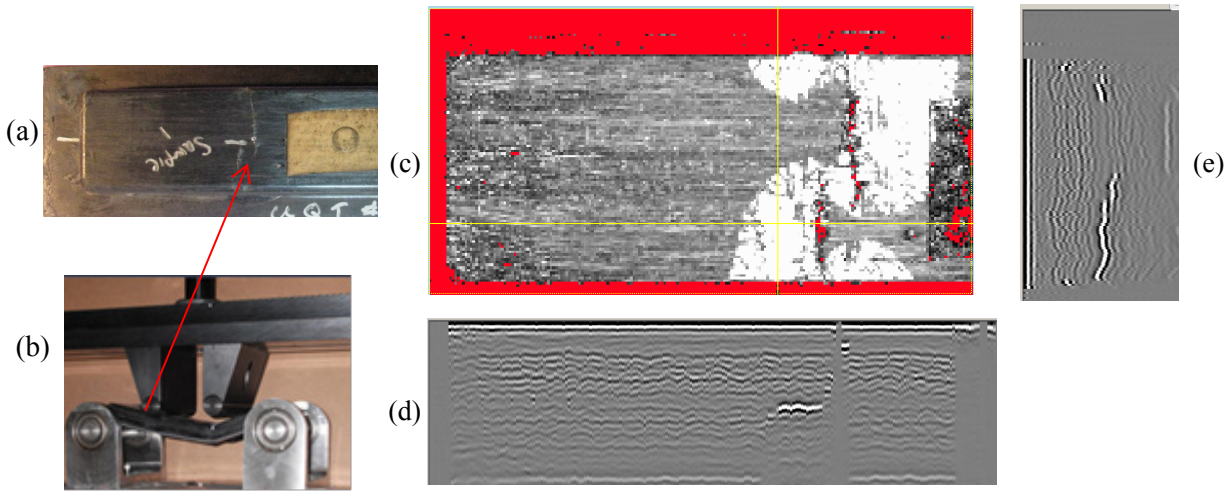

Figure IV-71: Ultrasonic inspection of (a) a hat section after (b) a four-point flex test. This is from the less-damaged end of a combined uni and woven-ply hat section with extensive inter-ply delamination. (c) Image of peak ultrasonic reflectivity. The yellow lines indicate location of a (d) horizontal section and a (e) vertical section through the damage.

The FBCC assembly is designed to be rivet-bonded. Crush tests have shown that the crush cans could fail in the adhesive if not properly bonded. To ensure adhesive bond quality, the selected NDE inspection methods were tested for capabilities to detect adhesive spread, thickness, and porosity. An example of a poorly bonded crush tube is shown in Figure IV-72.

Given the complex webbed and ribbed design of the bumper, alternative NDE inspection methods have been under discussion for the past year. CT is the best method for dealing with the complex shape of the FBCC assembly without complex surface scanning or difficult data-stitching. Resulting data can be readily compared with the CAD model. To exercise these capabilities, a 3D version of the crush can halves and part of the bumper were printed in nylon 6 by the stereolithography (SLA) additive manufacturing process. These were then "joined" using putty. The resulting assembly was CT scanned. Figure IV-73 shows three orthogonal slices and a perspective view of the assembly. The denser putty "adhesive" is readily visible. Two analyses were exercised on these CT scans. The first detects internal porosity. Unexpectedly, a small amount of porosity was detected in the nylon near the front end of the can. The second analysis determines the surface locations from the CT data and compares that to the original CAD surface model. For this SLA printed part, the surfaces differed by less than 0.5 mm. The analyses were judged to have performed well.

The bumper and crush can parts will also be inspected with an ultrasonic linear-phased array. For the inspections, the entire FBCC assembly or subassemblies will be immersed in a shallow tank. The array is mounted on a fixed-height fixture that is manually scanned along selected paths. Locations along the path are measured with a string encoder. The cans were specifically designed with flat facets to allow this inspection. These inspections are designed to detect (a) delamination, (b) foreign matter, and (c) fabric-orientation

deviations in the flat regions of the bumper and crush can, as well as (d) lack of adhesive wetting of the crush can flanges.

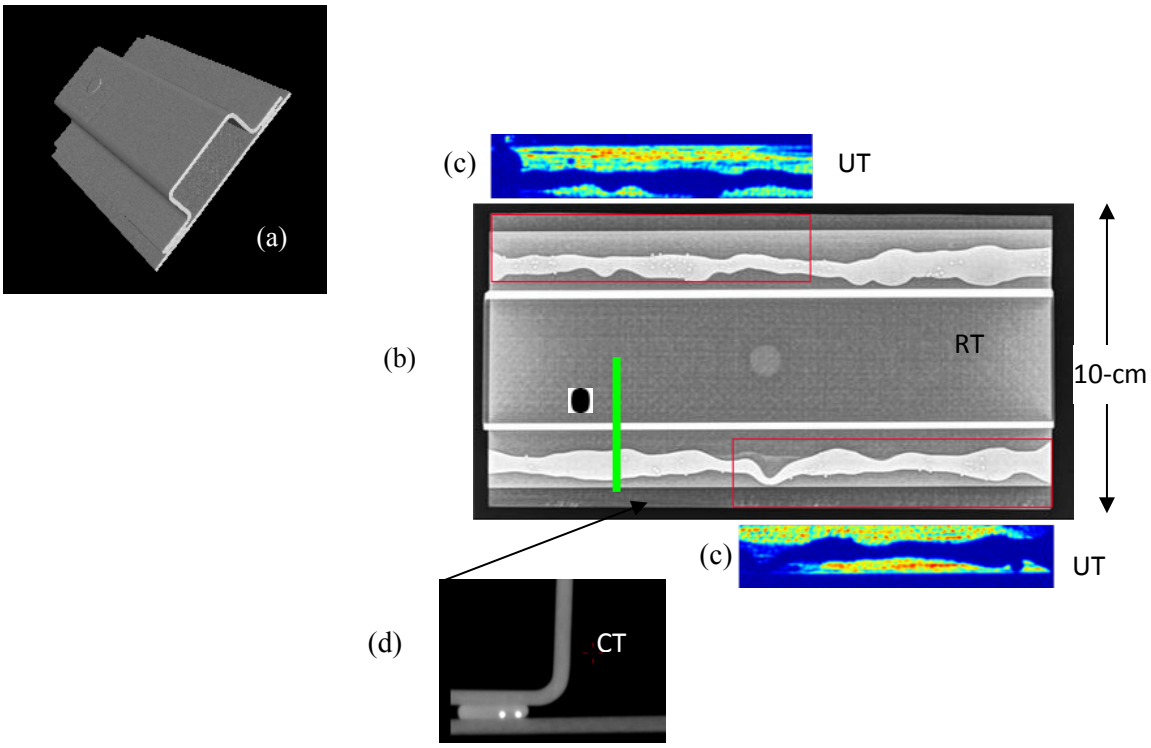

Figure IV-72: NDE inspections of a hat section adhesively bonded to a flat plate showing the two adhesive beads: (a) perspective view showing layup, (b) low-energy radiographic transmission (RT) of the 25-cm long section, (c) ultrasonic transmission (UT) pulse/echo image of adhesive bond, and (d) magnified CT section showing 1-mm glass beads used to limit minimum bead thickness.

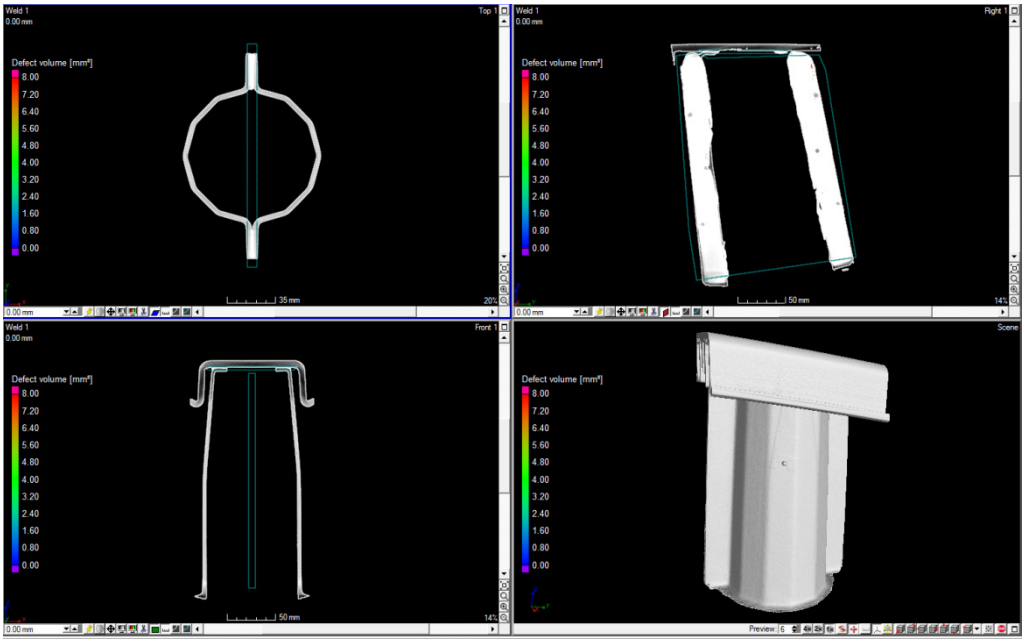

Figure IV-73: Orthogonal CT images of the nylon version of the FBCC assembly. The upper right image shows the adhesively bonded flanges of the crush cans.

The inspections are intended only as a final verification of the build process, not a 100% inspection of all components. When the molding and assembly processes appear to be under control, crush can subassemblies will be selected and inspected and FBCC assemblies will be selected. To ensure the capability of both the CT and ultrasonic inspections, a crush can and a bumper part will be produced with thin phantom discrepancies at each of the inter-plies.

Structural Health Monitoring: A general strategy for SHM in the automotive environment has been developed. While traditional NDE methods (such as tap tests and ultrasound) can be used in the manufacturing environment, they require too much training and capital expense for most repair shops. This drives the need for onboard sensors to detect in-service impacts that may have damaged the composites. While there is a deep literature for SHM of composites, most of these methods are probably too expensive for the automotive market. Our current, primary strategy is to evaluate very low-cost MEMS accelerometers (e.g., those found in cellphones), to determine optimal detector locations and the range of impact conditions that can be detected. These sensors will be mounted as self-powered, remotely accessible devices. A comparison study is being planned that would be used as an optical FBG strain sensor.

During FY 2015, a pendulum impact stand with a hemispherical impactor was built to compare the MEMS accelerometer and FBG sensors. A FBG vendor was also identified. However, the SHM activity has been mostly on hold while the NDE for the FBCC inspections is finalized. In Figure IV-73, the top slice is the top indentation, while the other slices are the local reflectivity in three orthogonal planes and indicate the conical damage zone. Damage propagates from the bottom surface toward the front. There is no visible damage on the impacted top surface. The vertical height is exaggerated with the sample at 2.5-mm thick.

Current plans call for straight, flat sections to be inspected with ultrasonic pulse/echo using raster scanning in an immersion tank as described above. Curved sections would be inspected with the surface-following ultrasonic phased-array that has also been demonstrated.

A general strategy for SHM in the automotive environment has been developed. While traditional NDE methods (e.g., tap tests and ultrasound) can be used in the manufacturing environment, they require too much training and capital expense for most repair shops. This drives the need for onboard sensors to detect in-service impacts that may have damaged the composites. While there is deep literature for SHM of composites, most of these methods are probably too expensive for the automotive market. Our current, primary strategy is to evaluate very low-cost MEMS accelerometers (e.g., those found in cellphones) to determine optimal detector locations and the range of impact energies that can be detected. These will be mounted as self-powered, remotely accessible devices. A comparison study is being planned that would use an optical FBG strain sensor. Multiple locations (i.e., gratings with different spacing) will be accessed on a single fiber using wavelength-division multiplexing.

Technology Transfer Path

FBCC was selected because it is a primary energy absorbing structural member in frontal crashes and is a challenging structural application of composites for crash energy management.

Six load cases are being evaluated for the crush cans and bumper beam application in predictive modeling followed by validation with fabricated structures via crash and physical testing and analyses. At all levels, a broad group of technology stakeholders are involved in modeling with academic materials models and four commercial codes (LS-DYNA, RADIOSS, PAM-CRASH, and ABAQUS) to help accelerate evaluation of the models for early identification of key knowledge gaps and to develop best practices. Advances made in crash modeling will be quickly implemented by respective crash code vendors into major commercial crash codes for crash analyses of carbon composite structures. As stated under Task 3.2, ESI has implemented UM's meso-scale RUC material model in PAM-CRASH and will release it during FY 2016 for broader evaluation by industry.

Successful demonstration of challenging structures such as FBCCs opens new lightweighting application opportunities for composites in passenger vehicles and light trucks, with the near-term potential to drive U.S. industrial capacity and economies of scale in carbon fiber production. Project outcomes are expected to advance the readiness levels of composite material modeling and crash-modeling technologies to prove their feasibility for broader application of primary automotive composite structures. Periodically, intermediate research results are reported by OEMs, vendors, and academic experts in task-specific reports, as well as disseminated through publications in open literature and/or subject-matter conferences.

Conclusion

During the project's Year 3, considerable progress was made in CAE analysis and finalization of the composite FBCC design so that tooling and molding process design could be addressed simultaneously with manufacturability, joining/assembly, and NDE considerations. Intermediate part shapes (such as hat section crush tubes) were fabricated, joined and crush tested to validate the proposed joining assumptions and develop correlations with corresponding CAE simulations. Final predictions of FBCC crash behavior were obtained from academic collaborators and an engineering design house, while the crash predictions in the other three codes are expected in FY 2016. Tooling and assembly fixture procurement were completed toward the end of Year 3 and initial molding trials were conducted. A detailed NDE methodology has been developed for characterization of the fabricated composite FBCC and adhesive joining. The team is positioned well to commence component-level and system-level physical crash testing of composite FBCCs in early FY 2016.

REFERENCES

1. S. Song; A. M. Waas; K. W. Shahwan et al., 2007, "Braided textile composites under compressive loads: Modeling the response, strength and degradation," *Composites Science and Technology*, 67(15-16); pp. 3059-3070.
2. S. C. Quek; A. M. Waas; K. W. Shahwan; and V. Agaram, 2003, "Analysis of 2D Flat Triaxial Braided Composites," *Int.J. Mechanical Sciences*, 45(6-7); pp. 1077-1096.
3. S. Song; A. M. Waas; K. W. Shahwan; O. Faruquec; and X. Xiao, 2009, "Compression response, strength and post-peak response of an axial fiber reinforced tow," *International Journal of Mechanical Sciences*, 51; pp. 491–499.
4. F. C. Caner; Z. P. Bazant; C. G. Hoover; A. M. Waas; and K. W. Shawan, 2011, "Microplane Model for Fracturing Damage of Triaxially Braided Fiber-Polymer Composites," *Journal of Engineering Materials and Technology*, 133(021024-1-12).
5. G. Cusatis; A. Beghini; and Z. P. Bazant, 2008, "Spectral Stiffness Microplane Model for Quasibrittle Composite Laminates – Part 1: Theory," *Journal of Applied Mechanics*, 75 (021009-1-6).
6. F. K. Chang and K. Y. Chang, 1987, "A progressive damage model for laminated composites containing stress concentrations," *Journal of Composite Materials*, 21; pp. 834-855.
7. P. Feraboli; B. Wade; F. Deleo; M. Rassian; M. Higgins; and A. Byar, 2011, "LS-DYNA MAT54 modeling of the axial crushing of a composite tape sinusoidal specimen," *Composites (Part A),* 42; pp. 1809-1125.
8. A. Matzenmiller; J. Lubliner; and R. L. Taylor, 1995, "A Constitutive Model for Anisotropic Damage in Fiber-Composites," *Mechanics of Materials* 20; pp. 125–152.
9. X. Xiao, 2008, "Simulation of Composite Tubes Axial Impact with a Damage Mechanics Based Composite Material Model," *10th International LS-DYNA Users Conference*, Dearborn, Michigan, June 8 through 10, 2008; pp. 43-54.
10. R. K. Goldberg and K. S. Carney, 2006, "Modeling the Nonlinear, Strain Rate Dependent deformation of Shuttle Leading Edge Materials with Hydrostatic Stress Effects Included," *8th International LS-DYNA Users Conference*, Dearborn, Michigan, June 4 through 6, 2006; pp. 45-56.

11. M. Gatti; L. Vescovi; M. Sperati; P. Pagano; and L. Ferrero, 2007, "Characterization of Composite Materials, Unidirectional and Fabric Samples," *Autosim Technology Workshops and Csc*, Paris, France, July 5 through 6, 2007.
12. S. W. Tsai and E. M. Wu, 1971, "A general theory of strength for anisotropic material," *J. Compos. Mater.*, 5(1); pp. 58–80.
13. I. M. Daniel and O. Ishai, 2006, "Engineering Mechanics of Composite Materials," 2nd Edition, New York, New York: Oxford University Press; pp. 122-147.
14. P. Ladevèze and E. Le Dantec, 1992, "Damage Modelling of the elementary ply for laminated composites," *Composites Science and Technology*, 43(3); pp. 257-267.
15. A. K. Johnson; A. K. Pickett; and P. Rozycki, 2001, "Computational methods for predicting impact damage in composite structures," *Composites Science and Technology*, 61(15); pp. 2183-2192.
16. Z. Hashin, 1980, "Failure Criteria for Unidirectional Fiber Composites," *Journal of Applied Mechanics*, (47); pp. 329–334.
17. "Abaqus Analysis User's Manual," v6.11. Dassault Systemès Simulia Corp.
18. S. Heimbs, 2011, "Bird Strike Simulations on Composite Aircraft Structures," *2011 Simulia Customer Conference*, Providence, Rhode Island, May 19, 2011.
19. Y. Pan; L. Iorga; and A. A. Pelegri, 2008, "Numerical generation of a random chopped fiber composite RVE and its elastic properties," *Composites Science and Technology,* 68; pp. 2792–2798.
20. N. D. Flesher and F.-K. Chang, 2003, "Effect of Cross-Section Configuration on Energy Absorption of Triaxially Braided Composite Tubes," *18th Annual Technical Conference American Society for Composites*, University of Florida, Gainesville, Florida, October 19 through 22, 2003.
21. Z. Yuan and J. Fish, 2008, "Hierarchical Model Reduction at Multiple Scales," *International Journal for Numerical Methods in Engineering*.
22. ASTM D1002, "Standard Test Method for Apparent Shear Strength of Single-Lap-Joint Adhesively Bonded Metal Specimens by Tension Loading."
23. ASTM D3807, "Standard Test Method for Strength Properties of Adhesives in Cleavage Peel by Tension Loading."
24. ISO 11343, "Determination of Dynamic Resistance to Cleavage of High Strength Adhesive Bonds Under Impact Conditions - Wedge Impact Method."

Bibliography

L. Berger; O. Faruque; and M. Mehta, 2015, "Validation of Material Models for Crash of Carbon Fiber Composites: Setting Targets and Initial Design," *Society for the Advancement of Material and Process Engineering, Spring Technical Conference*, Baltimore, Maryland.

L. Berger; O. Faruque; and M. Mehta, 2014, "Validation of Crash Models for Carbon Fiber Composites: A Project Overview," *17th U.S. National Congress on Theoretical and Applied Mechanics*, Michigan State University, East Lansing, Michigan, June 15 through 20, 2014.

C. J. Dasch; G. J. Harmon; and M. H. Jones, 2015, "Ultrasonic and X-ray Inspection of a High Performance Carbon Fiber Composite for Automotive Applications," *American Society for Composites, 2015 Technical Conference*, East Lansing, Michigan, September 2015.

K. Kirane; M. Salviato; and Z. P. Bazant, 2014, "A Multi-Scale Microplane Model for Fracturing Damage of Woven Composites," *17th U.S. National Congress on Theoretical and Applied Mechanics*, Michigan State University, East Lansing, Michigan, June 15 through 20, 2014.

A. S. Yaghoubi; G. Newaz; P. Begeman; D. Board; Y. Chen; and O. Faruque, 2014, "Rigid Angular Impact Response of Generic Steel FBCC Samples: Correlation of Multiple Velocity-Measurement Techniques," *2014 Society of Experimental Mechanics' Conference and Exposition on Experimental and Applied Mechanics*, Greenville, South Carolina, June 2 through 5, 2014.

A. S. Yaghoubi; G. Newaz; P. Begeman; D. Board; Y. Chen; and O. Faruque, 2014, "Rigid Full Frontal Response of Generic Steel FBCC Samples," *Society of Automotive Engineers 2014 World Congress*, Detroit, Michigan, April 8 through 10, 2014.

A. S. Yaghoubi; G. Newaz; P. Begeman; D. Board; Y. Chen; and O. Faruque, 2014, "Generic Steel FBCC Samples Subjected to Rigid Offset Frontal Impact," *Society of Automotive Engineers 2014 World Congress*, Detroit, Michigan, April 8 through 10, 2014.

A. S. Yaghoubi; G. Newaz; P. Begeman; D. Board; Y. Chen; and O. Faruque, 2014, "Load History Assessment of Generic Steel FBCC Samples Subjected to Rigid Center Pole Impact," *2014 Society of Experimental Mechanics' Conference & Exposition on Experimental and Applied Mechanics*, Greenville, South Carolina, June 2 through 5, 2014.

W. Xu and A. M. Waas, 2014, "Crush Analysis and Energy Absorption of Woven Textile Composite Tubes," *17th U.S. National Congress on Theoretical and Applied Mechanics*, Michigan State University, East Lansing, Michigan, June 15 through 20, 2014.

IV.6. Integrated Computational Materials Engineering Development of Carbon-Fiber Composites for Lightweight Vehicles – Ford Motor Company

Project Details

Xuming Su, Principal Investigator
Ford Motor Company
2101 Village Road
Dearborn, MI 48124
Phone: 313-845-5643
E-mail: xsu1@ford.com

David Wagner, Principal Investigator
Ford Motor Company
2101 Village Road
Dearborn, MI 48124
Phone: 313-845-2547
E-mail: dwagner6@ford.com

Walter Parker, Program Manager
U.S. Department of Energy
National Energy Technology Laboratory
626 Cochrans Mill Road
Pittsburgh, PA 15236-0940
Phone: 412-386-7357
E-mail: walter.parker@netl.doe.gov

Carol Schutte, Technology Area Development Manager
U.S. Department of Energy
1000 Independence Avenue, SW
Washington, DC 20585
Phone: 202-287-5371
E-mail: carol.schutte@ee.doe.gov

Contractor: Ford Motor Company
Contract No.: DE-EE0006867

Executive Summary

The project will simultaneously develop a structural carbon-fiber composite subframe to support immediate weight reduction in light-duty vehicles while also developing Integrated Computational Materials Engineering (ICME) techniques to support a reduced development-to-deployment lead time in all lightweight materials systems.

In the current Phase I of the project, the focus is on developing ICME tools. Carbon-fiber reinforced polymer (CFRP) composite consists of a polymer matrix reinforced with strong carbon fibers. The mechanical properties of the composite depend strongly on the layout of the fibers and the bonding of the matrix and fibers. Design of the material and the manufacturing process have profound impact on final performance of the material. The numerical tools intended here are to predict material performances of CFRP based on fiber architecture, molding process, and curing history, with considerations of uncertainties and probabilistic nature of materials, processes, and in-service conditions. The tools will be implemented in a popular software package (such as LS-DYNA for stress and crash analysis, nCode for durability, MoldFlow for molding, and

ModeFrontier for optimization). With these tools, a design engineer can optimize components to achieve the most efficient usage of the material and a manufacture engineer can optimize the process to produce materials that are able to meet challenging requirements.

Later, during Phase II, this project will design, develop, and optimize a light-duty vehicle carbon-fiber composite subframe capable of achieving a ≥25% weight reduction and ≤$4.27 per pound (lb) of weight saved when compared to the baseline technology being replaced. The subframe will significantly contribute to the structural performance of the vehicle in driving and crash conditions. The developed carbon-fiber composite subframe will achieve the function and packaging requirements of the baseline subframe to be replaced.

Accomplishments

- Molded forty 1.2-mm thick and twenty-five 2.3–mm thick unidirectional (UD) CFRP plaques and distributed for characterization at Northwestern University (NU), the National Institute of Standards and Technology (NIST), and Ford Motor Company (Fiscal Year [FY] 2015).
- Completed quasi-static tensile tests on neat resin and UD plaques for mechanical property characterization at room temperature. The preliminary data showed properties as expected (FY 2015).
- Established testing procedures to characterize prepregs at elevated temperatures (FY 2015).
- Investigated methods for characterizing single fibers and established the key characterization requirement to support interphase/interface modeling (FY 2015).
- Developed a non-orthogonal material model to better predict fiber orientation during the preform process for woven prepregs (FY 2015).
- Conducted molecular dynamic analysis (MDA) using the general purpose DREIDING force field with harmonic covalent potential functions to study the thermomechanical properties of polymer resins. The predicted glassy transition temperature (T_g) and stress-strain relations agree well with test data (FY 2015).
- Completed buildup of a steered molecular dynamics (SMD) approach-based molecular dynamics (MD) model to investigate fiber-matrix interface behavior and identify the right failure modes for both uncured and cured carbon-fiber composites (FY 2015).
- Completed a multiscale model for CFRP using representative volume element (RVE); delivered an automated RVE package to provide elastic property input for crash and durability models with UD composites (FY 2015).
- Established the framework for metamodeling of a constitutive relation that is based on a developed RVE model with Kriging technique to efficiently generate a non-linear stiffness matrix for a non-orthogonal model (FY 2015).
- Developed a pressure strain rate and temperature-dependent visco-plastic material model to better capture the complex material stress-strain behavior in an epoxy resin matrix and incorporated it into the multiscale model. The predicted results agree with testing data very well (FY 2015).
- Applied a Voronoi diagram algorithm to reconstruct the 3D microstructure for a chopped sheet molding compound (SMC) to capture fiber tow structures. The reconstructed microstructure will be used as geometry input for SMC RVE modeling (FY 2015).
- Implemented a thermo-chemo-mechanical material model in LS-DYNA as MAT277 to simulate resin behavior during the curing process. The model is qualitatively validated to capture the expected deformation phenomenon. Quantitative model validation work is ongoing (FY 2015).
- Integrated the resin curing model MAT277 with the fabrics mechanical model to create a new material model MAT278 in LS-DYNA to simulate the compression molding process for woven fabric CFRP. Model validation is ongoing (FY 2015).

- Identified the material constitutive framework for crash analysis where RVE is utilized to provide input parameters required by LS-DYNA material models (FY 2015).
- Completed the preliminary fatigue tests to provide guideline information for specifications of test specimen and tapping methods for future experiments; generated a completed fatigue test matrix (FY 2015).
- Established the project database infrastructure via the DSpace online data repository at NIST. Data sharing and management will be facilitated through this database (FY 2015).
- Established a generic material testing data process and storage template to ensure better interfacing and communication between different modeling and simulation solutions (FY 2015).

Future Directions

- Complete molding of remaining UD and woven plaques, double dome, and hat sections requested by teams.
- Plan and build a second set of continuous CFRP plaque variations of molding processes. Characterize the new set of CFRP to provide experimental data for material models to have an ICME nature (i.e., reflecting changes in performance based on variations in the material design and manufacturing process).
- Mold specimens of chopped fiber CFRP with SMC, using various molding parameters. The molding parameters to be studied comparatively include mold temperature, compression pressure, and initial charge locations. Temperature and pressure data will be recorded by in-mold sensors during the molding process to verify and improve existing Moldflow models.
- Improve the non-orthogonal material model for preforming to include rate effects. The improved model needs to be able to predict fiber orientation and wrinkling after the part is taken out of the molding tool.
- Generate RVE models for woven CFRP and include predictions of the material failure process in the RVE models to provide necessary parameters for homogenized macroscopic models.
- Utilize Co-Kriging models to optimize the procedure of generating virtual test data using RVE simulations for material modeling. The total amount of RVE runs required will be largely reduced by this process, while keeping the current level of accuracy. This work has already started during the current year and is expected to complete in the coming year.
- Establish ICME crash models for safety analysis. While the current RVE is able to provide material inputs for material relations in LS-DYNA for stress analysis, improvements/new material relations shall be developed and implemented in LS-DYNA to describe special failure modes in CFRP crash tests, including degradation of material performance caused by delamination in a shell model.
- Complete fatigue tests of UD specimens and establish fatigue analysis procedures/models for UD CFRP. Establish fatigue models for non-crimped laminates that correlates fatigue strength to prepreg stack-ups. Start fatigue tests of woven CFRP and work on fatigue models of woven CFRP.
- Perform preliminary design and analysis of CFRP subframes. The feedback results will be passed to modeling teams to guide ICME modeling work. Study possible solutions to design, develop, and optimize a light-duty vehicle carbon-fiber composite subframe capable of achieving a ≥25% weight reduction and ≤$4.27/lb of weight saving when compared to the baseline technology being replaced, while meeting function and packaging requirements.

Technology Assessment

- Target: Developing a comprehensive material characterization method for CFRP and building up the ICME database to verify and validate ICME models.

- Status: Forty 1.2-mm thick and twenty-five 2.3-mm thick UD plaques has been molded and only tensile test data are available.
- Gap: Only part of first shipment of requested plaques have been delivered, with more needed for comprehensive characterization of CFRP.
- Gap: Plaques of CFRP with different resins and compression molding processes are not available to verify ICME models.
- Target: Preforming models accurately predicting fiber orientations and winkling
- Status: Non-orthogonal models are able to follow fiber orientation for woven fabrics
- Gap: Test data are not available to verify predicted fiber orientations using preforming models
- Gap: Nonlinear elasticity models are currently used in prediction of wrinkling, yet not able to describe development of wrinkling after parts are removed from mold as observed in the experiments. Creep and relaxation behavior needs to be incorporated into material models.
- Target: Using MDA to predict thermomechanical behavior of resins, explore mechanisms of resin and interphase failures, and provide key data for micro and macro material models.
- Status: MDA analyses are completed for two commercially available epoxy materials: EPON825/33DDS and EPON862/DETDA. Predicted glass transfer temperature, stress, and strain relation are close to test data.
- Gap: The resin analyzed is not the resin used for material characterization of the current project.
- Gap: Results obtained from MDA have not yet been directly employed at micro and macro models.
- Gap: Failure mechanisms need to be identified.
- Target: Developing RVE models for UD and woven composites relating mechanical properties of composite to properties of its constituents.
- Status: RVE for no crimped CFRP has completed for stress analysis.
- Gap: RVE for woven fabric has not been developed.
- Gap: RVE is not able to predict material failure, which is critical for performance analysis.
- Target: Use the Moldflow module for compression molding simulation of chopper fiber CFRP.
- Status: Unverified compression molding module completed.
- Gap: Test data are not available. Test data shall include impact of variations of molding parameters.
- Target: Developing fracture models and energy absorption models for vehicle component safety analysis.
- Status: RVE calibrated material relation has been used in LS-DYNA for stress analysis.
- Gap: Failure models are not yet well developed for crash analysis.
- Target: Developing fatigue and durability models to predict component life.
- Status: Test specimen agreed and test samples are available.
- Gap: Test data are not available.
- Target: Developing stochastic multiscale optimization models for ICME analysis.
- Status: Reconstruction of chopped fiber RVE configuration with a given fiber orientation tensor that has been proposed; Co-Kriging method is developed for optimized procedure relating to the microscale to macroscale model
- Gap: Description of the statistical nature of material features critical for material mechanical properties that need to be developed.
- Gap: Transfer of uncertainty from nanoscale to microscale and from microscale to macroscale needs to be studied.

Introduction

Vehicle lightweighting is very important for automotive manufacturers to meet the ever-increasing demand of fuel efficiency. CFRP composites, with a density of 1.55 g/cm^3 and tensile strength of about 2,000 MPa in the fiber direction, are among the most promising candidates for replacing metals for structural components. The project will design, develop, and optimize a light-duty vehicle carbon-fiber subframe capable of achieving a ≥25% weight reduction and ≤$4.27/lb of weight saved when compared to the baseline technology being replaced. The subframe will significantly contribute to the structural performance of the vehicle in driving and crash conditions. The developed subframe will achieve the function and packaging requirements of the baseline subframe being replaced.

Unlike many metals typically used in automotive vehicles, the mechanical properties of CFRP are highly direction-dependent. The strength of the material in the fiber-reinforced direction could be an order of magnitude higher than in the direction perpendicular to it. Fiber orientation in a component is decided not only by the initial fabric layout, but also by preform or molding processes. An optimized vehicle component design will need tools that predict the performance of CFRP, based on fiber architecture, molding process, and curing history, with consideration of uncertainties and the probabilistic nature of materials, processes, and in-service conditions. The current project will develop these ICME tools to meet this design challenge.

ICME tools developed during the project will do the following:

- Simulate the subframe's constitutive and assembly behavior.
- Develop robust, accurate, and reliable constitutive models for each constituent material and the composite assembly under expected service conditions, including high-strain rates using physics-based models.
- Address structure/property predictions and process/property predictions.
- Simulate the manufacturing process (including variability from both the process and the material), including te evolution of thermo-chemical-mechanical material properties of complex systems and defects such as voids.
- Provide capabilities to predict the full nonlinear response under severe loading conditions, including dynamic crush and damage.
- Be capable of predicting part and assembly properties (i.e., load to failure, failure location, failure mode, stiffness/deflection, dynamic performance, and energy absorption/crashworthiness) from the constituent properties (i.e., fiber/interphase/resin) and the process history.

This project will utilize ICME tools developed for design, development, and optimization of an integrated CFRP subframe chassis system with the performance, weight, and cost targets mentioned above.

Approach

The project will design, develop, and optimize a light-duty vehicle carbon-fiber subframe capable of achieving a ≥25% weight reduction and ≤$4.27/lb of weight saved when compared to the baseline technology being replaced. This objective is achieved by developing ICME tools and numerical procedures for optimizing both the design and manufacturing process so CFRP is the most efficiently used.

The ICME tools relate the performance requirements of the vehicle-to-material design and processes. While material performances are expressed at the continuum macroscale, they are decided by material microstructures and microstructural features at the microscale and again by molecular bonds and crosslinking at the nanoscale. The material microstructures and microstructural features, bonding, and crosslinking are results of the material design and manufacturing processes. Therefore, ICME tools are multiscale models and approaches that bridge the different material scales. The models are based on physical principles and testing

measurements and observations. Test data are also needed for validating material models. Modeling and testing are always hand-in-hand for successful development of ICME tools. The project team, which consists of Ford Motor Company (an automotive manufacturer), Dow Chemical (a material manufacturer), Northwestern University (an institution of highly regarded academics), and the National Institute of Standard and Testing (NIST) (a world renowned test laboratory), has all elements for making the breakthrough in developing ICME tools. The research team also includes software developers from Livermore Software Technology Corporation (LSTC) (LS-DYNA), Autodesk (Moldflow), ESTECO (ModeFrontier), and HMB(nCode); therefore ICME tools developed during the project can be numerically implemented and available through popular engineering software and disseminated.

The project is conducted with four budget periods. The budget periods are (1) CFRP material characterization and ICME model development, (2) ICME model database and validation, (3) ICME model integration and validation, and (4) ICME-based design and optimization. The first two budget periods constitute Phase I: Model Development and Model-Level Validation. The remaining two budget periods constitute Phase II: ICME Integration and System Design.

Results and Discussion

The project is organized in four main tasks: Task 1 is the material characterization and ICME database development, Task 2 is ICME model development and validation, Task 3 is ICME model integration and validation, and Task 4 is ICME-based design and optimization. FY 2015 is the first year of Phase I. Only Task 1 and Task 2 were active during FY 2015.

Task 1 - Material Characterization and ICME Database

Experimental characterization of each constituent of CFRP and characterization at the coupon level will be conducted in this task. Results will be collected and stored in the ICME database and be used to correlate with models in Task 2.

The materials to be tested are produced by Dow Chemical. Thermoset epoxy resin is chosen to make prepregs with continuous fibers and SMC with chopped fibers. The vacuum-assisted compression molding process is used in order to achieve an aggressive cycle time and cost requirements. Figure IV-74 shows the fiber system and fabric architecture considered during this project:

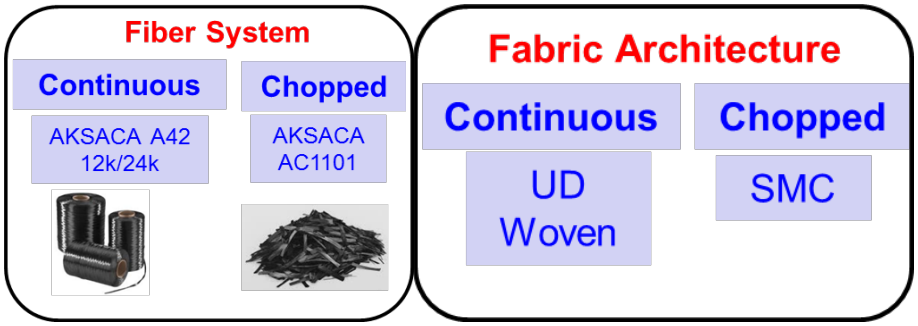

Figure IV-74: Material systems studied during the project.

About 1,000 12-in. × 12-in. plaques with various thicknesses are requested by task teams to characterize a variety of material properties. The requested plaques were prioritized and the shipment was split into different batches. Table IV-31 shows the initial request of material delivery.

Table IV-31: Initial molded plaques request for Dow Chemical.

Property	Thickness	First Shipment
UD	1.2 mm	40
UD	2.5 mm	25
UD	5.0 mm	15
Woven	1.0 mm	35
Woven	2.5 mm	25
Woven	5.0 mm	10

Two thermoset epoxy resins, A and A1, were tried. Resin A, an experimental resin, was tried first and turned out to not have the expected mechanical properties with the expected curing time. The expected curing time is set to be less than 5 minutes. The second resin, resin A1, which has been developed more for commercial use has since been used. UD plaques at 1.2 and 2.3-mm thicknesses were molded during the current year. In the meantime, Dow Chemical has shipped 5 gallons (gal) of uncured resin, 15 lb of twill woven dry fiber, and 40 lb of woven prepregs to NU to cast the neat resin plate onsite and characterize the uncured prepreg properties.

Task 1.1 – Resin Characterization

Tests were conducted on the neat resin plates of the new thermoset epoxy resin at Dow Chemical and NU. The results are compared in Table IV-32 and show good agreement. Further characterization on compression, shear properties, and properties at different temperatures is needed to provide all data necessary for material model inputs and validation in Task 2.

Table IV-32: Properties of Resin A1.

Property	NU Result	Dow Chemical Result
E (Young's Modulus)	3.85 GPa ± 2.75%	3.52 GPa ± 1.89%
ν (Poisson's Ratio)	0.38 ± 1.53%	NA
F_t (Tensile Strength)	68.2 MPa ± 6.85%	71.6 MPa ± 11.83%
Elongation	NA	2.47% ± 3.93%

Tests were also performed in a dynamic mechanical thermal analyzer (DMTA) at NU to obtain rudimentary information about viscoelastic behavior and the thermal response of epoxy. Tests were conducted across a range of cyclic loadings (i.e., 0.1 to 100 Hz) and through a sweep of temperatures (i.e., 34°C to 200°C). These tests generated data for the glass transition temperature of the epoxy, and the storage and loss modulus response as functions of frequency and temperature. The glass transition temperature was found to be between 133 and 171°C by considering the onset of a storage modulus decline and peak in tan delta, respectively.

Task 1.2 – Carbon Fiber and Fabric Characterization

A test plan was developed to characterize the prepreg to support preforming simulation. Initial tests in uniaxial tension and bias extension were conducted at elevated temperatures on woven prepregs at NU. The ends of the prepreg were cured to prevent resin from squeezing out of the grips during installation of the test specimen. However, the specimen slipped several times during testing and further development of the gripping method is needed to complete the characterization task.

Task 1.3 – Interfacial/Interphase Property Characterization

The key elements of interface/interphase characterization were decided; further discussions are ongoing to determine the best approach for developing a test plan and where the tests should be conducted (i.e., NU, Dow Chemical, or NIST).

Task 1.4 – Plaque Molding and Characterization

The 2.3-mm plaques were initially characterized at NU (results shown in Table IV-33). Further characterization is needed to measure the material response at different temperatures and strain rates.

Table IV-33: Mechanical properties of 2.3-mm thick plaques.

Property	Longitudinal	Transverse
E	125 GPa	8.89 GPa
v	0.33	0.023
F_t	2,100 MPa	61.7 MPa
v_f	About 50% (measured by bulk density)	

Preliminary microstructure work on the UD plaques was conducted at Ford. A typical optical microscope image in the transverse plane of the 2.3-mm UD plaque is shown in Figure IV-75.

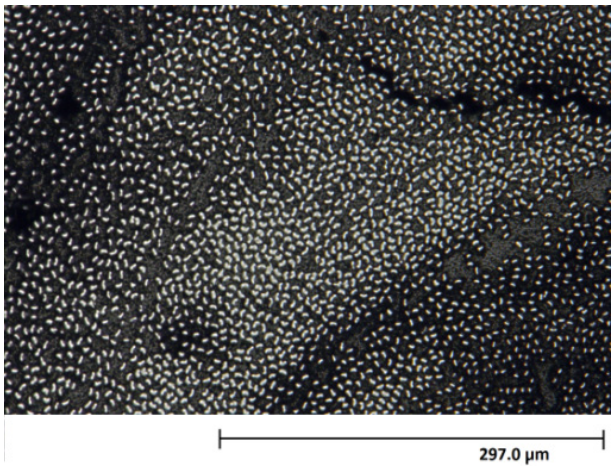

Figure IV-75: Cross-section in the transverse plane of the 2.3-mm UD composite.

The fibers are seen to have a kidney shape, which is a result of the fiber manufacturing process. The fibers have a nonhomogeneous distribution through the thickness direction of the plaque (i.e., left to right in the image). Further imaging is underway to better characterize fiber distribution throughout the plaque and distribution of voids.

Task 1.5 – ICME Database

Working with NIST, the existing online data repositories are reviewed. The DSpace online data repository was used. The basic functions and features of DSpace were introduced to the ICME team at the internal meetings and the team agreed on standardizing the data storage templates and specimen naming conventions. Example data templates were developed and are being revised with input from key collaborators.

Task 2 – ICME Model Development and Validation

A collection of process and material computational models and methodologies for predicting/optimizing CFRP performance in vehicle applications will be identified and/or developed and integrated into the ICME process.

Figure IV-76 provides a flowchart of the processes to be modeled in the ICME framework, including process modeling of performing, curing for UD and woven laminates, compression molding, and curing modeling for chopped fiber SMC. RVE models, which predict material constitutive and failure behaviors based on properties of constituents, bridge process models and performance analyses. Performance analyses are crash, durability, and NVH analyses. MDA will provide fundamental understanding of the thermomechanical behavior and failure mechanisms of resins and the resin and fiber interface. Statistical tools are needed to describe the distributions of process defects and uncertainties of processes.

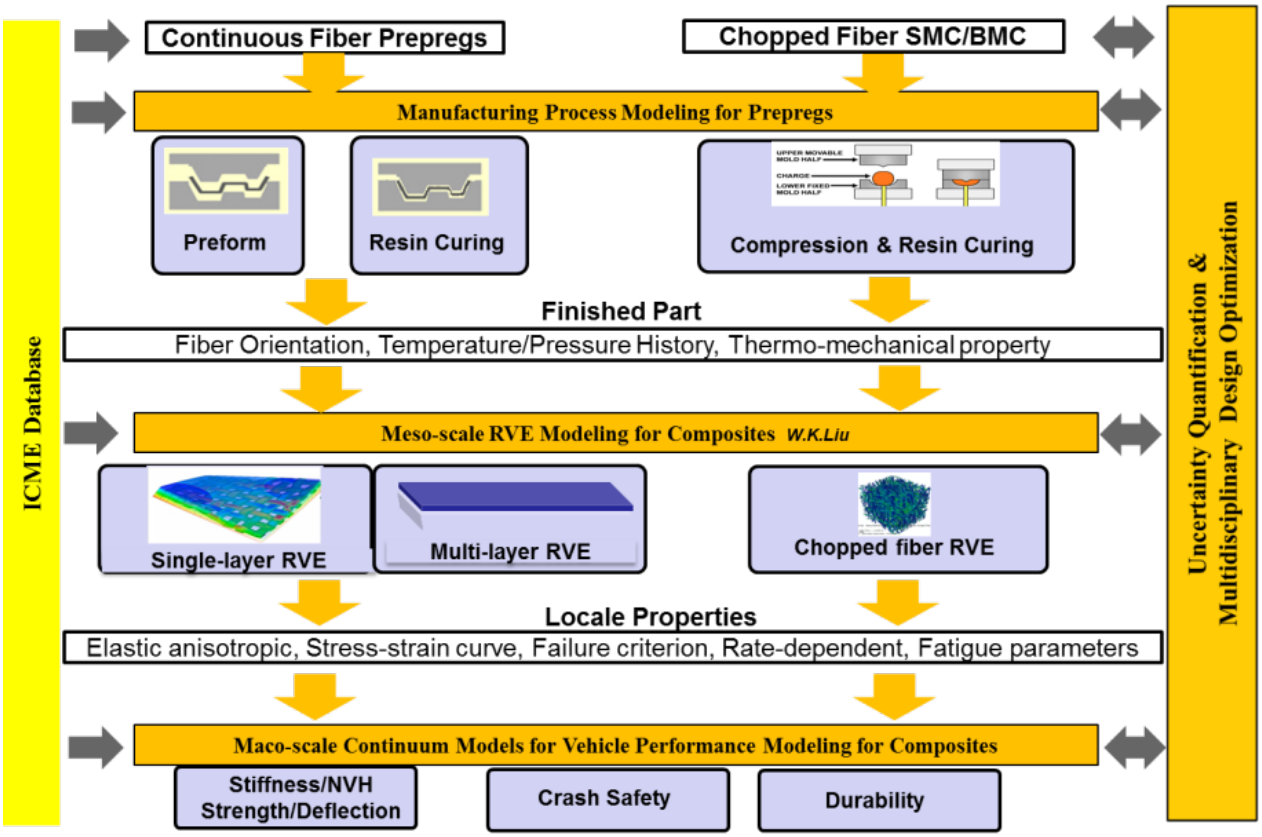

Figure IV-76: Models to be developed during the current project.

Integration of multiscale material models across the multiple stages of material processing and part operation is critical to the project. Figure IV-77 provides the material model integration flowchart. Data and information generated from simulation at each stage are passed as inputs to the next stage of modeling. The material state evolves from one stage to the next. Because local material properties depend on microstructure information (such as local fiber orientation and local detects), they vary from one location of the part to another due to influence from manufacturing processes. Micro-scale RVE models are used to obtain spatially varied material properties based on structure information obtained from forming and curing simulations. Properties estimated for each spatial location will be further used as inputs for macro-scale part structure simulations under operation loading conditions.

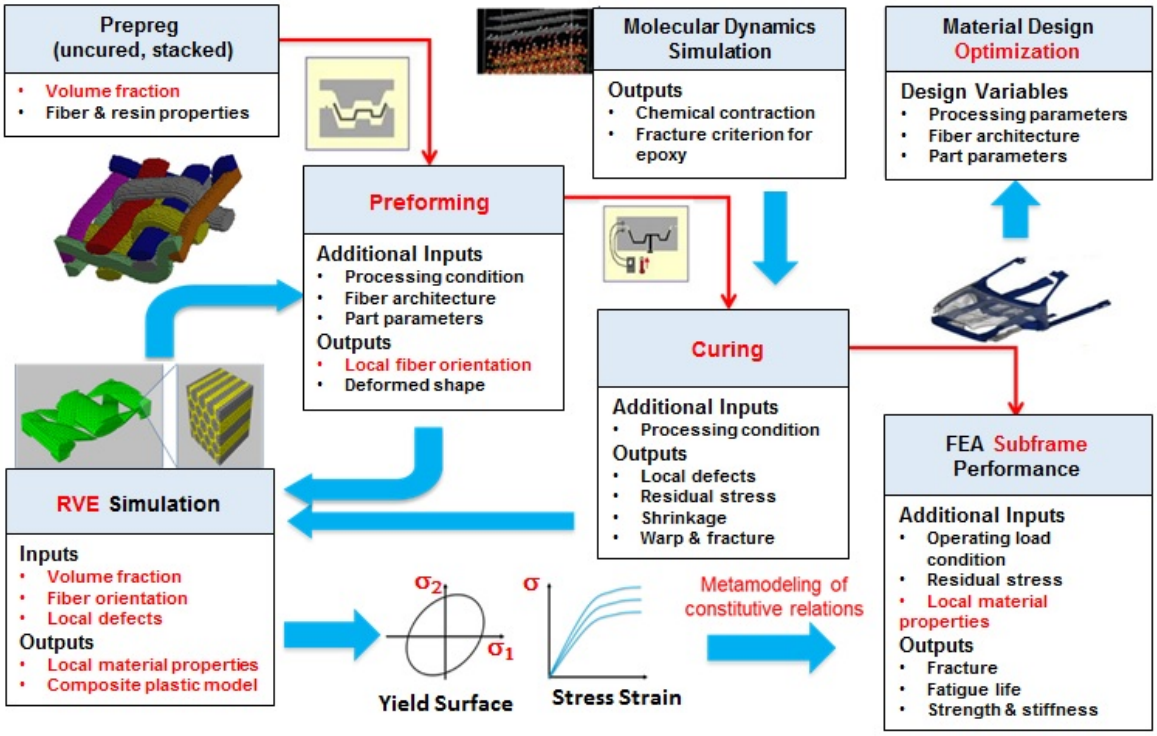

Figure IV-77: Integration of materials behavior modeling.

Task 2.1 – Atomistically Informed Resin Infusion Models

The reasonable crosslinking structures of two typical epoxy matrixes are developed: EPON825/33DDS and EPON862/DETDA. The material data were available and were very close to the resin used in the project for characterization from Dow Chemical. The general purpose DREIDING force field with harmonic covalent potential functions was employed during this stage. Using the developed crosslinking strategy, a very-high crosslinking conversion (i.e., up to 99%) could be reached. The resultingd density of a high crosslinking epoxy matrix, EPON825/33DDS, in room temperature is 1.14 g/cm^3, which is in agreement with the experimental value of about 1.2 g/cm^3.

The predicted thermo-mechanical properties are consistent with experimental and current literature results. The effect of curing degree on epoxy resin mechanical properties is investigated. Figure IV-78 shows that elastic moduli increase with an increase of curing degree. This trend is consistent with existing experimental and other computational studies.

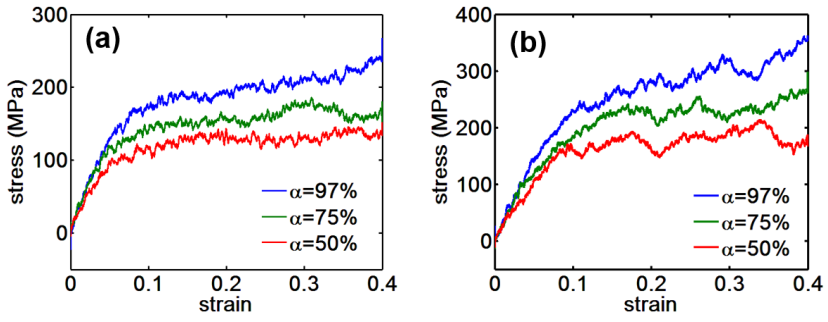

Figure IV-78: Mechanical behavior for a different curing degree of the epoxy matrix, EPON825/33DDS, during tension (a) and compression (b).

An atomistic model of multi-layer graphene (MLG)-reinforced epoxy composites was built to study the interaction between epoxy-based thermosets and carbon fibers. MLG consists of layers of graphene bound together via van der Waals interactions. The initial mass density of the epoxy matrix peaks at the interface indicates strong adhesion between the epoxy matrix and carbon surface. This strong adhesion might result in failure inside the epoxy instead of at the interface during carbon pull-out experiments.

Task 2.2 - Preform and Compression Molding Process Models

This task includes preform simulation and compression modeling simulation.

2.2.1 Preform Simulation

Two geometries were simulated using LS-DYNA with MAT234 developed for loose dry woven fabrics. One is the single dome geometry shown in Figure IV-79(a) and the other is a double dome. Different layups, such as [(0/90)]4 and [(0/90)/(±45)/(±45)/(0/90)] in Figure IV-79(b) and Figure IV-79(c), were simulated and compared. Wrinkles were predicted from simulations and a different layout yielded a different wrinkling pattern.

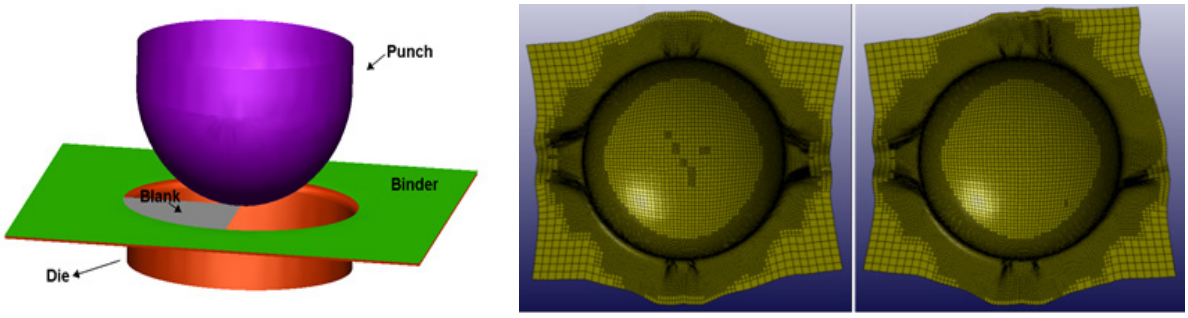

(a) (b) (c)

Figure IV-79: Case One (a) the single dome preform results with various layups (b) $[(0/90)]_4$ versus (c) [(0/90)/(±45)/(±45)/(0/90)].

A non-orthogonal phenomenological macro-scale model [1] is developed for woven fabrics. Because a non-orthogonal constitutive equation set is utilized for the fiber orientation coordinates, the non-linear and anisotropic material behavior of the woven fabric composites can be well captured in this model. Material parameters used in non-orthogonal constitutive equations are calculated by using output data from microscale RVE simulation. Figure IV-80 are simulations of bias extension tests using the new model with three different values of the shear modulus. Three different shear angle zones are clearly observed at the end of the simulation. It can be seen that as the shear modulus increases, the shear angle will decrease and the three sections of different shear angles will become less clear and even to the extent where the shear angles are similar throughout the whole specimen. Additionally, shrinkage at the central part of the specimen is found to be less obvious when the shear modulus is larger. These predictions are consistent with experimental observations.

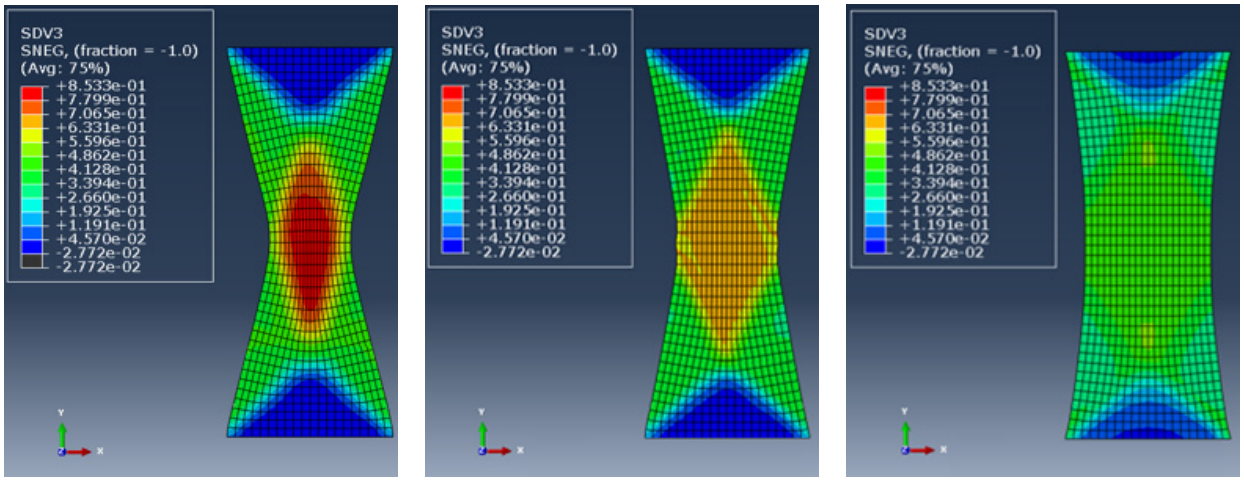

(a) 1.48 MPa shear modulus (b) 83.54 MPa shear modulus (c) 4.91 GPa shear modulus

Figure IV-80: Shear angle distribution in bias extension with different shear modulus.

2.2.2 Compression Molding Simulation

Dow Chemical, LSTC, and Ford integrated their efforts to develop LS-DYNA material model MAT277 for the simulation of resin curing behavior during the compression molding process. The curing model (i.e., Kamal model) has been implemented in LS-DYNA. Comparison between experimental data and the predicted curing degree by MAT277 is shown in Figure IV-81.

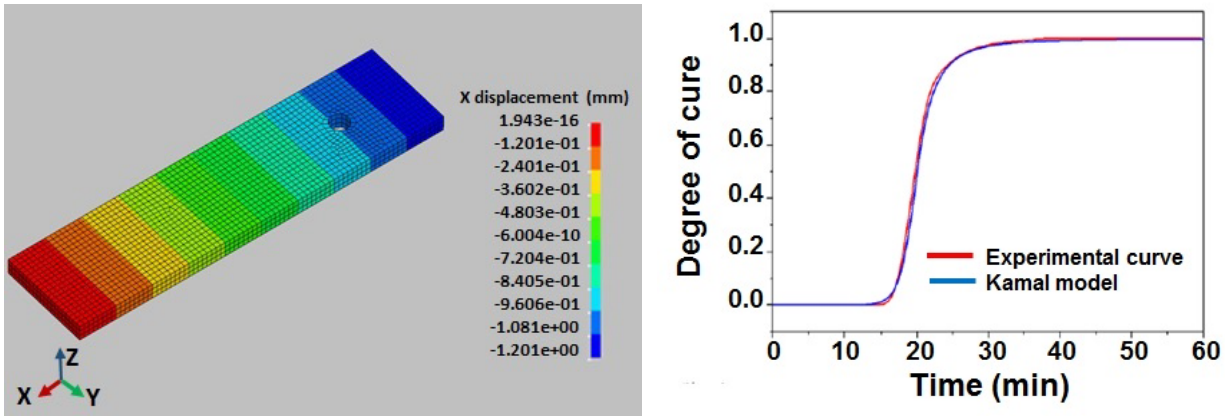

(a) (b)

Figure IV-81: (a) The test model using MAT277 and (b) a comparison between experimental results and the simulation curing degree.

The framework of the micromechanical curing-viscoelastic material model for woven fabric composites has been established and implemented in LS-DYNA as MAT278. The properties of the matrix phase in MAT278 is predicted through MAT277.

2.2.3 Compression Molding Modeling for Chopped Fiber Composites

Autodesk established the best-practice meshing methodology that is required for obtaining reliable compression molding process simulation of SMC using the double dome example model in Moldflow.

Figure IV-82(a) shows initial results obtained using default meshing parameters. This illustrates the false unfilled regions that will result in false weld lines. Figure IV-82(b) shows the eventual simulation obtained using the optimized meshing methodology. A test matrix has been established to further investigate the impact of process parameters on the quality of compression molding.

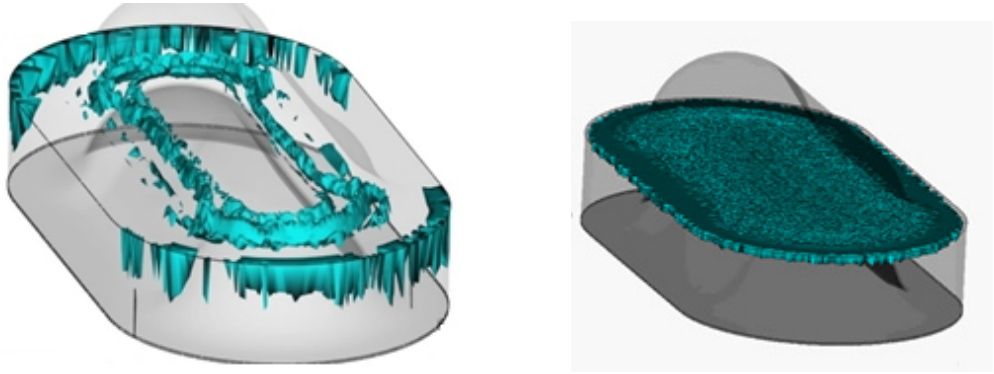

(a) Default meshing (b) Optimized meshing methodology

Figure IV-82: SMC compression molding process simulation.

Task 2.3 – Multiscale Models for Carbon-fiber Composites

Figure IV-83 illustrates the multiscale approach adopted to derive macroscopic mechanistic continuum models for different carbon-fiber-reinforced composites of interest to this project: UD fibers, woven fabrics, and chopped fiber composites. The goal is to find a macroscopic constitutive law with minimum experimental inputs by using a bottom-up hierarchical multiscale approach.

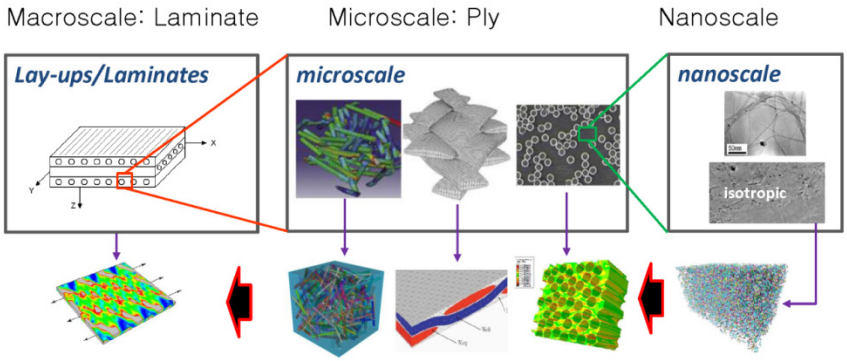

Figure IV-83: Multiscale approach toward mechanistic continuum models for carbon fiber composites.

The constitutive behavior of the polymer is of particular importance for predicting the behavior of composite material. At the micro-scale, a new continuum model for the epoxy was completed and experimentally validated for two different epoxies 3501-6 and Epon 862.

Various composite unit cells (i.e., statistical volume element [SVE] and RVE) were developed and micromechanical analyses were compared with experimental results. Predictions for transverse compression loads at different strain-rates are shown in Figure IV-84.

Simulation results obtained using classical paraboloidal yield criterion are included in order to compare with results obtained with the matrix's new constitutive model.

The RVE package for UD CFRP is completed and delivered to Ford to provide data for material relations used in crash and durability analyses.

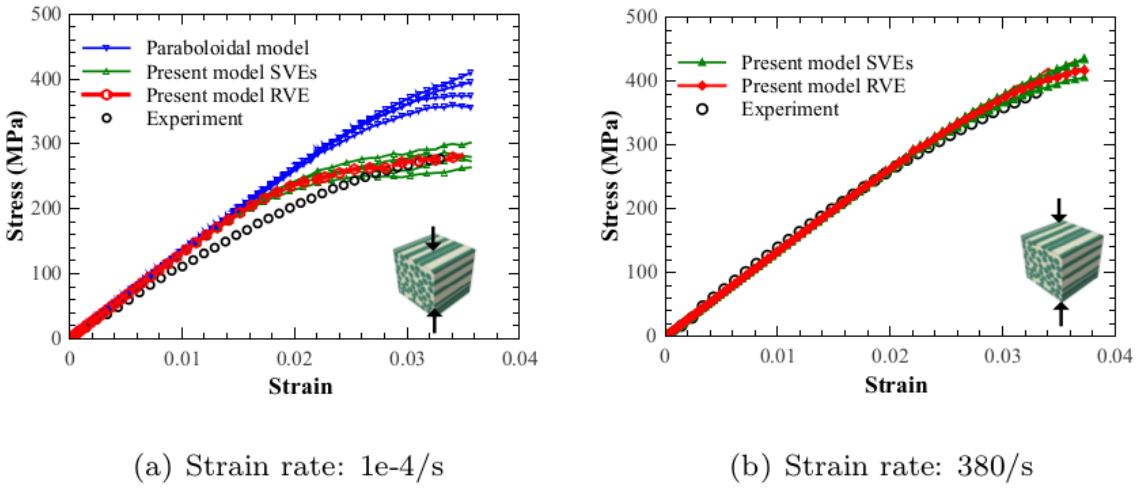

Figure IV-84: Comparison of the experiment and present model for transverse compression at different strain-rates.

Task 2.4 – Fracture Models and Energy Absorption Models

Three existing LS-DYNA carbon-fiber material models have been identified as the templates of macro model for NU's RVE model to extract macro-model properties. They are MAT54, MAT58, and MAT261, respectively. These three material models are popular ones with increasing sophistications.

Task 2.5 – Fatigue and Durability Models

A preliminary test plan has been laid out for S-N curves. The specimen will be cut in three fiber orientations, and tested at four stress ratios. Twenty-five reduplicates will be tested at each condition. It is estimated that, on average, 3 to 4 days is needed per test and four dedicated testing frames are needed to complete all testes within 1 year. Both Ford and nCode have pledged machines to perform the tests.

Task 2.6 – Stochastic Multiscale Characterization

2.6.1 Metamodeling of Constitutive Relations

Considering the spatial variation of processing conditions, the resulting fiber microstructures are different from one location to another. It is computationally prohibitive to embed RVE models into macro-scale FEA part structure simulations; therefore, this task involves constructing efficient surrogate models (i.e., metamodels) of material constitutive relations using RVE simulations for varying microstructure conditions that can capture a good range of materials properties as functions of microstructure.

As shown in Figure IV-85, a set of U.S. Department of Energy samples will be chosen as inputs to RVE simulations to obtain the responses of material constitutive relationships. Because the constitutive relation is a functional response represented by multiple highly correlated parameters, Co-Kriging techniques were proposed to construct surrogate models due to their excellent capability of handling multiple correlated responses. With the Co-Kriging models, the total amount of samples can be saved, while ensuring the accuracy of multiple correlated models.

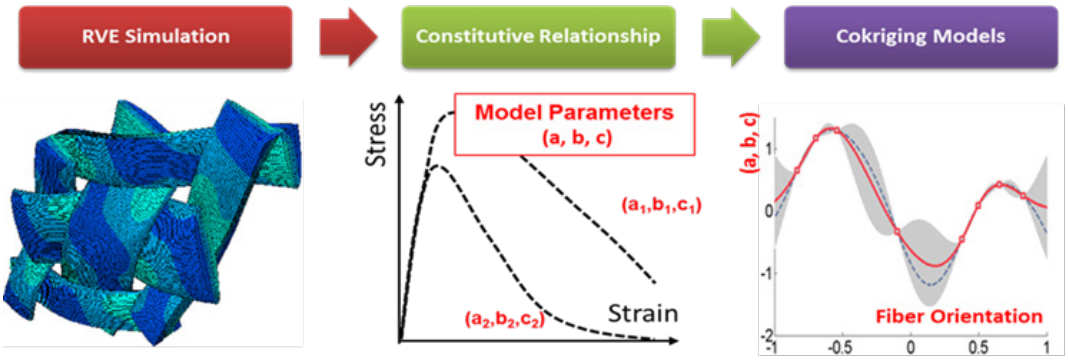

Figure IV-85: Co-Kriging metamodeling for constitutive relations.

2.6.2 Random Fiber Reconstruction

A Voronoi diagram algorithm is used to reconstruct the 3D microstructure of SMC to capture the fiber tow structure (Figure IV-86). The reconstructed microstructure will be used as geometry input for SMC RVE modeling.

Based on the 2D microscopic images, a preliminary 2D RVE is constructed first. The RVE domain is first divided into several subdomains. The voronoi diagram algorithm is then used to capture the boundaries between the ifferent tows. Each subdomain is filled with the aligned tow of fibers.

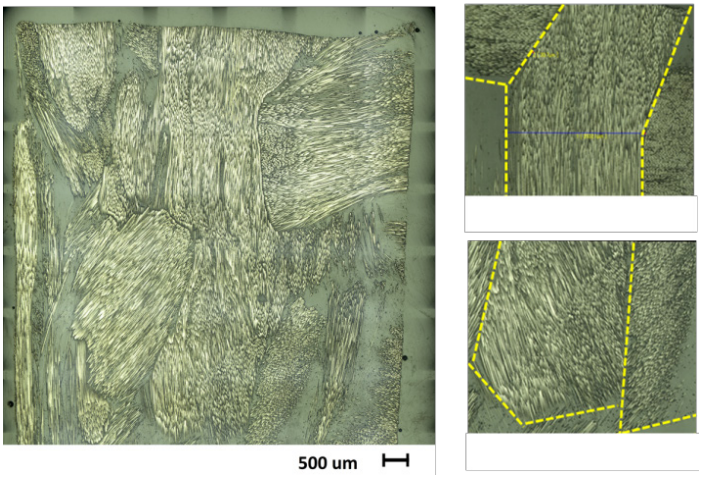

Figure IV-86: Microscopic images of chopped SMC.

To capture the 3D microstructure of SMC, a simulated annealing (SA) algorithm was employed to search for the solution of dividing the 3D domain, aiming for matching the target average cell area and aspect ratio; these parameters can be extracted from the 2D real microstructure images. Preliminary results from using the SA algorithm are shown in Figure IV-87. Results show that the optimization algorithm has significantly improved the reconstruction to match with the pre-specified characteristics.

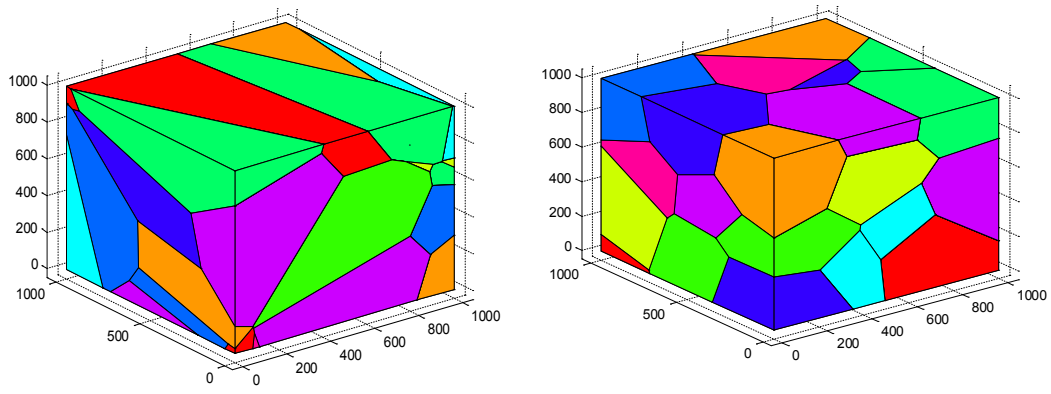

Figure IV-87: 3D Voronoi diagram optimized using the simulated annealing algorithm (left: target aspect ratio=3; right: target cell volume =10^3/30).

Technology Transfer Path

The project team includes the primary software developers in every aspect of the ICME application chain. LSTC's LS-DYNA is a popular FEA package for stress analysis. It is especially dominating in vehicle safety analysis. Moldflow has the largest user groups in polymer molding analysis. The same is true for HMB's nCode for fatigue and ESTECO's modeFrontier for optimization. All models developed by the project result from cooperation between the above-mentioned software developers, researchers in academia, and end users in OEMs and suppliers. The models are being implemented in the respective software when developed and are available to the general public once validated.

The second path of technology transfer is through infrastructure and methods identified by NIST. All test data and material models are being stored at the datacenter of NIST and will be open to the public once the project is completed. Research results are also being published in respective technical journals and conference proceedings.

The third path of technical transfer is direct usage of the results at Ford and Dow Chemical.

Conclusion

FY 2015 was the first year of this project and a research team, including Ford, NU, Dow Chemical, NIST and software developer LSTC, Autodesk, HBM, and ESTECO, has been assembled to design a subframe using CFRP composites and to develop ICME tools to enable design and optimization of the subframe.

Great progress has been made in the first year, with forty 1.2-mm thick and twenty-five 2.3-mm thick UD plaques being molded and distributed for characterization. A non-orthogonal material model has been developed for preform analysis. A local coordinate system that reflects fiber layout was used in the model with the impact of changing fiber orientation until it is better described. The model is confirmed by Bias extension tests to be able to track fiber direction change in the preforming process. MDA is used to study thermo-mechanical properties polymer resins. The predicted glassy transition temperature and material stress-strain relation are very close to the test data. MDA is also used to study interphase structure and properties, leading to interesting results that could inspire material failure models. A multiscale model for CFRP using RVE has been delivered. The new model implemented an improved resin model and is able to reproduce complex material stress-strain behavior. Generation and computation of RVE is automated using MATLAB script. Results from RVE simulation are used to produce material parameters to LS-DYNA inputs. A theory and process for reconstructing details about chopped fiber CFRP by using predicted fiber orientation tensor are developed. The reconstructed chopper fiber CFRP RVE model will be built soon.

LS-DYNA has implemented the curing model developed during the project as MAT277 for compression curing analysis. The model is being combined with MAT278 for compression molding simulation using LS DYNA.

The project is on schedule and has met every milestone set up at start of the project. Building on the above-mentioned success, most of the ICME work is expected to be completed in FY 2016. Design of a subframe with promised weight savings will also be initiated to guide direction of the modeling work.

References

1. X. Q. Peng and J. Cao, 2005, "A continuum mechanics-based non-orthogonal constitutive model for woven composite fabrics," *Composites Part A: Applied Science and Manufacturing,* 36(6); pp. 859-874.

Bibliography

X. Bai; M. A. Bessa; A. R. Melro; P. P. Camanho; L. Guo; and W. K. Liu, 2015, "High-fidelity micro-scale modeling of the thermo-visco-plastic behavior of carbon fiber polymer matrix composites," *Composite Structures*, 134; pp. 132 – 141.

N. Vu-Bac; M. A. Bessa; T. Rabczuk; and W. K. Liu, 2015, "A multi-scale model for the quasi-static thermo-plastic behavior of highly cross-linked glassy polymers," *Macromolecules* (accepted manuscript online).

IV.7. Development and Integration of Predictive Models for Manufacturing and Structural Performance of Carbon-Fiber Composites in Automotive Applications – General Motors, LLC

Project Details

Venkateshwar Aitharaju, Principal Investigator
Chemical Sciences and Material Systems Lab
General Motors (GM) R&D Center
MC 480-106-710
30500 Mound Road
Warren, MI 48090
Phone: 248-343-9500
E-mail: Venkat.aitharaju@gm.com

Walter Parker, Project Manager
National Energy Technology Laboratory
P.O. Box 880
3610 Collins Ferry Road
Morgantown WV 26507-0880
Phone: 412-386-7357
e-mail: walter.parker@netl.doe.gov

Carol Schutte, Technology Area Development Manager
U.S. Department of Energy
1000 Independence Avenue, SW
Washington, DC 20585
Phone: 202-586-1022
E-mail: carol.schutte@ee.doe.gov

Contractor: GM
Contract No.: DE-EE0006826

Executive Summary

The goal of this project is to develop an integrated suite of state-of-the-art computational modeling tools that are critically needed to enable structural carbon-fiber applications in automobiles. These tools help predict the manufacturing and structural performance of carbon-fiber composites, including stochastic effects. The project team is comprosed of researchers from General Motors (GM), ESI Group (i.e., a software company owner of the composite manufacturing tools PAM-RTM for resin transfer molding and PAM-FORM for forming of composites), Altair (i.e., a software company owner of the multiscale structural performance predictive tool for composites), Continental Structural Plastics (CSP) (i.e., molder/material supplier for composite materials and GM-Corvette composite parts supplier), and the University of Southern California (USC) (i.e., a leader in uncertainty quantification of the U.S. Department of Energy [DOE]-funded Scientific Discovery through Advanced Computing [SciDAC] Institute for Uncertainty Quantification). During the first phase of the project, both the manufacturing and structural performance tools, including a stochastic driver, will be calibrated and validated against coupon and component level tests. The difference between the predictions and experimental results is to be limited to less than 15%. During the second phase of the project, the manufacturing and performance tools will be integrated by mapping the manufacturing outcome (e.g., fiber angles, residual stresses, degree of cure, and defects, including voids, dry patches, and wrinkles) into structural models. Further, these integrated manufacturing and structural performance tools will be used to design a composite carbon fiber automotive assembly for a high-volume, medium-duty automobile that is currently made of steel. Various carbon fiber formats that are friendly to high-volume automotive manufacturing (e.g., non-crimp,

woven, and chopped systems) and manufacturing processes (e.g., resin transfer molding [RTM] and compression molding) will be studied. Cost models will be developed in parallel for these high volume manufacturing processes. The total number of parts in the carbon fiber assembly will be reduced through part consolidation and the weight will be reduced by strategic thickness optimization at critical and noncritical locations for each of the components. Each of the carbon-fiber composite components in the assembly will be optimized for weight, cost, and performance. The optimized carbon fiber automotive assembly will be certified and the developed numerical models will be validated by comparing the numerical and experimental results for performance of the assembly. Finally, for the optimized carbon fiber assembly design, the weight, cost, and performance will be compared with the existing steel design. The availability of the integrated computational tools for predicting stochastic manufacturing and structural performance of structural composites to an original equipment manufacturer (OEM) like GM can potentially eliminate significant bottlenecks that currently exist with large-scale implementation of carbon-fiber composites in an automobile.

Accomplishments

- Detailed side pole impact analysis of GM's 2016 Malibu was conducted to extract performance requirements for the chosen automotive assembly (Fiscal Year [FY] 2015).
- A local analysis method was developed for enabling the design, analysis, and optimization for the side impact that can be conducted on an assembly level rather than the entire vehicle level (FY 2015).
- The developed local analysis will allow design of an experimental setup comprised of a few critical assembly components, thereby eliminating full vehicle level testing for validation (FY 2015).
- Manufacturing processes suitable for high-volume automotive manufacturing were selected (i.e., resin transfer molding and compression molding) (FY 2015).
- Material systems suitable for high-volume automotive manufacturing were selected and plaques were molded for material testing (FY 2015).
- Experimental data for RTM of flat plaques using an instrumented tool and GM research and development (R&D) RTM machine at constant injection pressure was generated for defect-free panels (FY 2015).
- For the case of resin transfer molding, excellent correlations between the simulation and experimental results for fill time, pressure versus time, and degree of cure versus time were obtained for defect free panels.
- The multiscale structural performance tool predicts excellent correlation results for non–crimped fabric carbon-fiber composites for 0-degree tension, 0-degree flex, and 90-degree flex experiments.

Future Directions

- Generate experimental data for the resin transfer and compression molding processes for flat plaques and small components to validate the manufacturing prediction tool.
- Generate complete material testing data for coupons and components on three material systems for validation of the structural performance prediction tool.
- Validate manufacturing simulations to correlate manufacturing outcomes such as fiber angle changes, fill time, time for curing, residual stresses, and distortion.
- Validate structural performance simulations to correlate experimental results on coupons and components for three material systems chosen during the project.

Technology Assessment

- Target: Develop an integrated stochastic manufacturing and structural performance computation tool to design structural automotive composites and predict performance to within 15% of experimental results.

- Gap: Unknown manufacturing effects on structural performance of automotive composites.
- Gap: Commercial software packages capability to predict combined manufacturing and structural performance, including stochastic effects.
- Gap: Manufacturing process optimized to yield lower costs and higher quality for automotive composites.
- Gap: Certification procedure for an automotive composite assembly based on computer modeling alone.

Introduction

GM was the first North American automotive OEM to develop and commercialize carbon-fiber composites for Class-A body panel (i.e., closure) applications. Going forward, our objective is to look beyond closure components and implement carbon-fiber composites in body structural panels that undergo complex loading conditions represented in crash and durability. To enable these broader automotive structural applications of carbon-fiber composites, three key issues must be addressed. First, significant variability in material properties incurred during the manufacturing process need to be understood and predicted. Second, prediction of the structural performance of composites undergoing complex loading (i.e., crash) and environmental conditions is required. Third, the effect of manufacturing on performance of the final components needs to be understood and predicted. Without a good handle on the above issues, automotive designs can be overly conservative thereby increasing cost significantly and limiting the weight reduction potential of carbon-fiber composites. The present project addresses all of the above needs by developing a suite of integrated computational tools to predict the performance of manufacturing and structural performance of carbon-fiber composites, including stochastic effects.

Approach

Four key components of probabilistic integrated computational materials engineering (ICME) will be at the core of our approach, namely model integration, optimization, validation, and design certification. The computational engine will be constructed by integration of the state-of-the-art tools and capabilities from specific domains lead the project and integrate these modules: composites manufacturing (from GM and CSP), process simulation software for composites (from ESI), integrated multiscale-multiphysics structural software (using the multiscale design system [MDS] of Altair), probabilistic methods and probabilistic software (from USC), and, finally, the largest U.S. automaker with considerable expertise and record of accomplishments in the design and manufacturing of composite cars such as the Chevrolet Corvette (from GM). By model validation, we refer to making a prediction about the variables of interest and comparing specific variables under the same conditions. By certification of a component, we mean assurance that, once designed, manufactured, and loaded (i.e., crash test), the component will perform satisfactorily and up to preset specifications. Enabling model validation and component certification requires a retooling of the deterministic scientific process, specifically by requiring evidential attributes to be attached to model-based predictions. During this project, we will identify the limitations of existing software components comprising the computational engine and offer alternative technologies and solutions that facilitate integration for design optimization. Once the computational engine has been developed and validated, the chosen carbon-fiber assembly will be designed, optimized, tested, and certified and the resulting composite component will be compared to the current steel design.

The present carbon-fiber ICME project is organized into 10 tasks executed over a 48-month period. An outline of the tasks carried out during the current fiscal year is as follows:

Task 1.0: Project Planning, Coordination, and Reporting – ongoing

Task 2.0: Select Carbon-Fiber Assembly Preliminary Design – in progress

Task 3.0: Identify Preliminary Carbon-Fiber Material Systems and Manufacturing Processes – in progress

Task 4.0: Develop and Validate the Manufacturing and Crash Performance Engine – in progress

Task 5.0: Integrate the Manufacturing and Structural Models – not started

Task 6.0: Design and Optimize Automotive Assembly for Manufacturing and Performance – not started

Task 7.0: Design and Fabricate the Assembly and Test Fixture – not started

Task 8.0: Manufacture the Automotive Assembly – not started

Task 9.0: Certify the Automotive Assembly – not started

Task 10.0: Assessment of the Assembly – Correlations of Predictions and Experimental Results – not started.

Results and Discussion

Task 1.0. Project Planning Coordination and Reporting

Project team members consists of leading industrial and academic researchers, computational modeling professionals, experimental specialists, and management teams from GM, CSP, ESI, Altair, and USC. The project tasks were divided into three major subtasks: (1) manufacturing modeling, (2) structural performance modeling, and (3) stochastic modeling. Bi-weekly project meetings are held on these sub tasks to track progress of the project. GM coordinates the technical and management tasks for the entire project. Table IV-34 provides project timing.

Task 2.0 Select the Automotive Assembly Preliminary Design

The objective of this task is to determine the baseline performance requirements for design of a future carbon-fiber rocker floor by simulating side pole impact on the baseline vehicle. A medium-duty, high-volume vehicle (i.e., 2016 GM Malibu) was chosen as the baseline.

For this task, the entire finite element model of the 2016 Chevrolet Malibu vehicle, Epsilon 2, Sedan, Chevrolet (E2SC) was created in the framework of LS-DYNA for the side pole impact load [1]. Figure IV-88 shows the finite element model of the entire vehicle. For this model the mass of the vehicle is around 1,670 kg. The finite element model has 10,503 components, 6 million elements, and 5 million nodes. Each of the components of the vehicle is modeled with the corresponding material model available in the GM material database. Steel components in the vehicle are joined with welded joints and are modeled to include failure during the simulation.

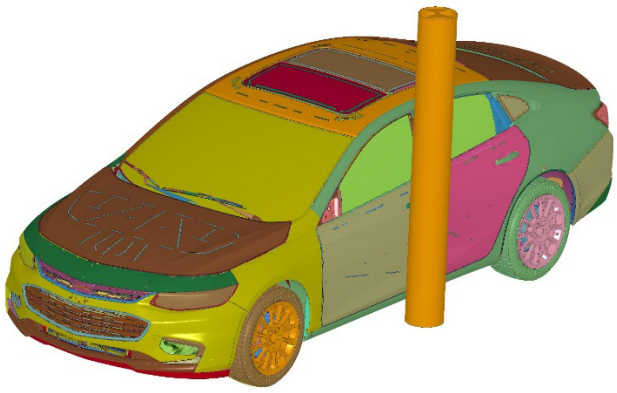

Figure IV-88: Finite element model of the 2016 Chevrolet Malibu vehicle for side pole impact.

Table IV-34: Project timing chart.

Table 1: Project Timing Chart

WBS ID #	Phase, Task, Subtask, and Milestone Descriptive Names	months	Q1 Mar-15	Apr-15	May-15	Q2 Jun-15	Jul-15	Aug-15	Q3 Sep-15	Oct-15	Nov-15	Q4 Dec-15	Jan-16	Feb-16	Q5 Mar-16	Apr-16	May-16	Q6 Jun-16	Jul-16	Aug-16	Q7 Sep-16	Oct-16	Nov-16	Q8 Dec-16	Jan-17	Feb-17	Q9 Mar-17	Apr-17	May-17	Q10 Jun-17	Jul-17	Aug-17	Q11 Sep-17	Oct-17	Nov-17	Q12 Dec-17	Jan-18	Feb-18	Q13 Mar-18	Apr-18	May-18	Q14 Jun-18	Jul-18	Aug-18	Q15 Sep-18	Oct-18	Nov-18	Q16 Dec-18	Jan-19	Feb-19
- Task 1.0	Project Planning, Coordination, and Reporting	48	PROJECT MANAGEMENT - GM / CSP - ESI - MDS - USC																																															
* Milestone 1.1 *	Go/No-Go #1 Decision Point	1													X																																			
* Milestone 1.2 *	Go/No-Go #2 Decision Point	1																				X																											
* Milestone 1.3 *	Phase 1 Topical Report Completed	1																				X																											
* Milestone 1.4 *	Go/No-Go #3 Decision Point	1																													X																	
* Milestone 1.5 *	FEP Models Delivered to DOE	1																																														X
* Milestone 1.6 *	Phase 2 Topical Report Completed	1																																														X
Phase 1	**Model Development and Model-Level Validations**	21	PHASE 1 - MODEL DEV+VAL																																														
- Task 2.0	Select the Automotive Assembly Preliminary Design	9	GM																																													
* Milestone 2.1 *	Performance Requirements (loads, energy absorption) Determined	1									X																																					
- Task 3.0	Identify Preliminary CF Material Systems & Manufacturing Process	9	GM / CSP - ESI																																													
* Milestone 3.1 *	Appropriate Materials Selected (2-3 material systems)	1									X																																					
* Milestone 3.2 *	Appropriate Manufacturing Processes Selected	1									X																																					
- Task 4.0	Develop and Validate the Manufacturing and Crash Simulation Engines	21	GM / ESI - MDS - USC																																													
- - Subtask 4.1	Develop Stochastic Process Simulation Engine	21	USC / MDS																																													
- - Subtask 4.2	Develop & Validate Manufacturing Process & Link Simulation Models	21	ESI / MDS - USC - CSP - GM																																													
* Milestone 4.2.1 *	Manufacturing of Small Plaques Completed and Data Generated	1													X																																		
* Milestone 4.2.2 *	Development of Manufacturing Process & Linking of Models Completed	1																				X																											
- - Subtask 4.3	Develop & Validate Stochastic Performance Model	18				MDS / USC																																										
* Milestone 4.3.1 *	Development of Mechanical Tests for Model Development Completed	1													X																																		
* Milestone 4.3.2 *	Stochastic Performance Model Developed & Compared with Experiments	1																				X																											
Phase 2	**Integration and Design**	30																			PHASE 2 - INTEGRATION+DESIGN																															
- Task 5.0	Integrate the Manufacturing and Structural Models	6																			ESI / MDS - USC																															
* Milestone 5.1 *	Mapping of Manufactured Properties to Structural Models Achieved	1																					X																											
- Task 6.0	Design & Optimize Automotive Assembly for Manufacturing & Performance	12																			GM / MDS - ESI - USC - CSP																															
* Milestone 6.1 *	Design and Optimization for Manufacturing and Performance Completed	1																													X																		
- Task 7.0	Design and Fabricate the Assembly and Test Fixture	6																															CSP / GM																	
* Milestone 7.1 *	Assembly and Test Fixture Designs Completed	1																																X																
- Task 8.0	Manufacture Automotive Assembly	12																											CSP / GM																					
- - Subtask 8.1	Design and Build Tools	6																											CSP																				
- - Subtask 8.2	Fabricate the Components	6																															CSP																
- - Subtask 8.3	Assemble the Components	6																																			CSP												
* Milestone 8.3.1 *	Build of Ten Assemblies for Testing Completed	1																																							X								
- Task 9.0	Certify Automotive Assembly	6																															GM / MDS - CSP - ESI - USC																
- - Subtask 9.1	Certify Manufacturing Process	6																															GM / MDS - CSP - ESI - USC																
* Milestone 9.1.1 *	Certification of Manufacturing Process Completed	1																																													X		
- - Subtask 9.2	Certify Automotive Assembly and Components	6																															GM / MDS - CSP - ESI - USC																
* Milestone 9.2.1 *	Certification & Validation of Components and Assembly Completed	1																																													X		
- Task 10.0	Assessment	9																																					GM / MDS - ESI - USC										
* Milestone 10.1 *	Final Cost & Performance Comparison of Composite & Steel Completed	1																																															X

During analysis, the vehicle was moved toward the stationary pole with a speed of 32 km/hour and energy absorption in the selected assembly was measured.

Local Analysis of the Assembly

A local analysis method was developed for the reference vehicle to make design/analysis iterations more efficient. The local analysis method was targeted to provide results for the chosen assembly that are the same as those from the global vehicle level analysis.

The global/local analysis procedure of Noor was used [2]. From extensive analysis, the local analysis method was able to provide results for energy absorption values very close to the global vehicle level results.

Summary

1) Performance requirements for components of the chosen automotive assembly were established by analyzing the side impact of the 2016 Malibu vehicle.
2) A local analysis was developed for the chosen assembly to yield results the same as a full vehicle level analysis. This will help the following:
   a) Design/analysis iterations on the future carbon-fiber assembly will be very efficient because the analysis model involved a few components only.
   b) An experimental setup for validating the automotive assembly is available without the need for full vehicle level testing.

Task 3.0: Identify Preliminary Carbon-Fiber Material Systems and Manufacturing Processes

The objective of this task is to select appropriate materials and manufacturing processes that are friendly for high-volume automotive manufacturing. GM and CSP, based on their experience and following the state-of-the-art in composite manufacturing technologies, broadly selected RTM and compression molding as the preferred choices for high-volume manufacturing methods for the chosen carbon-fiber assembly.

Corresponding to the manufacturing processes chosen above, GM appropriately selected several candidates for carbon-fiber material systems. Table IV-35 shows the reduced matrix of material systems in the study. As shown in Table IV-35, this matrix provides a variety of resin and reinforcement choices.

A list of actual materials being studied during this project is provided Table IV-36. Table IV-37 shows how these materials fit into the category chart.

Table IV-35: Carbon-fiber material systems – reduced matrix.

Carbon-Fiber Material Systems		Continuous Reinforcement			Discontinuous Reinforcement
		Unidirectional	Non–Crimped Fabric - QI	Woven	Long Fiber
Thermoset	RTM	Epoxy $[0]_n$, $[0/90]_{ns}$	Epoxy $[0/-45/45/90]_{ns}$	Epoxy 2x2 twill	Epoxy Spray-chop Random
	Composite Molding	Epoxy [0]n, $[0/90]_{ns}$	Epoxy $[0/-45/45/90]_{ns}$	Epoxy 2x2 twill	Vinyl-Ester Sheet Molding Compound (SMC) Random
Thermoplastic	Composite Molding	Polyamide [0]n, $[0/90]_{ns}$		Polyamide 2x2 twill	Polyamide Direct-Injection Long Fiber Technology Random

Table IV-36: Carbon composite materials used in this study.

	Carbon Fiber				Resin			Processing		Additonal Comments
Material Designation	Chop	Cont	Manufacturer	Lay-up	Class	Manufacturer	Designation	RTM	Comp	
Material #0		X	Toray T700-12K	$[0/45/-45/90]_S$	Epoxy	GMR		X		
Material #1	X		Toray T700	Random	Vinyl-Ester				X	39% by volume (55% by weight) carbon fiber
Material #2A	X		SGL - Recatex	$[0]_n$	Epoxy	Hexion	Epikote Resin Trac 06170/Epikure TRAC 06170	X		SGL / Recatex Oriented fiber n°: M48-P79-W3018/778
Material #2B	X		SGL - Recatex	$[0/90]_{4S}$	Epoxy	Hexion	Epikote Resin Trac 06170/Epikure TRAC 06170	X		SGL / Recatex Oriented fiber n°: M48-P79-W3018/779
Material #3		X	Chomarat - Zoltek Panex 35	$[45/-45]_{4S}$	Epoxy	Hexion	Epikote Resin Trac 06170/Epikure TRAC 06170	X		Chomarat C-Ply SP BX 240 C3.4 50K HS
Material #4A		X	Chomarat - Zoltek Panex 35	$[0/90/45/-45]_{2S}$	Epoxy	Hexion	Epikote Resin Trac 06170/Epikure TRAC 06170	X		C-PLY SP BT 240 : C-PLY SP BX 240 C3.4 50K HS
Material #4B		X	Chomarat - Zoltek Panex 35	$[3K\ twill/45/-45/0/90/45/-45]_S$	Epoxy	Hexion	Epikote Resin Trac 06170/Epikure TRAC 06170	X		C-WEAVE 245T 3K HS : C-PLY SP BT 240 : C-PLY SP BX 240 C3.4 50K HS
Material #5	X		Mitsubishi - Pyrofil TR50	DLFT - Random/Flowed	PA6	Lanxess	Durethan PA6		X	
Material #6		X	?	2 x 2 Twill, 3K	PA66	Lanxess	?		X	Tepex Dynalite 201-C200(7)/50%
Material #7a		X	Tencate - *Zoltek Panex 35*	$[0]_{13}$	PA6	Tencate/BASF	Polyamide 6 *(B3G or 8202)*		X	Tencate CETEX 910 - Carbon Fiber, 13L, 49% by Volume CF
Material #7b		X	Tencate - *Zoltek Panex 35*	$[0/90]_7$	PA6	Tencate/BASF	Polyamide 6 *(B3G or 8202)*		X	Tencate CETEX 910 - Carbon Fiber, 13L, 49% by Volume CF
Material #7c		X	Tencate - *Zoltek Panex 35*	2 x 2 Twill, 3K	PA6	Tencate/BASF	Polyamide 6 *(B3G or 8202)*		X	Tencate Woven 3K Carbon-PA6 - 7L, *49% by Volume CF*
Material # 8A		X	*Zoltek Panex 35*	$[0]_{4S}$	Epoxy	Cytec	XMTM54FRB (EF4511)		X	Prepreg
Material # 8B		X	*Zoltek Panex 35*	$[0/90]_{2S}$	Epoxy	Cytec	XMTM54FRB (EF4511)		X	Prepreg
Material # 8C		X	*Zoltek Panex 35*	Woven 2 x 2 twill $[0/90]_{2S}$	Epoxy	Cytec	XMTM54FRB (EF4511)		X	Prepreg
Material # 8D		X	*Zoltek Panex 35*	Woven 2 x 2 twill QI $[0/45/-45/90]_S$	Epoxy	Cytec	XMTM54FRB (EF4511)		X	Prepreg

Note: Information provided in *italicized blue* is currently being confirmed.

Table IV-37: Carbon-fiber material systems – placement of materials within the matrix.

Carbon-Fiber Material Systems		Continuous Reinforcement			Discontinuous Reinforcement
		Unidirectional	Non–Crimped Fabric - QI	Woven	Long Fiber
Thermoset	RTM	Mat 2A Mat 2B Mat 3	Mat 0, Mat 4A	Mat 4B	
	Composite Molding	Mat 8A Mat 8B	Mat 8D	Mat8C	Mat 1
Thermoplastic	Composite Molding	Mat 7A, Mat 7B		Mat 6 Mat 7C	Mat 5

Testing for tensile, flexural, and compression properties is carried out on either an Instron 5582 or an Instron 5984 test frame using appropriate grips and fixtures. Specific energy absorption measurements are made using an Engenuity crush fixture operating in an Instron Dynatup 9250HV drop tower at GM. Table IV-38 shows the test and ASTM test method, or other appropriate method, used in the study.

Table IV-38: Table of mechanical property evaluations.

Property	Test Method
Tensile Modulus Tensile Strength Tensile Elongation	**ASTM D3039-08** – Standard Test Method for Tensile Properties of Polymer Matrix Composite Materials
Flexural Modulus Flexural Strength Flexural Elongation	**ASTM D790-03** – Standard Test Methods for Flexural Properties of Unreinforced and Reinforced Plastics and Electrical Insulating Materials
Specific Energy Absorption	**Engenuity Crush Protocol**
Compression Modulus Compression Strength Compression Elongation	**ASTM D3410 – 03 (Reapproved 2008)** – Standard Test Method for Compressive Properties of Polymer Matrix Composite Materials with Unsupported Gage Section by Shear Loading

Microscopic Analysis

Microscopic analysis of the size and orientation of the carbon-fiber tows in the various systems is required in order to create unit cell models of the different microstructures for use with the modeling efforts of the project. A representative image of a quasi-isotropic is shown in Figure IV-89.

From these images, we can determine the average width, thickness, and spacing of the carbon-fiber tows in each substrate material. These parameters will be provided to the performance modeling team in order to construct unit cell models of the various microstructures in this study.

Figure IV-89: Captured Image of a quasi-isotropic carbon-fiber composite (Material 4A) imaged perpendicular to the 0-degree fibers. The length, thickness, and spacing of the 0-degree two is clearly visible. All 16 layers of the composite are distinguishable.

Summary

All mechanical property specimens have been excised from their parent composite plaques and are in process for collecting appropriate information.

Next Steps

All material testing and microstructure analysis raw data collection is anticipated to be completed by the end of the next quarter.

Task 4.0: Develop and Validate Manufacturing and Crash Models, including Stochastic Methods

The objective of this task is to develop and validate stochastic manufacturing and structural performance models.

Task 4.1 involves development of a stochastic driver and Task 4.2 involves development of manufacturing a performance model.

Task 4.1: Development of the Stochastic Driver

During this performance period, computer scripts in Python and MATLAB® have been completed to do the following tasks.

Basis Adaptation and Application to the RTM Simulation

Basis adaptation is developed to reduce the required number of function evaluations from several thousands to a few dozen. Adaptation is done with respect to the quantity of interest defined by the fill time in RTM

simulation. Adaptations to other quantities of interest can be readily developed and do not require any special attention. The basis adaptation was demonstrated on PAM-RTM software with the uncertainty parameters shown in Table IV-39.

Table IV-39: Input parameters for uncertainty analysis.

	Random Variable	Deterministic Values	COV*
1	K1 of plaque (mm^2)	4.235E-10	0.75
2	K2 of plaque (mm^2)	4.235E-10	0.75
3	K of racetrack (mm^2)	3.0E-8	0.5
4	K of channel (mm^2)	3.32E-6	0.5
5	Density of the resin (kg/m^3)	1,100	0.005
6	Specific heat of the resin	1,205	0.01
7	Thermal conductivity of the resin	0.11	0.01
8	Density of the fabric (kg/m^3)	1,700	0.005
9	Specific heat of the fabrix	700	0.01
10	Thermal conductivity of the fabric along direction one	2	0.01
11	Thermal conductivity of the fabric along direction two	0.5	0.01
12	Specific heat of the laminate	700	0.01
13	Thermal conductivity of the laminate	0.1	0.01
14	Thickness of each layer (mm)	0.225	0.01
15	Porosity of each layer	0.52	0.25
16	Density of the channel (kg/m^3)	1,000	0.01
17	Specific heat of the channel	700	0.01
18	Thermal conductivity of the channel	0.02	0.01

*Coefficient of variation

Figure IV-90 shows a comparison of the histogram of the fill time obtained using different methods. The results using Monte Carlo sampling are not even converged because they require a very large number of samples.

A cost comparison of different methods for computing the fill time is shown in Table IV-40, where polynomial chaos expansion is referred to by PCE.

Work is underway to extend this formalism to situations combining curing and distortion into the simulation sequence.

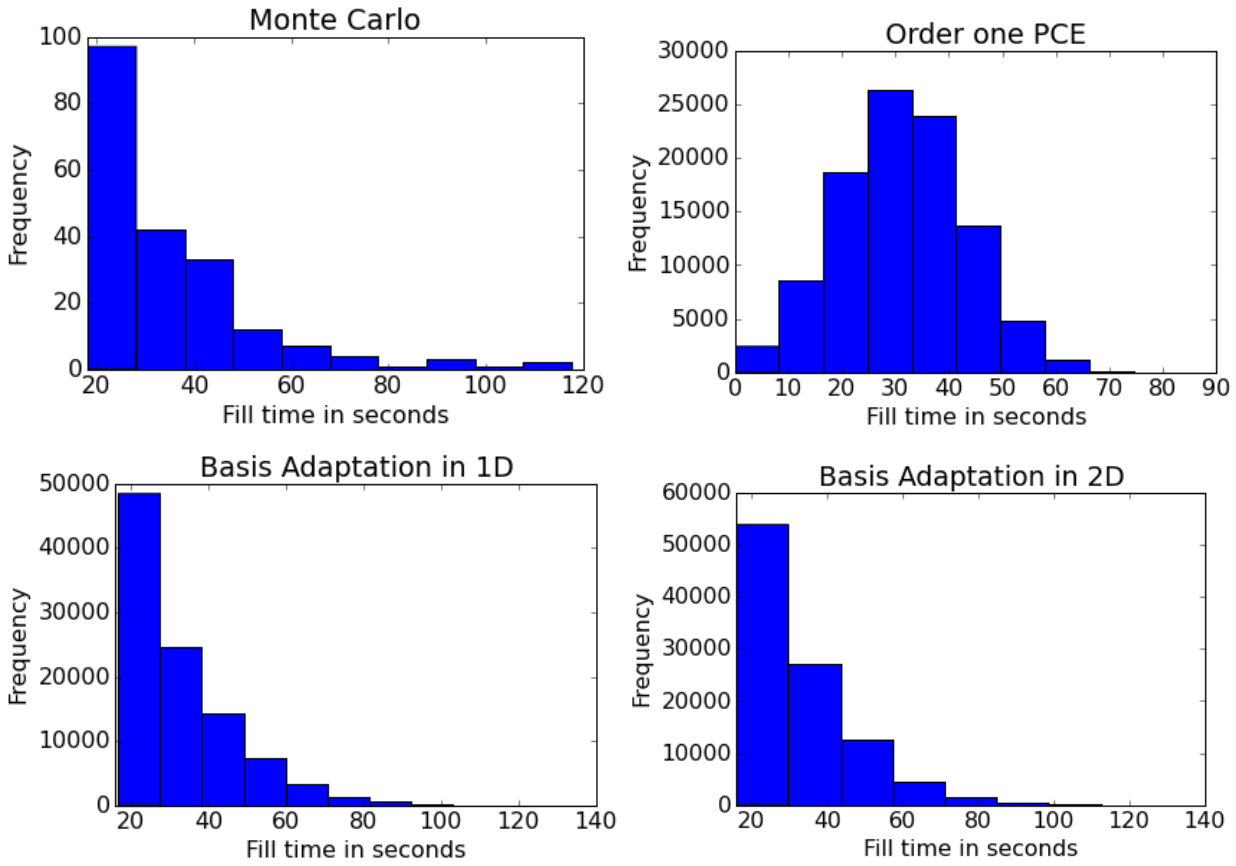

Figure IV-90: Histogram of fill time obtained with Monte Carlo samples (top left), first order polynomial chaos expansion (top right), with a one-dimensional adapted basis (bottom left), and an adapted basis (bottom right).

Table IV-40: Cost comparison for different methods.

	Method	Number of Samples	Comments
1	MCMC* and Orders of	Orders of Millions	Computationally expensive
2	PCE with Quadrature	n^d (2^{18})	Map between input and output, curse of dimensionality
3	PCE with Sparse Grid	$< n^d$(10597 for Level 3)	Map between input and output, curse of dimensionality
4	PCE with Adopted Basis	Cost of first order + one-dimensional (37+9)	Map between input and output, very efficient

* Markov Chain Monte Carlo

Random Matrix for Elasticity Problems

The objective of this exercise is to construct a probability model of linear elasticity matrices from experimentally observed or numerically generated realizations of macroscale behavior. These are 6×6 matrices. This probability model is constructed using the maximum entropy principle with constraints reflecting the mean of the elasticity matrix and scatter of realizations around the mean. These matrices will be used for improving the interface between the microscale analysis software, multiscale design system (MDS), and the structural-scale analysis software LS-DYNA.

Given N_{exp}experiments, the upper and lower bounds for the linear elasticity tensor from each of them can be obtained respectively as

$$[\mathbf{C}]_u^{(j)} = \mathbf{arg\,min} \,||\, [\mathbf{C}]\varepsilon^{(j)} - \sigma^{(j)}||_{R^6},\ j = 1, \dots, N_{exp} \quad (1)$$

$$[\mathbf{C}]_l^{(j)} = \mathbf{arg\,min} \,||\, \varepsilon^{(j)} - [\mathbf{C}]^{-1}\sigma^{(j)}||_{R^6},\ j = 1, \dots, N_{exp} \ . \quad (2)$$

Denoting decomposition of the mean matrix $[\bar{\mathbf{C}}]$ by

$$[\bar{\mathbf{C}}] = [\bar{\mathbf{N}}][\bar{\mathbf{N}}]^T \ . \quad (3)$$

Let the random matrix $[\mathbf{C}]$ be expressed as

$$[\mathbf{C}] = [\bar{\mathbf{N}}][\mathbf{H}][\mathbf{H}]^T[\bar{\mathbf{N}}]^T \ . \quad (4)$$

Then it can be shown that the rows of the lower triangular matrix $[\mathbf{H}]$ are statistically independent. The probability density function of each row is given as

$$p_{[H]}(\mathbf{h}^{(i)}) = c_i\left(\mathbf{h}_{ii}^{d-1-i+2\alpha}\right)\exp\left(-\mu_i\left(\sum_{l=1}^{i} h_{il}^2\right) - \sum_{i=1}^{i}\tau_i\left(\sum_{l=1}^{i} h_{il}^2\right)^2\right) \quad (5)$$

where, the coefficients τ_i, μ_i, α, and c_i are computed from the maximum entropy optimization problem.

Current work is underway to capture spatial correlation in the fluctuation of these matrices.

Random Matrix for Permeability

In a similar manner to the elasticity random matrix above, a random matrix is constructed to represent random permeability matrices. The difference from the previous case is that the present matrix is a 3 × 3 matrix.

Darcy's law can be stated as

$$< \mathbf{u} >= \frac{\mathbf{1}}{\mu}[\mathbf{K}]\ \nabla < \mathbf{P} > \quad (6)$$

where, matrix $[\mathbf{K}]$ is obtained as

$$[\mathbf{K}]^{(j)} = \arg\min \|\nabla < \mathbf{P} >^{(j)} - \mu[K]^{(j)-1} < \mathbf{u} >^{(j)} \|_{R^3}; j = 1, \dots, N_{exp} \quad (7)$$

where,N_{exp}refers to the number of experiments available.

Next Steps

Once realizations of the permeability matrix are available, a procedure similar to the one developed for the random elasticity is implemented to compute the density function and sample from it.

Task 4.2: Development and Validation of Manufacturing Process and Joining Simulation Models

The objective of this task is to develop and validate the stochastic manufacturing simulation models. The following manufacturing methods are considered for simulation:

1) Resin transfer molding (traditional RTM, compression (C)-RTM and high pressure (HP)-RTM)
2) Prepreg compression molding.

Instrumented RTM: Molding of Flat Plaques

A small, GM, custom-built RTM apparatus was used for molding experiments. The RTM apparatus is a two-stream machine that uses hydraulic cylinders to pump the resin and the curing agent. Precise control of flow rates is achieved via computer-controlled pumping of hydraulic oil with gear pumps. Linear variable

distance transducers (LVDTs) are used to measure displacement of the cylinder pistons, thereby monitoring the volume of resin pumped. Figure IV-91 shows a schematic of the apparatus. The GM RTM system is capable of delivering a preheated, mixed resin to a mold at up to 250 psi with flow rates up to 50 cc/s.

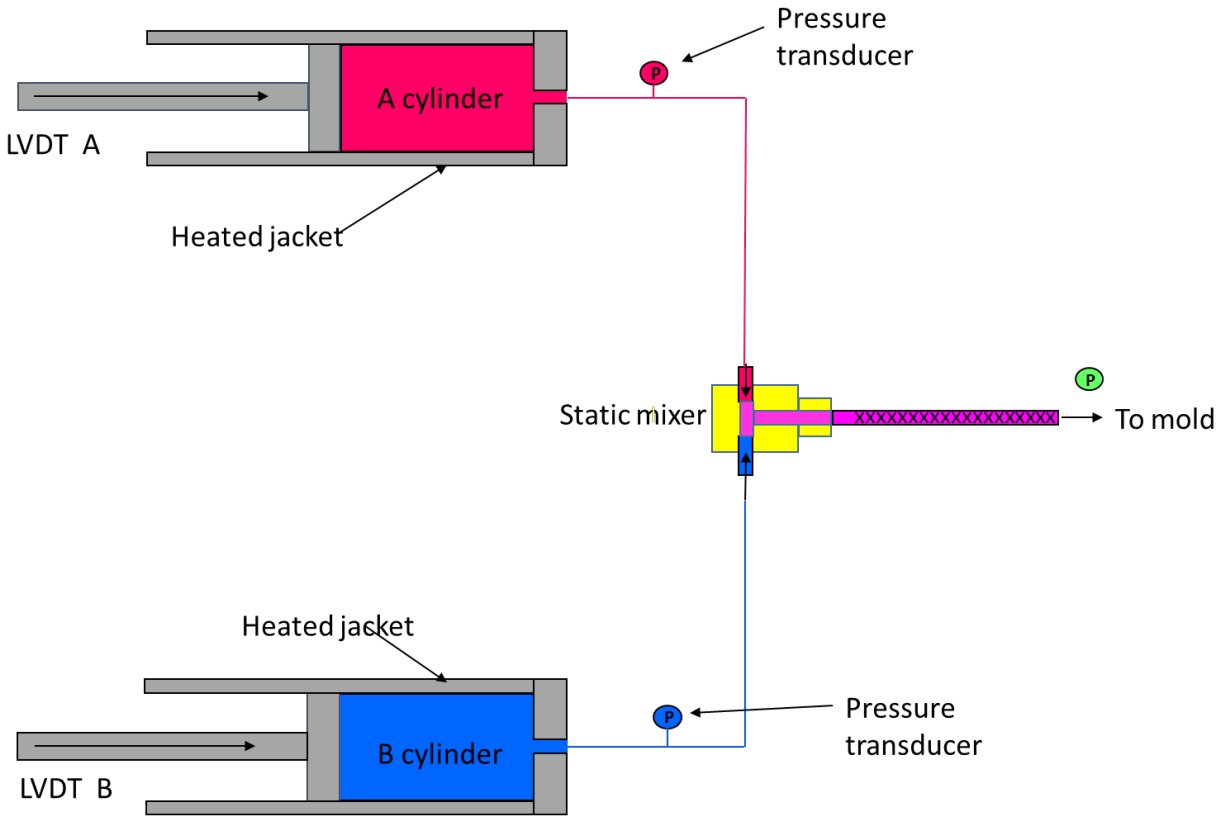

Figure IV-91: Schematic of GM research two-stream RTM.

An instrumented plaque mold was designed for use with the RTM apparatus. This mold cavity is 17.5-in. long, 17.5-in. wide, and 0.12-in. thick. Opposing, centered end gates are used for the inlet and vent ports of the mold. Three flush-mounted dielectric cure sensors and three flush-mounted pressure transducers are positioned in the top half of the mold. Their locations are along the centerline of the mold near the inlet, at the midpoint, and near the vent. Thermocouples are integrated into the dielectric cells and additional thermocouple ports are located near each of the four corners of the mold. Figure IV-92 shows the mold design.

With the flow rate control available from the GM RTM apparatus, fill times as short as 10 seconds and as long as 60 seconds can be attained. A data acquisition computer controls the RTM experiment and records the LVDT signals, pressures, and temperatures. The dielectric cure data are collected via a Lambient Dielectric Cure system running on a second computer.

With the objective of facilitating computer simulations of RTM molding, a well characterized epoxy resin system was selected. This system requires a catalyst to enable short cure times. With the limitation of the two-stream RTM apparatus, the catalyst must be soluble and stable in either the epoxy resin or the anhydride. For this resin, a quaternary ammonium salt was chosen as the catalyst because it could be safely dissolved into the epoxy resin stream at a 3% loading. The resin formulation is provided in Table IV-34.

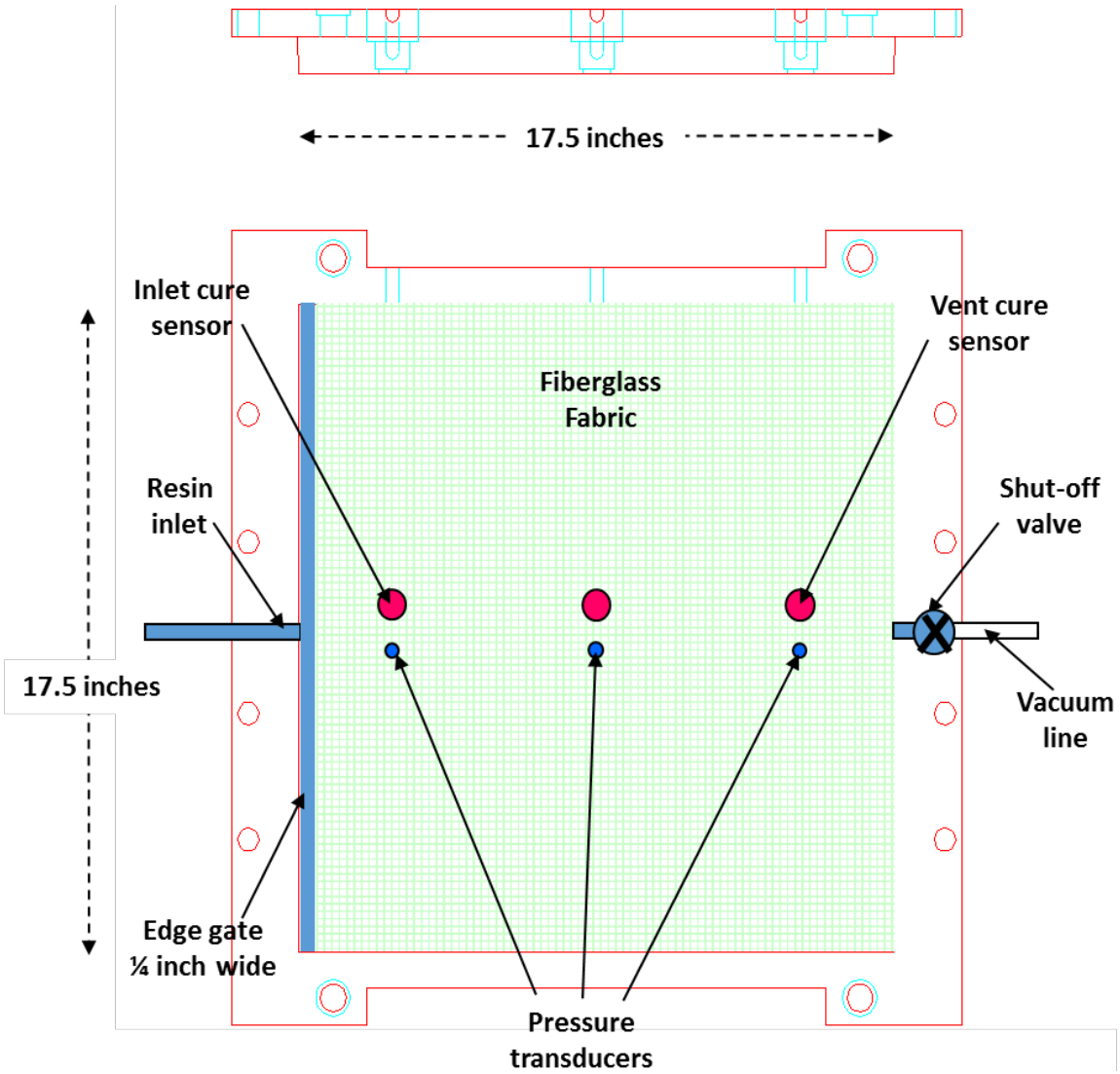

Figure IV-92: Instrumented plaque mold for RTM.

Table IV-41: RTM epoxy resin formulation.

Component	Source	Formulation Amount
Epoxy resin	Dow 383	100
Methyltetrahydrophthalic anhydride (MTHPA)	Lonza (now Broadview Chemical)	80
Catalyst (t-butyl ammonium bromide)	Aldrich	3

Resin viscosity as a function of temperature was previously measured for this system. These viscosity measurements were carried out by omitting the catalyst from the formulation in order to allow sufficient time to take data before the curing reaction began. The viscosity (in centipoise) versus temperature (in degrees Centigrade) data for the chosen RTM resin are presented in Figure IV-93.

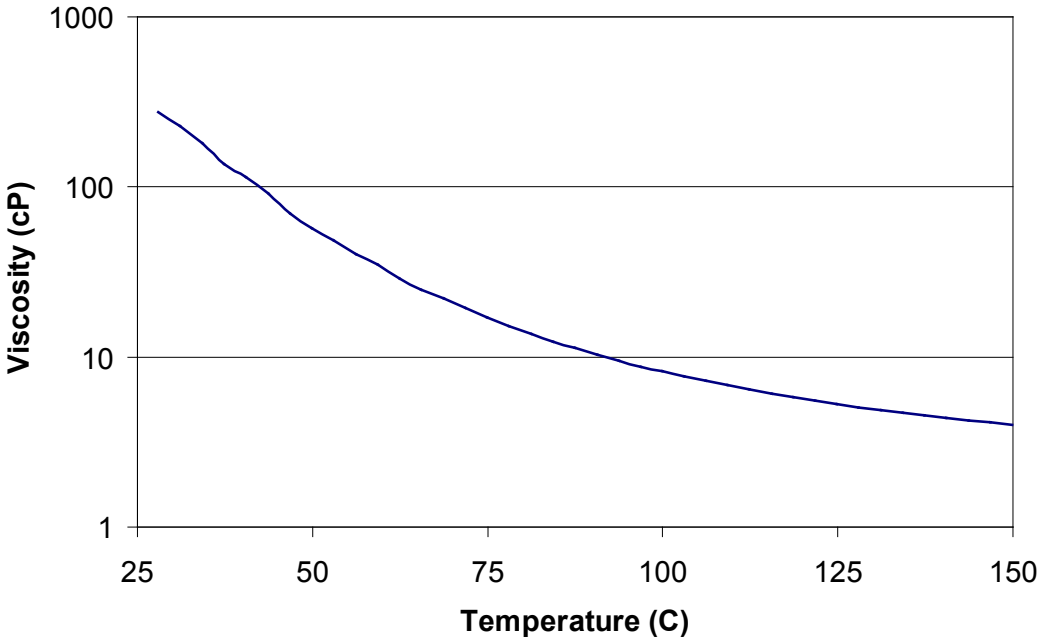

Figure IV-93: Viscosity versus temperature for the epoxy/MTHPA resin system.

Cure kinetics for the chosen RTM resin system were characterized via a series of constant heating rate differential scanning calorimetry (DSC) experiments [3]. By varying the heating rates from 2 to 20°C/min, temperature dependence of the complex chemical kinetics can be modeled to yield a numerical model. With the 3% catalyst loading, cure times of approximately 5 minutes can be attained when the mold temperature is 140°C.

An accurate chemical kinetics model is essential for modeling RTM. Development of this model requires experimental measurement of chemical reaction rates as a function of both temperature and degree of cure. In the case of epoxy resin systems, the exothermic nature of the curing reactions can be used to follow the state of cure. DSC can be used to measure heat flows from a small sample of mixed resin as the curing reaction proceeds.

Development of Kinetics Model for the Curing Analysis

In this work, a set of seven constant heating rate DSC experiments were performed using the epoxy resin system. Isothermal DSC experiments can also be used, but analysis of the data is made difficult by the inevitable curing that can take place during rapid heating to the isothermal temperature. Because of this difficulty, we have found better results using constant heating rate experiments with heating rates ranging from 2 to 20°C/min. The DSC curves from these constant heat rate experiments are presented in the following sections, along with the best fit model predictions.

The chemical rate kinetic model fitting was performed using the PolyKinetic software program developed and written at Ecole Polytechnique de Montreal. For this work, the Kamal-Sourour kinetic model [4] was chosen. This model is an empirical model that has been found to yield reasonably accurate models for a large number of epoxy-based resin systems. Although an empirical model with six parameters, it is based on autocatalytic mathematics that can reproduce an apparent induction time, followed by an accelerating cure rate. The PolyKinetic software uses a least-square Levenberg-Marquardt nonlinear regression algorithm for the calculation of the unknown parameters of the kinetic models. As evidenced by Figure IV-94, the optimized parameters give a reasonable accurate prediction of reaction rates over a wide range of temperature and degree of cure.

$$\frac{d\alpha}{dt} = (0.1179e^{-\frac{4117}{T}} + 3.32E6 * e^{-\frac{7836.3}{T}}\alpha^{0.457})(1-\alpha)^{1.199} \quad (8)$$

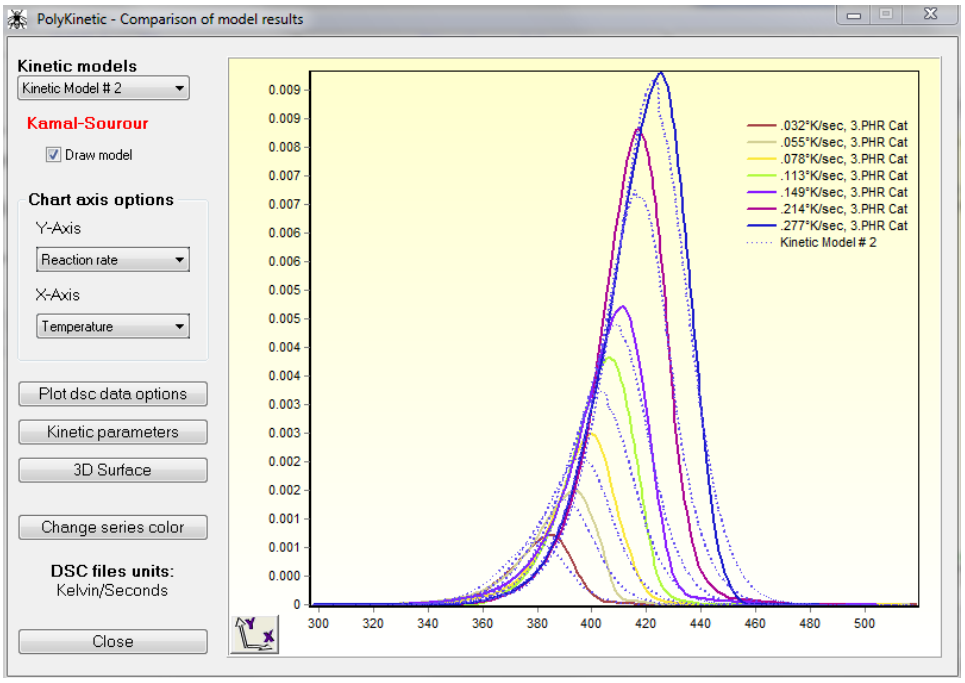

Figure IV-94: Development of Kamal-Sourour model and comparison of model and experimental results [4].

Manufacturing Simulation of Defect-Free Panels

Figure IV-95 shows the molding conditions of the flat plaque (dimensions 444.5 mm × 444.5 mm × 1.8 mm). Simulations were conducted with 2D and 3D finite element models. The 2D model has 115,660 triangular elements and 58.279 nodes; the 3D model has 1,503,580 tetrahedron elements and 291,379 nodes. The temperature-dependent viscosity of the resin was modeled by providing a curve (i.e., viscosity variation with temperature). The curing kinetics were modeled using Kamal-Sarour model.

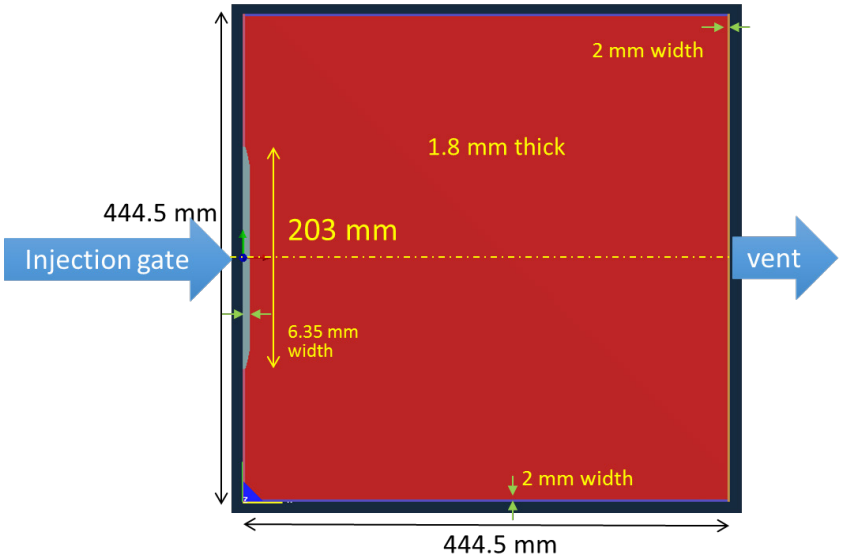

Figure IV-95: Plaque dimension for defect-free panel molding.

Defect Free Panels – Filling Simulation

For filling simulations, the material and thermal properties used for preform and resin were as given in Table IV-42. The permeability of the preform is calculated using an inverse method by matching the fill time of the experimental results (about 47 seconds). Figure IV-96 shows the filling time results for the plaque. The permeability results obtained from the inverse analysis for the 0-degree orientation are provided in Table IV-43.

Table IV-42: Thermal properties for materials in the numerical simulation.

Thermal Property	Non–Crimped Fabric Preform	Epoxy Resin	Air
Thermal Conductivity (W/mK)	2, 0.5, 0.5 (principal directions)	0.11	0.02
Specific Heat (J/kg.K)	710	1,205	1,013
Density (kg/m^3)	1,700	1,100	1.2

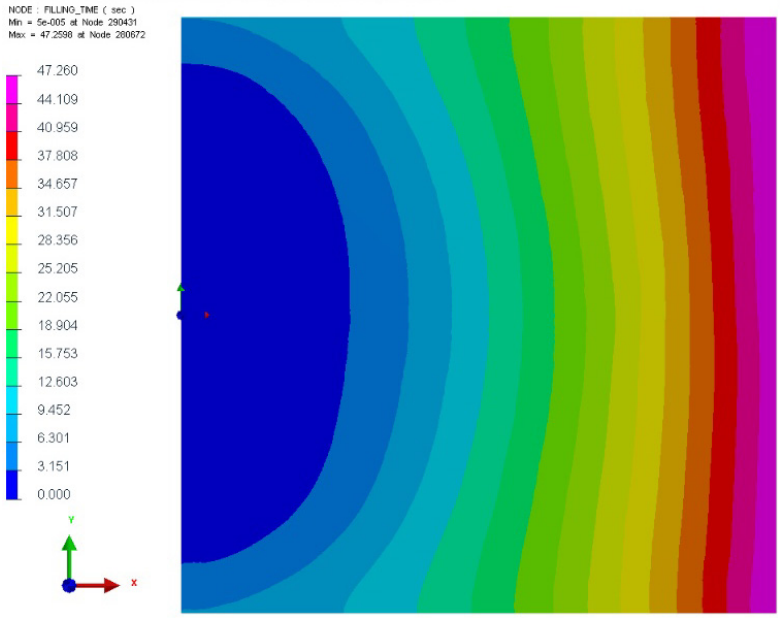

Figure IV-96: Filling time contour for the constant pressure RTM infusion process.

Table IV-43: Permeability of the preform in the principal directions from inverse analysis (0-degree fabric).

Principal Permeability	Non–Crimped Fabric Preform
K_{11} (mm^2)	3.5^{e-11}
K_{22}(mm^2)	6.7^{e-11}
K_{33}(mm^2)	3^{e-12}

Comparisons of pressure buildup in the tool between the simulation results and experimental pressure transducer results are shown in Figure IV-97 from the 3D models. The results with 2D models are very close to the 3D results; therefore, they are not shown. There is good agreement between the simulation and experimental results for the three locations in the mold (i.e., inlet, midpoint of the mold, and at the vent location).

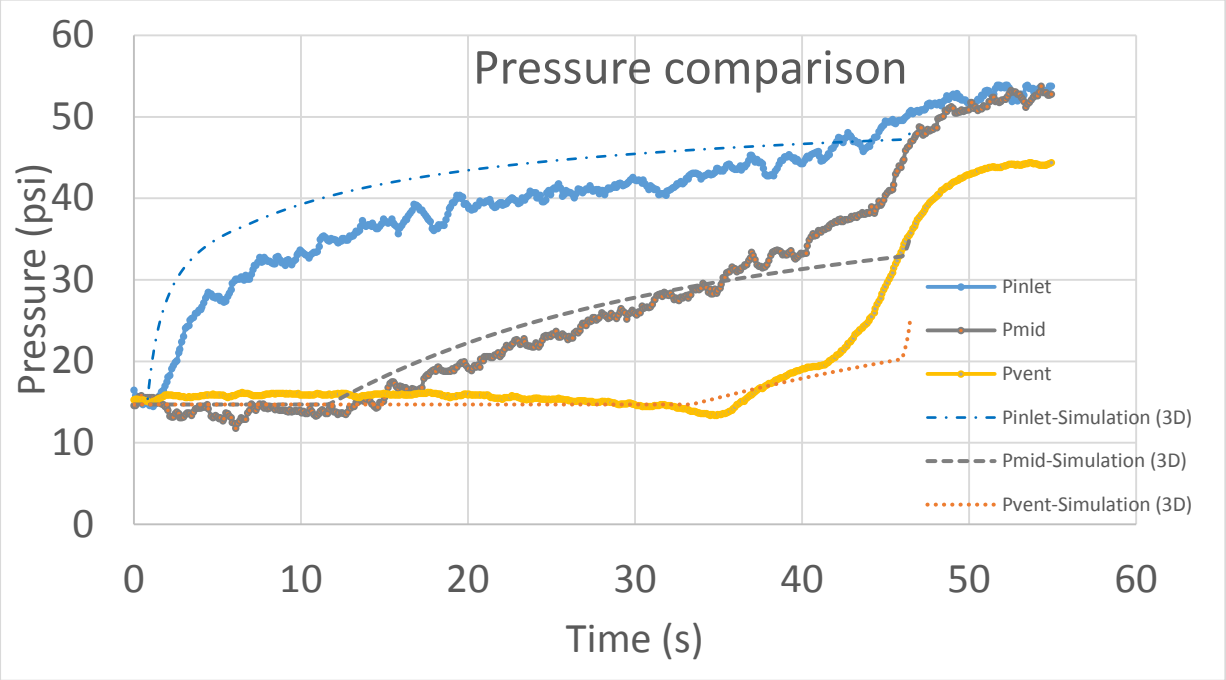

Figure IV-97: Pressure correlation between 2D RTM simulation and experimental results.

Defect-Free Panels – Curing Simulation

To predict resin curing, te Kamal-Sourour kinetic model was used. The enthalpy was assumed to be 350,000 J/Kg. Figure IV-98 shows the simulated curing cycle. Figure IV-99 shows the degree of cure after the filling stage.

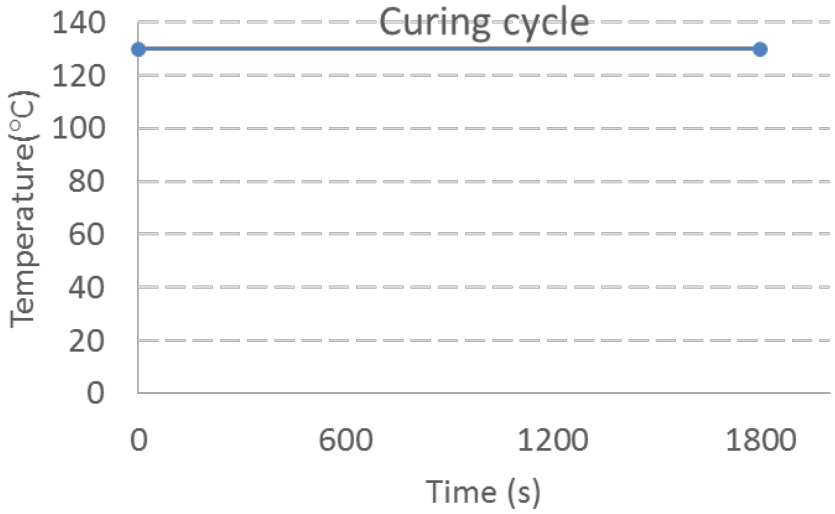

Figure IV-98: Curing cycle for the plate-in curing process.

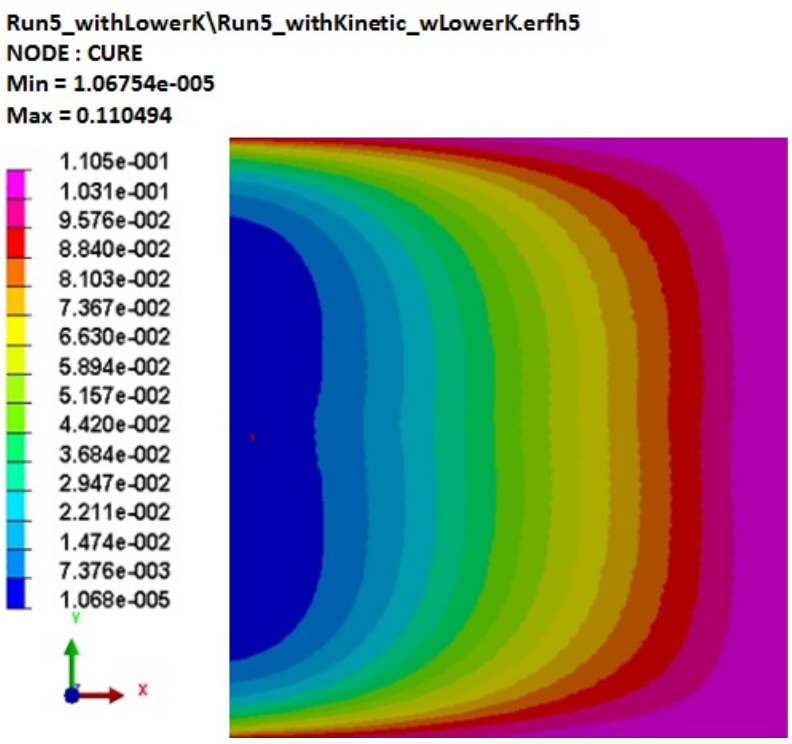

Figure IV-99: Percentage of curing during the filling stage.

From Figure IV-99, according to the model, the system has reached 10% cure during the filling stage. Figure IV-100 shows comparison of the percent of cure obtained from the simulation results and the dielectric cure sensor readings. The scale on the Y-axis is different, but it is worth noting the trend and time to reach the 100% cure matching between simulation and experimental results.

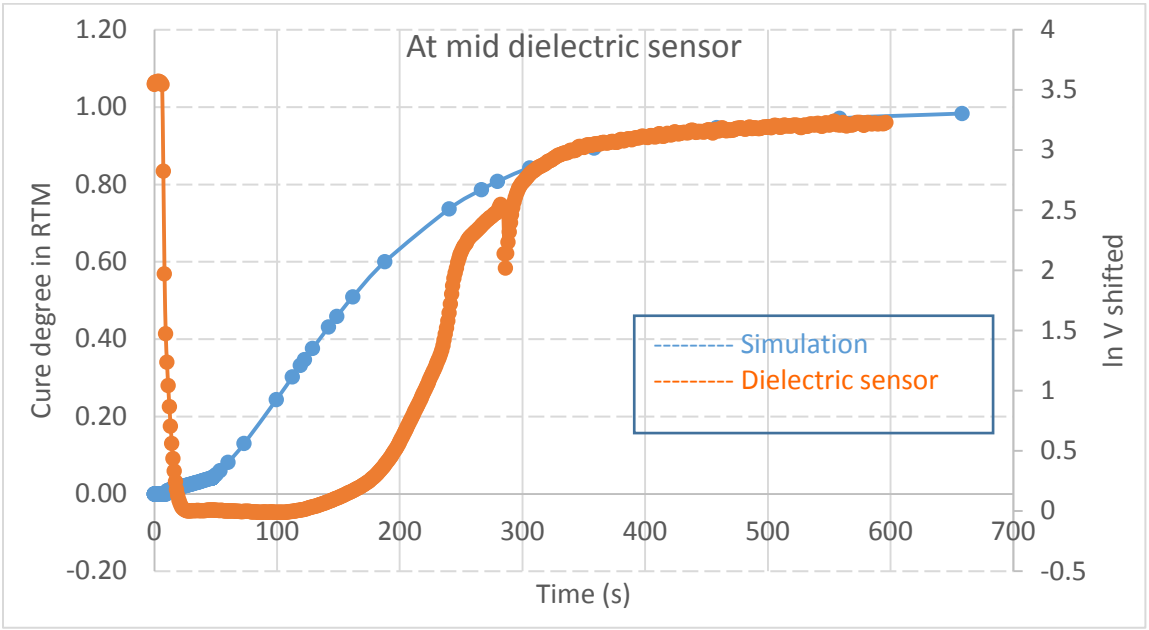

Figure IV-100: Comparison of the cure percentage results from simulation and log ionic viscosity readings from the dielectric cure sensors.

Defect Panels and Correlations (Obstacle in the Mold)

In this section, correlations of simulation results for the panel with a defect are presented. Figure IV-101 shows molding conditions of the plaque with an obstruction. A square thin plate with dimensions of 100 mm x 100 mm x 0.4 mm was placed on the fabric, creating a high-volume fraction/low-permeability region.

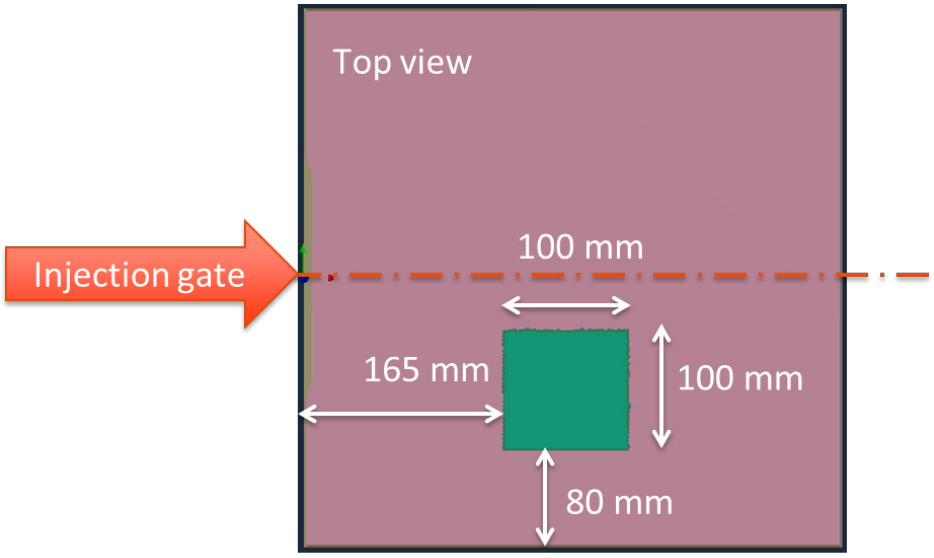

Figure IV-101: Schematic for the metal obstacle location.

During this simulation, the elements corresponding to the obstruction's location were assigned new permeability values that are lower than the preform permeability. The permeability of this obstruction region was modeled with permeability based on the Gebart model [5]

$$k = \frac{8r^2}{c}\frac{(1-V_f)^3}{{V_f}^2} \tag{9}$$

Equation 9 relates the permeability values to the volume fraction of the fabric. The new permeability values are calculated using the following equation:

$$\frac{K_{new}}{K_{ref}} = \frac{(1-V_f)^3}{{V_f}^2} * \frac{V_{f\,ref}}{(1-V_{f\,ref})^3} \tag{10}$$

Figure IV-102(a) and Figure IV-102(b) shows the panel's filling results, with the obstruction and void prediction at 36 seconds and 41.5 seconds of filling. At this time, more results are needed to complete this correlation study.

Summary

1) Simulation results predicting the buildup of pressure versus time in the mold correlates very accurately with the experimental results.
2) Simulation results predict this trend and 100% cure time of dielectric curing sensor measurements very closely.
3) The simulation model predicts defects at the obstruction site, but more work is needed for validation.

Next Steps

1) Conduct simulation of defect-free panels for the remaining crucial steps, such as prediction of residual stresses and warpage in the plaque.

2) Conduct simulations of panels with defects to compare with the experimental results for filling time, defect location, defect size, residual stresses, and distortion.

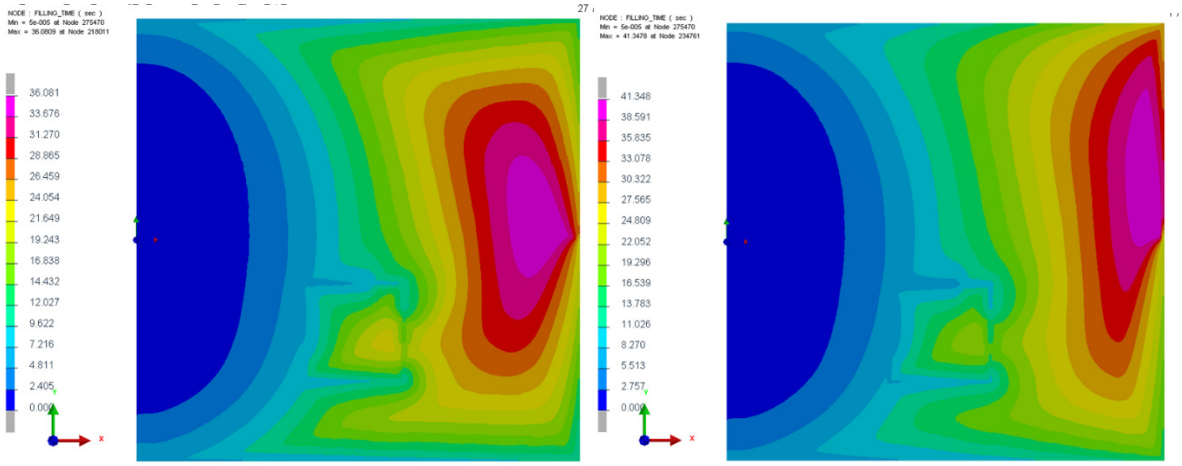

(a) (b)

Figure IV-102: Filling time contour for the panel with obstacle (a) t = 36 seconds and (b) t = 41.5 seconds.

Nondestructive Evaluation (NDE) of Molded Plaques (with Defects)

The following sections describe the background of a pulsed thermography NDE technique and its application to detect the size of the defects in the manufacturing of plaques.

Background

Pulsed thermography is a full-field and contactless non-destructive technique. It can quickly detect and qualitatively assess structure defects located below the surface. The types of detectable flaws could be resin-rich areas, blisters, delaminations, and foreign inclusions or any insert that has different thermal characteristics than the composite. Basically, during this process, the specimen is briefly heated by a thermal stimulation pulse that lasts less than 10 ms. The part's surface temperature gradient and decay curve is recorded by an infrared camera with time. The transient heat flow in areas with subsurface defects is different from areas without defects. Transmission rate discrepancies of pulse heat at areas with and without defects can be classified by an image post-processing data analysis system, which converts the measured data into a temperature versus time map. The first derivate and the second derivative of this temperature versus time curve, which represent cooling rate and cooling acceleration, are usually implemented for reconstructing the enhanced infrared (IR) image.

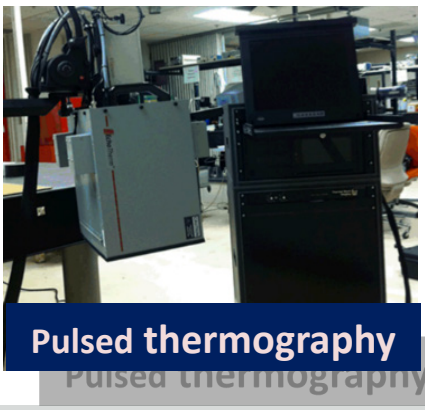

Figure IV-103: Pulsed thermography system (GM R&D).

The Thermal Wave Imaging Thermoscope II IR system is shown in Figure IV-103. The system consists of two high-intensity xenon flash lamps, an IR camera, and a data acquisition system. In our experiments, an exposure time of about 4 ms at a light intensity of about 9.6 kilojoule (kJ) per flash was used as the heat source for uniform illumination on the target surface. The IR camera was equipped with a 13-mm lens and a 640 x 512 resolution indium-antimony (InSb) detector, with a snapshot focal-plane array (FPA) of 3 to 5 um and a 14-bit digital data output. Its frame rate can reach up to 30 frames per second (fps) at a resolution of 650 x 512 and up to 120 fps at a resolution of 320 x 256.

The sample is made of an 8-ply quasi-isotropic (QI) carbon-fiber non–crimped fabric, which was molded in an RTM machine with constant pressure resin injection. In order to study occurrence of voids and provide experimental data for simulation, a 100 x 100 x 0.4-mm piece of sheet metal was placed between the non-crimped fabric and the bottom half of the mold as an obstacle during molding; it was removed after part de-molding. Images of the top and bottom surface of the plaque are shown in Figure IV-104. The molded part had a thickness of about 1.68 mm and 1.29 mm at the location of the obstacle. The pulsed flash was applied from the sample top surface at the first inspection location, roughly 250 mm by 250 mm. The intensity of the flash lamps was set to 100% with a 30-fps camera speed for a 25-second data acquisition window. The distance from the sample to the IR camera was set at 220 mm, while the flash event occurred 200 mm away from the sample top surface.

The thermal images shown in Figure IV-105 are post-processed by Thermal Signal Reconstruction (TSR) at particular times after the flash event. The large square on the left is where the obstacle was with internal voids due to resin race-tracking. The small square on the right of the image is from a glass veil placed between the top half of the mold and the fabric surface, to prevent short circuit of the dielectric curing sensor. The fiber volume fraction is much higher at the obstacle location than the rest of the part, thus it shows a lower grey intensity (i.e., darker) due to a rapid heat transfer through the carbon fiber at a time 0.1 second after the flash event.

In Figure IV-105, the fiber orientations with (0^0/-45^0/$+45^0$/90^0) are revealed, which is very important information for both FEA simulation and molding studies. In order to measure the size of the voids in the vicinity of the obstacle, histogram equalization was used that focused on the obstacle region and expanded the grey scale for resolution enhancement. The size of the void is 29.4 mm by 47.3 mm, with a measured area of about 950 mm^2 (Figure IV-106(a)).

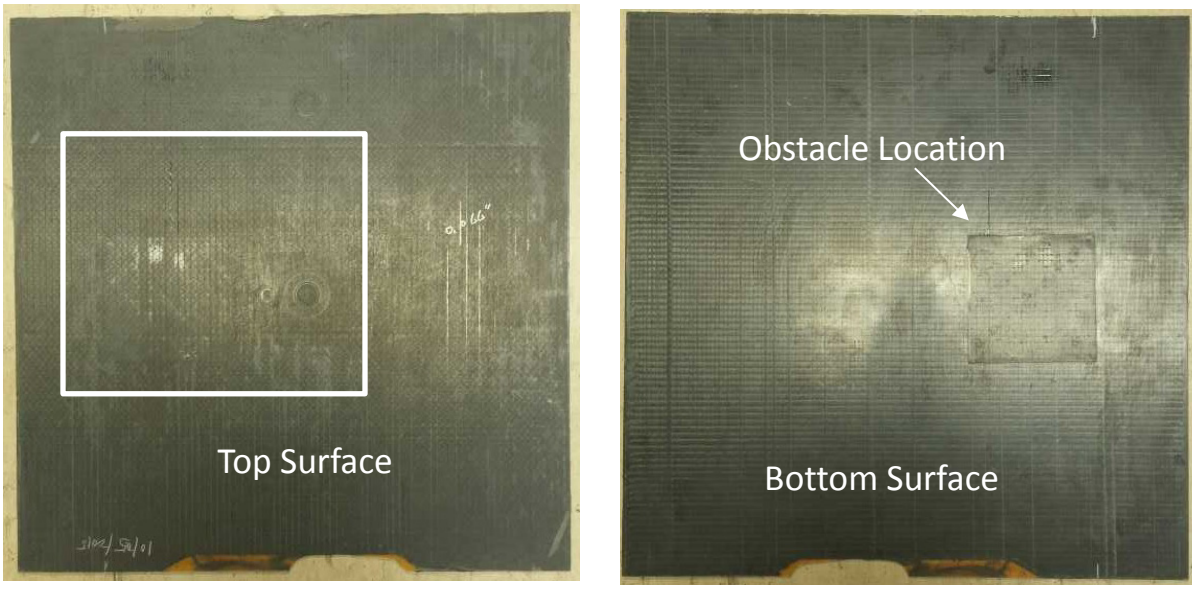

Figure IV-104: Top and bottom surface of the plaque (molded panels with obstruction).

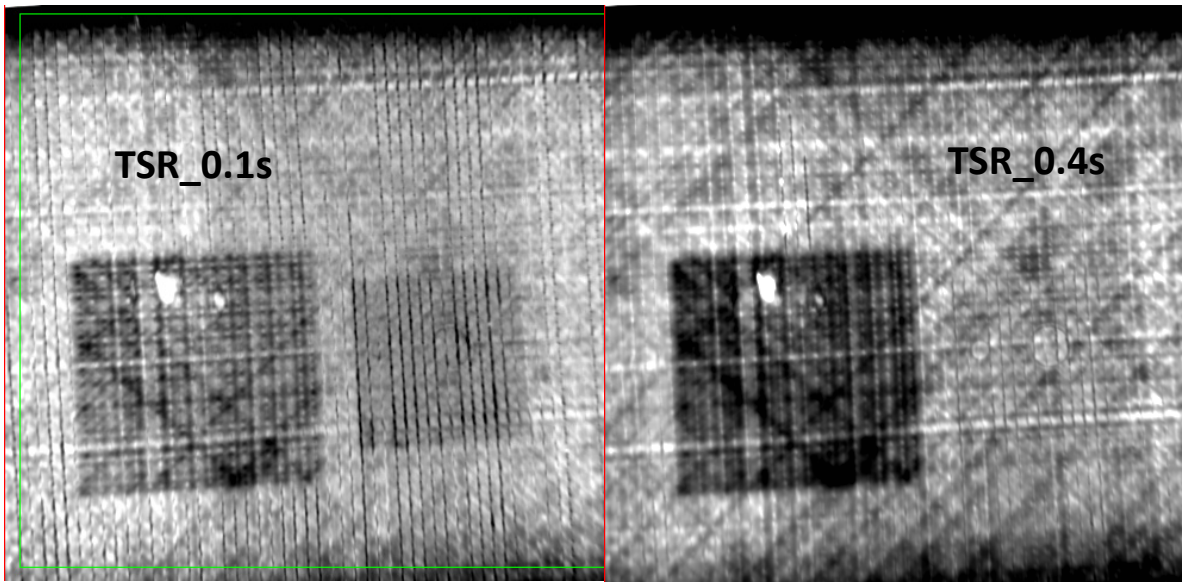

Figure IV-105: Post processor thermal image (by TSR) at 0.1 seconds and 0.4 seconds after the flash event.

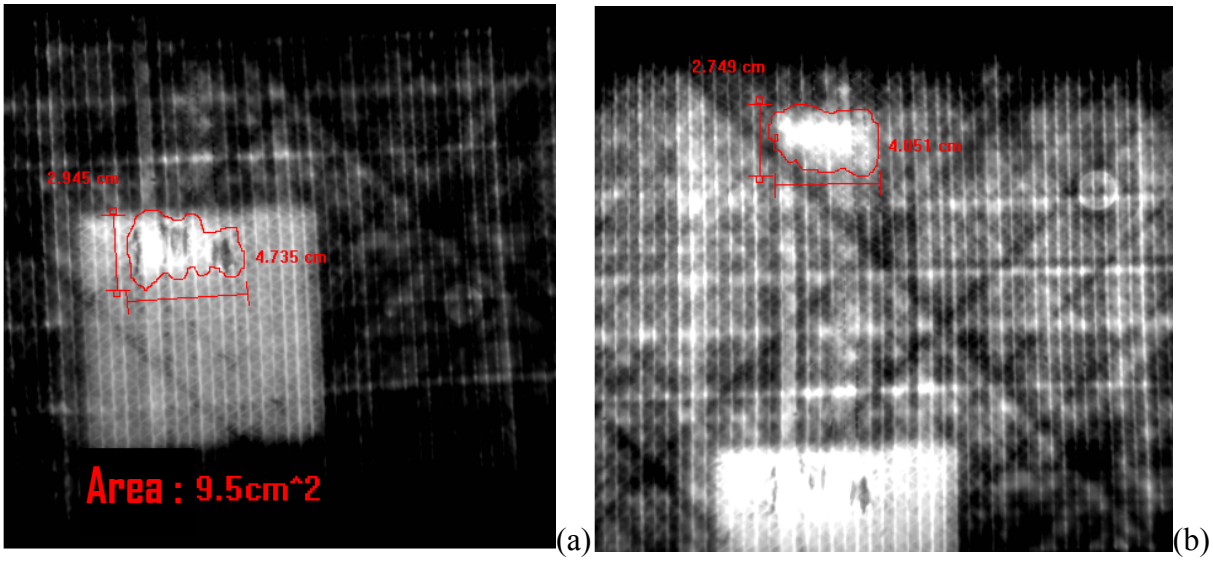

(a) (b)

Figure IV-106: (a) Void size from histogram equalization at the obstruction area and (b) void size at the vent.

A second void was found at a location close to the vent and right above the obstacle with a size of about 27.5 mm by 40.5 mm (Figure IV-106(b)).

Summary

It can be concluded that pulsed thermography NDE is suitable for materials that are of interest in the present research. Also, this is a promising method for measuring defects with different thermal properties (e.g., fiber orientation, void content, density, and delamination).

Next Steps

Pulsed thermography NDE will be used to measure defects for future RTM moldings and provide correlation data for manufacturing simulations.

Task 4.3: Development and Validation of a Stochastic Performance Model

The contribution to this project from Altair this year consisted of calibration of a multiscale material model for simulation of a laminated, non–crimped fabric, carbon-fiber composite material system. Robust calibration of the material model is crucial to developing predictive crash simulations and provides groundwork for stochastic analysis of the mechanical properties of the material system. A major challenge in calibrating material models to a small number of experiments is the possibility that the solution is not unique, meaning there potentially are an infinite number of material parameter combinations that match well with the given data. Using as many experiments as possible for calibration eliminates this issue because as more experimental data is added to the calibration process, the potential number of matching parameter combinations decreases. For the non–crimped fabric material system, single-ply data were not available. This is a challenge the entire industry faces, because it arises from manufacturing difficulties in producing single-ply specimens with the correct volume fraction of carbon fiber. As a workaround, calibration was performed by simultaneously using tensile and three flexural experiments on the laminate. While modeling flexure substantially increases the computational demands on the calibration procedure, the calibrated model matches all available experimental data within the given accuracy targets. Because the calibrated model simultaneously matches several complex experiments, the results are robust.

The non–crimped fabric material system is a 1.8-mm thick, $[0/+45/-45/90]_S$ laminate consisting of unidirectional carbon fiber – epoxy resin plies. The average carbon-fiber content of the laminate as determined by ASTM D3171 is 47.8%. The carbon fibers are Toray T700SC, which possess a 230 gigapascal (GPa) modulus. A summary of each level of the material system is given in Table IV-44.

Table IV-44: Summary of available data for each level of the non–crimped fabric material system.

Level	Details and Available Data
Carbon Fiber – T700SC	• Axial modulus and fiber diameter from data sheet
Epoxy Resin	• Strength and stiffness properties from experiments on resin only samples
Tow	• 12K fibers specified per tow • Volume fraction of fiber in the tow estimated as 80 to 90% • Ellipse shaped with radii 1.85 mm and 0.1 mm • No mechanical testing data
Lamina	• 5-mm by 0.225-mm unit cell • Tow volume fraction = 51.7% • Carbon-fiber volume fraction = 47.8% • No mechanical testing data
Laminate	• $[0/+45/-45/90]_S$ layup • Stiffness and strength properties available for tension and flexure

Experiments were performed on the laminate by GM for tension and flexure, each with 0 degree, 45 degree, and 90 degree orientations. A summary of the average stiffness and strength properties from each experiment are given in Table IV-45 and Table IV-46. Additionally, plots of the experimental curves are shown in Figure IV-107 and Figure IV-108. Significant scatter, particularly for the strength properties, can be observed.

Table IV-45: Overview of the average stiffness properties of the eight-layer non–crimped fabric laminate.

Experiment	Property Measured	Average Value
0 and 90-degree tension	E11 and E22	39.6 GPa
45-degree tension	G12	16.2 GPa
0-degree flex	0-degree flexural modulus	60.9 GPa

Experiment	Property Measured	Average Value
45-degree flex	45-degree flexural modulus	24.8 GPa
90-degree flex	90-degree flexural modulus	16.0 GPa

Table IV-46: Overview of the average strength properties of the eight-layer non–crimped fabric laminate.

Experiment	Property Measured	Average Value
0 and 90-degree tension	Tensile strength	598 MPa
0 and 90-degree tension	Ultimate tensile strain	1.71%
0-degree flex	0-degree flexural strength	876 MPa
0-degree flex	0-degree ultimate flexural strain	1.53%
45-degree flex	45-degree flexural strength	618 MPa
45-degree flex	45-degree ultimate flexural strain	3.19%
90-degree flex	90-degree flexural strength	428 MPa
90-degree flex	90-degree ultimate flexural strain	3.91%

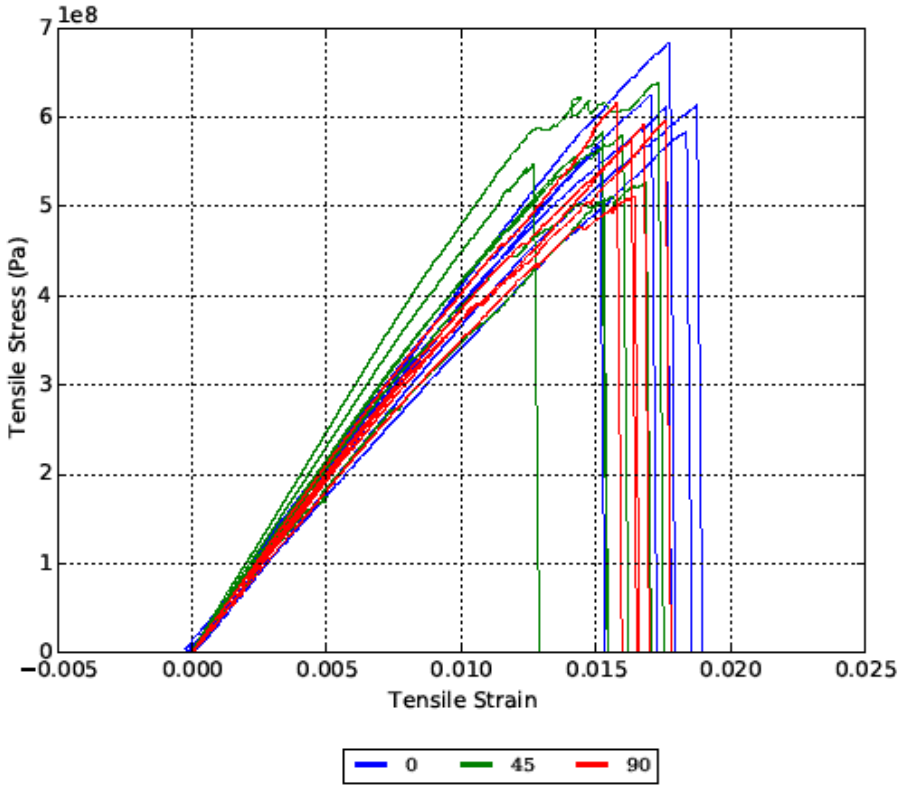

Figure IV-107: Tensile stress strain curves from experiments. Blue is for 0-degree samples, green is for 45-degree samples, and red is for 90-degree samples.

The calibration problem for the non–crimped fabric may be stated as follows: identify the in situ tow and resin properties such that the simulated homogenized response of the laminate system matches experimental data. An accuracy target of 15% was adopted to determine the acceptability of the results.

The unit cell for the non–crimped fabric, which is a single ellipsoidal-shaped tow in a brick-shaped matrix, is shown in Figure IV-109. The unit cell model is defined parametrically in MDS (i.e., an Altair product for composites) and the parameters are given as follows:

Tow major radius – 1.85 mm

Tow minor radius – 0.1 mm

Center-on-center tow spacing – 5 mm

Tow volume fraction – 51.7%.

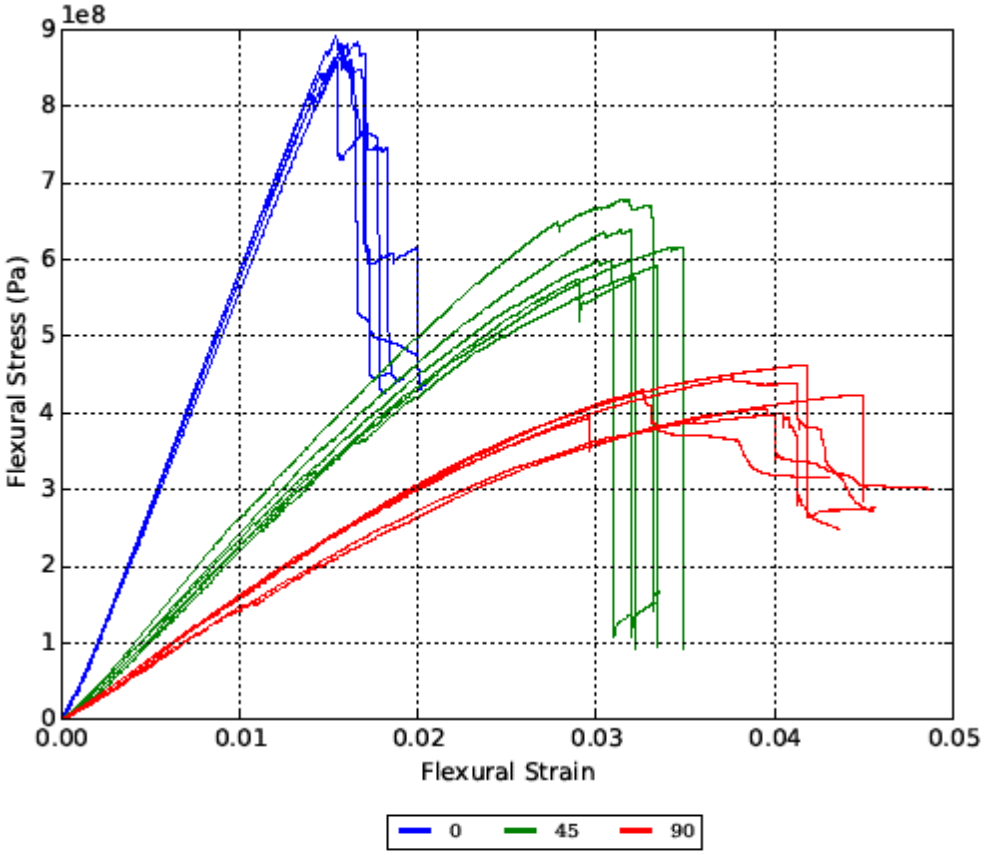

Figure IV-108: Flexural stress strain curves from experiments. Blue is for 0-degree samples, green is for 45-degree samples, and red is for 90-degree samples.

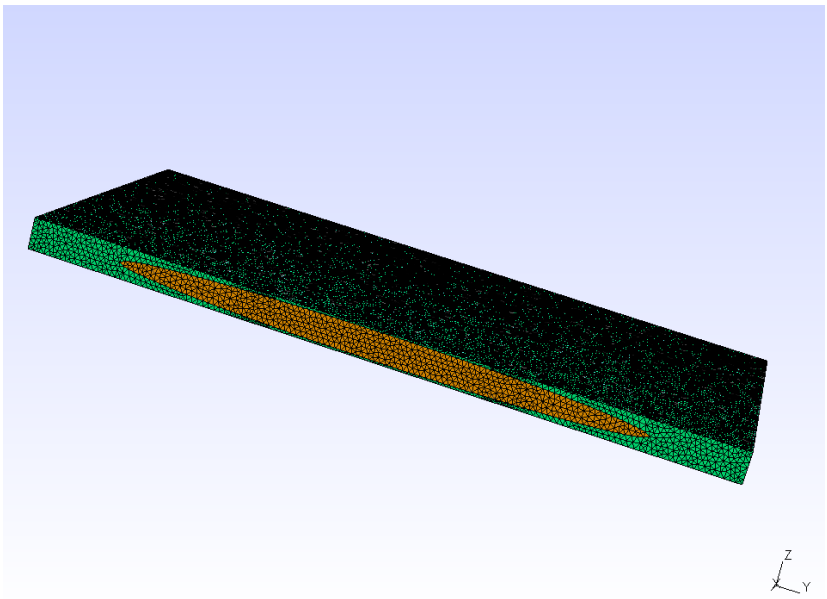

Figure IV-109: Unit cell of the non–crimped fabric composite considered for the study.

The tow is modeled as transversely isotropic, while the matrix is modeled as isotropic. Elastic calibration must identify a total of seven parameters (i.e., five for the tow and two for the matrix) representing the in situ constituent micro properties so the homogenized laminate properties computed by MDS match experimental data in Table IV-45. Because the laminate is QI in tension, an infinite amount of combinations of the seven parameters can match closely with the tensile experiments. Ideally, when experiments on the unidirectional lamina are available, this problem is eliminated by simultaneously calibrating to multiple tensile experiments on different orientations of the lamina. Each additional experiment constrains the calibration procedure and increases the likelihood that the final result will be predictive. Unfortunately, testing on the lamina is not available for this material due to manufacturing difficulties in producing single-ply specimens with the correct volume fraction. This is an issue faced by the whole industry and is a hurdle for obtaining robust calibrated models.

The group's solution to this problem was to simultaneously calibrate seven parameters to the QI tension results and the three flexural results. Because the behavior of the laminate is not QI in flexure and the distribution of stress in the layers will be different for each of the three flexural tests, the calibration procedure is well constrained. This means the results can be considered very robust. The tradeoff of using flexural data for the laminate versus tensile data on the individual plies is numerical. Determination of tensile stiffness properties requires only linear homogenization, while determination of flexural stiffness properties requires linear homogenization followed by a linear finite element model of the three-point bending test. The load on the three-point bend test is created by maintaining an average downward displacement across the top and center of three-point bend finite element model. This average downward displacement is implemented using multipoint constraints in an ABAQUS finite element model. The computational effort required for calibration is substantially increased by including the three-point bend models; however, this process has successfully produced a set of parameters that simultaneously match all available data to within the 15% accuracy target. The calibrated micro-properties of the tow and matrix may be found in Table IV-47; comparison of the homogenized properties of the laminate to the observed properties may be found in Table IV-48.

Table IV-47: Calibrated micro-properties for the tow and matrix.

Matrix Micro Properties

Property Name	Symbol	Value
Elastic Modulus	E	2.00e9 Pa
Poisson's Ratio	N	0.37

Tow Micro Properties

Property Name	Symbol	Value
Transverse Elastic Modulus	E_T	2.21e9 Pa
Axial Elastic Modulus	E_A	1.70e11 Pa
Transverse Poisson Ratio	v_T	0.4
Axial Poisson Ratio	v_A	0.015
Transverse Shear Modulus	G_T	48.1e9 Pa

Table IV-48: Comparison of homogenized laminate properties to experiments.

Property Name	Computed Laminate Property from Homogenization	Observed Laminate Property From Experiments	Error
Tensile Modulus	39.6 GPa	39.6 GPa	0.0%
0-Degree Flex Modulus	60.9 GPa	60.9 GPa	0.0%
45-Degree Flex Modulus	24.8 GPa	24.8 GPa	0.0%
90-degree Flex Modulus	16.0 GPa	16.0 GPa	0.0%

The nonlinear response of the resin in the non-crimped fabric is modeled using a bilinear isotropic damage law and, similarly, the nonlinear behavior of the tow is described by a bilinear orthotropic damage law. The parameters of the damage laws were determined by a trial and error inspection of the load displacement curves in Figure IV-110 versus the simulated response of the same experiments. The nonlinear damage parameters are described in Table IV-49.

Table IV-49: Calibrated nonlinear properties for the tow and matrix.

Matrix Damage Properties

Property Name	Value
Stress at Damage Initiation	4.00e8 Pa
Failure Strain	0.02

Tow Damage Properties

Property Name	Value
Transverse Stress at Damage Initiation	4.00e7 Pa
Transverse Failure Strain	0.0175
Axial Stress at Damage Initiation	2.60e9 Pa
Axial Failure Strain	0.0150

Results for simulations versus experiments are shown with the experimental curves in blue and the simulated response in red (Figure IV-110 through Figure IV-114). Simulation results are in excellent agreement with experimental results for tension, 0-degree three-point bend test, and 90-degree three-point bend flex tests.

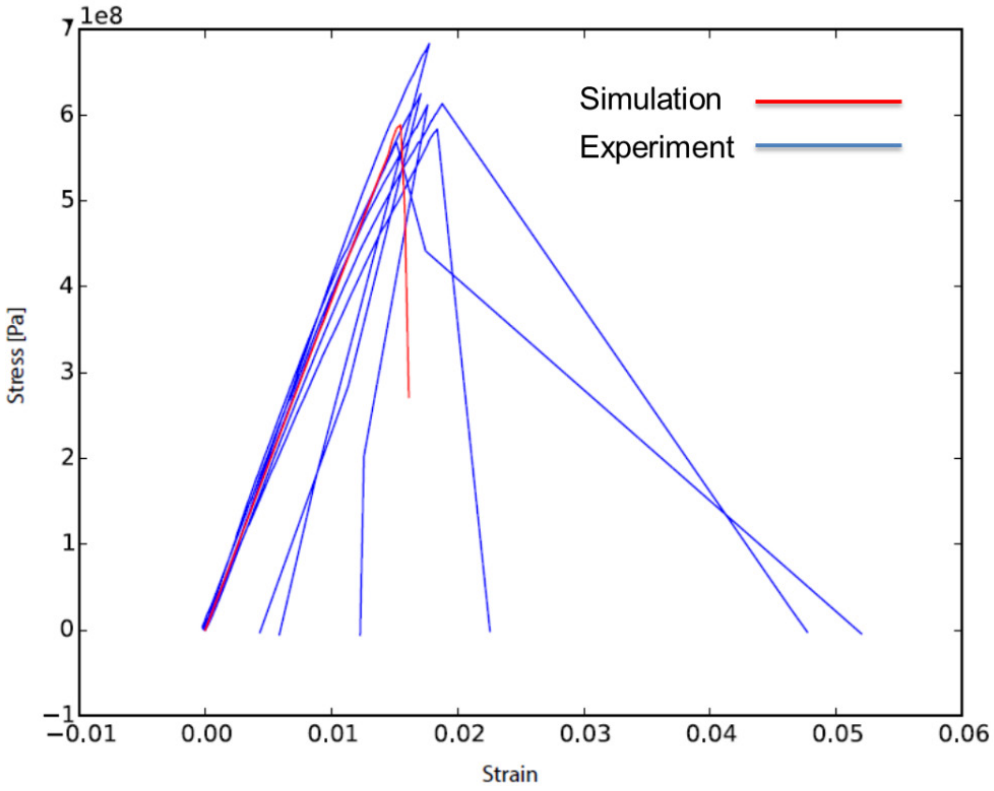

Figure IV-110: QI tension (stress versus strain).

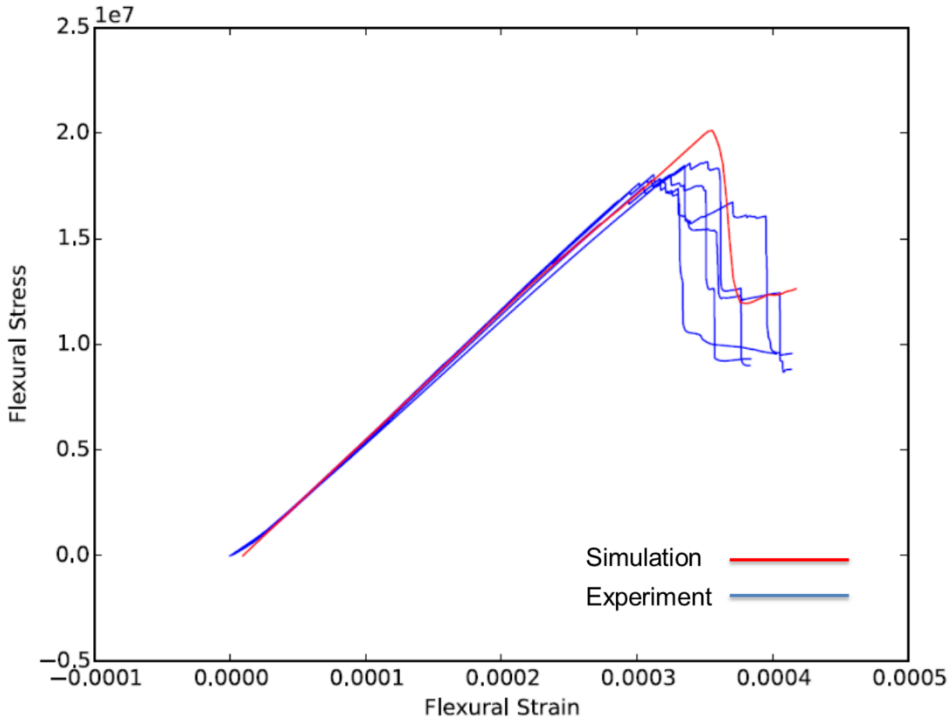

Figure IV-111: Bending with 0-degree top ply (flexural stress versus strain).

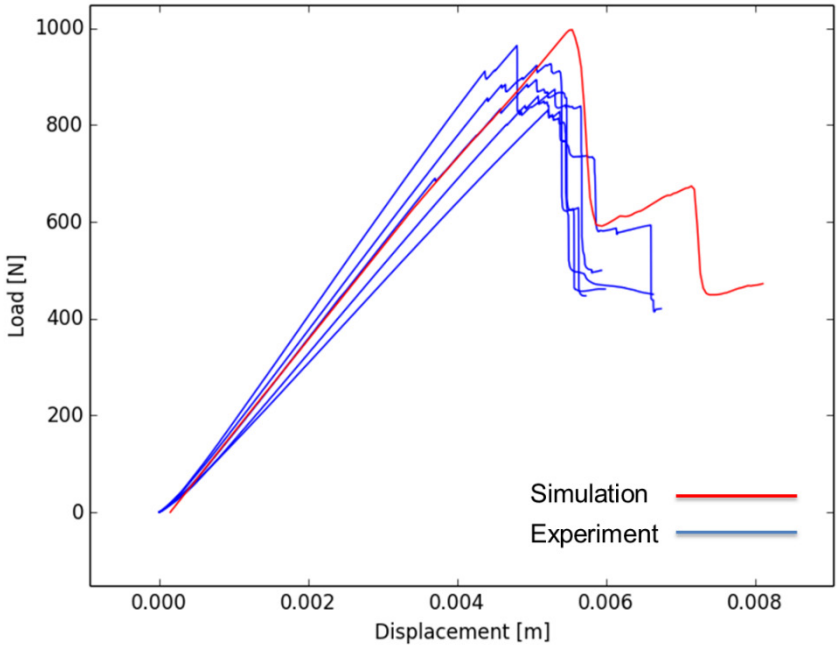

Figure IV-112: Bending with 0-degree top ply (load versus displacement).

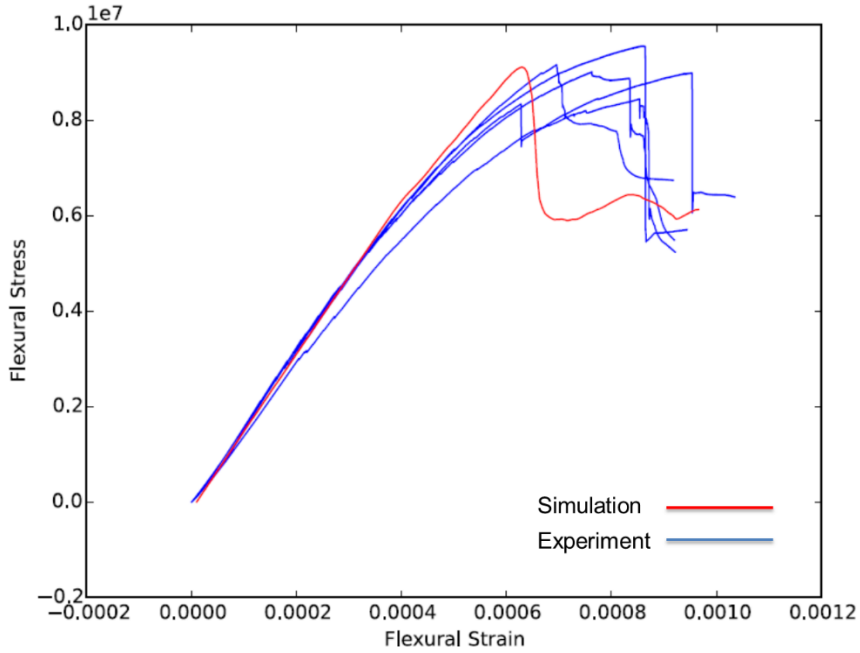

Figure IV-113: Bending with 90-degree top ply (flexural stress versus strain).

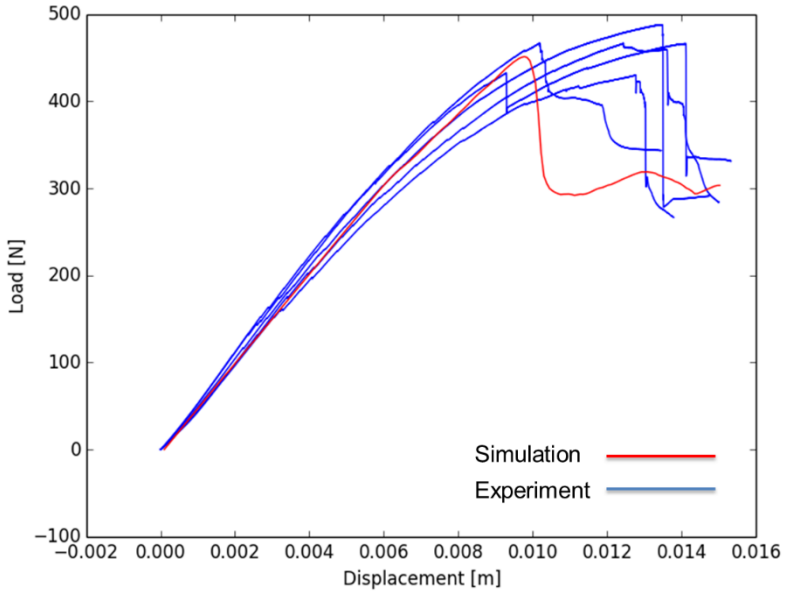

Figure IV-114: Bending with 90-degree top ply (load versus displacement).

Technology Transfer Path

The project's primary objective, which is development of an integrated stochastic manufacturing and structural performance predictive tool, is currently not available in the market. Successful development of these tools will help the automotive industry and its suppliers in optimizing the manufacturing process, predicting performance accurately, and accounting for manufacturing effects. The project team comprised of important stakeholders such as GM (i.e., the current largest automotive company using carbon-fiber composites by volume); ESI (i.e., owner of the commercial software company for manufacturing simulation of composites such as PAM-RTM, PAM-FORM, and PAM-DISTORTION; Altair (i.e., owner of the software company for

predicting performance using multiscale simulation for composites); CSP (i.e., molder/material supplier for composite materials and the GM-Corvette composite parts supplier); and USC (i.e., leader in stochastic model development). These stakeholders hold and command a wide influence in implementing advanced carbon-fiber composites in automobiles by providing valuable input from each of the steps from choosing the raw constituent materials and manufacturing the components to final implementation in an automobile. The developed models will transform current automotive composite design and manufacturing practices from a slow trial-and-error approach to a fast physics-based approach with improved quality, cost, and performance. The modeling approach will significantly reduce the validation and testing effort required to meet necessary confidence levels for composites. Demonstrating use of the developed models to reduce vehicle weight and meet cost targets for a representative body assembly common to light-duty vehicles enhances the value of this project significantly. Finally, the project is believed to accelerate widespread application of carbon-fiber composites in the automotive industry. The U.S. supply base for component manufacturing is also expected to expand through use of predictive technologies to enable high-volume carbon-fiber composites manufacturing with lower costs to automotive OEMs.

Conclusion

During the first year of the project, a solid framework of development work between the various project teams was established (i.e., tools to be used during the process and a detailed experimental plan for validating the manufacturing and structural performance tools). For the task of determining the performance requirements of automotive assembly, the 2016 GM Malibu vehicle was chosen and pole side impact was modeled. A local method was developed to make future design and analysis iterations efficient compared to full vehicle-level analysis. The local analysis will help provide experimental setup for validating the automotive assembly. Two manufacturing processes suitable for high-volume automotive manufacturing were chosen: RTM and compression molding. Experimental results were collected using GM's instrumented RTM tool to validate the manufacturing simulation tool for void-containing and void-free panels. Simulation results for void-free panels were correlated and excellent correlations were observed. In parallel, multiscale performance simulation was conducted on non–crimped fabric composites and excellent correlations were predicted for 0-degree tension, 0-degree flex, and 90-degree flex experiments. A stochastic model that works for both manufacturing and structural performance was developed and is being applied to predict the results, including variation.

References

1. FMVSS214 Final Rule – [Docket No. NHTSA-07- 29134] RIN 2127-AJ10.
2. A. K. Noor, 1986, "Global-Local Methodologies and their application to nonlinear analysis," *Finite Elements in Analysis and Design*, 2; pp. 333-346.
3. J. M. Castro and C. W. Macosko, 1980, ''Kinetics and Rheology of Typical Polyurethane Reaction Injection Molding Systems,'' *SPE Technical Paper*, 26; pp. 434–438.
4. M. R. Kamal and S. Sourour, 1973, "Kinetics and thermal characterization of thermoset cure," *Polymer Engineering and Science*, 13; pp. 59-64.
5. B. R. Gebert, 1992, "Permeability of Unidirectional Reinforcements for RTM," *Journal of Composite Materials*, 26; pp. 1100-1133.

IV.8. Spider Silk MaSp1 and MaSP2 Proteins as Carbon-fiber Precursors – Utah State University

Project Details

Randolph V. Lewis, Principal Investigator
9820 Old Main Hill
Logan, UT 84322-9820
Phone: 435-797-9291
E-mail: randy.lewis@usu.edu

Felix L. Paulauskas, Co-Principal Investigator
Building 5800, Room A107
P.O. Box 2008
Oak Ridge, TN 37831-6053
Phone: 865-576-3785
E-mail: paulauskasfl@ornl.gov

Cheryl Hayashi, Co-Principal Investigator
2318 Spieth Hall
University of California
Riverside, CA 92521
Phone: 951-827-4322
E-mail: cheryl.hayashi@ucr.edu

Soydan Ozcan, Co-Principal Investigator
Building 5800
P.O. Box 2008
Oak Ridge, TN 37831-6053
Phone: 865-576-3785
E-mail: ozcans@ornl.gov

Carol Schutte, Technology Area Development Manager
U.S. Department of Energy
1000 Independence Avenue, SW
Washington, DC 20585
Phone: 202-287-5371
E-mail: carol.schutte@ee.doe.gov

Contractor: Utah State University (USU)
Contract No.: DE-EE0006857/0002

Executive Summary

The objective of this project is to develop an unconventional non-petroleum-based carbon-fiber precursor with the potential for production in high yield and quantities. Methods will be developed to produce pilot-scale quantities of fibers from spider silk proteins with mechanical properties at least 75% that of the natural dragline silk fibers in tensile strength and elongations of less than 5%. The precursor fibers will be converted to carbon fibers, with a goal of greater than 250 kilopound per square inch (Ksi) strength and 1 to 2% elongation. The results of this project will include a cost analysis and an optimized process.

Task 1. Fiber Synthesis

Subtask 1. Fiber production: Results to-date exceeded the go/no go milestone of 1.0 gram per liter (g/L) of one of the spider silk proteins—purified major ampullate spidroin 2 (MSp2). The 6.2 grams (g) of protein were purified from 5 liters (L) of culture media. Another protein has yielded nearly 4 g/L from fermentation. The two other proteins are at the 1.0-g level. Future efforts are for expressing and scaling up to a production level of the aciniform spider silk. This silk contains a higher proportion of larger amino acids, aiding in carbonization.

Subtask 2. Fiber spinning: An eight-fiber product was successfully spun with several different proteins under various conditions, but during the post-spin draw needed for maximal mechanical properties (which is done in aqueous based baths), the individual fibers tend to fuse. This leads to lower mechanical properties than desired. Altering the post-spin process to allow the fibers to dry more before placing them on the winder spool should resolve this problem.

Subtask 3. Silkworm silk: Using the proposed method of gene replacement produced new lines of silkworms. The best silk from those cocoons is greater than 90% of the strength of spider silk and contains up to 10% spider silk protein, both of which are better than previous work from our laboratory and others. We have generated several hundred meters of 25-fiber thread and delivered it to Oak Ridge National Laboratory (ORNL) to start developing the carbonization process.

Task 2. Carbonization

Preliminary work leading up to the milestones for Task 2, which involved using silk from transgenic silkworms began in Fiscal Year (FY) 2015. This work began because large quantities are available and the milestone has been surpassedand for the mechanical strength of this silk fiber. Differential scanning calorimetry at different heating rates in air and a nitrogen (N_2)-controlled atmosphere and thermo-gravimetric analysis of fibers in air and N_2 have been initiated.

Task 3. Techno-Economic Analyses

Two system models were created with variable inputs to be able to analyze three scenarios. Material prices were sourced online from a variety of industrial vendors from Alibaba.com and Sigma Aldrich. The Results and Discussion section later in this report discusses price inputs for three scenarios. All of the models include a setup of 24 fermenters, each with a capacity of 20,000 L of expression media to be representative of a large-scale production facility. Total protein production is then dependent on the level of protein expression used for the given scenario and represents a foundational input.

Capital expenses related to equipment were determined on the size and specifications of the given process. Equipment modeling was done with any of the following methods or a combination of them, depending on the availability of information (i.e., material consumption for equipment construction with a manufacturing and resale scale-up factor, Aspen plus economic analyzer, or industrial equipment pricing from various sources scaled to the model production size). We integrated operational and capital expenses with standard techno-economic considerations on price calculations, including interest on loans, capital investment, and depreciation.

Accomplishments

- We have exceeded the go/no go milestone of 1.0 g/L of one of the purified spider silk proteins (MaSp2). We were able to purify 6.2 g of protein from 5 L of culture media. Another protein has yielded nearly 4 g/L from fermentation. The two other proteins are at the 1.0-g level (FY 2015).
- We have successfully spun an eight-fiber thread with several different spider silk proteins under various conditions (FY 2015).

- We determined that the best silk from the transgenic cocoons is greater than 90% of the strength of the spider silk and contains up to 10% spider silk protein, both of which are better than previous work from our laboratory and others.
- We created a techno-economic model that describes the relative percent costs of all inputs to spider silk protein production via fermentation.

Future Directions

- Increase spider silk protein production via fermentation.
- Further improve the tensile strength of the transgenic silkworm silk.
- Generate methods that thermally stabilize the spider silk-derived carbon fibers.
- Complete the techno-economic model to determine the best estimate of cost.

Technology Assessment

- Target: Increase spider silk protein production up to 2 g/L of recovered protein.
- Gap: Bacterial production and purification technology both have to be improved.
- Target: Transgenic spider silk tensile strength equal to spider silk.
- Gap: Percentage of spider silk in the fiber needs increased to 50% from the current 10%.
- Target: Stabilize spider silk fibers by photo-crosslinking to prevent thermal degradation before forming carbon fibers.
- Gap: Preliminary data indicate that the fibers in their native state will not remain stable at the temperatures needed to convert them to carbon fibers.
- Target: Complete a techno-economic analysis that will accurately predict a cost basis for carbon fibers derived from spider silk.
- Gap: Data sets are still incomplete concerning the oxidative conversion process.

Introduction

The project proposal was to develop efficient carbon fibers by using unconventional, non-petroleum precursors that are high strength, low cost, and high yield. To our knowledge, the use of spider silk as a carbon-fiber precursor is entirely novel. Specifically, during this 2-year project, we will assess the feasibility of spider silk fiber as a model for engineering biomimetic polymer precursors to replace petroleum-based polyacrylonitrile (PAN) precursors. Utilization of this unconventional precursor has several potential impacts. From a material science perspective, spider silk has many desirable properties, including tensile strength as high as Kevlar® and elongation equivalent to nylon, which would impart new properties to carbon fiber. From a sustainability perspective, silks are proteins and, thus, are renewable resources. Finally, from the perspective of national competitiveness and security, unlike PAN precursors, spider silk can be U.S. sourced. Future efforts include techno-economic modeling to understand the commercial feasibility of the production processes under investigation, with data feedback used to highlight key areas for research focus that will improve the economics of the processes.

The technical target for this feasibility project is to produce carbon fibers with uniform mechanical properties of at least 250 Ksi (1.72 gigapascals [GPa]) tensile strength, 25 million pounds per square inch (Msi) (172 GPa) tensile modulus, and 1% ultimate tensile strain. Future efforts include a pilot-scale level of multiple 500-L fermenters to produce spider silk protein via Escherichia coli (E. coli) fermentation. Recent advances in

fermentation and protein expression indicate that this production level at the pilot scale will produce in excess of 1kilogram (kg) per fermentation, resulting in approximately 330,000 meters (m) of silk fiber.

The three major goals of this project are (1) develop methods for producing large (pilot-scale) quantities of fibers from spider silk proteins with mechanical properties at least 75% that of the natural dragline silk fibers in tensile strength and elongations of less than 5%, (2) develop procedures to convert these fibers into carbon fibers with mechanical properties of 250 Ksi and elongations of 1 to 2%, and (3) conduct a techno-economic assessment of key process cost points to determine where to minimize costs and the most cost-effective alternative method.

Approach

Task 1. Fiber Synthesis

There are two separate approaches for producing sufficient spider silk protein-based fibers (i.e., Project Objective 1): (1) spin fibers from *E.coli*-produced protein and (2) create transgenic silkworms that produce cocoon silk fibers with mechanical properties similar to spider silk (see Figure IV-115 for flowchart). Our major deliverable depends on achieving this task.

Current production methods for spider silk fibers have two deficits: (1) lack of production capacity and/or (2) inferior mechanical properties. Bacterial production suffers from both deficits, but our current research has increased protein production. We plan to improve both bacteria mass per L and the amount of protein produced per gram of bacteria. We will do this by determining the optimal bacterial host and the best expression system. In theory, the transgenic silkworm system is infinitely expandable and low cost, but the fibers we produced and those produced by others, lack the needed mechanical properties. To overcome this, we have two strategies: (1) directly replace the major silkworm silk protein gene with our spider silk protein gene or knockout that silkworm silk gene in our current transgenic silkworm line we already have and (2) allow for substitution of the spider silk protein in the spinning process.

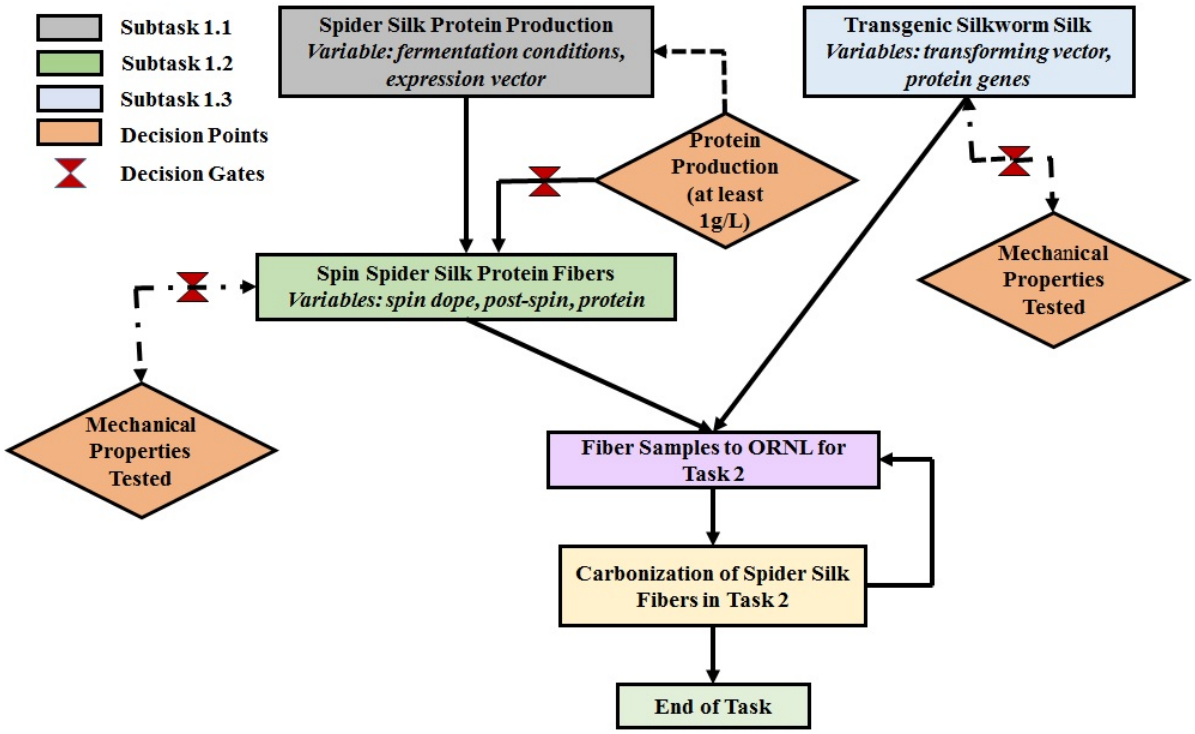

Figure IV-115: Flowchart for Task 1.

Subtask 1: Fiber Production

The objective of Subtask 1 was to produce 1 g/L of spider silk protein from *E.coli* fermentation. Spider silk protein production increased almost five-fold from the baseline of 100 mg/L in only a few months [1]. The combination of increased bacteria cell mass and increased protein production should achieve the objective of 1 g/L. To achieve greater bacterial mass, we will optimize fermentation conditions where possibly the timing and levels of sugar limit the amount of bacteria produced. Protein production can be limited by the amount of transfer ribonucleic acids (tRNAs), amino acids, and energy available. This may be especially true for spider silk proteins, which are extraordinarily biased in using only six to eight amino acids out of the usual 20. We have developed two different protein expression vector systems for increasing the levels of crucial tRNAs, which led to part of the five-fold increase noted above.

Future tests include two approaches for increasing amino acids. The first is simply to add amino acids to the media at the time of inducing spider silk protein production. This approach may interfere with other metabolic pathways. However, if fed continuously instead of as a bolus, then the amino acid may be consumed rapidly enough not to interfere with other pathways. Secondly, an expression system was developed that produces larger levels of glycine (i.e., the most common amino acid in spider silk). We can improve that system to include other amino acids if that turns out to be a key limiting factor (we are currently testing fermentation media and bacteria at successive time points during fermentation to assess this). In addition, as a backup, new bacterial strains are available that may be more amenable to protein production, although they have not been tested with spider silk proteins.

The second phase of Subtask 1 is to produce sufficient protein for fibers to perform testing for conversion to carbon fibers. This will follow our current fermentation schedule, augmented by the addition of two 500-L fermenters and all the needed purification equipment in a new pilot-scale bio-production facility near our research building. The differing approaches described in the summary above may overcome possible problems. There are two milestones for Subtask 1:

Milestone 1.1.1: The initial milestone is 0.5 g of purified protein per L of fermentation.

Milestone 1.2.1: The go/no go milestone is 1 g of purified protein per L of fermentation.

Both milestones were accomplished in FY 2015 as result of improved fermentation methods and use of a vector to provide additional tRNAs to the cells. In particular, we found that adding additional antibiotic at the time of induction of protein synthesis and lowering the temperature of the fermentor to 25°C resulted in substantially greater protein production. The additional tRNAs were provided by producing them from a single vector, which included the protein gene to be produced and/or a separate vector (i.e., two vector system). We found that using the two-vector system was consistently as good or better than the one vector system for all proteins tested and, due to the smaller size of the vectors, was much easier to use. Amino acid additions did not have a substantial impact on protein production and were likely to increase the production price beyond a commercially viable level.

Subtask 2: Fiber Spinning

The objective of Subtask 2 was to spin fibers from the spider silk protein with tensile strengths approaching natural spider silk and extension less than 10%. We will continue to develop the aqueous-based spinning methods we have devised in the past several months [2]. To our knowledge, all other spider silk fiber spinning methods use organic solvents that cannot be scaled to commercial production due to cost and health effects. The aqueous system is similar to our published methods [3] using an organic solvent because fibers are extruded and then post-spin draw in an aqueous solution is used to generate the final fibers. We have improved the published methods by using a custom-built spinning instrument (Figure IV-116), which allows for fine control of the rate of fiber movement as well as the stretch occurring in each of the spin draw baths. A camera system allows measurement of, in real time, the diameter of the fiber and its opacity (the clearer the fibers; the better the mechanical properties). However, we did not produce fibers that match the natural fibers in tensile strength.

Figure IV-116: New fiber spinning instrument at USU.

To achieve that goal, we have three distinct approaches with multiple combinations. The first will continue to improve the actual spinning conditions and will involve changing the post-spin draw conditions, particularly the aqueous baths and additives to the baths (such as glutaraldehyde or L-3,4-dihydroxyphenylalanine [l-DOPA]) that crosslink the protein chains and that have greatly improved our spider silk films [4].

The second is to use proteins of larger size. We have recently developed methods for producing proteins in *E.coli* much larger than previously produced [1], which can be as large as 240 kD (kilodalton) in comparison to the standard 50 to 60 kD or smaller proteins currently used. These are likely to achieve higher tensile strengths, as is the case for most synthetic polymers, and we observed that in the transgenic silkworms the larger proteins resulted in substantially higher tensile strengths for the fibers.

The third approach will be to alter the protein sequence itself. MaSp1 is the most likely initial candidate for high tensile strength and low stretch, but the final fiber will be carbon fiber. The spider silk fiber properties needed to produce the best carbon fibers are unknown at this time. MaSp2, minor ampullate spidroin (MiSp), and the protein sequences like MaSp1 or MaSp2 that have differing lengths or ratios of the strength sequences are also candidates. Evaluation will measure tensile strength and elongation by using methods we have used for over 20 years on an MTS Systems Corporation (MTS) system with a custom load cell [5]. The differing approaches are described above to overcoming possible problems. There is one milestone for Subtask 2:

Milestone 1.2.1: Achieve a tensile strength at least 75% that of natural spider silk, with an elongation of less than 5%.

The tensile strength achieved was, at most, 60% of the natural dragline spider silk. However, we did not produce sufficient amounts of the larger proteins to allow us to test various spinning methods. Using a combination of MaSp1 and MaSp2 in a ratio of 80:20 gave better strength than either protein alone or in other ratios. A visible light-activated crosslinking system generated showed substantially increased the strength of spider silk protein materials in preliminary studies. This will be much easier to implement than a chemical system.

Subtask 3: Silkworm Silk

The objective of Subtask 3 was to generate silkworms with at least 25% spider silk protein and a tensile strength of 75% of spider silk. We have already generated transgenic silkworms that produce cocoons of a mixture of silkworm and spider silk proteins [6]. The spider silk protein content is low (about 5%), but the tensile strength was still improved by about 50% above the natural cocoon fibers. This is about 45% of spider silk. The transgenesis was achieved using a standard baculovirus system, resulting in a random integration site. This led to a decrease in spider silk protein production in successive generations of some silkworm lines. In order to both improve the mechanical properties and generate stable silkworm lines, we plan to directly replace the natural silkworm silk gene with our spider silk genes.

We used two methods to achieve this. First, the transcription activator-like effectors to nucleases (TALEN) system uses proteins designed to specifically bind to the target site and direct an endonuclease to cut at that site. The approach used was to cut at both ends of the native silkworm gene and use homologous recombination to replace that gene with our spider silk genes. Only the repetitive region of the silkworm gene was replaced to keep all of the control elements and protein interaction regions of the silkworm protein.

The second is the much newer and widely heralded clustered regularly interspaced short palindromic repeats (CRISPR) system that accomplishes the same genome cutting as the TALEN system, but uses ribonucleic acid (RNA) guides to direct binding. This appears to lead to fewer non-specific sites cleaved and is much faster because the endonuclease is standard to all reactions and only the RNA-producing sequence needs changing for specific uses. We will target the same areas of the silkworm gene as in the TALEN method.

We designed and created the necessary plasmids to accomplish cleavage for both systems and are testing the best methods for getting the plasmids into silkworms. The standard method is to micro-inject into the eggs, but that is incredibly laborious and has a low success rate. To get the plasmids into the embryo, we are testing injection into the ovaries and testes of silkworms and electroporation of eggs with weakened membranes to allow for DNA uptake. Success was achieved by creating transgenic silkworms with baculovirus injection into the ovaries that have shown fluorescent protein gene uptake with electroporation into eggs. Expectations are that all of these methods will work and future work will proceed with the most efficient method.

Finally, as a fallback method, we will use the transgenic silkworms we have and knockout the silkworm gene to create hemizygous silkworms that should produce 50% of the normal amount of silkworm protein, increasing the level of spider silk protein in the fibers.

Overlaid on all of these methods is the need to achieve the added tensile strength in these fibers, which may be dependent on the protein we use. Two different proteins are available that may serve the purpose. The first is the MaSp1 protein from dragline silk, which is composed predominantly of sequences that contribute to strength and not elongation. The second is the MiSp protein from minor ampullate silk, which is also composed of strength and not elongation sequences. As a backup, we have protein genes where the strength regions are substantially longer or more frequent, either of which might make major contributions to increased strength.

Evaluation will be two-fold. First, we need to measure the percentage of spider silk protein produced in the cocoon fibers of the transgenic silkworms. Measurement is accomplished by dissolving the silk, running sodium dodecyl sulfate - polyacrylamide gel electrophoresis (SDS-PAGE), staining the proteins, and measuring their relative concentrations. Second, mechanical testing will be done as described [5].

Milestone 1.3.1: Tensile strengths of 75% or better of spider silk.

We exceeded this milestone, which was also a go/no go metric, by a substantial margin. Fibers with 900 megapascals (MPa) (i.e., roughly 90% of spider dragline silk) were generated using the MaSp2 protein as part of the cocoon silk. Use of the CRISPR system and replacing one copy of the silkworm silk heavy chain protein accomplished this result. There are six copies; therefore, we would expect about a 10% replacement of silkworm protein by spider silk protein and that is what we observed. We are currently breeding these silkmoths to determine if we can continue to improve the mechanical strength and the percentage of spider silk protein. We have also been able to knockout the heavy chain gene that effectively prevents nearly complete formation of the cocoon silk. Therefore, we are working to attenuate the effect to substantially decrease the heavy chain production, but not eliminate it.

Task 2. Carbonization

The overall technical objective of the proposed research is to demonstrate continuous mode conversion of spider silk protein fiber precursors to obtain carbonized fibers that are applicable in automotive industries. The specific objectives for this work include (1) develop modified spider silk protein fiber that can be rendered infusible, (2) demonstrate accelerated stabilization using thermal in air or thermochemical methods with a residence time comparable to traditional PAN fiber residence time, and (3) obtain carbonized fiber from the stabilized precursors by applying optimal conversion parameters. In Task 2 (Figure IV-117), we will conduct a systematic approach to optimizing the conversion parameters with an overarching goal of producing renewable source spider silk-based, low-cost carbon fiber for automotive application. The final project deliverable will be a continuously processed spider silk-based carbon fiber with satisfactory properties. All of these activities are

planned for the second year of performance; however, we have started work on Subtask 2.1, which is development of a chemical/physical pretreatment.

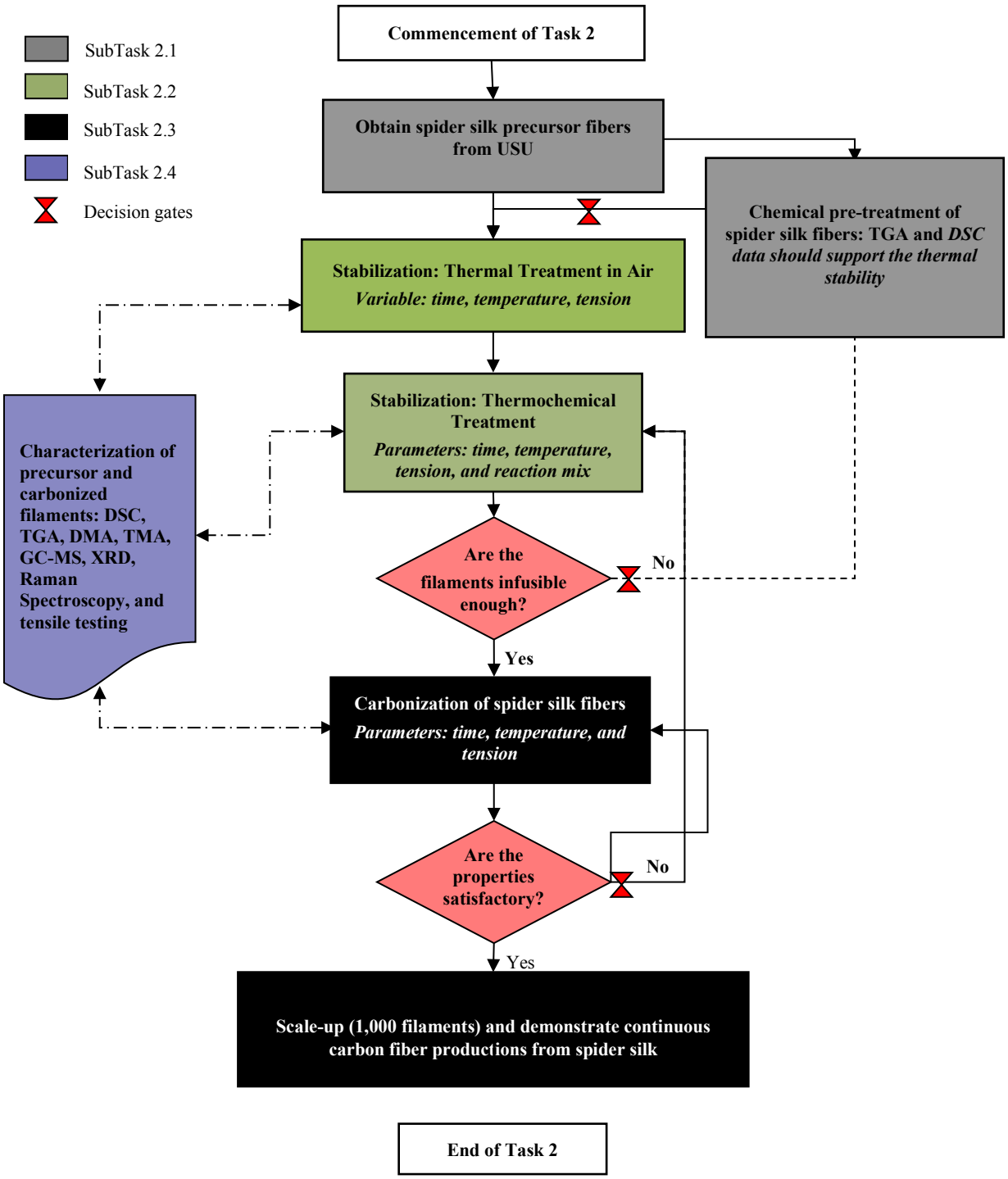

Figure IV-117: Flowchart for Task 2.

To achieve these goals, spider silk needs to be chemically/physically modified (to suppress crystallinity) without affecting fiber morphology. At the same time, fibers should exhibit high mechanical properties so they can withstand shrinkage force during crosslinking or stabilization. To accelerate stabilization, we will use a thermal component during the process. Therefore, spider silk precursor fibers need to be rendered for a gradual increase of temperature during the heat treatment process. The technical approach for developing carbonized filaments from a spider silk precursor will most likely involve modification of filaments by a chemical reaction to render them infusible. In the case of PAN-based fiber, thermal oxidation (i.e., incorporation of an oxygen heteroatom in the polymer) cross-links the fiber and increases the glass transition temperature above its melting point and pyrolysis temperature. In the case of spider silk fibers, chemical functionalization might need to be investigated after spinning to form a thermoset plastic. Achieving this occurs by either modifying the starting material prior to spinning without affecting its melt-rheology (spinnability) or through post-spinning modification of fibers. In addition, in order to achieve desired molecular orientation in fibers, pre-stretching would be applied in steam.

Task 3: Techno-Economic Analyses

The scope of the modeling work is focused on critical evaluation of the proposed process on the metrics of economics and environmental impact. A critical component of the modeling work is the integration of experimental data for validation and data feedback to experimental systems. Scope is divided into two performance periods. The first period focuses on the development of engineering process models and integration with economic evaluation. The second performance period will continue to refine economic modeling, while leveraging engineering process models for lifecycle assessment. Results from the first performance period will be an economic assessment of the proposed process and data feedback highlighting areas for improvement. Results from the second performance period will include updating economic models based on experimental results and quantifying the environmental impact of production and use of the proposed technology. Task 3 includes two subtasks.

Subtask 1: Development and Validation of an Engineering Process Model

The first phase of work will focus on development of representative models and integration with the techno-economic assessment. The engineering process model will be composed of multiple subprocess models intended to be representative of large-scale production. Experimental data will be leveraged for subprocess modeling validation. Alternative processing technologies will be evaluated through the modularity of the modeling effort. Proper model function will be assessed through comparison of traditional production systems and sensitivity analysis. Subtask 1 of Task 3 has two milestones:

Milestone 3.1.1: Development and preliminary validation of subprocess models.

Milestone 3.1.2: Integration of subprocess models into large-scale process models.

Subtask 2: Evaluation of the Economic Feasibility of the Proposed Process

Outputs from the subprocess models of the engineering system model will serve as primary inputs to economic modeling efforts. Subprocess models will be individually evaluated for capital and operational costs with results integrated into an equivalent uniform annual benefit assessment. Sensitivity to economic assumptions (such as return on investment) and uncertainty in future economics will be evaluated for an impact assessment. Results from the economics will be used to identify areas for experimental improvements. Subtask 2 has two milestones:

Milestone 3.2.1: Integration of the process model with techno-economic modeling.

Milestone 3.2.2: Processes optimization and identification of priority experimental parameters on the metric of economic viability.

We created two system models with variable inputs to be able to analyze three scenarios. Material prices were sourced online from a variety of industrial vendors from Alibaba.com and Sigma Aldrich. The Results and Discussion section presents a table that shows all price inputs for the three models. All of the models include a

setup of 24 fermenters, each with a capacity of 20,000 L of expression media to be representative of a large-scale production facility. Total protein production is then dependent on the level of protein expression used for the given scenario and represents a foundational input.

Capital expenses related to equipment were determined on the size and specifications of the given process. Equipment modeling was done with any of the following methods or a combination of them, depending on the availability of information (i.e., material consumption for equipment construction with a manufacturing and resale scale-up factor, Aspen Plus Economic Analyzer, or industrial equipment pricing from various sources scaled to model production size). Operational and capital expenses were integrated with standard techno-economic considerations on price calculations, including interest on loans, capital investment, and depreciation.

Results and Discussion

Task 1. Fiber Synthesis

Subtask 1. Fiber Production

We have exceeded the go/ no go milestone of 1.0 g/L of one purified spider silk protein (MaSp2). We were able to purify 6.2 g of protein from 5 L of culture media. Another protein has yielded nearly 4 g/L from fermentation. The two other proteins are at the 1.0-g level. The aciniform spider silk generated during the second quarter of FY 2015 is now being expressed and will be scaled up to production. This silk contains a higher proportion of larger amino acids, aiding in carbonization.

We are still working on a pH-dependent solubilization and precipitation method, which, for at least some proteins, will eliminate the affinity column step and greatly decrease production costs. It remains to be determined if this process can be adapted for all different silk proteins, but at least two of the first three tested worked. Figure IV-118 shows the results.

The purified spider silk protein can be seen as the band between 100 and 150 kD, which is correct for this 120-kD version of MaSp2. The improved purity is clear between Lanes 1 and 2 or 6. The protein is over 90% pure and full length with the new method and has a much lower level of smaller protein products. Lane 1 is below 75% of the full-length protein.

In addition, we are testing whether even lower fermentation temperatures during expression (16°C versus 25°C) will increase protein production when expression is allowed to continue for 16 hours versus the current 4 hours. Preliminary data with just one protein indicate more protein production with more of the protein remaining soluble. Finally, we have received our new flow-through centrifuge after the major manufacturing delay, which will allow us to speed up both bacteria collection from the fermenter and removal of cell debris.

Subtask 2. Fiber Spinning

We have successfully spun an eight-fiber thread (one of our goals from our second quarter FY 2015 report) with several different proteins under various conditions but have found that, during the post-spin draw needed for maximal mechanical properties (which is done in aqueous based baths), the individual fibers tend to fuse. This leads to lower mechanical properties than desired. Therefore, we are altering the post-spin process to allow the fibers to dry more before placing on the winder spool.

We have designed and tested the photo-induced crosslinking system for the fibers. This system will lead to internal crosslinks between the spider silk proteins and help stabilize the fiber to carbonization. We will continue this testing.

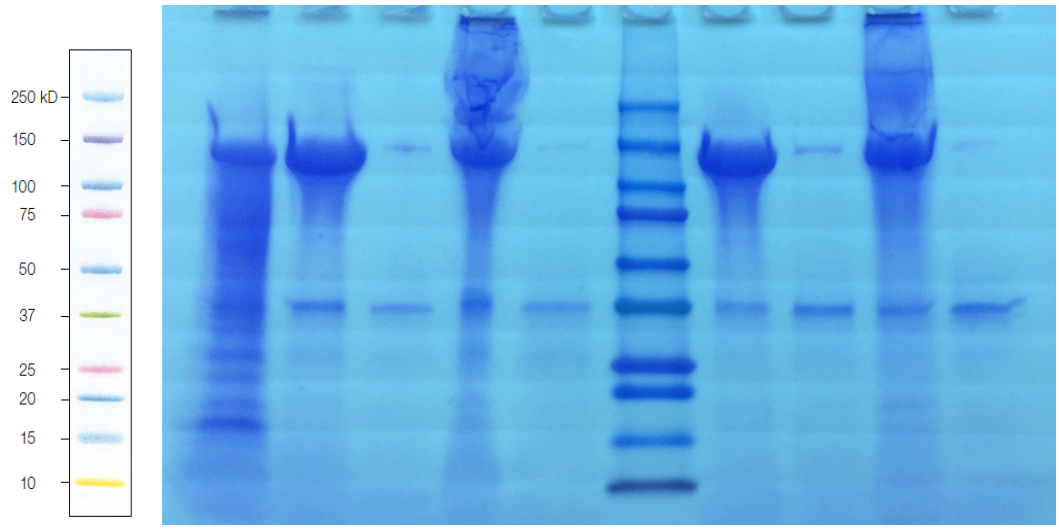

	1	2	3	4	5	Standard	6	7	8	9
Protein	MaSP2	MaSP2	MaSP2	MaSP2	MaSP2		MaSP2	MaSP2	MaSP2	MaSP2
Urea	2M	2M	2M	2M	2M		2M	2M	2M	2M
Heated, 90°C	No	Yes	Yes	Yes	Yes		No	No	No	No
Column	Ni	—	—	—	—		—	—	—	—
$(NH_4)_2SO_4$	—	10%	30%	10%	30%		10%	30%	10%	30%
Dired Sample	Yes	Yes	Yes	No	No		Yes	Yes	No	No
Protein (mg)		180					150			

1. MaSp2 (M4) from Ni column purification, 3 mg/ml.
2. Weight 5 g MaSp2 (M4) E coli cell pellet; add 15-ml lysis buffer with 2 M urea to the cell pellet; sonicate x 2 10 min at 20% power; heated to 90°C 20 minutes with stirring; centrifuge, take 10 ml supernatant and add 1 ml saturated $(NH_4)_2SO_4$; centrifuged; use the supernatant for sample 3; washed precipitant 3 times with pure water; free-dried overnight, weigh the protein and then add 2 ml H_2O to the precipitant; microwave heated to 130°C; centrifuge; mix supernatant 1:1 with sample buffer; heated at 99°C 20 minutes, centrifuged; load the solution to the gel.
3. Add another 2-ml saturated $(NH_4)_2SO_4$ to the supernatant in Sample 2; centrifuged; washed precipitant three times with pure water; free-dried overnight, weight the protein and then add 2-ml H_2O to the precipitant; microwave heated to 130°C; centrifuge; mix supernatant 1:1 with sample buffer; heated at 99°C 20 minutes, centrifuged; load the solution to the gel.8.5 mg M3 from Mike, 2.8 ml H_2O (3.0 mg/ml), dissolved by micro wave, mixed 1;1 with sample buffer, heated at 99°C 20 minutes, centrifuged.
4. Same as Sample 2, but the final sample was not dried ovenight at the freeze dryer.
5. Same as Sample 3, but the final sample was not dried ovenight at the freeze dryer.
6. Same as Sample 2, but the E. coli lysis solution was not heated at 90°C.
7. Same as Sample 3, but the E. coli lysis solution was not heated at 90°C.
8. Same as Sample 4, but the E. coli lysis solution was not heated at 90°C.
9. Same as Sample 5, but the E. coli lysis solution was not heated at 90°C.

Figure IV-118: SDS-PAGE analysis of extractions.

Subtask 3. Silkworm Silk

The proposed method of gene replacement, rather than the standard gene random integration, produced new lines of silkworms. The best silk from those cocoons is greater than 90% of the strength of spider silk and contains up to 10% spider silk protein, both of which are better than previous work from our laboratory and others. Table IV-50 shows the mechanical properties for the control and transgenic silk fiber and Figure IV-119 illustrates the stress-strain curves for control and transgenic silkworm silk. The HC samples are three different transgenic silkworm lines and the controls are non-transgenic lines. We have generated several hundred meters of 25-fiber thread and delivered this thread to ORNL to start developing the needed carbonization process. We are also using that thread to make knit fabrics.

Table IV-50: Control and transgenic silk fiber mechanical properties.

Sample	Energy to Break (MPa)	Max Stress (MPa)	Max Strain (ε)	Diameter (μm)
HC2-8	152	912	0.27	9.2
HC2-10	150	913	0.25	9
HC3-12	173	931	0.28	9.1
Control1-5	65	507	0.18	8.70
Control 2-6	75	554	0.21	8.6

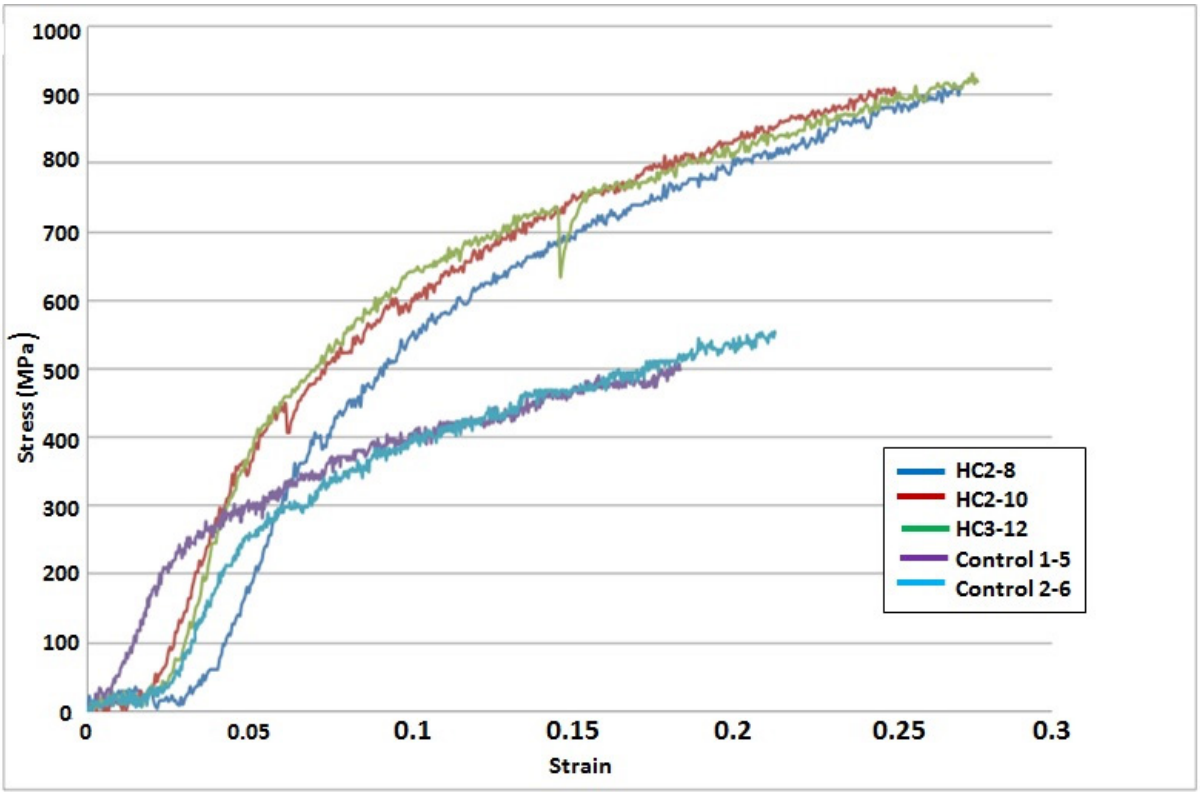

Figure IV-119: Stress-strain curves for control and transgenic silkworm silk.

Note that both the similar shapes and values for the different transgenic silkworm lines is very similar to variation in the controls.

Task 2. Carbonization

Although there are no milestones yet for Task 2, we have included preliminary work leading up to those milestones using transgenic silkworm silk because we have large quantities and, as described above, we have surpassed our milestone for the mechanical strength of this silk fiber.

Spider silk's (i.e., a protein fiber containing rich beta sheet confirmations) thermal characteristics are being investigated by means of differential scanning calorimetry (DSC) and thermogravimetric analysis (TGA)

techniques. Results shown in Figure IV-120 and Figure IV-121, respectively, are for analyses on the spider silk produced. The onset of exothermic and endothermic processes is apparent in the material at temperature around 250°C, depending on the atmosphere of the experiment. An inert nitrogen atmosphere produces a dominant endothermic reaction, while, in contrast, the presence of air yields an exothermic reaction. The exothermic reaction is likely due to polypeptide chains beginning to vaporize into variant gaseous species, while the endothermic reaction is possibly indicative of partial cross-linking processes.

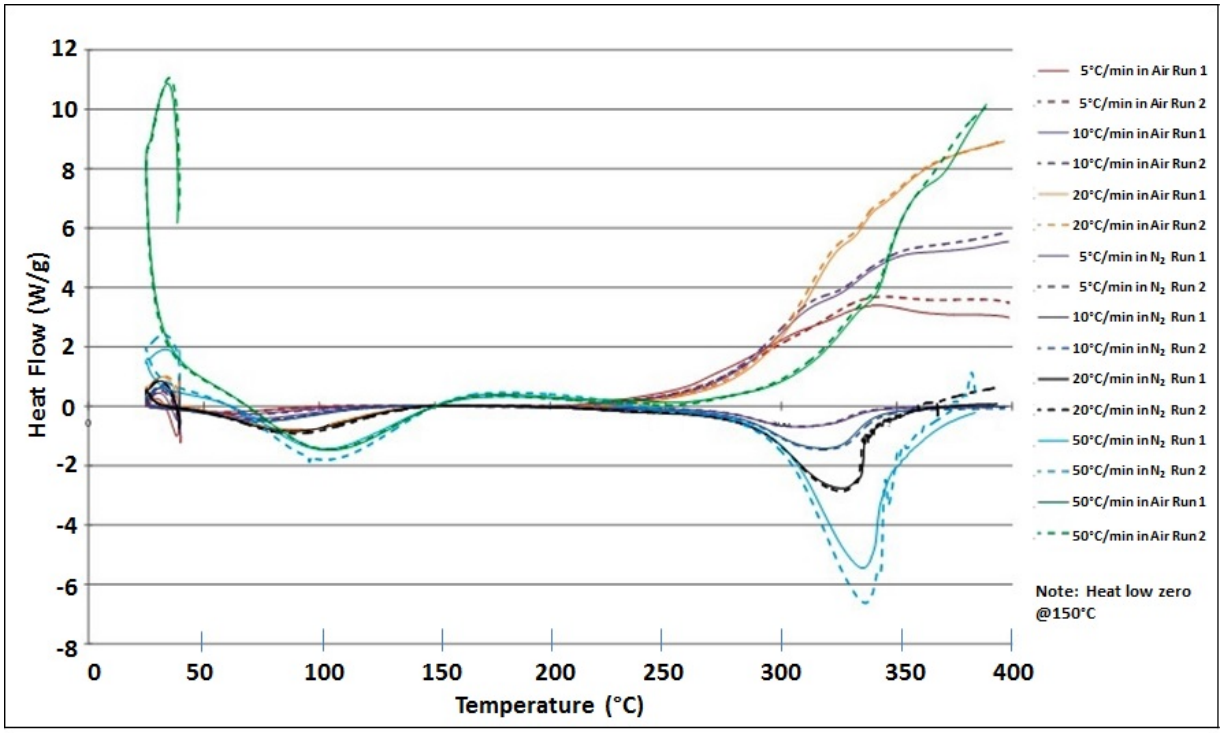

Figure IV-120: Differential scanning calorimetry study at different heating rates and in air and nitrogen-controlled atmospheres – silk runs at various ramps in nitrogen and air.

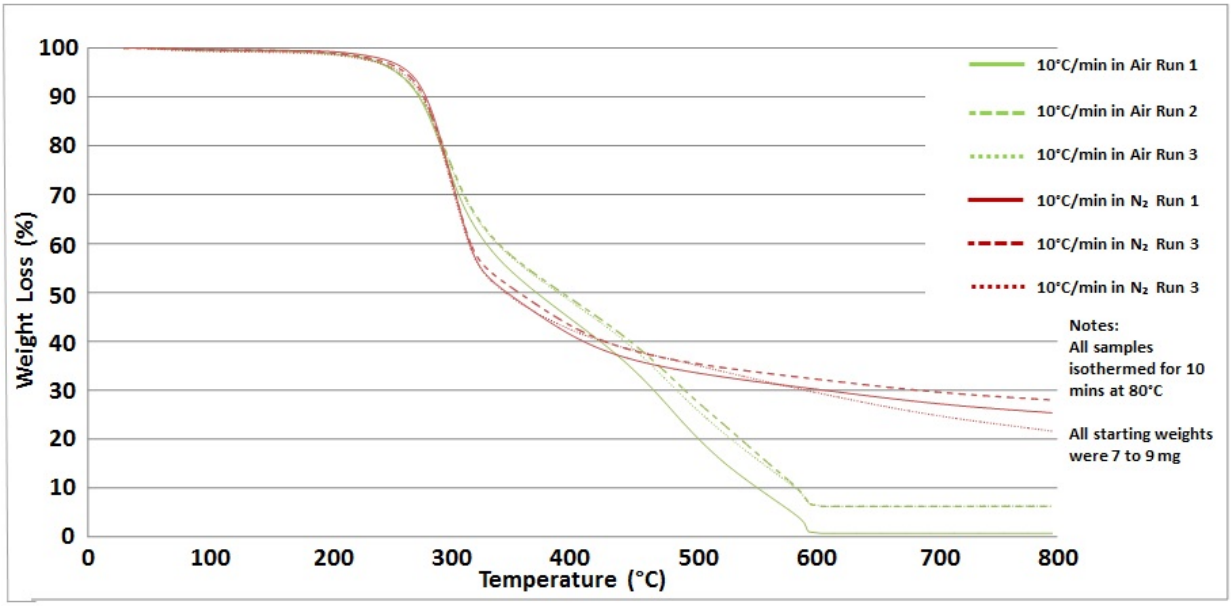

Figure IV-121: Thermogravimetric analysis of fibers in air and nitrogen – larger silk samples run in TGA.

The silk fibers tested under nitrogen shown in Figure IV-120 retain residual mass at around 20 to 30%, which could be associated with carbon yield. This mass loss behavior may be improved by increasing the stabilization time within the range of 150 to 250°C at the onset of the crosslinking process, while then maintaining an inert atmosphere at higher temperatures to avoid the destructive exothermic reaction.

Further TGA experimentation results shown in Figure IV-122 include isotherms at 150, 175, 200, 225, and 250°C for 45 minutes each with both air and nitrogen samples, then a constant ramp rate of 10°C/minute to a temperature of 600°C under an inert nitrogen atmosphere. This experiment depicts a stepwise slope as thermal degradation and stabilization start to take place in this temperature range. As seen in Figure IV-122, the increase in residence time within the temperature range of 150 to 250°C shows that the residual mass can be increased up to 40% at 600°C compared to 30% at 600°C. This experiment indicates that more of the material has stabilized and survived the heat treatment and has promising results for further optimization.

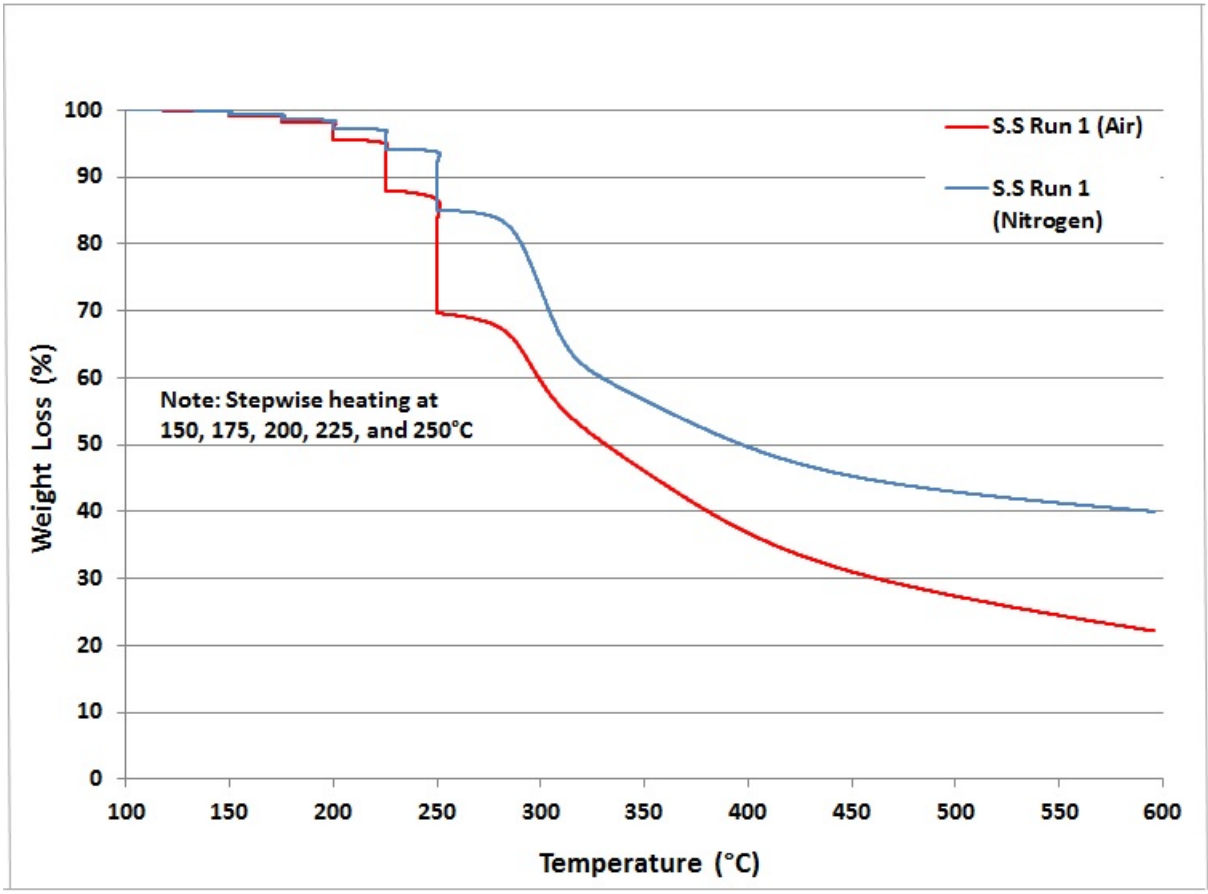

Figure IV-122: Simulation of stabilization TGA isotherm process with stepwise heating rate in between 150 and 250°C.

The conditions of the mechanical tests (Table IV-51) were at the onset of thermal degradation and stabilization by cross-linking. The strain at break percentage gradually decreased from 17.97 to 8.29% with an increase of temperature and residence time, which is indicative that more crosslinking has occurred and the fiber has become less elastic. Slight color changes to a darker hue were reported for temperatures above 200°C, signifying that the chemical reactions that had taken place were producing a partially crosslinked structure.

Based on preliminary results obtained, we will proceed with this study by using a continuous oven process. For this reason, we designed and purchased a stabilization oven and fiber movement system. Table IV-52 gives the design specifications for this system and Figure IV-123 shows the oven/stretcher assembly.

Table IV-51: Mechanical properties of spider silk precursor under varying conditions of residence time and temperature (RT – room temperature, VAC – vacuum).

Sample (Heated at Constant Temperature for 16 hours)	Diameters (µm)	Measurements		
	Optical Microscope	Peak Stress (Ksi)	Modulus (Msi)	Strain at Break (%)
Spider Silk As Received	9.07(1.32)	93.2(30.9)	2.7(1.0)	12.37(3.78)
Spider Silk Dried RT in VAC	10.38(1.25)	46.1(14.0)	1.7(.3)	10.49(7.22)
Spider Silk Dried 80C in VAC	10.60(1.25)	63.4(17.2)	1.7(.4)	18.05(3.82)
Sample(Heated at Constant Temperature in Nitrogen for Different Times)				
Spider Silk Dried at 160C Constant Length for 2 hours	10.12(.65)	81.9(19.2)	2.2(.4)	17.97(3.34)
Spider Silk Dried at 160C Constant Length for 4 hours	9.81(.76)	72.1(17.7)	2.1(.5)	15.61(4.57)
Spider Silk Dried at 200C Constant Length for 4 hours	10.09(1.14)	75.9(21.1)	2.7(1.0)	8.29(2.79)

Table IV-52: Design specifications for the stabilization oven and fiber movement system.

Overall Assembly	Stretcher	Oven	Load Cell
Length: about 8.5 feet	Process Speed: 0.18 to 32 mm/min	Operating Temperature: ambient to 250°C	For low count fiber tows (maximum 1 Newton)
Height: about 4.5 feet	Maximum Pulling Force: 10 kilogram	Air Flow: 5.4 cubic feet per minute	Replaceable to 100 Newton load cell for larger tow (24,000)
Width: 2 feet	Power Requirements: Alternating current, 208 Volts, 3 phase, 60 hertz	Heated Length: 24 inches	Power required: 110 Volt
—	—	Two proportional-integral-derivative controllers for temperature control	—
—	—	Power required: 110 Volt, 20 Amperes	—

Notes: Heights of oven, stretcher, and load cell are adjustable.

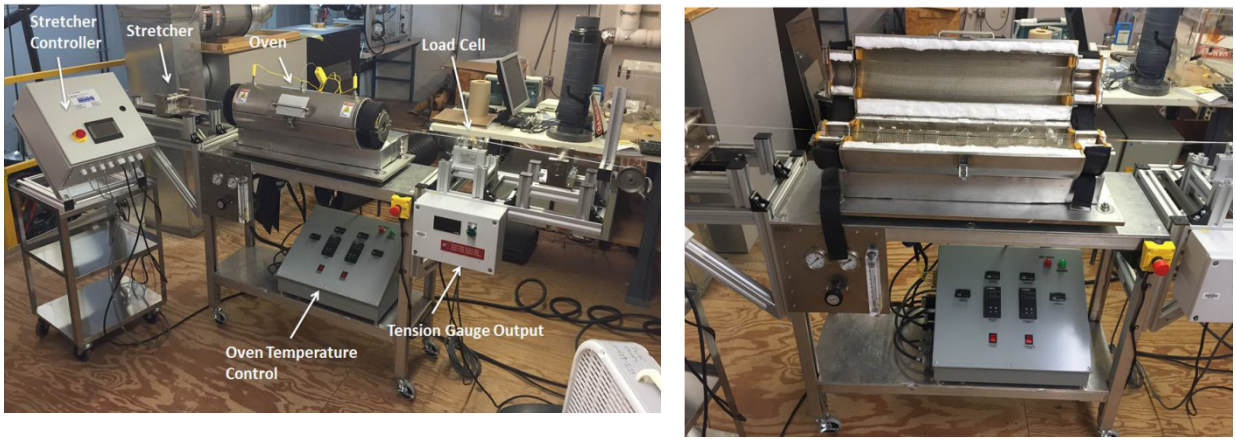

Figure IV-123: Two-foot oven/stretcher assembly.

Task 3. Techno-Economic Analyses

Milestone 3.2.1 was integration of a process model with techno-economic modeling. We created two system models with variable inputs to be able to analyze three scenarios. Material prices were sourced online from the industrial vendors Alibaba.com and Sigma Aldrich. All models include a setup of 24 fermenters, each with a capacity of 20,000 L of expression media to be representative of a large-scale production facility. Total protein production is then dependent on the level of protein expression used for the given scenario and represents a foundational input.

Capital expenses related to equipment were determined on the size and specifications of the given process. Equipment modeling was done with any of the following methods or a combination of them, depending on the availability of information, including material consumption for equipment construction with a manufacturing and resale scale-up factor, Aspen Plus Economic Analyzer, or industrial equipment pricing from various sources scaled to the model production size. Operational and capital expenses were integrated with standard techno-economic considerations on price calculations, including interest on loans, capital investment, and depreciation. Table IV-53 presents all economic inputs used in the analysis.

Table IV-53: Techno-economic analysis input variables.

Techno-Economic Analysis Inputs	Value
Investment Capital	40%
Loan Interest (Equity)	10%
Loan Term (Years)	10
Working Capital (% of FCI)	5%
Internal Rate of Return	10%
Income Tax Rate	35%
Plant Life (Years)	20
Depreciation Periond (Years)	7

The minimum selling price of spooled spider silk is shown in Table IV-54 in terms of dollars per kilogram ($/kg) and dollars per pound ($/lb).

Table IV-54: Minimum sale price for spider silk in three different industrial production scenarios.

Case	Scenario	$/kg	$/lb
1	Laboratory: Laboratory processes and production rates modeled to industrial scale	$537.79	$244.41
2	High Productivity: Laboratory processes with high production rates modeled to industrial scale	$192.96	$87.71
3	Optimized Commercial Production: Potential production rates with experimental processes at industrial scale	$11.12	$5.05

A breakdown of the cost further solidifies data observed in the sensitivity analysis, highlighting factors that affect minimum sale price most significantly. A cost breakdown for each of these scenarios (Table IV-54) is presented in detail in the following sections

Case 1: Laboratory

The total cost breakdown for this scenario is presented in Figure IV-124. The majority of the cost contribution comes from material consumption. In this scenario, each of the processes, material consumption, and production rates have been mapped and scaled directly from the laboratory to an industrial scale. Because the laboratory is primarily concerned with proof-of-concept and not cost, it is expected that the results are not favorable. Some of the materials being consumed are used in excess to improve protein recovery. Economic analysis shows material use is not justified based on economics.

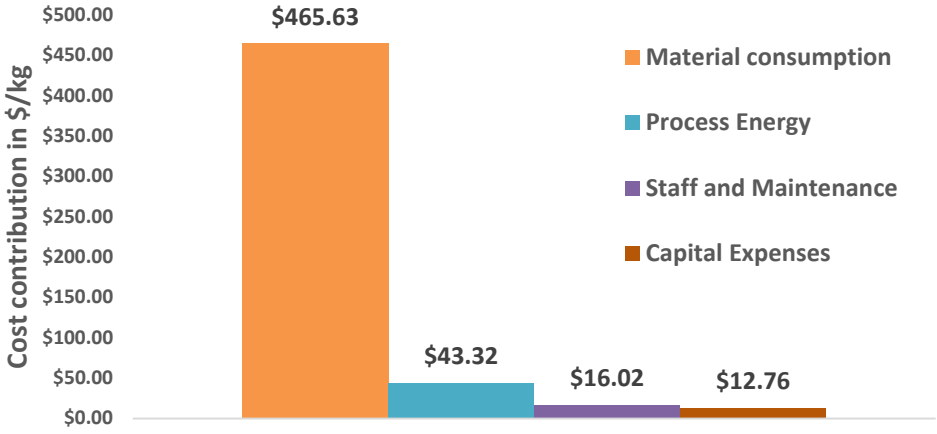

Figure IV-124: Basic price breakdown for Case 1 of industrial spider silk production.

Case 2: High Productivity

From observation in the laboratory, not all protein is harvested during the harvesting and purification steps. All inputs for Case 2 are identical to Case 1, except for the change in harvestable expressed protein. In this case, an assumption was that 2.8 grams per liter are harvested per liter of induced media. This value has been demonstrated in the laboratory and represents a realistic near-term production level. Figure IV-125 shows the total cost breakdown.

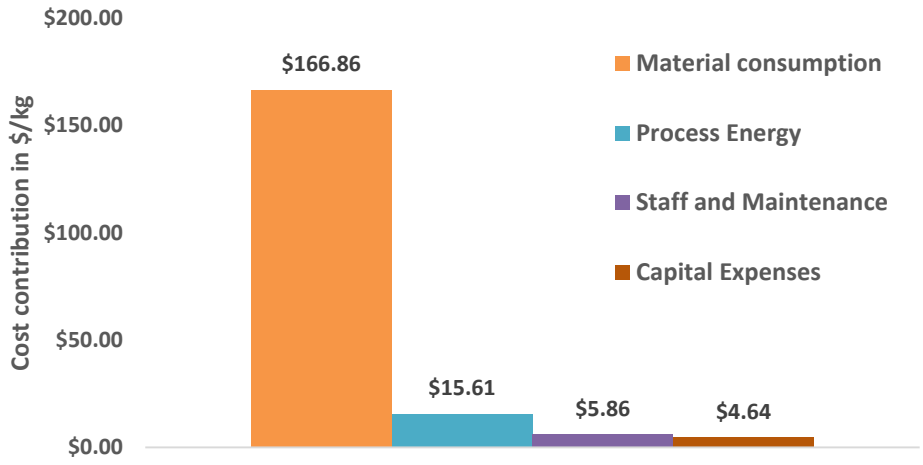

Figure IV-125: Basic price breakdown for Case 2 of industrial spider silk production.

The amount of harvested protein has minimal impact on material consumption; therefore, distribution of material costs is almost identical to that of Case 1. The only significant change in material consumption is the amount of material and energy expended during the fiber spooling process; however, because these are small

compared to the total, almost no change is observable in the overall distribution. The thing of most importance to note is the decrease in minimum selling price, which is directly impacted by the protein yield as it is the functional unit.

Case 3: Optimized Commercial Production

The final case involves integrating alternative subprocess technology that represents large-scale commercially viable alternative processing steps compared to laboratory processes. Several elements play a key role in reducing the cost of protein production for Case 3. The first of which begins with heat shock induction in the expression stage of fermentation. The laboratory uses isopropyl-β-D-thiogalactoside (IPTG) to induce the *E. coli*, which is a very costly substance. Because energy is not costly, this results in a dramatic decrease in material cost for production of protein. Conservatively assuming that the efficiency is low in transferring energy quickly to the reactor, the costs associated with this process are still much lower than that of using IPTG. Partial recycling of used media is also incorporated into this model, further offsetting the costs of fermentation in comparison to Case 1.

In this case, we accomplished harvesting by using a combination of salt precipitation extraction with Urea instead of a chromatography column, as done in the laboratory. With elimination of the chromatography column used in Case 1 and 2, the need for many of the expensive materials used in the buffers has been removed. Urea is a much cheaper substitute and, though large quantities are used, it does not affect the price adversely because it is a readily available and an inexpensive commodity. The decrease in disposed media also plays a big role in cost reduction. With less media needing to be disposed of, less bleach needs to be purchased as a sterilizing agent.

The final assumption in Case 3 is that harvestable protein expression has reached 20 g/L. This amount of harvestable protein represents a realistic near-term achievable amount because of a new harvesting method used. At a production rate of 20 g/L, the materials used in fermentation are being used at a highly efficient rate for protein production. Figure IV-126 shows the cost breakdown for Case 3.

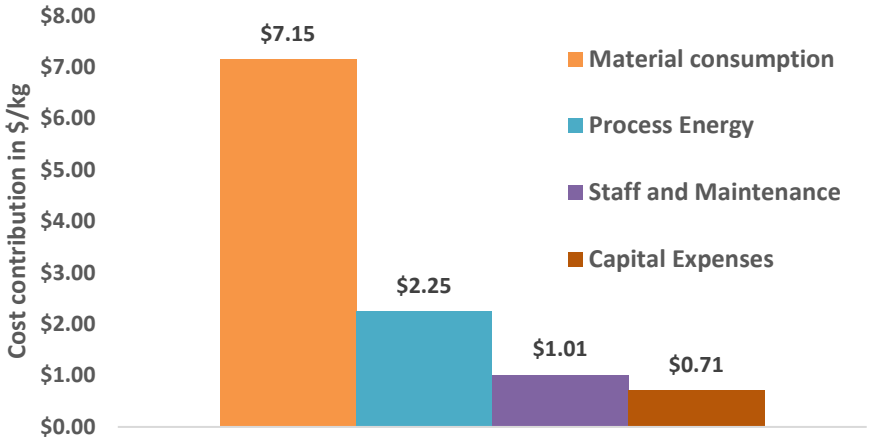

Figure IV-126: Basic price breakdown for Case 3 of industrial spider silk production.

At this point, energy consumption, staff, and maintenance begin to play a bigger part in the overall cost of spider silk production. The initial capital expenses, however, do not contribute much to the overall cost of production. In Case 3, more energy is consumed in a year by the production facility, but because production is so much higher, the contribution is a smaller fraction of the total cost than in Case 1.

Economics of Transgenic Silkworms

The economics of production of synthetic spider silk through silkworms will be similar to that of traditional silk from silkworm growers. The methods of sericulture for transgenic silk worms are identical to that of

traditional sericulture. From this point in the research, three growth options are available that protect intellectual property but also affect the minimum sale price. The first option is that sericulturists could pay a large initial cost to purchase transgenic eggs and then be able to grow their cocoons at their own rate. The second is to produce a hybrid spider silk worm such that the transgenic qualities are only present in a single generation. With every generation, the sericulturist would be required to purchase more transgenic eggs. The third option is similar to the first, except that as part of the transgenic development, a "kill switch" is provided. Essentially, the transgenic silkworms will need a special food or nutrient in their diet or they will die. The owner/operator of the intellectual property would sell this special food or nutrient.

The costs associated with production are the same as traditional silk, which currently sells at a price between $5 to $60/kg. Depending on the method used to secure intellectual property, the price of transgenic silk will vary. Based on supply and demand, the price silk from a spider silk silkworm could be reasonably assumed to initially have a higher price. However, as supply increases, the prices should normalize. Current work is being done to refine and better understand the actual selling price for synthetic spider silk through a silkworm production method.

Technology Transfer Path

We currently are discussing a joint research effort with an automobile parts designer in California and a presentation to the DOE Automobile Materials Team.

Conclusion

Task 1. Fiber Synthesis

Subtask 1. Fiber production: We have exceeded the go/no go milestone of 1.0 g/L of one purified spider silk protein (MaSp2). We were able to purify 6.2 g of protein from 5 L of culture media. Another protein has yielded nearly 4 g/L from fermentation. The two other proteins are at the 1.0-g level, allowing us to move forward with production to begin the carbonization process.

Subtask 2. Fiber spinning: We have successfully spun an eight-fiber thread with several different proteins under various conditions and are in the process of building a 25-fiber spinning head. We have designed and tested a photo-induced crosslinking system for the fibers. This system will lead to internal crosslinks between the spider silk proteins and help stabilize the fiber to carbonization. The ability to spin 25 fibers and photo-crosslink the proteins during the spinning process is critical to producing fiber bundles for carbonization.

Subtask 3. Silkworm silk: We produced new lines of transgenic silkworms using gene replacement rather than standard gene random integration. The best silk from those cocoons is greater than 90% of the strength of spider silk and contains up to 10% spider silk protein, both of which are better than previous work from our laboratory and others and exceed our milestones. We have generated several hundred meters of 25-fiber thread and delivered to ORNL for them to start developing the needed carbonization process. We are also using that thread to make knit fabrics.

Task 2. Carbonization

Although there are no milestones in Year 1 for Task 2, we have conducted preliminary work leading up to those milestones using transgenic silkworm silk because we have large quantities and (as described above) we have surpassed our milestone for the mechanical strength of this silk fiber. Based on obtained preliminary results, we will proceed with this study by using a continuous oven process. For this reason, a stabilization oven and fiber movement system were designed and installed.

Task 3. Techno-Economic Analyses

For Milestone 3.2.1 of Task 3, we created two system models with variable inputs to analyze three scenarios: laboratory, high production, and optimized commercial production scales. In all of these scenarios, the major cost is materials; therefore, efforts are now underway to reduce that as much as possible. Total protein production is dependent on the level of protein expression in all scenarios and increasing protein production leads to a direct linear decrease in fiber costs. For the silkworm model, there appear to be no barriers to production costs being similar to current silkworm silk prices.

References

1. P. Oliviera; G. Bhattacharyya; J. Jones; and R. V. Lewis, 2016, "High level expression of spider silk proteins," manuscript in preparation.
2. T. Harris; J. Jones; P. Oliviera; G. Bhattacharyya; and R. V. Lewis, 2016, "Aqueous spinning methods for spider silk protein fibers," manuscript in preparation.
3. C. Copeland; B. Bell; C. Christensen; and R. V. Lewis, 2015, "Development of a Process for the Spinning of Synthetic Spider Silk," *ACS Biomaterials Science and Engineering*, 7; pp. 577–584, DOI: 10.1021/acsbiomaterials.5b00092.
4. D. Gil; T. Harris; J. Jones; and R. V. Lewis, 2016, "Crosslinking improves strength in spider silk protein materials," manuscript in preparation.
5. F. Teulé; A. Cooper; W. Furin; D. Bittencourt; E. Rech; A. Brooks; and R. V. Lewis, 2009, "A protocol for the production of recombinant spider silk-like proteins for artificial fiber spinning," *Nature Protocols*, 4; pp. 341-355.
6. F. Teulé; Y. Miao; B. Sohn; Y. Kim; J. Hull; M. Fraser Jr.; R. V. Lewis; and D. Jarvis, 2012, "Silkworms Transformed with Chimeric Silkworm/ Spider Silk Genes Spin Composite Silk Fibers with Improved Mechanical Properties," *Proc Natl Acad Sci,* 109(3); pp. 923-928.

V. Multi-Material Joining

V.1. Friction Stir Scribe Joining of Aluminum to Steel – Pacific Northwest National Laboratory

Project Details

Yuri Hovanski, Principal Investigator
Pacific Northwest National Laboratory
902 Battelle Boulevard
Richland, WA 99352
Phone: 509-375-3940
E-mail: yuri.hovanski@pnnl.gov

Sarah Ollila, Technology Area Development Manager
U.S. Department of Energy (DOE)
1000 Independence Avenue, SW
Washington, DC 20585
Phone: 202-586-8027
E-mail: Sarah.Ollila@ee.doe.gov

Contractor: Pacific Northwest National Laboratory
Contract No.: DE-AC05-00OR22725 and DE-AC06-76RL01830

Executive Summary

The purpose of this project is to develop the joining technology needed to demonstrate fabrication of dissimilar aluminum (Al)/steel assemblies that will enable direct replacement of steel components with Al for high-volume applications. The objectives of the proposed work are to overcome the major obstacles of implementing friction stir scribe (FSS) technology in production and to demonstrate the required Al-steel joint strengths in industrially relevant components as defined by the weakest material in the dissimilar metal joint. Specifically, the project will develop the critical process technology, models, and tools necessary for advancing the FSS method through experimentation, validation at the laboratory scale, and integration into a production-like environment to demonstrate the technology on industrially relevant components. Additionally, the purpose is to successfully transfer technological understanding and design tools of FSS joining to the original equipment manufacturers (OEMs) and suppliers to aid in direct joining of Al and steel assemblies and components.

Accomplishments

- Selected three specific alloy and gage combinations for FSS joining; one for each of the three OEM partners according to their desired application (Fiscal Year [FY] 2015).
- Received and sized hundreds of Al and steel sheets from each of the three OEMs in preparation for weld development, characterization, testing, and validation (FY 2015).
- Designed, fabricated, and tested more than 50 FSS tools supporting development of each of the three combinations of Al/steel (FY 2015)
- Established welding parameters, tool design and process specifications to produce defect-free FSS joints with strength similar to parent steel sheet for a AA6022 (1.0 mm)/mild steel (0.7 mm) combination. (FY 2015)
- Developed weld parameters for Al sheet to martensitic steel, and cast Al to mild steel at strength levels required by the industrial partners for body and chassis applications. (FY 2015)

- Completed the stationary shoulder design supporting the Al roof ditch demonstration ahead of schedule. (FY 2015)

Future Directions

- Demonstrate the capability of the FSS process to extend to alternative material combinations including progressively higher strength steels up to and including fully martensitic steels.
- Evaluate the feasibility of extending advanced technologies like adjustable pin technology and stationary shoulder to the FSS process to allow greater process flexibility for industrial partners interested in implementing the process for multi-material joining.
- Demonstrate the ability to predict joint properties, failure mechanisms, and locations of FSS joints in Al/steel.
- Complete prototypical technology demonstrations at the facilities of each industrial partner.

Technology Assessment

- Target: Achieve 70% joint efficiency for dissimilar Al/steel joints between various combinations of Al and steel in production environments.
- Gap: Conventional linear solid-state joining techniques for dissimilar material combinations rely on bonding mechanisms that rarely approach the structural strengths of the base materials and cannot adequately manage the interfacial heat of dissimilar materials like Al and steel to remain truly solid state. The temperatures required to plastically form steel are higher than the melting temperature of Al; therefore, intermetallic formation at the joint interface cannot be managed to produce quality, uniform joints.
- Gap: Friction stir scribe has yet to be demonstrated in production environments.

Introduction

This project addresses the joining aspects of lightweight dissimilar metal structures made with Al and steel with the aim of achieving DOE's goal of increasing the efficiency of vehicle transportation by enabling more efficient multi-material solutions. Project collaborators include General Motors (GM), Honda R&D America (HRA), and Fiat Chrysler Automobiles (FCA). They are actively involved in the project by providing materials, demonstration parts, and unique expertise related to the specific hybrid joining needs. KUKA Systems, an automotive supplier and robotic integrator, is another project collaborator providing robotic implementation of the FSS joining method in the automotive supply chain.

The method to be developed, if successful, will enable low-cost joining of a wide range of Al alloys and products to existing steel structures. Success during this project will enable direct replacement of steel components with Al that can achieve a mass savings of more than 40%, while maintaining the form and function of existing steel components. The project provides a direct injection of joining technology to participating automotive OEMs for Al/steel assembly. Pacific Northwest National Laboratory (PNNL) will develop, characterize, and transfer unique joining parameters for specific applications provided by participating collaborators. This includes applications ranging from body structures to assembly of Al chassis components onto a steel substructure. Each specific application will be developed sufficiently to determine the overall properties, welding parameter operating window, tooling and fixture requirements, and computational design specifications. Upon successful completion of development at the laboratory-scale, each participant will demonstrate a prototypical application-specific mock-up utilizing the FSS process.

Approach

To develop joining technology that enables hybrid Al/steel structures and assemblies for high-volume automotive production lines, the project is divided into four main task areas. The first task focuses on initial joint development and characterization for each of the selected Al/steel combinations associated with the demonstration needs of each OEM. This includes developing weld parameters, tool design, and other process requirements to achieve acceptable joint performance. The second task is designed to expand the overall application of FSS, optimizing tooling, introducing stationary shoulder and retractable pin technologies, and applicability across numerous alloys, thicknesses, and material combinations. This task will ultimately lead to a decision gate for utilization of the developed knowledge base in prototypical demonstrations associated with Task 3 by providing the information necessary to justify capital investments and product design using Al/steel joints. Task 3 is divided into several subtasks areas that will emphasize preparing the process for commercialization and ultimately demonstrating the process in a production-like environment. This task focuses on supporting technology transfer into each of the OEMs facilities/suppliers to allow for prototypical demonstrations by each industrial participant. The final task will utilize information developed in Tasks 1 and 2 to calibrate a numerical modeling tool for prediction of joint performance, failure location, and failure mode, and, finally, to validate the predictive tool against new material combinations and demonstration parts.

Results and Discussion

The project started with a kickoff meeting at the beginning of the third quarter in FY 2014 with participation from the three OEMs (i.e., GM, HRA, and FCA) and one equipment supplier (i.e., KUKA Systems). Each participating member communicated their interests and expectations from the project and representative team, and a schedule for timely execution of the project was established. Combinations of specific Al/steel alloys and gages to be developed for FSS joining were ultimately established for each of the three OEMs based on their unique interests and application-specific needs. While materials were being prepared by OEMs to be shipped to PNNL facilities, associated tool designs and parameter matrices were developed. Figure V-1 shows the stackups of Al/steel combinations and gages used to support eventual technology transfer and demonstration by each industrial participant. Additionally, preliminary tool designs for each material set are also shown in the figure. The tools are depicted plunged into the material at the appropriate depth.

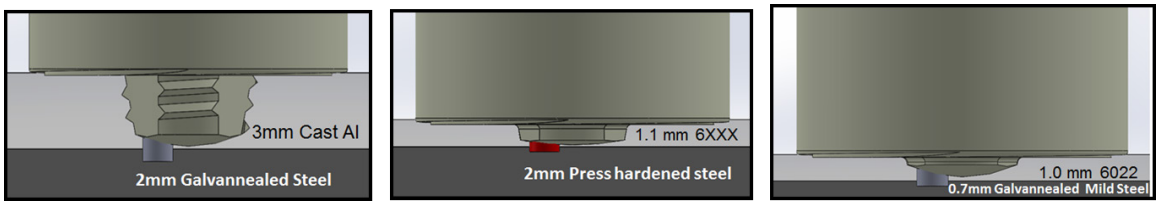

Figure V-1: Three sets of Al-steel combinations and associated FSS tool plunged into the stack up. Material combination was I of participating automotive manufacturers.

A variety of tool designs were considered based on relationships between the tool features and material flow during conventional friction stir welding. Tool geometric features, line radii of the pin tips, features in the pin threads, flats, and tapers have been specifically varied based on alloys and thickness of each unique application. An example of this variation in tool designed for a 3-mm thick cast Al to steel joint is shown in Figure V-2. Several FSS tools were fabricated in various geometries to evaluate the efficacy of material flow in the FSS process. Each tool was fitted with a scribe and had a hole drilled into the pin at an appropriate location, which was in turn fit with a scribe cutter. Care was taken to ensure that the bottom of the scribe was completely seated into the base of the hole to avoid any readjustment of the scribe length during joining.

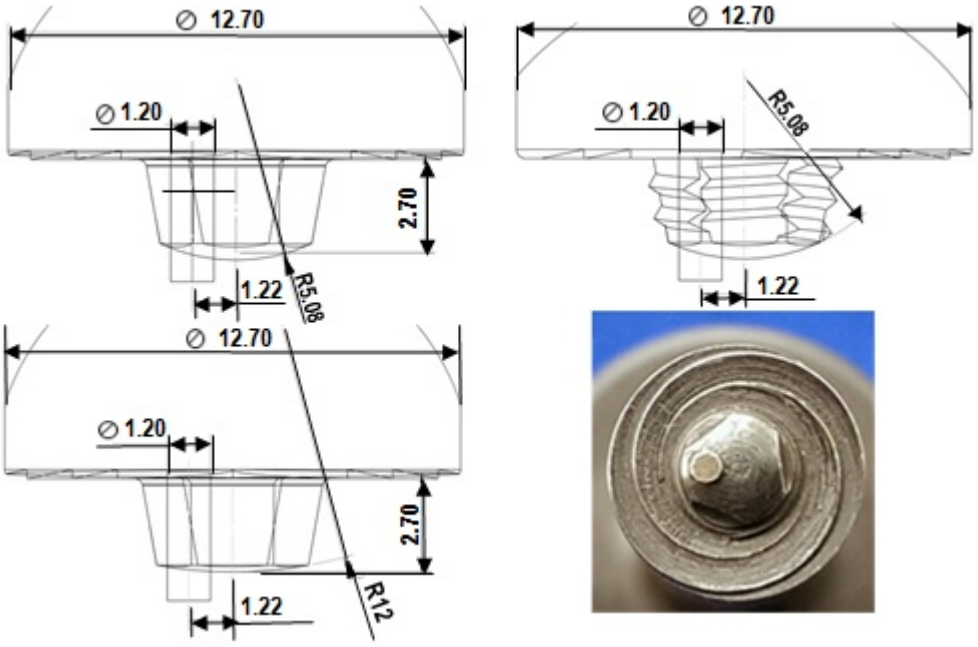

Figure V-2: Tool geometry and feature variation considered for the project. Top view of a typical friction stir scribe tool is shown on bottom right corner.

Several control parameters (such as welding speed, rotational speed, and plunge depth) were varied, which resulted in a wide array of welded coupons for each material combination. Samples were visually inspected and were subsequently evaluated via quasi-static lap-shear tensile testing. Representative joint panels for the three sets of material combinations are shown in Figure V-3.

Figure V-3: Examples of materials combinations being investigated for dissimilar FSS joining of Al-steel.

Owing to the early receipt of materials from our OEM partners, significant progress was made on the AA6022 (1.0 mm) mild steel (0.7 mm) combination. Figure V-4 shows load per unit weld length versus elongation obtained from several joint samples along the length of an Al/steel joint. For reference, the corresponding curve for the base metal properties of the mild steel (i.e., 0.7 mm) is also shown. Welds were produced at linear welding speeds from 250 to 3,000 mm/min and rotational velocities up to 2,000 rpm. For the material set represented in Figure V-4, all samples tested showed a peak load sustained by the joint very similar to that of the parent mild steel sheets. The image on the top left corner of Figure V-4 shows a fractured sample where necking and eventual failure took place away from the weld region. This result shows that for this case consistent joint strength on the order of the strength of mild steel can be obtained.

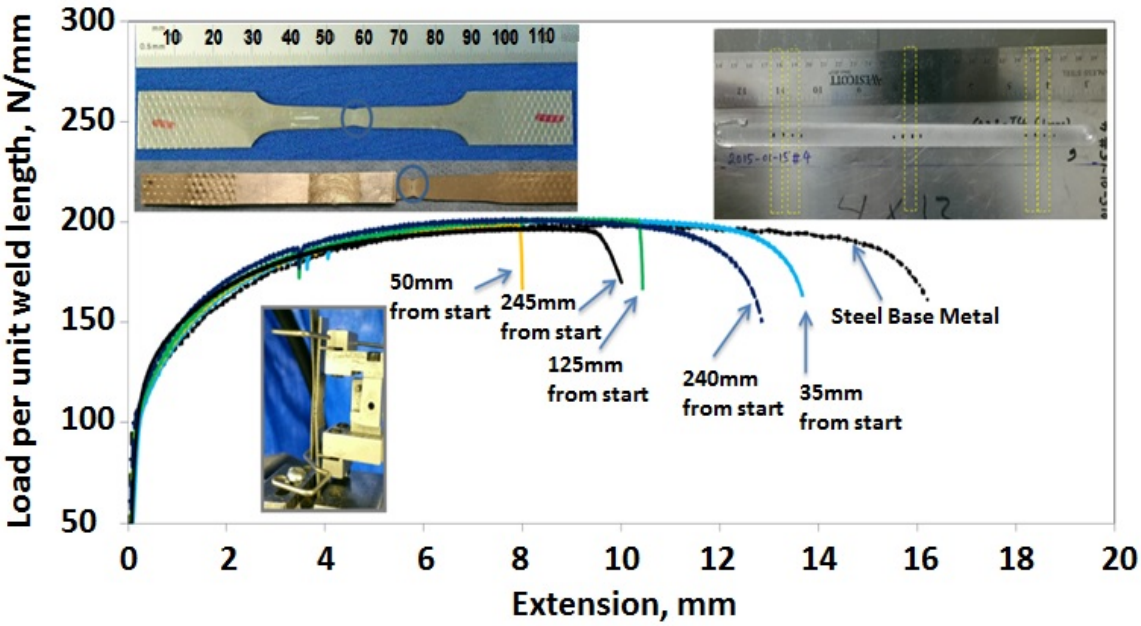

Figure V-4: Load per unit weld length versus extension for five FSS joint samples obtained over a length of the joint as indicated. An E8 subsize tensile sample for mild steel base metal is shown for side-by-side comparison. A representative FSS joint sampl,e showing the location of final fractures, is marked with blue circles (top left corner). A typical lap shear test setup is shown in the bottom left corner.

The morphology of the hook feature at the joint interface (Figure V-5) for three different locations shows very consistent hook formation. Although there are inclusions of some stray steel into the Al nugget, this does not lead to void formation or initiation sites for eventual fracture. There are two aspects of FSS joining that need to be fulfilled in order to obtain a defect-free joint that can perform well in tensile tests. While friction stir welding on the top sheet must be defect free, it is also important to have a complete hook feature at the bottom sheet to form an in-situ joint without causing voids in the plastically deformed Al sheet. This requirement demands precision of plunge depth and scribe length.

Figure V-5: Representative FSS joint cross section for welds made between Al and mild steel.

For every weld produced at PNNL, the process forces experienced by the tool during welding were recorded. This information is critical to equipment suppliers, because it allows informed design assessments necessary to implement robotic FSS joining. A typical force plot measured during the weld discussed above is shown in Figure V-6. Plots similar to this have been provided to the equipment supplier partner.

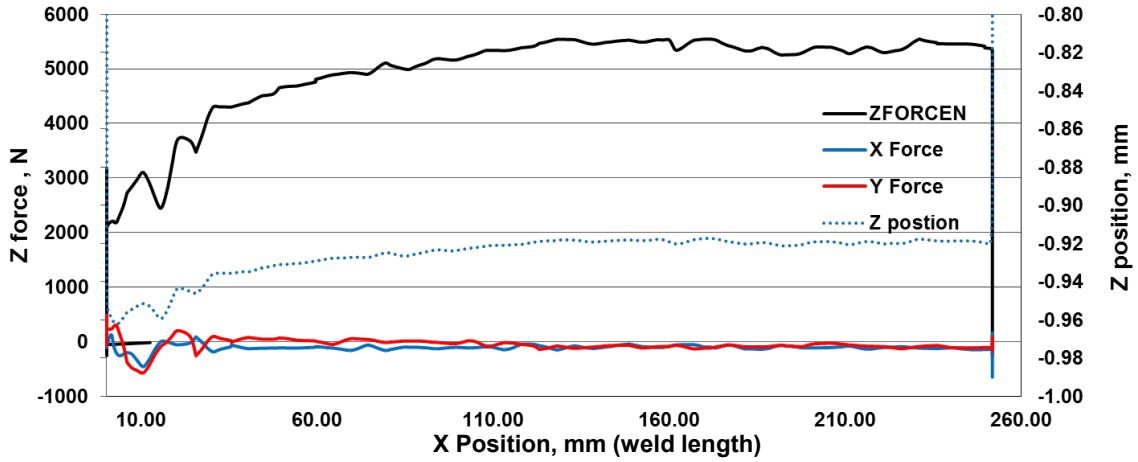

Figure V-6: X, y, and z forces experienced by the FSS tool during the process plotted against the tool position. Z position of the tool is also shown.

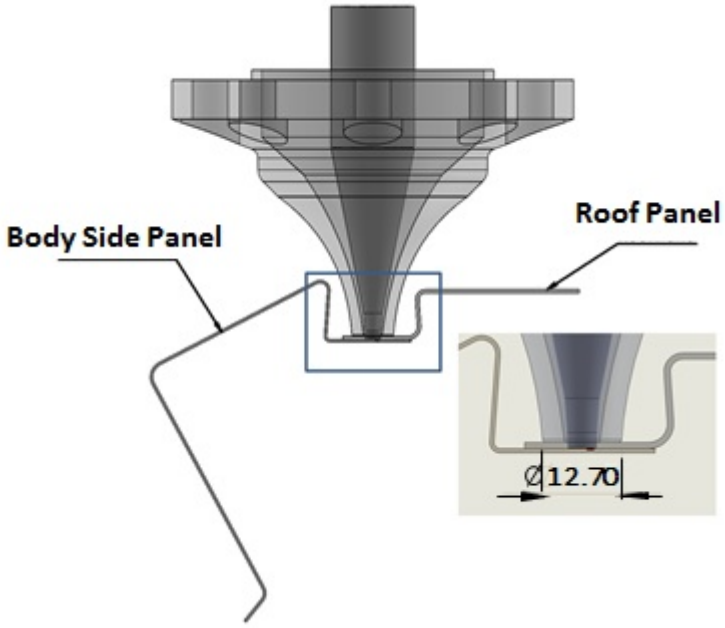

Figure V-7. Schematic of preliminary stationary shoulder FSS design for Al-steel joining for a roof-ditch application.

Moving forward with this material combination, the OEM has shown interest in using this technology to provide prototypical demonstrations on a roof ditch, joining an Al roof panel to a built-up steel structure. In order to accommodate design constraints associated with specific clamping needs, the FSS tool will be modified to a stationary shoulder setup. A stationary shoulder allows for a relatively narrow working space and provides uniformity through thickness material flow. Researchers at PNNL are currently working closely with the OEM team to develop tool design to effectively transfer the FSS process into the OEMs demonstration process. Figure V-7 shows a current conceptual design for the stationary shoulder FSS section for the roof ditch made in association with the OEM.

Progress has also been made on other material combinations. Figure V-8 shows a comparative dataset obtained from lap shear tests for FSS joints made from 3-mm cast Al and 2-mm mild steel. The effects of welding speed on lap shear performance can be gathered from the bar chart. Joints made at 400-mm/minute yield consistently higher joint strength along the length of the weld compared to those at higher welding speeds. Nevertheless, all samples across the welding speed exhibit a load-bearing capacity of 150 N/mm or greater. For higher welding speed cases, the strength corresponding to a joint near the start of the welding is relatively small. Further assessment of joint cross section is expected to provide a guideline for improving the joint strength in higher welding speeds.

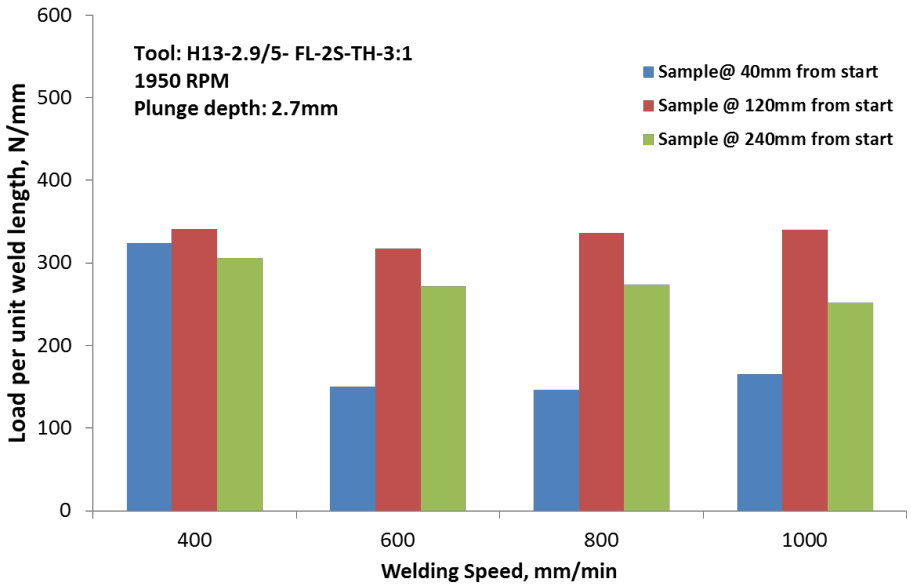

Figure V-8. Load per unit weld length versus welding speed for 3-mm cast Al – 2-mm mild steel FSS joint.

Technology Transfer Path

As one of the primary goals of this project, transferring the FSS process to industrial participants is part of everyday project execution. First, the team brings together multiple automotive OEMs and a robotic supplier into a single team to evaluate FSS of Al to steel in various and unique applications. The project team develops the welding process and provides mechanical testing and characterization throughout development to demonstrate how the technology is applied to various applications. This ranges from thin wrought Al alloys being joined to mild sheet steels to high-pressure vacuum die-cast Al being joined to advanced high-strength steels. Monthly calls bring together the team to evaluate the process, provide opportunities for education and discussion of the nuances of the process, and provide updates on the latest development. This forum provides design guidelines that establish a methodology for applying the FSS process across a more diverse set of materials and, ultimately, strengthens the ability for industrial partners to make informed decisions regarding where and how to implement the FSS joining process for optimized multi-material designs.

Conclusion

Work completed during the first year of the project includes bringing together a team with multiple OEM partners into a working group to develop and transfer the FSS technology to automotive producers. Materials and designs were obtained from each partner to allow for development of process parameters that would meet the needs of each specific prototypical demonstration by the industrial partners. The unique material combinations, thicknesses, and alloys provided ultimately led to the development of numerous unique tool

designs and process parameters specific to each material set. The first year focused on development and validation of each of these initial material sets, demonstrating quasi-static lap-shear tensile results that were consistent and repeatable joint strengths that were appropriate for each specific application. In the development of welding parameters, various characterization methods were used to evaluate the interfacial relationships that ultimately led to the desired performance.

References

None.

Bibliography

Y. Hovanski; P. Upadhyay; S. Jana; and L. S. Fifield, 2015, "Joining Dissimilar Materials with Friction Stir Scribe Technology," presented by Y. Hovanski (invited speaker) at the *4th International Conference on Scientific and Technical Advances on Friction Stir Welding & Processing*, Ordizia, Spain, October 2, 2015, PNNL-SA-112917, PNNL, Richland, Washington.

Y. Hovanski; P. Upadhyay; S. Jana; and L. S. Fifield, 2015, "Joining Dissimilar Materials with Friction Stir Scribe Technology," presented by Y. Hovanski at *MS&T 2015*, Columbus, Ohio, October 7, 2015, PNNL-SA-112917, PNNL, Richland, Washington.

P. Upadhyay; Y. Hovanski; L. S. Fifield; and S. Jana, 2015, "Joining Dissimilar Materials with Friction Stir Scribe Technology," in *The 4th International Conference on Scientific and Technical Advances on Friction Stir Welding & Processing*, PNNL-SA-111642, PNNL, Richland, Washington.

V.2. Chrysler Upset Protrusion Joining Techniques for Joining Dissimilar Metals – FCA US LLC

Project Details

Stephen Logan, Principal Investigator
FCA US LLC
800 Chrysler Drive
Auburn Hills, MI 48326
Phone: 248-512-9485
E-mail: stephen.logan@fcagroup.com CIMS #482-00-13

Chuck Alsup, Project Officer
National Energy Technology Laboratory
3610 Collins Ferry Road
P.O. Box 880
Morgantown, WV 26507-0880
Phone: 304-285-5432
E-mail: charles.alsup@netl.doe.gov

Sarah Ollila, Technology Area Development Manager
U.S. Department of Energy (DOE)
1000 Independence Avenue, SW
Washington, DC 20585
Phone: 202-586-8027
E-mail: sarah.ollila@ee.doe.gov

Contractor: FCA US LLC
Contract No.: DE-EE0006442

Executive Summary

The overall project goal is to develop and demonstrate a robust, cost-effective, and versatile joining technique, known as upset protrusion joining (UPJ), for joining challenging dissimilar metal combinations. UPJ is well suited for joining metal combinations where one of the metals is die cast magnesium (Mg). This project has developed process variants that enable joining Mg die castings to aluminum (Al) and steel sheet components of various thicknesses, strengths, and coating configurations. A variant of the UPJ process, known as upset cast riveting (UCR), is being evaluated for joining mixed metals that do not include die cast components.

Joints produced from these techniques are evaluated with conventional microstructure characterization, joining-induced defect characterization, tensile lap shear testing, cross-tension testing, fatigue energy tests, and drop tower impact energy tests. The joint's galvanic corrosion performance is evaluated using FCA US LLC's prescribed accelerated corrosion testing procedure American Society for Testing Materials (ASTM) G85-A2. This is a cyclic salt fog test that incorporates a small amount of acetic acid. At the end of the corrosion test, selected configurations are re-evaluated for quasi-static, fatigue, and impact performance.

Accomplishments

- Pretreated appropriate Mg die castings for round boss UPJ joining (Fiscal Year [FY] 2014, FY 2015).
- Optimized boss geometry for oval boss configurations using computer-aided engineering simulation tools (FY 2014, FY 2015).
- Produced over 650 round boss UPJ joints from 11 unique material/coating configurations to support mechanical/structural and corrosion evaluation (FY 2015).

- Completed initial (pre-corrosion) mechanical/structural evaluation of round boss UPJ joints, including microstructure evaluations, joining-induced defect characterization, and quasi-static, impact, and fatigue tests of shear and cross-tension joint configurations of 355 Mg to Al and Mg to steel joints (FY 2015).
- Commenced 12 weeks of round boss UPJ accelerated corrosion exposure and post-corrosion evaluation of 350 round boss UPJ joints in 11 unique material/coating configurations of shear and cross-tension joint configurations (FY 2015).
- Obtained 1,200 oval boss test coupons (each including two bosses for a total of 2,400 bosses) to support oval boss UPJ joining process development, modeling correlation work, and assembly of joining test coupons in later tasks (FY 2015).
- Machined and polished final optimized round boss electrode geometries to support process optimization and production of joined assemblies (FY 2015).
- Conducted numerous simulations and physical experiments of oval boss UPJ joints to compare the effects on joint development performance of varying force and current rates throughout the process. This information was utilized during the final process optimization used to produce joints for evaluation (FY 2015).
- Produced over 400 oval boss UPJ joints, including process development and optimization and 220 joints intended for mechanical/structural evaluation (FY 2015).
- Completed initial (pre-corrosion) mechanical/structural evaluation, including microstructure evaluations, joining-induced defect characterization, and quasi-static, impact, and fatigue tests of shear and cross-tension joint configurations of 220 Mg to Al and Mg to steel oval boss joints (FY 2015).
- Developed and optimized UCR geometry using computer-aided engineering simulation tools (FY 2015).
- Obtained 1,000 UCR rivets for process development and test coupon production (FY 2015).
- Optimized UCR joint electrode shapes and process parameters using a combination of extensive simulation and actual physical experiments in order to develop optimum robust head shapes (FY 2015).
- Machined and polished final optimized UCR electrode geometries to support process optimization and production of joined assemblies (FY 2015).
- Conducted numerous simulations and physical experiments of UCR joints comparing the effects on joint development performance of varying force and current rates throughout the process. This information was utilized during final process optimization used to produce UCR joints for evaluation (FY 2015).
- Pretreated appropriate Mg die castings for UCR joining (FY 2015).
- Produced over 500 UCR joints during process development and test assembly production, including 384 test assemblies (FY 2015).
- Initiated pre-corrosion mechanical/structural evaluation, including microstructure evaluations, joining-induced defect characterization, and quasi-static, impact, and fatigue tests of shear and cross-tension joint configurations of 384 steel to Al and Al to steel UCR joints. Sixty tests were completed at the time of this writing. The remaining tests are expected be completed by the end of December 2015 (FY 2015).

Future Directions

- Finish corrosion testing and post-corrosion evaluation of round boss UPJ joints.

- Finish producing UCR joints and conducting mechanical/structural evaluation of these joints, as well as conduct accelerated corrosion evaluation and post-corrosion evaluation of these joints.

Technology Assessment

- Target (Project): Develop a robust, low-cost method of joining Mg die-castings to dissimilar metal components such as Al and steel sheet.
- Gap: No method is currently available for joining Mg die castings to dissimilar metals.
  - Fusion welding cannot be used to join Mg to dissimilar metals because of the formation of brittle intermetallic structures.
  - Although solid state welding should theoretically offer some advantages for joining Mg to dissimilar metals without forming brittle intermetallic formations, experimentation has shown that processing windows must be very narrow in order to be successful.
  - Mechanical joining of Mg die castings with steel fasteners creates a strong potential for galvanic corrosion between the materials. Attempts to rectify this effect were only partially successful because (1) any coatings on the steel fastener typically got damaged during fastener insertion, and (2) attempts to use Al fasteners were typically cost prohibitive.
- Target (Task 1): Develop optimized joint geometry and process parameters for producing robust UPJ joints between Mg and dissimilar metals at industry acceptable cycle times without damaging coatings (where applicable) on the cathodic material.
- Gap: Robust boss and electrode design and process parameters have not been developed to ensure UPJ can be used reliably in volume production applications.
- Gap: Insufficient thermo-mechanical compression material data exists for common die cast Mg alloys.
- Gap: Most common die cast Mg alloys do not have ideal forming characteristics and may be susceptible to cracking during the forging process, even with substantial heat application.
- Target (Task 2): Produce joined assemblies for testing and evaluation.
- Gap: No joined assemblies are currently available for testing and evaluation.
- Target (Task 3): Conduct initial (pre-corrosion) mechanical/structural testing and evaluation.
- Gap: Data do not exist to compare performance of UPJ process to existing joining processes for strength and durability.
- Target (Task 4): Conduct accelerated corrosion testing and evaluation on benchmark self-pierce riveting (SPR) joints and UPJ variants.
- Gap: Data do not exist to compare corrosion performance of the UPJ process to existing joining processes.

Introduction

The UPJ process, shown conceptually in Figure V-9, is similar to heat staking of plastic components. The simplest form of the process uses a cast-in protrusion on a die cast component, which is aligned with a clearance hole in a mating component. An application of force and heat are used to upset forge the protrusion into a larger diameter boss that fills the clearance hole and forms a mushroom-shaped head that solidly locks the two components together.

Die casting is the most common and cost-effective process for producing lightweight Mg components. The UPJ process was conceived primarily for joining Mg die-castings to each other and for joining Mg die-castings

to dissimilar metals. However, prior to this study, there has been relatively little work, other than bolting, aimed at joining components produced from this process.

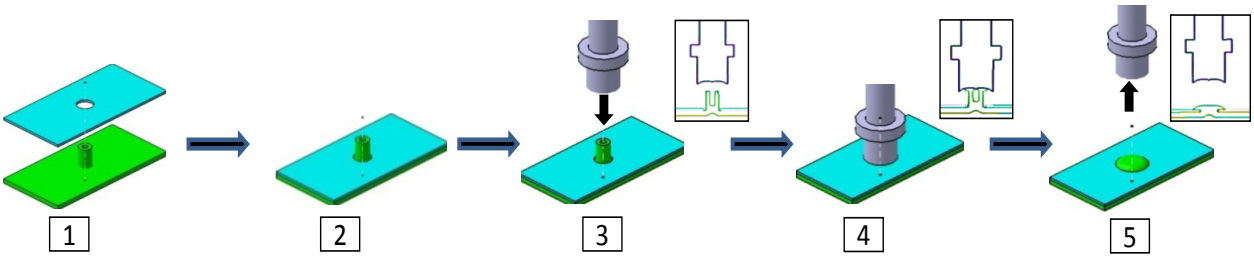

Figure V-9: Initial conceptual UPJ process schematic – assembling parts, applying heat and force, and completing the assembly.

Alternative dissimilar metal joining processes have been investigated with varying levels of success; however, galvanic corrosion has consistently been demonstrated to be a key challenge. Particularly for the followin:

1) Metallic bonding, such as fusion or solid-state welding processes, requires a clean (i.e., either no coatings or a specific coating that is designed to improve intermetallic bonding rather than corrosion performance) surface on both metals and does not allow for any isolation between the two metals.
2) Fasteners (e.g., rivets or bolts) that are typically made of steel for high strength and low cost tend to promote galvanic corrosion in Al and aggressively promote galvanic corrosion in Mg. The galvanic activity is increased if one of the two light metals is joined to a steel component. Coatings intended for corrosion protection on steel fasteners tend to get damaged during the installation process. Fasteners also typically damage coatings on the components being joined. One result is that the preliminary coatings are rendered useless because galvanic isolation has been broken. Another result is that the galvanic attack on the anode can be magnified if a small defect is created in the anode coating. Figure V-10 shows an example of this magnified galvanic attack, where coated steel screws were driven into a coated magnesium component and then exposed to a corrosive environment.

Figure V-10: Galvanic corrosion effects of steel screws in an Mg component exposed to 240 hours of ASTM B117 salt spray testing.

The UPJ process, by contrast, relies on a robust mechanical joint rather than intermetallic bonding; therefore, cathodic material can be coated prior to joining to protect against galvanic attack on the anodic material. Additionally, because the UPJ protrusion is going through a hole that is drilled or punched prior to coating, the UPJ process is much less likely to damage the coating when the joint is being made. Furthermore, there is no joining-induced galvanic activity beyond that between the two parent materials because no additional cathodic material (such as a steel fastener) is used to create the joint.

Approach

The project technical approach is summarized as follows:

1. Establish the benchmark performance of Mg to Al joints produced with SPR (a currently available commercial process) for comparison purposes only.
2. Obtain additional knowledge and understanding about the thermo-mechanical behavior of Mg alloys through Gleeble® testing conducted in Canada at no cost to DOE.
3. Supplement existing FCA UPJ process knowledge with computer-aided engineering forming simulation results based on knowledge gained through Gleeble® testing. Use this information to develop optimized cast protrusion and welding electrode shapes to reduce electrical current requirements and provide a more robust, repeatable forming performance for each of the joint configurations being considered.
4. Evaluate all material configurations (e.g., AM60B to Al6022, Al6013, and high-strength steel [HSS] materials in bare, pretreated, and coated conditions for round and oval-shaped joints). For each configuration, produce tensile shear and cross-tension test coupons. Apply additional coating layers to select joint configurations prior to the mechanical/structural and corrosion evaluations.
5. Subject five samples of each configuration to the initial mechanical/structural tests described above.
6. Subject a substantial number of samples to FCA's accelerated corrosion tests, reviewing visually every 2 weeks and removing three samples of each configuration at 4-week intervals for quasi-static testing.
7. Finally, at the end of the 12-week accelerated corrosion exposure, subject select configurations to fatigue and impact testing for comparison to pre-corrosion performance.

Validate joint performance through the following:

- Characterization of material microstructure in the joint region
- Characterization of joining-induced defects in the joint region
- Quasi-static tensile shear tests
- Quasi-static cross-tension tests
- Drop tower impact tests of select tensile shear and cross-tension samples
- Cyclic fatigue testing of select tensile shear and cross-tension samples
- FCA's 12-week accelerated corrosion test (ASTM G85-A2) with quasi-static lap shear failure and cross-tension failure being evaluated after each 4-week increment and fatigue testing and impact testing to be re-evaluated on select samples at the end of corrosion exposure
- Characterization of failure mechanisms for each of the mechanical tests described above.

Results and Discussion

This report focuses on results of UPJ and UCR joint process development and joint performance testing. A comparison of round boss UPJ joint performance to the benchmark SPR joint performance (reported in the FY 2014 annual report) is also included.

The team developed optimized round boss UPJ boss and head geometries. The team also developed process parameters to facilitate production and testing of a substantial number of unique joint configurations. The configurations discussed in this report are defined in Table V-1.

Table V-1: Round boss UPJ material and coating configurations.

Configuration Number	Upper Sheet			Bottom Sheet			Assembly Coating Configuration
	Material	Thickness (mm)	Coating	Material	Thickness (mm)	Coating	
UPJ8-1	HSS DP-590	2.0	Galvanized	Mg AM60B	4.0	Pretreated	Uncoated
UPJ8-2	Al 6013-T4	2.2	Bare	Mg AM60B	4.0	Bare	Uncoated
UPJ8-3	HSS DP-590	2.0	Galvanized	Mg AM60B	4.0	Pretreated	Powdercoated
UPJ8-4	Al 6013-T4	2.2	Pretreated	Mg AM60B	4.0	Pretreated	Powdercoated
UPJ8-5	Al 6013-T4	2.2	Powdercoated	Mg AM60B	4.0	Pretreated	Uncoated
UPJ8-6	Al 6013-T4	2.2	Powdercoated	Mg AM60B	4.0	Pretreated	Powdercoated
UPJ8-7	Mg AM60B	2.0	Bare	Mg AM60B	4.0	Bare	Uncoated

Figure V-11 shows several round boss head formations produced with Al, Mg, and steel top sheets in bare, pre-treated, and coated configurations. It can be seen that well-formed, crack-free head formations were produced for all of these material and coating configurations.

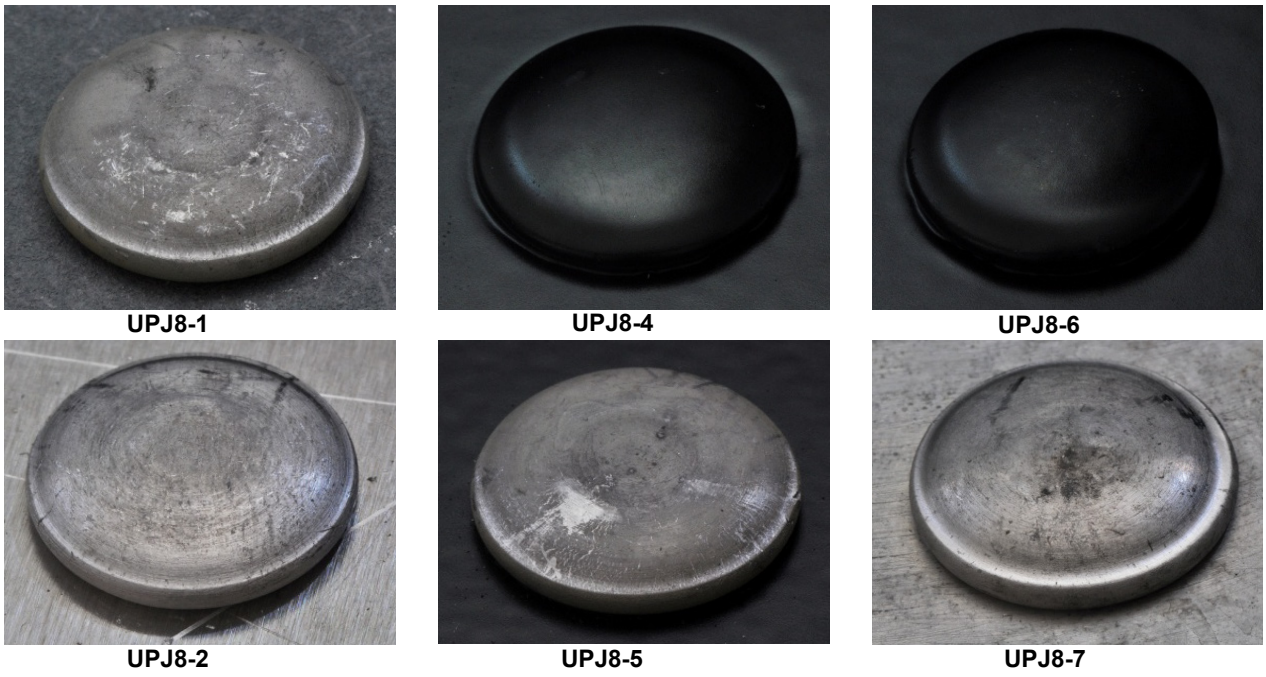

Figure V-11: Round boss UPJ head formations.

Figure V-12 shows two examples of round boss UPJ joint cross-sections. Figure V-12(a) shows a section through an Mg to steel joint, while Figure V-12(b) shows a section through an Mg to Al joint. There is no evidence of cracking or porosity in either of these joints. The boss expanded to completely fill the clearance hole in the top sheet, while the head shape is well-formed and provides a substantial overlap to the joined sheet material to produce high cross-tension joint strength.

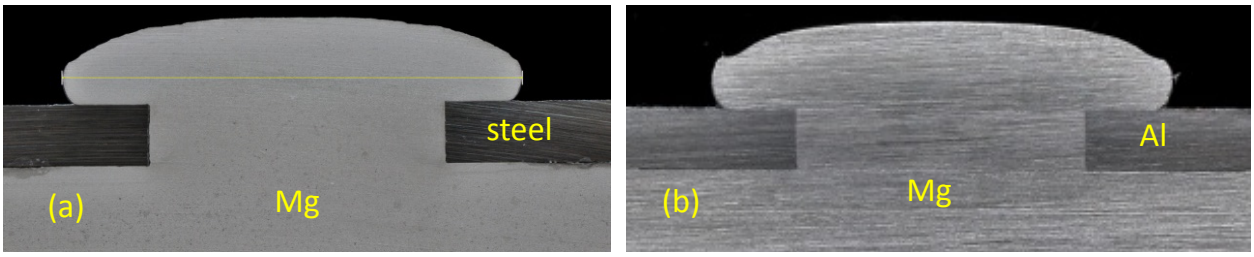

Figure V-12: Metallurgical cross sections of round boss UPJ joints.

Figure V-13 shows quasi-static and impact lap shear tension testing results of samples using seven different coating configurations. The different coating configurations were not expected to show any substantial performance difference in these pre-corrosion mechanical/structural tests. However, it should be noted that UPJ8-1 and UPJ8-3 are Mg-steel joints and are expected to show slightly higher strength than Mg-Al joints. UPJ8-6 is a powder coated assembly, which may have experienced an increase in joint strength as a result of the paint bake temperature cure of the Al-6013 material. The three impact configurations performed as expected with UPJ8-1 (Mg-steel) displaying higher strength than UPJ8-2 (Mg-Al), which is in turn higher than UPJ8-7 (Mg-Mg).

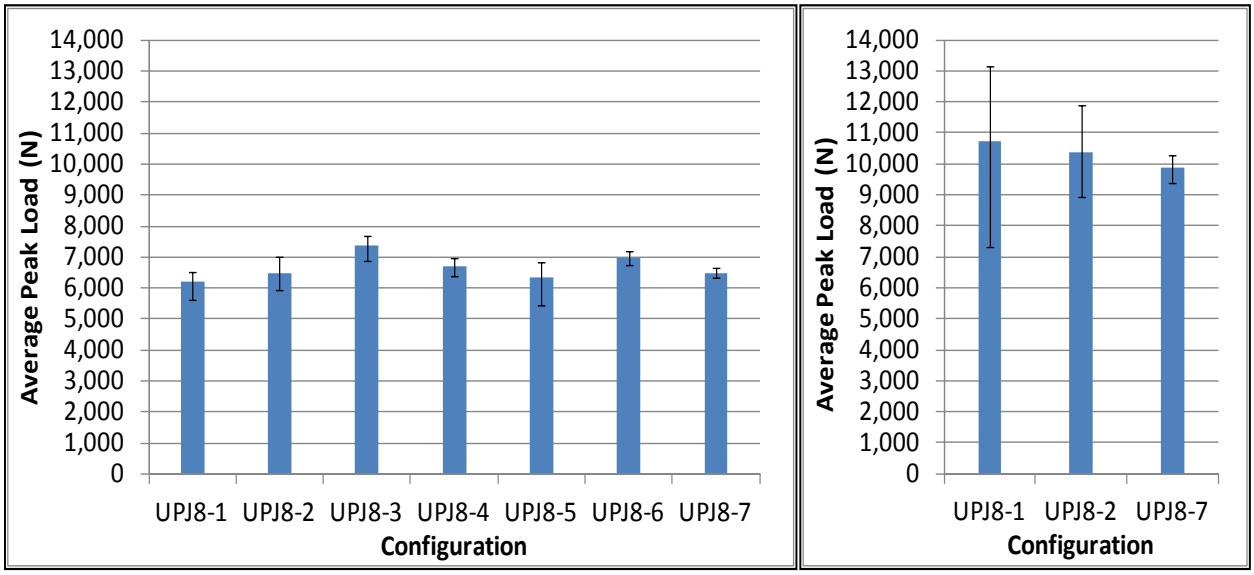

Figure V-13: Round boss UPJ quasi-static (left) and impact (right) lap shear test results.

Figure V-14 shows the quasi-static and impact cross-tension testing results. There are no unexpected results in this study. The Mg-steel joints (i.e., UPJ8-1 and UPJ8-3) again show slightly higher joint strength levels than the Mg-Al and Mg-Mg joints.

Figure V-15 and Figure V-16 show lap shear tension and cross-tension fatigue testing results of 8-mm round boss joints for Mg-steel, Mg-Al, and Mg-Mg joints. The Mg-steel joints are shown in red, the Mg-Al joints are shown in blue, and the Mg-Mg joints are shown in green. It is notable that the Mg-steel joints showed greater high-cycle fatigue strength than the Mg-Al and Mg-Mg joints despite the fact that all high-cycle joint failures occurred in the die cast Mg bottom plate. This result shows that the high-cycle fatigue strength could be affected by overall joint stiffness.

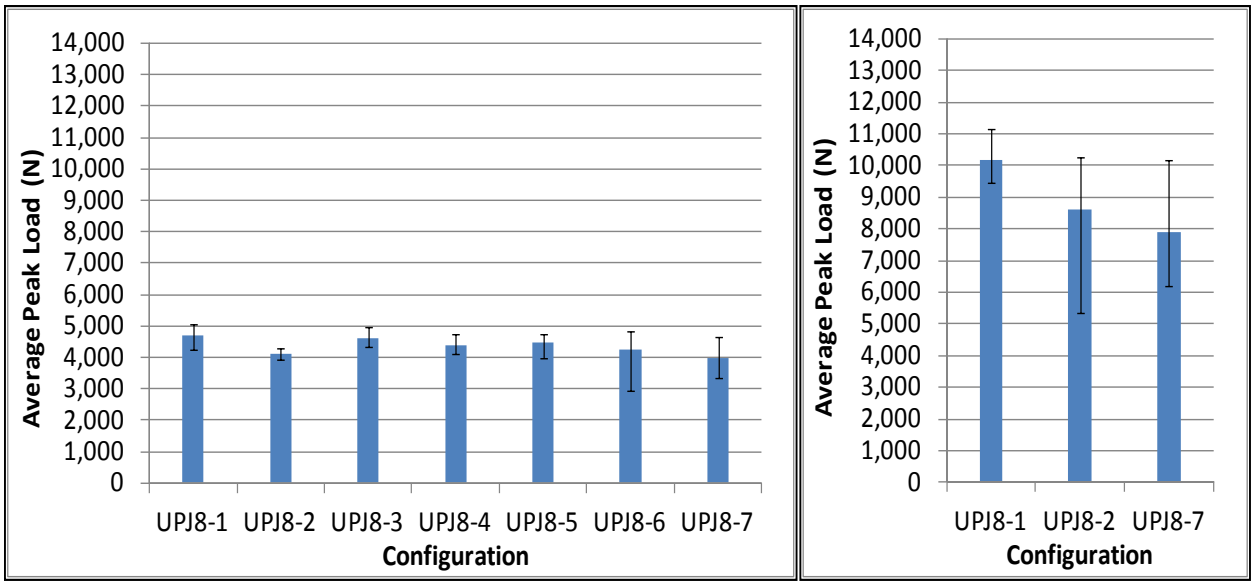

Figure V-14: Round boss UPJ quasi-static (left) and impact (right) cross-tension test results.

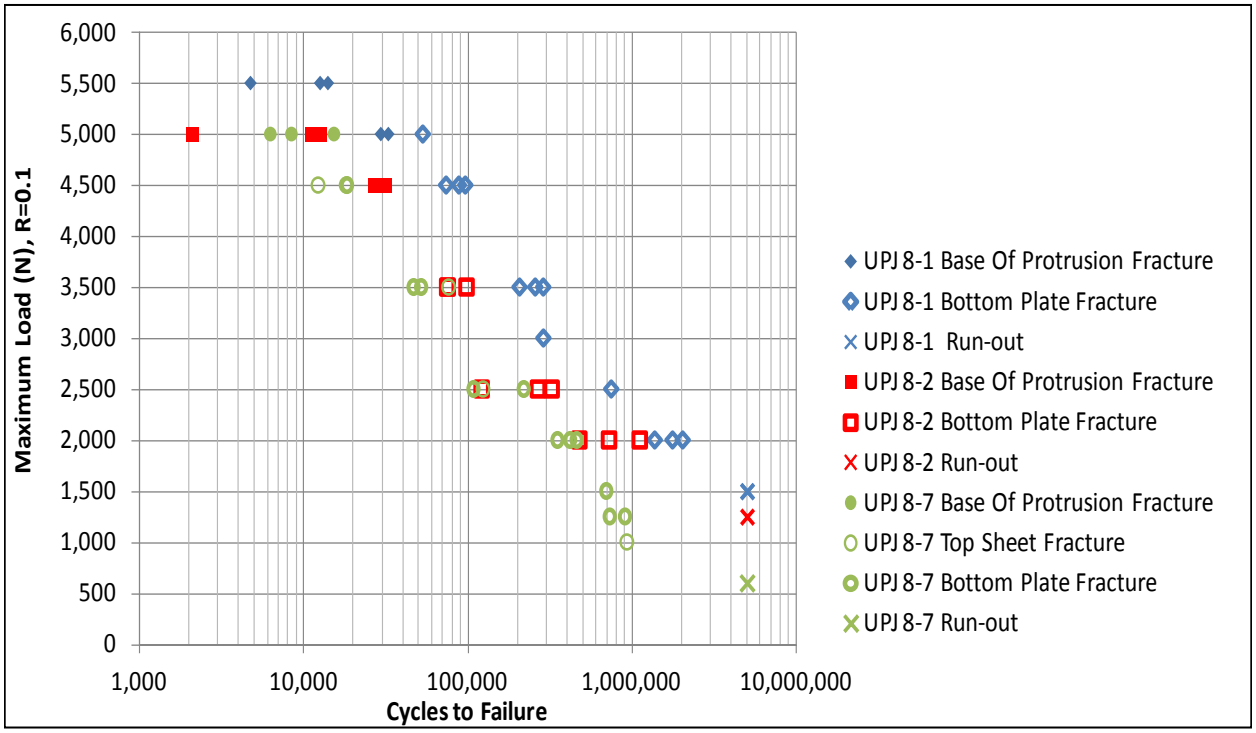

Figure V-15: Round boss UPJ lap shear fatigue curves.

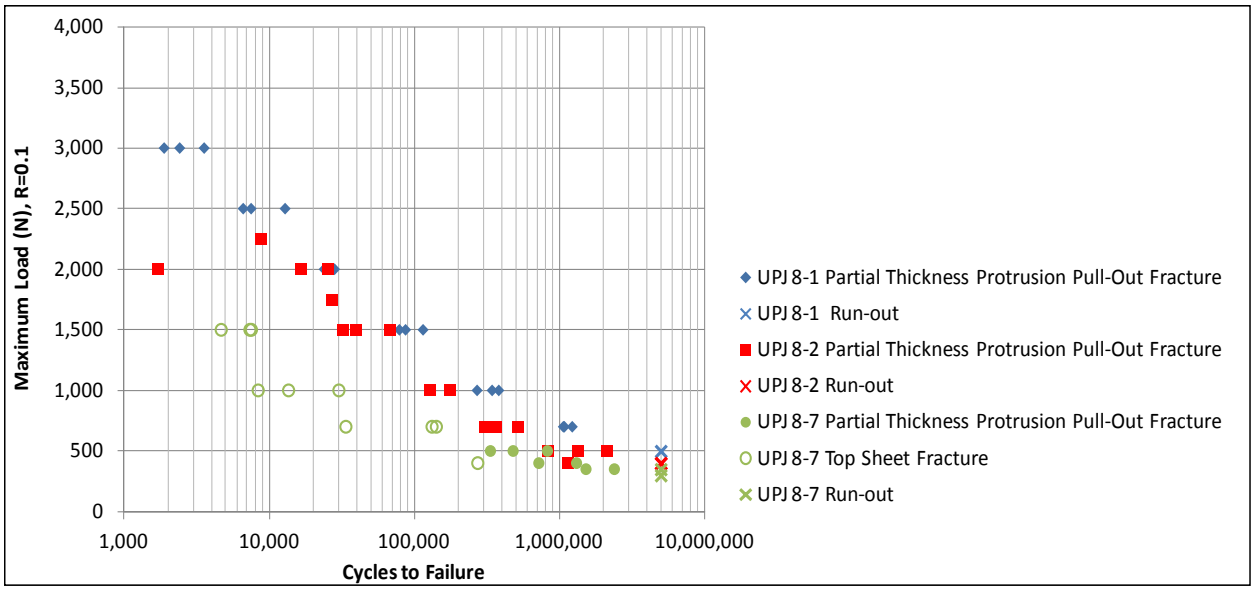

Figure V-16: Round boss UPJ cross-tension fatigue curves.

Figure V-17 shows results of bare Mg to bare Al6013 joints that separated after 8 weeks (i.e., about 1,350 hours) of exposure to FCA's ASTM G85-A2 accelerated corrosion procedure. This is a cyclic salt spray test with the addition of acetic acid. Although galvanic attack of the Mg sheet by the Al sheet was expected to be the source of failure for this combination, the actual source of failure turned out to be exfoliation corrosion of the Al6013 alloy. This alloy contains more copper than most conventional automotive Al alloys; therefore, it is very sensitive to acidic environments such as those experienced in the FCA corrosion procedure. Figure V-18 shows more extensive exfoliation corrosion and more extensive joint damage of Mg-Al 6013 joints after 12 weeks (i.e., about 2,000 hours) of exposure.

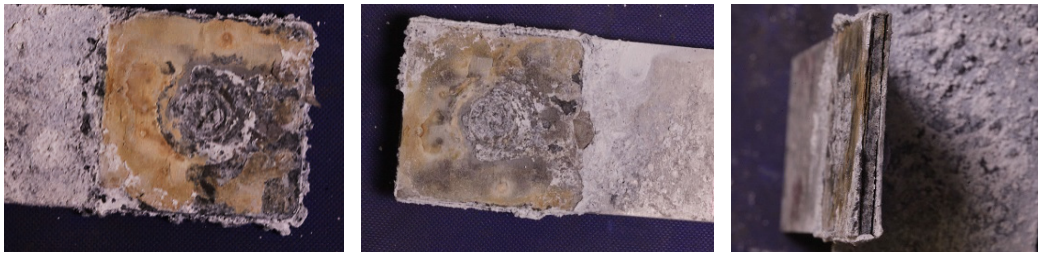

Figure V-17: UPJ8-2 (bare Mg to bare Al 6013) after 8-weeks of accelerated corrosion exposure.

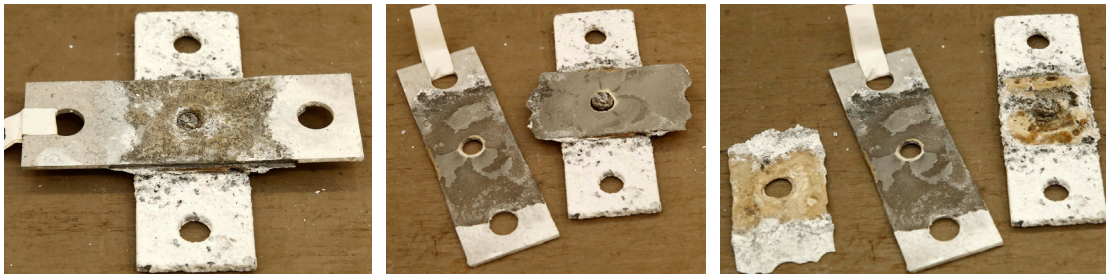

Figure V-18: UPJ8-2 (bare Mg to bare Al 6013) after 12-weeks of accelerated corrosion exposure.

Figure V-19 shows results of Mg-steel joints that separated after less than eight weeks of accelerated exposure. In this case, the failure mode was as expected (i.e., galvanic attack from the steel to Mg sheets), but slightly

more severe. The photos show that crevice corrosion around the edges of the joints is the biggest challenge. Even the combination of galvanizing, e-coating, and sealing around the edges was not sufficient to prevent corrosion damage. Although this is a very severe test and may not be reflective of performance in the field, these results do indicate that a complete top coating of the steel panel (prior to joining to Mg), followed by extensive precautionary sealing and coating of the full assembly, may be advisable.

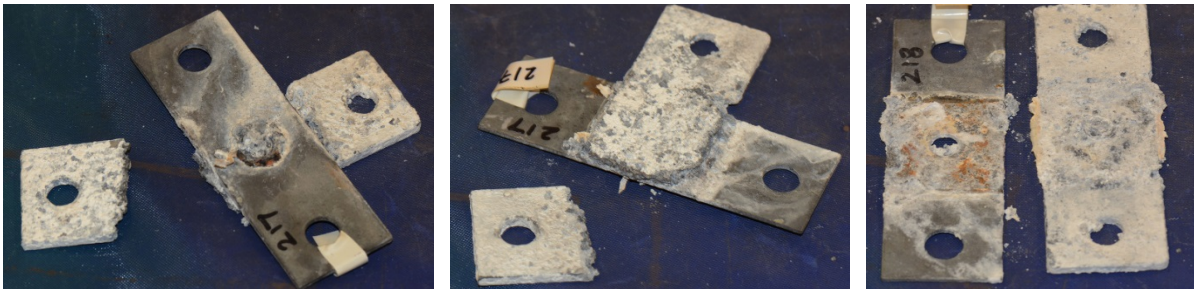

Figure V-19: UPJ8-1 (Mg-steel) after 8-weeks of accelerated corrosion exposure.

Quasi-static lap shear test results for round boss UPJ joints are shown in Figure V-20 both prior to corrosion testing and after 4, 8, and 12 weeks of accelerated corrosion exposure. For reasons cited in the previous paragraph, none of the Mg-steel joints (i.e., UPJ8-1 and UPJ8-3) remained intact after 8-weeks. All coated Mg-Al configurations (i.e., UPJ8-4, UPJ8-5, and UPJ8-6) maintained good joint strength performance even after 12 weeks of accelerated corrosion testing exposure. For comparison, the uncoated (i.e., bare) Mg-Al configuration (i.e., UPJ8-2) remained intact but exhibited lower overall joint strength. Cross-tension test results showed similar performance retention to the lap shear tension tests after corrosion testing.

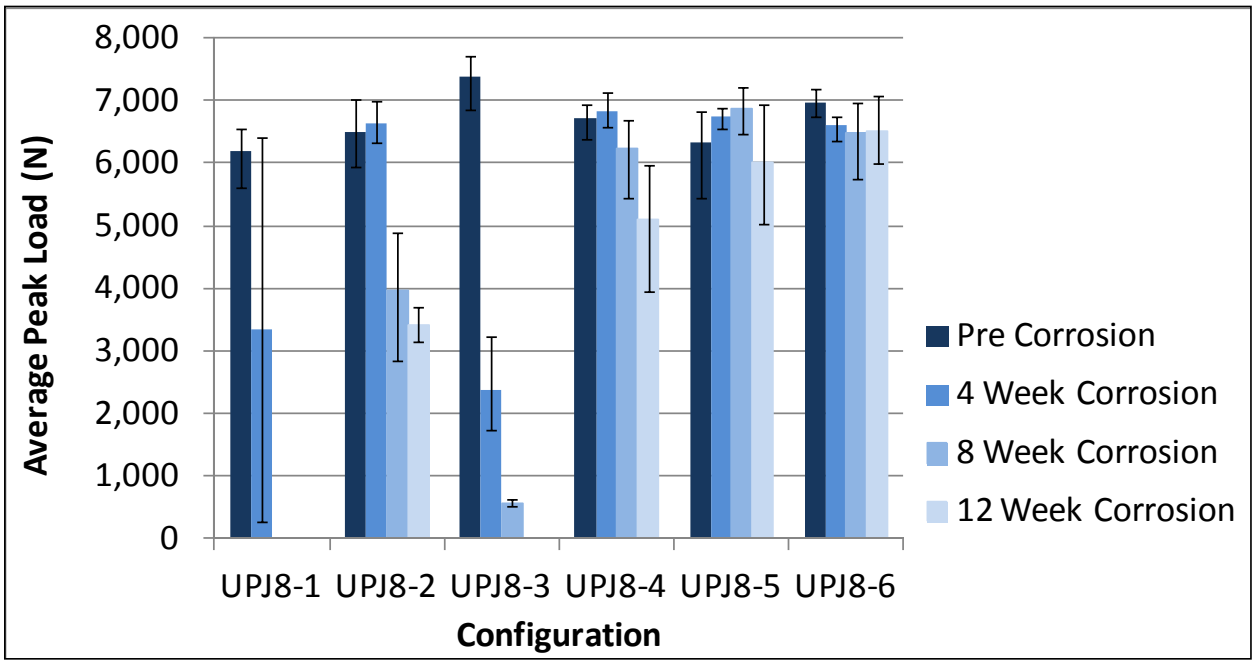

Figure V-20: Round boss UPJ lap shear tension performance prior to corrosion testing and at 4, 8, and 12 weeks of accelerated corrosion exposure.

Comparisons of quasi-static lap shear tensile test and cross-tension test results for round boss UPJ joints and benchmark SPR joints are shown in Figure V-21 and Figure V-22 prior to accelerated corrosion exposure and after 4 weeks, 8 weeks, and 12 weeks of exposure. The benchmark SPR data were presented in the FY 2014 annual report, but are repeated here to facilitate comparison with the round boss UPJ joints. When viewing

these figures, note that (1) UPJ8-2 and SPR1 are both bare Mg to bare Al joints; (2) UPJ8-4 and SPR2 are pretreated Mg to pretreated Al with the whole assembly being powder-coated; (3) UPJ8-5 and SPR3 are pretreated Mg to powder-coated Al; and (4) UPJ8-6 and SPR4 are pre-treated Mg to powder-coated Al with the whole assembly being powder-coated after assembly.

The figures indicate that substantially higher levels of joint strength were achieved for all UPJ configurations (primarily a function of geometry in this case). However, the real purpose of this comparison was to evaluate performance retention after corrosion exposure. Both SPR and UPJ joints performed reasonably well when Mg was pretreated and Al was powder-coated (i.e., SPR3, SPR4, UPJ-5, and UPJ-6). Even so, there were two rivet fractures in the SPR3 configuration. Both the SPR and UPJ joints failed to survive 12 weeks of exposure in the bare Mg to bare Al configurations (i.e., SPR1 and UPJ2). The configurations with the greatest distinction between similar UPJ and SPR configurations were SPR2 and UPJ8-4, where both the Mg and Al samples were pretreated and the assembly was powder-coated after assembly. In this configuration, there were multiple rivet fractures in the SPR joints at 8 weeks. This resulted in no SPR samples surviving to 12 weeks of exposure. Only two UPJ joints of this configuration failed before reaching 12 weeks of exposure.

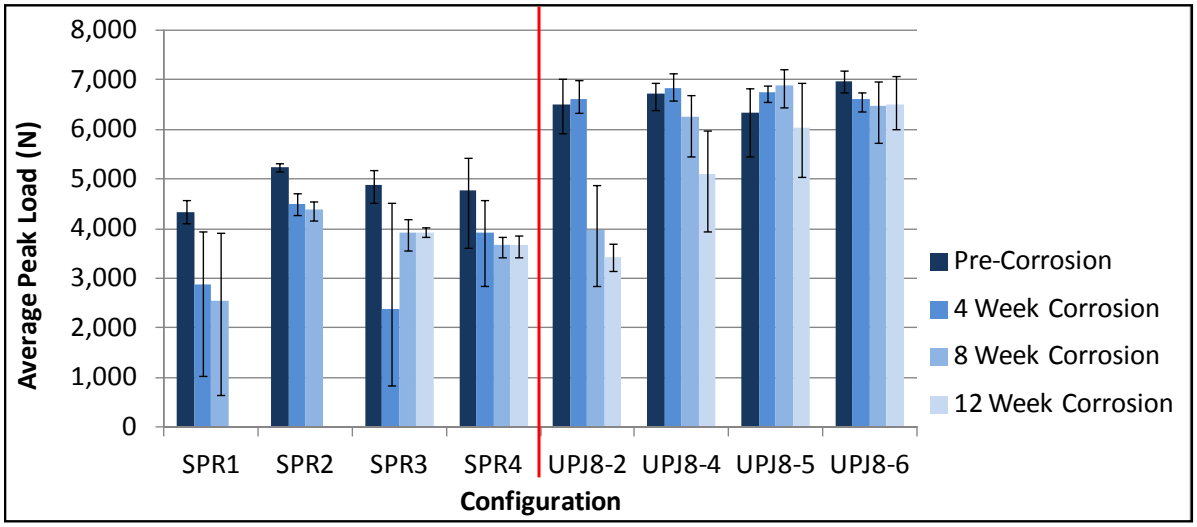

Figure V-21: Round boss UPJ lap shear tension performance comparison to benchmark SPR joints prior to corrosion testing and at 4, 8, and 12 weeks of accelerated corrosion exposure.

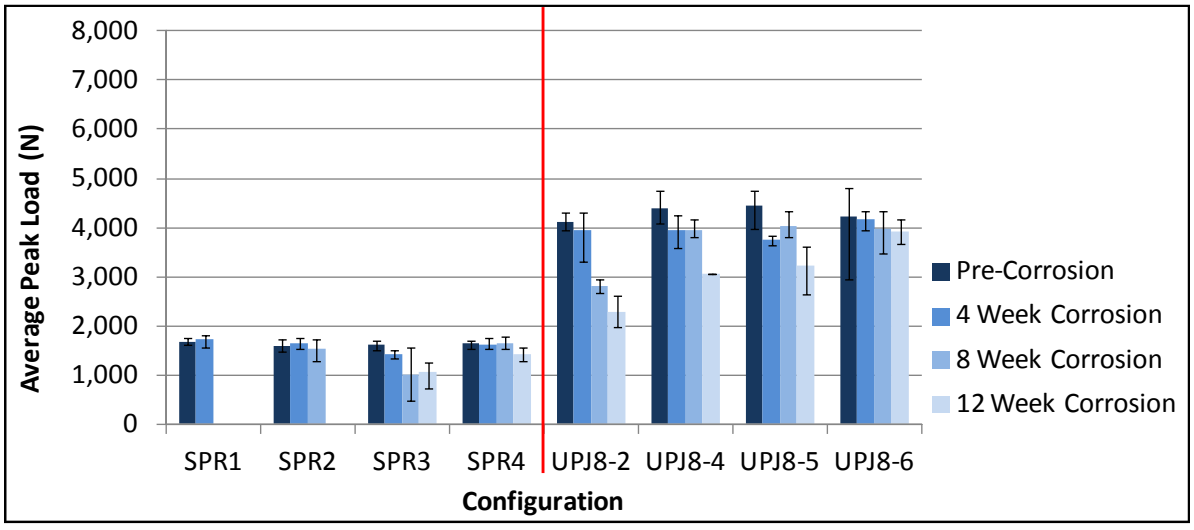

Figure V-22: Round boss UPJ cross-tension performance comparison to benchmark SPR joints prior to corrosion testing and at 4, 8, and 12 weeks of accelerated corrosion exposure.

The team also developed optimized joint geometries and process parameters for oval boss configurations. Figure V-23 shows three oval boss UPJ head formations that resulted from increasing temperature and force. The superimposed yellow oval indicates the top sheet clearance-hole shape. As the head formation was squeezed harder to improve coverage over the clearance hole, the head shape deviated further from the original oval proportions and began to approach a circular shape. While this did not significantly affect joint strength, it did limit the ability of the oval boss joint design to enable use of narrower joint flanges.

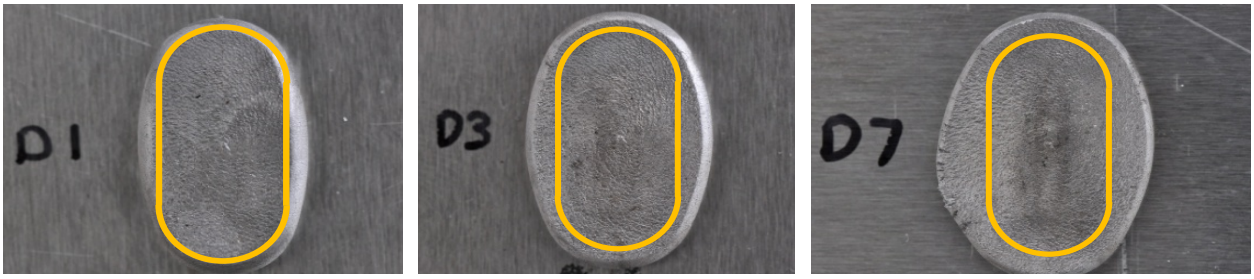

Figure V-23: Effect of increasing force and temperature on oval boss UPJ head shape and size.

Figure V-24 shows metallurgical cross-sections for oval boss Mg-Al UPJ joints. The sections shown along the top row are cut through the transverse axis, while the sections along the bottom row are cut through the longitudinal axis. These sections illustrate the substantial difference in overlap to a clearance hole in the top sheet in longitudinal and transverse directions that result from the tendency of oval joints to tend closer to round joints as they are deformed.

Figure V-24: Metallurgical cross sections of oval boss UPJ joints through the transverse axis (top) and the longitudinal axis (bottom).

Figure V-25 shows quasi-static joint performance comparisons between oval boss joints and 8-mm round boss Mg-steel joints. Lap shear tension joint strength is significantly higher for the oval boss joints than the round boss joints, primarily as a result of the shear area of the oval boss joints being substantially larger than the round boss joints. In the case of cross-tension testing, the strength of these joints is known to be highly correlated to the stiffness of the top sheet and the strength of the UPJ head. The result is the cross-sectional boss area does not have such a great effect as it does for lap shear tension.

Finally, the team optimized the electrode geometry and force/current application for UCR joints for steel-Al joints using computer-aided engineering simulation tools and physical experimentation. Over 20 unique rivet and electrode concepts were evaluated with computer simulations. The optimum rivet and electrode geometry was very similar to the optimized UPJ boss and electrode geometry. Figure V-26 shows the head form of four unique material/coating configurations, while Figure V-27 shows the metallographic cross-sections of five samples of one of these configurations (typical for all four configurations). Clearly all of these configurations

can be produced with good quality head formations and very little cracking. The figure also shows that the rivet expands to fill the clearance holes even when they are misaligned.

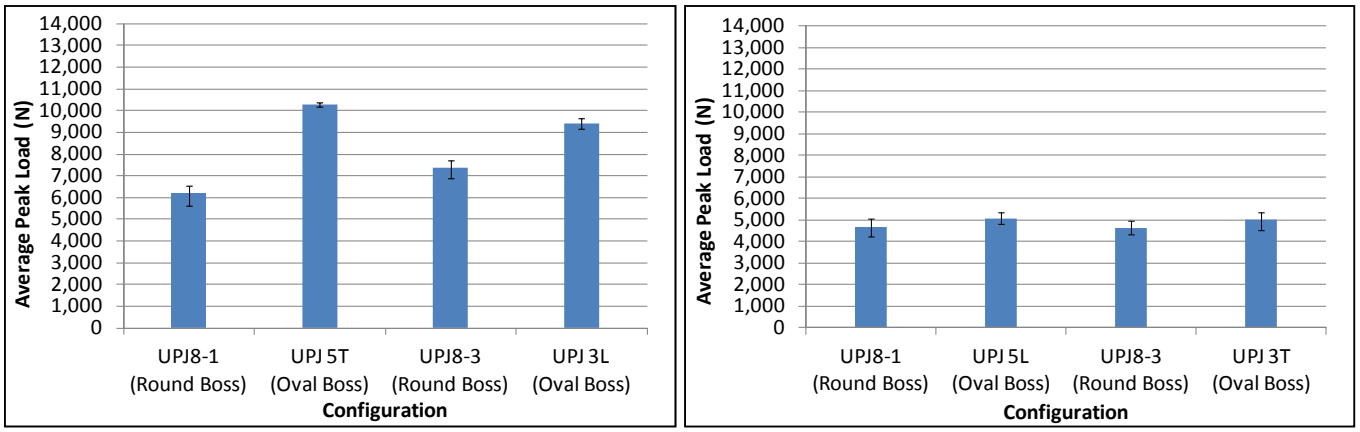

Figure V-25: Comparison of oval boss joints to 8-mm round boss Mg-steel joints in quasi-static lap shear tension (left) and cross-tension testing (right).

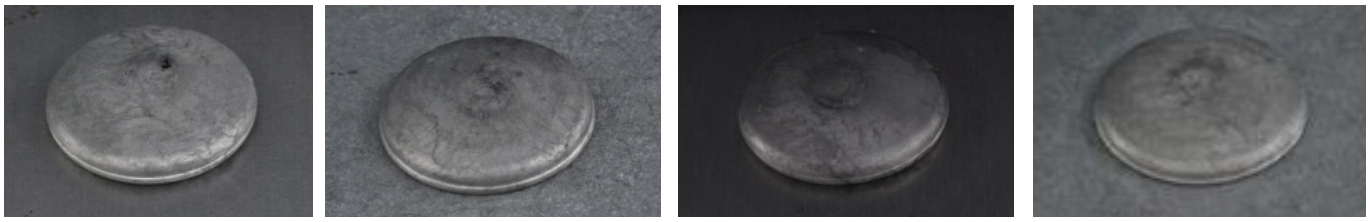

Figure V-26: UCR head formations for four unique material/coating configurations.

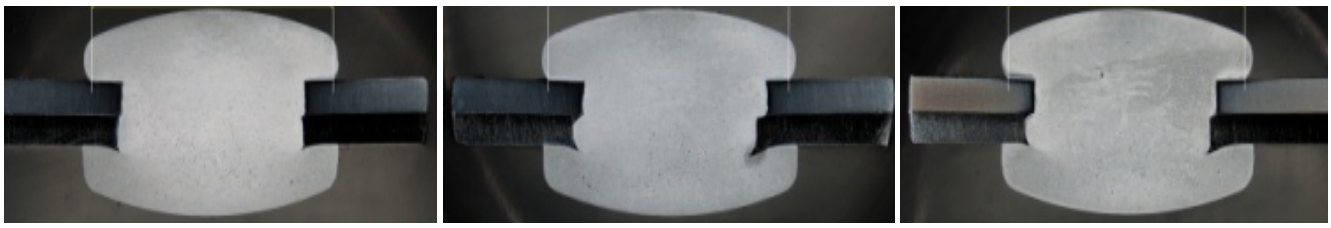

Figure V-27: Metallographic cross sections for a typical UCR material/coating configuration.

Figure V-28 shows initial lap shear and cross-tension test performance of four UCR Al-steel joint configurations (the rivet is Mg AM60B). The red bars indicate lap shear performance, while the blue bars indicate cross-tension performance. The chart on the left shows results for joints of 1.4-mm thick steel sheet to 1.3-mm thick Al6016 sheet. The chart on the right shows results for joints of 1.0-mm thick steel sheet to 1.3-mm thick Al6016. The results are quite interesting because the lap shear tension results for joints with thicker steel sheet are slightly lower than those for joints with thinner steel sheet. A review of the failure modes shown in Figure V-29 indicates that the reason for this unusual result may be related to the fact that bending of the thinner steel sheet results in an entirely different failure mode.

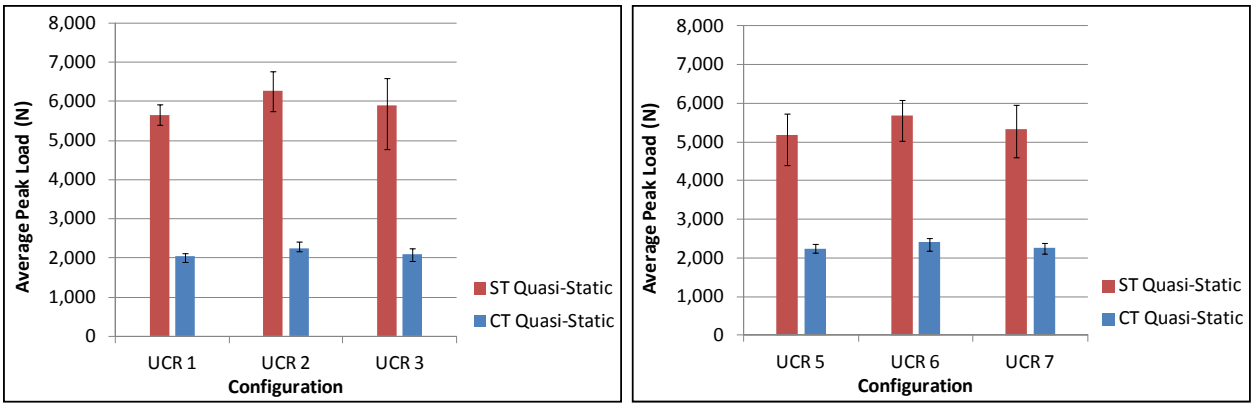

Figure V-28: UCR initial quasi-static lap shear and cross-tension test results for 1.4-mm steel to 1.3-mm Al (left) and 1.0-mm steel to 1.3-mm Al (right).

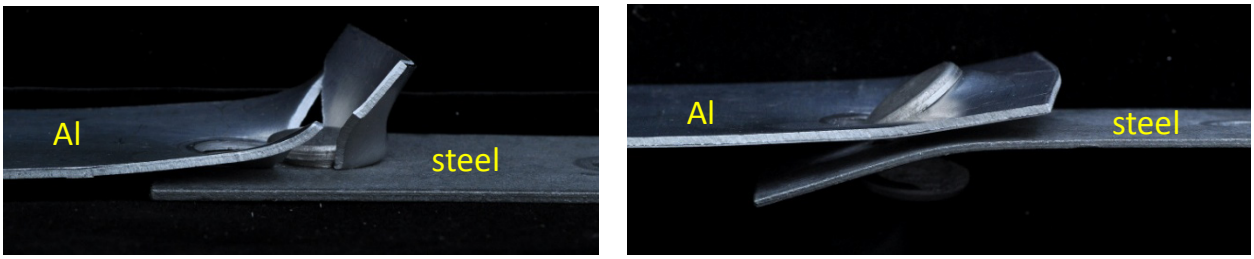

Figure V-29: UCR initial quasi-static lap shear and cross-tension failure modes for 1.4-mm steel to 1.3-mm Al (left) and 1.0-mm steel to 1.3-mm Al (right).

Technology Transfer Path

Two of the key obstacles preventing more widespread use of light metals in high-volume automotive applications are lack of robust joining techniques (especially for dissimilar metal joining) and susceptibility to galvanic corrosion. Successful completion of this project will provide a key enabler to high-volume application of lightweight materials. This will allow FCA (and other manufacturers) to accelerate development of new lightweight vehicle designs that utilize multiple lightweight materials in order to aggressively reduce mass on future vehicle programs.

Conclusion

During FY 2015, the team has demonstrated UPJ to be capable of providing good, repeatable joints in several material/coating configurations and boss geometry configurations. Extensive thermo-mechanical material characterization, modeling/simulation, and physical experimentation were used to optimize process parameters for round boss UPJ joints. A full test matrix of over 350 round boss UPJ joints were produced and evaluated for mechanical/structural performance, were subjected to FCA's accelerated corrosion exposure, and were compared to the benchmark SPR process. Neither UPJ nor SPR passed the full corrosion test in the bare Mg to bare Al combination. However, UPJ showed significant improvement over SPR for at least one of the coated joint configurations. It also had improved lap shear strength and dramatically improved cross-tension strength in all configurations.

Additionally, oval joint UPJ joining processes were developed for use on narrow flange applications. These joints displayed improved joint strength over round boss UPJ due to increased boss shear area, but did not offer quite the level of reduced flange width capability as anticipated due to a tendency of the head formations to veer away from oval and toward round.

UCR joining processes have also been developed for joining dissimilar metals where neither metal is cast Mg. These joints have shown exceptionally good formation with very little to no cracking tendencies.

References

None.

Bibliography

S. D. Logan, 2015, "Upset Protrusion Joining Techniques for Joining Dissimilar Metals," presented at the *2015 U.S. DOE Hydrogen and Fuel Cells Program and Vehicle Technologies Office Annual Review and Peer Evaluation Meeting*, Washington, D.C., June 12, 2015.

S. D. Logan, 2015, "Evaluating the Upset Protrusion Joining (UPJ) Method to Join Magnesium Castings to Dissimilar Metals," presented at the *2015 Global Automotive Lightweight Materials Detroit Conference*, Detroit, Michigan, August 19, 2015.

V.3. Brazing Dissimilar Metals with a Novel Composite Foil – Johns Hopkins University

Project Details

Timothy P. Weihs, Principal Investigator
Johns Hopkins University
3400 North Charles Street
Baltimore MD, 21218
Phone: 410-516-4071
E-mail: weihs@jhu.edu

David Ollett, Project Officer
National Energy Technology Laboratory
626 Cochrans Mill Road
P.O. Box 10940
Pittsburgh, PA 15236-0940
Phone: 412-386-7339
E-mail: david.ollett@netl.doe.gov

Sarah Ollila, Technology Area Development Manager
U.S. Department of Energy
1000 Independence Avenue, SW
Washington, DC 20585
Phone: 202-586-8027
E-mail: sarah.ollila@ee.doe.gov

Contractor: Johns Hopkins University
Contract No.: DE-EE0006441

Executive Summary

The aim of this project is to develop, characterize, and assess novel reactive foils that are based on reduction-oxidation (redox) chemical reactions for use in dissimilar alloy bonding applications. Upon ignition, the reactions within these foils self-propagate through the bond area and produce heat and molten metal. This represents a significant advantage over traditional joining techniques (e.g., welding, soldering, and furnace brazing), because the heat and braze are delivered locally and heating of the bulk components is not required. In the interest of cost and scalability, the redox foils are fabricated from powder compacts that are swaged and rolled into thin foils. The reactive properties can be tailored by altering the extent of mechanical processing and varying the starting chemistry. Bond strength is expected to depend on a number of factors, including joining materials, foil chemistry, foil microstructure, foil thickness, and bonding parameters such as applied pressure, surface preparation, and bond area.

In the past fiscal year, we have focused strongly on refinement of the redox foil powder constituents through ball milling. The reactivity of fully processed redox foils can be enhanced by reducing spacing between the aluminum and the oxide powders. High-energy collisions between milling media embed oxide fragments into softer aluminum powders. Milling process parameters can be tailored to maximize reactivity, which occurs when reactant spacing is small and there is little or no reaction during fabrication. Our primary focus has been on the Al:Cu_2O system. Of the three major systems we have studied (Al:NiO, Al:CuO, and Al:Cu_2O), Al:Cu_2O produces the largest braze-to-alumina ratio by volume when the reactants are held at their stoichiometric ratio. In addition, we have empirically observed that copper has better wetting characteristics than nickel. Thin, multilayer thermite foils have also been manufactured via magnetron sputtering. These foils

are prone to stresses that evolve during the deposition process, but we show that stresses can be controlled by adjusting deposition parameters such as bilayer thickness and sputtering pressure.

Accomplishments

- Processed ball-milled, composite powders into diluted redox foil with a higher reactivity using conventional swaging and rolling techniques.
- Performed studies to identify a set of ball-milling parameters that maximizes the heat of reaction in Al:Cu_2O and Al:NiO composite powders.
- Characterized stresses in Al:NiO multilayer films fabricated via magnetron sputtering as a function of three sputtering pressures and two distinct bilayer spacings.
- Increased the amount of diluent that can be added to redox foils before self-propagating reaction quenches in bond interface using ball-milled powders
- Achieved dissimilar bond strengths as high as 10 MPa.

Future Directions

- Fabricate free-standing, sputter-deposited redox foils to understand how changes in microstructure affect velocity, heat of reaction, and gas generation.
- Alter dilution chemistry to tailor the reaction braze product for specific bonding substrates.
- Continue optimizing bonding parameters for given redox foil/base metal couples, including optimization of surface preparation, bonding pressure, and foil thickness.
- Create statistically significant datasets for shear strengths of bonds and determine the modes of failure in the joint.
- Analyze the braze and base metal interface for any changes in mechanical properties of base metal due to heating from the reaction of the redox foil.

Technology Assessment

- Target: Bonds with a lap shear strength of 20 MPa.
- Gap: Current bonds fabricated with redox foil are on the order of 10 MPa; shear strength can be increased by decreasing the porosity of the bond area and improving wetting.
- Target: Gasless propagation of Al:Cu2O redox foils.
- Gap: Current bonds fabricated with redox foil show significant porosity that is likely due to the evolution of gases upon heating.

Introduction

The last two decades have seen the development and commercialization of reactive, self-propagating multilayer foils as local heat sources for joining materials [1,2]. When used in conjunction with solder or braze, these foils can join dissimilar materials without heating either component significantly, as only the area near the interface is heated [3,4]. The standard NanoBond practice of pre-wetting components with solder, however, adds cost, slows dissemination of the technology, and limits bond strength to the strength of the solder being used within the joining process. Ideally, no pre-wetting would be required and stronger braze bonds would be enabled.

The aim of this project is to develop, characterize, and assess novel reactive foils that are based on reduction-oxidation chemical reactions. Many redox reactions are noted for their exothermic heats of reaction and molten metallic products, making them intriguing candidates for solder-free bonding applications. These are typically known as thermite reactions. Figure V-30 gives a schematic of a possible bonding configuration using a redox foil. In addition, the reactive properties of thermite foils may be tailored in a controllable manner by altering the chemistry of the reactants and refining the foil microstructure. We seek to understand the relationships between the foil properties and bond characteristics for several thermite systems and dissimilar alloys, including Al 3003, Mg AZ31, and high strength boron steel (HSBS). Of particular interest are the shear strengths of the bond, mass ejection (i.e., gas and particle) during the reaction, wettability of braze materials, and the extent of joint corrosion.

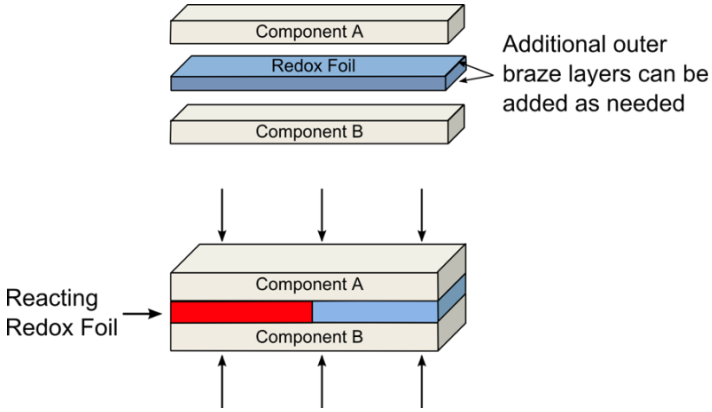

Figure V-30: A schematic representation of bonding with a redox foil. After ignition, a reaction within the foil self-propagates through the bond interface.

Approach

Diluting redox foils with excess metal has been shown to decrease gas production and increase the amount of braze present in the joint interface [5]. However, the presence of diluent also reduces the heat generated in the reaction because the total amount of reactants decreases and the average reactant spacing increases. When highly diluted redox foils are ignited in a joining configuration, the resulting self-propagating reaction tends to quench in the bond interface because the rate of heat loss exceeds the rate of heat generation. One way to preserve small reactant spacings while diluting the reaction is to create composite thermite powders that are comprised of small oxide inclusions embedded in softer aluminum powders. Figure V-31 and Figure V-32 provide a schematic and micrograph, respectively, showing how these powders change during ball milling. These two-phase powders are then mixed with diluent powders and processed via swaging and rolling.

Ball milling was used to create thermite composite powders with average reactant spacings of less than 1 µm. Initials experiments were performed using Al and NiO powders to explore the effect of changing various ball-milling parameters, particularly the ball-to-powder mass ratio (BPR), ball size, and milling time. Once these variables were better understood, we generated several batches of ball-milled powders and varying ball sizes and milling times in an effort to maximize the heat of reaction. Heats of composite powders were measured using differential scanning calorimetry (DSC) and compared to redox foils prepared from single-phase powders. After the best milling parameters were identified, we diluted the ball-milled powders and packed them into steel tubes to be swaged and rolled into redox foils.

We have also begun to prepare thermite-based multilayer films via physical layer deposition. A magnetron sputtering system was used to sputter fully dense films with controllable layer spacings. Multilayer films produced in this manner provide an ideal basis for comparison to mechanically processed redox foils, which are nearly fully dense and whose reactant spacings are less uniform. NiO and Cu_2O targets were diluted with 20 wt% Ni/Cu and Cu, respectively, to increase conductivity of the targets for direct current (DC) sputtering.

The NiO target was doped with a $Ni_{60}Cu_{40}$ alloy (by wt%) to make the diluent non-magnetic at room temperature. To generate the multilayer structure, substrates were rotated past aluminum and oxide targets in an alternating fashion.

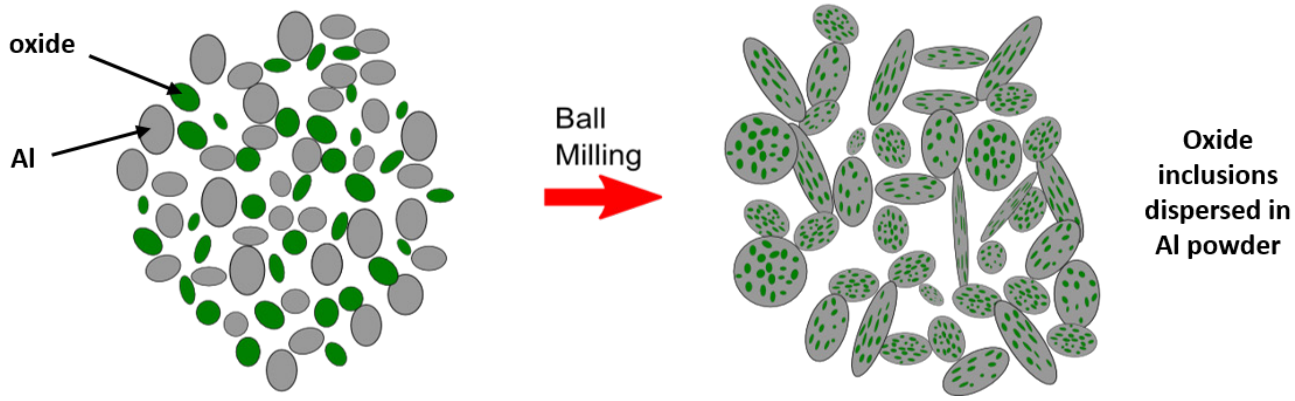

Figure V-31: Schematic of powder evolution during ball milling process. Collisions between the milling media and single-phase powders create composite powders containing oxide fragments dispersed in softer aluminum powders.

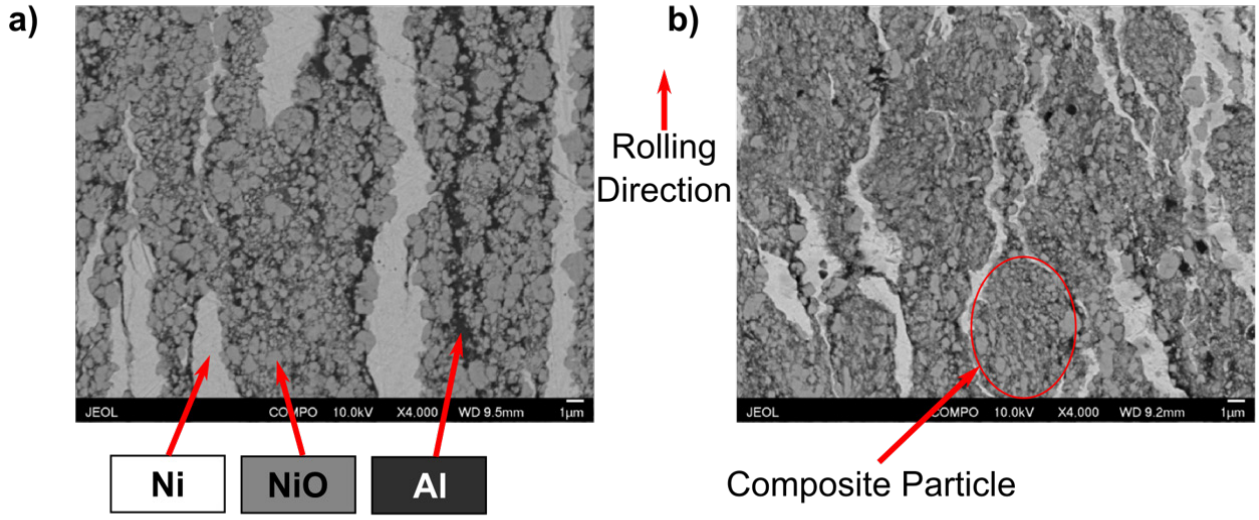

Figure V-32: Scanning electron micrographs of Al:NiO:Ni redox foil fabricated from (a) single-phase powders, and (b) ball-milled composite powders.

Stresses that evolve during the deposition process represent a significant obstacle in the effort to produce thick, free-standing multilayer films. If the magnitude of these stresses is significant, the film tends to crack or delaminate from the substrate, depending on whether the stress is tensile or compressive. The focus of FY 2015 was to understand how these stresses develop in Al:NiO films as a function of layer spacing, sputtering pressure and substrate-film interaction. Films with a total thickness of about 1 µm and varying layer spacings were deposited on silicon wafer substrates at different sputtering pressures. A wafer curvature rig was used to measure the change in wafer curvature that occurred due to the deposition of the film. The change in substrate curvature was related to the biaxial stress of the film using the Stoney equation. The orientation of each wafer was tracked throughout the experiment in order to measure the stresses in two orthogonal directions, one of which corresponds to the direction of rotation in the sputtering chamber.

Results and Discussion

We attempted to dilute Al:NiO redox foils produced from single-phase powders with copper instead of nickel. We have empirically observed that copper wets the base metals better than nickel and the Al:NiO system produces less gas than the Al:CuO and Al:Cu_2O systems (Figure V-33b).

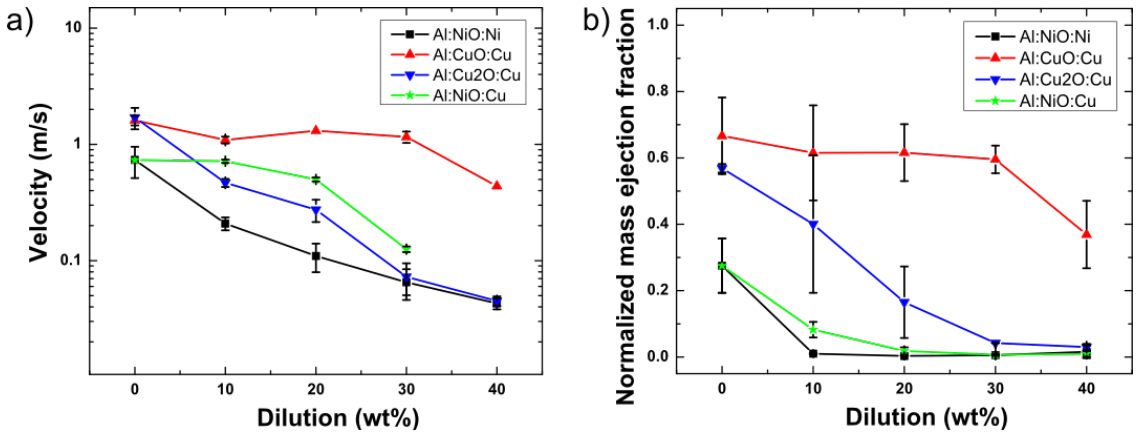

Figure V-33: (a) Velocity of selected thermite systems as a function of dilution. When changing the diluent of the Al:NiO system from nickel to copper, the velocity increases by a factor of 2 to 3. (b) Mass ejection fraction of selected thermite systems as a function of dilution. The Al:NiO:Cu system produces slightly more gas at lower dilutions, but the mass ejection fraction plateaus near zero at 20 wt% dilution.

Changing the diluent of the Al:NiO system from nickel to copper increased the velocity of reaction by a factor of 2 to 3 across the range of dilutions. We attribute this increase in velocity, in part, to increased thermal conductivity along the length of the redox foil due to the presence of copper. In addition, DSC experiments indicate that the onset of the reaction occurs at a lower temperature when the Al:NiO system is diluted with copper. Figure V-34 gives DSC traces for Al:NiO redox foil diluted with copper and nickel. A shift of the second exotherm from 635°C to about 550 to 560°C is evident for both copper-diluted samples. This exotherm corresponds to melting of aluminum. Because these reactions are diffusion-limited, we expect the rate of diffusion to increase upon melting of the reactant. The melting point of aluminum is lowered due to alloying with copper. These phenomena explain the observed increase in velocity.

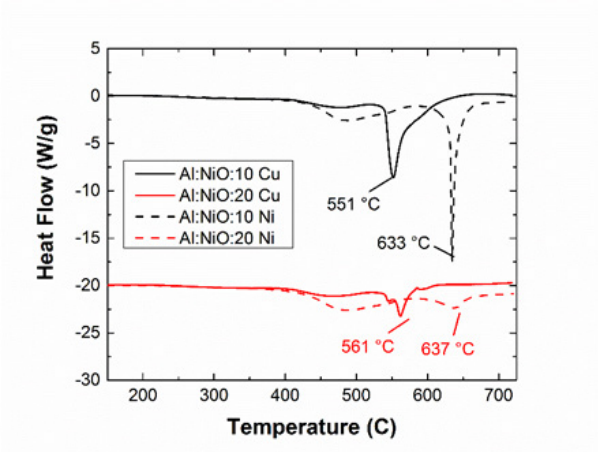

Figure V-34: DSC traces of Al:NiO redox foil diluted with copper (solid lines) and nickel (dashed lines), for both 10 and 20 wt% dilutions. There is a shift of the second exotherm to lower temperatures, indicating that the onset of the reaction occurs at a lower temperature. This shift offers one explanation as to why we see enhanced velocity when diluting with copper as opposed to nickel.

A focus in FY 2015 was on fabrication, testing, and application of redox foils produced from ball-milled, composite powders. Initials experiments were performed using Al and NiO powders to explore the effect of changing various ball-milling parameters, particularly the BPR, ball size, and milling time, on heat of reaction. Samples were tested using DSC. The BPR was fixed at 10 for this set of experiments. The results are shown in Figure V-35.

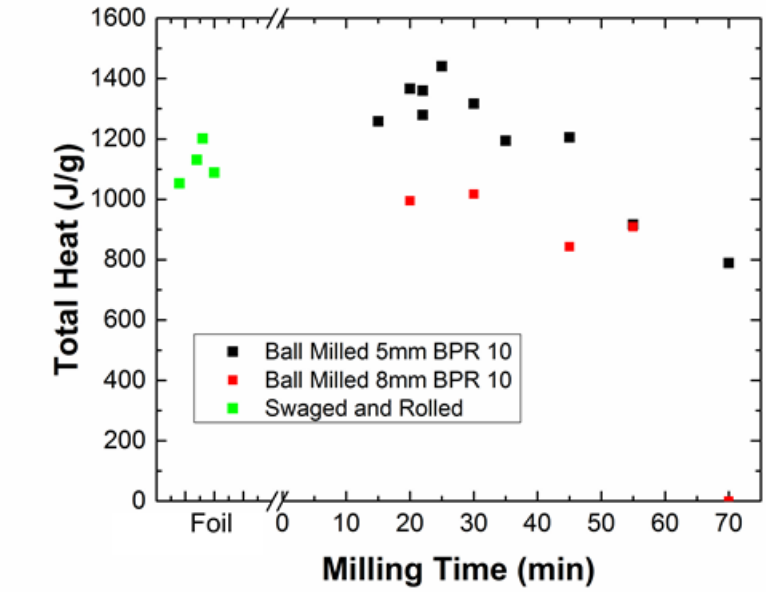

Figure V-35: Heats of reaction of ball-milled, composite Al:NiO powders as a function of ball diameter and milling time compared to conventionally processed, undiluted redox foil. Heats of reaction are maximized at a ball diameter of 5 mm and a milling time of 25 minutes.

At comparable milling times, the 5-mm diameter balls generated powders with higher heats of reaction. This is attributed to the nature of the interactions between the milling media and powders. For instance, 9-mm diameter balls are more massive, but the velocities and mean free paths between collisions are different than those seen in 5-mm diameter balls. In general, collisions that minimize reactant spacing between aluminum and the metal oxide without leading to significant reaction will maximize the heat of reaction. The highest heats of reaction were measured in powders that were milled with 5-mm diameter balls and were generally found to be higher than heats observed in fully processed redox foils prepared with single-phase powders. Thus, reduction in reactant spacing induced by the milling process is likely larger than that induced by the swaging and rolling processes.

A similar study was performed using Al:Cu_2O composite powders, because the Al:Cu_2O system is predicted to produce more braze by volume than either the Al:CuO or Al:NiO systems. Heat of reaction data were collected using DSC and are shown in Figure V-36. In this case, the highest heat of reaction was observed in powders milled with 8-mm diameter balls for 30 minutes. X-ray diffraction (XRD) experiments were also performed before thermal analysis to correlate the heats of reaction with the relative amounts of Al and Cu_2O present. The XRD traces are shown in Figure V-37. The extent of reaction was assessed by searching for Cu peaks, which indicate that some of the reaction had occurred given the samples were undiluted. The Al:Cu_2O powders with the highest heat of reaction (8 to 30 min) yielded the highest peak intensities of reactant phases, with insignificant Cu peaks. Conversely, the 5 to 60-minute sample yielded the highest peak intensities for Cu, indicating significant reaction had occurred. This sample produced the lowest measured heat of reaction.

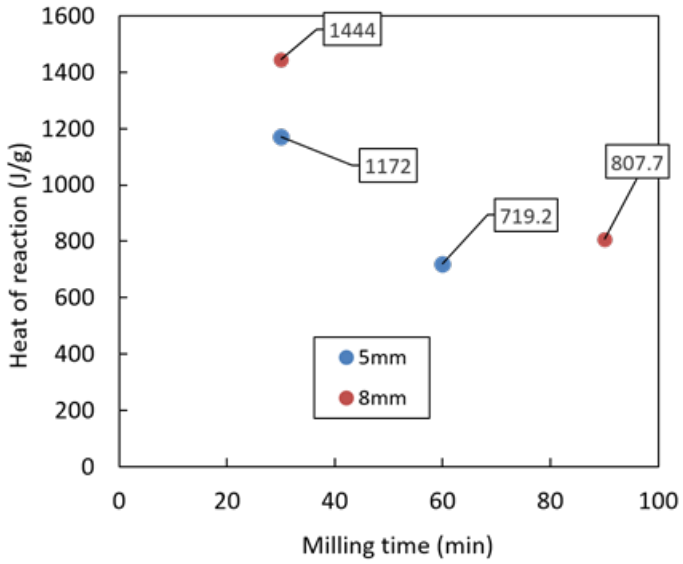

Figure V-36: Measured heats of reaction of Al:Cu_2O ball-milled powders as a function of ball diameter and milling time. The highest heat of reaction was measured in powders milled with 8-mm diameter balls for 30 minutes.

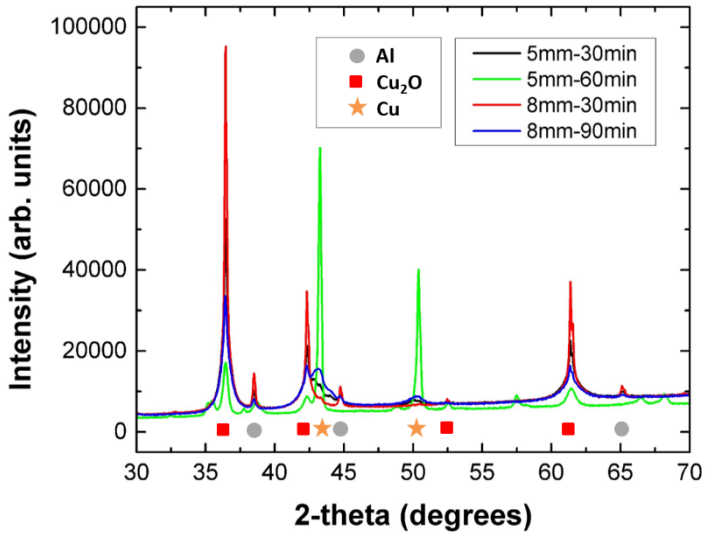

Figure V-37: XRD traces of undiluted Al:Cu_2O ball-milled powders at various ball diameters and milling times. Small/absent Cu peaks suggest that little or no reaction has taken place and correlate with large reactant (Al, Cu_2O) peak intensities.

In order to assess reactivity in REDOX FOILS fabricated from ball-milled powders, we compared reaction propagation velocities to those measured for redox foils prepared from single-phase powders. The velocity data are shown (Figure V-38) as a function of braze volume. For the Al:Cu_2O system, we found that ball milling increases the average propagation velocity by a factor of 3 in 20 wt% diluted foils and a factor of nearly 7 in 40 wt% diluted foils. This is a promising finding, because it suggests we can significantly increase the reactivity of redox foils that approach 75% braze content by volume. All ball-milled powder redox foils propagated faster than their single-phase counterparts.

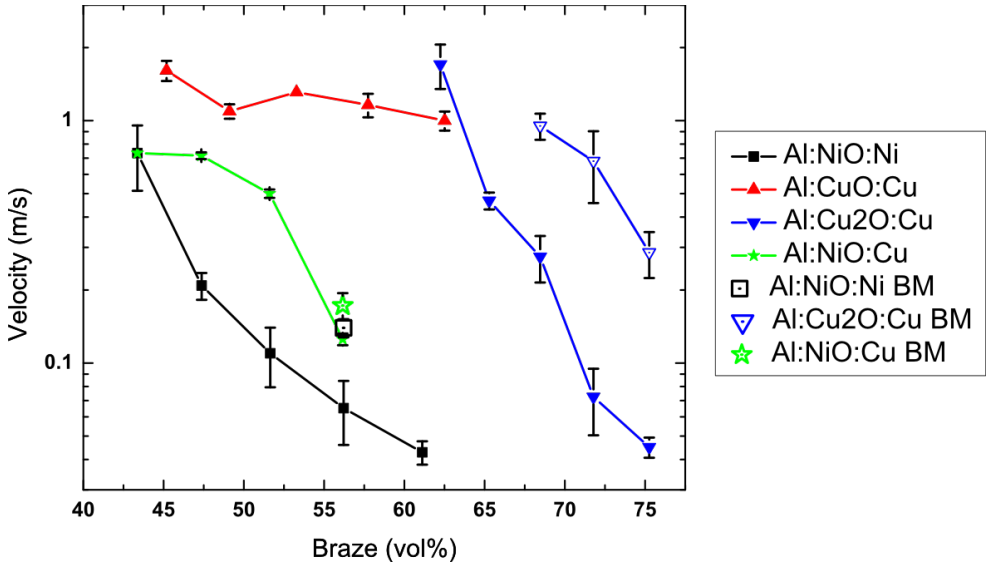

Figure V-38: A comparison of propagation velocities for thermite systems produced from single-phase powders and ball-milled (BM) composite powders. Velocities are plotted as a function of expected braze percent by volume, where the balance is the expected alumina content. Diluent increases from moving left to right.

We also tested ball-milled redox foils in a joining configuration to determine whether the reactions would quench in the bonding interface. Quenching tests were performed in bonds where similar alloys were joined together (Mg AZ31 to Mg AZ31 and Al 6061 to Al 6061) using conventional and ball-milled redox foils. The results are shown in Figure V-39. In all cases, the highest dilution that could be fully propagated through a bond interface was increased by at least 20 wt% when bonding with ball-milled redox foils.

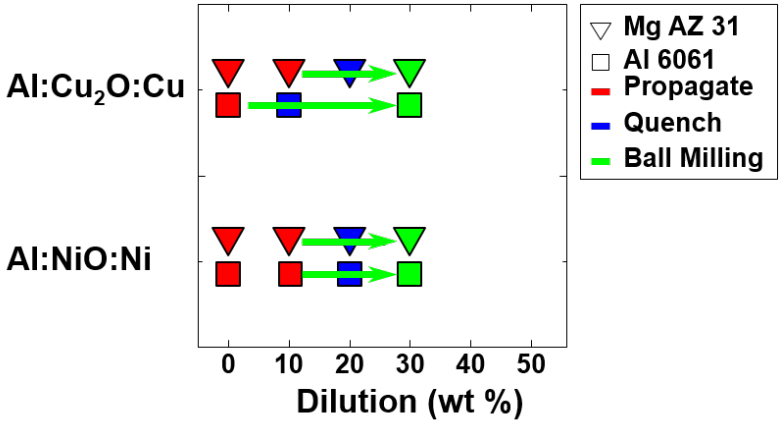

Figure V-39: Quenching limits for Al:Cu_2O:Cu and Al:NiO:Ni systems using conventional and ball-milled powders. Foils created from ball-milled powders could be subjected to higher levels of dilution before quenching in the bond interface.

Experiments to determine the nature and magnitude of stresses in thermite films that are deposited via magnetron sputtering were performed. Stresses were calculated as functions of three deposition parameters: the first deposited layer (Al or NiO), sputtering pressure, and film bilayer thickness. The calculated stresses are shown in Figure V-40 and Figure V-41. For each figure, x-stress refers to the film stress acting in the direction of rotation (i.e., horizontal), while y-stress refers to film stress acting in the vertical direction. For the regime of sputter pressures tested, film stress becomes increasingly compressive as sputter pressure increases for all first layer and direction combinations (Figure V-40. Stresses in the rotation direction decrease in a linear fashion, while y-stresses tend to level off. The trends suggest that stresses in both directions can be minimized at a

sputter pressure of about 2.5 mtorr. Figure V-41 shows film stress as a function of bilayer spacing. For the regime of bilayer spacings tested, the film stress gradually decreases in magnitude as the bilayer spacing increases from 53 nm to 106 nm.

In accordance with the discussion above, we have attempted to deposit 20-µm thick Al:NiO multilayer films using a bilayer spacing of 106 nm and a sputter pressure of 2.5 mtorr. Large aluminum and brass substrates were included in the stress experiments to assess the viability of using these substrates for large-scale film deposition. For particularly thick multilayer films, we have deposited on both thermal oxide silicon wafers (with a 500-nm thick silicon oxide layer) and large aluminum substrates. In the event that films cannot be pulled from aluminum substrates, measurements of velocity can be performed on films deposited on thermal oxide wafers. Unfortunately, issues with various components of our sputtering system prevented successful deposition of this film. We have purchased larger, rectangular oxide targets to help control film stress and give us better control of our sputtering rates.

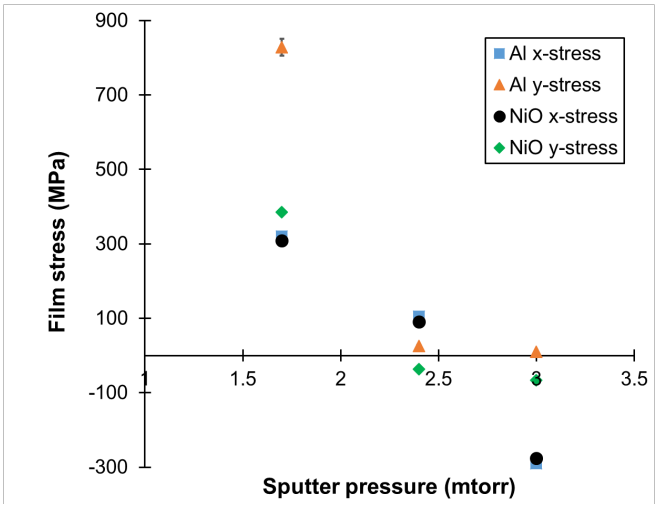

Figure V-40: Biaxial stresses in Al:NiO-Ni/Cu multilayer films as a function of sputter pressure. Total film thickness is about 1 µm and bilayer thickness is 106 nm. Positive values indicate tensile stresses. The legend indicates which layer was deposited first.

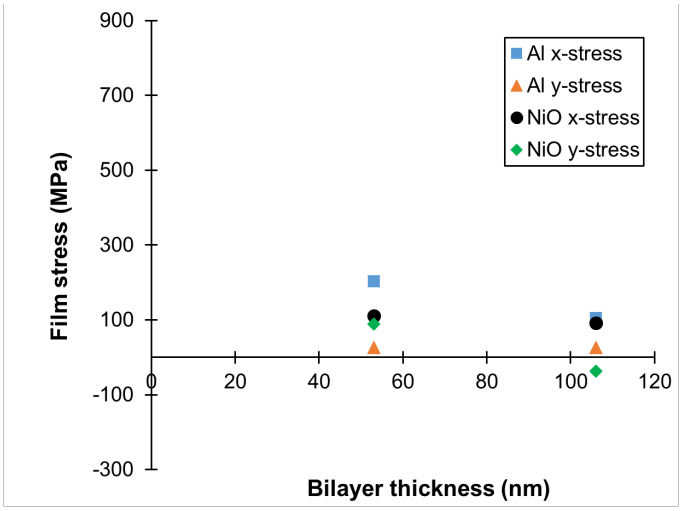

Figure V-41: Biaxial stresses in Al:NiO-Ni/Cu multilayer films as a function of bilayer thickness. Total film thickness is about 1 µm and sputter pressure is 2.4 mtorr. Positive values indicate tensile stresses. The legend indicates which layer was deposited first.

Technology Transfer Path

We have submitted a provisional patent for this technology and other possible embodiments of the redox foil. In the future, we plan to license the technology to a materials manufacturer, who will then sell to the automobile industry.

Conclusion

In FY 2015, we focused on fabrication and characterization of redox foils prepared with ball-milled composite powders. Micrographs confirm that the ball-milling process reduces the average distance between the aluminum and oxide phases when compared to redox foils prepared with single-phase powders. The decrease in reactant spacing is expected to increase reactivity in diffusion-limited reactions, which is supported by the observed increase in average propagation velocity and the shift in exothermic activity to lower temperatures. In addition, we have successfully identified ball-milling parameters for which heats of reaction are maximized in undiluted Al:NiO and Al:Cu_2O ball-milled powders. Quench test data indicate that ball milling can be used to enable bonding at higher dilutions for Al:NiO and Al:Cu_2O redox foils. This is essential for reducing porosity caused by gas production and increasing the amount of braze available for bonding. We have characterized stresses in Al:NiO-Ni/Cu multilayer films produced by magnetron sputtering and identified a set of sputtering parameters that reduces the magnitude of the stress to an acceptable level. Understanding how these stresses evolve during deposition is critical for scaling up the film thickness to produce free-standing films.

References

1. E. Ma; C. V. Thompson; L. A. Clevenger; and K. N. Tu, 1990, *Appl. Phys. Lett.*, 57; pp. 1262.
2. A. Duckham; J. E. Newson; M. V. Brown; T. R. Rude; O. Knio; E. M. Heian; and J. S. Subramanian, 2008, "Method For Fabricating Large Dimension Bonds Using Reactive Multilayer Joining."
3. J. Wang; E. Besnoin; A. Duckham; S. J. Spey; M. E. Reiss; O. M. Knio; M. Powers; M. Whitener; and T. P. Weihs, 2003, *Appl. Phys. Lett.,* 83; pp. 3987.
4. A. J. Swiston; T. C. Hufnagel; and T. P. Weihs, 2003, *Scr. Mater.,* 48; pp. 1575–1580.
5. K. Woll; J. D. Gibbins; K. A. Slusarski; A. H. Kinsey; and T. P. Weihs, in review for publication in *Combustion and Flame.*

Bibliography

A. H. Kinsey; A. Ku; K. A. Slusarski; J. D. Gibbins; K. Woll; and T. P. Weihs, 2014, "Mechanically Processed Thermite Foils for Bonding Metals," presented at the *2014 MRS Fall Meeting & Exhibit*, Boston, Massachusetts.

K. A. Slusarski; E. Krumheuer; A. H. Kinsey; and T. P. Weihs, 2014, "Temperature, Velocity, and Mass Ejection Measurements in Thermite Composite Foils," presented at the *2014 MRS Fall Meeting & Exhibit*, Boston, Massachusetts.

K. Woll; J. D. Gibbins; K. A. Slusarski; A. H. Kinsey; and T. P. Weihs, 2014, "The Utilization of Metal/Metal Oxide Core-Shell Powders Optimizes the Dilution of Thermite Mixtures," presented at the *43rd International Conference on Metallurgical Coatings and Thin Films*, San Diego, California.

K. Woll; J. D. Gibbins; K. A. Slusarski; A. H. Kinsey; T. P. Weihs, "Metal/Metal Oxide Core-Shell Powders to Optimize the Dilution of Thermite Mixtures," in review for publication in *Combustion and Flame.*

V.4. Active, Tailorable Adhesives for Dissimilar Material Bonding, Repair and Reassembly – Michigan State University

Project Details

Mahmoodul Haq, Principal Investigator
428 S. Shaw Lane
Room 3569 Engineering Building
Michigan State University
East Lansing, MI 48824
Phone: 517-402-3409
E-mail: haqmahmo@egr.msu.edu

Lawrence T Drzal, Principal Investigator
428 S. Shaw Lane
Room 2100 Engineering Building,
Michigan State University
East Lansing, MI 48824
Phone: 517-353-5466
E-mail: drzal@egr.msu.edu

Adrienne Riggi, Project Officer
National Energy Technology Laboratory
3610 Collins Ferry Road
P.O. Box 880
Morgantown, WV 26507-0880
Phone: 304-285-5223
E-mail: Adrienne.riggi@netl.doe.gov

Sarah Ollila, Technology Area Development Manager
U.S. Department of Energy
1000 Independence Avenue, SW
Washington, DC 20585
Phone: 202-586-8027
E-mail: sarah.ollila@ee.doe.gov

Contractor: Michigan State University
Contract No.: DE-EE0006424

Executive Summary

Joining of materials and components is necessary as it allows versatility in assembly and repair along with reduction in time and cost of manufacturing. This work uses ‘active adhesives’ that inherit all the benefits of bonded joints (e.g., lightweight, elimination of holes, and associated stress concentrations) and overcome the shortcomings of disassembly and repair. Thermoplastic adhesives modified by the incorporation of electrically conductive graphene nanoplatelets (GnP) at a concentration above the percolation point provide a unique synergy of mechanical, thermal and electrical properties. While the choice of thermoplastic is governed by desired application, the addition of GnP allows energy to be deposited primarily in the adhesive. The percolated network of graphene particles in the adhesive at less than 2 wt.% can quickly couple to a high frequency radiation (microwave [MW]) via non-contact methods and increase the adhesive temperature to above the required processing temperatures. The adhesive melts and flows over the adherends and, upon cooling, forms a structural adhesive bond. Furthermore, the process can be used to disassemble the adhesive joint if repair or reworking is required.

During this work, the concept of the aforementioned active adhesives was studied using varying graphene contents in nylon-6 adhesive. Successful activation, assembly, and disassembly was achieved using variable frequency microwave activation on in-plane (i.e., lap-shear) joints. Structural behavior of reassembled joints was found to be better than similar thermally bonded joints. Additionally, chemical functionalization of GnP and its effect on enhancement of mechanical, thermal, damage resistance, and interaction with MWs was studied. An integrated experimental and numerical approach that adopts novel non-destructive evaluation techniques at every length scale is used in this project. This allows for development of experimentally validated design tools and databases, along with the possibility of a wide range of industrial and large-scale structural joining. The work-to-date has shown great promise in use of the active adhesives for multi-material joining. Critical experiments and parametric studies are in progress to fully exploit the benefits offered by these active adhesives.

Accomplishments

- Successful development of active adhesives films comprising pristine (non-functionalized) and functionalized GnP (Fiscal Year [FY] 2015).
- Completed experimental characterization of tensile properties of functionalized active adhesive (FY 2015).
- Successful proof-of-concept of activation (i.e., effective bonding and debonding of composite adherends using variable frequency microwave [VFM]) (FY 2015).
- Evaluated tensile behavior of active adhesives under varying temperature conditions; for example, 25°C (75°F), 100°C (212°F), and 177°C (350°F) (FY 2015).
- Developed numerical simulations to obtain effective properties of novel adhesives and study the structural behavior of resulting joints (FY 2015).

Future Directions

- Experimental evaluation of enhancements in toughness (i.e., impact strengths and delamination resistance) due to chemical functionalization of GnP.
- Environmental testing of multi-material joints to evaluate the effects of corrosion on material properties.
- Experimental evaluation of repair (i.e., selective activation of adhesive after impact to heal the joint), followed by destructive testing to evaluate efficiency of repair.
- Experimental characterization of multi-material joints (a) in-plane (i.e., lap-joints), (b) out-of-plane (i.e., T-joints), and (c) torsional joints (rotors, will be tested in collaboration with EATON).
- Evaluate the reassembly/repair of joints using an array of nondestructive evaluation (NDE) tools.
- Development of experimentally validated numerical simulations.

Technology Assessment

- Target: Develop active adhesive technology for structural joining of similar and dissimilar materials, with the ability of reversible bonding (disassemble/reassemble), in-service repair, enhanced mechanical properties, and acceptable industrial practices.
- Gap: Joints are commonly considered the weak links of a structure due to the complex phenomena and interactions of either similar or dissimilar materials. Strategic incorporation of nanographene in adhesives allows for improvements in stiffness, toughness, and delamination resistance.
- Gap: Unlike bolted joints, adhesive/bonded joints do not allow disassembly and repair. Industry use of bonded joints is limited due to moderate strengths and inability to dis-assemble or repair.

Introduction

The objective of the project is to demonstrate the feasibility of the proposed active adhesive technology for structural joining of dissimilar materials, with the ability to disassemble/reassemble and perform in-service repair. The outcomes of this work will accelerate development of efficient active adhesive technology to join multi-material lightweight structures in different sectors (e.g., automotive, aerospace, and marine applications).

Thermoplastic adhesives modified by incorporation of electrically conductive GnP at a concentration above the percolation point provide a unique synergy of mechanical, thermal, and electrical properties. While the choice of the thermoplastic is governed by the desired application, the addition of GnP allows energy to be deposited primarily in the adhesive. The percolated network of graphene particles in the adhesive at less than 2 wt.% can quickly couple to ultra-high frequency (UHF) MW radiation via non-contact methods and increase the adhesive temperature to above the required processing temperatures. The adhesive melts and flows over the adherends and, upon cooling, forms a structural adhesive bond. Furthermore, the process can be used to disassemble the adhesive joint if repair or reworking is required. A schematic of the proposed technology and the overall approach is provided in Figure V-42. To the best of the investigators' knowledge, these active adhesives with repeatable healing/repair and facile disassembly are unique and have not been used in structural joining; they offer a possibility in a wide range of applications.

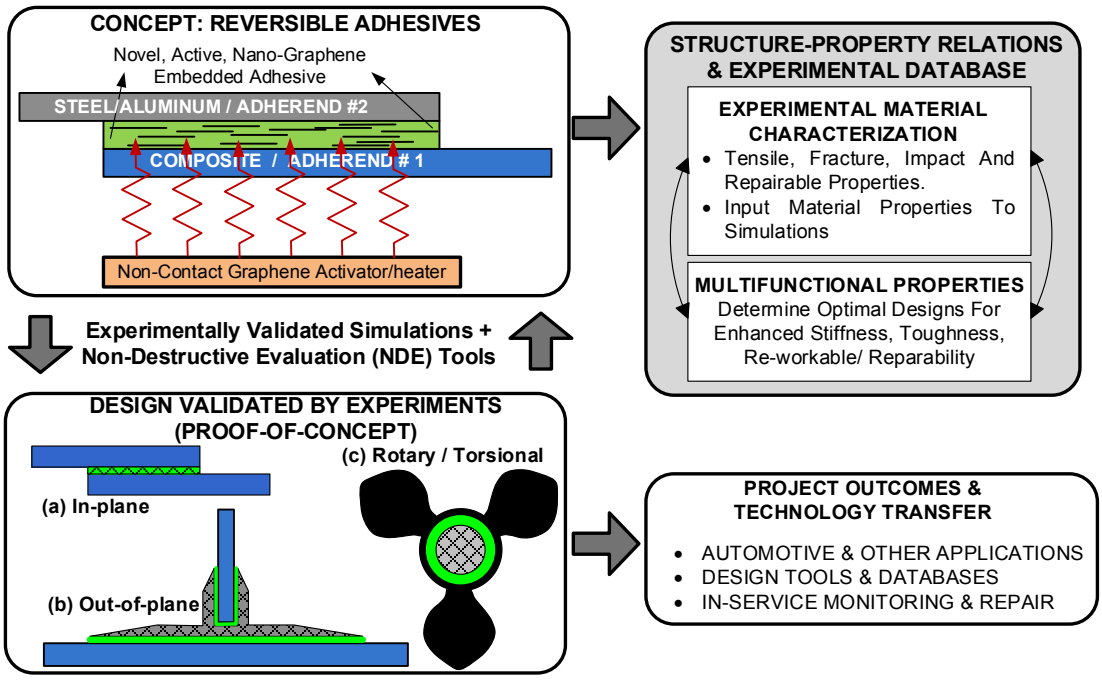

Figure V-42: Schematic of the concept and overall approach.

Most structural joint development studies focus solely on in-plane behavior. This work evaluates the feasibility of the proposed technique on (a) in-plane (i.e., lap-joints), (b) out-of-plane (i.e., 3D-woven Pi/T-joints), and (c) torsional/rotatory (i.e., super-charger) joints. Measurement techniques (such as embedded fiber-Bragg optic sensors and infrared thermography) will be used to accurately measure the in-service performance and observe the repair efficiency of resulting dissimilar material joints. This thorough of a study is directed to cover all possible automotive and ground vehicle applications.

The above mentioned approach of developing active adhesives will be achieved through the following subobjectives/tasks:

A. Processing, material development, and optimization of active adhesives
B. Lab-scale evaluation and detailed material characterization
C. Design, testing, and applications:

The detailed subtasks for the aforementioned categories were provided in the FY 2014 annual report [1] and, for brevity, are not included in this report.

Approach: Experimental Methods and Processing of Adhesives

Processing of Active (GnP-Modified) Adhesives

During this work, nylon-6 was selected as the thermoplastic material. The choice of thermoplastic depends on the desired application and instead of studying multiple thermoplastics, a single adhesive was selected. The processing of thermoplastics with GnP and associated experimental characterization can be directly extended to other thermoplastics. During this work, a melt extrusion process was used to blend GnP into nylon-6. The nylon-6 pellets were exposed to 70°C for 4 hours to eliminate any presence of moisture. Then, melt extrusion of pristine and GnP-modified nylon-6 was carried out in a Dutch State Mines (DSM) Micro 15 cc Compounder (vertical, co-rotating, twin-screws micro-extruder) operating at 260°C for 3 minutes at a screw speed of 100 rpm. The melted material was then directly transferred in to a Daca micro-injector with the $T_{barrier}$=260°C and T_{mold}=100°C. The injection pressure applied for injection molding of tensile, impact, flexural coupons and discs was around 0.97 MPa. The resulting injection-molded samples were used for experimental testing and the discs were used for adhesive film production.

The discs from the injection molded specimens were placed between stainless steel plates covered by a high-temperature-resistant polyimide film, Kapton® (DuPont®) to enable ease of adhesive film removal. To control/maintain the adhesive film thickness, 0.09-mm thick aluminum spacers were placed between the top and bottom plates. To eliminate/reduce entrapped air, the entire setup was covered by a vacuum bag and subjected to a vacuum pressure of one atmosphere. While maintaining the vacuum pressure, the plates were heated at a rate of 5°C/minute up to 260°C, followed by an isothermal process for 5 minutes. In order to obtain the desired film thickness, successive pressures of 30, 60, and 90 MPa were applied to the plates with a time interval of 3 to 5 minutes. Additional spacers were placed in the center of the plates to ensure uniform adhesive thickness. The overall process is shown schematically in Figure V-43.

Enhancements in mechanical thermal and damage resistance properties offered by addition of GnP in polymers can be further enhanced by proper chemical functionalization (i.e., creating compatibility between the host polymer and GnP). During this work, three types of GnP functionalization were studied: (1) aliphatic epoxy (AE), (2) phase-separated carboxyl-terminated acrylonitrile butadiene rubber (CTBN), and (3) styrene-butadiene-methyl-methacrylate (SBM) triblock. Grafting of the aforementioned functional groups to epoxy has found considerable enhancements in toughness and fracture resistance [2,3]. Similar work on thermoplastics is not explored elsewhere and is studied in this work.

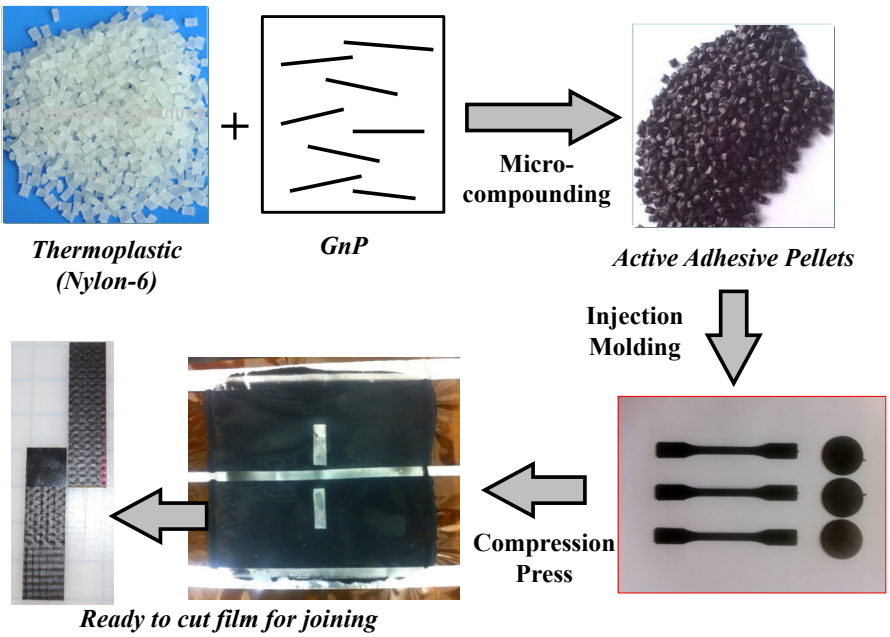

Figure V-43: Production of active adhesives functionalization of GnP.

Material Characterization of Pristine and GnP-Modified Nylon

Tensile and flexural tests were performed using a universal testing system (UTS) electro-mechanical equipment. A minimum of five specimens per case were tested and only the average values are reported. The tensile tests were performed according to ASTM D638. A 1,000-lb (454 kg) standard load cell attached to the UTS frame and external laser extensometer were used to measure applied force and resulting longitudinal strain, respectively. On the other hand, flexural tests (i.e., three-point bending mode) were performed according to the ASTM D770-10 on the same machine with a load cell of 100 lb (45.4 kg). The dimensions of the samples for flexural tests were 62.7 mm ×12.24 mm×3.2 mm. The span length was set at 50.8 mm. The crosshead speed was calculated based on specimen geometry, according to ASTM standard, and was set at 1.27 mm/min. A linear variable differential transformer (LVDT) was used to measure deflection in flexural tests. Impact resistance tests (i.e., Izod type) were carried out according to the ASTM D256 standard test. The dimensions of the samples for impact resistance tests were 62.7 mm x 10.72 mm×3.91 mm cross-sectional area at the mid-notch.

Results and Discussion:

Tensile Behavior of GnP-Modified Adhesives

The enhancements in tensile, flexure, and impact behavior due to pristine (i.e., non-functionalized) GnP in nylon-6 were reported in FY 2014 [1]. For 5 wt.% GnP content, the flexural strengths and modulus improved by 10% and 30%, respectively, while the tensile strengths reduce by about 15% [1]. Figure V-44 and Figure V-45 provide the effects of functionalization on tensile modulus and strengths, respectively. The experimental characterization of AE-functionalized GnP was still in progress and not included. The effect of functionalization is very clear from the observations of Figure V-44 and Figure V-45. CTBN modifications had adverse effects on both tensile modulus and strengths, while SBM modification showed enhancements in tensile modulus and minimal drop in strengths. The biggest advantage (and need) of functionalization is the improvements in toughness and resistance to fracture without sacrificing stiffness. Experimental characterization on toughness is in progress. Nevertheless, the enhancement in tensile stiffness along with equal or better tensile strengths (as seen in Figure V-44 and Figure V-45 for 3 and 5 wt.% SBM) shows that

the stiffness-toughness balance can be achieved using functionalized GnP. From earlier evidence in thermosets [2,3], the fracture toughness should considerably increase due to improved functionalization.

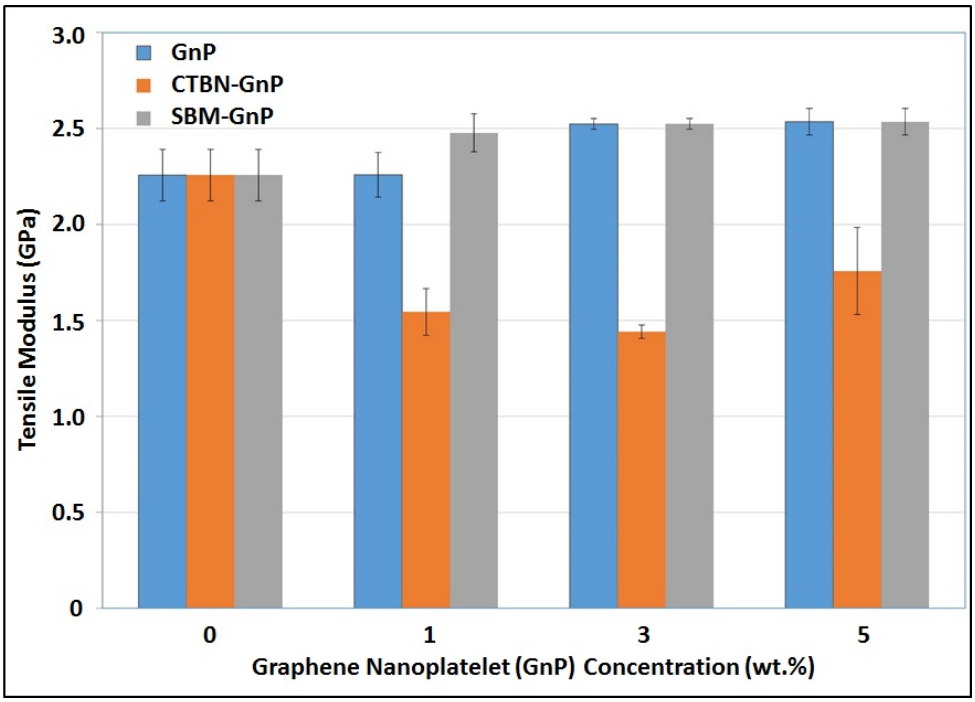

Figure V-44: Effect of functionalization on tensile modulus of GnP-modified nylon-6.

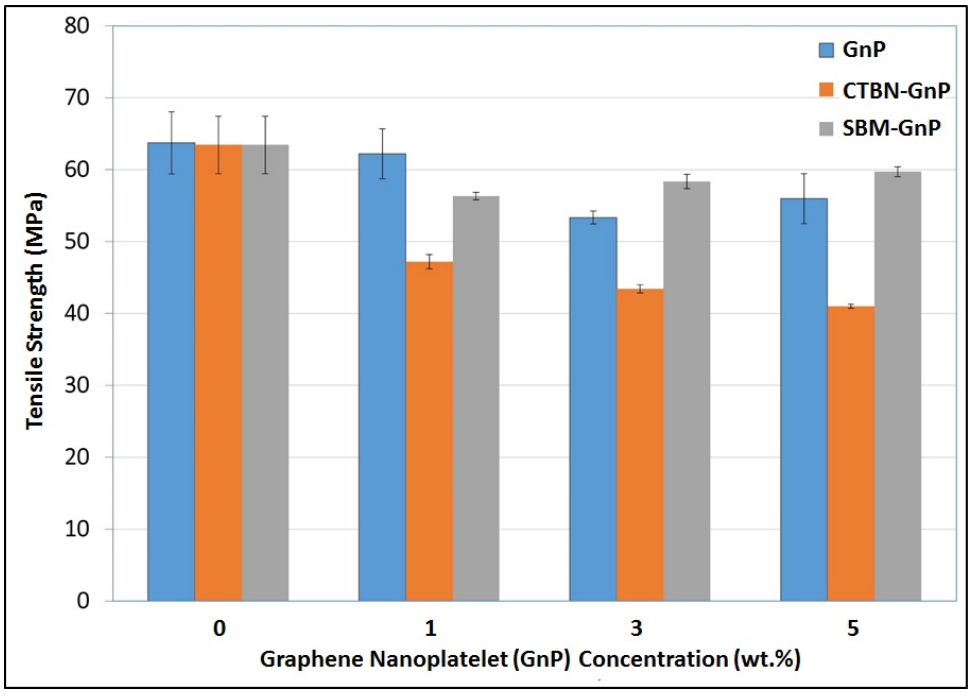

Figure V-45: Effect of functionalization on tensile strengths of GnP-modified nylon-6.

Temperature-Dependent Tensile Behavior of GnP-Modified Adhesives

In order to understand the behavior of GnP-modified adhesives at high temperatures, tensile tests were performed at three temperature states: (1) room temperature 25°C (75°F), (b) 100°C (212°F), and (c) 177°C (350°F). All tests were performed in displacement control at a rate of 2 mm/minute in a universal testing machine equipped with an environmental chamber at the EATON research facility.

Figure V-46 shows representative plots of high-temperature tensile behavior corresponding to pristine nylon-6 (i.e., 0 wt.%) and 3 wt.% GnP contents. The 1 and 5 wt.% GnP contents are not shown for clarity, plus the 3 wt.% response was found to be intermediate and bounded by the 1 and 5 wt.% responses. Figure V-46a shows the entire tensile response, while Figure V-46b shows the linear regime depicting stiffness variations. The pristine case (0 wt.%) for each temperature is shown in a solid line, while the 3 wt.% is shown with a dotted line. As expected, embedment of non-functionalized GnP in nylon-6 reduces ductility while increasing stiffness. As the temperature increased, the stiffness dropped considerably and ductility increased. The increase in ductility is attributed to an increased ability of the polymer chains to move at higher temperatures. While considerable reduction in ductility was observed due to GnP reinforcement at room temperature; this drastic reduction was not observed at higher temperatures. Instead a balance in stiffness-toughness was observed relative to pristine nylon for similar temperature.

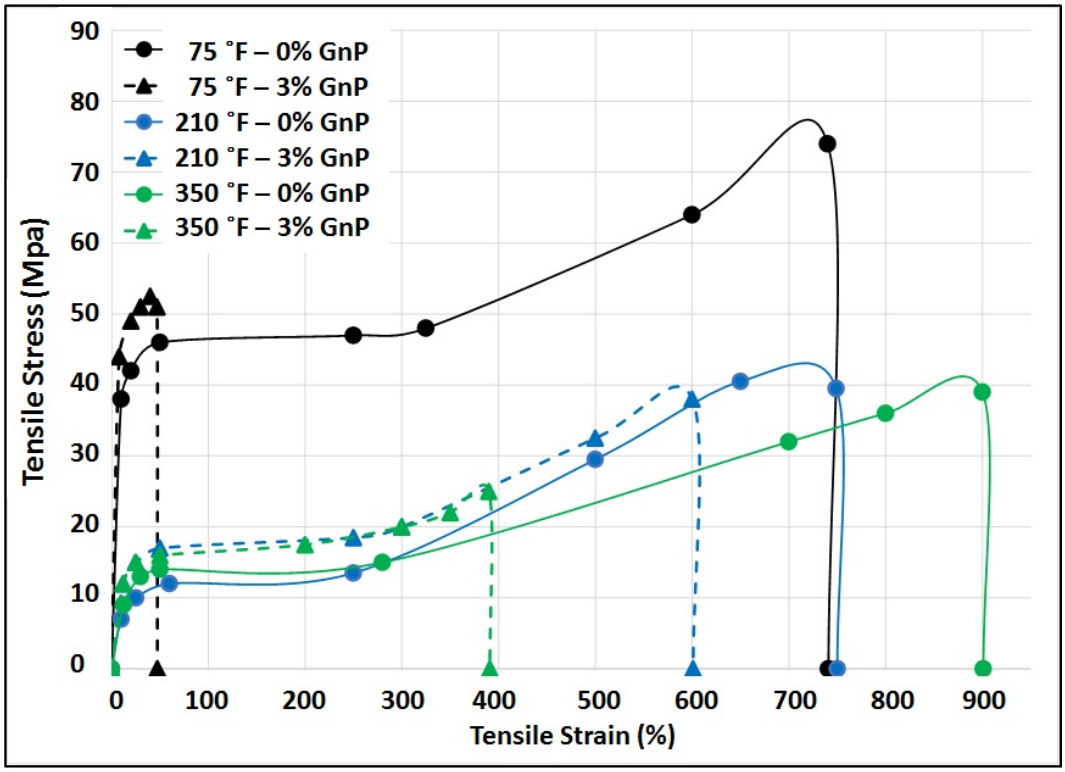

(a)

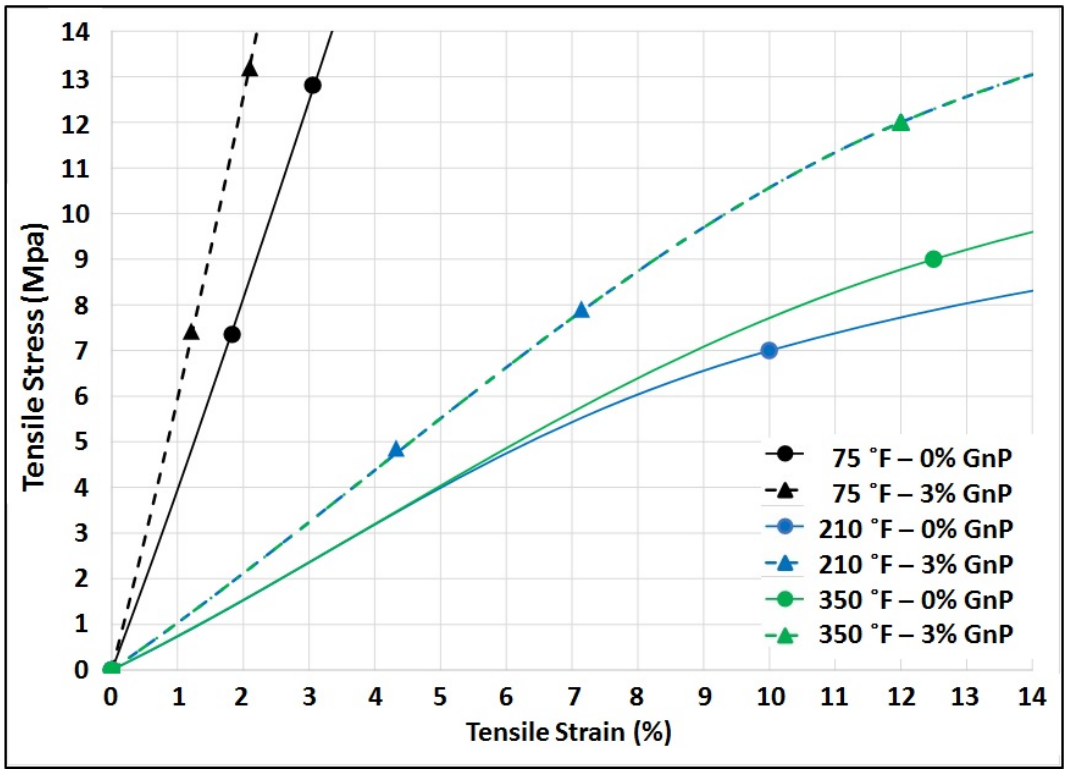

(b)

Figure V-46: Tensile behavior of GnP-reinforced nylon-6 with varying temperature: (a) entire response and (b) linear regime.

Microwave-Activated Joining: Assembly and Disassembly

To demonstrate the concept of selective activation of the GnP-modified nylon-6 adhesive, the joints were exposed to microwave radiations using a variable frequency microwave (VFMW) Model MC2100 supplied by Lambda Technologies, Inc. NC, USA. For bonding, the two adherends and GnP modified nylon-6 film were placed inside the VFMW cavity with quartz rods as dead-weights. Additionally, Teflon spacers were placed to maintain uniform adhesive thickness as the adhesive heats and flows during VFMW activation. Figure V-47a and Figure V-47b show the schematics of the assembly and disassembly setup prior to microwave activation. Figure V-48 describes the entire assembly/bonding procedure.

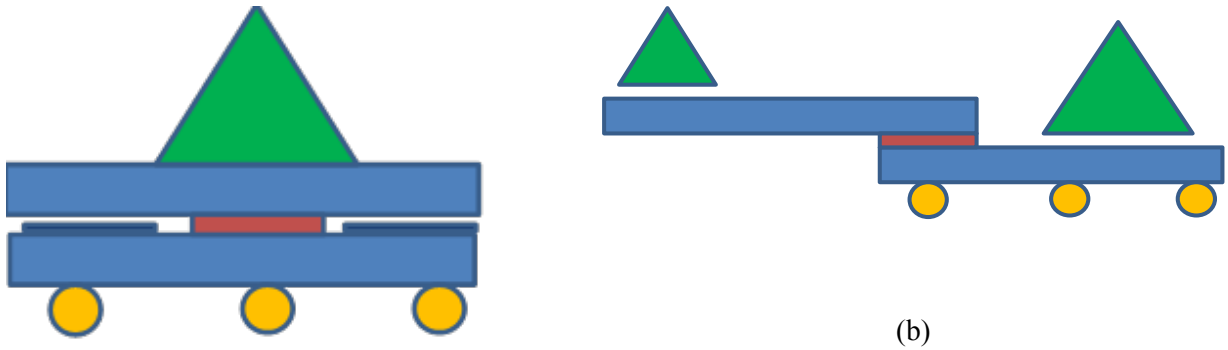

(a) (b)

Figure V-47: Schematics of microwave setup (a) assembly/bonding and (b) dis-assembly. The green triangles are dead-weight and the red rectangle represents the active adhesive.

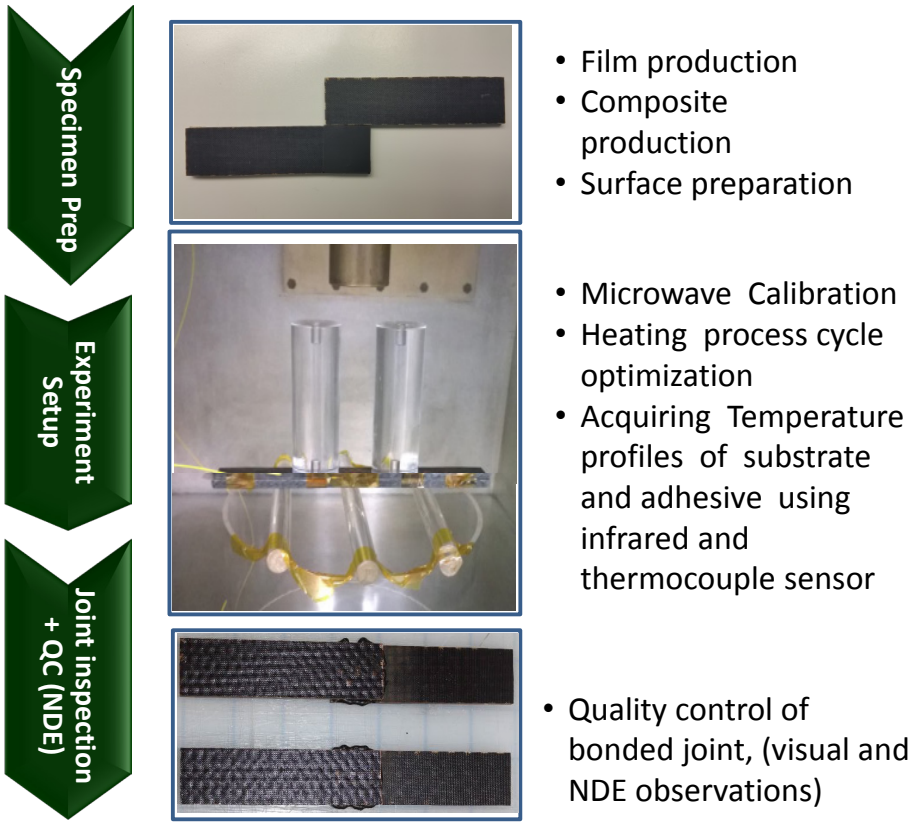

Figure V-48: Process of microwave-activated assembly/bonding.

A fiber optic contact probe was attached to the bond-line region of the assembly. An aluminum/quartz block weighing approximately 200 g was used to provide hold down weight; this was the desired load balance that allows bondind (Figure V-48) and debonding (Figure V-49) of the joint. For bonding of the joint, three and four-step processes were used. For brevity, only the four-step process is described here: (1) ramp at 2°C/s to 100°C and hold for 1 minute; (2) ramp at 1.5°C/s to 115°C and hold for 1 minute; (3) ramp at 1°C/s to 150°C and hold for 2 minutes, and (4) ramp at 0.5°C/s to 230°C and hold for 4 minutes. For the debonding process, a two-step VFM process was used: (1) ramp at 2°C/s to 200°C and hold for 1 second followed by (2) a ramp of 0.5°C/s to 240°C and hold for 1 minute. The quartz rods were placed such that they create a cantilever/lift-off mechanism to debond the joint. Figure V-49 shows the debonding setup and the actual test sample.

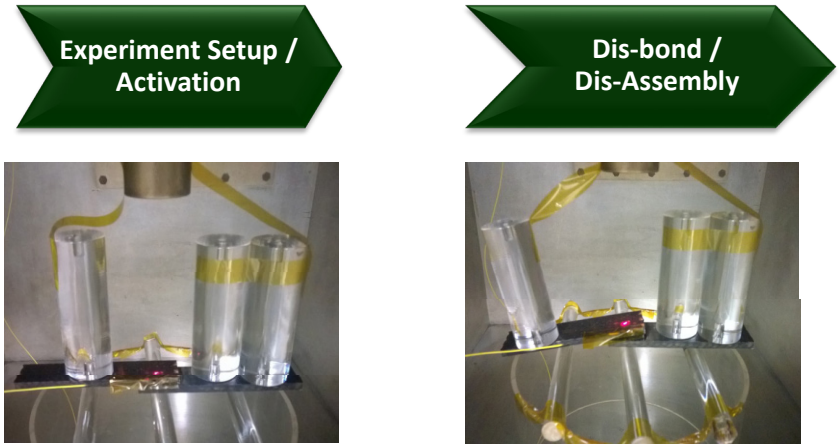

Figure V-49: Process setup and actual test sample of the microwave-activated disassembly

Quality Control and Measurement of Temperature in the Bond-Line During Bonding and Debonding

The temperature profiles of the substrate and the adhesive were recorded using both infrared and thermocouple sensors. Additionally, fiber-optic sensors were embedded in the adhesive to measure the temperature in the bond line. Figure V-49a and Figure V-49b show temperature profiles for adhesive during the bonding and debonding process for varying GnP contents in the adhesive film. As expected, the temperature profile within the bond line changed with varying GnP content during both bonding and debonding. Specifically, as the GnP content increased, the higher the change in adhesive temperature was expected. This was clearly observed during the bonding process (Figure V-50a) and not so distinctly observed during the debonding process. This discrepancy is primarily attributed to differences in the location of the temperature sensor as the opening gap increases during debonding and changes in the length of the cantilever portion in the current setup (Figure V-49). Experiments currently in progress address this issue by carefully maintaining the location of the cantilever portion and with embedment of sensors in the adhesive at a similar location for all samples.

Another expected observation was that the substrate would also heat up due to interactions with microwave; however, the hypotheses was to selectively heat just the adhesive. Figure V-51 shows the increase in temperature of the substrates during the bonding process. The concentration shown in Figure V-51 corresponds to the adhesive and not the substrate. As a result, the substrates seem to heat up more uniformly, independent of GnP content. Another observation is that the maximum temperature reached by the substrate was 200°C, whereas the adhesives reached higher than 200°C (see Figure V-50a), indicating relatively better interaction of adhesives to microwaves. In all of the above-mentioned experiments, the microwave applicator was controlled by the temperature of the adhesive over a constant duration and the power applied varied based on feedback from the temperature probe. During this process, the substrate and adhesive both heated up according to their dielectric properties. In order to better understand selective heating of just the adhesive, instead of using temperature control, constant power was selected to control the applicator and the temperature of the adhesive and substrate was measured (Figure V-52). At a power of 350 Watts or more, the adhesive heated up much more rapidly than the substrate for the same duration. This indicates the possibility of selective activation of just the adhesive. Statistically significant experiments are in progress to validate this observation for a wide range of substrates.

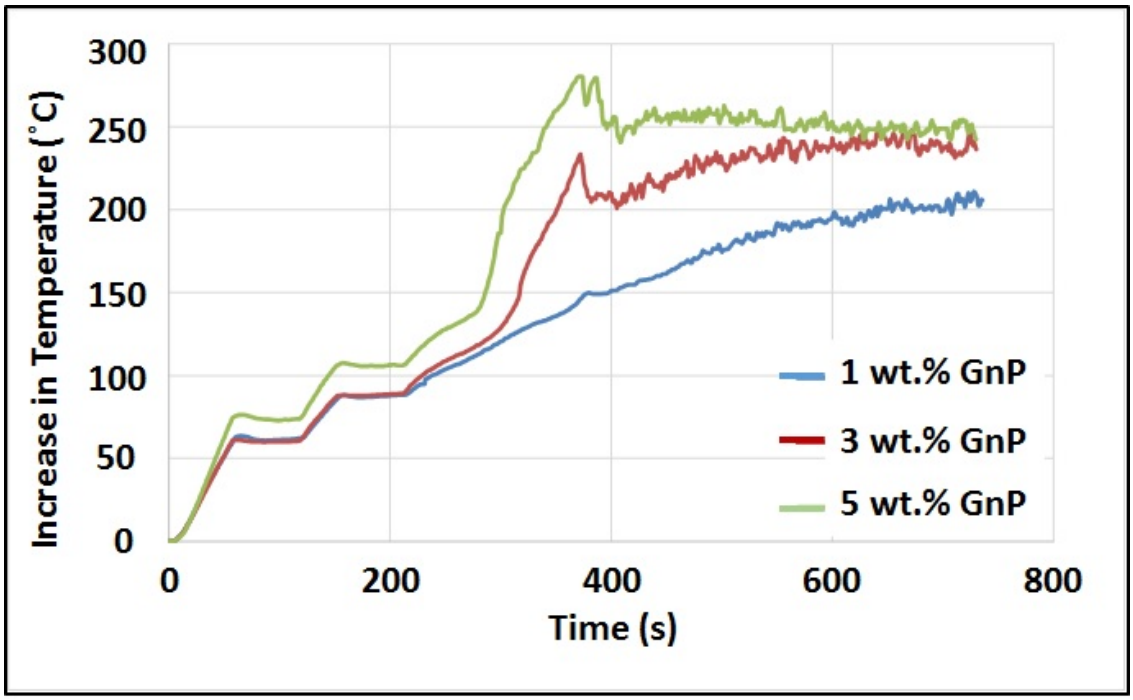

(a)

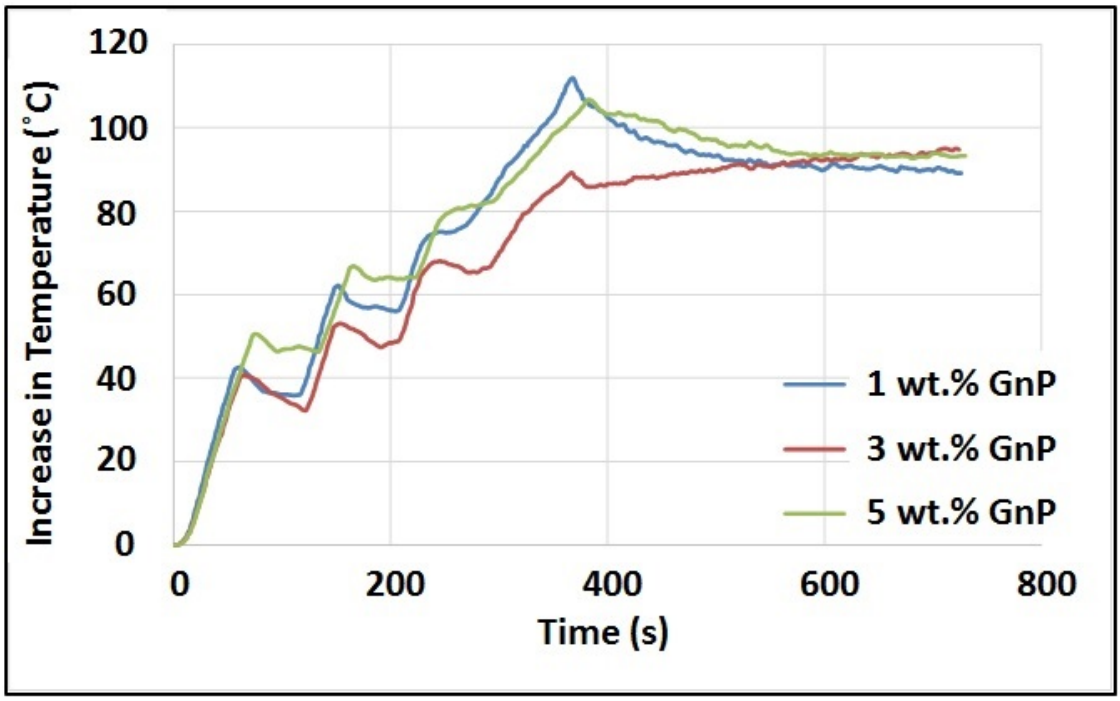

(b)

Figure V-50: Adhesive temperature profile during (a) bonding and (b) debonding.

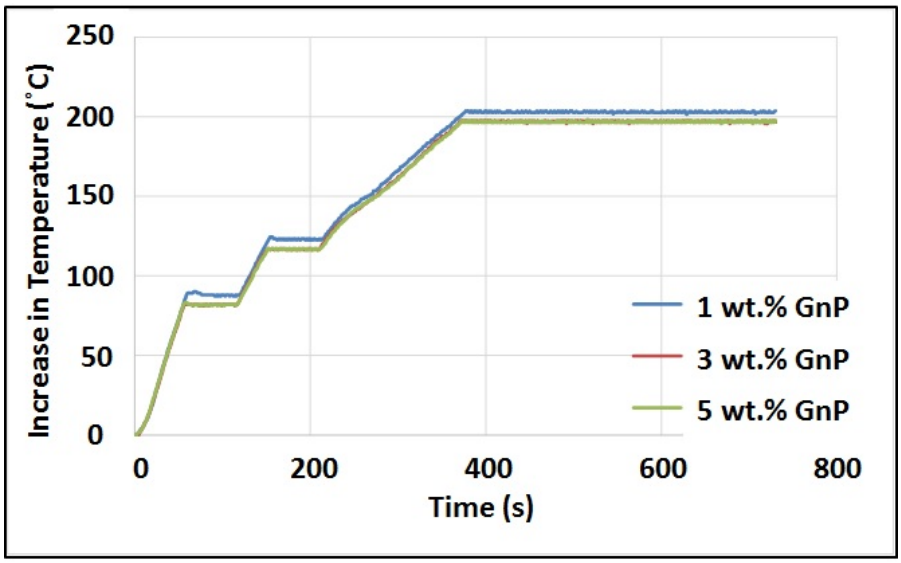

Figure V-51: Substrate temperature profile during bonding.

Comparison of Lap-Shear Properties: Thermally Bonded – Convection Oven Versus Microwave-Assisted Bonding

In order to understand the efficacy of active adhesives, lap-shear joints were tested from both the microwave-assisted bonding process and the conventional thermally bonded process. All parameters (e.g., processing, film thickness, GnP content, batch, and testing conditions) were the same, except the bonding process. Figure V-52 shows comparison of the lap-shear strengths for varying GnP contents from the microwave–assisted and thermally bonded joints.

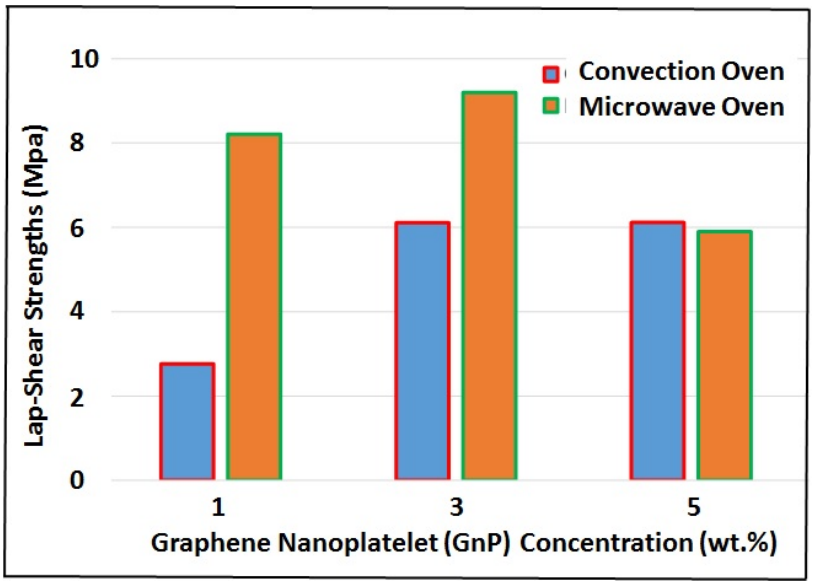

Figure V-52: Comparison of lap-shear joints strengths for conventional thermal-bonded and microwave-activated assembled joints.

The lap-shear tests from both the microwave-assisted and thermally bonded joints were expected to be similar. Interestingly, the microwave-assisted joints showed much better performance. This could be for several reasons. First, the adhesive heats up relatively uniformly as it is activated by the microwave. In thermal systems, the heat is transferred via conduction from the substrates to the adhesives and via convection through the edges of the adhesives. This leads to non-uniform heating of the adhesives and may be degrading the adhesive near the edges. Unfortunately, the edges are locations where the stress concentrations are maximum and this could affect joint behavior significantly. Second, in microwave-assisted heating, the substrate does not degrade as the adhesive is heated rapidly. This should increase the stiffness of the substrate and the joint, thereby increasing the load-transfer rate and resulting strength of the joint. Statistically significant testing and embedded sensors and NDE tests are currently in progress to further validate the observed results. Overall, the results are very promising and further prove the concept and the possibility of a wide range of applications.

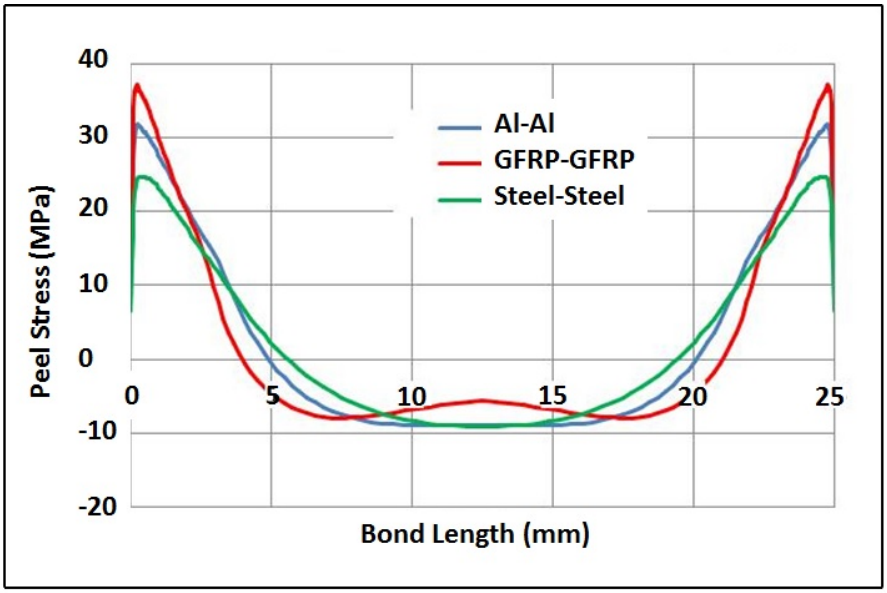

(a)

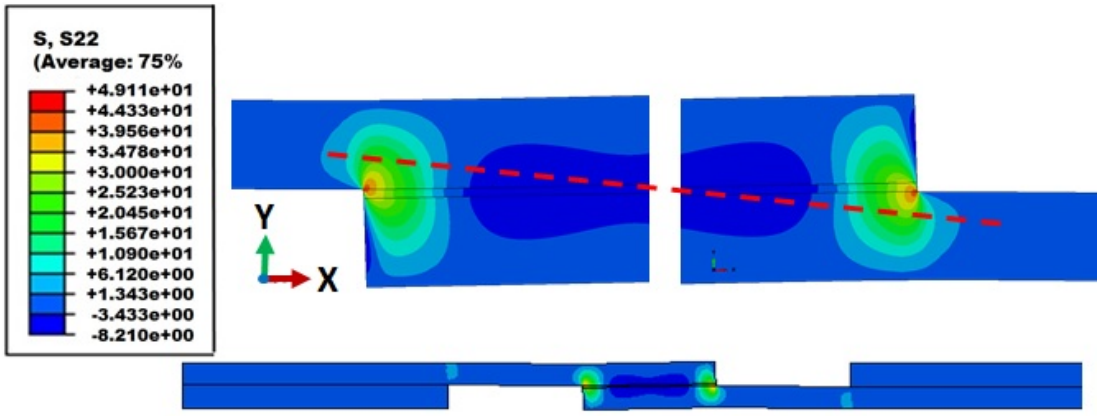

(b)

Figure V-53: Variation of peel stresses (S_{22}) along the adhesive mid-plane in a lap-joint (a) along the length of the bonded area and (b) S_{22} stress contours showing stress contours in the two ends.

Numerical Simulations

Finite element-based numerical simulations were performed to obtain the effective properties of novel adhesives and to study the structural behavior of resulting joints. The effective properties of the adhesives (such as the modulus being taken into account due to variation in GnP content, its morphology, and random distribution) were obtained through numerical homogenization using finite element-based unit cells as reported in the FY 2014 report [1]. The structural simulation of a lap-joint was performed using the commercial finite element software ABAQUS. The material properties of the substrate and the adhesives input in the software were experimentally obtained. Figure V-53 shows a typical peel stress distribution in a lap-joint. As expected, stress concentrations occur at the ends of the joints (Figure V-53b). An interesting possibility is to develop active adhesive films with oriented GnP platelets and place these films along the direction of the loads (Figure V-53a) to reduce stress concentrations, delay onset of failure, and increase the load-carrying capacities and fully exploit the benefits offered by GnP. While this has not yet been attempted in this work, it shows the possibility of tailoring the adhesives to enhance structural performance while taking advantage of reversible bonding.

Technology Transfer Path

The deliverables (i.e., procedures and results) of this project will be transferred to industry through collaboration with EATON. EATON is an industrial partner as a part of this project. Additionally, the results and findings will be shared with the U.S. Army Tank Automotive Research Development and Engineering Center to facilitate applications on ground vehicles.

Conclusion

During the past year, considerable progress was made in developing active adhesive technology for multi-material joints in lightweight structures. Microwave-activated assembly and disassembly was successfully performed on joints with a wide-range of GnP contents. The process was found to be repeatable and efficient. Microwave-activated joints had improved lap-shear strengths over those of conventional thermally bonded joints. This is attributed to uniform heating throughout the bondline due to microwave-activation rather than non-uniform heating from conventional thermal bonding. Work is in progress on additional joints in out-of-plane and torsional configurations and improved modeling and simulations.

GnP were chemically functionalized to increase compatibility between the host polymer and GnP. Three types of GnP functionalization were studied: AE, CTBN, and SBM triblock. Successful processing and tensile

property characterization were completed. SBM-based functionalization showed enhancements in tensile modulus with minimal drop in strengths. The biggest advantage (and need) of functionalization is improvements in toughness and resistance to fracture without sacrificing stiffness. Impact resistance and toughness characterization are in progress.

Overall, the progress and results from this work show great promise in use of GnP-reinforced thermoplastics as active adhesives for dissimilar material joining.

References

1. "FY 2014 Annual Progress Report for Lightweight Materials R&D," http://energy.gov/sites/prod/files/2015/07/f24/DOE%20VTO%202014%20Materials%20Annual%20report.pdf, accessed November 10, 2015.
2. M. A. Downey and L. T. Drzal, 2014, "Toughening of aromatic epoxy via aliphatic epoxy copolymers," *Polymer*; pp. 6658-6663.
3. N. K. Kamar and L. T. Drzal, 2016, "Micron and Nanostructured Rubber Toughened Epoxy: A Direct Comparison of Mechanical, Thermomechanical and Fracture Properties," *Polymer* (in review)
4. M. Haq; L. T. Drzal; and E. A. Patterson, 2011, "Adhesively Bonded Structural Composite Pi-Joints: Damage-induced Behavior, Modeling and Experiments," *ASME 2011 Applied Mechanics and Materials Conference*, Chicago, Illinois, May 31 through June 2, 2011.

Bibliography

M. Haq, 2015, "Examining Novel, Tailorable Reversible Bonded Joints for Multi-material Joining," invited lecture at the *4th Annual Global Automotive Lightweight Materials Detroit 2015*, symposium, August 18 through 20, 2015.

M. Haq; E. G. Koricho; L. T. Drzal; and R. J. Gerth, 2015, "Tailorable Adhesives for Multi-material Joining, Facile Repair and Re-assembly," *American Society of Composites (ASC2015) Conference*, Michigan, September 28 through 30, 2015.

M. Haq; L. T. Drzal; and Koricho, "Reversible Adhesive Compositions and Related Methods," U.S Prov. Patent App. No. 62/137,023.

V.5. Laser-Assisted Joining Process for Aluminum and Carbon-Fiber Components — Oak Ridge National Laboratory

Project Details

Adrian S. Sabau, Principal Investigator
Oak Ridge National Laboratory
1 Bethel Valley Road
Oak Ridge, TN 37831
Phone: 865-241-5145
E-mail: sabaua@ornl.gov

C. David Warren, Principal Investigator
Oak Ridge National Laboratory
1 Bethel Valley Road
Oak Ridge, TN 37831
Phone: 865-574-9693
E-mail: warrencd@ornl.gov

Sarah Ollila, Technology Area Development Manager
U.S. Department of Energy
1000 Independence Avenue, SW
Washington, DC 20585
Phone: 202-287-6020
E-mail: Sarah.Ollila@ee.doe.gov

Contractor: Oak Ridge National Laboratory
Contract No.: DE-AC05-00OR22725

Executive Summary

The project objective is to demonstrate a breakthrough laser-structuring technology for joining carbon-fiber polymer composites (CFPCs) and aluminum (Al) components. Innovations include the texturing of both the Al surface and the CFPC surface and engineering "rough" surfaces on Al and CFPC before an adhesive bonding operation. 3M Company (3M) formulated the adhesives; Plasan Carbon Composites, Inc. (Plasan) provided the composite; and Cosma, Inc. (Cosma) provided the Al. All three companies are partners on this project.

In this second year of the project, the effort focused on demonstrating the effect of the laser-structured surfaces of the Al and CFPC materials on joint performance. The following quality indicators were used for assessing joint performance: lap-shear strength, maximum load, displacement at which the maximum load was recorded, and mode of failure (i.e., failure in the joint or failure in one component).

A significant increase in the mechanical properties of the lap-shear joints, which were made with laser-structured surfaces, compared to the baseline data demonstrates the proof-of-concept for use of laser structuring and/or laser-ablation technology for surface preparation of both CFPC and Al coupons before adhesive joining. Data indicate that mechanical properties of the joints can be significantly increased by laser structuring the Al and CFPC with a 6-millimeter (mm) beam size and increasing the bond line thickness of the adhesive from 0.25 to 0.85 mm.

Accomplishments

- A minimum of six specimens were used per each condition to obtain range, mean, and standard deviation data on quality indicators for characterization of joint performance (e.g., shear-lap strength, maximum load, displacement at which the maximum load was recorded, and mode of failure).

- Demonstrated increases in the measured lap-shear strength up to 40% compared to the "the abraded and ethanol cleaned" baseline.
- Demonstrated up to 35% increases in the maximum load for single-lap Al-CFPC joints.
- Demonstrated 90% increases in the elongation or displacement at failure of Al-CFPC joints.
- Demonstrated a 100% increase in the total energy absorbed during tensile testing of double-lap Al CFPC joints.
- Attained the maximum possible mechanical strength of the double-lap Al-CFPC joints, with 50% of double-lap Al-CFPC joints failed in the Al away from the joint.

Future Directions

- Demonstrate joint performance for samples created in an in-line setup resembling an actual production line.
- Conduct a proof-of-concept for joining CFPC with magnesium (Mg), advanced high-strength steel, and Al using typical wavelengths used in industry (i.e., 1 micrometer [µm] optical-fiber friendly).
- A follow-on effort is needed to demonstrate, in a production environment, this multi-material joining capability for wide acceptance by the automotive industry.

Technology Assessment

- Target: Achieve 20% improvement over baseline samples prepared without laser structuring in dynamic super lap-shear strength of a double lap-shear joint produced by using Al and CFPCs, both with laser-structured surfaces.
- Gap: Conventional adhesive joining techniques for CFPCs and Al use extensive surface preparation techniques such as grit blasting and solvent wiping, followed by abrading with Scotch-Brite.
- Gap: Conventional adhesive joining techniques for CFPCs and Al exhibit significant process variability.

Introduction

This technology will enable the increased use of both Al and carbon-fiber composites in primary automotive structures. Body structures make up a significant fraction of the weight of a vehicle and represent a significant opportunity for reducing the weight of a vehicle. According to multiple analyses by the United States Council for Automotive Research, the U.S. Department of Energy, and Oak Ridge National Laboratory (ORNL), Al alloys have the potential to reduce component weight by 30 to 60% and carbon-fiber composites have the potential to reduce component weight by 40 to 70%.

To date, CFPC and Al 5000, 6000, or 7000 series components are joined by simply overwrapping the Al with the CFPC or using specially formulated adhesives coupled with extensive surface preparation techniques. Traditional industrial techniques used to prepare Al surfaces for bonding include grit blasting, solvent wiping followed by abrading, and anodizing. The results from grit blasting and abrasion techniques are inconsistent; a more controlled process would be an improvement. In addition, these processes are empirical, use multiple steps, and are labor-intensive surface preparation methods that are incompatible with the degree of automation required in automotive applications.

Approach

Cosma supplied Al 5182 samples that were 1.5 mm gauge, 100 mm width, and 300 mm long. Plasan supplied CFPC specimens made from the T70 prepreg (T700S carbon fiber and an epoxy resin); the samples were 12 in. × 12 in., four plies thick, and 0/90 lay-up plaques. Three adhesives were selected for this project based on their compatibility with the Al alloy and CFPC. The selection process took place at 3M. These structural adhesives were selected: DP460 (an epoxy), DP620 (a polyurethane), and DP810 (a low-odor acrylic). By using a laser-structuring technique [1] before the adhesive bonding operation, the untreated, smooth adhesive composite interface was replaced with a rough fiber-reinforced interface, which was expected to increase the bond strength of the CFPC-AL joint.

A 10-hertz (Hz), Q-switched neodymium-doped yttrium aluminum garnet (Nd:YAG) laser (Quanta-Ray PRO 230, Spectra Physics) was used in this study. With only 10 nanoseconds (ns), the laser pulse duration is very short, creating an extremely high power above 100 megawatts (MW) and resulting in greater than 1,012 degree Kelvin per second (°K/s) heating rates. The beam diameter was 8 mm. The fundamental emission with a wavelength of 1,064 nm was transformed to 355 nm and 266 nm using nonlinear crystals. The maximum laser energy per pulse was 0.15 Joules (J) at 355 nm and 0.038 J at 266 nm. Patterns could be dot, line, and ring-shaped [2–6]; however, only dot patterns were used in this work.

Two types of laser structuring were used: (1) rastering, where the laser beam was translated over the sample surface while the laser was on and (2) spot-by-spot, where the laser beam was held over each spot for a certain amount of time to allow multiple laser shots over the same area. Conditions for the laser rastering and laser spot-by-spot processing modes were selected based on a sensitivity study for DP810 adhesive conducted in the last quarter of FY 2015. Surface preparation conditions were as follows.

Baseline surface preparation: Surfaces of Al and composite samples were abraded using Scotch-Brite and ultrasonically cleaned using ethanol.

Laser-structured surfaces: Both CFPCs and Al specimens, in the as-received condition, were laser structured using the interference technique without any additional surface preparation steps. The laser-structured samples were not cleaned with ethanol before joining.

Results and Discussion

Adhesive effect on single-lap joint strength for 0.25-mm thick bond line. To assess the adhesive effect on joint strength, a total of 60 Al and CFPC joints were bonded using the three adhesives provided by 3M, as follows: 24 joints with DP810, 18 joints with DP460, and 18 joints with DP620 (Table V-2).

Table V-2: Six joint specimens made for each joint type to assess the effect of adhesive with laser-structured surface preparation compared to conventional surface preparation.

Adhesive	Joint Type	Preparation of CFPC	Preparation of Al
DP810	Baseline	Abraded and ethanol cleaned	Abraded and ethanol cleaned
DP460NS	Baseline	Abraded and ethanol cleaned	Abraded and ethanol cleaned
DP620NS	Baseline	Abraded and ethanol cleaned	Abraded and ethanol cleaned
DP810	2B-raster	Laser raster #2	Laser raster B
DP810	3B-raster	Laser raster #3	Laser raster B
DP810	3C-spot	Laser spot-by-spot #3	Laser spot-by-spot C
DP460NS	2B-raster	Laser raster #2	Laser raster B

Adhesive	Joint Type	Preparation of CFPC	Preparation of Al
DP460NS	2B-spot	Laser spot-by-spot #2	Laser spot-by-spot B
DP620NS	2B-raster	Laser raster #2	Laser raster B
DP620NS	2B-spot	Laser spot-by-spot #2	Laser spot-by-spot B

Figure V-54 shows baseline shear-lap strengths with each of the three adhesives compared to samples with laser-structured surfaces. Table V-3 shows the increase in mean lap-shear strength as a percentage for the laser-structured joints with respect to their corresponding baselines for the three adhesives considered. The results show that the shear-lap strength of Al-CFPC joints increased by 12 to 35% using laser-interference structuring.

To identify an optimum adhesive, several criteria have to be reviewed, including curing temperature and curing time. Depending on the actual production line, a cost analysis that would include the impact of curing time and temperature would have to be performed. This cost analysis is not presented. The laser-assisted technique will both increase joint strength and eliminate the sanding and solvent cleaning steps. The largest impact of the laser structuring was seen in the no heat-cure adhesive (DP620), which attained strength increases 35% higher than its baseline. This allowed the DP620 adhesive to attain strength comparable to the 810 adhesive that requires a 10-minute curing at 66°C. Based on data shown in Figure V-54, adhesives DP810 and DP620NS are recommended for use, because the joint strength of the baseline and laser-structured samples of the DP460NS falls between these two adhesives and requires a much longer curing time.

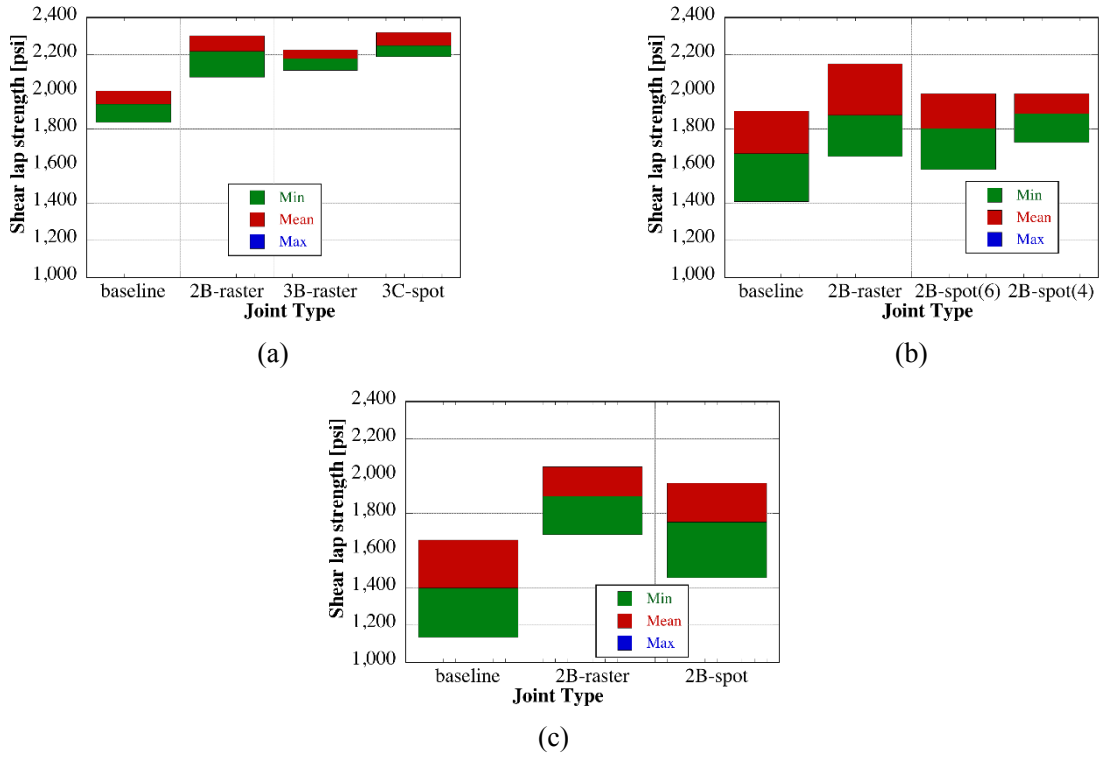

Figure V-54: The single-lap shear strength (in pounds per square inch [psi]) results for minimum, mean, and maximum values for baseline and laser-interference structured surfaces for both CFPC and Al for the following adhesives: (a) DP810, (b) DP460NS, and (c) DP620Ns.

Table V-3: Increase in mean shear-lap strength shown as a percentage for the laser-structured joints with respect to their corresponding baselines.

Adhesive	Percent Increase by Laser-Raster	Percent Increase by Laser Spot-By-Spot
DP810	12.7 to 14.8	16.3
DP460NS	12.8	8.2 to 12.8
DP620NS	35.3	25.4

Dynamic single lap-shear strength properties for 0.25-mm thick bond line. To assess the effect of the loading rate on the lap-shear strength, a total of 48 Al-CFPC joints were bonded using the DP810 adhesive. Six specimens each were used for loading rates of 0.02, 0.2, 2, 20, and 200 inches per second (in./s). The results from the lap-shear-strength mechanical testing are shown in Table V-4 and Table V-5 for the mean and minimum and maximum values, respectively. The results show that at loading rates of 0.2, 2, and 20 in./s, the dynamic shear-lap strength has improved for the laser-structured specimens with respect to the baseline. The improvement is evidenced by the large mean shear-lap strength, which was obtained by averaging the data for six specimens, as well as by the data range (i.e., from minimum to maximum). The data for the slowest loading rate showed the greatest improvement, indicating that fiber reinforcement of the interface is load-rate dependent. The data at 2 in./s showed the least improvement in both the mean shear-lap strength and range. At 200 in./s the mean values for both the baseline and laser-structured joints were very close. Another quality indicator is the minimum-to-maximum range variation of the shear-lap strength. Table V-5 shows the minimum-to-maximum data range for both the baseline and laser-structured joints. The range of shear strength variation for the laser-structured specimens was just a fraction of that for the baseline at loading rates of 0.2, 2, and 20 in./s.

Table V-4: Increase in mean lap-shear strength (psi) for the laser-structured joints with respect to their corresponding baselines.

Loading Rate (in./s)	τ (psi) Baseline Joints	τ (psi) Laser Raster-Structured Joints	Percent Increase by Laser-Raster
0.02	1,933.7	2,219.6	14.78
0.2	2,203.7	2,374.2	7.74
2	2,228.3	2,236.7	0.37
20	2,220.8	2,316.2	4.67
200	3,980.6	3,970.8	-0.24

Table V-5: Minimum shear-lap strength, τ_{min} (psi); maximum shear-lap strength, τ_{max} (psi); and range $\Delta\tau=\tau_{min}-\tau_{max}$ (psi) for baseline and laser-structured (LS) joints.

Loading Rate (in./s)	τ_{min} (psi) Baseline Joints	τ_{max} (psi) Baseline Joints	$\Delta\tau$ (psi) Baseline Joints	τ_{min} (psi) LS Joints	τ_{max} (psi) LS Joints	$\Delta\tau$ (psi) LS Joints	$\Delta\tau_{base}/\Delta\tau_{LS}$
0.02	1,835.5	2,005	169.7	2,078.6	2,303.1	224.5	1.32
0.2	1,784.4	2,370	585.9	2,306.5	2,424.2	117.7	0.2

Loading Rate (in./s)	τ_{min} (psi) Baseline Joints	τ_{max} (psi) Baseline Joints	$\Delta\tau$ (psi) Baseline Joints	τ_{min} (psi) LS Joints	τ_{max} (psi) LS Joints	$\Delta\tau$ (psi) LS Joints	$\Delta\tau_{base}/\Delta\tau_{LS}$
2	1,959.6	2,330	370.9	2,071.2	2,328.1	256.9	0.69
20	1,992.1	2,349	356.6	2,300.0	2,346.2	46.2	0.13
200	3,661.5	4,204	543.1	3,609.0	4,437.6	828.6	1.53

Single lap-shear joint strength for 0.85-mm thick bond line. The results from the mechanical testing of the lap-shear strength are shown in Figure V-55 for the minimum, mean, and maximum values when surface structuring was conducted using a laser beam size of 6 mm and the adhesive bond line thickness was 0.85 mm. In Table V-6, the increase in mean shear-lap strength [Figure V-55] is shown as a percentage for the laser-structured joints with respect to the corresponding baselines. The results show that the shear-lap strength of Al-CFPC joints increased more than 30% when Al and CFPC surfaces were interference structured, with one condition showing shear-lap strengths slightly greater than 40%. The load increase was about 20 to 28% of the mean baseline.

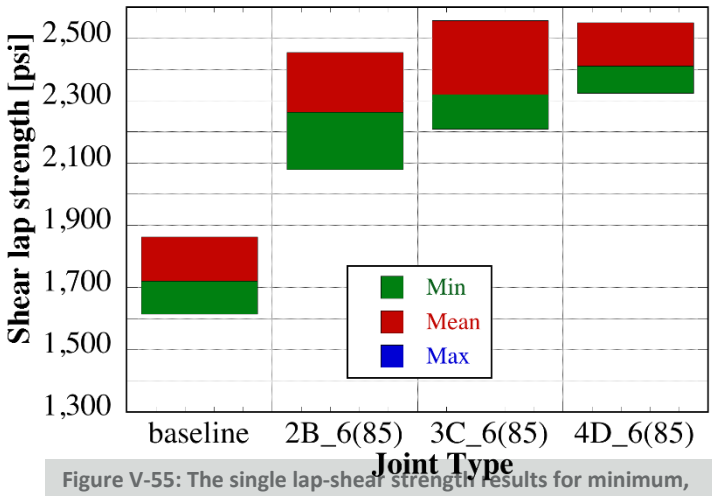

Figure V-55: The single lap-shear strength results for minimum, mean, and maximum values for baseline and laser interference-structured surfaces for both CFPC and Al for a bond line thickness of 0.85 mm and a laser beam size of 6 mm.

Table V-6: Increase in mean shear-lap strength shown as a percentage for the laser-structured joints with respect to the baseline for a bond line thickness of 0.85 mm (the laser beam size was 6 mm).

Joint Type	Percent Shear-Lap Increase (of mean)	Percent Load Increase (of mean)
2B_6	31.5	19.9
3C_6	34.8	23.3
4D_6	40.1	28

Displacement at failure for single-lap and double-lap joints with a bond line thickness of 0.25 mm. The displacement at maximum load in Newtons (N) is an indication of elongation and is a direct measure of the energy absorbed by the joint during the shear-lap test. Figure V-56 (a) shows evolution of the shear-lap stress during mechanical testing for three single-lap joint specimens: (1) baseline (no laser structuring), (2) laser-structured spot-by-spot, and (3) laser structured by rastering with a 4-mm laser beam. These data indicate that the laser-structured joints are much more ductile than without laser structuring. The displacement at failure increases from 0.145 in. for the baseline joint to more than 0.26 in. for the laser-structured joints. This behavior indicates an enhanced bonding of adhesive to both Al and CFPC. Laser-structured joints can absorb almost double the energy of the baseline joints (area under the stress-strain curve).

Results for the evolution of load during mechanical testing are shown in Figure V-56(b) for two representative double-lap joint specimens (i.e., a baseline specimen and another one using laser-structured surfaces). The double-lap joint was made with laser-structured surfaces using a laser beam size of 6 mm. These results show that elongation has increased by about 83% (0.77 in. for the laser-structured specimen and 0.42 in. for the baseline joint). By integrating the load with respect to displacement, the total energy absorbed by the joint with laser-structured surfaces showed an increase of about 100% over that for the baseline joint (202.03 J for the laser-structured specimen and 101.18 J for the baseline joint).

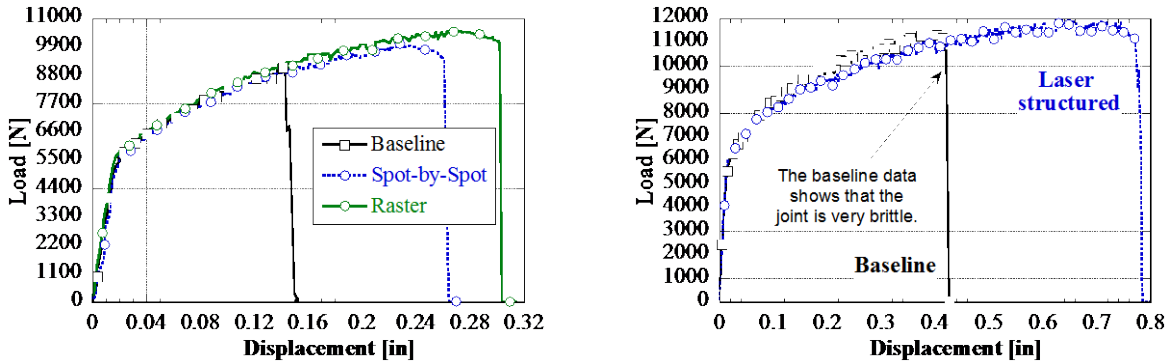

(a) (b)

Figure V-56: Load evolution during mechanical testing as a function of displacement for (a) single-lap joints and (b) double-lap joints.

Mode of failure: single-lap and double-lap joints with a bond line thickness of 0.25 mm. The failure mode was changed as a result of laser structuring for Al and CFPC surfaces. Pictures taken after mechanical testing of single-lap joints bonded with adhesive DP620 and a bond line thickness of 0.25 mm were used to identify fracture surfaces and/or failure modes for single-lap joints (Figure V-57). For the baseline joints, the large, clean fracture surfaces indicate an adhesive failure mode, where there is poor adhesion to either substrate [Figure V-57(a)]. The joints made with laser-structured surfaces exhibit residual adhesive on both surfaces, demonstrating a cohesive failure mode.

(a) (b)

Figure V-57: Pictures taken after mechanical testing of single-lap joints bonded with adhesive DP620 and a bond line thickness of 0.25 mm showing fracture surfaces and failure modes at (a) baseline joints *and* (b) joints with laser-structured surfaces using a laser beam size of 6 mm.

Figure V-58 shows pictures of baseline joints and joints made with laser-structured surfaces taken after mechanical testing of double-lap joints bonded with adhesive DP810 and a bond line thickness of 0.25 mm. Figure V-58(a) and Figure V-58(b) indicate that none of the baseline joints failed in the component Al or CFPC, while 50% of the joints made with laser-structured surfaces were found to fail in the Al component [Figure V-58(c)]. The fact that 50% of the joints made with laser-structured surfaces were found to fail in the Al component indicates that the maximum performance (i.e., load, shear-lap strength) for the joint was attained and that no further improvement could be attained irrespective of surface treatment.

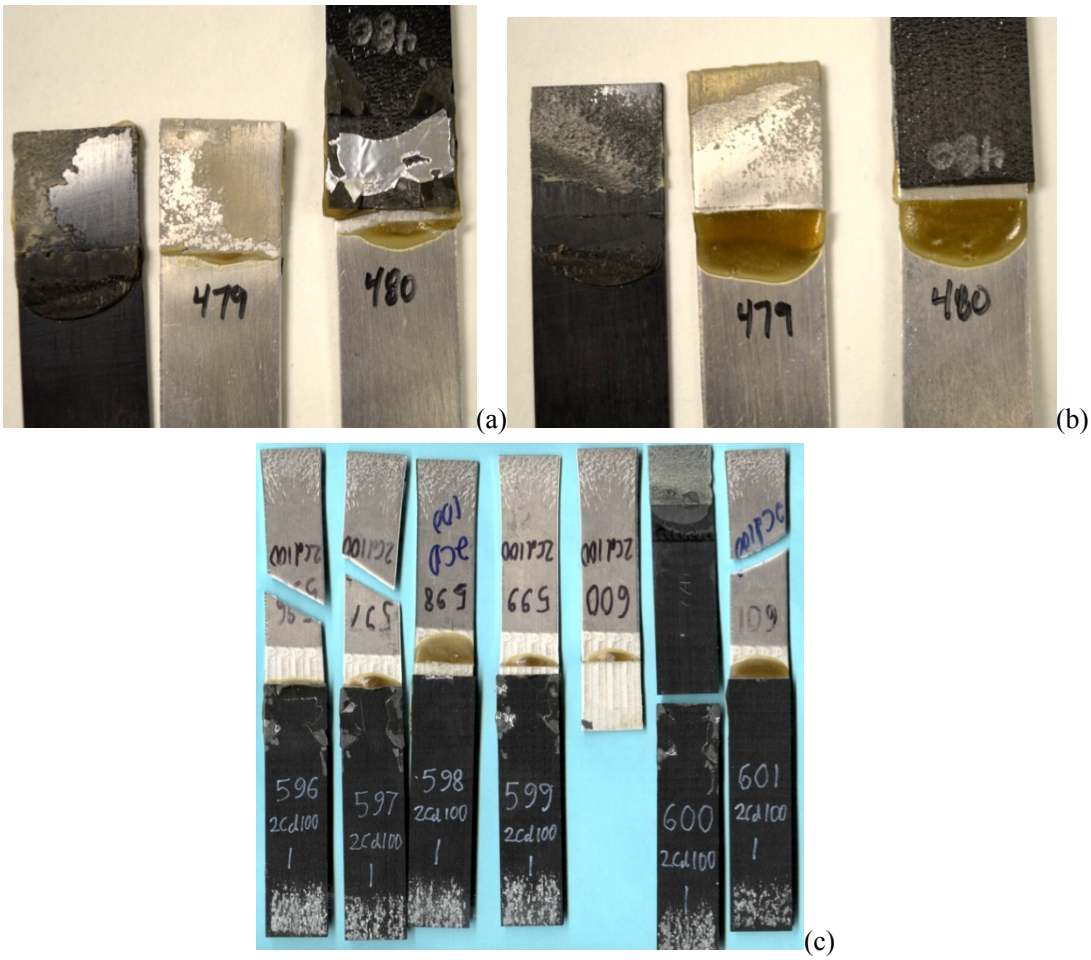

Figure V-58: Pictures taken after mechanical testing of double-lap joints bonded with adhesive DP810 showing fracture surfaces and/or failure modes at (a, b) baseline joints and (c) joints with laser-structured surfaces using a laser beam size of 6 mm.

Technology Transfer Path

Two project participants, Cosma and Plasan, are Tier I suppliers and have the ability to commercialize this technology. Issues related to process scaleup will be addressed by the industrial partners.

The following steps are being taken to ensure commercialization potential of the joining technology developed during this project.

- Cosma, Plasan, and 3M identified materials that are commonly used in the automotive industry and reviewed industrial needs to ensure the materials used during this project were the same or comparable.

- 3M selected the adhesives based on the commercialization plans of the two Tier I suppliers participating in the project: Cosma (Al structures) and Plasan (carbon-fiber composites structures).
- The project team has engaged a supplier of high-speed industrial laser systems that currently supplies the automotive industry as a future scaleup partner.

Conclusion

The project has demonstrated significant improvement in the mechanical properties of shear-lap joints made with laser-structured surfaces compared to those of baseline joints, demonstrating the proof-of-concept for laser structuring and/or laser ablation for surface preparation of both CFPC and Al coupons before adhesive joining. The joints demonstrated higher loads to break and a significant increase in energy absorption during failure. This was due to the failure mode shifting from being an adhesive-to-adherend interfacial failure to a failure cohesively through the bulk of the adherend, either in the region of the joint or in regions away from the joint.

Data indicate that mechanical properties of the joints can be significantly increased by laser structuring the Al and CFPC. This method can be robotically controlled, eliminating the need for labor intensive and variable manual processes.

This technology is attractive because use of lighter weight, adhesively joined materials in automotive applications would reduce gas consumption and production of greenhouse gasses. The proof-of-concept for laser structuring to enable joining of these lightweight substrates for this work gives credibility to incorporating them into a larger structure for automotive testing.

References

1. C. Daniel; F. Mücklich; and Z. Liu, 2003, "Periodical Micro-Nano-Structuring of Metallic Surfaces by Interfering Laser Beams," *Appl. Surf. Sci.*, 208–209; pp. 317–321.
2. C. Daniel and F. Mücklich, 2004, "Quantification of Periodical Surface Structures by White Light Interferometry," *Prakt. Metallogr.*, 41(6); pp. 277–285.
3. F. Mücklich; C. Daniel; A. Lasagni; and F. Yu, 2004, "Direct Surface Patterning Induced by Interfering Laser Beams," *Mat. Res. Soc. Symp. Proc.*, EXS-2, M11.1.
4. F. Mücklich; A. Lasagni; and C. Daniel, 2005, "Laser Interference Metallurgy—Periodic Surface Patterning and Formation of Intermetallics," *Intermetallics*, 13(3–4); pp. 437–442.
5. F. Mücklich; A. Lasagni; and C. Daniel, 2006, "Laser Interference Metallurgy—Using Interference as a Tool for Micro/Nano Structuring," *Int. J. Mater. Res.*, 97(10); pp; 1337–1344.
6. C. Daniel, 2006, "Biomimetic structures for mechanical applications by interfering laser beams—more than only holographic gratings," *J. Mater. Res.*, 21; pp. 2098–2105.

Bibliography

J. Chen; A. S. Sabau; J. F. Jones; A. Hackett; G. D. Jellison; C. Daniel; and D. Warren, 2015, "Aluminum Surface Texturing by Means of Laser Interference Metallurgy," in *Proceedings of the 2015 TMS Annual Meeting & Exhibition: Light Metals 2015*, Aluminium Processing; TMS, Orlando, Florida; pp. 427–429.

H. M. Meyer III; A. S. Sabau; C. D. Warren; and C. Daniel, 2016, "Chemical Analysis of Laser Interference-Based Surface Treatment of Al and CFPC," in preparation for submission to *Applied Surface Science*.

A. S. Sabau; J. Chen; J. F. Jones; A. Hackett; G. D. Jellison; C. Daniel; D. Warren; and J. D. Rehkopf, 2015, "Surface Modification of Carbon Fiber Polymer Composites after Laser Structuring," in *Advanced Composites for Aerospace, Marine, and Land Applications II,* T. Sano and T. S. Srivatsan (eds.), John Wiley & Sons, Inc., Hoboken, New Jersey; doi: 10.1002/9781119093213.ch23.

A. S. Sabau; C. M. Greer; J. Chen; C. D. Warren; and C. Daniel, 2016, "Surface Characterization of Carbon Fiber Polymer Composites and Aluminum Alloys after Laser Interference Structuring," in preparation for submission to *JOM* and presentation at the *2016 TMS Annual Meeting and Exhibition*, Nashville, Tennessee, February 14 through 18, 2016.

A. S. Sabau; J. Chen; C. D. Warren; C. Daniel; T. Skszek; and M. M. Caruso Dailey, 2016, "Laser Interference-Based Surface Treatment of Al and Carbon Fiber Polymer Composites for Enhanced Bonding," in preparation for submission to the *Materials and Processes track of Nanocomposites, Nanotechnology Challenges and Solutions, SAMPE*, Long Beach, California, May 23 through 26, 2016.

A. S. Sabau; J. Chen; C. D. Warren; C. Daniel; T. Skszek; and M. M. Caruso Dailey, 2016, "Laser Interference-Based Surface Treatment for Enhanced Bonding of Al and Carbon Fiber Polymer Composites," in preparation for submission to the *Journal of Applied Physics*.

V.6. Collision Welding of Dissimilar Materials by Vaporizing Foil Actuator — The Ohio State University

Project Details

Glenn Daehn, Principal Investigator
The Ohio State University
141 Fontana Labs
116 W 19th
Columbus, OH
Phone: 614-292-6779
E-mail: daehn.1@osu.edu

Anupam Vivek, Co-Principal Investigator
MacQuigg Laboratory MQ
Building 348
105 W Woodruff Avenue
Columbus, OH 43210
Phone: 608-332-4892
E-mail: vivek.4@osu.edu

Adrienne Riggi, Project Officer
National Energy Technology Laboratory
3610 Collins Ferry Road
P.O. Box 880
Morgantown, WV 26507-0880
Phone: 304-285-5223
E-mail: Adrienne.riggi@netl.doe.gov

Sarah Ollila, Technology Area Development Manager
U.S. Department of Energy
1000 Independence Avenue, SW
Washington, DC 20585
Phone: 202-586-8027
E-mail: sarah.ollila@ee.doe.gov

Contractor: The Ohio State University
Contract No.: DE-EE0006451

Executive Summary

The feasibility of using vaporizing foil actuator welding (VFAW) technique for welding dissimilar material combinations of aluminum, steel, and magnesium alloys has been tested. Seventeen material systems were screened using VFAW in different configurations during the first year. Four additional combinations of high-performance aluminum and steel alloys were investigated during the second year. Of all screened combinations, seven were selected for further study with corrosion testing and mechanical testing. Half of the e-coated aluminum/iron (Al/Fe) samples retained >90% lap-shear strength after 30 cycles of ASTM B117 salt-spray testing. Thicker materials such as 2.0-mm AA6061-T4 and high-strength materials such as 1500-MPa boron steel were welded successfully and strong joints were achieved such that failure occurred in the base material, away from the weld, during lap-shear testing. Future work to study bond interfaces, using advanced microscopy, will help us obtain a deeper understanding of the factors that contribute to a strong bond. Emphasis will also be placed on industry readiness. An automated prototype system is being built that

will be able to perform welding at one cycle per minute. Industry partners are also being engaged to deploy VFAW in automotive manufacturing environments.

Accomplishments

- Since Fiscal Year (FY) 2014, screened 21 dissimilar metal combinations consisting of magnesium, steel, and aluminum alloys for welding using VFAW. More than 14 combinations successfully welded.
- Selected seven combinations for corrosion testing and mechanical testing.
- Made six weld coupons for each selected material combination for testing under three conditions: as welded, coated and corroded, and uncoated and corroded. Each coupon yielded two or three lap-shear test samples.
- Performed lap-shear tests on about 90 samples in various material combinations and conditions.
- Welded 2-mm thick AA6061-T4 flyers sheets to DP780 steel.
- Successfully welded JSC1500 boron steel with a tensile strength of 1500 MPa with AA5052 and AA6111-T4 flyers.
- E-coated samples of DP780/AA6061-T4, JAC270F/AA6061T4, and JAC980/AA5052 retained >90% lap-shear strength after 30 cycles of ASTM B117 salt-spray testing. In most cases, failure was in the base metal away from the weld. Strength decreases were due to reduction in material thickness due to corrosion.
- Studied fracture surfaces of peeled weld interfaces using scanning electron microscopy (SEM) and energy dispersive x-ray spectroscopy (EDS) mapping. Both ductile and brittle regions were identified.
- Obtained larger weld area using a pre-formed tent-shaped target.

Future Directions

- Characterize joining-induced defects and understand the failure mechanisms for samples that fail within the weld. Understand the factors that contribute to strong welds.
- Build an automated system for creating VFA welds with minimal manual involvement. This will increase repeatability and reduce experimental cycle time.
- For commercial application, besides material combination, find and focus on part geometries and stack thicknesses that are relevant to the industry.

Technology Assessment

- Target: Reduce the VFAW process time to one cycle/minute and increase reproducibility in weld quality.
- Gap: The stackup of foil, insulation, sheet metals, and standoffs being assembled separately before inserting into the VFA apparatus helps with increasing repeatability and reducing cycle time. However, for commercial implementation, a way for indexing the foil near the desired weld spot will need to be devised.
- Target: Eliminate the unwelded area in the center of the weld or its rebound effect.
- Gap: Spot welding of the aluminum-steel combinations that have been successfully welded in the patch configuration has been difficult because of the flat-impact region directly above the former position of the vaporized foil. This region of the flyer sheet tends to rebound and occasionally peel apart the perimeter weld. Alternate geometries may mitigate this issue.

Introduction

This report is a continuation of the FY 2014 annual report. This project aims to meet the challenge of effectively welding starkly dissimilar materials, namely, steel, aluminum, and magnesium for creating a multi-material automotive body structure. Traditional fusion-based welding between dissimilar combinations of aluminum, steel, or magnesium is difficult due to disparate melting points and commonly leads to formation of intermetallic compounds (IMCs), which are brittle. Upon mechanical testing, failure in such weld samples tends to happen within the weld. For instance, Al-Fe welds made by resistance spot welding often contain IMCs and are not tough enough to be applied in the body in white. Solid-state welding techniques (e.g., friction stir and impact welding) offer ways of avoiding or reducing the formation of IMCs.

This project used VFAW [1], a solid-state impact welding technique developed at Ohio State University. A schematic of the progress of a weld interface is shown in Figure V-59a. The main driver of these experiments is a 0.0762-mm thick aluminum foil, which is a consumable that is replaced after every experiment. When a high, short-duration current pulse, driven by a capacitor discharge, passes through the foil, the foil vaporizes rapidly due to Joule heating. The rapidly expanding gas drives the flyer sheet to high velocities toward the target plate. Standoff sheets between the flyer sheet and target plate provide the distance over which the flyer accelerates. Additionally, the height of the standoff sheets and the horizontal distance between them help create an oblique collision, which is necessary for weld creation. As shown in Figure V-59b, a good weld, represented by a wavy interface with no continuous layer of IMCs, is obtained when the impact angle and velocity are within the process window.

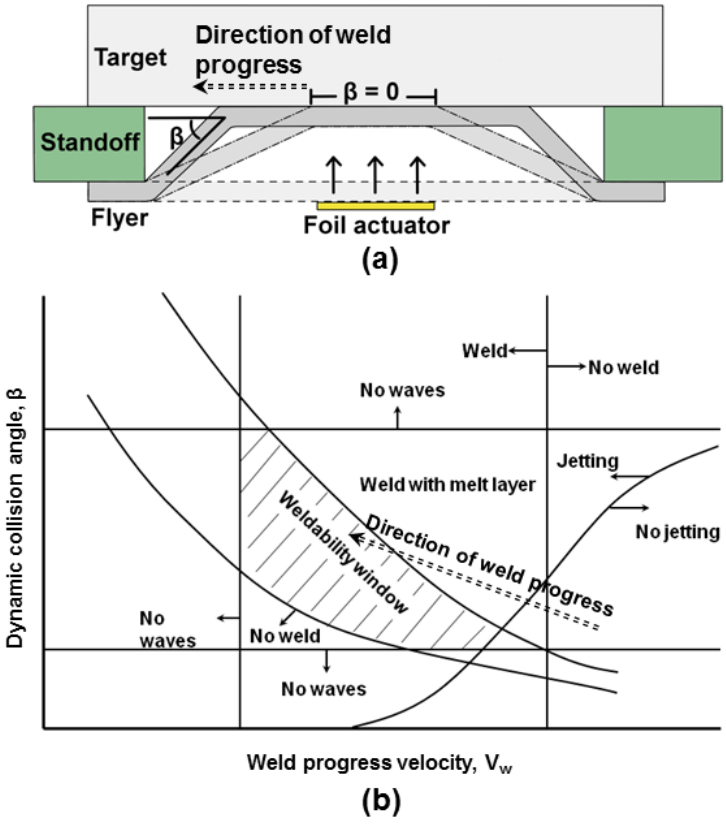

Figure V-59: (a) Mechanism of weld progress during current VFAW implementation. (b) A generic impact welding window depicting conditions that lead to different compositions and structure of the weld interface. The dotted arrow labeled as the direction of weld progress (single column).

The flyer sheet is chosen based on density, strength, and ductility of the joining members. Ideally, the flyer material should be one that is lighter, weaker, and more ductile between the two metals. However, in some cases where not all three criteria can be met simultaneously, the more ductile material is chosen. Flyer sheet thickness ranges from 0.5 to 2.0 mm. Target plates can be as thick as needed, since they are stationary. Many alternate flyer and target configurations are now under examination in separate investigations.

During FY 2015, we focused on corrosion behavior and its effect on mechanical performance, since corrosion due to disparate electrochemical potentials is a major issue with dissimilar material joining. Corrosion mitigation by using e-coating was pursued. In addition, we also studied electrochemical properties of some base materials, fracture surfaces, and some new welding configurations.

Approach

The following seven material combinations were studied during FY 2015 (target/flyer sheet):

- JAC270F/AA6061-T4
- AM60B/AA6061-T4
- DP780/AA6061-T4
- JAC980/AA5052
- JAC980/AA6111-T4
- JSC1500/AA5052
- JSC1500/AA6111-T4.

JAC270F and JAC980 are galvannealed steels with nominal tensile strengths of 270 and 980 MPa, respectively. The Zn coating was surface ground prior to welding by either belt-sanding or surface grinding. JSC1500 was also surface ground to remove its dull-colored surface layer. Because aluminum is light and ductile, it was a fitting flyer material in every test.

The main body of this work consists of mechanical testing of as-welded, corrosion-protected, and corroded samples. Six weld coupons were made for each material combination (Figure V-60). All samples were welded in the lap configuration using 10-kJ of input energy and a 1.7-mm standoff distance. With these input parameters and a 1-mm thick aluminum flyer sheet, the impact velocity was found to be approximately 700 m/s. Of the six samples, two were left as-welded, two were e-coated and then corrosion-tested, and two were left uncoated and then corrosion-tested (Figure V-61). All six samples were sectioned by abrasive water jet machining and lap-shear tested. Each weld coupon yields either two or three useable 12.7-mm-wide lap-shear test samples, depending on the dimensions of the available materials.

E-coating was performed by Electro Prime Inc., using POWERCRON 6000CX cationic epoxy electrocoat. Corrosion testing was done according to ASTM B117 (i.e., 35°C, spray of 5% sodium chloride [NaCl] solution, 24 hours/cycle) for 30 cycles. Lap-shearing testing was done in an MTS Systems Corporation mechanical testing frame at a rate of 0.1 mm/s.

Electrochemical characterization of the base metals was conducted for AA5052, AA6111-T4, JAC980, and JSC 1500, by polarization scans. Figure V-62 shows the corrosion cell. Because aluminum is typically anodic and iron cathodic, an anodic polarization scan was done on AA5052 and AA6111-T4 and a cathodic polarization scan was done on JAC980 and JSC1500 with current density measured.

The research analyzed the fracture surfaces of AM60B/AA6061-T4 and DP780/AA6061-T6 welds (from FY 2014) using SEM and EDS mapping.

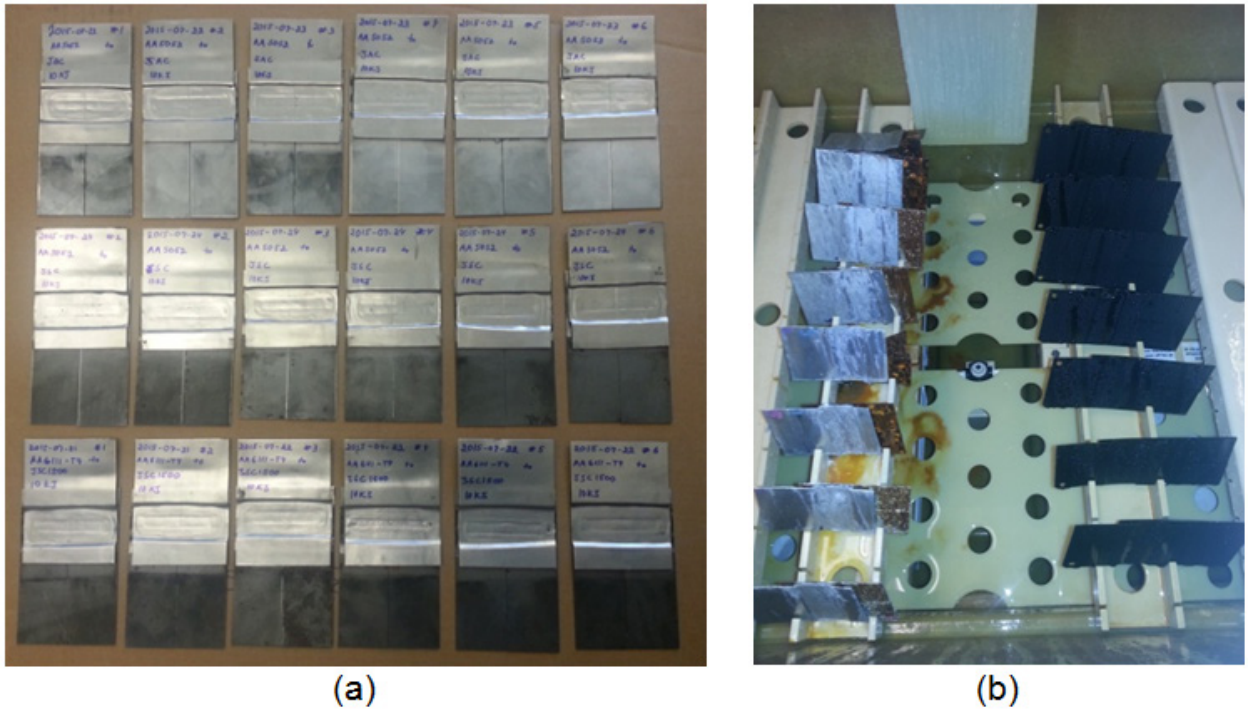

Figure V-60: (a) Al/Fe weld coupons. Six of the coupons are not shown. (b) Corrosion testing in progress (double column).

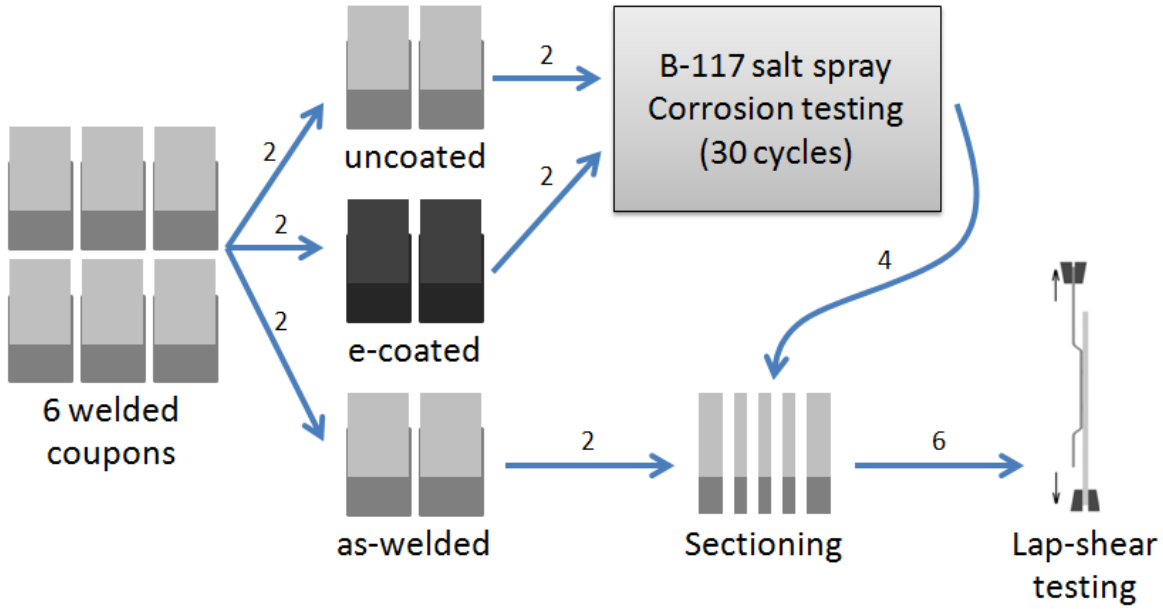

Figure V-61: Schematic of experiment plan (double column).

A new welding configuration involved a pre-formed, tent-shaped target sheet, with the intention of maximizing the area of oblique impact. Successful impact welding requires an oblique impact, but in the typical flat-on-flat configuration. The center of the impact area experiences a non-oblique impact; therefore, no welding occurs. Furthermore, this flat impact may cause the flyer sheet to rebound away from the target, which could put the weld under tensile stress. Therefore, we pre-formed the target sheet into a tent shape to maximize the area where oblique impact occurs (Figure V-63). Only the AA6061-T4/DP780 combination used this configuration with a flyer thickness of 1.5 and 2 mm.

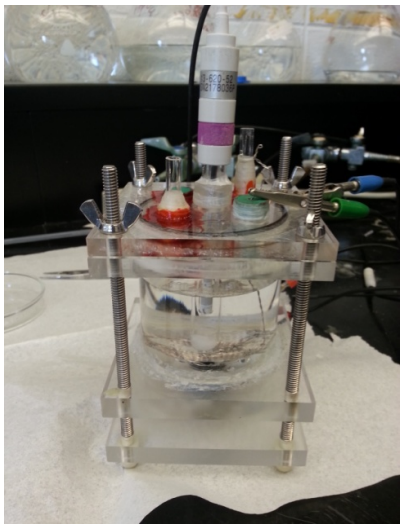

Figure V-62: Corrosion testing cell (single column).

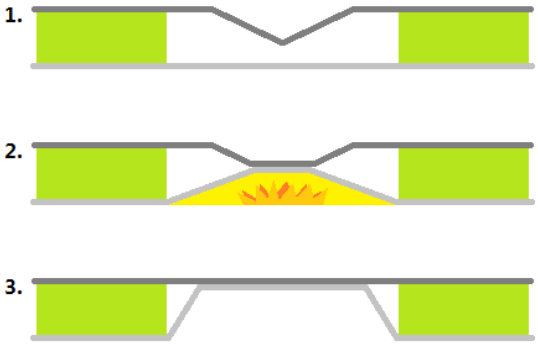

Figure V-63: Side-view schematic of welding process using a tent-shape-target (single column).

Results and Discussion

Mechanical Testing

Figure V-64 shows a sectioned sample of each test condition. In most cases, no clear sign of galvanic corrosion was observed, but rather general corrosion, especially with Fe/Al welds. More discussion on corrosion will follow in a later section.

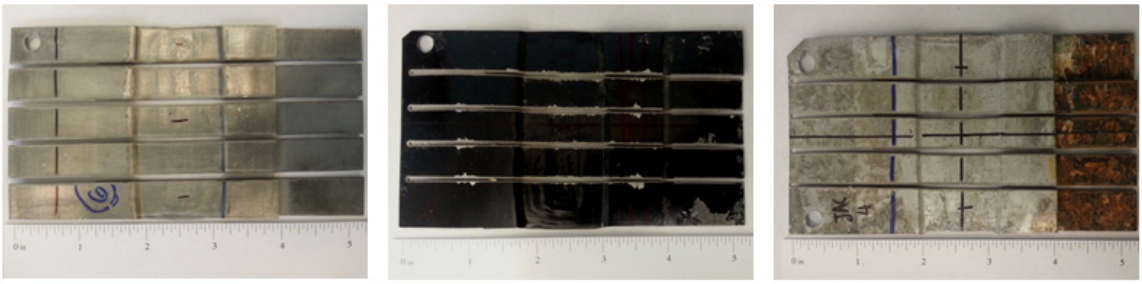

Figure V-64: Sectioned samples in the (a) as-welded, (b) e-coated and corroded, and (c) uncoated and corroded conditions (double column).

Figure V-65 summarizes mechanical testing data and reports the average lap-shear failure loads. For comparison, the chart also shows the expected failure loads calculated, based on reported tensile strength values.

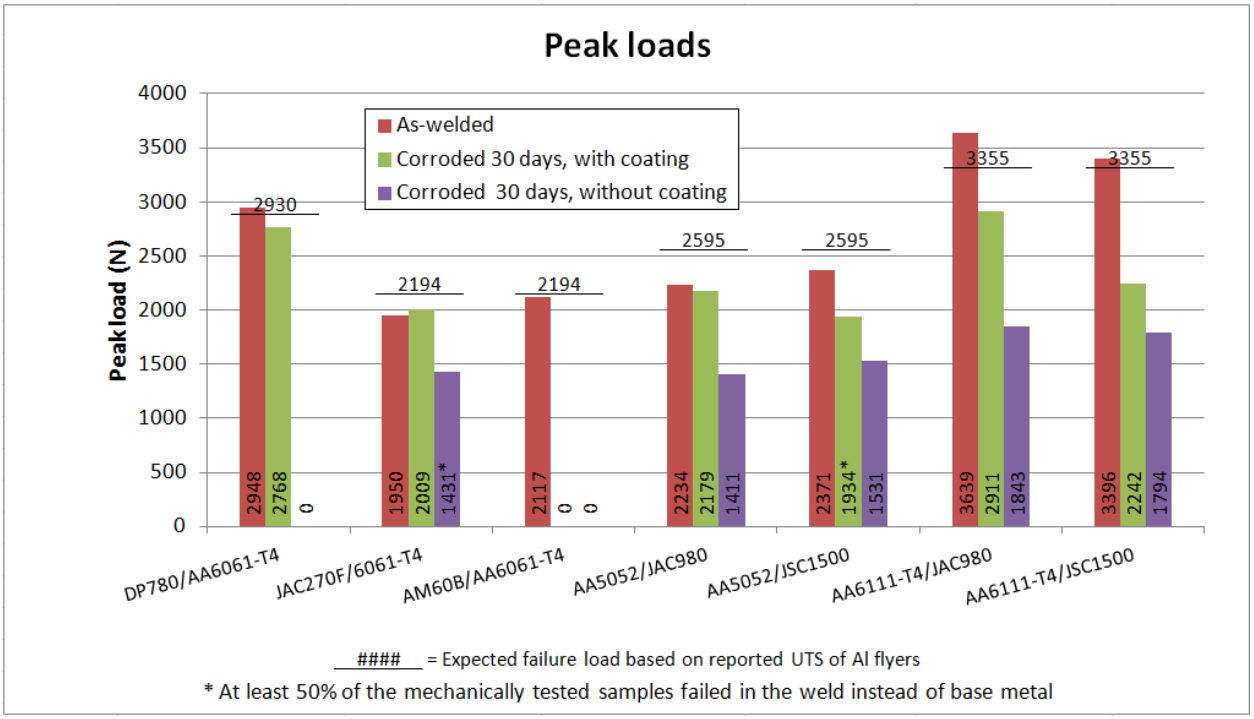

Figure V-65: Lap-shear data of various material combinations and conditions (double column).

Most of the welds failed in the base aluminum during mechanical testing for both uncorroded and corroded samples. Furthermore, in the as-welded condition, the average measured failure loads are generally quite close to the expected failure loads calculated based on reported ultimate tensile strength (UTS) values. This indicates that the mechanical knock-down due to the welding process is minimal. In other words, the welds are at least as strong as one of the base metals, indicating nearly 100% joint efficiency.

In the uncoated, corroded condition, two material pairs (DP780/AA6061-T4 and AM60B/AA6061-T4) delaminated along the weld during corrosion testing. On the positive side, the remaining five material combinations retained more than 50% of their strength after corrosion testing in the uncoated condition. Failure still mostly occurred in the base aluminum, indicating a retained joint efficiency of 100%, but the failure load was reduced due to reduction in the cross section of the aluminum.

E-coating was fairly effective in protecting the materials from corrosion. Again, in most cases, e-coated, corroded samples failed in the base aluminum. The e-coated samples of DP780/AA6061-T4, JAC270F/AA6061T4, and JAC980/AA5052 experienced strength degradations of less than 7% through corrosion testing. The most severe strength reduction of e-coated samples occurred with AM60B/AA6061-T4, where all samples delaminated along the weld during corrosion testing. This is largely because the e-coating used here was not appropriate for Mg alloys. Application of an intermediate conversion coating should result in better compatibility. A more appropriate corrosion test and coating method for that combination will need development in collaboration with industry experts.

Electrochemical Properties of Base Metals

Figure V-66 shows the polarization curves and open cell potentials (OCP) in volts (V) for a saturated calomel electrode (SCE) (Table V-7).

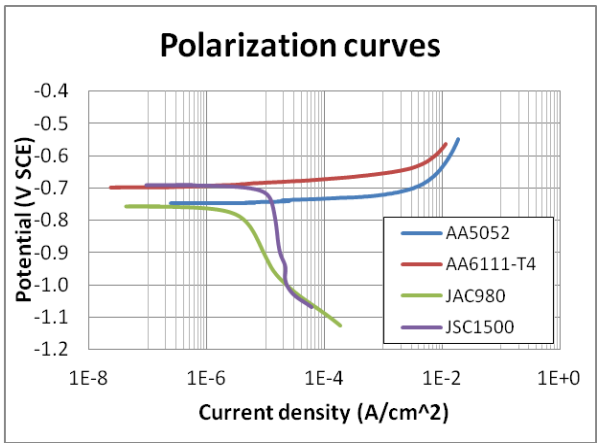

Figure V-66: Polarization curves of base metals (single column).

Table V-7: Open cell potentials of base metals.

Metal	OCP (V SCE)
AA5052	-0.746
AA6111-T4	-0.698
JAC980	-0.758
JSC1500	-0.690

The driving force for galvanic corrosion between two adjacent metals has to do with the difference in OCP between the two metals. In this case, the largest potential difference is the one between JAC980 and AA6111-T4, with a magnitude of 0.060 V, which is not very large. In other words, the propensity for galvanic corrosion is not very high. This is consistent with the fact that we mainly observed general corrosion during corrosion testing. JAC980 turned out to be more anodic than both aluminum alloys at hand, which is quite surprising, because aluminum alloys are typically more anodic than iron alloys. In any case, the potential differences are small enough that galvanic corrosion is not a major concern for the aluminum-steel joint combinations above. The microanalysis discussed in the following section concerns only pre-corrosion aluminum-steel and aluminum-magnesium weld samples.

Microanalysis: Interfacial Structure and Fracture Surfaces

Figure V-67 shows the weld interface of a DP780/AA6061-T6 sample welded at 8-kJ input energy and illustrates some features of a typical weld interface. Along the direction of weld progress initially, there are cracks or unwelded regions followed by wavy regions that contain intermittent layers of IMCs. A continuous layer of brittle IMCs provides an unhindered crack path and is not desirable. Regions with discontinuous IMCs are expected to be tougher.

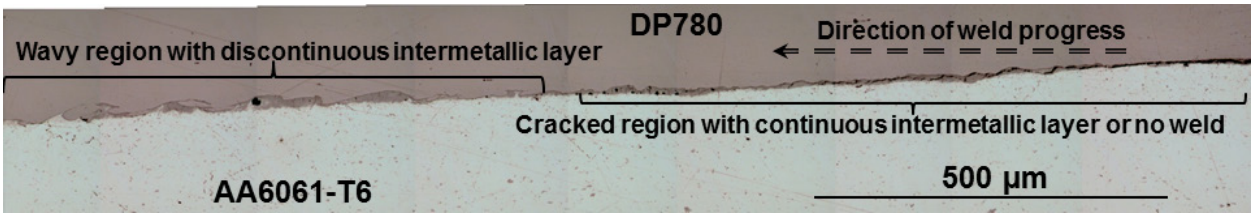

Figure V-67: DP780/AA6061-T6 weld interface showing wavy and cracked regions. The interfacial waves formed by gross material flow due to the severe shearing action of the collision process.

In addition to lap-shear testing, where most of the samples failed in the base material, we have also performed some peel testing, which had a higher tendency to cause failure along the weld, thus revealing the weld interface. DP780/AA6061-T6 and AM60B/AA6061-T4 were peeled in this fashion. SEM images and EDS maps of their peeled fracture surfaces of are shown in Figure V-68 and Figure V-69.

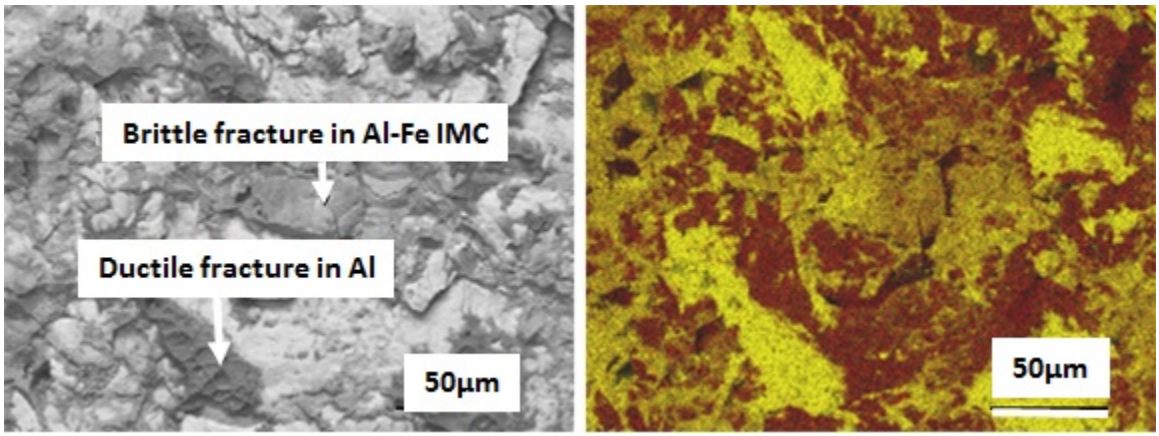

Figure V-68: Peeled fracture surface (left) and the corresponding EDS map (right) of a DP780/AA6061-T6 weld. Yellow = Al, red = iron.

A scanning electron fractograph of the iron side of DP780/AA6061-T4 is shown in Figure V-68 and the corresponding EDS map of the fracture surface is shown in Figure V-68b. As noted in the FY 2014 annual report, several samples created with T6 temper flyer sheets failed within the weld during mechanical testing. However, Figure V-65 illustrates that even though the overall failure of such sample seemed brittle, there were regions where ductile failure in the parent aluminum occurred. Because interfacial IMCs are usually brittle, one can infer that the areas where ductile fractures occurred were free of interfacial IMCs. Further microanalysis could validate this reasoning. Furthermore, based on past studies on the impact-welding window, the joint toughness can be improved by tailoring the welding conditions to minimize the formation of interfacial IMCs [3].

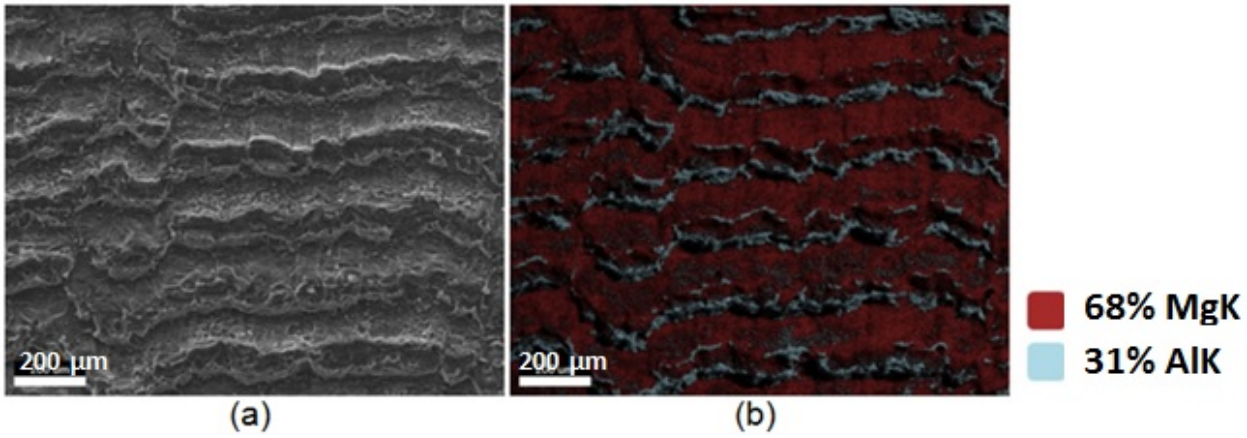

Figure V-69: Peeled fracture surface (left) and the corresponding EDS map (right) of a AM60B/AA6061-T4 weld.

AM60B is a cast Mg alloy and AA6061 is an age-hardenable aluminum alloy. This particular weld sample yielded an exceptionally large weld area and a peel strength of 32.5 N/mm. The fracture surface (Figure V-69) showed very pronounced and regular wavy features. The fracture surface appears to be primarily ductile, which corresponds with the high toughness of the joint in peel.

Both the peaks and valleys of the waves contain continuous lines of residual aluminum that were transferred over to the Mg side by ductile fracture, which occurred within the base material. This material transfer by ductile fracture indicates areas where the bond strength exceeds the strength of one of the base materials. In this case, areas of material transfer are continuous and regular, which are good for joint strength and toughness.

Figure V-70 shows SEM micrographs from the AA5052/JAC980 and AA6111/JSC1500, depicting slightly wavy interfaces. Regions with no IMCs were found at both welds and these areas are expected to be tougher than welds with large amounts of IMCs.

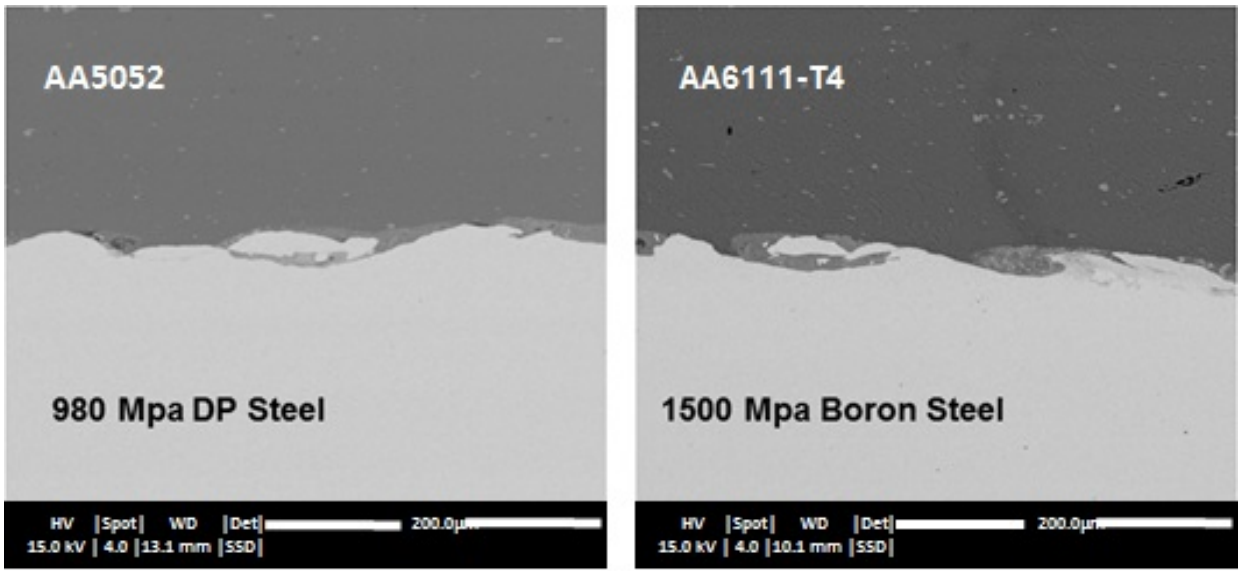

Figure V-70: Backscattered electron SEM images of the AA5052/JAC980 (left)) and AA6111/JSC1500 (right) weld interfaces.

Pre-Formed Tent-Shape Target

The peeled fracture surface of the tent-shape-target weld shows distinct bands in the welded regions (Figure V-71). A significant welded area is near the centerline. This is in contrast to the flat-on-flat weld where there is an unwelded area near the centerline. Because the area near the centerline experiences the highest driving pressure, obtaining welding in this area may be a more efficient way of creating good welds, even though the overall welded area does not seem much larger in this particular case.

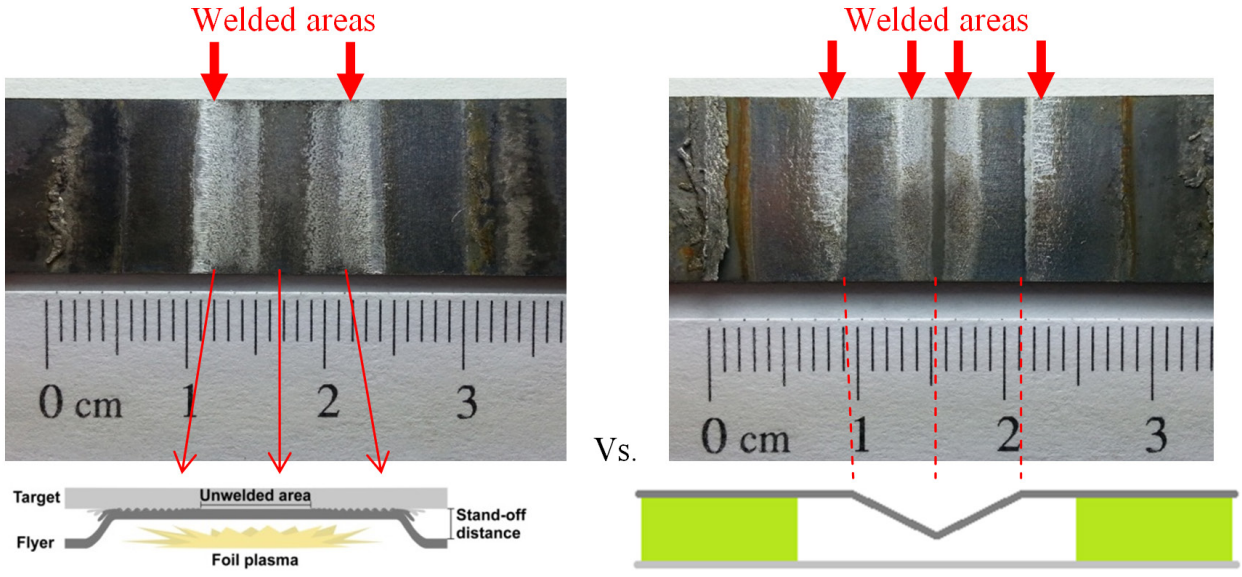

Figure V-71: Peeled fracture surfaces of a flat-on-flat weld (left) and a tent-shape-target weld (right).

Mechanical testing employed samples of two flyer thicknesses (1.5 and 2.0 mm) and two welding configurations (flat target with 1.6-mm standoff and tent target with 3.67-mm standoff). Table V-8 gives

results for both peel and lap-shear tests and the data indicate that tent-shape targets achieved higher peak failure loads, but there was much scatter in the data and the trend was not all consistent. Nevertheless, the tent configuration provides one workaround for the flat-impact problem and can be pursued further during industrial implementation.

Table V-8: Mechanical testing results of welds done with flat targets and with tent targets

Peel Test		
	Flat Target	Tent Target
1.5-mm flyer	9.1	23.9
2.0-mm flyer	21.7	23.5

Lap-Shear Test		
	Flat Target	Tent Target
1.5-mm flyer	317.1	376.4
2.0-mm flyer	420.5	423.4

Units: N/mm (failure load normalized by sample width)

Technology Transfer Path

From the work performed under the auspices of this project, VFAW is a flexible process for welding a variety of material combinations in patch and spot configurations. Because of the lack of heat-affected zones, the welds have nearly 100% joint efficiency, even for advanced high-strength materials. With these value propositions at its core, a customer alignment process was initiated under the I-Corps@Ohio program, wherein 80 customer interviews were conducted within the automotive industry. Besides providing the research team with key insights on industry pain points, supply chai, and ways to implement new processes in the industry, this program also enabled wider dissemination of the knowledge gained from this project. A few original equipment manufacturers and Tier 1 and Tier 2 parts, systems, and material suppliers have expressed interest in conducting validation studies with the aim of ultimately implementing the VFAW process on their production floors.

A major breakthrough in process innovation has been further miniaturization of the weld apparatus and the reduction in the electrical energy requirement (Figure V-72). An impact spot welding head that weighs less than 20 lb was used to create a weld between two sheets of 1-mm thick AA6111-T4 material with a spot size of 10 mm at an energy level of 1 kJ. Figure V-72c shows the experimental apparatus. Demonstration of an impact spot weld with such low input energies is encouraging. As much lower energies are used, noise and gas generation are also dramatically reduced.

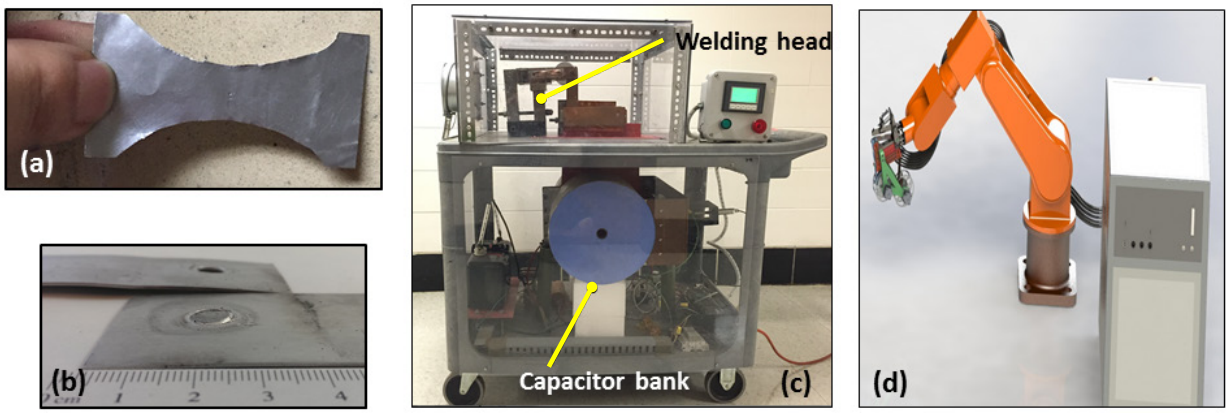

Figure V-72: Low-energy welding (a) 2-in. long "spot welding" foil, (b) a mechanically tested AA6111-T4 weld specimen, (c) lab-built apparatus with a small spot welding head and a fast, low-energy capacitor bank, and a (d) schematic of possible robotic implementation.

Conclusion

During FY 2015, six combinations of aluminum/steel and one combination of aluminum/magnesium alloys were impact welded using VFAW. These combinations were down-selected for prototype build based on the screening tests of FY 2014 and suggestions from our industrial collaborators. Multiple coupons of each combination were created in order to subject them to various post-weld treatments. In lap shear, most of the as-welded specimens failed outside the welded region at nearly 100% theoretical strength of one of the base metals. Based on that result, the base material properties are not degraded due to heat or from plastic work. Furthermore, all samples used the same input parameters of energy and standoff distances. This illustrates the wide process window and flexibility of the method for welding a variety of material combinations. Post-corrosion mechanical testing of the e-coated samples revealed that the aluminum/steel samples retained most of their uncorroded strength, which indicated that e-coating was successful in mitigating galvanic or other forms of corrosion. However, aluminum/magnesium samples did not survive 30 days of the corrosion treatment chosen for these tests. The low-energy spot welding results are particularly encouraging with regard to feasibility of the technology, and the Ohio State University team is committed to collaborating with equipment builders, system integrators, tier suppliers, and original equipment manufacturers to bring this process to market.

References

1. A. Vivek; S. R. Hansen; B. C. Liu; and G. S. Daehn, 2013, "Vaporizing foil actuator: a tool for collision welding," *Journal of Materials Processing Technology*.
2. S. A. A. Akbari Mousavi and S. P. Farhadi, 2009, "Experimental investigation of explosive welding of cp-titanium/AISI 304 stainless steel," *Mater. Des.*, 30(3); pp. 459-468.
3. A. Szecket, 1985, "A wavy versus straight interface in the explosive welding of aluminum to steel," *J. Vac. Sci. Technol. A Vacuum, Surfaces, Film.*, 3(6); pp. 2588.
4. A .Vivek; B. C. Liu; S. R. Hansen; and G. S. Daehn, 2014, "Accessing collision welding process window for titanium/copper welds with vaporizing foil actuators and grooved targets," in *Journal of Materials Processing Technology*, 214(8); pp. 1583-1589.

Bibliography

G. S. Daehn; A. Vivek; B. C. Liu et al., 2015, "Novel joining and process design," *Global Automotive Lighweight Manufacturing Summit,* Novi, Michigan.

G. S. Daehn; A. Vivek; B. C. Liu et al., 2015, "Keynote: Application of impulse for dissimilar metal joining," *MS&T,* Columbus, Ohio.

B. C. Liu; A. Vivek; and G. S. Daehn, 2015, "Use of Vaporizing Foil Actuator for Impact Welding of Aluminum Alloy Sheets with Steel and Magnesium Alloys," *Light Metals*; pp. 463-468.

A. Vivek; S. Hansen; J. Benzing; M. He; and G. S. Daehn, 2014, "Impact Welding of Aluminum to Copper and Stainless Steel by Vaporizing Foil Actuator: Effect of Heat Treatment Cycles on Mechanical Properties and Microstructure," in *Metallurgical and Materials Transactions A*; pp. 1-11.

A. Vivek; G. S. Daehn; B. C. Liu et al., 2014, "Impulse Manufacturing: Multi-material Joining," presented at *Global Lightweight Vehicle Manufacturing Congress,* Troy, Michigan.

A. Vivek and G. S. Daehn, 2014, "Welding in Lap and Spot Configurations with Vaporizing Foil Actuator," provisional patent application, Ohio State University.

A. Vivek; B. Liu; D. Sakkinen; M. Harris; and G. Daehn, 2015, "Impact Welding of Aluminum Alloy 6061 to Dual Phase 780 Steel Using Vaporizing Foil Actuator (No. 2015-01-0701)," Society of Automotive Engineers Technical Paper.

VI. Crosscutting

VI.1. Vehicle Lightweighting: Mass Reduction Spectrum Analysis and Process Cost Modeling – IBIS Associates, Inc.

Project Details

Anthony Mascarin, Principal Investigator
1601 Trapelo Road, Suite 163
Waltham, MA 02451
Phone: 781-290-0400
E-mail: tony@ibisassociates.com

James Francfort, Project Manager
Idaho National Laboratory
2525 Fremont Avenue
Idaho Falls, ID 83415
Phone: 208-526-6787
E-mail: james.francfort@inl.gov

Carol Schutte, Technology Area Development Manager
U.S. Department of Energy (DOE)
1000 Independence Avenue, SW
Washington, DC 20585
Phone: 202-287-5371
E-mail: carol.schutte@ee.doe.gov

Contractor: IBIS Associates, Inc.
Contract No.: ID14517

Executive Summary

The third phase of the technical cost modeling for vehicle lightweighting effort for the DOE Vehicle Technologies Office (VTO) Materials Program was undertaken with two goals: (1) lightweighting spectrum analysis and (2) process cost modeling.

Lightweighting Spectrum Analysis – In light of the extreme challenges of cost-effectively reaching ≥40% vehicle weight reduction and to best align with DOE's impact on vehicle mass reduction, the FY 2015 effort was directed at applying the existing tools, knowledge base, and team structure to develop a meaningful lightweighting solution cost spectrum. The spectrum analysis developed a framework of strategy risk regimes that incorporates the confidence of demonstrated manufacturing viability and economics with the potential impact on market acceptance. The strategies were ordered within each risk regime based on the cost premium. The cost of iteratively adopting successively more expensive options at the vehicle level was assessed. "Low risk" strategies involve well-understood materials and processes that can be employed in the near-term to reduce the overall vehicle weight of a conventional North American midsize vehicle by up to 17%. This weight savings costs approximately $2.00 per pound and assumes high-volume implementation using world class practices. "Medium risk" strategies can reduce overall vehicle weight up to 27%. This is primarily done through increased magnesium usage for components, component redesign, system downsizing, and lightweight interior material and glazing. These strategies are considered moderate risk due to questions of high-volume pricing or market resistance to reducing performance and/or luxury features for the sake of weight and fuel economy. "High-risk" strategies are needed to achieve the highest levels of weight reduction that approach 45% overall vehicle weight savings. Principal among these strategies is using carbon-fiber composites for

many vehicle structures. Even with optimistic manufacturing economics, the best cost-effectiveness is around $6.00 per pound saved. Significantly reduced carbon-fiber material price is needed to further reduce costs.

Process Cost Modeling – Aluminum, magnesium, and carbon fiber are critical materials on the path to significant reduction of vehicle mass and improvement of fuel economy. Technical cost models (TCM) were developed and used to better understand these priority lightweight material manufacturing technologies to evaluate cost structures and understand the relative leverage of key cost drivers. The processes targeted were aluminum extrusion, magnesium sheet forming, and carbon-fiber composite molding. Aluminum manufacturing, whether stamping, casting, or extrusion, is well understood. The raw aluminum material cost dominates the modelled aluminum extrusion process (for both simple and complex parts). Magnesium presents more processing challenges and industry does not yet have the same level of processing familiarity as aluminum. Ongoing magnesium sheet production and sheet forming development will expand its use for automotive weight reduction. The modelled magnesium sheet forming process is heavily and primarily dependent on the raw magnesium sheet material cost. While there are multiple aluminum suppliers, the availability of the required magnesium alloy sheet is extremely limited. Carbon-fiber composite molding is on the brink of achieving actual automotive volume production. Carbon-fiber feedstock price is still the primary obstacle to more widespread adoption. The modelled process (based on the BMW i3) is highly-automated and primarily uses robots. There is very little labor cost or tooling investment cost involved, but capital equipment costs are high; therefore, part costs are sensitive to cycle time/production rate. Materials handling techniques and rapid molding cycle time improvements need to be developed and widely demonstrated to continue carbon fiber's market growth and weight savings benefits.

Accomplishments

- Developed framework for comparing 107 lightweighting strategies employed across multiple engineering studies on different vehicle platforms on a common basis (FY 2015).
- Applied framework to assess a coherent adoption path in terms of weight savings impact and cost reduction across different levels of technical and market adoption risk (FY 2015).
- Created TCMs for three lightweight material manufacturing operations (i.e., aluminum extrusion, magnesium sheet forming, and carbon-fiber composite molding) in order to assess cost drivers and sensitivity to process improvements (FY 2015).

Future Directions

- The current scenario and process cost modeling task is complete. The TCM approach and framework can be applied to perform in-depth cost analyses of specific vehicle subsystems and components (e.g., powertrain) to identify detailed optimal pathways for reducing weight. Therefore, expanding the approach to investigate additional areas is being explored.

Technology Assessment

- Target: Develop an understanding of the relative merits of weight-reduction strategies from disparate vehicle programs across government and industry in terms of functional equivalence and manufactured cost impact. Use this understanding to prioritize technology research and adoption.
- Gap: Reported achievements and concepts often only report specific weight reductions on a specific component or system. Sizing to an equivalent vehicle platform bases and development of manufactured cost is required for comparisons.
- Target: Understanding the manufacturing cost of lightweight material production processes that are currently in development or in only limited use relative to mainstream automotive production levels.
- Gap: Costing data for developmental processes is not apparent through pricing transactions either because such transactions do not yet exist or are obscured by other cost factors in low-level production. Understanding the potential cost structure must be developed through economic

simulation of the processes through TCM, requiring collection and interpretation of difficult-to-obtain information.

Introduction

DOE VTO initiated a technical cost modeling effort with IBIS Associates, Inc. (IBIS) in 2013 to evaluate the cost-effectiveness of various materials-based weight reduction technologies that were being considered or were under development by the DOE Lightweighting Program. The overall goal was to model and assess the manufacturing economics of alternative design and production strategies for a series of lightweight vehicle concepts to achieve a high level of overall mass reduction. The weight-reducing strategies consisted of multiple combinations of lightweight structural materials, advanced manufacturing technologies, alternative subsystem technologies, and vehicle design approaches. The effort performed over the previous 2 years, developed and fully evaluated these concepts' ability to achieve two tiers (40% and 45%) of overall vehicle mass reduction over a 2013 baseline vehicle. The study's primary objective was to conceptualize these strategies, to construct a detailed techno-economic simulation of the vehicle design and manufacturing costs, and to project the relative commercial and retail cost position of each concept. The second goal was to identify the material, processing, and economic requirements for achieving these reductions at an effective cost of $3.42 per pound saved, a metric developed by the DOE as described in the Phases 1 and 2 report for this program. The results were clear that the weight reductions are technically possible, but meeting the required cost-effectiveness was not. A better understanding of the best approach for maximizing vehicle fleet weight reduction on a cost and cost-effectiveness basis was needed to best focus DOE's investment.

Approach

The results from Years 1 and 2 highlight the extreme challenges these required improvements would be to the automotive industry in the near future. Therefore, to best align with DOE's impact on vehicle mass reduction, the Year 3 effort was directed into two areas: (1) spectrum analysis and (2) process cost modeling.

Lightweighting Spectrum Analysis – This analysis applied the existing tools, knowledge base, and team structure from Years 1 and 2 toward developing a meaningful lightweighting solution cost spectrum. The developed weight-reduction spectrum analysis was built through visual and data mapping of multiple lightweighting technologies, ranging from existing practices through low-risk early stage advanced technologies to high-risk speculative projected achievements. The existing model structures and data allowed these assessments to be made on a consistent scenario basis to allow for direct "apples-to-apples" comparisons. This spectrum analysis approach provides DOE, vehicle manufacturers, and system manufacturers with a means of determining and understanding the most cost-effective approach for achieving a given level of mass savings over a broad range. Furthermore, this analysis provides a framework for assessing future designs, inventions, or development efforts against those that have already been analyzed.

The spectrum analysis started with developing weight reduction path scenarios. This was accomplished by reviewing Year 1 and 2 technologies, identifying data collection needs, and then prioritizing the list by impact and cost. Model scenarios were then developed, using data collection and industry review, and vehicle models were updated. The spectrum analysis was completed by a path analysis and optimization, in which the model was refined, and the preliminary results were reviewed and presented.

Process Cost Modeling – The results of the first two phases of this program highlighted that aluminum, magnesium, and carbon-fiber composites are critical materials for achieving significant vehicle mass reduction (e.g., ≥40%). The process cost modeling task developed TCMs and supporting analyses of these critical manufacturing technologies. The results provide DOE and industry with an understanding of the process parameters that have the greatest impact on component and/or system cost and the specific goals for technology development needed to achieve a desired cost target.

The process cost modeling effort began with identifying the critical manufacturing processes for each of the materials (i.e., aluminum, magnesium, and carbon-fiber composites). Process priorities were selected from the vehicle scenarios evaluated in the broader effort. Model resources and data gaps were thn identified. Relevant data were collected via literature review, interviews with subject matter experts, and with site visits. The process cost models were developed using these inputs. The resulting models were validated with collected data.

The developed models were used to analyze the processes. Preliminary analyses were performed and reviewed for accuracy and completeness. Additional data collection and analysis refinement were performed to improve the models. This included interacting with DOE, topic experts, and relevant industry members to validate the approach, model construction, and analysis. The results were used to define the goal for each process improvement.

The effort focused on following manufacturing process operations: carbon-fiber composite molding (i.e., weave, cut, kit, stack and staple, preform, ultrasonic trim, and molding), aluminum extrusion (i.e., extrude, cut, bend, machine, drill, and deburr), and magnesium sheet metal forming (i.e., blank, heat, stamp/pressure-form, and trim). The process parameters and data sources were then outlined and the preliminary models were presented and reviewed. After completing this initial stage, the model was refined and analyzed using data collection, interviews, and site visits. This final model, after being presented and reviewed, was used to complete a preliminary analysis. Additional data collection and other analysis refinement were done before the work was validated by DOE, topic experts, and industry. The final step in this process was reporting of results.

Technical cost modeling provides a powerful tool for estimating and simulating manufacturing costs. The technique is an extension of conventional process modeling, with particular emphasis on capturing the cost implications of material and process variables and changing economic scenarios.

For process modeling TCMs, a cost is assigned to each unit operation from the manufacturing process flow diagram. For each unit operation, the total cost is broken down into separately calculated elements: variable cost elements (e.g., materials, labor, and utilities [i.e., energy use]), and fixed-cost elements (e.g., equipment, tooling, building, maintenance, overhead labor, and cost of capital). Itemizing the cost down in this way, allows the complex task of cost estimation to be reduced down to a series of more simplified engineering and economic calculations.

Each TCM contains a module for each individual operation in the process being modeled. Each module contains sections for user-defined process inputs, intermediate calculations used by the model, and cost summaries for the process step. Information is also linked between modules where there are important relationships between process steps (e.g., production rate linkages, yield loss impact, and rework rates). Each input and intermediate calculation is given a range name, so that the source of data can be identified in downstream algorithms.

The user-defined inputs start with the process description, material description, part geometry, and weight. The next group of inputs relate to process parameters, capital equipment, energy, floor space, and process material consumption. Materials and specific pieces of equipment can be selected from lists contained in internal databases. Production rate, equipment and tooling, power, and space requirements can either be calculated by the model or be provided as an override entry by the user.

Each TCM module performs several intermediate calculations to determine the total production need to meet the target, calculate total capital investments, and allocate the annual costs on a per piece basis. The cost summary output for each TCM module lists the overall capital investment requirement for the operation, along with both the annual costs for production and the per piece costs (e.g., material, energy, labor, equipment, tooling, building, maintenance, overhead, and the cost of capital).

Cost Modeling Assumptions in this Analysis

- The full details of functionally equivalent, crashworthy designs are not available for many proposed advanced concepts. Therefore, the analysis results are speculative and most likely represent a best possible case scenario. Real-world application of these concepts may involve additional processing, performance, comfort, safety, and corrosion measures that are not fully understood at this time.
- Costing was performed in regard to fully implemented high-volume processes, with automation and expected learning curve improvements, not as current developmental or low-volume introductory practices. Particularly in the case of carbon-fiber structures, the ultimate analysis includes the predictions of processing cost reductions professed by material suppliers currently engaged in automotive production. To provide a conservative estimate for the carbon-fiber composite-intensive scenario, the analysis also addressed results with costs based on current production experience, under which the cost of weight savings is considerably beyond the stated target.
- An economic comparison was made in terms of the OEMs' direct manufacturing cost per vehicle. Therefore, when considering subsystems, analysis accounted for margins of one or more supplier levels that would be included in the OEM purchase cost. Those systems manufactured by the OEM (such as engines and body structures) include the costs of tooling, production capital, energy, direct and indirect manufacturing labor, and material. Engineering costs; selling, general, and administrative costs; profit; and dealer margins are not included at this level of analysis.

Results and Discussion

Lightweighting Spectrum Analysis

Data from several vehicle lightweighting opportunity studies, including the Ford Motor Company/Vehma International Multi-Material Lightweight Vehicle (MMLV) study [1], Lotus [2], and FEV Inc. (FEV) [3] are presented in Figure VI-1. These data are used to compare the evaluated weight reduction strategies in terms of the amount of weight saved relative to the cost per pound of savings. The negative cost of weight savings indicates that a strategy reduces both cost and mass at the same time, most likely from downsizing, feature decontenting (i.e., an auto industry term for removing features from upcoming model years, usually to save money), or system elimination. While such strategies are technically viable, they pose risk in terms of functional-equivalency and consumer acceptance as described in the conclusions from the Year 2 report. The figure also highlights materials-based weight savings strategies (opposed to savings achieved through component downsizing) and identifies the significant amount of mass reduction potential of carbon-fiber composite, aluminum, and multi-material body structures and magnesium powertrain and chassis components.

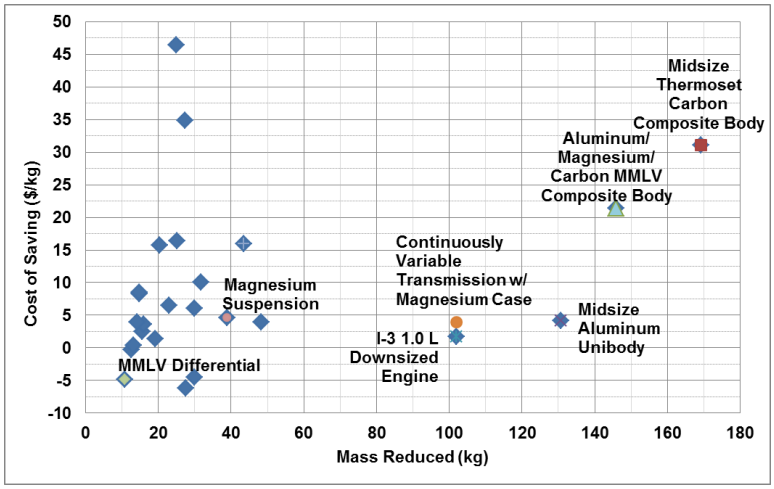

Figure VI-1: Priority materials-based weight reduction strategies.

The mass saved and cost data for each weight reduction strategy were assembled. A coherent rationale for strategy prioritization was developed using this information. The developed rationale was used to create a technology adoption path that was used to construct a spectrum of optimum vehicle weight savings. The analysis approach was adopted to accomplish this: (1) identify substitution type, (2) evaluate technical and economic risk factors, (3) prioritize strategies by cost per pound and total mass saved, (4) model the step-by-step system adoption at the vehicle level, and (5) construct an adoption path by weight reduction and cost across the mass spectrum. Each lightweighting strategy was assigned a code for the type of substitution relative to the baseline system it replaces, using the following categories: high-strength steel, aluminum, magnesium, carbon-fiber composites, plastic, multi-material, design changes, process changes, size reductions, and functionality reduction. A risk factor rating was also assigned to each strategy.

Low risk strategies can be readily implemented now by automakers because of both material and processing familiarity and confidence in the perfomance and economics. **Moderate risk** strategies are considered to be technically viable, but for which there is less familiarity in high-volume production and/or less certainty of performance, quality, and/or cost relative to incumbent practices. **High-risk strategies** require significant material and/or process cost reductions or significant changes in vehicle perfomance or features. The weight-reduction strategies were grouped into three risk categories (from low to high risk) and prioritized by cost of weight savings in each category. The resulting prioritized list of weight-reduction strategies was used to evaluate the impact on overall vehicle mass and cost using the vehicle system technical cost model that was developed in Years 1 and 2.

The analysis began with the baseline vehicle. Each weight-reducing strategy was incrementally assessed, moving from low to high risk, in terms of impact on overall vehicle mass and cost as each additional strategy is adopted. The sequence of strategy adoption, resulting vehicle mass and cost, percentage of mass reduction, and cost of weight savings are shown in Table VI-1 and Table VI-2. Note that data for each adoption step are cumulative, which means it includes all previous employed strategies. For several systems, more than one strategy was available. In these cases, adoption of a later strategy replaced the earlier lightweight strategy, rather than the baseline system. The model also accounts for secondary and tertiary lightweighting that results from the reduced requirements of chassis components from lighter weight body structures and further reduction of powertrain size needed for equivalent performance.

Scenario of Mass Reduction versus Cost of Savings

Figure VI-2 presents the amount of weight savings with the cost per pound of weight reduction for each strategy in the developer priority order. As described in the reports for Years 1 and 2, the cost projections involve various amounts of optimism based on their source and risk factor. Dividing the plot into regimes of low risk (green), moderate risk (blue), and high risk (red) and reflecting on the strategies included in each regime makes the overall shape more understandable. These figures also show the cost-effectiveness for the achieved weight savings for each strategy. Within each risk regime, the order of adoption was determined by the overall cost of incorporating the strategy. The steep increase in cost per pound saved between 7 to 10% weight saved is due to the cost of the multi-material body-in-white (BIW). (Replacing the high-strength steel BIW results in 0 to 3% mass savings). The negative slope from 13 to 17% is due to adoption of the all-aluminum BIW. The aluminum BIW costs more than the multi-material BIW it replaces, but saves more weight and has a better cost per pound saved; therefore, this further reduces overall cost per pound saved.

The moderate risk regime contains several lightweighting strategies from the FEV and MMLV studies involving lower-density materials or downsized interior and chassis components. Most of these were predicted at very little, if any, additional cost (resulting in negative slope from 17 to 22%), but are considered to have risk in terms of performance and consumer acceptance.

Table VI-1: Scenario masses and costs of incremental lightweighting strategy adoption (Part 1).

Component, Lightweighting Study (When Relevant)	Vehicle Mass (lb)	Vehicle Cost ($)	Total Weight Reduced (%)	Cost of Weight Reduction ($/lb)
Baseline Vehicle	3,304	15,723	0	0.00
Body-in-White, Lotus High-Strength Steel Unibody	3,206	15,723	3	0.00
Fuel System, High-Density Polyethylene	3,178	15,723	4	0.00
Fuel System, Multi-Material Lightweight Vehicle (MMLV)	3,172	15,723	4	0.00
Powertrain Electronics, MMLV Mach 1	3,154	15,723	5	0.00
Emission Control Electronics, MMLV Mach 1	3,151	15,723	5	0.00
Braking System, Aluminum Brake Rotors, Stainless	3,129	15,723	5	0.00
Cradle, Extruded Aluminum	3,100	15,728	6	0.03
Wheels and Tires, Aluminum 15"	3,064	15,787	7	0.27
Cradle, Extruded Aluminum	3,062	15,838	7	0.47
Body-in-White, MMLV Mach 1 Unibody	2,994	16,366	9	2.07
Front/Rear Bumpers, Extruded Aluminum	2,986	16,386	10	2.08
Corner Suspension, Aluminum	2,920	16,566	12	2.19
Panels, Stamped Aluminum	2,869	16,715	13	2.28
Body-in-White, Aluminum Unibody	2,748	16,728	17	1.81
Front/Rear Bumpers, FEV, Inc. (FEV) Lightweight	2,755	16,719	17	1.81
HVAC, Subcompact	2,737	16,719	17	1.76
Body Hardware, FEV MuCell®/ PolyOne	2,732	16,719	17	1.74
Seating and Restraints, FEV Lightweight	2,694	16,719	18	1.63
HVAC, FEV Lightweight	2,706	16,719	18	1.67
Driveshaft/Axle, FEV Scalloped, Aluminum and Plastic Beaming Carriers	2,703	16,719	18	1.66
Corner Suspension, FEV Aluminum, Magnesium and Steel Tube	2,675	16,539	19	1.30
Exhaust System, FEV Mubea Tubing	2,659	16,537	20	1.26
Instrument Panel, FEV Magnesium Beam, MuCell®	2,645	16,537	20	1.24
Body Hardware, MMLV Mach 1 MuCell®	2,640	16,537	20	1.23
Interior Electrical, MMLV Mach 1	2,638	16,537	20	1.22
Exterior Electrical, MMLV Mach 1	2,636	16,537	20	1.22
Door Modules, Long Fiber Injection Molded	2,632	16,537	20	1.21
Interior Electrical, FEV	2,623	16,539	21	1.20
Chassis Electrical, FEV	2,622	16,540	21	1.20
Wheels and Tires, Toyota Prius-based	2,615	16,509	21	1.14
Exterior Electrical, FEV	2,616	16,510	21	1.14
Trim and Insulation, MuCell® and Foamed Plastic	2,582	16,549	22	1.14
Glass, FEV Lightweight	2,573	16,563	22	1.15
Transmission, FEV Magnesium Housing	2,525	16,671	24	1.22
Transmission, Continuously Variable Transmission with Magnesium Case	2,467	16,755	25	1.23
Steering System, FEV Lightweight	2,463	16,765	25	1.24
Steering System with Magnesium Wheel, Column Assembly	2,458	16,781	26	1.25
Glass, Lightweight Mix	2,435	16,892	26	1.34
Seating and Restraints, Magnesium, MuCell®, Structural Foam	2,427	17,212	27	1.70

Table VI-2: Scenario masses and costs of incremental lightweighting strategy adoption (Part 2).

Component, Lightweighting Study (When Relevant)	Vehicle Mass (lb)	Vehicle Cost ($)	Total Weight Reduced (%)	Cost of Weight Reduction ($/lb)
HVAC, None	2,385	16,762	28	1.13
Body Hardware, Magnesium	2,382	16,770	28	1.14
Engine, Multi-Material Lightweight Vehicle (MMLV) I-3 1.0 L	2,158	16,940	35	1.06
Corner Suspension, Aluminum, Carbon, Hollow Springs	2,166	17,120	34	1.23
Front/Rear Bumpers, Magnesium	2,157	17,149	35	1.24
Instrument Panel, Carbon Fiber Beam	2,138	17,272	35	1.33
Seating and Restraints, Carbon Fiber Seat Backs, Reduced Design	2,113	17,272	36	1.30
Wheels and Tires, Carbon with Reduced Mass Wheel	2,059	17,940	38	1.78
Braking System, Carbon-Ceramic Brake Rotors and Magnesium	2,026	18,351	39	2.06
Body-in-White, MMLV Ultra High Strength Steel, Aluminum, Carbon Composite Body	1,993	20,932	40	3.97
Body-in-White, Carbon Composite Body	1,941	23,068	41	5.39
Panels, Stamped Magnesium	1,932	23,869	42	5.94
Panels, Carbon Composite	1,937	24,080	41	6.11
Interior Electrical, Internal Network	1,920	24,678	42	6.47
Chassis Electrical, Internal Network	1,903	25,277	42	6.82
Exterior Electrical, Internal Network	1,895	25,576	43	6.99

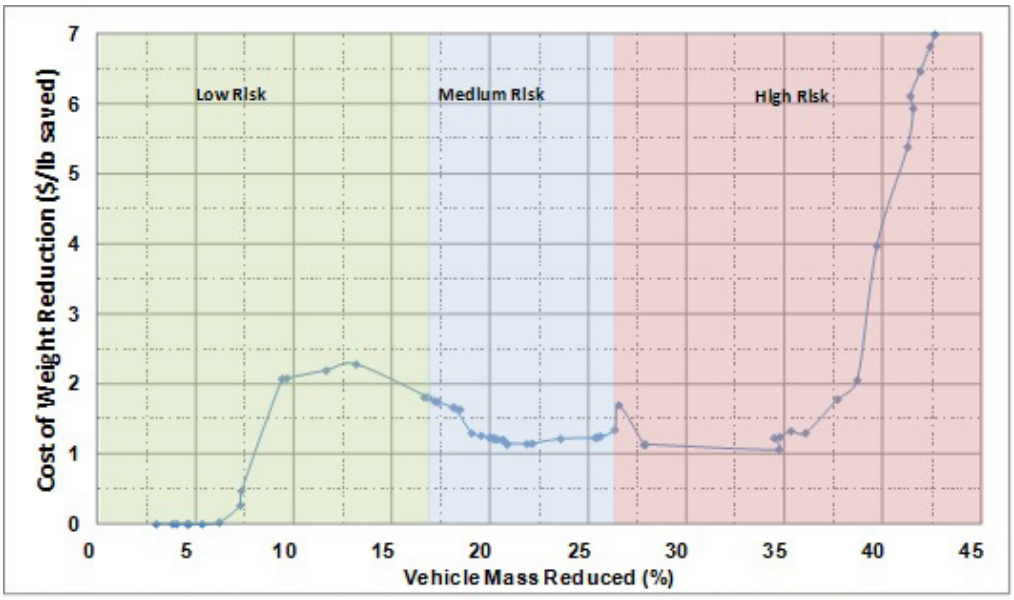

Figure VI-2: Mass reduction and cost of weight savings for adoption path of incremental mass savings strategies.

Two strategies in the high-risk regime are responsible for the negative slope for the cost per pound saved in the 27 to 35% weight saved range: (1) eliminating the heating, ventilating, and air-conditioning system and (2) significantly downsizing the engine/transmission. Both strategies reduce weight and cost, but are unlikely to be acceptable in today's market.

Figure VI-3 combines the weight reduction of each strategy and the cost of weight savings for the individual strategy (red line) and cost of weight savings as cumulatively adopted into the baseline vehicle.

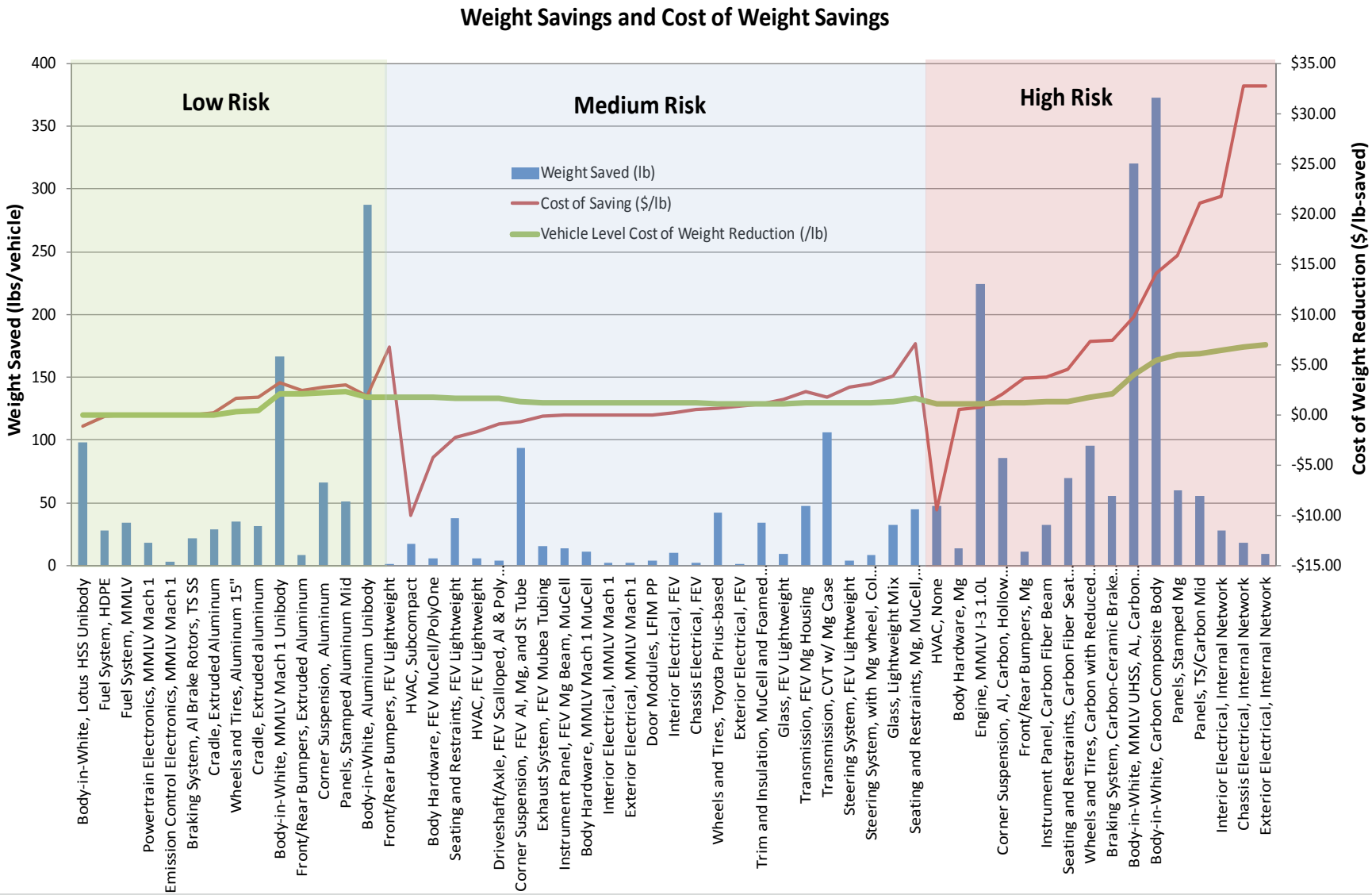

Figure VI-3: Weight savings of individual strategies and overall vehicle cost of weight reduction.

Strategies with a negative or zero cost of weight reduction involve system downsizing or decontenting and are only considered in the medium or high-risk regimes because of the lower likelihood of market acceptance. Each of these technology risk regimes is shown in more detail, respectively, in Figure VI-4, Figure VI-5, and Figure VI-6 to allow for deeper interpretation. (The arrows and numbers show the couple very high values to allow the bulk of the data to be shown in more detail) These figures, put in order of risk and cost of adoption, compare the impact of individual weight-reduction strategies. The aluminum intensive body and chassis components are clearly the low hanging fruit for significant near-term weight reduction. Overall vehicle mass reduction between 15 to 20% is readily-achievable at moderate cost premiums. However, many individual system strategies must be pursued to achieve higher levels of mass reduction. Magnesium and carbon-fiber composites, in addition to aluminum, are key materials needed to achieve vehicle weight reductions greater than 30%. Current material pricing and manufacturing practices pose significant obstacles to high volume adoption. Understanding the process economics is the first step toward achieving commercial viability for these materials systems, which is needed to achieve significant reduction in vehicle mass and improve average vehicle fuel economy.

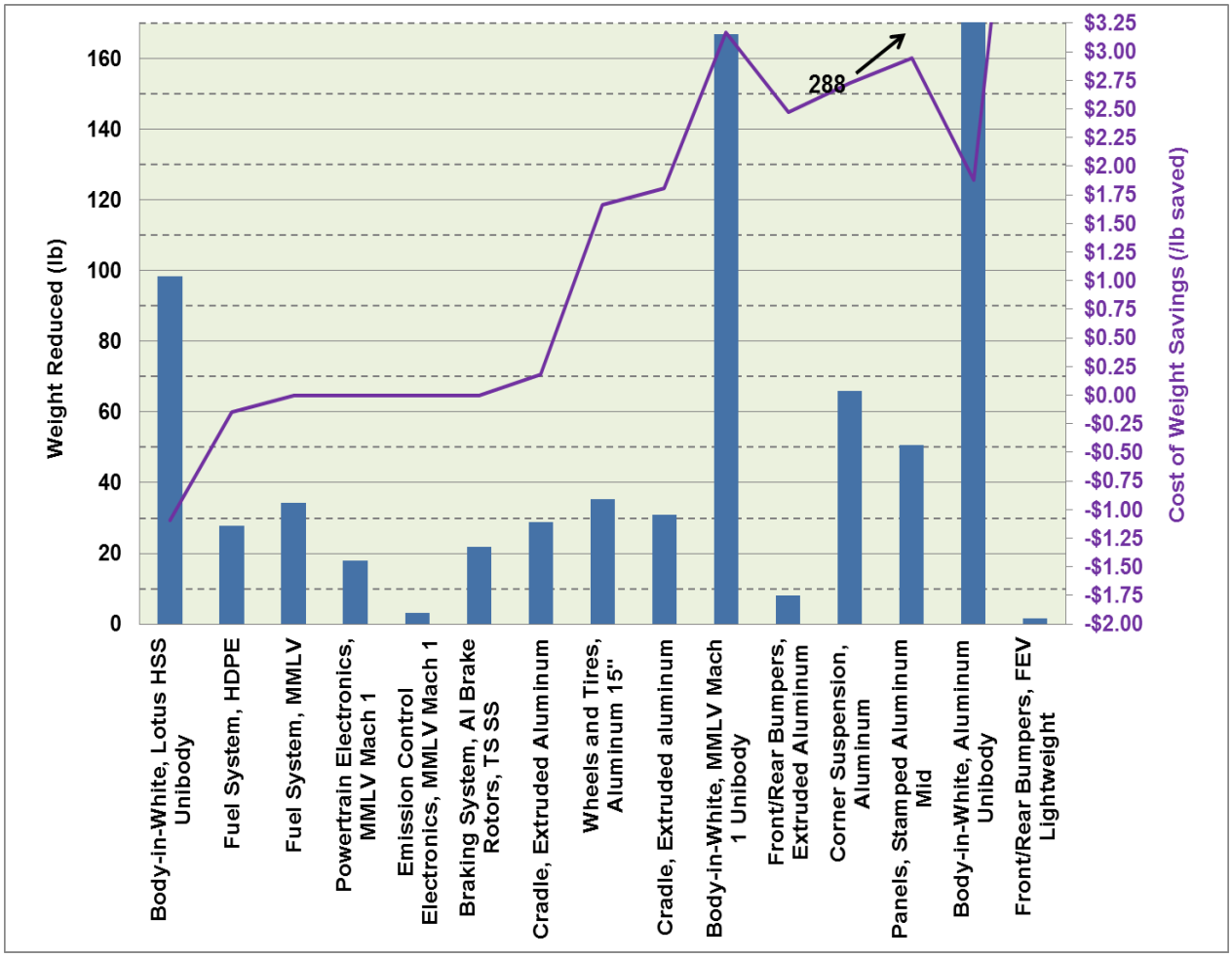

Figure VI-4: Weight-reduction strategies by risk factor and cost of weight savings (low risk).

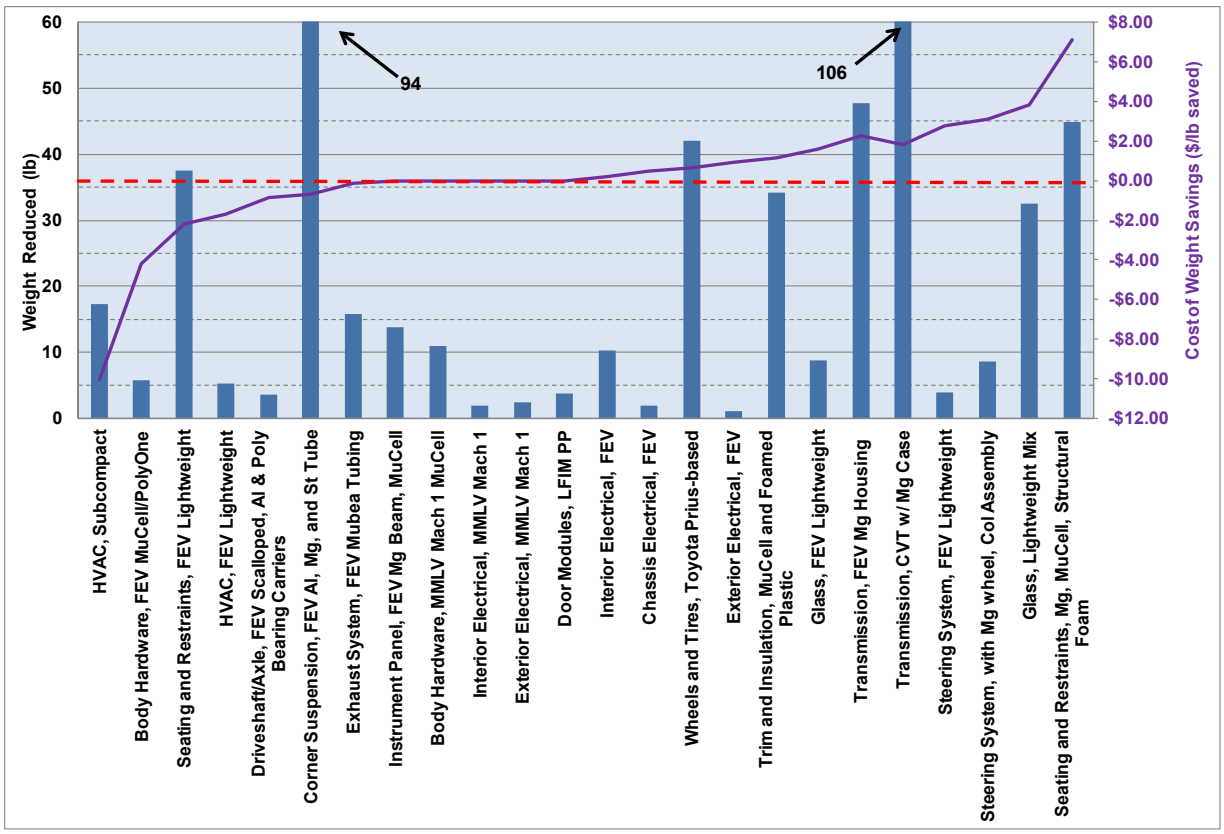

Figure VI-5: Weight-reduction strategies by risk factor and cost of weight savings (moderate risk).

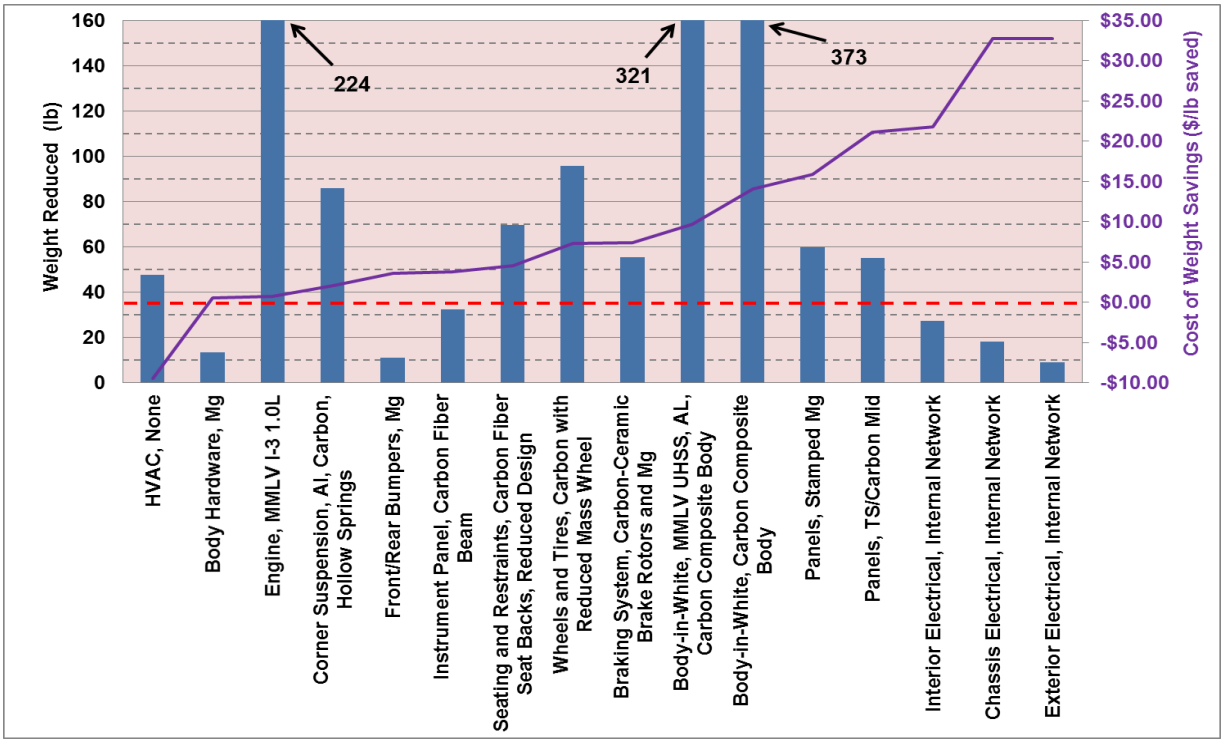

Figure VI-6: Weight-reduction strategies by risk factor and cost of weight savings (high risk).

Process Cost Modeling

Aluminum Extrusion — Simple

Aluminum extrusion is the process of using great pressure to force material through a die to create a longitudinal shape with a desired continuous cross section. In simplest form, aluminum extrusion consists of an aluminum billet, an extrusion press (including a part-specific die assembly), and a cut-off saw. The "simple" example describes an easy-to-manufacture part. As shown in Figure VI-7, aluminum extrusion is a very material cost-intensive process. The extrusion press itself can be expensive, but process rates are relatively high and tooling is inexpensive; therefore, the capital cost per part is very low. Production rates are high and yield loss is very low for extrusion. As such, large changes to the production rate and yield do not have a great deal of impact relative to the cost of material. The only important factors for simple extrusion cost reduction are aluminum price and part weight (i.e., design and changes to the thickness or cross section). Economy of scale is achieved at less than 20,000 units per year.

	Part Cost ($/part)	Annual Cost ($/year)	Percentage of Total Cost
VARIABLE COST ELEMENTS			
Material Cost	$2.58	$258,373	81.5%
Labor Cost	$0.11	$11,310	3.6%
Utility Cost	$0.01	$957	0.3%
FIXED COST ELEMENTS			
Equipment Cost	$0.14	$14,229	4.5%
Tooling Cost	$0.11	$10,501	3.3%
Building Cost	$0.00	$483	0.2%
Maintenance Cost	$0.09	$8,800	2.8%
Overhead Labor Cost	$0.02	$1,823	0.6%
Cost of Capital	$0.11	$10,658	3.4%
TOTAL MANUFACTURING COST	$3.17	$317,134	100%
Cost per Unit Weight ($/lb)	$1.44		

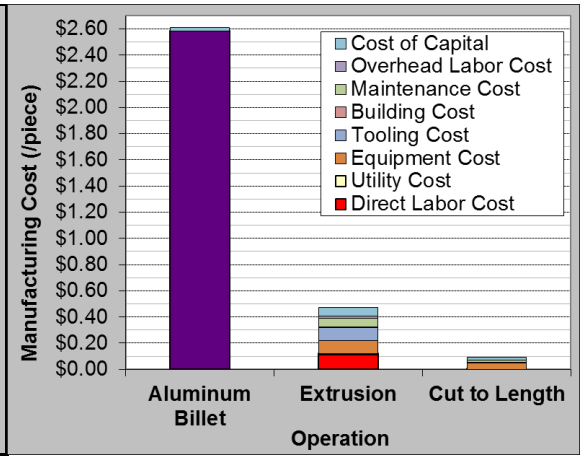

Figure VI-7: Aluminum extrusion (simple) cost summary by element and part cost breakdown by operation.

Aluminum Extrusion — Complex

The previous analysis examined aluminum extrusion in its simplest form, but more complex aluminum parts can also be made using extrusion. Continuous straight parts can have various parts machined and drilled to create different cross sections. Furthermore, the entire component can be bent into a curve or partially forged into a different shape. Post-forming heat treatment may also be applied. The cost summary and breakdown in Figure VI-8 shows that even with additional operations, complex aluminum extrusion is still mostly a material price-intensive operation; however, it has more capital and labor cost content than simple extrusion. A sensitivity analysis revealed that complex extrusion is still primarily sensitive to material price and part weight, but is also affected by the amount and complexity of bending and machining. Economy of scale is achieved at slightly less than 20,000 units per year.

Another interesting sensitivity that can be addressed with the TCM approach is historical price sensitivity. Taking a market price history over 20 years as an input to the model, it can be seen how wildly the price of a single component may have changed over time. Aluminum price volatility has traditionally been one of the obstacles to its adoption in the automotive market.

	Part Cost ($/part)	Annual Cost ($/year)	Percentage of Total Cost
VARIABLE COST ELEMENTS			
Material Cost	$2.58	$258,373	69.4%
Labor Cost	$0.29	$29,437	7.9%
Utility Cost	$0.01	$1,298	0.3%
FIXED COST ELEMENTS			
Equipment Cost	$0.32	$32,032	8.6%
Tooling Cost	$0.11	$10,901	2.9%
Building Cost	$0.01	$1,032	0.3%
Maintenance Cost	$0.17	$16,570	4.5%
Overhead Labor Cost	$0.05	$4,745	1.3%
Cost of Capital	$0.18	$17,948	4.8%
TOTAL MANUFACTURING COST	$3.72	$372,338	100%
Cost per Unit Weight ($/lb)	$1.69		

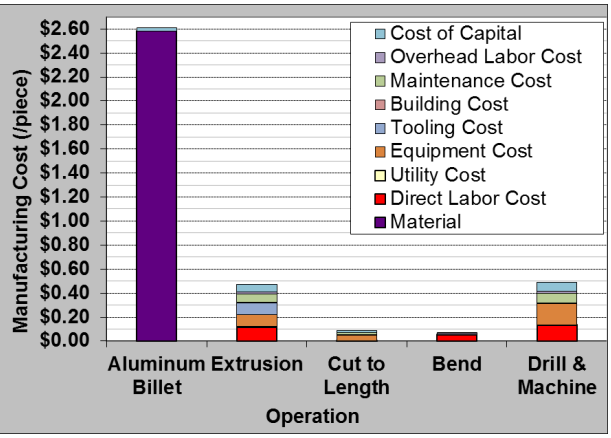

Figure VI-8: Aluminum extrusion (complex) cost summary by element and part cost breakdown by operation.

Magnesium Sheet Forming

The modeled magnesium sheet forming example was similar to the process developed by the U.S. Automotive Materials Partnership Automotive Metals Division, "*Development of High-Volume Warm Forming of Low-Cost Magnesium Sheet"* project [4]. The project developed an integrated forming cell that utilized a continuous belt furnace, robotic transfer, and stamping press. The complexity of deformation for such parts is unclear; therefore, a fairly simple panel was assumed for the analyzed example. Figure VI-9 summarizes the manufacturing cost summary. The developed process that is prototyped by General Motors Company is not particularly complex, with tooling and energy being secondary cost drivers behind magnesium sheet price. Magnesium sheet supply is particularly an issue with only one known supplier (POSCO). A sensitivity analysis revealed that part weight (i.e., design and changes to thickness or cross section) is the key important cost factor. Economy of scale is achieved at around 40,000 units per year.

	Part Cost ($/part)	Annual Cost ($/year)	Percentage of Total Cost
VARIABLE COST ELEMENTS			
Material Cost	$15.91	$1,591,111	74.8%
Labor Cost	$1.07	$106,516	5.0%
Utility Cost	$0.06	$5,658	0.3%
FIXED COST ELEMENTS			
Equipment Cost	$0.57	$57,003	2.7%
Tooling Cost	$1.93	$193,105	9.1%
Building Cost	$0.02	$2,184	0.1%
Maintenance Cost	$0.73	$73,262	3.4%
Overhead Labor Cost	$0.17	$17,169	0.8%
Cost of Capital	$0.82	$82,338	3.9%
TOTAL MANUFACTURING COST	$21.28	$2,128,346	100%
Cost per Unit Weight ($/lb)	$5.40		

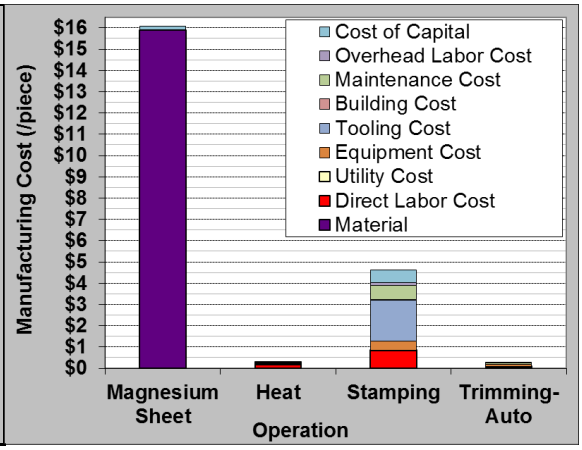

Figure VI-9: Magnesium sheet forming cost summary by element and part cost breakdown by operation.

Carbon-Fiber Composites

Carbon-fiber composite manufacturing was modeled as the high-volume, automated, high-pressure resin transfer molding operation employed by BMW on the BMW i3 "Life Module" passenger compartment. In order to model this process, BMW's process was extensively researched, including fabric production, reinforcement kitting and preforming, materials handling, and molding. A single large complex component was examined for this case study, specifically, the body side inner of the i3 "Life Module". The fiber itself is manufactured by a joint-venture with Mitsubishi Rayon and supplied directly to the BMW plant in

Wackersdorf, Germany for fabric production. Because of this, there is no market price for the 50K carbon-fiber yarn. A price of $12.50 per pound for the carbon fabric was used by utilizing a $9 per pound price for a similar Zoltek product and unidirectional fabric production modeling.

Figure VI-10 shows that material cost is, not surprisingly, the greatest cost driver. However, equipment cost is still very high for this process because of the long cycle times. The modeled process is highly automated; therefore, it requires several robots per component for preforming, trimming, and molding operations. There is very little labor or tooling investment involved in the BMW process. However, the capital equipment cost is high and is very sensitive to production rate. The conducted analysis assumed the 10-minute cycle time reported by BMW and SGL Group. Sensitivity analysis shows the impact of molding cycle time on part cost. A 50% cycle time reduction (i.e., 5-minute cycle) would decrease the cost by approximately $150 (23%).

	Part Cost ($/part)	Annual Cost ($/year)	Percentage of Total Cost
VARIABLE COST ELEMENTS			
Material Cost	$309.78	$30,977,778	47.7%
Labor Cost	$69.46	$6,946,452	10.7%
Utility Cost	$3.26	$326,075	0.5%
FIXED COST ELEMENTS			
Equipment Cost	$171.74	$17,173,678	26.4%
Tooling Cost	$1.18	$118,165	0.2%
Building Cost	$0.65	$65,353	0.1%
Maintenance Cost	$43.56	$4,355,637	6.7%
Overhead Labor Cost	$8.08	$808,391	1.2%
Cost of Capital	$42.10	$4,209,551	6.5%
TOTAL MANUFACTURING COST	$649.81	$64,981,081	100%
Cost per Unit Weight ($/lb)	$21.07		

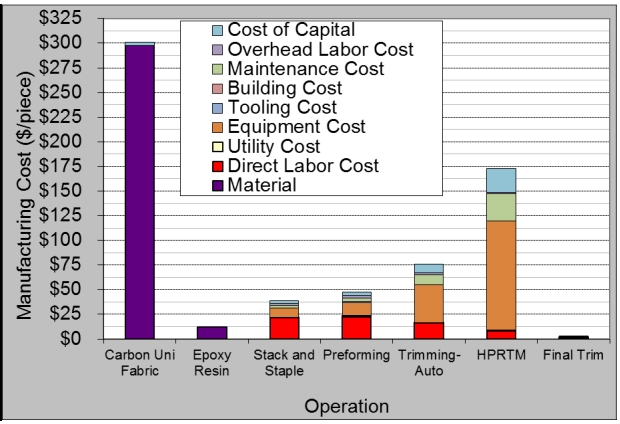

Figure VI-10: Carbon-fiber composites (side inner panel) cost summary by element and part cost breakdown by operation.

Technology Transfer Path

The analysis performed for and conclusions drawn from this study inform the U.S. DOE VTO's Lightweight Materials Program of the opportunities, barriers, and technical gaps for applying significant lightweighting to mainstream light-duty vehicles. The technical and economic conclusions are intended to guide DOE's definition for future vehicle lightweighting goals to focus them on enabling the largest, most cost-effective fleetwide petroleum fuel savings possible. Spectrum analysis results are presented in a manner that allows industry to use the findings as a tool for determining the priority and to use a combination of strategies to evaluate and incorporate into vehicle designs to reduce weight. Process cost analysis results inform DOE about the critical parts of the manufacturing process that must be improved to reduce the overall component costs.

Conclusion

Lightweighting Spectrum Analysis – The spectrum analysis determined that low-risk strategies that involve well-understood materials and processes can be employed in the near-term to reduce the overall vehicle weight of a conventional North American midsize vehicle by up 17%. This weight savings costs approximately $2.00 per pound saved and assumes high-volume implementation and world class practices. These low-risk strategies involve extensive use of aluminum structural components. Medium-risk strategies can be used to reduce overall vehicle weight up to a total of 27%. This is primarily done through increased magnesium usage for components, component redesign, system downsizing, and lightweight interior materials and glazings. These strategies are considered moderate risk due to questions of high-volume pricing or market resistance to reducing performance and/or luxury features for the sake of weight and fuel economy. High-risk strategies are needed to achieve the highest levels of weight reduction that approach 45% overall vehicle weight savings. Principal among these strategies is use of carbon-fiber composites for many vehicle structures. However, even with optimistic manufacturing economics, the best cost-effectiveness of weight savings is around $6.00 per

pound saved (relative to the $3.42 cost per pound saved target at the start of the program). Significantly reduced carbon-fiber material price is needed to reduce costs further. Magnesium, smaller lightweight propulsion systems, and next generation electrical and control systems will be required to achieve greater than 30% weight reduction.

Process Cost Modeling – Aluminum, magnesium, and carbon fiber are critical materials on the path to significant reduction of passenger car mass and improvement of fuel economy. Aluminum manufacturing, whether stamping, casting, or extrusion is well understood. The modelled aluminum extrusion process (for both simple and complex parts) is heavily and primarily dependent on raw aluminum material cost. Magnesium presents more processing challenges and does not yet have the same level of processing familiarity in the industry as aluminum or steel. Ongoing development of magnesium sheet production and sheet forming will expand the possibilities for automotive weight reduction.

The magnesium sheet forming process is heavily and primarily dependent on the raw magnesium sheet material cost. There are multiple aluminum suppliers, but there is only one magnesium sheet manufacturer (i.e., POSCO). The lack of market competition likely results in higher costs.

Carbon-fiber composite molding is on the brink of achieving automotive volume production. The carbon-fiber feedstock price is still the primary obstacle to more widespread adoption. The modelled process was highly automated and primarily uses robots. There is very little labor cost or tooling investment cost involved in BMW's process. Capital equipment costs are high; therefore, part costs are sensitive to cycle time/production rate. Processing improvements (such as materials handling and rapid molding cycle times) also need to be developed and widely demonstrated in order to continue growth of the market and its weight-savings benefits.

References

1. T. Skszek and M. Zaluzec, 2012, "Demonstration Project for a Multi-Material Lightweight Prototype Vehicle - Vehma International of America, Inc.," presented to the U.S. Department of Energy Vehicle Technologies Office, Washington DC, April 2012.
2. EPA, *Peer Review of Light-Duty Vehicle Mass-Reduction and Cost Analysis — Midsize Crossover Utility Vehicle (FEV Report),* 2012, EPA-420-R-12-019, Washington, DC, U.S. Environmental Protection Agency, accessed March 2, 2016, https://www3.epa.gov/otaq/climate/documents/420r12019.pdf.
3. Lotus Engineering Inc., 2010, *An Assessment of Mass Reduction Opportunities for a 2017-2020 Model Year Vehicle Program,* submitted to the International Council on Clean Transportation, accessed March 2, 2016, http://www.theicct.org/sites/default/files/publications/Mass_reduction_final_2010.pdf.
4. *United States Automotive Materials Partnership LLC and Department of Energy Final Report Compilation: Cooperative Agreement DE-FC26-02OR22910 Projects from January 1, 2002 through January 31, 2011,* 2011, Southfield, Michigan, United States Automotive Materials Partnership, LLC, accessed on March 2, 2016, http://www.osti.gov/scitech/servlets/purl/1038533.

Bibliography

EIS, 2011, *Annual Energy Outlook 2011,* Washington, DC, United States Energy Information Administration, accessed March 2, 2016, http://www.eia.gov/pressroom/presentations/newell_02082011.pdf.

EIS, 2014, *Annual Energy Outlook Retrospective Review: Evaluation of 2013 and Prior Reference Case Projections,* Technical Report No. PB2014105313, U.S. Energy Information Administration, Washington, DC, accessed March 2 2016, http://www.eia.gov/forecasts/aeo/retrospective/.

A. Bandivadekar; K. Bodek; L. Cheah; C. Evans; T. Groode; J. Heywood; E. Kasseris; M. Kromer; and M. Weiss, 2008, *On the Road in 2035: Reducing Transportation's Petroleum Consumption and GHG Emissions,*

MIT Laboratory for Energy and the Environment Report No. LFEE 2008-05 RP, Cambridge, Massachusetts, Massachusetts Institute of Technology, accessed March 2, 2016, http://web.mit.edu/sloan-auto-lab/research/beforeh2/otr2035/On%20the%20Road%20in%202035_MIT_July%202008.pdf.

L. Berger, 2014, *Cheaper carbon fibre will slash auto making costs-manufacturer,* prepared for Reuters Industries, March 28, 2014, accessed March 2, 2016, http://www.reuters.com/article/sgl-fibres-idUSL5N0MP2RP20140328.

A. Broda and R. Casadei, 2007, "Impact of Vehicle Weight Reduction on Fuel Economy for Various Vehicle Architectures Project FB769," presented to The Aluminum Association, Inc., Arlington, Virginia, accessed on March 2, 2016, http://www.drivealuminum.org/research-resources/PDF/Research/2008/2008-Ricardo-Study.pdf.

L. Cheah, 2010, *Cars on a Diet: The Material and Energy Impacts,* Ph.D. Thesis, Cambridge, Massachusetts, Massachusetts Institute of Technology.

DOT, 2010, *Corporate Average Fuel Economy for MY 2012-MY2016 Passenger Cars and Light Trucks Final Regulatory Impact Analysis,* March 2010, Washington, DC, U.S. Department of Transportation National Highway Traffic Safety Administration, accessed on March 2, 2016, www.nhtsa.gov/staticfiles/rulemaking/pdf/cafe/CAFE_2012-2016.

S. C. Davis; S. W. Diegel; and R. G. Boundy, 2015, *Transportation Energy Data Book: Edition 34,* ORNL-6991 (Edition 34 of ORNL-5198) Table 3.12, Oak Ridge, Tennessee, Oak Ridge National Laboratory, accessed March 2, 2016, http://cta.ornl.gov/data/index.shtml.

L. D'Orazio; F. Visintainer; M. Darin, 2011, "Sensor Networks on the Car, State of the Art and Future Challenges," prepared for Design Automation and Test in Europe 11, Grenoble, France, March 14 through 18, 2011, Special Interest Group on Design Automation (SIGDA), 6 pp, accessed March 2, 2016, https://www.researchgate.net/publication/221341817_Sensor_networks_on_the_car_State_of_the_art_and_future_challenges.

Edmunds.com, 2013, data retrieved from website, http://www.edmunds.com.

K. Ernst, 2013, "World's First 'One-Piece' Carbon Fiber Wheels Now Available In U.S.," Motor Authority, accessed March 2, 2016, http://www.motorauthority.com/news/1081602_worlds-first-one-piece-carbon-fiber-wheels-now-available-in-u-s.

J. Francfort et.al., 2015, *Vehicle Lightweighting: 40% and 45% Weight Savings Analysis: Technical Cost Modeling for Vehicle Lightweighting,* INL/EXT-14-33863, Idaho Falls, Idaho, Idaho National Laboratory, accessed on March 2, 2016, http://avt.inl.gov/pdf/TechnicalCostModel40and45PercentWeightSavings.pdf.

Freescale Semiconductor, 2013, "Future Advances in Body Electronics," accessed March 2, 2016, http://cache.freescale.com/files/automotive/doc/white_paper/BODYDELECTRWP.pdf.

B. Halvorson, 2012, "Carbon Fiber Wheels: A Costly Upgrade, but Better Performance?," Motor Authority, accessed March 2, 2016, http://www.motorauthority.com/news/1081342_carbon-fiber-wheels-a-costly-upgrade-but-better-performance.

IBIS Associates, Inc., 2005, *Aluminum Association Aluminum Vehicle Structure - Manufacturing and Lifecycle Cost Analysis,* Results Report, Arlington, Virginia, The Aluminum Association, accessed March 2, 2016, http://www.drivealuminum.org/research-resources/PDF/Research/2005/2005_IBIS_Cost_Study.pdf.

IBIS Associates, Inc., 2008, "Advantages of Automotive Aluminum and Advanced Powertrains," presented to The Aluminum Association, Inc., Arlington, Virginia, accessed on March 2, 2016, http://www.drivealuminum.org/research-resources/PDF/Research/2008/2008-IBIS-Study.pdf.

IBIS Associates, Inc., 2010, *Technical Cost Model Analysis for a Structural Composite Underbody, Supporting USCAR – ACC Composite Underbody Program,* Southfield, Michigan, United States Council for Automotive Research LLC.

IBIS Associates, Inc., 2014, Internal Proprietary Data, Concord, Massachusetts.

Lithium Pros, Frequently Asked Questions, Knoxville, Tennessee, http://lithiumpros.com/support/faqs-2/.

Lu, S., 2006, *Vehicle Survivability and Travel Mileage Schedules,* DOT HS 809 952, Washington, DC: U.S. Department of Transportation, National Highway Traffic Safety Administration, accessed March 2, 2016, www.nrd.nhtsa.dot.gov/Pubs/809952.PDF.

United States Council for Automotive Research, 2006, *Magnesium Vision 2020: A North American Automotive Strategic Vision for Magnesium,* Southfield, Michigan, United States Automotive Materials Partnership, accessed March 2, 2016, http://iweb.tms.org/Communities/FTAttachments/MG_2020_-_Released_11_1_[1].1.06.pdf.

A. Mascarin, 2016, "Vehicle Lightweighting: Mass Reduction Spectrum Analysis and Process Cost Modeling," presentation submitted for the *2016 Society of Automotive Engineers World Congress and Exhibition*, Detroit, Michigan, April 12 through 14, 2016.

C.-K. Park; C.-D. Kan;W. T. Hollowell; and S. I. Hill, 2012, *Investigation of Opportunities for Lightweight Vehicles Using Advanced Plastics and Composites,* DOT HS 811 692, Washington, DC, U.S. Department of Transportation, National Highway Traffic Safety Administration, accessed March 2, 2016, http://www-nrd.nhtsa.dot.gov/pdf/esv/esv23/23ESV-000023.PDF.

T. Skszek and J. Conklin, 2013, "Multi-Material Lightweight Prototype Vehicles Demonstration," presented at the *U. S. Department of Energy FY 2013 Annual Merit Review*, Arlington, Virginia, accessed March 2, 2016, http://energy.gov/eere/vehicles/vehicle-technologies-office-annual-merit-review-presentations.

T. S. Stephens; A. K. Birky; and J. Ward, 2014, "Vehicle Technologies Program Government Performance and Results Act (GPRA) Report for Fiscal Year 2015," ANL/ESD-14/3, Argonne, Illinois, Argonne National Laboratory, accessed March 2, 2016, https://anl.app.box.com/s/db1r5oo3omow10hqdy79py6qlwuvkqup.

C. Thomas, 2013, "Honda's Study and Report on the Study Commissioned by NHTSA 'Mass Reduction for Light-Duty Vehicles for Model Years 2017-2025' Contract No. DTNH22-11-C-00193," *NHTSA Mass-Size-Safety Workshop,* Washington, DC, May 13 and 14, 2013, Department of Transportation, accessed on March 2, 2016, www.nhtsa.gov/staticfiles/rulemaking/pdf/MSS/4-Thomas-Honda_Report.pdf.

Aluminum Association, 2013, *VENZA Aluminum BIW Concept Study,* Arlington, Virginia, accessed March 2, 2013, http://www.drivealuminum.org/research-resources/PDF/Research/2013/venza-biw-full-study/view.

Wards Automotive Yearbook, 2013, http://wardsauto.com/wards-automotive-yearbook-2013.

C. D. Warren, 2013, "Lightweighting Composites and Lower Cost Carbon Fiber," Oak Ridge National Laboratory presentation to U.S. Department of Energy, accessed March 2, 2016, http://www.raspet.msstate.edu/wp-content/uploads/Oak-Ridge-NL.pdf.

DOE VTO, *Workshop Report: Light-Duty Vehicles Technical Requirements and Gaps for Lightweight and Propulsion Materials,* DOE/EE-0868, Washington, DC, U.S. Department of Energy Vehicles Technologies Office, accessed on March 2, 2016, https://www1.eere.energy.gov/vehiclesandfuels/pdfs/wr_ldvehicles.pdf.

VI.2. Safety Data and Analysis – Lawrence Berkeley National Laboratory

Project Details

Tom Wenzel, Principal Investigator
Lawrence Berkeley National Laboratory (LBNL)
1 Cyclotron Road, 90R4000
Berkeley, CA 94720
Phone: 510-486-5753
E-mail: TPWenzel@lbl.gov

Carol Schutte, Technology Area Development Manager
U.S. Department of Energy (DOE)
1000 Independence Avenue, SW
Washington, DC 20585
Phone: 202-586-1022
E-mail: carol.schutte@ee.doe.gov

Contractor: LBNL
Contract No.: DE-AC02-05CH11231

Executive Summary

During Fiscal Year (FY) 2015, LBNL conducted analysis of the sensitivity of its 2012 Phase 2 results on the relationship between mass reduction, crash frequency, and fatality risk per crash to the exclusion of non-severe crashes from the analysis. This analysis also used several years of odometer readings in Texas to adjust the vehicle miles traveled (VMT) weights that the U.S. Department of Transportation's National Highway Traffic Safety Administration (NHTSA) used in its 2012 baseline model and tested the sensitivity of the results from that model to the VMT weights used. Adding the curb weight of the other vehicle in a two-vehicle crash to the 2012 Fatality Analysis Reporting System (FARS) and state-induced exposure databases will allow estimation of the relationship between changes in the ratio of masses between both vehicles in a two-car crash and fatality risk. These estimates will be used to model the change in total fatalities as a fleet of new vehicles transitions to a lighter median mass. The 2012 study update to cover model year 2003 to 2010 vehicles between calendar years 2005 and 2011 will be included in the technical assessment report for the mid-term review of the 2017 through 2025 fuel economy/carbon dioxide (CO_2) emission standards to be published in early FY 2016. Participation in monthly conference calls of the inter-agency team studying the historical relationship of vehicle mass and risk using recent data allowed for continued collaboration on current efforts. Finally, analysis continued on trends in vehicle miles of travel, both at the state level, using national data, and for individual vehicles and households, using odometer readings and vehicle registration data over several years in California and Texas. This permitted an estimation of the effect recent changes in gasoline prices and economic conditions have had on vehicle miles of travel.

Accomplishments

- Participated in monthly discussions by the interagency working group that included DOE, NHTSA, the U.S. Environmental Protection Agency (EPA), and the California Air Resources Board (CARB) on updating research on the relationship between vehicle weight/size and safety in support of federal agency rulemakings on fuel economy/greenhouse gas emission standards for new light-duty vehicles.
- Tested the sensitivity of our 2012 Phase 2 results on the relationship between mass reduction, crash frequency, and fatality risk per crash to exclude non-severe crashes from the analysis. This sensitivity was conducted to determine if not accounting for crash severity is the cause for the unexpected signs of several control variables in the regression models.

- Tested the sensitivity of NHTSA's 2012 baseline results on the relationship between mass reduction and societal fatality risk per VMT to the VMT weights NHTSA developed. Examination of NHTSA's VMT weights revealed some inconsistencies when compared to calculated annual VMT from annual odometer readings of millions of vehicles in Texas between 2003 and 2013. Adjusted NHTSA's VMT weights using Texas odometer data and tested the sensitivity of the results to these revised VMT weights.
- Began updating the 2012 study to cover model year 2003 to 2010 vehicles between calendar years 2005 and 2011 to be included in the technical assessment report for the mid-term review of the 2017 to 2025 fuel economy/CO_2 emission standards to be published in early FY 2016.
- Provided comments on the safety section of the draft report of the National Research Council (NRC) Committee on Fuel Economy for Light-Duty Vehicles.

Future Directions

- Complete the update of the 2012 Phase 1 analysis using more recent data provided by NHTSA.
- Complete the update of the 2012 Phase 2 analysis using more recent state data on police-reported crashes.
- Construct a model for estimating the change in total fatalities as the distribution of masses of on-road vehicles changes from incentives to reduce mass, especially in heavier light trucks. The first step is to add the weight of the crash partner in a two-vehicle crash to the 2012 FARS and state-induced exposure databases and then estimate the relationship between changes in the ratio of the masses of the two vehicles (as opposed to mass reduction in the case vehicle) and fatality risk in two-vehicle crashes.

Introduction

Reducing vehicle mass is perhaps the easiest and least-costly method of reducing fuel consumption and greenhouse gas emissions from light-duty vehicles. However, the extent to which government regulations should encourage manufacturers to reduce vehicle mass depends on what effect, if any, light-weighting vehicles is expected to have on societal safety. As part of an interagency analysis effort between NHTSA, EPA, and DOE, LBNL has been examining the relationship between vehicle mass and size and U.S. societal fatality and casualty risk, using historical data on recent vehicle designs. This research effort informs the agencies on the extent to which vehicle mass can be reduced in order to meet fuel economy and greenhouse gas emissions standards without compromising the safety of road users.

In FY 2014 LBNL published two draft reports. The first examined the sensitivity of the relationship between vehicle mass/size, crash frequency, and fatality risk per crash to regression models that exclude non-severe crashes [1]. The second tested the sensitivity of the relationship between vehicle mass/size and societal fatality risk per VMT from NHTSA's 2012 baseline regression model to the VMT weights NHTSA used [2,3].

Results and Discussion

Accounting for Crash Severity

The LBNL Phase 2 study, which analyzed the effect of mass reduction on crash frequency and casualty risk per crash, and the Dynamic Research Incorporated (DRI) and LBNL simultaneous two-stage regression models that analyzed the effect on crash frequency and U.S. fatality risk per crash, found that mass reduction was associated with increases in crash frequency, but had no effect on or even decreases in risk per crash for all types of vehicles [4,5]. These results were unexpected because one would expect that lighter vehicles, with

better maneuverability and shorter braking distances, would have lower crash frequency than heavier vehicles and that heavier vehicles would have lower risk than lighter vehicles once a crash has occurred. LBNL examined the sensitivity of the results on crash frequency to adding several additional explanatory variables to the baseline NHTSA regression model; none of these variables, either independently or combined, changed the relationship between mass reduction and increased crash frequency [6].

Kahane suggested two possible explanations for these unexpected results: (1) that the analysis did not account for the severity of the crash and (2) possible bias in the crashes reported to police in different states, with less severe crashes being underreported for certain vehicle types [7]. In his preliminary report, Kahane speculated that owners of heavier vehicles (e.g., sport utility vehicles [SUVs] and pickups) would be less likely to report minor crashes than owners of lighter passenger cars, because the heavier vehicles would sustain less damage in a two-vehicle crash; however, this suggestion was removed from the final report. On the other hand, it would seem just as likely that owners of vehicles that are uninsured or under-insured would refrain from reporting a minor crash; their vehicles are likely to be inexpensive passenger cars rather than heavier and more expensive pickups or SUVs.

LBNL analyzed the first of Kahane's explanations for the unexpected result of mass reduction being associated with decreased risk per crash (i.e., regression models do not account for the severity of the crash). Of the 13 states whose police-reported crash data were used, seven report the severity of the damage sustained by the subject vehicle, two report whether the vehicle had to be towed from the crash scene, and three report both. Because Washington does not report either of these measures of crash severity, their data had to be excluded from the analysis. For the seven states that report crash damage severity, vehicles that were described as "disabled" were included, while vehicles with functional, none, or unknown damage were excluded.

We compared the regression coefficients from the NHTSA baseline model with those from a model that excludes all crashes that occurred in Washington. Only a small effect occurred on the estimated coefficients for crash frequency and casualty risk per crash by excluding the Washington crashes. Table VI-3 compares the estimates for selected variables from the NHTSA baseline model, excluding Washington crashes ("Ex WA") with a model that includes only vehicles in crashes where at least one involved vehicle was so disabled from the crash that it had to be towed from the crash scene (i.e., excludes non-severe crashes, labeled "Ex NS" in Table VI-3). Values in red are statistically significant at the 95% level, while the estimates shaded green are in the expected direction, and those shaded yellow are in the opposite direction.

As Kahane and LBNL noted in their 2012 studies, certain vehicle technologies (such as anti-lock braking system [ABS] and electronic stability control [ESC]) should reduce crash frequency, while others (such as side airbags in cars and crossover utility vehicles [CUVs]/minivans, and supplementary frontal bumpers [BLOCKER1] or greater bumper overlap [BLOCKER2] on light trucks) should reduce casualty risk once a crash has occurred. And one might expect that, all else held equal, mass reduction would reduce braking distance and footprint reduction (or more specifically, wheelbase) would improve maneuverability, both of which would result in reduced crash frequency. On the other hand, one might expect that the added mass of AWD might increase braking distance and thus increase crash frequency, while it might reduce risk per crash in the subject vehicle, but perhaps increase societal risk per crash.

Table VI-3 presents the estimated effects on crash frequency (crashes per VMT) and casualty risk per crash for selected variables by vehicle type. As expected, the four side airbag variables all are associated with a decrease in risk per crash (although only two are statistically significant) in the "Ex WA" model; however, two are also associated with an unexpected decrease in crash frequency and COMBO is associated with an unexpected increase in crash frequency. Excluding the most severe crashes in the "Ex NS" model has little effect on these variables. Results are reported for cars, light trucks, and CUVs and minivans. Control variables are shown for several vehicle safety technologies and include the following: improving the overlap of light truck bumpers with those of other vehicles (BLOCKER1); a secondary energy-absorbing structure (known as a "blocker beam") behind and below the bumper so it engages the bumper of the other vehicle (BLOCKER2); ROLLCURT airbags used only in regression models of rollover crashes involving cars or CUVs/minivans; and CURTAIN, COMBO, and TORSO types of airbags. Other control variables include whether the driver is a

male (DRVMALE), eight variables that represent the driver's gender and age group (i.e., M14_30 for males 14 to 30 years old or F14_30 for females) and NITE, RURAL, and SPDLIM55 representing crashes occurring at night, in rural counties, or on roads with speed limits of 55 miles per hour or higher.

Table VI-3: Estimated effect on crash frequency (crashes per mile traveled) and casualty risk per crash, excluding crashes in Washington ("Ex WA") and excluding non-severe crashes ("Ex NS").

	Crash Frequency (Crashes per VMT)						Casualties per Crash					
	Cars		Light Trucks		CUVs/Minivans		Cars		Light Trucks		CUVs/Minivans	
Variable	Ex WA	Ex NS	Ex WA	Ex NS	Ex WA	Ex NS	Ex WA	Ex NS	Ex WA	Ex NS	Ex WA	Ex NS
BLOCKER1	—	—	-1.09%	-0.35%	—	—	—	—	0.67%	1.64%	—	—
BLOCKER2	—	—	-0.28%	-2.04%	—	—	—	—	-4.75%	-2.69%	—	—
ROLLCURT	-1.88%	-1.74%	—	—	-0.81%	-0.74%	-3.91%	-3.75%	—	—	-1.81%	-1.80%
CURTAIN	0.00%	0.20%	—	—	-2.94%	-0.58%	-2.94%	-3.48%	—	—	-3.03%	-5.99%
COMBO	2.55%	2.82%	—	—	-0.79%	-1.60%	-1.66%	-1.58%	—	—	5.49%	7.26%
TORSO	-5.07%	-5.93%	—	—	-4.59%	-7.09%	-10.4%	-9.12%	—	—	-2.91%	-0.26%
ABS	-5.73%	-7.62%	—	—	-19.0%	-19.0%	-1.98%	-1.39%	—	—	-9.08%	-6.16%
ESC	-16.7%	-16.4%	-15.1%	-19.8%	-1.28%	-5.08%	-12.4%	-12.2%	-18.3%	-14.4%	-10.2%	-7.65%
AWD	—	—	39.4%	37.6%	8.84%	10.5%	—	—	1.07%	0.42%	-4.14%	-6.69%
DRVMALE	6.66%	10.2%	-1.12%	-0.54%	2.02%	3.76%	-0.01%	-4.53%	-0.06%	-1.94%	8.09%	7.50%
M14_30	4.36%	5.51%	3.76%	4.42%	5.03%	6.06%	1.02%	-0.07%	0.63%	-0.32%	0.52%	-0.78%
M30_50	0.33%	0.66%	0.40%	0.56%	0.18%	0.40%	0.02%	-0.25%	-0.17%	-0.37%	-0.15%	-0.35%
M50_70	0.16%	0.35%	0.31%	0.34%	0.63%	0.85%	1.27%	1.22%	1.11%	1.16%	1.28%	1.12%
M70_96	3.93%	4.86%	4.42%	5.05%	3.27%	4.03%	2.36%	1.66%	1.87%	1.52%	1.95%	1.17%
F14_30	3.46%	4.70%	3.53%	4.72%	3.61%	4.85%	0.75%	-0.20%	0.62%	-0.44%	1.24%	0.03%
F30_50	-0.05%	0.06%	0.03%	-0.11%	0.00%	-0.04%	-0.43%	-0.67%	-0.12%	-0.14%	-0.18%	-0.23%
F50_70	0.70%	1.13%	0.91%	0.93%	1.09%	1.34%	1.08%	0.86%	1.32%	1.39%	2.08%	1.86%
F70_96	4.33%	5.21%	3.31%	3.42%	3.36%	4.18%	1.86%	1.23%	-0.16%	-0.03%	0.58%	-0.18%
NITE	32.4%	41.1%	37.2%	47.3%	25.2%	30.5%	43.1%	33.7%	40.9%	29.2%	32.0%	29.7%
RURAL	20.9%	23.8%	19.3%	22.1%	15.2%	19.1%	48.4%	44.1%	41.4%	37.5%	43.3%	42.9%
SPDLIM55	60.4%	98.0%	41.7%	79.6%	33.4%	68.5%	82.9%	60.6%	88.2%	62.3%	88.3%	71.7%

*Values in red are statistically significant at the 95% level. Estimates shaded green are in the expected direction and those shaded yellow are in the opposite direction.

The crash avoidance technologies (i.e., ABS and ESC) are associated with a large decrease in crash frequency for cars, as expected, in the "Ex WA" model (a 5.73% and 16.7% decrease, respectively); however, they also are associated with large unexpected decreases in risk per crash for cars (a 1.98% decrease for ABS and a 12.4% decrease for ESC). Excluding the most severe crashes has little effect on crash frequency for ABS (from a 5.73% decrease to a 7.62% decrease) or ESC (from a 16.7% decrease to a 16.4% decrease); excluding severe crashes has little effect on casualty risk per crash for ESC (from a 12.4% decrease to a 12.2% decrease), but results in a small decrease in risk per crash for ABS (from a 1.98% decrease to a 1.39% decrease).

Regarding driver gender, male drivers are associated with an expected large increase in crash frequency for cars (6.66%), but no effect on risk per crash in the "Ex WA" model. Excluding severe crashes increases the expected large increase in crash frequency to 10.2%, but also results in a large decrease in risk per crash (to 4.53%) in the "Ex NS" model. This result is expected, because men are assumed to be more robust and better able to withstand injury than women in a severe crash. Regarding driver age, the youngest and oldest drivers are associated with the largest increase in crash frequency in the "Ex WA" model, as expected; and seven of the eight age groups are also associated with increases in risk per crash, suggesting that drivers older than 50

are less robust than 50-year old drivers. Excluding the most severe crashes increases the association between driver age and crash frequency for the youngest and oldest drivers, while decreasing the association between driver age and risk per crash.

Under the "Ex WA" model, driving at night, in a rural county, and on a high-speed road are each associated with large increases in crash frequency (i.e, 32.4%, 20.9%, and 60.4%, respectively), but even larger increases in risk per crash (i.e., 43.1%, 48.4%, and 82.9%), particularly on high-speed roads. Excluding the most severe crashes shifts some of the estimated effect from risk per crash to crash severity for each variable in the "Ex NS" model; however, each variable is still associated with a fairly large increase in risk per crash (i.e., 33.7% for night, 44.1% for rural roads, and 60.6% for high-speed roads). For example, driving on a high speed road is associated with a 60% increase in crash frequency and a 83% using all crashes; excluding the most severe crashes increases the association of driving on a high-speed road to a 98% increase in crash frequency, while reducing the association to a 61% increase in risk per crash. The results described above for cars are similar for light trucks and CUVs/minivans.

Table VI-4 compares results from the simultaneous two-stage model, which simultaneously estimates the two components of U.S. fatality risk per VMT (i.e., crash frequency and fatality risk per crash). As in Table VI-3, values in red are statistically significant at the 95% level, while the estimates shaded green are in the expected direction, and those shaded yellow are in the opposite direction.

Comparing the "Ex WA" estimates in Table VI-3 with the "Base" model estimates in Table VI-4, we see that the simultaneous two-stage model estimates several substantial differences in the effectiveness of side airbags in fatality risk per crash: a smaller decrease in fatality risk per crash for torso airbags in cars (a 1.36% versus a 10.4% decrease) and a large increase in risk per crash for combination side airbags (a 9.48% decrease versus a 5.49% increase) and a large increase in risk per crash for torso side airbags (a 5.61% increase versus a 2.91% decrease) in CUVs/minivans. While the two-stage fatality model estimates comparable decreases in crash frequency, as expected, from ABS and ESC to those in the casualty model for all three types of vehicles, the two-stage fatality model estimates larger decreases in risk per crash for ABS in cars (a 5.14% decrease versus a 1.98% decrease), but unexpected increases in risk per crash for ESC in cars (a 6.22% increase rather than a 12.4% decrease), for ABS in CUVs/minivans (a 5.39% increase rather than a 9.08% decrease), and for ESC in light trucks (a 2.53% decrease rather than a 18.3% decrease) and CUVs/minivans (a 1.39% decrease rather than a 10.2% decrease). For AWD, the two-stage fatality model estimates a similar increase in crash frequency in light trucks and CUVs/minivans to the baseline casualty risk model, as expected, but also estimates unexpected, very large reductions in risk per crash (a 49.2% decrease for light trucks and a 30.3% decrease for CUVs/minivans).

For the most part, the estimated effects of driver age on the two-stage fatality risk model are comparable to those in the casualty risk model; however, the two-stage fatality risk model estimates large, unexpected increases in risk per crash for male drivers for each vehicle type (i.e., 31% for cars, 24% for light trucks, and 36% for CUVs/minivans). Similarly, the large unexpected increases in risk per crash in the casualty risk model are even higher in the two-stage fatality risk model.

The effect of removing non-severe crashes from the analysis using the two-stage fatality model can be seen by comparing the two sets of estimates in Table VI-4. As in Table VI-3, removing the non-severe crashes somewhat improves the estimated effects for some variables, but does not "correct" the unexpected results from the baseline model. For example, combination and torso side airbags in cars are associated with larger decreases in risk per crash after removing non-severe crashes (from a 2.45% to a 4.36% decrease for combination side airbags and from a 1.36% decrease to a 3.36% decrease for torso side airbags); however, combination side airbags continue to be associated with an increase and torso side airbags with a decrease in crash frequency in cars. Crash avoidance technologies continue to be associated with expected large decreases in crash frequency, but also a large decrease in risk per crash in cars.

Table VI-4: Simultaneous two-stage model estimated effect on U.S. crash frequency (crashes per mile traveled) and fatality risk per crash, baseline ("Base") and excluding non-severe crashes ("Ex NS").

	Crash Frequency (Crashes per VMT)						Casualties per Crash					
	Cars		Light Trucks		CUVs/minivans		Cars		Light Trucks		CUVs/Minivans	
Variable	Base	Ex NS	Base	Ex NS	Base	Ex NS	Base	Ex NS	Base	Ex NS	Base	Ex NS
BLOCKER1	—	—	-0.93%	-1.38%	—	—	—	—	-1.86%	-1.01%	—	—
BLOCKER2	—	—	-0.70%	-2.26%	—	—	—	—	-1.18%	0.29%	—	—
ROLLCURT	-1.19%	-1.16%	—	—	-0.66%	-0.59%	-0.38%	-1.04%	—	—	-1.42%	-1.05%
CURTAIN	-0.04%	0.58%	—	—	-3.87%	-0.97%	-0.06%	-1.21%	—	—	1.11%	-1.92%
COMBO	2.00%	2.54%	—	—	0.00%	-2.68%	-2.45%	-4.36%	—	—	-9.48%	-6.70%
TORSO	-6.35%	-6.32%	—	—	-4.48%	-7.71%	-1.36%	-3.36%	—	—	5.61%	11.5%
ABS	-5.99%	-8.44%	—	—	-19.4%	-17.8%	-5.14%	-3.68%	—	—	5.39%	2.38%
ESC	-17.1%	-16.6%	-17.1%	-19.1%	-1.52%	-4.71%	6.22%	3.09%	-2.53%	-0.90%	-1.39%	-2.79%
AWD	—	—	44.8%	31.5%	10.0%	8.05%	—	—	-49.2%	-47.0%	-30.3%	-32.6%
DRVMALE	5.54%	9.77%	-2.86%	-1.68%	0.53%	2.59%	30.9%	23.1%	24.4%	21.5%	36.3%	32.5%
M14_30	4.48%	5.45%	3.71%	4.36%	4.93%	5.89%	0.24%	-0.79%	-0.07%	-0.82%	-1.01%	-2.28%
M30_50	0.50%	0.73%	0.44%	0.64%	0.26%	0.49%	0.97%	0.71%	0.79%	0.53%	0.71%	0.60%
M50_70	0.11%	0.30%	0.24%	0.26%	0.59%	0.83%	2.34%	2.17%	1.16%	1.09%	1.59%	1.53%
M70_96	4.26%	4.93%	4.33%	4.79%	3.47%	4.04%	4.00%	2.99%	3.35%	2.89%	3.66%	2.49%
F14_30	3.68%	4.77%	3.46%	4.72%	3.64%	4.97%	-0.53%	-1.69%	0.37%	-0.98%	1.36%	-0.25%
F30_50	0.05%	0.11%	0.01%	-0.12%	-0.01%	-0.08%	0.09%	-0.03%	0.27%	0.35%	-0.40%	-0.12%
F50_70	0.74%	1.08%	0.81%	0.82%	1.04%	1.22%	2.67%	2.24%	2.62%	2.53%	2.55%	2.50%
F70_96	4.51%	5.24%	3.68%	3.46%	3.42%	4.12%	3.55%	2.62%	2.21%	2.67%	3.93%	3.25%
NITE	31.2%	37.1%	41.0%	44.6%	30.5%	29.8%	119%	110%	93.0%	90.1%	86.2%	96.5%
RURAL	24.3%	22.4%	23.9%	19.4%	25.1%	20.8%	162%	177%	145%	159%	149%	167%
SPDLIM55	66.7%	97.4%	51.4%	80.8%	44.6%	69.7%	205%	153%	222%	164%	232%	186%

* Values in red are statistically significant at the 95% level. Estimates shaded green are in the expected direction and those shaded yellow are in the opposite direction.

While removing severe crashes somewhat decreases the unexpected increases in risk per crash for male drivers and, in some cases, driving at night, in rural counties, or on high-speed roads, these unexpected increases in risk per crash remain quite large in the two-stage fatality model after removing severe crashes.

These results suggest that accounting for crash severity by excluding crashes where all involved vehicles were able to be driven away from the crash scene, for the most part, has little effect on the unexpected relationships between crash frequency, casualty risk per crash, vehicle characteristics, driver age and gender, and crash circumstances in either of the two separate crash frequency and casualty risk per crash models developed during Phase 2 (Table VI-3) or the simultaneous two-stage U.S. fatality risk model (Table VI-4).

Sensitivity to Changes in Estimates of Vehicle Miles of Travel

NHTSA developed a mileage accumulation schedule for all light-duty vehicles, based on mileage accumulation rates for cars and light trucks combined, that wasvtaken from the 2001 National Household Transportation Survey (NHTS). The schedule indicates the number of annual VMT by vehicle age. NHTSA applied this schedule to all vehicles in the FARS public database, based on the age of the vehicle. NHTSA then adjusted the estimated miles by vehicle age for individual vehicle models based on odometer data obtained from IHS Automotive (formerly R.L. Polk & Co.). IHS used the most recent odometer reading for each vehicle between April 2008 and October 2010 and estimated the average odometer reading by model year for every

vehicle model. Using the proprietary data purchased from IHS Automotive, NHTSA calculated VMT adjustment factors for every vehicle model by dividing the average odometer reading by model year for each model by the overall average odometer reading by model year. NHTSA then applied each of these model VMT adjustment factors to the mileage accumulation schedule.

This methodology assumes that, overall, vehicles of the same age have the same annual VMT, regardless of calendar year. However, VMT by vehicle age is adjusted by the VMT ratios NHTSA obtained from Polk odometer readings, by model year. Any changes in VMT by model year (or calendar year) of vehicles of a certain age are attributable to differences by model year in the ratio of odometer readings of individual vehicle models to all vehicles in the Polk database.

Figure VI-11 shows the percent change in average annual VMT from 2004 for 2-year old vehicles by vehicle type; these data are derived from the NHTSA public database and are obtained by dividing the sum of the VMT weights by the sum of the registration weights by vehicle type. Figure VI-12 shows the same data obtained from odometer readings of six million vehicles reporting for testing in the Texas emission inspection and maintenance (I/M) program. The Texas I/M program requires annual testing of all light-duty vehicles 2-years-old or older in the 17 counties comprising the Houston, Dallas, Austin, and El Paso metropolitan areas. The cumulative changes in average VMT since 2004 in Table VI-3 and Table VI-4 are fairly similar, with the exception of those indicated in red. NHTSA's method indicates that CUV VMT increased 3.1%, small pickups 6.3%, and large pickups 20.5%, between 2004 and 2008, while the Texas odometers indicate that all three vehicle types reduced VMT between 2004 and 2008.

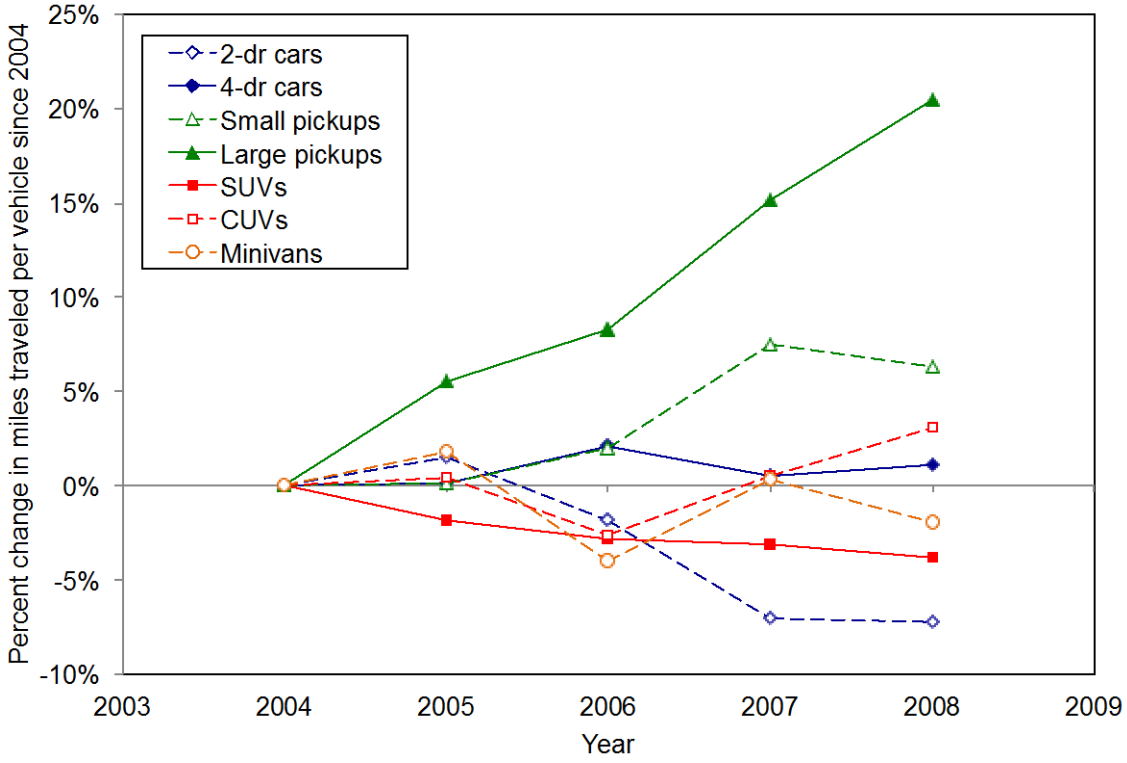

Figure VI-11: Change in average annual VMT since 2004 for 2-year-old vehicles by vehicle type: NHTSA method.

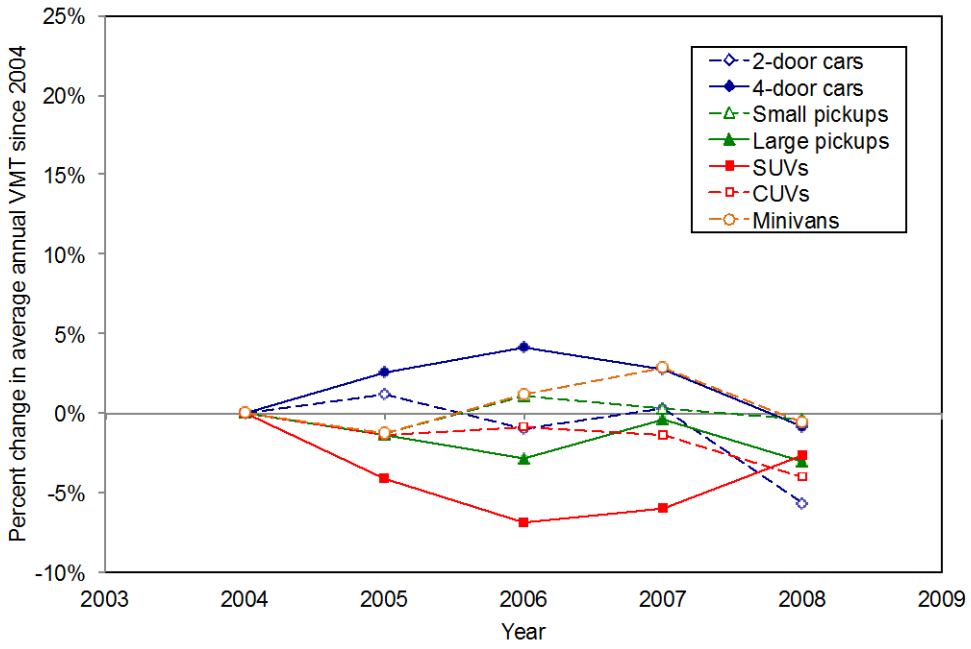

Figure VI-12: Change in average annual VMT since 2004 for 2-year-old vehicles by vehicle type: Texas odometer readings.

There are two ways the VMT weights estimated by NHTSA could be incorrect. First, NHTSA applied a single VMT schedule by vehicle age to both cars and light trucks and used the same schedule for each calendar year. If average VMT varies by calendar year due to economic conditions or gas prices or if VMT varies substantially by vehicle type, the NHTSA method may state the average VMT incorrectly. In addition, the VMT schedule is derived from reported annual VMT from the 2001 NHTS. Although all households were surveyed twice at least two months apart in order to obtain two odometer readings for each vehicle, only 48% of survey respondents provided two useable odometer readings. For vehicles without two odometer readings, Oak Ridge National Laboratory estimated VMT based on self-reported VMT for the previous year, applying the reported odometer reading to a proscribed VMT schedule by vehicle age or estimated annual VMT based on the daily VMT reported in the survey. (The 2009 NHTS contacted households only once, which means that only one odometer reading is available for any of the vehicles included in the survey.)

A comparison of the VMT schedule by vehicle age and calendar year from the 2001 NHTS and Texas odometer data between 2003 and 2010 indicates that the VMT schedules derived from the 2001 NHTS has shallower slopes than those from the Texas data, meaning newer vehicles in Texas had higher VMT than those in the 2001 NHTS and older vehicles in Texas had lower VMT than those in the 2001 NHTS.

The second way NHTSA's VMT weights could be incorrect is the ratio of the average odometer reading for each model relative to the odometer reading for all light-duty vehicles. The percent difference from the average odometer reading in the U.S. Polk data by vehicle type and model year indicates that the average percent difference varies substantially by model year for two-door cars, small pickups, large pickups, and CUVs. For example, the average odometer reading for large pickups ranges from 1.2% lower than the average reading for all vehicles in model year 2000 to 23% higher than average in 2006. The odometer reading for CUVs ranges from 13% below average in 2000 to 3% below average in 2007.

The same information from the Texas odometer data indicates that, for the most part, the percent difference from the overall average in each model year is fairly consistent across model years for most vehicle types. In the Texas data, the odometer reading for two-door cars ranges from 7.6% below average in 2000 to 16% below average in 2007, and the odometer reading for large pickups ranges from 33% above average in 2000 to 44% above average in 2007; however, these ranges are much smaller than observed in the U.S. odometer data obtained by Polk.

The large range in percent differences across model years may be caused by what data Polk included in their averages by vehicle model. Polk included the most recent odometer reading of a particular vehicle within the previous 30 months, while odometer data from the Texas I/M program were evenly distributed across the previous 12 months. If the average odometer reading for some vehicle models, or types, were taken substantially earlier than for other vehicle models or types, this would introduce bias into the adjustment factors.

Figure VI-13 takes the VMT schedule by vehicle age that NHTSA used from the 2001 NHTS and applies the VMT adjustment factors from the Texas odometers by vehicle model. Using the Texas odometer readings rather than the national odometer readings from Polk result in changes in VMT since 2004 that are more comparable to the actual Texas VMT data in Figure VI-12. Now VMT increased only 2.0% for small pickups, 4.8% for large pickups, and 2.6% for CUVs between 2004 and 2008, which is much less than the large increases originally estimated by NHTSA using the national odometer readings (Figure VI-11). However, the results can be substantially different in certain years; for example, under the NHTSA method, VMT of four-door cars increased 1.1% between 2004 and 2008, whereas using the NHTS VMT schedule and Texas odometer data results in the VMT of four-door cars increasing 5.1% between 2004 and 2008.

Figure VI-14 compares regression results using the VMT weights from the NHTSA baseline regression model (shown in light blue) with the new VMT weights derived using the NHTS VMT schedule by vehicle age and adjustment factors by vehicle model from the Texas odometer data (shown in orange). The purpose of Figure VI-14 is not to indicate the relationship between mass or footprint reduction and risk using the "correct" VMT weights; rather, it is merely to test the sensitivity of the results from the baseline regression model to changes in the VMT weights. The figure indicates that using different VMT weights reduces the estimated detrimental effect of mass reduction on fatality risk for cars and light trucks, but increases the detrimental effect of mass reduction on fatality risk for CUVs/minivans. Using different VMT weights increases the estimated effect of footprint reduction on risk for cars and light trucks, but decreases the estimated effect of footprint reduction for CUVs/minivans. Figure VI-14 also shows the sensitivity model from the Phase 1 LBNL report, which uses vehicle registration years rather than estimated VMT as the measure of exposure (shown in teal). This sensitivity estimates even smaller effects from mass or footprint reduction on U.S. societal fatality risk per vehicle, with the exception of mass reduction in heavier-than-average cars, which is estimated to have a much higher risk than under the baseline estimate and the sensitivity using different VMT weights.

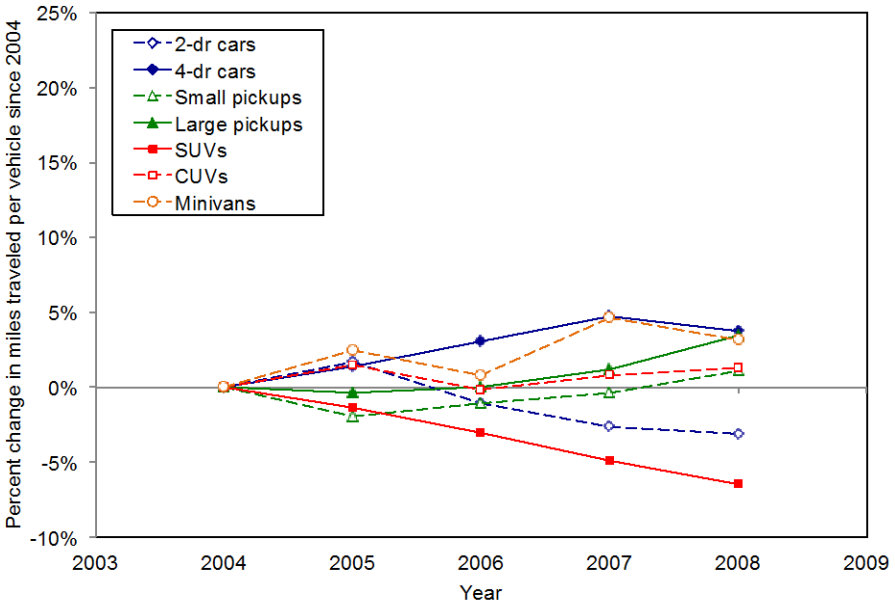

Figure VI-13: Change in average annual VMT since 2004 for 2-year-old vehicles, by vehicle type: NHTS VMT schedule with Texas odometer data.

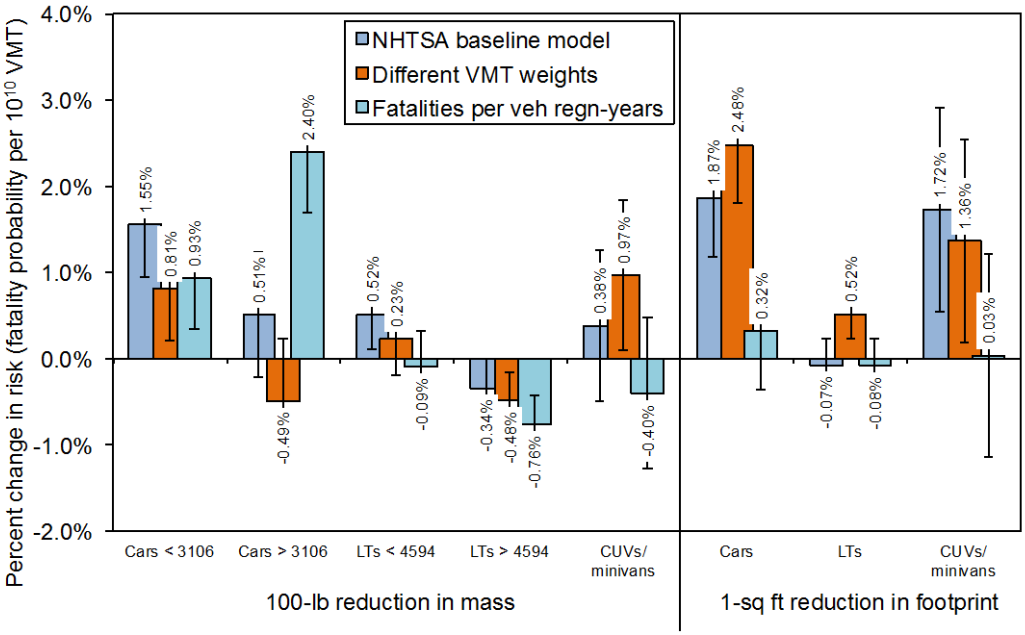

Figure VI-14: Estimated effect on U.S. societal fatality risk per VMT, under baseline model and using different VMT weights.

Analysis Updates of the Relationship Between Vehicle Weight, Size, and Societal Fatality Risk per VMT

An update began for the 2012 study to cover model year 2003 to 2010 vehicles between calendar years 2005 and 2011, which will be included in the technical assessment report for the mid-term review of the 2017 through 2025 fuel economy/CO_2 emission standards, which will be published in early FY 2016. Six preliminary versions of the updated safety database provided by Volpe (i.e., the National Transportation Systems Center) have been analyzed and comments on anomalies in the database were provided to Volpe. With NHTSA and EPA, an agreement was reached for a baseline regression model and coefficients using the methodology from NHTSA's 2012 study. Nineteen alternate regression models from the 2012 study were initiated, as well as several new alternate models, to test the sensitivity of the NHTSA baseline model to changes in the measure of risk and data and control variable used.

Conclusion

In FY 2015 LBNL conducted several analyses to better understand the relationship between vehicle mass, footprint, and societal fatality risk per VMT. Excluding non-severe crashes did not substantially "correct" some unexpected relationships between various control variables and crash frequency or risk once a crash had occurred. Examination of NHTSA's VMT weights revealed some inconsistencies when compared to calculated annual VMT from annual odometer readings of millions of vehicles in Texas between 2003 and 2013. Adjusting NHTSA's VMT weights using the Texas odometer data resulted in substantial differences in the estimated relationship between vehicle mass and societal fatality risk per VMT from the 2012 NHTSA baseline model. Volpe provided several preliminary versions of the updated safety database of model year 2003 to 2010 vehicles between calendar years 2005 and 2011; LBNL helped Volpe and NHTSA finalize the database for the preliminary update of the 2012 analysis. The results of the preliminary analysis will be included in the technical assessment report for the mid-term review of the 2017 through 2025 fuel economy/CO_2 emission standards to be published in early FY 2016 and a complete report at a later date. LBNL was asked to provide comments on the safety section of the draft report of the NRC Committee on Fuel Economy for Light-Duty Vehicles.

References

1. T. Wenzel, 2015, *Effect of Accounting for Crash Severity on the Relationship between Mass Reduction and Crash Frequency and Risk per Crash,* draft report prepared for the Office of Energy Efficiency and Renewable Energy, DOE, LBNL.
2. T. Wenzel, 2015, *Sensitivity of Baseline Results to Changes in NHTSA's Estimate of Vehicle Miles of Travel,* draft report prepared for the Office of Energy Efficiency and Renewable Energy, DOE, LBNL.
3. T. Wenzel, 2015, *Recent Sensitivity Analyses on NHTSA Baseline Regression Model of U.S. Societal Fatality Risk,* presentation to EPA Office of Transportation and Air Quality and CARB staff, Ann Arbor, Michigan.
4. T. Wenzel, 2012, *An Analysis of the Relationship between Casualty Risk per Crash and Vehicle Mass and Footprint for Model Year 2000-2007 Light-Duty Vehicles,* LBNL-5697E, final report prepared for the Office of Energy Efficiency and Renewable Energy, DOE, LBNL.
5. T. Wenzel, 2013, *Assessment of DRI's Two-Stage Logistic Regression Model Used to Simultaneously Estimate the Relationship between Vehicle Mass or Size Reduction and U.S. Fatality Risk, Crashworthiness/Compatibility, and Crash Avoidance,* draft report prepared for the Office of Energy Efficiency and Renewable Energy, DOE, LBNL.
6. T. Wenzel, 2014, *Sensitivity of Light-Duty Vehicle Crash Frequency per Vehicle Mile of Travel to Additional Vehicle and Driver Variables,* draft report prepared for the Office of Energy Efficiency and Renewable Energy, DOE, LBNL.
7. C. J. Kahane, 2012, "Relationships Between Fatality Risk, Mass, and Footprint in Model Year 2000-2007 Passenger Cars and LTVs," final report prepared for the National Center for Statistics and Analysis, National Highway Traffic Safety Administration, Department of Transportation Highway Safety (DOT HS) 811 665.

U.S. DEPARTMENT OF
ENERGY
Energy Efficiency &
Renewable Energy

For more information, visit: energy.gov/eere

DOE/EE-1337 • September 2016